NUMERICAL QUADRATURES FOR
NEARLY SINGULAR INTEGRALS IN 3-D
THREE DIMENSIONAL BOUNDARY ELEMENT METHOD

3次元境界要素法における
近特異積分の数値積分法の研究

福水 毅

(1)

NUMERICAL QUADRATURES FOR NEARLY SINGULAR INTEGRALS IN THE THREE DIMENSIONAL BOUNDARY ELEMENT METHOD

3次元境界要素法における近特異積分の数値積分法の研究

by

KEN HAYAMI

速水 謙

THESIS SUBMITTED FOR THE DEGREE OF
DOCTOR OF PHILOSOPHY OF
THE UNIVERSITY OF TOKYO

OCTOBER, 1992

日本語概要

境界要素法は、境界のみを離散化すればよいという特質などから近年工学において幅広く定着しつつある。しかしながら、数値解析上未解決の課題も多い。その一つが数値積分の問題である。境界要素法において大半の計算時間は境界要素上の積分に費やされ、手法の精度も積分の計算精度に支配される。ここで生じる積分は一般に解析的に求めることが不可能である。また、場を計算しようとするソース点（基本解の特異点）が積分する要素から十分遠い場合は従来のガウスの数値積分法で十分求まるが、ソース点が要素に近い場合は積分核がソース点の近傍で急激に変化するため（近特異性）、従来の方法では精度良く求めることができない。このような近特異積分は工学において頻繁に出現する薄い構造や狭い間隙、及び境界近傍の場を境界要素法を用いて計算する際に生じる。

本論文は3次元境界要素法で生じる一般曲面上の近特異積分の高精度数値積分法を提案し、その有効性を理論及び数値実験により検証するものである。

第1章は序文であり、境界要素法における特異積分、近特異積分の数値積分の重要性と困難性に触れ、本研究の動機づけを示す。

第2章は3次元ポテンシャル問題の境界要素法による定式化を与える。

第3章は3次元ポテンシャル問題で生じる積分核の性質について論じる。特に、従来明確でなかった弱特異積分核（ソース点が境界上にある場合）の性質を明らかにする。具体的には、ソース点が境界上にある場合は、基本解の法線方向微分が、ソース点での境界の曲率と基本解の積に比例すること、従ってソース点を中心とする極座標の導入によって容易に積分できることを示す。次に、近特異積分核の基本的性質を明らかにし、動径方向のモデル積分を導出する。これは新手法の導出、理論誤差解析の基礎となる。

第4章は境界要素法における特異積分、近特異積分の数値積分に関する従来の手法を紹介する。中でも有効とされているのは、ソース点距離（ソース点と積分する境界要素の間の距離）に対して適応的な3次の変数変換を用いるTellesの方法である。しかし、この方法もソース点距離が要素のサイズの5％以下になると十分な精度を与えない。

第5章では3次元境界要素法の近特異積分の新しい数値積分法: Projection and Angular & Radial Transformation Method (PART法) を提案する。同手法はまずソース点（場を計算しようとする点、基本解の特異点） x_s から最も近い曲面要素 S 上の点 $\overline{\mathrm{x}}_s$ を求める。ここでソース点と要素 S の間の距離（ソース点距離）を d とする。次に $\overline{\mathrm{x}}_s$ における S の接平面上の多角形 $\overline{S}$ に S を近似射影し、近特異性が本質的に動径方向の成分であることに着目し、$\overline{S}$ に $\overline{\mathrm{x}}_s$ を中心とする極座標 (ρ,θ) を導入する。更に、積分核の特異性を緩和するための動径方向の変数変換 $R(\rho)$、及び $\overline{\mathrm{x}}_s$ が $\overline{S}$ の辺に近い場合に生じる偏角方向の近特異性を緩和する変数変換 $t(\theta)$ を施した後に変換された動径方向の変数 R 及び偏角方向の変数 t に関して Gauss-Legendre 法により数値積分を行なう。

ここで、動径方向の変数変換としていかなる変換を用いるかが重要となる。一般に境界要素法の近特異積分核の支配的な成分は、ソース点 x_s と積分する境界要素上の点 x の間の距離を r として、$1/r^{\alpha}$（α は自然数）で表される。そこでまず $1/r^{\alpha}$ を打ち消すような変数変換 $\rho\,\mathrm{d}\rho = r^{\alpha}\mathrm{d}R$ を考える。しかし、これに対する $R(\rho)$ は曲面要素の場合、陽に求まらない。そこで、x を上記の $\overline{\mathrm{x}}_s$ での接平面上の多角形 $\overline{S}$ に射影して得られる近似距離を $r' = \sqrt{\rho^2 + d^2}$ として、変換 $\rho\mathrm{d}\rho = r'^{\alpha}\mathrm{d}R$ を導入する。この変換は陽に求まり、平面一定要素の場合、動径方向の積分点一点のみで積分値が正確に求まる。しかし、一般の曲面要素や、積分核が内挿多項式を含む場合は効率的でない。但し、この変換で $\alpha = 2$ に対応する $\log$-L_2 変換： $R(\rho) = \log\sqrt{\rho^2 + d^2}$ は、ポテンシャル計算で生じる曲面要素上の積分 $\int_S 1/r^{\alpha}\mathrm{d}S\,(\alpha = 1 \sim 5)$ に対しては有効である。

ところが、この $\log$-L_2 変換もフラックスの計算で生じる積分の計算では極端に精度が落ちる。

これは、フラックスの計算で生じる積分が $\int_S \rho/r^n dS$ を含み、その場合 log-L_2 変換の ρ^2 の項のために変換された動径方向の被積分関数が積分区間の端点で無限大の勾配を持つことに起因する。そこで、この問題を克服する新しい変換として log-L_1 変換： $R(\rho) = \log(\rho + d)$ を提案する。また、フラックスの計算で生じる近特異積分を更に効率的に計算するための変換として $L_1^{-1/5}$ 変換:$R(\rho) = -(\rho + d)^{-1/5}$ を導入する。

偏角方向の変数変換としては、対数型の変換
$t(\theta) = h_j/2 \log[\{1 + \sin(\theta - \alpha_j)\} / \{1 - \sin(\theta - \alpha_j)\}]$　を導入する。

第6章では Taylor 展開と Gauss-Legendre 法の誤差評価式を用いた初等的な誤差解析により、ポテンシャル計算で生じる近特異積分 $\int_S 1/r^\alpha \, dS$ に対して log-L_2 変換は、動径方向の積分点数を n として、積分誤差は漸近的に $n^{-2\alpha}$ と非常に有効であるのに対し、$\alpha \neq 2$ に対応する他の変換は効率が悪いことを示す。

第7章では複素関数論を用いたより厳密な誤差解析を行なう。具体的には、n を動径方向の積分点数として、Gauss-Legendre の積分公式の誤差の特性関数 $\Phi_n(z)$ を用いて積分誤差を、積分区間を含み、変換された被積分関数の特異点を中に含まないような複素平面内の経路上の周回積分で表し、$\Phi_n(z)$ の漸近近似を用いて評価する。

log-L_2 変換の場合、ポテンシャル計算に対しては積分誤差が n^{-2n} で収束するが、フラックス（ポテンシャル勾配）で生じる積分に対しては、積分区間の端点が分岐点になるため、誤差が n^{-3} でしか収束しないことを示す。

一方、log-L_1 変換では、被積分関数の近特異性の原因となる複素平面上の特異点が積分区間 [-1,1] から十分離れているので、周回積分の経路として、$z = \pm 1$ を焦点とする楕円 $|z + \sqrt{z^2 - 1}| = \sigma$ で、特異点を中に含まないなるべく大きなものを選び、漸近近似として $\Phi_n(z) \sim 2\pi(z + \sqrt{z^2 - 1})^{-2n-1} (n \gg 1)$ を用いることにより、積分誤差がポテンシャル、フラックス共に σ^{-2n} で収束することを示す。但し σ は比ソース点距離 D（ソース点距離 d を要素の代表的な長さで割ったもの）の単調増加関数で $D : 10^{-3} \sim 10^{-1}$ に対して $\sigma : 1.31 \sim 1.63$ である。

また、$L_1^{-1/5}$ 変換に対しても同様に、積分誤差がポテンシャル、フラックス共に σ^{-2n} で収束し、そのとき $D : 10^{-3} \sim 10^{-1}$ に対して $\sigma : 1.41 \sim 1.67$ である。

以上の誤差解析は数値実験結果と符合している。また、これらの誤差解析により、最適な動径方向の変数変換 $R(\rho)$ とは、$r = \sqrt{\rho^2 + d^2} = 0$ に対応する特異点 $\rho = \pm di$ をできるだけ遠く（積分区間を含むできるだけ大きな楕円の上に来るように）写像するような変換であるという見通しが得られる。

第8章では数値実験の手続きと使用する曲面要素について述べる。

第9章では PART 法が3次元境界要素法の係数行列の対角項の計算で生じる弱特異積分の計算に有効なことを平面及び曲面要素上の数値実験により示す。この場合は動径方向の変数変換は恒等変換でよい。

第10章では PART 法の近特異積分に対する有効性を数値実験により検証する。まず、動径方向のモデル積分に対して、log-L_1 変換及び $L_1^{-1/5}$ 変換の有効性を示し、従来の二重指数変換よりも有効なことを示す。次に、曲面要素上の近特異積分に対する実験より、比ソース点距離 D が 0.06 より小さいときは PART 法は従来の方法（例えば Telles 法）より有効で、その傾向は D が小さいほど顕著なことを示す。今のところ動径方向の変数変換としては、ポテンシャルの計算に対しては log-L_1 変換が最も有効で、フラックスの計算には $L_1^{-1/5}$ 変換が最も有効である。更に、$\overline{x}_s$ と $\overline{S}$ の辺の間の距離がソース点距離 d よりも小さい場合は、$\overline{x}_s$ を強制的に対応する S の辺上に移動することにより大幅に積分点数を減らすことができることを示す。

第11章は、境界上のフラックスの計算などで生じる特異積分（コーシーの主値）の計算に対しても、近特異の極限とみなして PART 法が応用可能なことを示す。

第12章で結論を述べる。

NUMERICAL QUADRATURES FOR NEARLY SINGULAR INTEGRALS IN THE THREE DIMENSIONAL BOUNDARY ELEMENT METHOD

by

KEN HAYAMI

ABSTRACT

This thesis proposes an accurate and efficient numerical integration method for nearly singular integrals over general curved surfaces, arising in three dimensional boundary element analysis. Nearly singular integrals frequently occur in engineering problems involving thin structures or gaps and when calculating the potential or flux near the boundary.

The proposed Projection and Angular & Radial Transformation (PART) method finds the source projection, which is the closest point on the curved element over which the integration is performed, from the source point; approximately projects the element on to a polygon in the plane tangent to the element at the source projection; introduces polar coordinates in the planar polygon centred at the source projection; applies a radial variable transformation in order to weaken the near singularity of the integral kernel; applies an angular variable transformation to weaken the angular near singularity which arises when the source projection is near the edge of the polygon; and finally uses the Gauss-Legendre rule to integrate in the transformed radial and angular variables.

As the near optimum radial variable transformations, the log-L_1 transformation: $R(\rho) = \log(\rho + d)$ and the $L_1{}^{-1/5}$ transformation: $R(\rho) = -(\rho + d)^{-1/5}$ are proposed. Also, an efficient log-type angular variable transformation is introduced.

Numerical experiments on planar and curved boundary elements for potential and flux integrals containing interpolation functions arising in three dimensional potential problems, show that the method is far more efficient compared to previous methods such as Telles' method, for nearly singular integrals with relative source distance D less than 0.06, and the tendency becomes more pronounce as the relative source distance decreases. Here, the relative source distance D is defined as the source distance relative to the element size. The proposed method is robust concerning the type of integral kernel and position of the source point.

Experiments also show that the log-L_1 transformation is suited to potential calculations, while the $L_1^{-1/5}$ transformation is suited to flux calculations. When the source projection lies outside the element, or when it is closer to the element edge than the source point, it is shown that moving the source projection to the nearest element edge improves the efficiency of the method substantially.

Theoretical error estimates using complex function theory are derived, which quantatively explain the efficiency of the proposed radial variable transformation.

The PART method is also shown to be applicable, with some modifications, to weakly singular integrals and Cauchy principal value integrals arising in three dimensional potential problems.

ACKNOWLEDGEMENTS

I wish to thank Prof. M. Iri for his advice and supervision in preparing the present thesis.

I am grateful to Dr. C. A. Brebbia, Prof. W. S. Hall, Prof. J. C. F. Telles, Dr. S. Amini, Dr. W. Tang, Dr. M. H. Aliabadi, Dr. M. Sugihara, Dr. K. Kishimoto among many others, for stimulating discussions, valuable remarks and encouragements.

I am indebted to my company, NEC Corporation, in particular, Dr. K. Iinuma, Mr. K. Nakamura, among many others, for their support and understanding for the present work. I am grateful to Mr. H. Matsumoto and Mr. K. Moroga of NEC Scientific Information System Development Co. Ltd. for helping with some of the numerical experiments. I would also like to thank Ms. N. Tsurukai and Ms. N. Watanabe for their excellent typing.

Last, but not the least, I would like to thank my wife Emiko, for her constant support and encouragement.

TABLE OF CONTENTS

PART I

THEORY AND ALGORITHMS

CHAPTER 1

INTRODUCTION

In three dimensional boundary element analysis, computation of integrals is an important aspect since it governs the accuracy of the analysis and also because it usually takes the major part of the CPU time.

The integrals which determine the influence matrices, the internal field and its gradients contain (nearly) singular kernels of order $1/r^{\alpha}$ ($\alpha=1,2,3,4,\cdots$) where r is the distance between the source point and the integration point on the boundary element.

For planar elements, analytical integration may be possible [1,2,6]. However, it is becoming increasingly important in practical boundary element codes to use curved elements, such as the isoparametric elements, to model general curved surfaces. Since analytical integration is not possible for general isoparametric curved elements, one has to rely on numerical integration.

When the distance d between the source point and the element over which the integration is performed is sufficiently large compared to the element size ($d>1$), the standard Gauss-Legendre quadrature formula [1,3] works efficiently.

However, when the source is actually on the element ($d=0$), the kernel $1/r^{\alpha}$ becomes singular and the straight forward application of the Gauss-Legendre quadrature formula breaks down. These integrals will be called singular integrals. Singular integrals occur when calculating the diagonals of the influence matrices.

When the source is not on the element but very close to the element ($0<d\ll 1$), although the kernel $1/r^{\alpha}$ is regular in the mathematical sense, the value of the kernel changes rapidly in the neighborhood of the source point and the standard Gauss-Legendre quadrature formula is not practical since it would require a huge number of integration points to achieve the required accuracy.

These integrals will be called nearly singular integrals . Nearly singular integrals occur in practice when calculating influence matrices for thin structures, where distances between different elements can be very small compared to the element size. They also occur when calculating the field or its derivatives at an internal point very close to the boundary element.

Singular Integrals ($d=0$)	Nearly Singular Integrals ($0<d\ll 1$)
I. Analytical (for planar elements only)	
II. Numerical	
(1) Weighted Gauss	(1) Element Subdivision
(2) Singularity Subtraction (+Taylor Expansion)	(2) Variable Transformation
	(i) Double Exponential Transformation
(3) Variable Transformation	(ii) Cubic Transformation
(4) Coordinate Transformation	(3) Coordinate Transformation
(i) Triangle to Quadrilateral Transformation	Polar Coordinates (+ modification)
(ii) Polar Coordinates	
(5) Finite Part Integrals	
Present Method : Projection and Angular & Radial Transformation (PART)	

Table 1.1 Classification of quadrature methods for (nearly) singular integrals in three dimensional boundary element method.

Numerous research works have already been published on this subject and they may be classified as in Table 1.1. These are numerical methods based on the Gaussian quadrature formula or the truncated trapezium rule with modifications

to suit the (nearly) singular kernels which appear in the Boundary Element Method (BEM).

Let us first briefly review the methods for singular integrals.

The weighted Gauss [4,5,19,20] method uses the kernel $1/r$ as the weight function for generating the Gauss integration points.

The singularity subtraction [21] with Taylor expansion [6] method expands the singular kernel by the local parametric coordinates. The main terms containing the singularity is subtracted and integrated analytically and the remaining well behaved terms are integrated by Gaussian quadrature.

Then there are the coordinate transformation methods. The first type is the method of transforming a triangular region into a quadrilateral region so that the node corresponding to the singularity is expanded to an edge of the quadrilateral, so that the singularity is weakened [7,8,21]. The second type is that of using polar coordinates (ρ, θ) around the source point in the parameter space [9,15]. This introduces a Jacobian which cancels the singularity $1/r$.

For higher singularities of order $1/r^2$ which appear in elastostatics, the method for calculating finite part integrals [10,11] may be used.

Although a rigorous comparison is not attempted, the use of polar coordinates seems to be the most natural and effective way. In the present work this idea is extended to taking polar coordinates around the source point in the plane tangent to the curved element at the source point. Further, an angular variable transformation is introduced which considerably reduces the number of integration points in the angular variable.

Nearly singular integrals turn out to be more difficult and expensive to calculate compared to singular integrals. They are becoming more and more important in practical boundary element codes, since the ability and efficiency to calculate nearly singular integrals governs the code's versatility in treating objects containing thin structures, which occur in many important problems in engineering. Examples are the electrostatic analysis of electron guns with

complex geometry, calculation of the magnetic flux in thin gaps occurring in electric motors, to mention a few. The use of discontinuous elements [1] also increases the chances of encountering nearly singular integrals. The stress of the present work is on a new quadrature scheme for the accurate and efficient evaluation of these nearly singular integrals.

The orthodox way to treat the problem is to increase the number of integration points as the source to element distance d becomes small, and further to subdivide the element so that the integration points are concentrated near the source point [7,12]. Subdivision tends to be a cumbersome procedure and would be inefficient when d is very small compared to the element size.

A recent trend is to transform the integration variables so as to weaken the singular behaviour of the kernel, such as using the double exponential transformation with trapezium rules [13,14]. A more efficient self-adaptive method using cubic transformation[15] has been proposed. However, this method does not give accurate results when the ratio of the distance d to the typical element size is smaller than the order of 10^{-2}, which is required in practice.

The use of polar coordinates in the parametric space with correction procedures is reported to be efficient for potential problems [16].

In the present work a new coordinate transformation method is introduced, in which the curved boundary element is approximately projected to the tangent plane at the point on the curved element nearest to the source point, and then polar coordinates are employed in the tangent plane with a further transformation of the radial variable in order to weaken the near singularity, after which the standard Gauss-Legendre quadrature scheme [17] is applied.

As the radial variable transformations, the log-L_1 and $L_1^{-1/5}$ transformations are introduced and shown to be robust and efficient for near singularities of different orders.

Furthermore, the method is generalized to cope with arbitrary geometry of the curved element, such as curved triangular as well as quadrilateral elements.

Then, an angular variable transformation is introduced to reduce the number of integration points in the angular variable.

The method, which will be referred to as the Projection and Angular & Radial Transformation (PART) method, enables one to calculate nearly singular integrals accurately and efficiently, even when the distance d to element size ratio is smaller than 10^{-2}. The method is also applicable to different types of nearly singular kernels because of the robustness of the proposed radial variable transformations.

CHAPTER 2

BOUNDARY ELEMENT FORMULATION OF 3-D POTENTIAL PROBLEMS

Although the quadrature methods to be proposed are applicable to general problems, let us take potential problems to illustrate the nature of the (near) singularities of integrals and how the quadrature methods can be applied.

2.1 Boundary Integral Equation

The potential problem in a three dimensional domain V with boundary surface S can be described by the following Laplace equation:

$$\Delta u(\mathbf{x}) = 0 \quad , \tag{2.1}$$

where

$$\Delta u \equiv \frac{\partial^2 u}{\partial x^2} + \frac{\partial^2 u}{\partial y^2} + \frac{\partial^2 u}{\partial z^2} \quad ,$$

with the boundary condition;

$$\begin{aligned} u(\mathbf{x}) &= \bar{u}(\mathbf{x}) \qquad \text{on } S_1 \subset S \quad , \\ q(\mathbf{x}) &\equiv \frac{\partial u}{\partial n} = \bar{q}(\mathbf{x}) \quad \text{on } S_2 = S - S_1 \quad , \end{aligned} \tag{2.2}$$

where $\partial/\partial n$ is the derivative along the unit outward normal vector $\mathbf{n}$ of the boundary surface S at point $\mathbf{x}$.

The fundamental solution $u^*(\mathbf{x}, \mathbf{x}_s)$ of the Laplace equation:

$$\Delta_x u^*(\mathbf{x}, \mathbf{x}_s) = -\delta(\mathbf{x}, \mathbf{x}_s) \tag{2.3}$$

in the infinite domain is given by

$$u^*(\mathbf{x}, \mathbf{x}_s) = \frac{1}{4\pi r} \tag{2.4}$$

where

$\delta(\mathbf{x}, \mathbf{x}_s)$: Dirac's delta function,

$\mathbf{x}$: field point,

$\mathbf{x}_s$: source point,

$r = |\mathbf{r}|$,

and

$\mathbf{r} = \mathbf{x} - \mathbf{x}_s$,

as shown in Fig. 2.1.

Using Green's identity:

$$\int_V (F\Delta G - G\Delta F)\,dV = \int_S (F\frac{\partial G}{\partial n} - G\frac{\partial F}{\partial n})\,dS \tag{2.5}$$

taking $F = u$ and $G = u^*$, we obtain

$$\int_V (u\,\Delta u^* - u^*\,\Delta u)\,dV = \int_S (u\,q^* - u^*\,q)\,dS \quad , \tag{2.6}$$

where

$$\begin{aligned} q^*(\mathbf{x}, \mathbf{x}_s) &= \frac{\partial u^*(\mathbf{x}, \mathbf{x}_s)}{\partial n} \\ &= -\frac{(\mathbf{r}, \mathbf{n})}{4\pi r^3} \end{aligned} \tag{2.7}$$

Substituting equations (2.1) and (2.3) into equation (2.5) gives

$$\int_V u(\mathbf{x})\,\delta(\mathbf{x}, \mathbf{x}_s)\,dV = \int_S (q\,u^* - u\,q^*)\,dS \tag{2.8}$$

where

$$\int_V u(\mathbf{x})\,\delta(\mathbf{x}, \mathbf{x}_s)\,dV = u(\mathbf{x}_s) \quad \text{for} \quad \mathbf{x}_s \in V, \tag{2.9}$$

and

$$\int_V u(\mathbf{x})\,\delta(\mathbf{x}, \mathbf{x}_s)\,dV = 0 \quad \text{for} \quad \mathbf{x}_s \notin V, \tag{2.10}$$

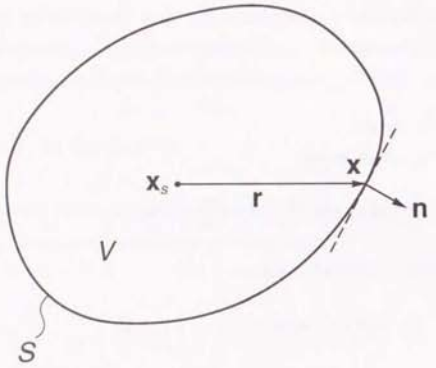

Fig.2.1 Source point $\mathbf{x}_s$ in region V

For the case when $\mathbf{x}_s \in S$, i.e. when the source point $\mathbf{x}_s$ is actually on the surface S, the property of the Dirac's delta function yields

$$\int_V u(\mathbf{x})\,\delta(\mathbf{x},\mathbf{x}_s)\,dV = \frac{\omega}{4\pi}\,u(\mathbf{x}_s) \tag{2.11}$$

where ω is the solid angle subtended by V at $\mathbf{x}_s$ on S as show in Fig. 2.2. For instance, $\omega = 2\pi$ when the surface S is smooth at $\mathbf{x}_s$.

From equations (2.8-11),

$$c(\mathbf{x}_s)\,u(\mathbf{x}_s) = \int_S (q\,u^* - u\,q^*)\,dS \tag{2.12}$$

where

$$c(\mathbf{x}_s) = \begin{cases} 1 & (\mathbf{x}_s \in V) \\ 0 & (\mathbf{x}_s \notin V) \\ \omega/4\pi & (\mathbf{x}_s \in S) \end{cases} \tag{2.13}$$

Instead of using the Dirac's delta function of equation (2.11), equation (2.12) can be derived for the case when $\mathbf{x}_s \in S$ as follows:

Consider a part of a sphere S_ϵ of radius ϵ centered at $\mathbf{x}_s$ as in Fig. 2.3, where $S = S' + S_\epsilon$. Since now $\mathbf{x}_s \in V$, the left hand side of equation (2.8) is

$$\int_V u(\mathbf{x})\,\delta(\mathbf{x},\mathbf{x}_s)\,dV = u(\mathbf{x}_s) \tag{2.14}$$

Next, the first term of the right hand side of equation (2.8) is

$$\int_S q\,u^*\,dS = \int_{S'} q\,u^*\,dS + \int_{S_\epsilon} q\,u^*\,dS \tag{2.15}$$

where

$$\int_{S_\epsilon} q\,u^*\,dS = \int \frac{q}{4\pi r}\,dS$$

$$= \frac{q}{4\pi r}(4\pi - \omega)\,\epsilon^2 \xrightarrow[\epsilon \to 0]{} 0 \tag{2.16}$$

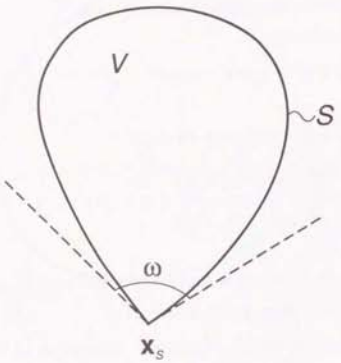

Fig.2.2 Use of Dirac's delta function at $\mathbf{x}_S \in S$

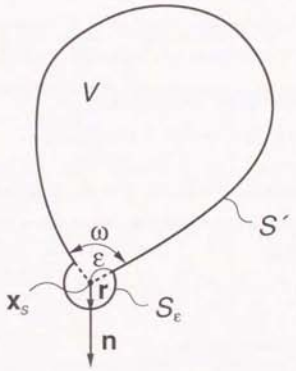

Fig.2.3 Treatment of $\mathbf{x}_S \in S$ without the use of Dirac's delta function

The second term of the right hand side of equation (2.8) is

$$-\int_S u\, q^*\, dS = -\int_{S'} u\, q^*\, dS - \int_{S_\varepsilon} u\, q^*\, dS \tag{2.17}$$

where

$$-\int_{S_\varepsilon} u\, q^*\, dS = \int_{S_\varepsilon} \frac{(\mathbf{r},\mathbf{n})}{4\pi r^3}\, u\, d$$

$$= \frac{\varepsilon}{4\pi\varepsilon^3}\, u(\mathbf{x})\,(4\pi-\omega)\varepsilon^2 \xrightarrow[\omega\to 0]{} \left(1-\frac{\omega}{4\pi}\right) u(\mathbf{x}_s) \tag{2.18}$$

From equations (2.8), (2.14) and (2.15-18),

$$u(\mathbf{x}_s) = \lim_{\varepsilon\to 0}\int_{S'} (q\,u^* - u\,q^*)\,dS + \left(1-\frac{\omega}{4\pi}\right) u(\mathbf{x}_s) \tag{2.19}$$

Since for potential problems, $u^* \sim O(1/\varepsilon)$, $q^* \sim O(1/\varepsilon)$ (cf. equation (3.40)) and $dS \sim O(\varepsilon^2)$ for $\mathbf{x}\in S$ in the neighborhood of $\mathbf{x}_s$, where S now indicates the original smooth surface, we obtain

$$\lim_{\varepsilon\to 0}\int_{S'} (q\,u^* - u\,q^*)\,dS = \int_S (q\,u^* - u\,q^*)\,dS \tag{2.20}$$

Hence, equations (2.19) and (2.20) give

$$\frac{\omega}{4\pi}\, u(\mathbf{x}_s) = \int_S (q\,u^* - u\,q^*)\,dS \tag{2.21}$$

which corresponds to equation (2.12) for the case when $\mathbf{x}_s \in S$.

2.2 Treatment of the Exterior Problem

One advantage of the boundary element method, especially when treating electromagnetic or acoustic problems is that exterior problems can be treated without meshing the infinite exterior regions. A brief explanation will be given in the following for the three dimensioned potential problem.

Let us consider an exterior problem

$$\Delta u(\mathbf{x}) = 0 \quad \text{in } V \tag{2.22}$$

with boundary condition

$$\begin{cases} u(\mathbf{x}) = \bar{u}(\mathbf{x}) & \text{on } S_1 \subset S \\ q(\mathbf{x}) = \bar{q}(\mathbf{x}) & \text{on } S_2 = S - S_1 \end{cases} \tag{2.23}$$

where the region V is an infinite region as shown in Fig. 2.4.

Since the Green's identity of equation (2.5) is also valid for a multi connected region, let us take a sphere S_R of radius R centered at the source point $\mathbf{x}_s \in V$, such that S is included in the sphere S_R, as shown in Fig. 2.5. The boundary integral formulation of equation (2.12) becomes valid for the region V_R enclosed between surface S and S_R, i.e.

$$c(\mathbf{x}_s)\, u(\mathbf{x}_s) = \int_S (q\,u^* - u\,q^*)\, dS + \int_{S_R} (q\,u^* - u\,q^*)\, dS \tag{2.24}$$

On S_R,

$$u^* = \frac{1}{4\pi r} = \frac{1}{4\pi R}$$

$$q^* = -\frac{(\mathbf{r},\mathbf{n})}{4\pi r^3} = -\frac{1}{4\pi R^2}$$

$$dS = R^2 dR\, \sin\theta\, d\theta\, d\phi \tag{2.25}$$

where (r, θ, ϕ) is the polar coordinate system centered at $\mathbf{x}_s$, and $R = |\mathbf{R}|$.

Let us take the limit of $R\to\infty$. The value of u, q, on S_R can be considered as a solution of

$$\Delta u = -Q\,\delta(\mathbf{x}, \mathbf{x}_s) \tag{2.26}$$

where Q is the sum of the source term (e.g. electric charge) inside S, since S may be considered as a point source of finite magnitude Q when observed from a distant point $\mathbf{x} \in S_R$ as $R\to\infty$.

Hence, on S_R

$$u \sim \frac{Q}{4\pi R} \sim O\left(\frac{1}{R}\right) \tag{2.27}$$

$$q \sim \frac{-(\mathbf{R},\mathbf{n})\,Q}{4\pi R^3} \sim O\left(\frac{1}{R^2}\right) \tag{2.28}$$

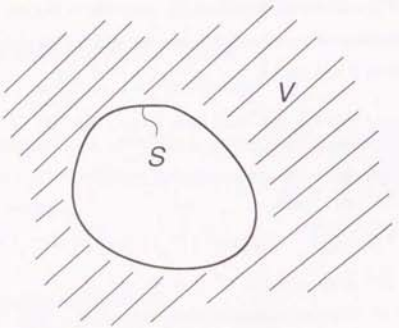

Fig.2.4 Exterior region V

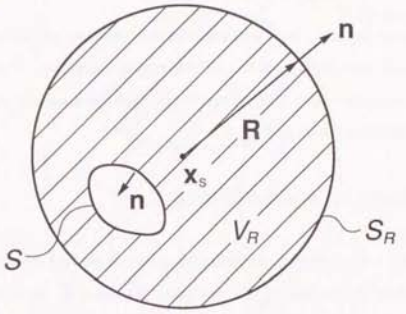

Fig.2.5 Multi connected region V_R

as $R \to \infty$, so that the third term of equation (2.24) tends to zero as $R \to \infty$, since

$$\int_{S_R} (q u^* - u q^*) dS \sim \int_{S_R} \left[O\left(\frac{1}{R^2}\right) \frac{1}{4\pi R} + O\left(\frac{1}{R}\right) \frac{1}{4\pi R^2} \right] dS \sim 4\pi R^2 O\left(\frac{1}{R^3}\right) \to 0 \quad (2.29)$$

as $R \to \infty$.

Hence, equation (2.24) becomes

$$c(\mathbf{x}_s)\, u(\mathbf{x}_s) = \int_S (q u^* - u q^*)\, dS \quad (2.30)$$

for the exterior problem. Note that the boundary that has to be discretized is only S and no mesh discretization in the infinite region is involved. Note also that the unit outward normal $\mathbf{n}$ on S is defined in the opposite direction compared to the interior problem as shown in Fig.2.5.

2.3 Discretization into Boundary Elements

Now the boundary element formulation can be derived from equation (2.12) by discretizing the surfaces S into boundary elements S_e, as shown in Fig.2.6. Each element contains nodes $\mathbf{x}_e^j$ $(j = 1 \sim n_e)$, where u (or q) is defined from the boundary condition, and q (or u) is to be solved.

The element is described by the parameters (η_1, η_2) and interpolation functions $\phi_e^j(\eta_1, \eta_2), (j = 1 \sim n_e)$, which are defined so that

$$f(\eta_1, \eta_2) = \sum_{j=1}^{e} \phi_e^j(\eta_1, \eta_2) f_e^j \quad , \quad (2.31)$$

where f_e^j is the value of $f(\eta_1, \eta_2)$ at node $\mathbf{x}_e^j$. f can represent the potential u, its normal derivative $q = \partial u / \partial n$ or coordinates $\mathbf{x}$, i.e.

$$u(\eta_1, \eta_2) = \sum_{j=1}^{n_e} \phi_e^j(\eta_1, \eta_2) u_e^j \quad , \quad (2.32)$$

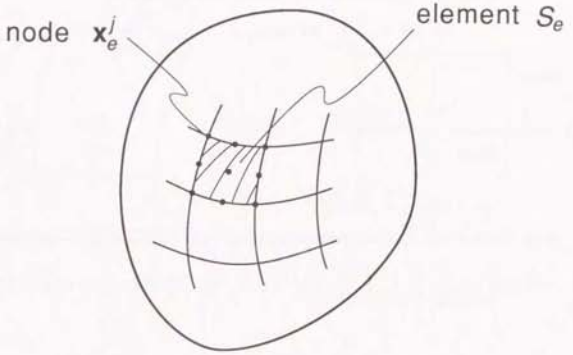

Fig.2.6 Discretization of S into boundary elements S_e

$$q(\eta_1, \eta_2) = \sum_{j=1}^{n_e} \phi_e^j(\eta_1, \eta_2)\, q_e^j \quad , \tag{2.33}$$

and

$$\mathbf{x}(\eta_1, \eta_2) = \sum_{j=1}^{n_e} \phi_e^j(\eta_1, \eta_2)\, \mathbf{x}_e^j \quad . \tag{2.34}$$

For a curved quadrilateral element shown in Fig.2.7,

$$\int_{S_e} dS = \int_{-1}^{1}\int_{-1}^{1} |G|\, d\eta_1 d\eta_2 \tag{2.35}$$

where

$$G = \frac{\partial \mathbf{x}}{\partial \eta_1} \times \frac{\partial \mathbf{x}}{\partial \eta_2} \quad .$$

Since

$$\int_S dS = \sum_{e=1}^{m} \int_{S_e} dS$$

where m is the total number of elements, equation (2.12) can be discretized as

$$c(\mathbf{x}_e^k)\, u(\mathbf{x}_e^k) = \sum_{e=1}^{m}\sum_{j=1}^{n_e} \int_{-1}^{1}\int_{-1}^{1} \left\{ \phi_e^j q(\mathbf{x}_e^j)\, u^*(\mathbf{x}, \mathbf{x}_e^k) - \phi_e^j u(\mathbf{x}_e^j)\, q^*(\mathbf{x}, \mathbf{x}_e^k) \right\} |G|\, d\eta_1 d\eta_2 \tag{2.36}$$

or

$$c_e^k u_e^k = \sum_{e=1}^{m}\sum_{j=1}^{n_e} \left(g_{e\,e}^{k\,j} q_e^j - h_{e\,e}^{k\,j} u_e^j \right) \tag{2.37}$$

where

$$c_e^k = c(\mathbf{x}_e^k) \quad , \qquad \phi_e^j = \phi_e^j(\eta_1, \eta_2)$$

$$u_e^j = u(\mathbf{x}_e^j) \quad , \qquad G = G(\eta_1, \eta_2)$$

$$q_e^j = q(\mathbf{x}_e^j) \quad , \qquad \mathbf{x} = \mathbf{x}(\eta_1, \eta_2)$$

and

$$g_{e\,e}^{k\,j} = \int_{-1}^{1}\int_{-1}^{1} \phi_e^j |G|\, u^*(\mathbf{x}, \mathbf{x}_e^k)\, d\eta_1 d\eta_2 \tag{2.38}$$

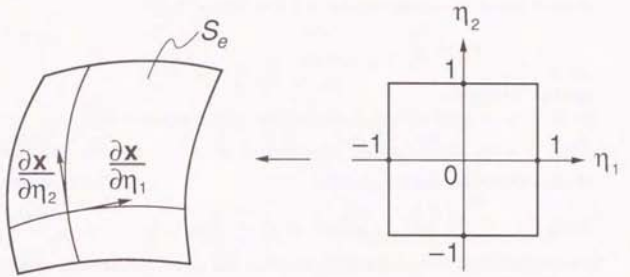

Fig.2.7 Curved quadrilateral element S_e and parametric space (η_1, η_2)

$$h^{k\,l}_{e^{\prime}e} = \int_{-1}^{1}\int_{-1}^{1} \phi^{l}_{e} |G| q^{*}(x, x^{k}_{e^{\prime}}) \, d\eta_1 d\eta_2 \qquad (2.39)$$

Reordering the nodes throughout S, equation (2.37) can be written as

$$c_i u_i = \sum_{j=1}^{N} G_{ij} q_j - \sum_{j=1}^{N} \bar{H}_{ij} u_j \qquad (2.40)$$

where N is the total number of nodes on S. If we define

$$H_{ij} = \begin{cases} \bar{H}_{ij} & (i \neq j) \\ \bar{H}_{ij} + c_j & (i = j) \end{cases} \qquad (2.41)$$

equation (2.40) gives

$$\sum_{j=1}^{N} H_{ij} u_j = \sum_{j=1}^{N} G_{ij} u_j \qquad (2.42)$$

which can be written in matrix form as

$$H\begin{pmatrix} u \\ \bar{u} \end{pmatrix} = G\begin{pmatrix} q \\ \bar{q} \end{pmatrix} \qquad (2.43)$$

u represents the Dirichlet boundary condition and q the Neumann boundary condition.

Equation (2.43) can be rewritten as

$$A\begin{pmatrix} u \\ q \end{pmatrix} = B\begin{pmatrix} \bar{u} \\ \bar{q} \end{pmatrix} \qquad (2.44)$$

so that the unknown u and q can be obtained by solving the system of linear equations (2.44).

From equation (2.12) the potential $u(x_s)$ at an internal point $x_s \in V$ is given by

$$u(x_s) = \int_S (q u^{*} - u q^{*}) \, dS \qquad (2.45)$$

where

$$u^{*} = \frac{1}{4\pi r}, \qquad q^{*} = \frac{\partial u^{*}}{\partial n} = -\frac{(r, n)}{4\pi r^3}$$

and the potential gradient at an internal point $x_s \in V$ is given by

$$\frac{\partial u}{\partial x_s} = \int_S \left(q \frac{\partial u^{*}}{\partial x_s} - u \frac{\partial u^{*}}{\partial x_s} \right) dS \qquad (2.46)$$

where

$$\frac{\partial u^{*}(x, x_s)}{\partial x_s} = \frac{1}{4\pi} \frac{r}{r^3} \qquad (2.47)$$

and

$$\frac{\partial q^{*}(x, x_s)}{\partial x_s} = \frac{1}{4\pi} \left[\frac{n}{r^3} - \frac{3r(r, n)}{r^5} \right] \qquad (2.48)$$

Correspondingly, after the discretized equation (2.44) is solved for the boundary values u and q, the potential $u(x_s)$ at an internal point x_s can be calculated by

$$u(x_s) = \sum_{e=1}^{m} \sum_{l=1}^{n_e} \left(g^{sl}_{e} q^{l}_{e} - h^{sl}_{e} u^{l}_{e} \right) \qquad (2.49)$$

where

$$g^{sl}_{e} q^{l}_{e} = \int_{-1}^{1}\int_{-1}^{1} \phi^{l}_{e} |G| u^{*}(x, x_s) d\eta_1 d\eta_2 \qquad (2.50)$$

$$h^{sl}_{e} q^{l}_{e} = \int_{-1}^{1}\int_{-1}^{1} \phi^{l}_{e} |G| q^{*}(x, x_s) d\eta_1 d\eta_2 \qquad (2.51)$$

and

$$x(\eta_1, \eta_2) = \sum_{l=1}^{n_e} \phi^{l}_{e}(\eta_1, \eta_2) \, x^{l}_{e} \qquad (2.52)$$

Similarly, the potential gradient at an internal point $x_s \in V$ can be calculated by

$$\frac{\partial u}{\partial x_s}(x_s) = \sum_{e=1}^{m} \sum_{l=1}^{n_e} \left(a^{sl}_{e} q^{l}_{e} - b^{sl}_{e} u^{l}_{e} \right) \qquad (2.53)$$

where

$$a_e^{sl} = \frac{\partial}{\partial \mathbf{x}_s} g_e^{sl}$$

$$= \int_{-1}^{1}\int_{-1}^{1} \phi_e^l |G| \frac{\partial u^*}{\partial \mathbf{x}_s} d\eta_1 d\eta_2$$

$$= \int_{-1}^{1}\int_{-1}^{1} \frac{\phi_e^l |G|}{4\pi} \frac{\mathbf{r}}{r^3} d\eta_1 d\eta_2 \qquad (2.54)$$

and

$$b_e^{sl} = \frac{\partial}{\partial \mathbf{x}_s} h_e^{sl}$$

$$= \int_{-1}^{1}\int_{-1}^{1} \phi_e^l |G| \frac{\partial q^*}{\partial \mathbf{x}_s} d\eta_1 d\eta_2$$

$$= \int_{-1}^{1}\int_{-1}^{1} \frac{\phi_e^l |G|}{4\pi} \left\{ \frac{\mathbf{r}}{r^3} - \frac{3\mathbf{r}(\mathbf{r},\mathbf{n})}{r^5} \right\} d\eta_1 d\eta_2 \qquad (2.55)$$

where $\mathbf{r} = \mathbf{x}(\eta_1, \eta_2) - \mathbf{x}_s$, and $\mathbf{n}$ is the unit outward normal vector of the boundary element S_e at $\mathbf{x} \in S_e$.

2.4. Row Sum Elimination Method

The calculation of $c(\mathbf{x}_s)$ in equation (2.13) when $\mathbf{x}_s$ is a node shared by two or more elements as shown in Fig.2.8 involves the calculation of the solid angle ω subtended by the region V at $\mathbf{x}_s$ on S. In order to avoid this, one many use the row sum elimination method in many cases.

For the three dimentional potential problem defined in the interior region, consider the equipotential solution $u(\mathbf{x}) = 1$ to the original Laplace equation $\Delta u(\mathbf{x}) = 0$. This implies that $q(\mathbf{x}) = \partial u(\mathbf{x})/\partial n = 0$ on the boundary S.

Hence equation (2.12)

$$c(\mathbf{x}_s) = -\int_S q^* \, dS \qquad (2.56)$$

and $u_j \equiv 1, (j = 1 \sim N)$ and $q_j \equiv 0, (j = 1 \sim N)$ in equation (2.42) gives

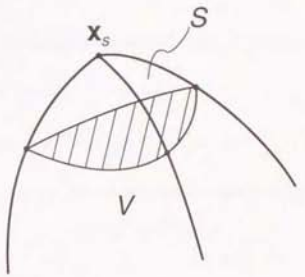

Fig.2.8 The solid angle ω at x_s subtending V

$$\sum_{j=1}^{N} H_{ij} = 0 \tag{2.57}$$

Hence,

$$H_{ij} = -\sum_{j=1(j\neq i)}^{N} H_{ij} \tag{2.58}$$

For the exterior problem, a similar technique can be used with some modification.

In the equation

$$c(\mathbf{x}_s)\, u(\mathbf{x}_s) = \int_S (q u^* - u q^*)\, dS + \int_{S_R} (q u^* - u q^*)\, dS \quad , \tag{2.24}$$

let us assume the equipotential solution $u(\mathbf{x}) \equiv 1$ in the region V_R of Fig.2.5.

Since

$$q = \frac{\partial u}{\partial n} = 0 \tag{2.59}$$

$$c(\mathbf{x}_s) = -\int_S q^*\, dS - \int_{S_R} q^*\, dS \tag{2.60}$$

Hence,

$$\int_{S_R} q^*\, dS = \int_{S_R} \frac{(\mathbf{r}, \mathbf{n})}{4\pi r^3}\, dS = -\int_{S_R} \frac{R}{4\pi R^3}\, dS = -1 \tag{2.61}$$

Equation (2.61) is satisfied in the limit of $R \to \infty$.

Hence, equation (2.60) gives

$$c(\mathbf{x}_s) = -\int_S q^*\, dS + 1 \tag{2.62}$$

The discretization of this equation as in equation (2.40) gives

$$c_i = -\sum_{j=1}^{n} \bar{H}_{ij} + 1 \quad , \tag{2.63}$$

which gives

$$H_{ii} = H_{ii} + c_i = 1 - \sum_{j=1(j\neq i)}^{n} H_{ij} \tag{2.64}$$

From the above argument, the diagonal element H_{ii} can be indirectly calculated by the row sum of H_{ij} ($i \neq j$), so that the calculation of the solid angle at node $\mathbf{x}_i$ given by

$$c_i = \frac{\omega(\mathbf{x}_i)}{4\pi} \tag{2.65}$$

and the calculation of the singular integral

$$H_{ii} = \sum_{\mathbf{x}_e^k = \mathbf{x}_i} h_{ee}^{kk} \tag{2.66}$$

$$h_{ee}^{kk} = \int_{-1}^{1}\int_{-1}^{1} \phi_e^k\, |G|\, q^*(\mathbf{x}, \mathbf{x}_e^k)\, d\eta_1\, d\eta_2 \tag{2.67}$$

where

$$q^* = \frac{\partial u^*}{\partial n} = -\frac{(\mathbf{r}, \mathbf{n})}{4\pi r^3}$$

become unnecessary. This technique is equivalent to what is known as the use of rigid body motion in elastostatics. On the other hand, it is a good check to calculate H_{ii} directly from c_i and H_{ij}. For discontinuous elements[1], $c_i = 1/2$ for $i = 1 \sim N$, and calculating the singular integrals H_{ii} directly are reported to give more accurate results[15].

The diagonal element G_{ii} has to be calculated directly by the singular integral

$$g_{ee}^{kk} = \int_{-1}^{1}\int_{-1}^{1} \phi_e^k\, |G|\, u^*(\mathbf{x}, \mathbf{x}_e^k)\, d\eta_1\, d\eta_2 \quad , \tag{2.68}$$

where $u^* = 1/(4\pi r)$ and

$$G_{ii} = \sum_{\mathbf{x}_e^k = \mathbf{x}_i} g_{ee}^{kk} \tag{2.69}$$

One also has to calculate integrals

$$h_{ee}^{kk} = \int_{-1}^{1}\int_{-1}^{1} \phi_e^k |G|\, u^*(\mathbf{x}, \mathbf{x}_e^k)\, d\eta_1\, d\eta_2 \tag{2.70}$$

and

$$g_{ee}^{kk} = \int_{-1}^{1}\int_{-1}^{1} \phi_e^l |G|\, q^*(\mathbf{x}, \mathbf{x}_e^k)\, d\eta_1\, d\eta_2 \quad , \tag{2.71}$$

which contribute to the non-diagonal element H_{ij} and G_{ij}. It will be shown in Chapter 3 that the integrals $h_{ee}{}^{kl}$, $g_{ee}{}^{kl}$ $(k \neq l)$ are not singular for three dimensional potential problems in the sense that the integral kernels are order $O(1)$ or $O(r)$, where $r = |\mathbf{x} - \mathbf{x}_e{}^k|$, since $\phi_e{}^l(\mathbf{x}_e{}^k) = 0$ for $k \neq l$.

CHAPTER 3

NATURE OF INTEGRALS IN 3-D POTENTIAL PROBLEMS

From the previous chapter, the integrals which appear in three dimensional potential problems are the following :

$$\int_S q\, u^*\, dS = \int_S \frac{q}{4\pi}\,\frac{1}{r}\, dS \tag{3.1}$$

$$\int_S u\, q^*\, dS = -\int_S \frac{u}{4\pi}\,\frac{(\mathbf{r}, \mathbf{n})}{r^3}\, dS \quad , \tag{3.2}$$

related to the calculation of the potential $u(\mathbf{x}_s)$ and the coefficients of the H, G matrices, and

$$\int_S q\,\frac{\partial u^*}{\partial \mathbf{x}_s}\, dS = \int_S \frac{q}{4\pi}\,\frac{\mathbf{r}}{r^3}\, dS$$

$$\int_S u\,\frac{\partial q^*}{\partial \mathbf{x}_s}\, dS = \int_S \frac{u}{4\pi}\left\{\frac{\mathbf{n}}{r^3} - \frac{3\mathbf{r}(\mathbf{r}, \mathbf{n})}{r^5}\right\} dS \tag{3.3}$$

related to the calculation of the flux $\partial u/\partial \mathbf{x}_s$ at $\mathbf{x}_s$.

As mentioned in the introduction (Chapter 1), these integrals may be classified by the distance d between the source point $\mathbf{x}_s$ and the boundary surface S (or the boundary element S_e).

When $d = 0$, they are called singular integrals.

When $0 < d \ll 1$, they are called nearly singular integrals.

When $d > 1$, the integrals do not cause difficulties since they may be calculated accurately using the standard Gauss-Legendre formula [1, 3] with relatively few integration points. (Here the distance d is defined relative to the element size which is set to 1.)

It is for the singular ($d = 0$), and nearly singular integrals ($0 < d \ll 1$) that special attention is necessary in order to calculate their values accurately.

3.1 Weakly Singular Integrals

Weakly singular integrals ($d=0$) arise when calculating the diagonal terms of the G and H influence matrices. This corresponds to integrals $g_{e'e}^{kl}$ and $h_{e'e}^{kl}$ in equations (2.38) and (2.39), when $e'=e$ and $k=l$.

$e'=e$ means that the source point $\mathbf{x}_s$ is actually on the element surface S_e, so that $r=|\mathbf{x}-\mathbf{x}_s|$ becomes 0 at $\mathbf{x}=\mathbf{x}_s$.

Furthermore, when $k=l$, one has to calculate

$$g_{ee}^{ll} = \int_{-1}^{1}\int_{-1}^{1} \phi_e^l(\eta_1,\eta_2)\,|\mathbf{G}|\,u^*(\mathbf{x},\mathbf{x}_e^l)\,\mathrm{d}\eta_1\,\mathrm{d}\eta_2 \tag{3.5}$$

$$h_{ee}^{ll} = \int_{-1}^{1}\int_{-1}^{1} \phi_e^l(\eta_1,\eta_2)\,|\mathbf{G}|\,q^*(\mathbf{x},\mathbf{x}_e^l)\,\mathrm{d}\eta_1\,\mathrm{d}\eta_2 \tag{3.6}$$

where

$$u^*(\mathbf{x},\mathbf{x}_e^l) = \frac{1}{4\pi r} \tag{3.7}$$

$$q^*(\mathbf{x},\mathbf{x}_e^l) = -\frac{(\mathbf{r},\mathbf{n})}{4r^3} \tag{3.8}$$

and

$$\mathbf{r} = \mathbf{x} - \mathbf{x}_e^l \quad .$$

Interpolation functions are generally constructed so that

$$\mathbf{x}(\eta_1,\eta_2) = \sum_{l=1}^{n_e} \phi_e^l(\eta_1,\eta_2)\,\mathbf{x}_e^l \tag{3.9}$$

where

$$\phi_e^l(\eta_1^l,\eta_2^l) = 1$$

and

$$\mathbf{x}(\eta_1^l,\eta_2^l) = \mathbf{x}_e^l \quad .$$

In other words, ϕ_e^l is the interpolation function corresponding to node $\mathbf{x}_e^l$.

Hence, the numerator of the kernels of integrals g_{ee}^{ll}, h_{ee}^{ll} of equations (3.5) and (3.6) take a nonzero value at $\mathbf{x}=\mathbf{x}_e^l$, whilst the denominator is zero since $r=|\mathbf{x}-\mathbf{x}_e^l|=0$. This means that the kernel of the integrals are singular, and special care is required for the evaluation of the integrals.

Let us now consider the order of singularity of the kernels of integrals g_{ee}^{ll} and h_{ee}^{ll}.

For g_{ee}^{ll}, since $\phi_e^l(\eta_1,\eta_2)=1$ and $|\mathbf{G}|\neq 0$ at $\mathbf{x}_e^l=\mathbf{x}(\eta_1^l,\eta_2^l)$, the order of singularity is $1/r$.

For h_{ee}^{ll}, the order of singularity is also $1/r$, since $(\mathbf{r},\mathbf{n})/r^3$ has a singularity of order $1/r$ when $d=0$, as shown in the following theorem.

Theorem 3.1

$$\frac{(\mathbf{r},\mathbf{n})}{r^3} \sim \frac{K_n}{2r} \qquad \text{for} \quad 0<r\ll 1 \quad , \tag{3.10}$$

where $K_n(\lambda)$ is the normal curvature of the curved element along a direction $\lambda=\mathrm{d}\eta_2/\mathrm{d}\eta_1$ at a source point $\mathbf{x}_s$ on the element, and η_1, η_2 are the parameters describing the curved element.

Proof:

Let the curved element be expressed by $\mathbf{x}=\mathbf{x}(\eta_1,\eta_2)$ and the source point be

$$\mathbf{x}_s = \mathbf{x}(\bar{\eta}_1,\bar{\eta}_2)$$

with

$$\mathbf{r} = \mathbf{x} - \mathbf{x}_s \quad .$$

The unit normal is given by

$$\mathbf{n} = \mathbf{G}/|\mathbf{G}| \tag{3.11}$$

where

$$\mathbf{G} = \frac{\partial \mathbf{x}}{\partial \eta_1} \times \frac{\partial \mathbf{x}}{\partial \eta_2} = \frac{\partial \mathbf{r}}{\partial \eta_1} \times \frac{\partial \mathbf{r}}{\partial \eta_2} \quad . \tag{3.12}$$

Taking Taylor expansions around $\mathbf{x}_s$ one obtains,

$$\mathbf{r} = \bar{\mathbf{r}}_{,1}\,d\eta_1 + \bar{\mathbf{r}}_{,2}\,d\eta_2 + \frac{1}{2}\left(\bar{\mathbf{r}}_{,11}\,d\eta_1^2 + 2\,\bar{\mathbf{r}}_{,12}\,d\eta_1 d\eta_2 + \bar{\mathbf{r}}_{,22}\,d\eta_2^2\right) + O(d\eta^3) \tag{3.13}$$

where $\mathbf{r}_{,i} \equiv \partial \mathbf{r}/\partial \eta_i$ etc. and the bar $\bar{}$ indicates the quantity at $\mathbf{x}_s = \mathbf{x}(\bar{\eta}_1, \bar{\eta}_2)$.

$$O(d\eta) = O(d\eta_1, d\eta_2) \quad ,$$

$$O(d\eta^2) = O(d\eta_1^2,\ d\eta_1 d\eta_2,\ d\eta_2^2)$$

and

$$O(d\eta^3) = O(d\eta_1^3,\ d\eta_1^2 d\eta_2,\ d\eta_1 d\eta_2^2,\ d\eta_2^3) \tag{3.14}$$

denote the first, second and third order terms of $d\eta_1$ and $d\eta_2$, respectively.

Similarly one can express the derivatives of $\mathbf{r}$ as,

$$\frac{\partial \mathbf{r}}{\partial \eta_i} = \bar{\mathbf{r}}_{,i} + \bar{\mathbf{r}}_{,i1}\,d\eta_1 + \bar{\mathbf{r}}_{,i2}\,d\eta_2 + O(d\eta^2) \quad , \quad (i = 1, 2) \tag{3.15}$$

Hence, the cross product can be expressed by the following expression

$$\mathbf{G} = \frac{\partial \mathbf{r}}{\partial \eta_1} \times \frac{\partial \mathbf{r}}{\partial \eta_2} = \left[\bar{\mathbf{r}}_{,1} + \left(\bar{\mathbf{r}}_{,11}\,d\eta_1 + \bar{\mathbf{r}}_{,12}\,d\eta_2\right) + O(d\eta^2)\right] \times \left[\bar{\mathbf{r}}_{,2} + \left(\bar{\mathbf{r}}_{,21}\,d\eta_1 + \bar{\mathbf{r}}_{,22}\,d\eta_2\right) + O(d\eta^2)\right] \quad , \tag{3.16}$$

and $(\mathbf{r}, \mathbf{G})$ can be calculated from equations (3.13) and (3.16) as follows:

$$O(1)\ \text{term} = 0 \quad , \tag{3.17}$$

$$O(d\eta)\ \text{term} = \left(\bar{\mathbf{r}}_{,1}\,d\eta_1 + \bar{\mathbf{r}}_{,2}\,d\eta_2\right) \cdot \left(\bar{\mathbf{r}}_{,1} \times \bar{\mathbf{r}}_{,2}\right) = 0 \quad , \tag{3.18}$$

since

$$\bar{\mathbf{r}}_{,i} \cdot \left(\bar{\mathbf{r}}_{,1} \times \bar{\mathbf{r}}_{,2}\right) = 0 \quad , \quad (i = 1, 2) \tag{3.19}$$

The $O(d\eta^2)$ term is given by

$$O(d\eta^2)\ \text{term} = O_1(d\eta^2) + O_2(d\eta^2) \tag{3.20}$$

where, from the $O(d\eta)$ term of equation (3.13) and the $O(d\eta)$ term of equation (3.16),

$$\begin{aligned} O_1(d\eta^2) &= \left(\bar{\mathbf{r}}_{,1}\,d\eta_1 + \bar{\mathbf{r}}_{,2}\,d\eta_2\right) \cdot \left[\bar{\mathbf{r}}_{,1} \times \left(\bar{\mathbf{r}}_{,12}\,d\eta_1 + \bar{\mathbf{r}}_{,22}\,d\eta_2\right) - \bar{\mathbf{r}}_{,2} \times \left(\bar{\mathbf{r}}_{,11}\,d\eta_1 + \bar{\mathbf{r}}_{,12}\,d\eta_2\right)\right] \\ &= -\bar{\mathbf{r}}_{,1} \cdot \left[\bar{\mathbf{r}}_{,2} \times \left(\bar{\mathbf{r}}_{,11}\,d\eta_1 + \bar{\mathbf{r}}_{,12}\,d\eta_2\right)\right] d\eta_1 + \bar{\mathbf{r}}_{,2} \cdot \left[\left(\bar{\mathbf{r}}_{,1} \times \left(\bar{\mathbf{r}}_{,12}\,d\eta_1 + \bar{\mathbf{r}}_{,22}\,d\eta_2\right)\right] d\eta_2 \\ &= -\bar{\mathbf{r}}_{,1} \cdot \left(\bar{\mathbf{r}}_{,2} \times \bar{\mathbf{r}}_{,11}\right) d\eta_1^2 + \left[-\bar{\mathbf{r}}_{,1} \cdot \left(\bar{\mathbf{r}}_{,2} \times \bar{\mathbf{r}}_{,12}\right) + \bar{\mathbf{r}}_{,2} \cdot \left(\bar{\mathbf{r}}_{,1} \times \bar{\mathbf{r}}_{,12}\right)\right] d\eta_1 d\eta_2 \\ &\qquad + \bar{\mathbf{r}}_{,2} \cdot \left(\bar{\mathbf{r}}_{,1} \times \bar{\mathbf{r}}_{,22}\right) d\eta_2^2 \\ &= -\left(\bar{\mathbf{r}}_{,11}\,d\eta_1^2 + 2\,\bar{\mathbf{r}}_{,12}\,d\eta_1 d\eta_2 + \bar{\mathbf{r}}_{,22}\,d\eta_2^2\right) \cdot \left(\bar{\mathbf{r}}_{,1} \times \bar{\mathbf{r}}_{,2}\right) \quad , \end{aligned} \tag{3.20}$$

since

$$\mathbf{a} \cdot (\mathbf{b} \times \mathbf{c}) = \mathbf{c} \cdot (\mathbf{a} \times \mathbf{b}) \quad , \tag{3.21}$$

and, from the $O(d\eta^2)$ term of equation (3.13) and the $O(1)$ term of equation (3.16),

$$O_2(d\eta^2) = \frac{1}{2}\left(\bar{\mathbf{r}}_{,11}\,d\eta_1^2 + 2\,\bar{\mathbf{r}}_{,12}\,d\eta_1 d\eta_2 + \bar{\mathbf{r}}_{,22}\,d\eta_2^2\right) \cdot \left(\bar{\mathbf{r}}_{,1} \times \bar{\mathbf{r}}_{,2}\right) \quad , \tag{3.22}$$

so that equation (3.20) becomes

$$O(d\eta^2)\ \text{term} = -\frac{1}{2}\left(\bar{\mathbf{r}}_{,11}\,d\eta_1^2 + 2\,\bar{\mathbf{r}}_{,12}\,d\eta_1 d\eta_2 + \bar{\mathbf{r}}_{,22}\,d\eta_2^2\right) \cdot \left(\bar{\mathbf{r}}_{,1} \times \bar{\mathbf{r}}_{,2}\right) \tag{3.23}$$

Hence, from equations (3.17), (3.18) and (3.23),

$$(\mathbf{r}, \mathbf{G}) = -\frac{1}{2}\left(\bar{\mathbf{r}}_{,11}\,d\eta_1^2 + 2\,\bar{\mathbf{r}}_{,12}\,d\eta_1 d\eta_2 + \bar{\mathbf{r}}_{,22}\,d\eta_2^2\right) \cdot \bar{\mathbf{G}} + O(d\eta^3) \tag{3.24}$$

From equation (3.16),

$$G = \bar{G} + (\bar{r}_{,1} \times \bar{r}_{,12} - \bar{r}_{,2} \times \bar{r}_{,11})\, d\eta_1 + (\bar{r}_{,1} \times \bar{r}_{,22} - \bar{r}_{,2} \times \bar{r}_{,12})\, d\eta_2 + O(d\eta^2)$$

$$= \bar{G} + O(d\eta) \quad , \tag{3.25}$$

$$|G|^2 = (G \cdot G)$$

$$= |\bar{G}|^2 + O(d\eta)$$

$$= |\bar{G}|^2 \left\{ 1 + O(d\eta) \right\} \quad , \tag{3.26}$$

$$|G| = |G| \left\{ 1 + O(d\eta) \right\}^{\frac{1}{2}}$$

$$= |G| + O(d\eta) \tag{3.27}$$

and

$$|G|^{-1} = |G|^{-1} + O(d\eta) \tag{3.28}$$

Hence, from equations (3.11), (3.24) and (3.28),

$$(r, n) = \left(r, \frac{G}{|G|} \right)$$

$$= (r, G)\, |G|^{-1}$$

$$= \left\{ -\frac{1}{2} (\bar{r}_{,11} d\eta_1^2 + 2\bar{r}_{,12} d\eta_1 d\eta_2 + \bar{r}_{,22} d\eta_2^2) \cdot \bar{G} + O(d\eta^3) \right\} \left\{ |\bar{G}|^{-1} + O(d\eta) \right\}$$

$$= -\frac{1}{2} (\bar{r}_{,11} d\eta_1^2 + 2\bar{r}_{,12} d\eta_1 d\eta_2 + \bar{r}_{,22} d\eta_2^2) \cdot \bar{n} + O(d\eta^3)$$

$$= O_3(d\eta^2) + O(d\eta^3)$$

On the other hand, from equation (3.13),

$$r^2 = (r, r) \tag{3.29}$$

$$= \bar{r}_{,1} \cdot \bar{r}_{,1} d\eta_1^2 + 2\bar{r}_{,1} \cdot \bar{r}_{,2} d\eta_1 d\eta_2 + \bar{r}_{,2} \cdot \bar{r}_{,2} d\eta_2^2 + O(d\eta^3) \tag{3.29}$$

$$= O_4(d\eta^2) + O(d\eta^3) \tag{3.30}$$

and

$$r = O(d\eta) \quad . \tag{3.31}$$

Hence,

$$\frac{(r, n)}{r^2} = \frac{O_3(d\eta^2)\{1 + O(d\eta)\}}{O_4(d\eta^2)\{1 + O(d\eta)\}}$$

$$= \frac{O_3(d\eta^2)}{O_4(d\eta^2)} \{1 + O(d\eta)\}$$

$$= -\frac{1}{2} \cdot \frac{(\bar{r}_{,11} d\eta_1^2 + 2\bar{r}_{,12} d\eta_1 d\eta_2 + \bar{r}_{,22} d\eta_2^2) \cdot \bar{n}}{(\bar{r}_{,1} \cdot \bar{r}_{,1} d\eta_1^2 + 2\bar{r}_{,1} \cdot \bar{r}_{,2} d\eta_1 d\eta_2 + \bar{r}_{,2} \cdot \bar{r}_{,2} d\eta_2^2)} + O(d\eta)$$

$$= \frac{K_n}{2} + O(d\eta) \tag{3.32}$$

where

$$K_n = -\frac{(\bar{r}_{,11} d\eta_1^2 + 2\bar{r}_{,12} d\eta_1 d\eta_2 + \bar{r}_{,22} d\eta_2^2) \cdot \bar{n}}{\bar{r}_{,1} \cdot \bar{r}_{,1} d\eta_1^2 + 2\bar{r}_{,1} \cdot \bar{r}_{,2} d\eta_1 d\eta_2 + \bar{r}_{,2} \cdot \bar{r}_{,2} d\eta_2^2} \tag{3.33}$$

is the normal curvature of the curved element at x_s. (See for instance [24].)

Here, K_n depends only on the direction specified by

$$\lambda = \frac{d\eta_2}{d\eta_1} \quad .$$

i.e.

$$K_n = -\frac{(\bar{r}_{,11} + 2\lambda \bar{r}_{,12} + \lambda^2 \bar{r}_{,22}) \cdot n}{\bar{r}_{,1} \cdot \bar{r}_{,1} + 2\lambda \bar{r}_{,1} \cdot \bar{r}_{,2} + \lambda^2 \bar{r}_{,2} \cdot \bar{r}_{,2}}$$

From equation (3.31) and (3.32),

$$\frac{(r, n)}{r^3} = \frac{K_n}{2} \frac{1}{r} + O(1)$$

$$\sim \frac{K_n}{2}\,\frac{1}{r} \qquad \text{for} \qquad 0 < r \ll 1 \tag{3.34}$$

Q.E.D.

Hence, for potential problems, singular integrals arising from the diagonal term of the H and G matrices are both of order

$$\int_S O(\frac{1}{r})\, dS \tag{3.35}$$

where (r, θ) are the polar coordinates on the plane tangent to the element at $\mathbf{x}_s$, and

$$O(\frac{1}{r})\, dS \sim O(\frac{1}{r})\, r\, dr\, d\theta$$

$$= O(1)\quad dr\, d\theta \tag{3.36}$$

This means that the integrals defining $g_{ee}{}^{ll}$ and $h_{ee}{}^{ll}$ in equations (3.5) and (3.6) are only weakly singular. They can be calculated efficiently using polar coordinates on the plane tangent at $\mathbf{x}_s$, as will be shown by numerical experiments in Chapter 7.

For the case when $e' = e$ but $k \neq l$, it is shown in the following that the numerators of the integral kernels also become zero at the source point $\mathbf{x}_e{}^l$, so that the integrals $g_{ee}{}^{kl}$ and $h_{ee}{}^{kl}$ have a even weaker singularity compare to $g_{ee}{}^{ll}$ and $h_{ee}{}^{ll}$. From equations (2.38) and (2.39),

$$g_{ee}^{kl} = \int_{-1}^{1}\int_{-1}^{1} \phi_e^l |G|\, u^*(\mathbf{x}, \mathbf{x}_e^k)\, d\eta_1 d\eta_2 \tag{3.37}$$

$$h_{ee}^{kl} = \int_{-1}^{1}\int_{-1}^{1} \phi_e^l |G|\, q^*(\mathbf{x}, \mathbf{x}_e^k)\, d\eta_1 d\eta_2 \tag{3.38}$$

where

$$u^*(\mathbf{x}, \mathbf{x}_e^k) = \frac{1}{4\pi r} \sim O(\frac{1}{r}) \tag{3.39}$$

$$q^*(\mathbf{x}, \mathbf{x}_e^k) = \frac{(\mathbf{r}, \mathbf{n})}{4\pi r^3} \sim O(\frac{1}{r}) \tag{3.40}$$

and

$$\mathbf{r} = \mathbf{x} - \mathbf{x}_e^k$$

Let us take, as an example, a 9-point (quadrilateral) Lagrangian element where

$$f(\eta_1, \eta_2) = \sum_{p=-1}^{1} \phi_p(\eta_1) \sum_{q=-1}^{1} \phi_q(\eta_2)\, f(p, q) \tag{3.41}$$

and

$$\phi_{-1}(\eta) = \eta\,(\eta - 1)/2$$

$$\phi_0(\eta) = 1 - \eta^2 \tag{3.42}$$

$$\phi_1(\eta) = \eta\,(\eta + 1)/2$$

and let the source $\mathbf{x}_e{}^k$ be x(0, 0). Then for $k \neq l$, $\phi_e{}^l$ in equation (3.37) and (3.38) will be of the order $O(\eta_1)$ or $O(\eta_2)$ or $O(\eta_1\eta_2)$ in the neighborhood of $\mathbf{x}_e{}^k$ = x(0, 0) and will not include a constant term. Also, in general $|\mathbf{G}| \sim O(1)$ in the neighborhood of $\mathbf{x}_e{}^k$. Hence, the kernel of the integrals in $g_{ee}{}^{kl}$, $h_{ee}{}^{kl}$ $(k \neq l)$ are either of the order $O(\eta_1/r)$, $O(\eta_2/r)$ or $O(\eta_1\eta_2/r)$.

From equation (3.30), for $\mathbf{x}_e{}^k = \mathbf{x}(0, 0)$,

$$r^2 = (\mathbf{r}, \mathbf{r}) = a_{11}\eta_1^2 + 2a_{12}\eta_1\eta_2 + a_{22}\eta_2^2 + O(\eta^3) \tag{3.43}$$

where

$$a_{11} = (\bar{\mathbf{r}}_{,1} \cdot \bar{\mathbf{r}}_{,1}), \quad a_{12} = (\bar{\mathbf{r}}_{,1} \cdot \bar{\mathbf{r}}_{,2}), \quad a_{22} = (\bar{\mathbf{r}}_{,2} \cdot \bar{\mathbf{r}}_{,2}) \tag{3.44}$$

Here,

$$\frac{\eta_1^2}{r^2} = \frac{\eta_1^2}{a_{11}\eta_1^2 + 2a_{12}\eta_1\eta_2 + a_{22}\eta_2^2 + O(\eta^3)} \tag{3.45}$$

If we let $\eta_1 = 0$ and $\eta_2 \to 0$,

$$\frac{\eta_1^2}{r^2} = \frac{0}{a_{22}\eta_2^2 + O(\eta^3)} = 0 \quad , \tag{3.46}$$

since generally $a_{22} = (\mathbf{r}_{,2} \cdot \mathbf{r}_{,2}) > 0$.

If we let $\eta_1 \neq 0$,

$$\frac{\eta_1^2}{r^2} = \frac{1}{a_{22}\lambda^2 + 2a_{12}\lambda + a_{11} + O(\eta^3)} \tag{3.47}$$

and

$$f(\lambda) = a_{22}\lambda^2 + 2a_{12}\lambda + a_{11} \quad , \tag{3.48}$$

since

$$D/4 = a_{12}^2 - a_{11}a_{22} = (\mathbf{r}_{,1} \cdot \mathbf{r}_{,2})^2 - (\mathbf{r}_{,1} \cdot \mathbf{r}_{,1})(\mathbf{r}_{,2} \cdot \mathbf{r}_{,2}) < 0 \tag{3.49}$$

(because $\mathbf{r}_{,2} \neq c\,\mathbf{r}_{,1}$),

and $a_{22} > 0$,

$$f(\lambda) > 0 \quad \text{for all } \lambda \quad . \tag{3.50}$$

Hence,

$$\frac{\eta_1^2}{r^2} = \frac{1}{f(\lambda) + O(\eta^3)} \sim O(1) \quad ,$$

so that

$$\frac{\eta_1}{r} \sim O(1) \quad . \tag{3.51}$$

Similarly,

$$\frac{\eta_2}{r} \sim O(1) \quad . \tag{3.52}$$

Similarly,

$$\left(\frac{\eta_1\eta_2}{r}\right)^2 = \frac{\eta_1^2\eta_2^2}{a_{11}\eta_1^2 + 2a_{12}\eta_1\eta_2 + a_{22}\eta_2^2 + O(\eta^3)} \quad . \tag{3.53}$$

If $\eta_1 = 0$, $\eta_2 \to 0$,

$$\frac{\eta_1\eta_2}{r} = 0 \quad .$$

If $\eta_1 \neq 0$,

$$\left(\frac{\eta_1\eta_2}{r}\right)^2 = \frac{\eta_2^2}{f(\lambda) + \dfrac{O(\eta^3)}{\eta_1^2}} \sim O(\eta_2^2) \tag{3.54}$$

Hence

$$\frac{\eta_1\eta_2}{r} \sim O(\eta_1) \sim O(r) \quad . \tag{3.55}$$

To sum up,

$$\frac{\eta_1}{r} \sim O(1), \qquad \frac{\eta_2}{r} \sim O(1), \qquad \frac{\eta_1\eta_2}{r} \sim O(r) \quad . \tag{3.56}$$

Hence, the kernel of the integrals in g_{ee}^{kl}, h_{ee}^{kl} $(k \neq l)$ are of the order $O(1)$ or $O(r)$, which means that they have a even weaker singularity compared to $O(1/r)$ for integrals in g_{ee}^{II} and h_{ee}^{II}, and will not cause any substantial difficulty when integrating them numerically.

This will also imply that, for problems where $u^* \sim O(1/r^2)$, $q^* \sim O(1/r^2)$ as in three dimensional elastostatic problems, the nondiagonal terms g_{ee}^{kl}, h_{ee}^{kl} $(k \neq l)$ can be calculated using polar coordinates around the source point $\mathbf{x}_e^k$, since for these terms

$$\phi_e^l \sim O(\eta_1, \eta_2, \eta_1\eta_2) \quad , \tag{3.57}$$

$$\frac{\phi_e^l}{r^2} \sim O\left(\frac{1}{r}\right) \text{ or } O(1) \quad , \tag{3.58}$$

so that the Jacobian r in $dS = r\,dr\,d\theta$ will cancell the singularity in ϕ_e^l / r^2 and hence in g_{ee}^{kl} and h_{ee}^{kl}, $(k \neq l)$. The diagonal terms h_{ee}^{kk} can be calculated by using the row sum elimination (rigid body motion) technique. The calculation of

g_{ee}^{kk} may require the calculation of the finite part of a hyper singular integral by, for instance, Kutt's method [10].

3.2 Hyper Singular Integrals

For problems including higher order singularity i.e. $\int_S 1/r^\alpha \, dS$ ($\alpha \geqq 2$), the singular integrals do not exist in the normal sense.

This can be illustrated by taking S as a circular disc of radius a with the source point $\mathbf{x}_s$ at its centre. (Figure 3.1) Consider now taking a smaller concentric circular disc of radius ϵ away from S and calculating the integral at the limit as $\epsilon \to 0$. This gives

$$\begin{aligned}
\int_S \frac{dS}{r^\alpha} &= \lim_{\epsilon \to 0} \int_0^{2\pi} d\theta \int_\epsilon^a \frac{1}{r^\alpha} \, r \, dr \\
&= \lim_{\epsilon \to 0} 2\pi \int_\epsilon^a \frac{dr}{r^{\alpha-1}} \\
&= \lim_{\epsilon \to 0} \begin{cases} \log a - \log \epsilon & (\alpha = 2) \\ \dfrac{1}{2-\alpha}\left(\dfrac{1}{a^{\alpha-2}} - \dfrac{1}{\epsilon^{\alpha-2}} \right) & (\alpha > 2) \end{cases} 2\pi \\
&= +\infty
\end{aligned} \tag{3.59}$$

This means that the Cauchy principal value for $\int_S 1/r^\alpha \, dS$ does not exist for $\alpha \geqq 2$. Instead, the integral must be defined by its finite part [10, 50], which corresponds to $2\pi \log a$, $(\alpha = 2)$ and $2\pi \, a^{2-\alpha}/(2-\alpha)$, $(\alpha > 2)$ respectively in equation (3.59).

Alternatively, the physical concept equivalent to rigid body motion in elasticity may be used to calculate the diagonal coefficients of the influence matrices.

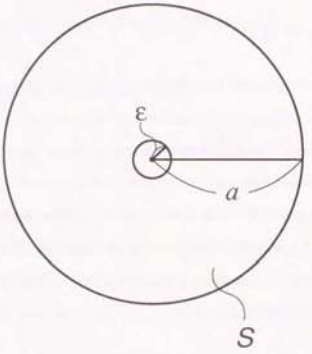

Fig.3.1 Circular disc S

For potential problems, integrals containing higher order singularities arise when calculating the derivative of the potential at a point on the element by

$$\frac{\partial u}{\partial \mathbf{x}_s} = \int_S \left(q \frac{\partial u^*}{\partial \mathbf{x}_s} - u \frac{\partial q^*}{\partial \mathbf{x}_s} \right) dS \tag{2.46}$$

where

$$\frac{\partial u^*}{\partial \mathbf{x}_s}(\mathbf{x}, \mathbf{x}_s) = \frac{1}{4\pi} \frac{\mathbf{r}}{r^3} \tag{2.47}$$

$$\frac{\partial q^*}{\partial \mathbf{x}_s}(\mathbf{x}, \mathbf{x}_s) = \frac{1}{4\pi} \left\{ \frac{\mathbf{n}}{r^3} - \frac{3\mathbf{r}(\mathbf{r}, \mathbf{n})}{r^5} \right\} \quad . \tag{2.48}$$

instead of interpolating on the boundary element. The integral of equation (2.46) does have a Cauchy principal value and can be calculated directly using a method similar to that of Gray [28] and Rudolphi et al. [51], or as a limit of a nearly singular integral by the method which will be proposed in Chapter 11.

Let the source point $\mathbf{x}_s$ be on the boundary element surface S. Since q and u in equation (2.46) generally contain constant terms q_0 and u_0 when expanded by Taylor series around the source point $\mathbf{x}_s$, the order of singularity of the integrals involved should be, roughly

$$\mathrm{I}_{\partial u^*} = \int_S q \frac{\partial u^*}{\partial \mathbf{x}_s} dS \sim \int_S O\left(\frac{1}{r^2}\right) dS \tag{3.60}$$

$$\mathrm{I}_{\partial q^*} = \int_S u \frac{\partial u^*}{\partial \mathbf{x}_s} dS \sim \int_S \left\{ O\left(\frac{1}{r^3}\right) - O\left(\frac{1}{r^2}\right) \right\} dS$$

$$\sim \int_S O\left(\frac{1}{r^3}\right) dS \quad . \tag{3.61}$$

since

$$(\mathbf{r}, \mathbf{n}) \sim \frac{K_n}{2} r^2 + O\left(r^3\right) \tag{3.62}$$

from equations (3.31) and (3.32). Hence, the apparent singularities in the integral in equation (2.46) is of order $O(1/r^2)$ and $O(1/r^3)$, suggesting that the integral does not have a finite value, which is contrary to the fact that $q \equiv \partial u/\partial n$ and $\partial u/\partial t$ ($\partial/\partial t$

: tangential derivative at $\mathbf{x}_s$ on the boundary S) usually have finite values on the boundary.

However, it will be shown in the following that the integrals $\mathrm{I}_{\partial u^*}$ and $\mathrm{I}_{\partial q^*}$ do have Cauchy principal values.

Since only the neighborhood of $\mathbf{x}_s$ is relevant, so long as the singularity is concerned, let us assume that the boundary S is smooth at $\mathbf{x}_s$ and take a local tangential planar disc S_a of radius a centered at $\mathbf{x}_s$ as shown in Fig. 3.2, and calculate the integrals $\mathrm{I}_{\partial u^*}$ and $\mathrm{I}_{\partial q^*}$ for the planar disc S_a :

$$\mathrm{I}_{\partial u^*}{}^a = \int_{S_a} q \frac{\partial u^*}{\partial \mathbf{x}_s} dS = \frac{1}{4\pi} \int_{S_a} q \frac{\mathbf{r}}{r^3} dS \tag{3.63}$$

$$\mathrm{I}_{\partial q^*}{}^a = \int_{S_a} u \frac{\partial q^*}{\partial \mathbf{x}_s} dS = \frac{1}{4\pi} \int_{S_a} u \left\{ \frac{\mathbf{n}}{r^3} - \frac{3\mathbf{r}(\mathbf{r}, \mathbf{n})}{r^5} \right\} dS \tag{3.64}$$

Cartesian coordinate (x, y, z) are introduced with the x, y, axis lying in the tangential disc with $(0, 0, 0)$ at the centre of the disc and the z-axis perpendicular to the disc towards the inside of the region (opposite to the normal $\mathbf{n}$).

For simplicity, let u and q in equation (2.46) be given by linear interpolation:

$$\begin{aligned} u &= u_0 + u_x x + u_y y \\ q &= q_0 + q_x x + q_y y \end{aligned} \tag{3.65}$$

By taking polar coordinates (ρ, θ) in the x, y plane centered at $(0, 0)$,

$$\begin{aligned} u &= u_0 + \rho (u_x \cos\theta + u_y \sin\theta) \\ q &= q_0 + \rho (q_x \cos\theta + q_y \sin\theta) \end{aligned} \tag{3.66}$$

In order to calculate the hyper singular integrals of equations (3.63), (3.64), let us assume that $\mathbf{x}_s = (0, 0, d)$ and take the limit as $d \to 0$, i.e.

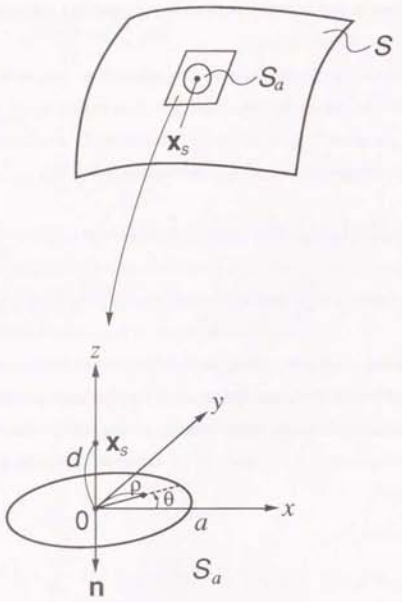

Fig.3.2 Polar coordinates (ρ,θ) on a planar disc S_a

$$\mathbf{I}_{\partial u^*}{}^a = \lim_{d \to 0} \mathbf{I}_{\partial u^*}{}^a(d) \tag{3.67}$$

and

$$I_{\partial q^*}{}^a = \lim_{d \to 0} \mathbf{I}_{\partial q^*}{}^a(d) \tag{3.68}$$

where

$$\mathbf{I}_{\partial u^*}{}^a(d) = \frac{1}{4\pi} \int_0^{2\pi} d\theta \int_0^a \left\{ q_0 + \rho\,(q_x \cos\theta + q_y \sin\theta) \right\} \frac{\mathbf{r}}{r^3}\, \rho\, d\rho$$

$$= \frac{1}{4\pi} (q_0 \mathbf{I}_{q_0} + q_x \mathbf{I}_{q_x} + q_y \mathbf{I}_{q_y}) \tag{3.69}$$

and

$$I_{\partial q^*}{}^a(d) = \frac{1}{4\pi} \int_0^{2\pi} d\theta \int_0^a \left\{ u_0 + \rho\,(u_x \cos\theta + u_y \sin\theta) \right\} \left\{ \frac{\mathbf{n}}{r^3} - \frac{3\,\mathbf{r}\,(\mathbf{r},\mathbf{n})}{r^5} \right\} \rho\, d\rho$$

$$= \frac{1}{4\pi} (u_0 + \mathbf{I}_{u_0} + u_x \mathbf{I}_{u_x} + u_y \mathbf{I}_{u_y}) \tag{3.70}$$

Noting that

$$\mathbf{r} = \mathbf{x} - \mathbf{x}_s = \begin{pmatrix} \rho\cos\theta \\ \rho\sin\theta \\ -d \end{pmatrix},$$

$$r = \sqrt{\rho^2 + d^2} \quad ,$$

$$\mathbf{n} = \begin{pmatrix} 0 \\ 0 \\ -1 \end{pmatrix},$$

and

$$(\mathbf{r}, \mathbf{n}) = d \quad , \tag{3.71}$$

we obtain

$$I_{q_0} = \int_0^{2\pi} d\theta \int_0^a \frac{\mathbf{r}}{r^3}\, \rho\, d\rho$$

$$= \int_0^a d\theta \int_0^a \frac{\begin{bmatrix} \rho^2\cos\theta \\ \rho^2\sin\theta \\ -\rho\, d \end{bmatrix}}{\sqrt{\rho^2+d^2}^{\,3}}\, d\rho$$

$$= \int_0^a \frac{\begin{bmatrix} 0 \\ 0 \\ -2\pi\rho\, d \end{bmatrix}}{\sqrt{\rho^2+d^2}^{\,3}}\, d\rho$$

$$= \begin{bmatrix} 0 \\ 0 \\ 2\pi d\left[\dfrac{1}{\sqrt{\rho^2+d^2}}\right]_0^a \end{bmatrix} = \begin{bmatrix} 0 \\ 0 \\ 2\pi\left(\dfrac{d}{\sqrt{a^2+d^2}} - 1\right) \end{bmatrix} \qquad (3.72)$$

so that

$$\lim_{d\to 0} \mathbf{I}_{q_0} = \begin{bmatrix} 0 \\ 0 \\ -2\pi \end{bmatrix} . \qquad (3.73)$$

and

$$\mathbf{I}_{q_x} = \int_0^{2\pi} d\theta \int_0^a \frac{r}{r^3}\, \rho^2\cos\theta\, d\theta$$

$$= \int_0^{2\pi} d\theta \int_0^a \frac{\begin{bmatrix} \rho\cos\theta \\ \rho\sin\theta \\ -d \end{bmatrix} \rho^2\cos\theta}{\sqrt{\rho^2+d^2}^{\,3}}\, d\rho$$

$$= \int_0^{2\pi} d\theta \int_0^a \frac{\begin{bmatrix} \rho^3\cos^2\theta \\ \rho^3\sin\theta\,\cos\theta \\ -\rho^2 d\,\cos\theta \end{bmatrix}}{\sqrt{\rho^2+d^2}^{\,3}}\, d\rho$$

$$= \int_0^a \frac{\begin{bmatrix} \pi\,\rho^3 \\ 0 \\ 0 \end{bmatrix}}{\sqrt{\rho^2+d^2}^{\,3}}\, d\rho \quad ,$$

since

$$\int_0^{2\pi} \cos^2\theta\, d\theta = \int_0^{2\pi} \frac{1+\cos 2\theta}{2}\, d\theta = \pi \qquad (3.75)$$

$$\int_0^{2\pi} \sin\theta\cos\theta\, d\theta = \int_0^{2\pi} \frac{\sin 2\theta}{2}\, d\theta = 0$$

Noting that,

$$\int_0^a \frac{\rho^3}{\sqrt{\rho^2+d^2}^{\,3}}\, d\rho = \int_0^a \left(\frac{\rho}{\sqrt{\rho^2+d^2}} - d^2 \frac{\rho}{\sqrt{\rho^2+d^2}^{\,3}} \right) d\rho \qquad (3.76)$$

$$= \left[\sqrt{\rho^2+d^2} + \frac{d^2}{\sqrt{\rho^2+d^2}} \right]_0^a$$

$$= \sqrt{a^2+d^2} + \frac{d^2}{\sqrt{a^2+d^2}} - 2d$$

$$\xrightarrow[d\to 0]{} a \quad . \qquad (3.77)$$

$$\lim_{d\to 0} \mathbf{I}_{q_x} = \begin{bmatrix} \pi a \\ 0 \\ 0 \end{bmatrix} . \qquad (3.78)$$

$$\mathbf{I}_{q_y} = \int_0^{2\pi} d\theta \int_0^a \frac{r}{r^3}\, \rho^2\sin\theta\, d\rho$$

$$= \int_0^{2\pi} d\theta \int_0^a \frac{\begin{bmatrix} \rho\cos\theta \\ \rho\sin\theta \\ -d \end{bmatrix} \rho^2\sin\theta}{\sqrt{\rho^2+d^2}^{\,3}}\, d\rho$$

$$= \int_0^{2\pi} d\theta \int_0^a \frac{\begin{pmatrix} \rho^3 \cos\theta \sin\theta \\ \rho^3 \sin^2\theta \\ -\rho^2 d \sin\theta \end{pmatrix}}{\sqrt{\rho^2+d^2}^3} \, d\rho$$

$$= \int_0^a \frac{\begin{pmatrix} 0 \\ \pi\rho^3 \\ 0 \end{pmatrix}}{\sqrt{\rho^2+d^2}^3} \, d\rho \quad , \tag{3.79}$$

since

$$\int_0^{2\pi} \sin^2\theta \, d\theta = \int_0^{2\pi} \frac{1-\cos 2\theta}{2} \, d\theta = \pi \tag{3.80}$$

Hence,

$$\lim_{d\to 0} \mathbf{I}_{q_y} = \begin{pmatrix} 0 \\ \pi \int_0^a d\rho \\ 0 \end{pmatrix} = \begin{pmatrix} 0 \\ \pi a \\ 0 \end{pmatrix} \tag{3.81}$$

From equations (3.69), (3.73), (3.78) and (3.81),

$$\mathbf{I}_{\partial u^*}{}^a = \lim_{d\to 0} \mathbf{I}_{\partial u^*}{}^a(d) = \lim_{d\to 0} \int_{S_a} u \frac{\partial q^*}{\partial \mathbf{x}_s} \, dS$$

$$= \frac{1}{4\pi} \begin{pmatrix} \pi a q_x \\ \pi a q_y \\ -\pi a q_0 \end{pmatrix} = \begin{pmatrix} \frac{a}{4} q_x \\ \frac{a}{4} q_y \\ -\frac{q_0}{2} \end{pmatrix} \tag{3.82}$$

As for $\mathbf{I}_{\partial q^*}{}^a$, since

$$\frac{\mathbf{n}}{r^3} - \frac{3\,\mathbf{r}(\mathbf{r},\mathbf{n})}{r^5} = \frac{1}{\sqrt{\rho^2+d^2}^3} \begin{pmatrix} 0 \\ 0 \\ -1 \end{pmatrix} - \frac{3d}{\sqrt{\rho^2+d^2}^5} \begin{pmatrix} \rho\cos\theta \\ \rho\sin\theta \\ -d \end{pmatrix} \tag{3.83}$$

in equation (3.70),

$$\mathbf{I}_{u_0} = \int_0^{2\pi} d\theta \int_0^a \left[\frac{\mathbf{n}}{r^3} - \frac{3\,\mathbf{r}(\mathbf{r},\mathbf{n})}{r^5} \right] \rho \, d\rho$$

$$= \begin{pmatrix} I_{u_0 x} \\ I_{u_0 y} \\ I_{u_0 z} \end{pmatrix} \tag{3.84}$$

where

$$I_{u_0 x} = -3d \int_0^{2\pi} d\theta \int_0^a \rho^2 \cos\theta \, d\rho = 0 \tag{3.85}$$

$$I_{u_0 y} = -3d \int_0^{2\pi} d\theta \int_0^a \rho^2 \sin\theta \, d\rho = 0 \tag{3.86}$$

$$I_{u_0 z} = \int_0^{2\pi} d\theta \int_0^a \left(\frac{-\rho}{\sqrt{\rho^2+d^2}^3} + \frac{3d^2\rho}{\sqrt{\rho^2+d^2}^5} \right) d\rho$$

$$= 2\pi \left[\frac{1}{\sqrt{\rho^2+d^2}} - \frac{d^2}{\sqrt{\rho^2+d^2}^3} \right]_0^a$$

$$= 2\pi \left(\frac{1}{\sqrt{a^2+d^2}} - \frac{d^2}{\sqrt{a^2+d^2}^3} - \frac{1}{d} + \frac{1}{d} \right)$$

$$= 2\pi \left(\frac{1}{\sqrt{a^2+d^2}} - \frac{d^2}{\sqrt{a^2+d^2}^3} \right) \tag{3.87}$$

Note that the singularities due to $\mathbf{n}/r^3$ and $-3\mathbf{r}(\mathbf{r},\mathbf{n})/r^5$ cancel each other out. Hence,

$$\lim_{d\to 0} \mathbf{I}_{u_0 z} = \frac{2\pi}{a} \tag{3.88}$$

and

$$\lim_{d\to 0} \mathbf{I}_{u_0} = \begin{pmatrix} 0 \\ 0 \\ \frac{2\pi}{a} \end{pmatrix} \tag{3.89}$$

Next,

$$I_{u_z} = \int_0^{2\pi} d\theta \int_0^a \left\{ \frac{n}{r^3} - \frac{3\,r\,(r,\,n)}{r^5} \right\} \rho^2 \cos\theta \; d\rho$$

$$= \begin{pmatrix} I_{u_{zx}} \\ I_{u_{zy}} \\ I_{u_{zz}} \end{pmatrix} \tag{3.90}$$

where

$$I_{u_{zx}} = -3d \int_0^{2\pi} d\theta \int_0^a \frac{\rho^3 \cos^2\theta}{\sqrt{\rho^2+d^2}^5} \; d\rho$$

$$= -3\pi d \int_0^a \frac{\rho^3}{\sqrt{\rho^2+d^2}^5} \; d\rho$$

$$= \pi \left(\frac{3d}{\sqrt{a^2+d^2}} - \frac{d^3}{\sqrt{a^2+d^2}^3} + 2 \right) \quad . \tag{3.91}$$

since

$$\int_0^a \frac{\rho^3}{\sqrt{\rho^2+d^2}^5} \, d\rho = \int_0^a \left(\frac{\rho}{\sqrt{\rho^2+d^2}^3} - \frac{d^2\rho}{\sqrt{\rho^2+d^2}^5} \right) d\rho$$

$$= \left[-\frac{1}{\sqrt{\rho^2+d^2}} + \frac{d^2}{3} \frac{1}{\sqrt{\rho^2+d^2}^3} \right]_0^a$$

$$= -\frac{1}{\sqrt{a^2+d^2}} + \frac{d^2}{3} \frac{1}{\sqrt{a^2+d^2}^3} - \frac{2}{3d} \quad . \tag{3.92}$$

Hence,

$$\lim_{d \to 0} I_{u_{zx}} = 2\pi \quad . \tag{3.93}$$

Noting that,

$$I_{u_{xy}} = -3d \int_0^{2\pi} d\theta \int_0^a \frac{\rho^3 \sin\theta \cos\theta}{\sqrt{\rho^2+d^2}^5} \; d\rho = 0 \tag{3.94}$$

$$I_{u_{xz}} = \int_0^{2\pi} d\theta \int_0^a \left(-\frac{\rho^2 \cos\theta}{\sqrt{\rho^2+d^2}^3} + \frac{3d^2\rho^2\cos\theta}{\sqrt{\rho^2+d^2}^5} \right) d\rho = 0 \quad , \tag{3.95}$$

we have

$$\lim_{d \to 0} I_{u_x} = \begin{pmatrix} 2\pi \\ 0 \\ 0 \end{pmatrix} \tag{3.93}$$

Similarly,

$$I_{u_y} = \int_0^{2\pi} d\theta \int_0^a \left\{ \frac{n}{r^3} - \frac{3\,r\,(r,\,n)}{r^5} \right\} \rho^2 \sin\theta \; d\rho$$

$$= \begin{pmatrix} I_{u_{yx}} \\ I_{u_{yy}} \\ I_{u_{yz}} \end{pmatrix} \quad , \tag{3.97}$$

where

$$I_{u_{yx}} = -3d \int_0^{2\pi} d\theta \int_0^a \frac{\rho^3 \sin\theta \cos\theta}{\sqrt{\rho^2+d^2}^5} \, d\rho = 0 \tag{3.98}$$

$$I_{u_{yy}} = -3d \int_0^{2\pi} d\theta \int_0^a \frac{\rho^3 \sin\theta}{\sqrt{\rho^2+d^2}^5} \, d\rho = -3\pi d \int_0^{2\pi} \frac{\rho^3}{\sqrt{\rho^2+d^2}^5} \, d\rho$$

$$= \pi \left(\frac{3d}{\sqrt{a^2+d^2}} - \frac{d^3}{\sqrt{a^2+d^2}^3} + 2 \right) \quad . \tag{3.99}$$

which gives

$$\lim_{d \to 0} I_{u_{yy}} = 2\pi \quad . \tag{3.100}$$

and

$$I_{u_{yz}} = \int_0^{2\pi} d\theta \int_0^a \left(-\frac{\rho^2 \sin\theta}{\sqrt{\rho^2+d^2}^3} + \frac{3d^2\rho^2\sin\theta}{\sqrt{\rho^2+d^2}^5} \right) d\rho = 0 \tag{3.101}$$

Hence ,

$$\lim_{d\to 0} \mathbf{I}_{u_y} = \begin{pmatrix} 0 \\ 2\pi \\ 0 \end{pmatrix} \tag{3.102}$$

From equations (3.70), (3.89), (3.96) and (3.102),

$$\mathbf{I}_{\partial q^*}{}^{a} = \frac{1}{4\pi} \begin{pmatrix} 2\pi u_x \\ 2\pi u_y \\ \frac{2\pi}{a} u_o \end{pmatrix} = \begin{pmatrix} \frac{u_x}{2} \\ \frac{u_y}{2} \\ \frac{u_o}{2a} \end{pmatrix} \tag{3.103}$$

To sum up, for the linear interpolation

$$u = u_o + u_x x + u_y y$$

$$q = q_o + q_x x + q_y y \quad , \tag{3.65}$$

$$\mathbf{I}_{\partial u^*}{}^{a} = \int_{S_a} q \frac{\partial u^*}{\partial \mathbf{x}_s} \mathrm{d}S = \frac{1}{4\pi} \int_{S_a} q \frac{\mathbf{r}}{r^3} \mathrm{d}S$$

$$= \begin{pmatrix} \frac{a q_x}{4} \\ \frac{a q_y}{4} \\ -\frac{q_o}{2} \end{pmatrix} \tag{3.104}$$

and

$$\mathbf{I}_{\partial q^*}{}^{a} = \int_{S_a} u \frac{\partial q^*}{\partial \mathbf{x}_s} \mathrm{d}S = \frac{1}{4\pi} \int_{S_a} u \left\{ \frac{\mathbf{n}}{r^3} - \frac{3\,\mathbf{r}\,(\mathbf{r},\mathbf{n})}{r^5} \right\} \mathrm{d}S$$

$$= \begin{pmatrix} \frac{u_x}{2} \\ \frac{u_y}{2} \\ \frac{u_o}{2a} \end{pmatrix} \tag{3.105}$$

Hence, the contribution of the integration in the local disc S_a including $\mathbf{x}_s$, to the singular integral of equation (2.46), which give the potential derivative $\partial u/\partial \mathbf{x}_s$ at $\mathbf{x}_s$ is

$$\left.\frac{\partial u}{\partial \mathbf{x}_s}\right|_{S_a} = \mathbf{I}_{\partial u^*}{}^{a} - \mathbf{I}_{\partial q^*}{}^{a} = \begin{pmatrix} \frac{a q_x}{4} - \frac{u_x}{2} \\ \frac{a q_y}{4} - \frac{u_y}{2} \\ -\frac{q_o}{2} - \frac{u_o}{2a} \end{pmatrix} , \tag{3.106}$$

which is finite. Since the integral for the boundary surface S excluding S_a is finite, the integral

$$\frac{\partial u}{\partial \mathbf{x}_s} = \int_S \left(q \frac{\partial u^*}{\partial \mathbf{x}_s} - u \frac{\partial q^*}{\partial \mathbf{x}_s} \right) \mathrm{d}S \quad , \quad \mathbf{x}_s \in S \tag{3.107}$$

gives a finite value (Cauchy principal value) when calculated in the above manner, although the integral kernel has an apparent hyper singularity of order $O(1/r^2) \sim O(1/r^3)$, as seen in equations (3.60) and (3.61).

This is reasonable since, physically, one would expect finite values for $\partial u/\partial \mathbf{x}_s$ from the interpolation of u, $\partial u/\partial n$, $\partial u/\partial t$ in the boundary S, where $d=0$.

3.3 Nearly Singular Integrals

When the source point is very near the surface, the integrals g_e^{sl}, h_e^{sl} of equations (2.50) and (2.51), and $\mathbf{a}_e^{sl}$, $\mathbf{b}_e^{sl}$ of equations (2.54) and (2.55) have finite values. But it is difficult to calculate them accurately and efficiently using the standard Gauss-Legendre product formula, since the value of the kernels vary very rapidly near the source point $\mathbf{x}_s$. In fact the nearly singular integrals

($0<d\ll 1$) turn out to be more difficult to calculate than the singular integrals ($d=0$).

The accurate calculation of these nearly singular integrals is of practical importance in boundary element codes. They may arise when calculating the H and G matrices in cases where the elements are very close to each other, when using discontinuous elements, or when it is necessary to calculate the potential and its gradients at a point very near the boundary. Good examples are the analysis of electron guns which have complex geometry and thin structures, or the analysis of electromagnetic fields in thin gaps arising in motors, to name a few.

To understand the problem, let us examine the nature of the near singularity ($0<d\ll 1$) in comparison with singularity ($d=0$), for the integral kernels u^*, q^*, $\partial u^*/\partial \mathbf{x}_s$ and $\partial q^*/\partial \mathbf{x}_s$, which occur in three dimensional potential problems.

Let $\bar{\mathbf{x}}_s$ be the nearest point on the curved boundary element S to the source point $\mathbf{x}_s$, and let the distance be

$$d = |\mathbf{x}_s - \bar{\mathbf{x}}_s| \tag{3.108}$$

as shown in Fig. 3.3. $\bar{\mathbf{x}}_s$ will be called the source projection.

In general, $\mathbf{r}/r$ is a unit vector.

Hence,

$$\left(\frac{\mathbf{r}}{r}, \mathbf{n}\right) = \cos\theta_{rn} \tag{3.109}$$

where θ_{rn} is the angle between $\mathbf{r}$ and $\mathbf{n}$ as shown in Fig. 3.4, so that

$$u^* = \frac{1}{4\pi r} \tag{3.110}$$

$$q^* = -\frac{1}{4\pi}\frac{(\mathbf{r}, \mathbf{n})}{r^3} = -\frac{1}{4\pi}\frac{\cos\theta_{rn}}{r^2} \tag{3.111}$$

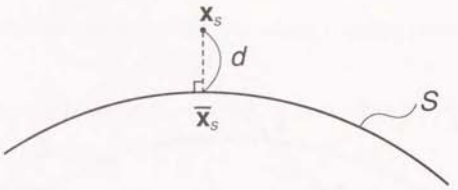

Fig.3.3 Source projection $\bar{\mathbf{x}}_S$ and source distance d

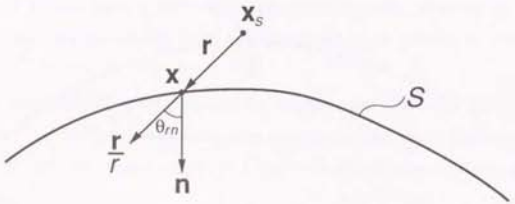

Fig.3.4 Angle θ_{rn} between **r** and **n**

$$\frac{\partial u^*}{\partial \mathbf{x}_s} = \frac{1}{4\pi}\frac{\mathbf{r}}{r^3} = \frac{1}{4\pi}\frac{1}{r^3}\left(\frac{\mathbf{r}}{r}\right) \tag{3.112}$$

$$\frac{\partial q^*}{\partial \mathbf{x}_s} = \frac{1}{4\pi}\left[\frac{\mathbf{n}}{r^3} - \frac{3\,(\mathbf{r},\mathbf{n})\,\mathbf{r}}{r^5}\right]$$

$$= \frac{1}{4\pi}\left[\frac{\mathbf{n}}{r^3} - \frac{3\cos\theta_{rn}}{r^3}\,\frac{\mathbf{r}}{r}\right] \tag{3.113}$$

Now let us examine the behaviour of these kernels when the limit of $\mathbf{x} \to \mathbf{x}_s$ is taken.

For the singular case ($d=0$), since $\hat{\mathbf{x}}_s = \mathbf{x}_s$, taking the limit of $\mathbf{x} \to \mathbf{x}_s$ i.e. $r \to 0$,

$$\frac{\mathbf{r}}{r} \to \mathbf{t}$$

where $\mathbf{t}$ is the unit tangent vector in the direction of $\mathbf{r}$ (as $r \to 0$), as shown in Fig. 3.5. Since,

$$\cos\theta_{rn} = \frac{(\mathbf{r},\mathbf{n})}{r} \to \frac{K_n}{2}\,r \tag{3.114}$$

from equation (3.10),

$$q^* \to -\frac{1}{4\pi}\,\frac{K_n}{2}\,\frac{1}{r} \tag{3.115}$$

$$\frac{\partial u^*}{\partial \mathbf{x}_s} \to \frac{1}{4\pi}\,\frac{\mathbf{t}}{r^2} \tag{3.116}$$

$$\frac{\partial q^*}{\partial \mathbf{x}_s} \to \frac{1}{4\pi}\left(\frac{\mathbf{n}}{r^3} - \frac{3}{2}\,K_n\,\frac{\mathbf{t}}{r^2}\right) \tag{3.117}$$

For the nearly singular case ($0<d\ll 1$), taking the limit of $\mathbf{x} \to \mathbf{x}_s$, i.e. $r \to d$,

$$\frac{\mathbf{r}}{r} \to \mathbf{n} \tag{3.118}$$

$$\cos\theta_{rn} \to 1 \tag{3.119}$$

as shown in Fig. 3.6.

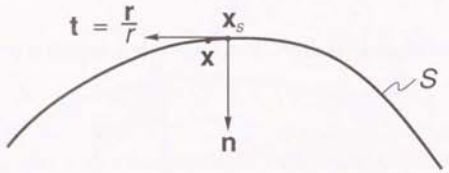

Fig.3.5 $\frac{\mathbf{r}}{r} \sim \mathbf{t}$ (singular case)

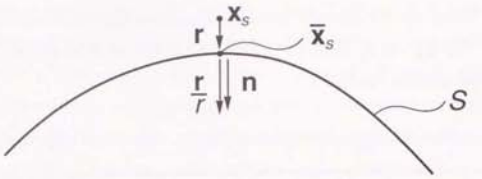

Fig.3.6 $\frac{\mathbf{r}}{r} \sim \mathbf{n}$ (nearly singular case)

Hence,

$$q^* \to -\frac{1}{4\pi}\frac{1}{r^2} \tag{3.120}$$

$$\frac{\partial u^*}{\partial \mathbf{x}_s} \to \frac{1}{4\pi}\frac{\mathbf{n}}{r^2} \tag{3.121}$$

$$\frac{\partial q^*}{\partial \mathbf{x}_s} \to \frac{1}{4\pi}\left(\frac{\mathbf{n}}{r^3} - \frac{3}{r^3}\mathbf{n}\right) = \frac{1}{4\pi}\left(-\frac{2\mathbf{n}}{r^3}\right) \tag{3.122}$$

To sum up, the nature of the singular and near singular kernels in the limit of $\mathbf{x} \to \bar{\mathbf{x}}_s$ is given in Table 3.1. Notice the difference of the nature of singular and near singular kernels.

Table 3.1 Nature of (near) singularity near source projection $\bar{\mathbf{x}}_s$

	singular $d=0$	near singular $0<d\ll 1$
$4\pi\ u^*$	$1/r$	$1/r$
$4\pi\ q^*$	$-K_n/(2r)$	$-1/r^2$
$4\pi\ \partial u^*/\partial \mathbf{x}_s$	$\mathbf{t}/r^2$	$\mathbf{n}/r^2$
$4\pi\ \partial q^*/\partial \mathbf{x}_s$	$\mathbf{n}/r^3 - 3/2\ K_n\ \mathbf{t}/r^2$	$-2\ \mathbf{n}/r^3$

For the singular case ($d=0$), u^* and q^* are of order $O(1/r)$ and the integrals are weakly singular in the sense that the singularity is cancelled by the Jacobian of the polar coordinate system centered at $\mathbf{x}_s$, i.e. $dS \sim O(r)\,dr\,d\theta$.

Integrals containing $\partial u^*/\partial \mathbf{x}_s$, $\partial q^*/\partial \mathbf{x}_s$ are hyper singular in the sense that the order of singularity is $O(1/r^2)$ and $O(1/r^3)$ respectively and the singularity cannot be cancelled by the Jacobian $O(r)$ of the polar coordinates. However, as shown in equations (3.104) and (3.105), these hyper singular integrals render finite values (Cauchy principal value), which can be calculated using polar coordinates centered at $\mathbf{x}_s$ on the plane tangent to S at $\mathbf{x}_s$.

For the nearly singular case ($0<d\ll 1$), the order of near singularity in the limit as $\mathbf{x} \to \bar{\mathbf{x}}_s$ is $1/r^{\alpha}$, ($\alpha=1\sim3$). However, as will be seen from numerical results in Chapter 7, the nature of the integral kernel at the limit of $\mathbf{x} \to \bar{\mathbf{x}}_s$ alone, does not explain the difficulty in integrating these near singular kernels numerically, using the log-L_2 transformation which will be proposed in Chapter 5. For instance, for a given source distance d, ($0<d\ll 1$), a given accuracy requirement ε, the integration of $\int_S \partial u^*/\partial \mathbf{x}_s\,dS$ and $\int_S \partial q^*/\partial \mathbf{x}_s\,dS$ related to the potential derivative $\partial u/\partial \mathbf{x}_s$, requires far more integration points compared to the integration of $\int_S u^*\,dS$ and $\int_S q^*\,dS$ related to the potential $u(\mathbf{x}_s)$, when the log-L_2 transformation is used. Looking at the nature of near singular kernels in the limit of $\mathbf{x} \to \bar{\mathbf{x}}_s$ (Table 3.1), this seems odd, since the order of near singularity for q^* and $\partial u^*/\partial \mathbf{x}_s$ are both $O(1/r^2)$, and one would expect that they can be integrated numerically with more or less the same number of integration points to obtain the same accuracy (relative error).

In order to explain the behaviour of the near singular kernels in numerical integration, it is necessary to consider not only the local behaviour of the kernels in the limit of $\mathbf{x} \to \bar{\mathbf{x}}_s$, but also the global behaviour of the kernels around $\mathbf{x} = \bar{\mathbf{x}}_s$ and in the total integration region S.

To do so, consider the case when the boundary element S is planar. Let the source point be $\mathbf{x}_s = (0, 0, d)$, where (x, y, z) are Cartesian coordinates. The planar element S lies in the xy-plane and the source projection is $\bar{\mathbf{x}}_s = (0, 0, 0)$, as shown in Fig. 3.7.

Taking polar coordinates (ρ, θ) in the xy-plane centred at $\bar{\mathbf{x}}_s$, the near singular kernels u^*, q^*, $\partial u^*/\partial \mathbf{x}_s$, $\partial q^*/\partial \mathbf{x}_s$ of equations (2.4), (2.7), (2.47) and (2.48) for three dimensional potential problems can be expressed as follows:

Noting that,

$$\mathbf{r} = \begin{pmatrix} \rho\cos\theta \\ \rho\sin\theta \\ -d \end{pmatrix} \tag{3.123}$$

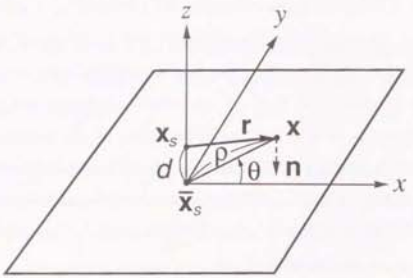

Fig.3.7 The planar element S

$$\mathbf{n} = \begin{pmatrix} 0 \\ 0 \\ -1 \end{pmatrix} \tag{3.124}$$

$$r = \sqrt{\rho^2 + d^2} \tag{3.125}$$

$$(\mathbf{r}, \mathbf{n}) = d \quad , \tag{3.126}$$

one obtains ,

$$u^* = \frac{1}{4\pi r} \tag{3.127}$$

$$q^* = -\frac{(\mathbf{r}, \mathbf{n})}{4\pi r^3} = -\frac{1}{4\pi}\frac{d}{r^3} \quad , \tag{3.128}$$

and

$$\frac{\partial u^*}{\partial \mathbf{x}_s} = \frac{1}{4\pi}\frac{\mathbf{r}}{r^3} = \frac{1}{4\pi}\begin{pmatrix} \frac{\rho\cos\theta}{r^3} \\ \frac{\rho\sin\theta}{r^3} \\ -\frac{d}{r^3} \end{pmatrix} , \tag{3.129}$$

$$\frac{\partial q^*}{\partial \mathbf{x}_s} = \frac{1}{4\pi}\left\{\frac{\mathbf{n}}{r^3} - \frac{3\,\mathbf{r}\,(\mathbf{r}, \mathbf{n})}{r^5}\right\}$$

$$= \frac{1}{4\pi}\begin{pmatrix} 0 - 3d\,\frac{\rho\cos\theta}{r^5} \\ 0 - 3d\,\frac{\rho\sin\theta}{r^5} \\ -\frac{1}{r^3} + 3d^2\,\frac{1}{r^5} \end{pmatrix} . \tag{3.130}$$

Since the (near) singularity is determined by the radial (ρ) component, we may neglect the angular (θ) component when discussing the nature of near singularity. Also, since for a planar element ($\mathbf{r}, \mathbf{n}$) = d is constant, the nature of

near singularity of the kernels u^*, q^* $\partial u^*/\partial x_s$, $\partial q^*/\partial x_s$ can be summarized as in Table 3.2.

Table 3.2 Nature of near singularity $(0<d\ll 1)$ for 3-D potential problems (planar element)

	Order of near singularity
u^*	$1/r$
q^*	$1/r^3$
$\partial u^*/\partial x_s$	$1/r^3$, ρ/r^3
$\partial q^*/\partial x_s$	$1/r^3$, $1/r^5$, ρ/r^5

Although the above analysis of near singularity was done for planar elements, it can be considered that the essential nature of near singularity for general curved elements is the same, since near singularity is dominant in the neighborhood of $\bar{x}_s$, where

$$(r, n) \sim d \tag{3.131}$$

Hence, the relative difficulty of numerically integrating $\int_S \partial u^*/\partial x_s \, dS$ and $\int_S \partial q^*/\partial x_s \, dS$, compared to $\int_S u^* \, dS$ and $\int_S q^* \, dS$, using the log-L_2 transformation, can be explained by the presence of kernels ρ/r^3 and ρ/r^5 in the first two integrals.

(cf. Chapter 5~7, 10)

For a constant planar element S,

$$I = \int_S F \, dS = \int_0^{2\pi} d\theta \int_0^{\rho_{\max}(\theta)} F \rho \, d\rho \tag{3.132}$$

where (ρ, θ) are the polar coordinates centered a the source projection $\hat{x}_s$ in S and $\rho_{\max}(\theta)$ is defined as in Fig. 3.8 .

Hence, the near singular integrals in three dimensional potential problems involving the kernels u^*, q^*, $\partial u^*/\partial x_s$ and $\partial q^*/\partial x_s$ in Table 3.2 can be expressed as

$$I = \int_0^{2\pi} d\theta \int_0^{\rho_{\max}(\theta)} \frac{\rho^\delta}{r^\alpha} d\rho \tag{3.133}$$

where $\alpha = 1, 3, 5$ and $\delta = 1, 2$ and

$$r = \sqrt{\rho^2 + d^2} \quad , \tag{3.134}$$

since S is a planar element.

Since the near singularity is essentially due to the radial component, consider the radial component of the integral in equation (3.133) :

$$J = \int_0^{\rho_{\max}} F \rho \, d\rho = \int_0^{\rho_{\max}} f(\rho) \, d\rho \tag{3.135}$$

where

$$\begin{aligned}
f(\rho) = \quad f_1(\rho) &= \frac{\rho}{r} = \frac{\rho}{\sqrt{\rho^2+d^2}} \\
f_3(\rho) &= \frac{\rho}{r^3} = \frac{\rho}{\sqrt{\rho^2+d^2}^3} \\
f_{3,2}(\rho) &= \frac{\rho^2}{r^3} = \frac{\rho^2}{\sqrt{\rho^2+d^2}^3} \\
f_5(\rho) &= \frac{\rho}{r^5} = \frac{\rho}{\sqrt{\rho^2+d^2}^5} \\
f_{5,2}(\rho) &= \frac{\rho^2}{r^5} = \frac{\rho^2}{\sqrt{\rho^2+d^2}^5}
\end{aligned} \tag{3.136}$$

so that, essentially, the nature of near singularity of the radial component of integrals containing the kernels u^*, q^*, $\partial u^*/\partial x_s$, $\partial q^*/\partial x_s$ is given by Table 3.3.

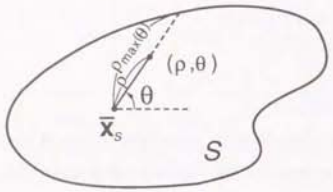

Fig.3.8 Definition of $\rho_{max}(\theta)$ for a planar element S

Table 3.3 Nature of near singular kernels of the radial component integrals in 3-D potential problems

	Order of near singularity
u^*	ρ/r
q^*	ρ/r^3
$\partial u^* / \partial x_s$	ρ/r^3, ρ^2/r^3
$\partial q^* / \partial x_s$	ρ/r^3, ρ/r^5, ρ^2/r^5

The graphs of the near singular kernels f_1, f_3, $f_{3,2}$, f_5 and $f_{5,2}$ of the radial component integrals are given in Figures 3.9 to 3.13. The characteristic feature of the kernels $f_{3,2}$ and $f_{5,2}$, which appear in the calculation of the flux $\partial u/\partial x_s$, is that

$$\frac{d f_{3,2}}{d \rho} = \frac{d f_{5,2}}{d \rho} = 0 \qquad (3.137)$$

For planar elements, the radial component integral of equation (6.135) for the kernel functions f_1, f_3, $f_{3,2}$, f_5 and $f_{5,2}$ of equation (6.136) can be expressed in closed form as follows:

$$\begin{aligned} J_1 &= \int_0^{\rho_{max}} \frac{\rho}{r} \, d\rho \\ &= \left[\sqrt{\rho^2 + d^2} \right]_0^{\rho_{max}} \\ &= \sqrt{\rho_{max}^2 + d^2} - d \end{aligned} \qquad (3.138)$$

$$J_3 = \int_0^{\rho_{max}} \frac{\rho}{r^3}\, d\rho$$

$$= \left| -\frac{1}{\sqrt{\rho^2 + d^2}} \right|_0^{\rho_{max}}$$

$$= \frac{1}{d} - \frac{1}{\sqrt{\rho_{max}^2 + d^2}}$$

$$J_{3,2} = \int_0^{\rho_{max}} \frac{\rho^2}{r^3}\, d\rho$$

$$= \left| \log\left(\rho + \sqrt{\rho^2 + d^2}\right) - \frac{\rho}{\sqrt{\rho^2 + d^2}} \right|_0^{\rho_{max}}$$

$$= \log\left(\rho_{max} + \sqrt{\rho_{max}^2 + d^2}\right) - \frac{\rho_{max}}{\sqrt{\rho_{max}^2 + d^2}} - \log d \qquad (3.140)$$

$$J_5 = \int_0^{\rho_{max}} \frac{\rho}{r^5}\, d\rho$$

$$= \left| -\frac{1}{3}\frac{1}{\sqrt{\rho^2 + d^2}^3} \right|_0^{\rho_{max}}$$

$$= \frac{1}{3}\left(\frac{1}{d^3} - \frac{1}{\sqrt{\rho_{max}^2 + d^2}^3}\right) \qquad (3.141)$$

$$J_{5,2} = \int_0^{\rho_{max}} \frac{\rho^2}{r^5}\, d\rho$$

$$= \left| \frac{\rho^3}{3d^2\sqrt{\rho^2 + d^2}^3} \right|_0^{\rho_{max}}$$

$$= \frac{\rho_{max}^3}{3d^2\sqrt{\rho_{max}^2 + d^2}^3} \qquad (3.142)$$

These closed form integrals are useful for performing the integration in the radial variable analytically for planar elements, as will be mentioned in Chapter 5. They are also useful in checking numerical integration methods for the radial variable, and will be used in Chapter 10.

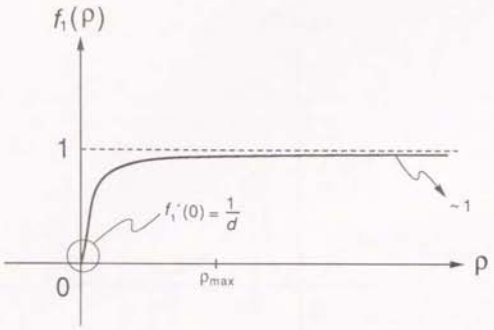

Fig.3.9 Graph of $f_1 = \dfrac{\rho}{\sqrt{\rho^2+d^2}}$

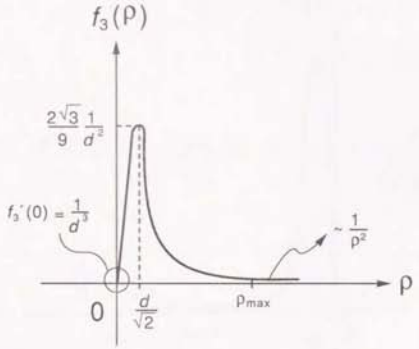

Fig.3.10 Graph of $f_3 = \dfrac{\rho}{\sqrt{\rho^2+d^2}^3}$

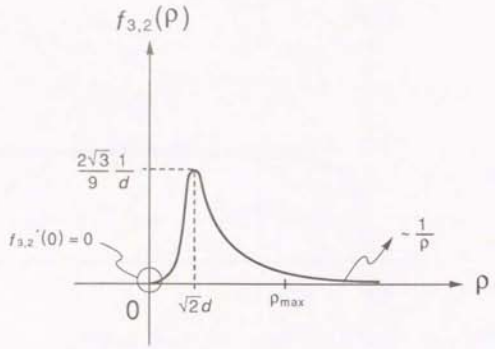

Fig.3.11 Graph of $f_{3,2} = \dfrac{\rho^2}{\sqrt{\rho^2+d^2}^3}$

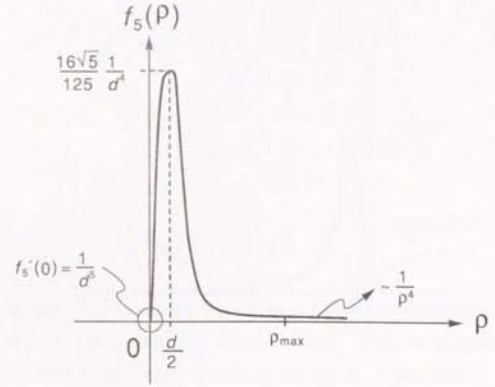

Fig.3.12 Graph of $f_5 = \dfrac{\rho}{\sqrt{\rho^2+d^2}^5}$

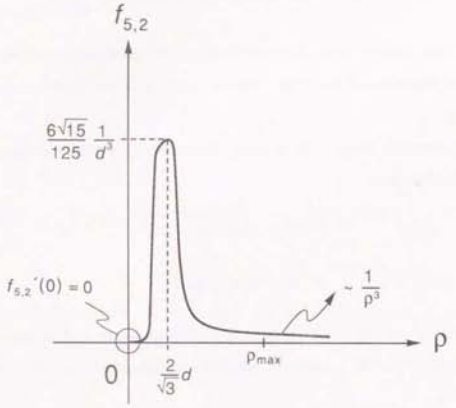

Fig.3.13 Graph of $f_{5,2} = \dfrac{\rho^2}{\sqrt{\rho^2+d^2}^5}$

CHAPTER 4

SURVEY OF QUADRATURE METHODS FOR 3-D BOUNDARY ELEMENT INTEGRALS

In this chapter we shall review some of the quadrature methods related to the three dimensional boundary element method in the literature according to Table 1.1.

As shown in Chapter 2, in three dimensional boundary element analysis, integrals of the form

$$g_{e}^{k\,l} = \int_{-1}^{1}\int_{-1}^{1} \phi_e^l\,|\mathrm{G}|\; u^*(\mathbf{x},\mathbf{x}_e^k)\,d\eta_1\,d\eta_2 \tag{4.1}$$

$$h_{e}^{k\,l} = \int_{-1}^{1}\int_{-1}^{1} \phi_e^l\,|\mathrm{G}|\; q^*(\mathbf{x},\mathbf{x}_e^k)\,d\eta_1\,d\eta_2 \tag{4.2}$$

are necessary for the calculation of H and G matrices and potential u at an internal point. For the potential gradient $\partial u/\partial \mathbf{x}_s$ at an internal point $\mathbf{x}_s$, integrals of the form

$$a_{e}^{sl} = \int_{-1}^{1}\int_{-1}^{1} \phi_e^l\,|\mathrm{G}|\,\frac{\partial u^*}{\partial \mathbf{x}_s}\,d\eta_1\,d\eta_2 \tag{4.3}$$

$$b_{e}^{sl} = \int_{-1}^{1}\int_{-1}^{1} \phi_e^l\,|\mathrm{G}|\,\frac{\partial q^*}{\partial \mathbf{x}_s}\,d\eta_1\,d\eta_2 \tag{4.4}$$

become necessary.

Here $\phi_e^l(\eta_1, \eta_2)$ is the interpolation function corresponding to node $\mathbf{x}_e^l$, and is a polynomial of (η_1, η_2). The field point $\mathbf{x}$ on the boundary element e is given by

$$\mathbf{x}(\eta_1,\eta_2) = \sum_{l=1}^{n_e} \phi_e^l(\eta_1,\eta_2)\,\mathbf{x}_e^l \tag{4.5}$$

where $\mathbf{x}_e^l$, $(l=1\sim n_e)$ are the coordinates of the nodes belonging to the element S_e. The Jacobian of the transformation $\mathbf{x}(\eta_1, \eta_2)$ is given by

$$\mathrm{G} = (g_1, g_2, g_3)^{\mathrm{T}} = \frac{\partial \mathbf{x}}{\partial \eta_1} \times \frac{\partial \mathbf{x}}{\partial \eta_2} \tag{4.6}$$

$$|\mathrm{G}| = \sqrt{g_1^2 + g_2^2 + g_3^2} \tag{4.7}$$

For potential problems,

$$u^*(\mathbf{x},\mathbf{x}_s) = \frac{1}{4\pi r} \tag{4.8}$$

$$q^*(\mathbf{x},\mathbf{x}_s) = -\frac{1}{4\pi}\,\frac{(\mathbf{r},\mathbf{n})}{r^3} \tag{4.9}$$

and

$$\frac{\partial u^*}{\partial \mathbf{x}_s}(\mathbf{x},\mathbf{x}_s) = \frac{1}{4\pi}\,\frac{\mathbf{r}}{r^3} \tag{4.10}$$

$$\frac{\partial q^*}{\partial \mathbf{x}_s}(\mathbf{x},\mathbf{x}_s) = \frac{1}{4\pi}\left\{\frac{\mathbf{n}}{r^3} - \frac{3\mathbf{r}(\mathbf{r},\mathbf{n})}{r^5}\right\} \tag{4.11}$$

where

$$\mathbf{r} = (r_1, r_2, r_3)^{\mathrm{T}} = \mathbf{x} - \mathbf{x}_s = \sum_{l=1}^{n_e} \phi_e^l(\eta_1,\eta_2)\,\mathbf{x}_e^l - \mathbf{x}_s \tag{4.12}$$

$$r = |\mathbf{r}| = \sqrt{r_1^2 + r_2^2 + r_3^2} \tag{4.13}$$

4.1 Closed Form Integrals

Closed form or analytical integration formulas for equations (4.1)~(4.4) are available for constant planar triangular elements [1], planar parallelograms [6] and for planar triangular elements with higher order interpolation functions [2, 29], in the case of potential problems.

However, for general curved elements with constant or higher order interpolation functions, it seems impossible to derive closed form integrals for equation (4.1)~(4.4), let alone for potential problems. The main reason for this is that the integrands include $1/r^{\alpha}$, $(\alpha=1\sim5)$ and $|\mathrm{G}|$, where r and $|\mathrm{G}|$ are given by the square root of a general polynomial of (η_1, η_2), the order of which is higher

than 4 for η_1 and η_2 respectively, for general curved elements which are expressed by quadratic or higher order polynomials $\phi_e{}^j(\eta_1, \eta_2)$ in equation (4.5).

4.2 Gaussian Quadrature Formula

Since closed form integrals are not available, numerical quadrature schemes must be employed for general curved elements.

Let us consider a one dimensional integral

$$I = \int_a^b f(x)\,dx \tag{4.14}$$

Numerical integration formulas for (4.14) is given in the form

$$I \sim I_A = \sum_{j=1}^{n} w_i\, f(x_i) \tag{4.15}$$

where x_i and w_i are the position and weight of the i-th integration point, respectively. The Gaussian quadrature formula [3] is known to give optimum results, so long as $f(x)$ does not include any singularity or near singularity. The formula is derived in the following manner. Let $a=-1$, $b=1$ and

$$E_n(f) = \int_{-1}^{1} f(x)\,dx - \sum_{j=1}^{n} w_j\, f(x_i) \tag{4.16}$$

The weights $\{w_i\}$ and positions $\{x_i\}$ are determined to make the error $E_n(f) = 0$ for as high a degree polynomial $f(x)$ as possible. Since,

$$E_n\Big(\sum_{j=1}^{n} a_j x^j\Big) = \sum_{j=1}^{n} a_j\, E_n(x^j) \tag{4.17}$$

$E_n(f)=0$ for every polynomial of degree $\leq m$ if and only if $E_n(x^j)=0$; $i=0, 1, \cdots, m$. Since the formula has $2n$ free parameters $\{x_i\}$ and $\{w_i\}$, the equation

$$E_n(x^j) = 0 \quad j = 0, 1, \cdots, 2n-1 \tag{4.18}$$

is solved to obtain $\{x_i\}$ and $\{w_i\}$, $i = 1 \sim n$.

It turns out that equation (4.18) is satisfied if $x_1, \cdots, x_n$ are taken as the zero points

$$P_n(x_i) = 0 \qquad (i = 1, 2, \cdots, n) \tag{4.19}$$

of the Legendre polynomial :

$$P_n(x) = \frac{1}{2^n\, n!}\,\frac{d^n\,(x^2-1)^n}{dx^n} \tag{4.20}$$

and

$$w_i = \frac{2}{n P_n'(x_i)\, P_{n-1}(x_i)} \qquad (i = 1, 2, \cdots, n) \tag{4.21}$$

The table for the Gauss-Legendre quadrature formula is given in [3], and an efficient algorithm for generating the table has been proposed by Golub and Welsch [38].

The error for the Gauss-Legendre quadrature formula when applied to a function $f(x)$ defined in the interval $x \in [-1, 1]$ is given by

$$E_n(f) = \frac{2^{2n+1}(n!)^4}{(2n+1)\,[(2n)!]^3}\, f^{(2n)}(\eta) \tag{4.22}$$

for some $-1<\eta<1$. [3,33]

For integration over the interval $[a, b]$, equation (4.22) can be applied to

$$\int_a^b f(t)\,dt = \frac{b-a}{2}\int_{-1}^{1} f\left[\frac{a+b+x(b-a)}{2}\right] dx \tag{4.23}$$

as will be shown in Chapter 6.

For two dimensional integrals, the product formula

$$\int_{-1}^{1}\int_{-1}^{1} f(\eta_1, \eta_2)\,d\eta_1 d\eta_2 = \sum_{i=1}^{n} w_i \sum_{j=1}^{n} w_j\, f(x_i, x_j) \tag{4.24}$$

can be employed.

The Gauss-Legendre quadrature formula is optimal in the sense that it gives exact results for polynomials of up to order $2n-1$ with n integration points. However, the formula does not give exact results when the integrand $f(x)$ is singular or nearly singular.

Hence, the Gauss-Legendre quadrature formula itself may be used to calculate the 3D boundary element integrals of equation (4.1)~(4.4) so long as the distance d between the source point $\mathbf{x}_s$ and the boundary element S is sufficiently large compared to the element size.

4.3 Quadrature Methods for Singular Integrals

Singular integrals arise when the source point $\mathbf{x}_s$ lies in the boundary element S over which the integration is performed. The straight forward application of the Gauss-Legendre quadrature formula fails, since the integrand goes to infinity when $\mathbf{x}$ coincides with $\mathbf{x}_s$, i.e. when $r=|\mathbf{x}-\mathbf{x}_s|=0$

Various methods have been proposed to overcome this difficulty. Some of them will be explained briefly in the following.

(1) The weighted Gauss method [4,5,11,19,20]

In the one dimensional Gaussian formula, one can obtain $\{x_i\}$ and $\{w_i\}$ so that they would give optimum results for a particular weight function $w(x)$, i.e.

$$I=\int_{-1}^{1} w(x)f(x)\,dx = \sum_{i=1}^{n} w_i f(x_i) \qquad (4.25)$$

For instance, Kutt [10] has obtained quadrature points $\{x_i\}$ and weights $\{w_i\}$ for the calculation of the finite part of the singular integral

$$\int_{-1}^{1} \frac{f(x)}{(x+1)^{\lambda}}\,dx = \sum_{i=1}^{n} w_i f(x_i) \quad , \quad \lambda \geq 1 \qquad (4.26)$$

where $w(x)=1/(x+1)^{\lambda}$ is singular at $x=-1$.

This can be applied to three dimensional boundary element integral, for instance to equation (4.1) in the form

$$\int_{-1}^{1}\int_{-1}^{1} \frac{1}{(\eta_1+1)(\eta_2+1)} \left\{ \frac{(\eta_1+1)(\eta_2+1)\phi_e^l(\eta_1,\eta_2)|\mathbf{G}|}{4\pi r} \right\} d\eta_1\, d\eta_2 \qquad (4.27)$$

when the source point is at $\mathbf{x}_s=\mathbf{x}(-1,-1)$, since the term in { } is well behaved, because the singularity due to $1/r$ is cancelled by $(\eta_1+1)(\eta_2+1)$.

This method was improved [4,5,19] by using a two dimensional weight function

$$\left\{(\eta_1-\bar{\eta}_1)^2+(\eta_2-\bar{\eta}_2)^2\right\}^{\frac{1}{2}} \qquad (4.28)$$

where $\mathbf{x}(\bar{\eta}_1,\bar{\eta}_2)$ is the source point. Equation (4.28) approximates the distance r so that the singularity cancellation is improved.

A further modification was introduced [20] where the first term of the Taylor approximation for the distance r is employed. This method is reported to give good results for planar parallelograms but relatively poor results on a spherical patch.

(2) Singularity subtraction and Taylor expansion method [6,21]

A classical way of dealing with kernel singularities is to subtract them out so that $F(\mathbf{x},\mathbf{x}_s)$, an integrand containing a singularity, would be dealt with using

$$\int_S F(\mathbf{x},\mathbf{x}_s)\,dS = \int_S \left\{F(\mathbf{x},\mathbf{x}_s)-F^*(\mathbf{x},\mathbf{x}_s)\right\} dS + \int_S F^*(\mathbf{x},\mathbf{x}_s)\,dS \quad , \qquad (4.29)$$

where $F^*(\mathbf{x},\mathbf{x}_s)$ is a function which has the same singularity as $F(\mathbf{x},\mathbf{x}_s)$ but is of simpler form which can be integrated exactly. Then, $F(\mathbf{x},\mathbf{x}_s)-F^*(\mathbf{x},\mathbf{x}_s)$ is non-singular and can be integrated accurately using, for example, the Gauss-Legendre quadrature formula.

This method was introduced in three dimensional boundary elements in [21], where the exact integration of the subtracted singularity $F^*(\mathbf{x},\mathbf{x}_s)$ for planar elements was calculated.

Aliabadi, Hall and Phemister [6] introduced the idea of using Taylor series expansion of the complete singular integrand to provide subtracted terms which can be exactly integrated, though these integrations can be very laborious. They also recognized that subtraction of only the first term containing the actual singularity was not sufficient to produce a well behaved remainder integral and that there was an advantage in subtracting further terms of the series. The method is reported [6] to give an error of 6×10^{-7} with only 64 integration points for planar parallelograms. However, for a spherical patch, $24\times24=576$ integration points are required to achieve an error of 10^{-6}.

(3) Variable transformation methods

Variable transformation is a well-known technique for the evaluation of improper integrals [36,13].

For a one dimensional integral

$$I = \int_{-1}^{1} f(x)\,dx \quad , \tag{4.30}$$

the variable x is transformed by

$$x = \phi(u) \tag{4.31}$$

so that

$$I = \int_{a}^{b} f(\phi(u))\,\phi'(u)\,du \tag{4.32}$$

where

$$\phi(a) = -1 \ , \qquad \phi(b) = 1 \tag{4.33}$$

and

$$\phi'(u) = \frac{d\phi}{du} \tag{4.33}$$

The transformation $x=\phi(u)$ is chosen so that

$$g(u) = f(\phi(u))\,\phi'(u) \tag{4.34}$$

is no longer an improper integrand. Hence, one can apply a standard quadrature rule to

$$I = \int_{c}^{d} g(u)\,du \tag{4.35}$$

to calculate the original integral.

One such transformation is the error function transformation [13,30]

$$x = \mathrm{erf}(u) = \frac{2}{\sqrt{\pi}} \int_{0}^{u} e^{-y^2}\,dy \tag{4.36}$$

which transforms the integral of equate (4.30) to

$$I = \frac{2}{\sqrt{\pi}} \int_{-\infty}^{\infty} f(\mathrm{erf}(u))\, e^{-u^2}\,du \tag{4.37}$$

The integrand is now dominated by e^{-u^2} and may be approximated accurately by a truncated trapezium rule [31]. This method has been applied in the boundary element analysis of a three dimensional acoustic problem [22] for weakly singular integrals by using the transformation of equation (4.36) in each direction of the two dimensional rectangular region.

The double exponential transformation [32] was applied [27] in the form

$$x(u) = \frac{\pm e^{\pm\eta}}{e^{\eta} + e^{-\eta}} \qquad (\pm \text{ for } x \gtrless 0)$$

$$\eta = \frac{\pi}{2} \sinh\left\{ \frac{\pi}{2}\left(\frac{1}{1-u} - \frac{1}{1+u}\right)\right\} \tag{4.38}$$

in each direction of the two dimensional element for weakly singular integrals in a three dimensional electrostatic problem.

Both methods are reported to give accurate results. However these methods use extra CPU-time in the calculation of the exponential and error functions, unless they are prepared before hand as a table of integration points and weights. Hence, as far as weakly singular integrals are concerned, the simple polar coordinate transformation, which will be explained in the next section, seems more efficient in cancelling the weak singularity of order $1/r$. For hyper singular

integrals of order $1/r^{\alpha}$ ($\alpha \geqq 2$), the variable transformations mentioned here do not work. For such cases the finite part of the integral may be calculated by the method of equation (4.26) proposed by Kutt [10].

(4) Coordinate transformation methods

(i) Triangle to quadrilateral transformation

Lachat and Waston [7] introduced the transformation of a triangular element to a square in the parameter space (η_1, η_2). In this transformation the corner at which the singularity is placed becomes the fourth side of the square on which the Jacobian of the transformation is zero. For example,

$$\int_{-1}^{1}\int_{\eta_1}^{1} \frac{f(\eta_1,\eta_2)\,|\mathbf{G}(\eta_1,\eta_2)|}{|\mathbf{x}(\eta_1,\eta_2)-\mathbf{x}(-1,-1)|}\,d\eta_1\,d\eta_2$$

$$=\int_{-1}^{1}\int_{-1}^{1} \frac{f(\eta_1,\eta_2)\,|\mathbf{G}(\eta_1,\eta_2)|\,J(\eta_1,\eta_2)}{|\mathbf{x}(\eta_1,\eta_2)-\mathbf{x}(-1,-1)|}\,d\gamma_1\,d\gamma_2 \qquad (4.39)$$

where

$$\eta_1 = \gamma_1$$

$$\eta_2 = \frac{(1+\gamma_1)\,\gamma_2-(1-\gamma_1)}{2}$$

$$J(\eta_1,\eta_2) = \frac{(1+\gamma_1)}{2} \qquad (4.40)$$

The above Jacobian $J(\eta_1, \eta_2)$ regularizes the integration so that the Gauss-Legendre quadrature formula can be applied.

(ii) Polar coordinates

Rizzo and Shippy [9] introduced the method of using the polar coordinate system (ρ, θ) centered at the source point (η_1, η_2) in the (η_1, η_2) parameter space, so that

$$d\eta_1 d\eta_2 = \rho d\rho\, d\theta \qquad (4.41)$$

The Jacobian of the transformation : ρ cancels the singularity of order $1/r$. The method is also mentioned in [15, 25].

As shown in Chapter 2, the order of singularity of both u^* and q^* are of order $1/r$ for weakly singular integrals arising in three dimensional potential problems. This explains the fact that the use of polar coordinates regularizes these singularities, so that the Gauss-Legendre quadrature formula can be safely applied to the variables ρ and θ.

In this thesis, this idea is extended to taking polar coordinates around the source point in the plane tangent to the curved element at the source. This enables one to treat near singular integrals and singular integrals in the same frame work by introducing a variable transformation $R(\rho)$ of the radial variable ρ, which regularizes the (near) singularity. Further, an angular variable transformation $t(\theta)$ is introduced, which considerably reduces the number of integration points in the angular direction.

4.4 Quadrature Methods for Nearly Singular Integrals

Nearly singular integrals turn out to be more difficult and expensive to calculate compared to the (weakly) singular integrals mentioned in the proceeding section.

Nearly singular integrals become important when treating thin structures, where the distance between elements are very small compared to the element size as shown in Fig. 4.1. The use of discontinuous elements is another source of nearly singular integrals, since the distance between an element node and an adjacent element can be very small compared to the element size, as shown in Fig. 4.2. Another important source of nearly singular integrals is the calculation of the potential or potential derivatives at an internal point very near the boundary. This arises for instance in the simulation of electron guns in cathode ray tubes,

where the accurate value of the electric flux near the cathode is required in order to calculate the trajectory of electrons.

The stress of this thesis is on the calculation of these near singular integrals, although singular integrals can be treated efficiently in the same frame work.

Previous methods will be briefly reviewed in the following.

(1) Element subdivision

The orthodox way to treat nearly singular integrals is to increase the number of integration points as the source to element distance d diminishes (compared to the element size) [7,12]. However, the number of necessary integration points with the standard Gauss-Legendre quadrature increases rapidly as d decreases, as will be shown in Chapter 10.

The next thing to do is to subdivide the element so that the integration points are concentrated near the source point [7,12].

Element subdivision tends to be a cumbersome procedure and would still be inefficient when d is very small compared to the element size. Another disadvantage of element subdivision is that it suffers from the fact that the highest polynomial degree which can be integrated exactly by the Gauss-Legendre quadrature depends on the local number of integration points selected for each sub-element. For instance, a one-dimensional quadrature which is subdivided into three subelements and uses 2, 3 and 4 Gauss points, respectively, can integrate exactly polynomial integrands of degrees 3,5 and 7 over each part $(2n-1)$, whereas if 9 points are used to integrate over the complete element, a 17th-degree polynomial is allowable [15].

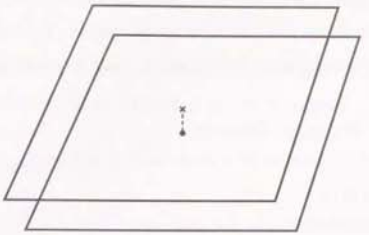

Fig.4.1 Boundary elements for thin structures

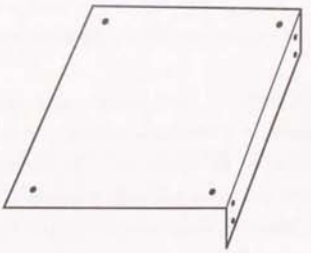

Fig.4.2 The use of discontinuous elements

(2) Variable transformation methods

A recent trend is to transform the integration variables so as to weaken the near singularity by the Jacobian of the transformation. The transformation also has the effect of concentrating the integration points near the source point.

(i) Double exponential transformation

The double exponential transformation was originally proposed by Takahashi and Mori [13].

The method is efficient for the integration

$$I = \int_{-1}^{1} f(x)\,dx \tag{4.42}$$

where $f(x)$ has integrable singularities at $x = \pm 1$.

The method introduces the variable transformation

$$x = \tanh\left\{\frac{\pi}{2}\sinh(t)\right\} \tag{4.43}$$

so that

$$I = \frac{\pi}{2}\int_{-\infty}^{\infty} f\left[\tanh\left\{\frac{\pi}{2}\sinh(t)\right\}\right]\frac{\cosh t}{\cosh^2\left\{\frac{\pi}{2}\sinh(t)\right\}}\,dt \tag{4.44}$$

The truncated trapezium rule is applied to equation (4.44) to evaluate the integral numerically.

This method has been applied to nearly singular integrals in boundary elements in [14, 26, 16]. However, it will be shown in Chapter 10 that it requires many integration points when the source distance d is very small, and the method consumes a lot of CPU-time for the evaluation of exponential functions in equations (4.43) and (4.44), unless they are prepared before hand in a table.

(ii) Cubic transformation method

A more efficient self-adaptive method using cubic transformation was proposed by Telles [15]. The method is briefly explained in the following.

For a one dimensional integral

$$I = \int_{-1}^{1} f(\eta)\,d\eta \quad , \tag{4.45}$$

let the projection of the source point $\mathbf{x}_s$ on to the element Γ be $\mathbf{x}(\bar{\eta})$, and the distance d as shown in Fig. 4.3, where the element is described by $\mathbf{x}(\eta), (-1 \leq \eta \leq 1)$.

A cubic transformation

$$\eta(\gamma) = a\gamma^3 + b\gamma^2 + c\gamma + d \tag{4.46}$$

is introduced, such that

$$I = \int_{-1}^{1} f(\eta(\gamma))\,J(\gamma)\,d\gamma \tag{4.47}$$

where

$$J(\gamma) = \frac{d\eta}{d\gamma}$$

and

$$\eta(-1) = -1 \quad ,$$

$$\eta(1) = 1 \quad ,$$

$$\eta(\bar{\gamma}) = \bar{\eta} \quad , \tag{4.48}$$

and $J(\gamma)$ takes a minimum value $\bar{r}(d)$ at $\gamma = \bar{\gamma}$, in order to weaken the near singular behaviour of $f(\eta(\gamma))$ near $\eta = \bar{\eta}$.

$\bar{r}(d)$ is an optimized function of the distance d given by

$$\bar{r}(d) = \begin{cases} 0.85 + 0.24\log d & (0.05 \leq d < 1.3) \\ 0.893 + 0.832\log d & (1.3 \leq d < 3.618) \\ 1 & (3.618 \leq d) \end{cases} \tag{4.49}$$

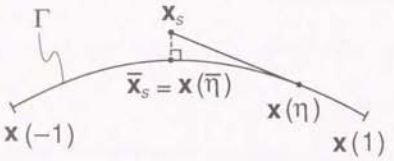

Fig.4.3 One dimensional integral over Γ.

In order to compare with methods proposed in this thesis for cases where $d<0.05$, the function $\bar{r}(d)$ is interpolated between $d=0$ and 0.05 to give

$$\bar{r}(d) = 2.62\,d \quad (0 \leq d < 0.05) \tag{4.50}$$

The standard Gauss-Legendre quadrature formula is then applied to equation (4.47).

For two dimensional integration, equations (4.45) and (4.47) are generalized to give.

$$I = \int_{-1}^{1}\int_{-1}^{1} f(\eta_1, \eta_2)\, d\eta_1 d\eta_2$$

$$= \int_{-1}^{1}\int_{-1}^{1} f(\eta_1(\gamma_1), \eta_2(\gamma_2))\, J_1(\gamma_1)\, J_2(\gamma_2)\, d\gamma_1 d\gamma_2 \tag{4.51}$$

where cubic transformations $\eta_1(\gamma_1)$, $\eta_2(\gamma_2)$ are applied to each direction η_1, η_2 respectively. In this case the distance parameters d_1, d_2 for each direction is determined by

$$d_1 = \frac{2d}{|x(1, \bar{\eta}_2) - x(-1, \bar{\eta}_2)|} \tag{4.47}$$

$$d_2 = \frac{2d}{|x(\bar{\eta}_1, 1) - x(\bar{\eta}_1, -1)|} \tag{4.52}$$

where $\bar{x}_s = x(\bar{\eta}_1, \bar{\eta}_2)$ is the source projection or the point on the curved element S nearest to the source point x_s. $(\bar{\eta}_1, \bar{\eta}_2)$ can be calculated by the Newton-Raphson method, as will be explain in Chapter 5.

Telles' method gives good results for $d>10^{-2}$, where d is the relative distance compared to the element size. However, when $0<d<10^{-2}$, the method does not give accurate enough results even when 32×32 integration points are used, as will be shown in Chapter 10.

(3) Polar coordinates

The use of polar coordinates in the (η_1, η_2) parameter space, as in the calculation of weakly singular integrals, alone does not give accurate results for nearly singular integrals, as will be shown in Chapter 10. A method to improve the result by correction procedures [16] is reported to be efficient for potential problems.

However, in this thesis we take a different view and introduce a new method by taking polar coordinates in the plane tangent to the element at the source projection. Further, radial and angular variable transformations are introduced in order to weaken the near singularity before applying the Gauss-Legendre quadrature formula.

CHAPTER 5

THE PROJECTION AND ANGULAR & RADIAL TRANSFORMATION (PART) METHOD

5.1 Introduction

Hayami and Brebbia [17] have proposed a new coordinate transformation method to calculate singular and nearly singular integrals for curved boundary elements [5].

Here, the method will be generalized to deal with arbitrary curved element geometries and different types of integral kernels which arise in three dimensional potential problems.

From Chapter 3 (cf. Tables 3.1 and 3.2), the (nearly) singular integrals involved in the boundary element analysis of three dimensional potential problems may be generally expressed as

$$I = \int_S \frac{f}{r^\alpha} dS \tag{5.1}$$

where

$\alpha = 1$ for (weakly) singular integrals necessary for the calculation of H and G matrices

and

$\alpha = 1, 3, 5$ for nearly singular integrals necessary for the calculation of potential and potential gradients at internal (external) points very near the boundary S.

Here $r = |\mathbf{x} - \mathbf{x}_s|$ is the distance between the source point $\mathbf{x}_s$ and the field point $\mathbf{x}$. f is a function of $\mathbf{x} \in S$, which does not have any (near) singularity in r.

Although the method is proposed for three dimensional potential problems, integrals arising in other areas such as acoustic problems (Helmholtz equation),

elastostatics etc., may be regarded to take the form of equation (5.1), so that the following analysis may also apply to such problems.

As the evaluation of (nearly) singular integrals becomes a difficult problem for the case of curved elements these are the elements to be treated here in detail. For planar elements, the problem becomes simpler and closed form integrals such as those given in Aliabadi, Hall and Phemister [6] or Kuwabara and Takeda [2,29] are available.

Although the quadrature method to be proposed can be applied to general curved elements (triangular as well as quadrilateral), we shall use the 9-point Lagrangian element as an illustration (cf. Fig. 5.1).

The interpolation in this element can be expressed as

$$f(\eta_1, \eta_2) = \sum_{j=-1}^{1} \sum_{k=-1}^{1} \phi_j(\eta_1)\, \phi_k(\eta_2)\, f(j,k) \quad , \tag{5.2}$$

where

$$\phi_{-1}(\eta) = \eta(\eta-1)/2$$

$$\phi_0(\eta) = 1-\eta^2$$

$$\phi_1(\eta) = \eta(\eta+1)/2 \tag{5.3}$$

The element is isoparametric in the sense that f can also represent the coordinates $\mathbf{x}(\eta_1, \eta_2)$. The element S is defined by

$$S = \left\{ \mathbf{x}(\eta_1, \eta_2) \mid -1 \leq \eta_1, \eta_2 \leq 1 \right\}$$

where

$$\mathbf{x}(\eta_1, \eta_2) = \sum_{j=-1}^{1} \sum_{k=-1}^{1} \phi_j(\eta_1)\, \phi_k(\eta_2)\, \mathbf{x}^{j,k}$$

and

$$\mathbf{x}^{j,k} = \mathbf{x}(j,k), \quad j,k = -1, 0, 1 \tag{5.4}$$

for a 9-point Lagrangian element.

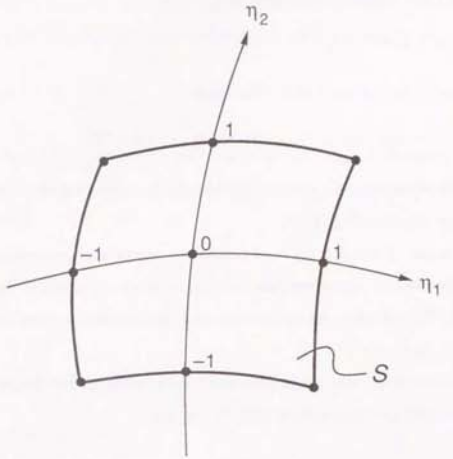

Fig. 5.1 The 9-point Lagrangian element

When calculating boundary element integrals, one needs to know a measure of the distance d between the source point $\mathbf{x}_s$ and the element S over which the integral is performed. A rough estimate of d can be obtained by the distance d' between $\mathbf{x}_s$ and the centre of element $\mathbf{x}(0,0)$, i.e.

$$d' = |\mathbf{x}(0,0) - \mathbf{x}_s| \quad . \tag{5.5}$$

Let us define the size l of the element by

$$l = \max\left(|\mathbf{x}(1,0) - \mathbf{x}(-1,0)|,\ |\mathbf{x}(0,1) - \mathbf{x}(0,-1)|\right) \tag{5.6}$$

If $d' \gg l$, the integration can be performed by the standard product Gauss-Legendre quadrature formula [1,3].

It is when $d' < l$ that we need to devise a new scheme, since the standard Gauss-Legendre formula alone does not give accurate estimates of the integral efficiently. (From here on, we shall assume that the element has been normalized, so that $l=1$ and $d=d'$.)

For such cases, this thesis proposes a new scheme : the Projection and Angular & Radial transformation (PART) method [18].

The proposed method consists of the following steps :

(1) Find the point $\hat{\mathbf{x}}_s$ on the element S nearest to the source point $\mathbf{x}_s$.

(2) Approximately project the curved element S on to a polygon $\bar{S}$ in the plane tangent to the element S at $\hat{\mathbf{x}}_s$.

(3) Introduce polar coordinates (ρ, θ) in the projected element $\bar{S}$.

(4) Transform the radial variable by $R(\rho)$ in order to weaken the (near) singularity f/r^{α} in the integral of equation (5.1).

(5) Transform the angular variable by $t(\theta)$ in order to weaken the near singularity in θ that arises when $\hat{\mathbf{x}}_s$ is close to the edges of $\bar{S}$.

(6) Apply the Gauss-Legendre quadrature formula to the transformed variables R and t in order to calculate the integral of equation (5.1) numerically.

5.2 Source Projection

The first step is to find the closest point $\hat{\mathbf{x}}_s = \mathbf{x}(\bar{\eta}_1, \bar{\eta}_2)$ on the curved element S to the source point $\mathbf{x}_s$. This point $\hat{\mathbf{x}}_s$ will be called the 'source projection'.

$(\bar{\eta}_1, \bar{\eta}_2)$ can be obtained by solving the set of nonlinear equations for (η_1, η_2):

$$\left(\mathbf{x} - \mathbf{x}_s \cdot \frac{\partial \mathbf{x}}{\partial \eta_i}\right) = 0 \quad , \quad (i = 1, 2) \quad , \tag{5.7}$$

since $\mathbf{x} - \mathbf{x}_s \perp \partial\mathbf{x}/\partial\eta_i$ $(i=1,2)$ is satisfied at $\hat{\mathbf{x}}_s = \mathbf{x}(\bar{\eta}_1, \bar{\eta}_2)$, as shown in Fig. 5.2.

Let $\mathbf{r} = \mathbf{x} - \mathbf{x}_s$. Then, $\partial\mathbf{r}/\partial\eta_i = \partial\mathbf{x}/\partial\eta_i$, $(i=1,2)$ so that equations (5.7) is equivalent to

$$\left(\mathbf{r} \cdot \frac{\partial \mathbf{r}}{\partial \eta_i}\right) = 0 \quad , \quad (i = 1, 2) \tag{5.8}$$

Here,

$$\begin{aligned} \mathbf{r} &= \mathbf{x} - \mathbf{x}_s \\ &= \sum_j \phi_j(\eta_1, \eta_2)\, \mathbf{x}^j - \mathbf{x}_s \\ &= \sum_j \phi_j \left(\mathbf{x}^j - \mathbf{x}_s\right) \\ &= \sum_j \phi_j\, \mathbf{r}^j \quad , \end{aligned} \tag{5.9}$$

where

$$\mathbf{r}^j = \mathbf{x}^j - \mathbf{x}_s \quad ,$$

since

$$\sum_j \phi_j\,(\eta_1, \eta_2) = 1 \quad ,$$

for complete interpolation functions. For instance for the 9-point Lagrangian element of equations (5.2)~(5.4),

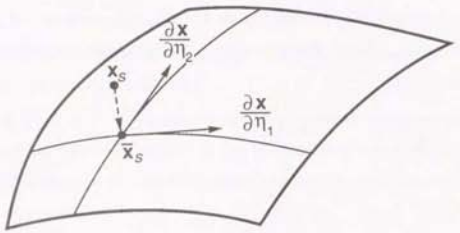

Fig. 5.2 The source projection $\bar{\mathbf{x}}_S$

$$\sum_j \phi_j = \sum_{k=-1}^{1} \phi_k(\eta_1) \sum_{l=-1}^{1} \phi_l(\eta_2) = \sum_{k=-1}^{1} \phi_k(\eta_1) = 1 \quad , \tag{5.10}$$

since

$$\sum_{k=-1}^{1} \phi_k(\eta) = \eta(\eta-1)/2 + 1-\eta^2 + \eta(\eta+1)/2 = 1 \quad .$$

From equation (5.9),

$$\frac{\partial \mathbf{r}}{\partial \eta_i} = \sum_j \frac{\partial \phi_j}{\partial \eta_i} \mathbf{r}^j \qquad (i = 1, 2) \quad . \tag{5.11}$$

Hence, equation (5.9) is equivalent to

$$\begin{cases} f_1(\eta_1, \eta_2) = 0 \\ f_2(\eta_1, \eta_2) = 0 \end{cases} \quad , \tag{5.12}$$

where

$$f_i(\eta_1, \eta_2) = \left(\sum_j \phi_j \mathbf{r}^j\right) \cdot \left(\sum_j \frac{\partial \phi_j}{\partial \eta_i} \mathbf{r}^j\right) \quad . \tag{5.13}$$

Let

$$\mathbf{f} = \begin{pmatrix} f_1 \\ f_2 \end{pmatrix}, \quad \boldsymbol{\eta} = \begin{pmatrix} \eta_1 \\ \eta_2 \end{pmatrix}, \quad \Delta\boldsymbol{\eta} = \begin{pmatrix} \Delta\eta_1 \\ \Delta\eta_2 \end{pmatrix} \quad . \tag{5.14}$$

Since

$$\mathbf{f}(\boldsymbol{\eta}+\Delta\boldsymbol{\eta}) = \mathbf{f}(\boldsymbol{\eta}) + \begin{bmatrix} \frac{\partial f_1}{\partial \eta_1} & \frac{\partial f_1}{\partial \eta_2} \\ \frac{\partial f_2}{\partial \eta_1} & \frac{\partial f_2}{\partial \eta_2} \end{bmatrix} \Delta\boldsymbol{\eta} + O(\Delta\eta^2) \quad , \tag{5.15}$$

if we have an initial solution $\boldsymbol{\eta}_0$ which is in the neighborhood of $\hat{\boldsymbol{\eta}}$: $\mathbf{f}(\hat{\boldsymbol{\eta}}) = \mathbf{0}$, i.e. $|\mathbf{f}(\boldsymbol{\eta}_i)| \ll 1$, the iteration

$$\boldsymbol{\eta}_{i+1} = \boldsymbol{\eta}_i + \Delta\boldsymbol{\eta}_i \tag{5.16}$$

where

$$\Delta\eta_i = -\begin{bmatrix} \frac{\partial f_1}{\partial \eta_1} & \frac{\partial f_1}{\partial \eta_2} \\ \frac{\partial f_2}{\partial \eta_1} & \frac{\partial f_2}{\partial \eta_2} \end{bmatrix}^{-1} \mathbf{f}(\eta_i) \tag{5.17}$$

should converge to the solution , i.e.

$$\lim_{i\to\infty} \eta_i = \bar{\eta}$$

This is what is known as the Newton-Raphson method , and η_i will converge to the true solution $\bar{\eta}$ very quickly, provided that the initial solution η_0 is in the neighborhood of $\bar{\eta}$. In fact the method has the property of second order convergence, i.e .

$$|\Delta\eta_{i+1}| \sim O(|\Delta\eta_i|)^2 \tag{5.18}$$

where $|\cdot|$ is a suitable norm for $\Delta\eta$.

For our problem of solving equation (5.7) to find the source projection $\bar{\mathbf{x}}_s$, the Newton-Raphson method converges within few (3~4) iterations to give a relative error of 10^{-6}, and consumes only about 1% of the total integration time. The convergence is very good, so long as the solution $\bar{\mathbf{x}}_s$ lies inside the element S . Then, the initial solution can be set to $\eta_0{}^T=(\eta_1, \eta_2)=(0, 0)$.

However, when the source projection lies far out side the element , i.e. $|\bar{\eta}_1|\gg 1$ and / or $|\bar{\eta}_2|\gg 1$, the method may not converge to the true solution $(\bar{\eta}_1, \bar{\eta}_2)$. This is because the interpolation function ϕ_j (e.g. 9-point Lagrangian element) diverges as $|\eta_1|\gg 1$ and / or $|\eta_2|\gg 1$, i.e. the interpolation function ϕ_j gives a good approximation of the function only when $|\eta_i|\leqq 1$, $(i=1, 2)$.

Hence, it may be safer to start with the initial solution

$$(\eta_1, \eta_2) = (j, k)$$

corresponding to the closest node $\mathbf{x}^{jk}$, $(j, k = -1, 0, 1)$ of the element, to the source point $\mathbf{x}_s$, particularly when $\bar{\mathbf{x}}_s$ lies near or outside the edge of the element.

In the actual application of the proposed integration method (PART), it turns out that it is only when the source distance $d=|\mathbf{x}_s-\bar{\mathbf{x}}_s|$ is relatively small compared to the element ($d\ll 1$), that the integral becomes (nearly) singular. This means that the method should be applied when the source point $\mathbf{x}_s$ is very close to the element. In this case, the source projection $\bar{\mathbf{x}}_s$ either lies inside the element S, or very close to the edges of S even when it lies outside the element. This justifies the use of the Newton-Raphson method to obtain the source projection $\bar{\mathbf{x}}_s$, since the convergence of the method is guaranteed in such cases due to the nature of the interpolation functions ϕ_j.

5.3 Approximate Projection of the Curved Element

Next, the curved element S is approximately projected on to the plane tangent to the curved element S at the source projection $\bar{\mathbf{x}}_s$.

First the unit normal vector $\mathbf{n}_s$ to the element S at $\bar{\mathbf{x}}_s=\mathbf{x}(\bar{\eta}_1, \bar{\eta}_2)$ is calculated by

$$\mathbf{n}_s = \mathbf{G}(\bar{\eta}_1, \bar{\eta}_2) / |\mathbf{G}(\bar{\eta}_1, \bar{\eta}_2)| \tag{5.19}$$

where

$$\mathbf{G} = \frac{\partial \mathbf{x}}{\partial \eta_1} \times \frac{\partial \mathbf{x}}{\partial \eta_2} \tag{5.20}$$

Denote the four corner nodes of the element by

$$\begin{aligned} \mathbf{x}_1 &= \mathbf{x}(1, 1) \\ \mathbf{x}_2 &= \mathbf{x}(-1, 1) \\ \mathbf{x}_3 &= \mathbf{x}(-1, -1) \\ \mathbf{x}_4 &= \mathbf{x}(1, -1) \end{aligned} \tag{5.21}$$

Then the perpendicular projection $\bar{x}_j$ of node x_j onto the plane tangent to the curved element S at $\hat{x}_s$ is given by

$$\bar{x}_j = x_j - \left\{ (x_j - \bar{x}_s) \cdot n_s \right\} n_s \quad , \qquad (j = 1 \sim 4) \tag{5.22}$$

The curved element S is then mapped onto the planar quadrilateral $\bar{S}$ defined by $\bar{x}_1$, $\bar{x}_2$, $\bar{x}_3$ and $\bar{x}_4$, as shown in Fig. 5.3. This is an approximate projection, since the exact projection of a curved edge of S would, in general, be a curve in the tangent plane.

The consideration of exact projection will be given in a later section. However, the approximate projection is shown to be sufficient and more efficient for introducing the source distance d into the radial variable transformation $R(\rho)$, considering that it is the local behaviour of $1/r^{\alpha}$, $r = |x - x_s|$, $x \in S$, that dominates the (near) singularity of the integrand.

Next, one divides the projected quadrilateral $\bar{S}$ into four triangular regions $\bar{\Delta}_j$, $(j = 1 \sim 4)$ centered at $\bar{x}_s$ as shown in Fig. 5.4.

In each triangular region $\bar{\Delta}_j$ defined by $\bar{x}_s$, $\bar{x}_j$ and $\bar{x}_{j+1}$, one defines the following, geometric quantities :

$$a_j = |\bar{x}_j - \bar{x}_s| \quad ,$$

$$a_{j+1} = |\bar{x}_{j+1} - \bar{x}_s| \quad ,$$

$$b_j = |\bar{x}_{j+1} - \bar{x}_j| \quad , \tag{5.23}$$

where $\bar{x}_5 \equiv \bar{x}_1$, and

edge-j : edge corresponding to $\bar{x}_{j+1} - \bar{x}_j$

$\bar{t}_j$: foot of perpendicular from $\bar{x}_s$ to edge-j

h_j : length of the perpendicular ($h_j = |\bar{t}_j - \bar{x}_s|$),

α_j : angle between vectors $\bar{t}_j - \bar{x}_s$ and $\bar{x}_j - \bar{x}_s$,

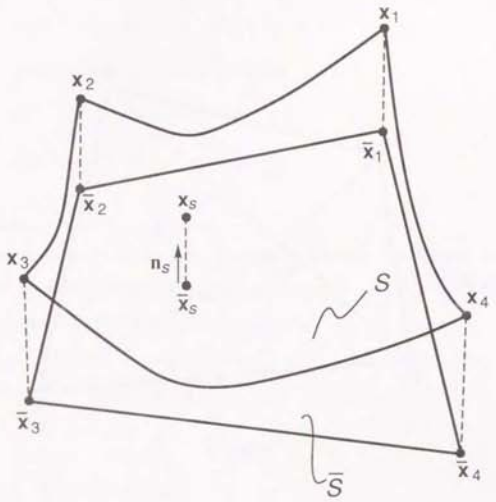

Fig. 5.3 Approximate projection of the curved element

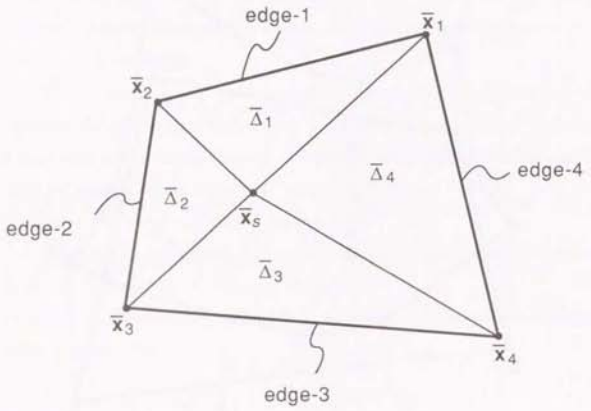

Fig. 5.4 Division of the projected quadrilateral $\bar{S}$ into four triangular regions

and

$\Delta\theta_j$: angle between $\hat{x}_{j+1}-\hat{x}_s$ and $\hat{x}_j-\hat{x}_s$. (5.24)

as shown in Fig. 5.5 .

Then ,

$$\cos\Delta\theta_j = (a_j^2 + a_{j+1}^2 - b_j^2)/(2a_j a_{j+1})$$

$$\sin\Delta\theta_j = \mathrm{sgn}(j)\sqrt{1-\cos^2\Delta\theta_j}$$

$$\cos\alpha_j = \mathrm{sgn}(j)\ (a_{j+1}\sin\Delta\theta_j)/b_j$$

$$\sin\alpha_j = \mathrm{sgn}(j)\ (a_j - a_{j+1}\cos\Delta\theta_j)/b_j$$

$$h_j = a_j\cos\alpha_j \qquad (5.26)$$

where sgn(j), $j=1\sim4$ for curved quadrilateral elements are defined by the position of the source projection ($\bar{\eta}_1$, $\bar{\eta}_2$) in the square $-1\leqq\eta_1$, $\eta_2\leqq1$ in the parameter space (Fig. 5.7), i.e.

$$\mathrm{sgn}(1) = \begin{cases} 1 & ; \quad \eta_2 < 1-\varepsilon \\ 0 & ; \quad 1-\varepsilon \leqq \eta_2 \leqq 1+\varepsilon \\ -1 & ; \quad 1+\varepsilon < \eta_2 \end{cases}$$

$$\mathrm{sgn}(2) = \begin{cases} 1 & ; \quad -1+\varepsilon < \eta_1 \\ 0 & ; \quad -1-\varepsilon \leqq \eta_1 \leqq -1+\varepsilon \\ -1 & ; \quad \eta_1 < -1-\varepsilon \end{cases}$$

$$\mathrm{sgn}(3) = \begin{cases} 1 & ; \quad -1+\varepsilon < \eta_2 \\ 0 & ; \quad -1-\varepsilon \leqq \eta_2 \leqq -1+\varepsilon \\ -1 & ; \quad \eta_2 < -1-\varepsilon \end{cases}$$

$$\mathrm{sgn}(4) = \begin{cases} 1 & ; \quad \eta_1 < 1-\varepsilon \\ 0 & ; \quad 1-\varepsilon \leqq \eta_1 \leqq 1+\varepsilon \\ -1 & ; \quad 1+\varepsilon < \eta_1 \end{cases} \qquad (5.27)$$

where $0<\varepsilon\ll1$ eg. $\varepsilon=10^{-6}$

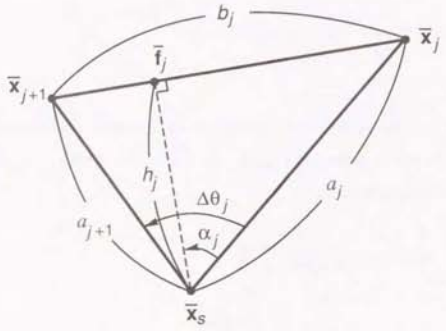

Fig. 5.5 Triangular region $\bar{\Delta}_j$

Here it should be noted that in equation (5.27), sgn(j) was defined according to the position of $(\bar{\eta}_1, \bar{\eta}_2)$ with respect to the square $-1 \leqq \eta_1, \eta_2 \leqq 1$ in the (η_1, η_2) parameter space, and not according to the position of the source projection $\hat{\mathbf{x}}_s = \mathbf{x}(\bar{\eta}_1, \bar{\eta}_2)$ with respect to the approximately projected quadrilateral $\bar{S}$.

There is a subtle but substantial difference, since when $\hat{\mathbf{x}}_s$ is very near the edge of a curved element S, it can happen that $\hat{\mathbf{x}}_s$ lies outside the projected element $\bar{S}$ in the tangent plane at $\hat{\mathbf{x}}_s$ even though $\hat{\mathbf{x}}_s$ lies inside the element S as shown in Fig. 5.6, or vice versa. It may also happen that $\hat{\mathbf{x}}_s$ lies on the edge-j of element S i.e. sgn(j)=0, but $\hat{\mathbf{x}}_s$ lies inside $\bar{S}$ or outside $\bar{S}$. In a word, the topology of $\hat{\mathbf{x}}_s$ with regard to S is not necessarily preserved for $\hat{\mathbf{x}}_s$ with regard to $\bar{S}$ when $\hat{\mathbf{x}}_s$ is near the edge of a curved element S. An example of such a case is given in chapter 10 for a 9-point Lagrangian element modelling a spherical quadrilateral element.

Since the integral of equation (5.1) of interest, is defined on the element S and on the (η_1, η_2) parameter space as in equation (5.28), the topology of the source projection $\hat{\mathbf{x}}_s = \mathbf{x}(\bar{\eta}_1, \bar{\eta}_2)$ should be maintained for the correct evaluation of the integral of equation (5.1) and hence (5.28). This is why sgn(j) of equation (5.27) was defined according to the position of $(\bar{\eta}_1, \bar{\eta}_2)$ with respect to the square $-1 \leqq \eta_1, \eta_2 \leqq 1$ in the (η_1, η_2) parameter space, and not according to the position of $\hat{\mathbf{x}}_s = \mathbf{x}(\bar{\eta}_1, \bar{\eta}_2)$ with respect to $\bar{S}$.

For the case of Fig. 5.6, sgn(4)=1 and $\Delta\theta_4$ is defined by equation (5.26) as $\Delta\theta_4 > 0$ even though $\hat{\mathbf{x}}_s \notin \bar{S}$. For the case when sgn (j)=0 but $\hat{\mathbf{x}}_s$ is not on the edge -j of $\bar{S}$, the integral I_j over Δ_j is zero since the area of Δ_j is zero, even though $\bar{\Delta}_j$ has a finite area. In this case, det $L_j = 0$ so that $I_j = 0$ in equation (5.39).

To sum up, the notion of mapping (approximately projecting) S onto $\bar{S}$ should be more rigorously interpreted as mapping each triangular region Δ_j in the (η_1, η_2) space to a triangular region $\bar{\Delta}_j$ in $\bar{S}$, maintaining the original topology of $(\bar{\eta}_1, \bar{\eta}_2)$ with respect to the square $-1 \leqq \eta_1, \eta_2 \leqq 1$ for $\hat{\mathbf{x}}_s = \mathbf{x}(\bar{\eta}_1, \bar{\eta}_2)$ in $\bar{S}$. Hence, the

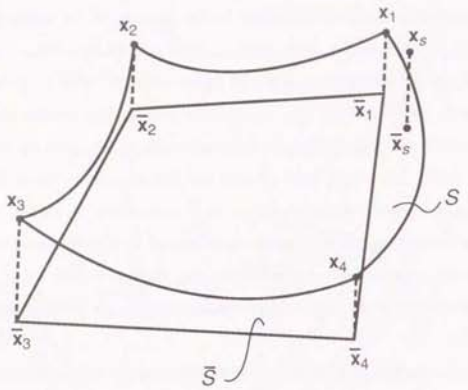

Fig. 5.6 Case where $\bar{\mathbf{x}}_S \in S$ but $\bar{\mathbf{x}}_S \notin \bar{S}$

orientation of each triangle Δ_j, sgn(j) or the sign of the angle corresponding to $\Delta\theta_j$ are maintained as Δ_j is mapped to $\bar{\Delta}_j$.

The procedure of approximate projection explained so far, can also be applied to curved triangular elements. In this case, $\bar{S}$ is divided in to three triangular regions $\bar{\Delta}_1$, $\bar{\Delta}_2$ and $\bar{\Delta}_3$.

5.4 Polar Coordinates in the Projected Element

As mentioned before, the singular and nearly singular integrals occurring in three dimensional boundary element method can be generally expressed as

$$I = \int_S \frac{f}{r^\alpha} \mathrm{d}S \qquad (\alpha > 0) \quad , \tag{5.1}$$

where f is a well behaved function of $\mathbf{x}$ on S. Since the singularity is related to the integration in the radial direction, it seems natural to separate the integral of equation (5.1) into its radial and angular components. In this way, one can tackle the problem of (near) singularity by considering only the radial component of the integral.

Hence, first consider integrating equation (5.1) using polar coordinates in the projected quadrilateral $\bar{S}$, centered at the source projection $\hat{\mathbf{x}}_s$, where $\hat{\mathbf{x}}_s$ is situated in the projected quadrilateral $\bar{S}$ as defined in the previous section.

Polar coordinates in the (η_1, η_2) parameter space have been previously used to deal with singular integrals [9,15], but here they are generalized by using polar coordinates in the projected quadrilateral and by introducing further variable transformations in the angular and radial directions.

Using the (η_1, η_2) parameters defined in equations (5.2)~(5.4) and Fig. 5.1, equation (5.1) becomes

$$I = \int_{-1}^{1} \int_{-1}^{1} \frac{f}{r^\alpha} |\mathrm{G}| \, \mathrm{d}\eta_1 \mathrm{d}\eta_2 \tag{5.28}$$

where

$$|G(\eta_1, \eta_2)| = |\frac{\partial \mathbf{x}}{\partial \eta_1} \times \frac{\partial \mathbf{x}}{\partial \eta_2}| \tag{5.29}$$

Next, divide the square region of the integration in equation (5.28) into four triangular regions Δ_j $(j=1\sim4)$ centered at $(\bar{\eta}_1, \bar{\eta}_2)$ and situated in the (η_1, η_2) space as shown in Fig. 5.7 . Notice that $(\bar{\eta}_1, \bar{\eta}_2)$ corresponds to the source projection.

Thus,

$$I = \sum_{j=1}^{4} I_j$$

where

$$I_j = \iint_{\Delta_j} \frac{f}{r^n} |G| \, d\eta_1 \, d\eta_2 \tag{5.30}$$

Let

$$\begin{aligned} &(\eta_1^1, \eta_2^1) = (\eta_1^5, \eta_2^5) = (1,1), \\ &(\eta_1^2, \eta_2^2) = (-1,1) \\ &(\eta_1^3, \eta_2^3) = (-1,-1), \\ &(\eta_1^4, \eta_2^4) = (1,-1) \end{aligned} \tag{5.31}$$

In order to map the projected quadrilateral $\bar{S}$ onto the curved element S, linearly map each triangular region $\bar{\Delta}_j$ in $\bar{S}$ (Fig. 5.4) onto each corresponding triangular region Δ_j in the (η_1, η_2) space (Fig. 5.7) . This is done by defining local Cartesian coordinates (ξ_1, ξ_2) for each triangular region $\bar{\Delta}_j$ in $\bar{S}$ (Fig. 5.5) as shown in Fig. 5.8 , and then mapping $\bar{\Delta}_j$ onto Δ_j (Fig. 5.9).

The linear map from $\bar{\Delta}_j$ to Δ_j which maps (0,0) to $(\bar{\eta}_1, \bar{\eta}_2)$, $(a_j, 0)$ to (η_1^j, η_2^j), and $(a_{j+1}\cos\Delta\theta_j, a_{j+1}\sin\Delta\theta_j)$ to $(\eta_1^{j+1}, \eta_2^{j+1})$ is given by

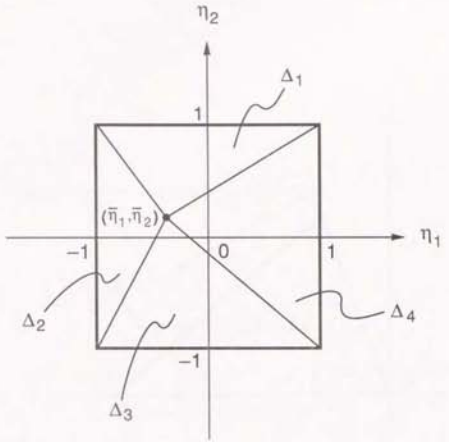

Fig. 5.7 Four triangular regions in (η_1, η_2) space

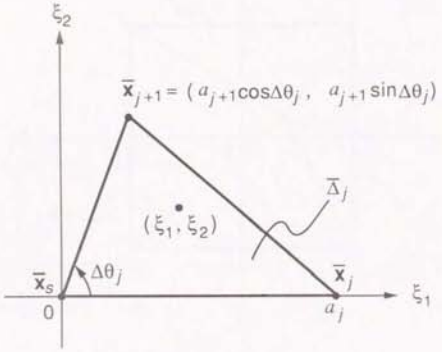

Fig. 5.8 (ξ_1, ξ_2) coordinates in region $\overline{\Delta}_j$ in $\overline{S}$.

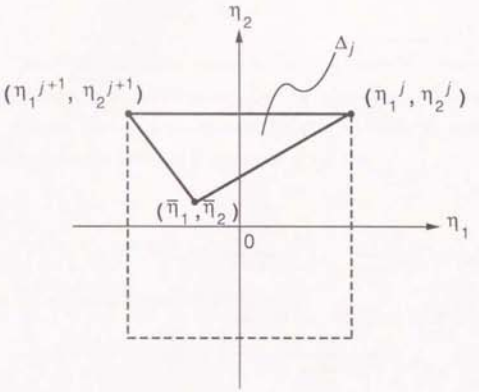

Fig. 5.9 Region Δ_j

$$\begin{pmatrix} \eta_1 \\ \eta_2 \end{pmatrix} = L_j \begin{pmatrix} \xi_1 \\ \xi_2 \end{pmatrix} + \begin{pmatrix} \bar{\eta}_1 \\ \bar{\eta}_2 \end{pmatrix} \tag{5.32}$$

where

$$L_j = \begin{pmatrix} l_{11}^{\,j} & l_{12}^{\,j} \\ l_{21}^{\,j} & l_{22}^{\,j} \end{pmatrix} \tag{5.33}$$

and

$$l_{11}^{\,j} = \frac{\eta_1^{\,j} - \bar{\eta}_1}{a_j} \quad ,$$

$$l_{12}^{\,j} = -\frac{\eta_1^{\,j} - \bar{\eta}_1}{a_j \tan \Delta\theta_j} + \frac{\eta_1^{\,j+1} - \bar{\eta}_1}{a_{j+1} \sin \Delta\theta_j} \quad ,$$

$$l_{21}^{\,j} = \frac{\eta_2^{\,j} - \bar{\eta}_2}{a_j} \quad ,$$

$$l_{22}^{\,j} = -\frac{\eta_2^{\,j} - \bar{\eta}_2}{a_j \tan \Delta\theta_j} + \frac{\eta_2^{\,j+1} - \bar{\eta}_2}{a_{j+1} \sin \Delta\theta_j} \tag{5.34}$$

From equations (5.32) and (5.33), one obtains

$$\frac{\partial \eta_1}{\partial \xi_1} = l_{11}^{\,j} \quad , \qquad \frac{\partial \eta_1}{\partial \xi_2} = l_{12}^{\,j}$$

$$\frac{\partial \eta_2}{\partial \xi_1} = l_{21}^{\,j} \quad , \qquad \frac{\partial \eta_2}{\partial \xi_2} = l_{22}^{\,j} \tag{5.35}$$

so that the Jacobian of the linear mapping from (ξ_1, ξ_2) to (η_1, η_2) is

$$\frac{\partial (\eta_1, \eta_2)}{\partial (\xi_1, \xi_2)} = l_{11}^{\,j}\, l_{22}^{\,j} - l_{12}^{\,j}\, l_{21}^{\,j} \tag{5.36}$$

Hence, the integral of equation (5.30) becomes

$$I_j = \iint_{\bar{\Delta}_j} \frac{f|G|}{r^{\alpha}} \left| \frac{\partial (\eta_1, \eta_2)}{\partial (\xi_1, \xi_2)} \right| d\xi_1 d\xi_2$$

$$= |\, l_{11}^{\,j} l_{22}^{\,j} - l_{12}^{\,j} l_{21}^{\,j} \,| \iint_{\bar{\Delta}_j} \frac{f|G|}{r^{\alpha}} \, d\xi_1 \, d\xi_2 \tag{5.37}$$

The above mentioned procedure for mapping the curved element S onto the planar polygon $\bar{S}$ via the parametric space (η_1, η_2) is illustrated in Fig. 5.10.

Now one can introduce polar coordinates (ρ, θ) in each triangular region $\bar{\Delta}_j$ of the projected quadrilateral $\bar{S}$, as shown in Fig. 5.11 .

$$\xi_1 = \rho \cos\theta$$

$$\xi_2 = \rho \sin\theta \tag{5.38}$$

Thus, the integral of equation (5.37) becomes

$$I_j = |\, l_{11}^{\,j} l_{22}^{\,j} - l_{12}^{\,j} l_{21}^{\,j} \,| \int_0^{\Delta\theta_j} \int_0^{\rho_j(\theta)} \frac{f|G|}{r^{\alpha}} \, \rho \, d\rho \, d\theta \tag{5.39}$$

and from equations (5.34) and (5.38) one can write

$$\eta_1 = \rho \, (l_{11}^{\,j} \cos\theta + l_{12}^{\,j} \sin\theta) + \bar{\eta}_1$$

$$\eta_2 = \rho \, (l_{21}^{\,j} \cos\theta + l_{22}^{\,j} \sin\theta) + \bar{\eta}_2 \tag{5.40}$$

The upper limit $\rho_j(\theta)$ of the integral in the radial direction $\rho_j(\theta)$ is given by

$$\rho_j(\theta) = \frac{h_j}{\cos(\theta - a_j)} \quad , \tag{5.41}$$

where h_j, a_j are defined in Fig. 5.5 of the previous section.

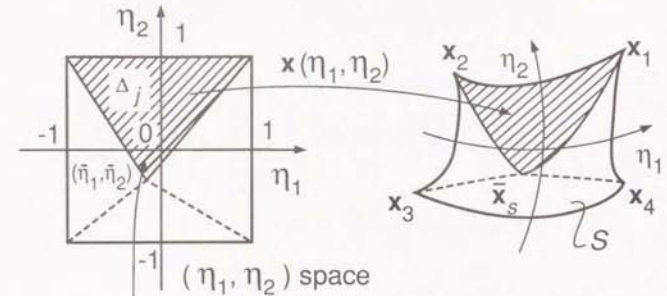

Linear map: L_j

$$I = \int_1^1 \int_{-1}^1 \frac{f|\mathbf{G}|}{r^\alpha} d\eta_1 d\eta_2$$

$$= \sum_{j=1}^4 I_j$$

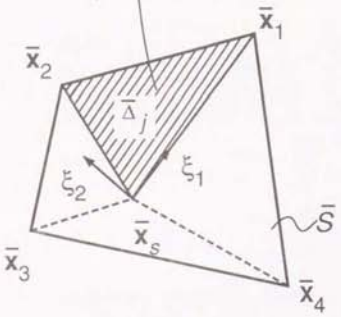

$$I_j = |L_j| \iint_{\bar{\Delta}_j} \frac{f|\mathbf{G}|}{r^\alpha} d\xi_1 d\xi_2$$

Fig. 5. 10 Mapping from S to $\bar{S}$ via the parametric space (η_1, η_2)

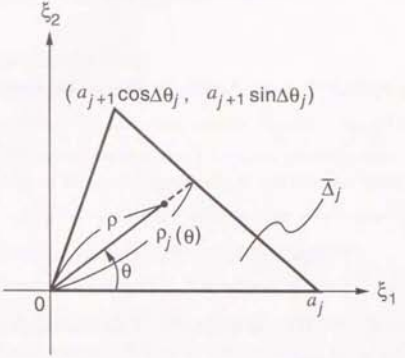

Fig. 5.11 Polar coordinates (ρ, θ) in $\bar{\Delta}_j$

5.5 Radial Variable Transformation

This section deals with two cases ;

(i) when the source point $\mathbf{x}_s$ is on the element and produces weak singularity ($\alpha=1$)

and

(ii) when the source point $\mathbf{x}_s$ is very near the element and results in a near singularity.

These types of singularities or near singularities can be investigated by looking at the integral in the radial direction in equation (5.39), i.e.

$$J(\theta) = \int_0^{\rho_j(\theta)} \frac{f|\mathbf{G}|}{r^\alpha}\,\rho\,\mathrm{d}\rho \tag{5.42}$$

In order to cope with the near singularity, a transformation of the radial variable ρ will be introduced.

(i) Weakly Singular Integrals

As shown in section 3.1 , the singular integrals ($d=0$) arising in the calculation of H and G matrices in three dimensional potential problems are only weakly singular and have kernels of order at most $O(1/r)$, i.e. $\alpha=1$ in equation (5.42).

Since $r\sim\rho$ in the proximity of $\mathbf{x}_s$, where ρ is the radial length along the tangent plane at $\mathbf{x}_s$, the singularity $O(1/r)$ is cancelled by ρ to give a regular kernel of order $O(1)$. Hence, no extra transformation in the radial variable is necessary for the weakly singular integrals. It will be shown in the numerical results in Chapter 10 that the use of polar coordinates with the angular variable

transformation enables one to calculate the weakly singular integrals very efficiently, irrespective of the position of the source point $\mathbf{x}_s$ on the element .

It is worth noting that in this method, the same set of integration points can be used for the calculation of both H and G matrices since the order of singularity involved is the same, as demonstrated in Chapter 3.

(ii) Nearly Singular Integrals

It will be shown that nearly singular integrals ($0<d\ll 1$) are much more difficult to calculate efficiently compared to singular integrals ($d=0$). Using polar coordinates alone, for instance, does not give accurate results when $0<d\ll 1$.

(1) Singularity cancelling radial variable transformation

To overcome this difficulty, Hayami and Brebbia [17] have proposed a transformation of the radial variable ρ for the integral of equation (5.42). This is done by approximating the distance $r=|\mathbf{x}-\mathbf{x}_s|$ by $r'=\sqrt{\rho^2+d^2}$ as shown in Fig. 5.12, which is equivalent to approximating the curved element by its projection on to its tangent plane at $\hat{\mathbf{x}}_s$.

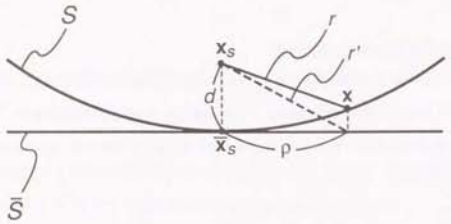

Fig. 5.12 Approximate distance $r' \equiv \sqrt{\rho^2 + d^2}$ of r

Here it is worth noting that for general curved elements, r' does not approximate r very well when $\mathbf{x}$ is far from the source projection $\hat{\mathbf{x}}_s$. However, the (near) singularity $1/r^{\alpha}$ is only dominant in the neighborhood of $\bar{\mathbf{x}}_s$, where $r \sim r'$, so that the transformation $R(\rho)$ based on this approximation $r' \sim r$ should work efficiently for (near) singular integrals ($0 \leqq d \ll 1$), even when the curvature of the element is relatively large.

Hence, a radial variable transformation $R(\rho)$ is introduced such that

$$\rho \, d\rho = r'^{\alpha} dR = \sqrt{\rho^2 + d^2}^{\,\alpha} \, dR \tag{5.43}$$

This transforms the radial integral of equation (5.42) as follows :

$$J(\theta) = \int_0^{\rho_j(\theta)} \frac{f|G|}{r^{\alpha}} \, \rho \, d\rho$$

$$= \int_{R(0)}^{R(\rho_j(\theta))} \frac{f|G|}{r^{\alpha}} \, r'^{\alpha} \, dR \tag{5.44}$$

This operation has the effect of cancelling the singular behaviour of $1/r^{\alpha}$ by r'^{α}. The transformation $R(\rho)$ is defined by equation (5.43) as

$$R(\rho) = \int \frac{\rho}{\sqrt{\rho^2 + d^2}^{\,\alpha}} \, d\rho \quad , \tag{5.45}$$

which can be integrated analytically as follows :

From the definition of the approximate distance

$$r' = \sqrt{\rho^2 + d^2} \tag{5.46}$$

$$r'^2 = \rho^2 + d^2 \tag{5.47}$$

$$r' dr' = \rho \, d\rho \tag{5.48}$$

so that

$$R(\rho) = \int \frac{\rho}{r'^{\alpha}} \, d\rho$$

$$= \int \frac{r'}{r'^{\alpha}} \, dr'$$

$$= \int r'^{(1-\alpha)} \, dr'$$

$$= \begin{cases} \dfrac{r'^{(2-\alpha)}}{2-\alpha} & \text{for } \alpha \neq 2 \\ \log r' & \text{for } \alpha = 2 \end{cases} \tag{5.49}$$

$$= \begin{cases} \dfrac{(\rho^2+d^2)^{\frac{2-\alpha}{2}}}{2-\alpha} & \text{for } \alpha \neq 2 \\ \log (\rho^2+d^2)^{\frac{1}{2}} & \text{for } \alpha = 2 \end{cases} \tag{5.50}$$

From equation (5.50), the inverse function $\rho(R)$ of $R(\rho)$ is given by

$$\rho(R) = \begin{cases} \left| \{(2-\alpha)R\}^{\frac{2}{2-\alpha}} - d^2 \right|^{\frac{1}{2}} & , \quad (\alpha \neq 2) \\ (e^{2R} - d^2)^{\frac{1}{2}} & , \quad (\alpha = 2) \end{cases} \tag{5.51}$$

From equation (5.49) the function $r'(R)$ is given by

$$r'(R) = \begin{cases} \{(2-\alpha)R\}^{\frac{1}{2-\alpha}} & , \quad (\alpha \neq 2) \\ e^{R} & , \quad (\alpha = 2) \end{cases} \tag{5.52}$$

$R(\rho)$, $\rho(R)$ and $r'(R)$ are given in Table 5.1 for $\alpha = 1 \sim 5$.

It is found that the radial transformation (5.45) exactly cancels out the (near) singularity in equation (5.44) when $f \equiv$constant for the case of planar parallelogram elements and planar triangular elements ($|G| \equiv$constant). This means that only one integration point is required for the radial integration to give

Table 5.1 Radial variable transformation $R(\rho)$ and $\rho(R)$, $r'(R)$ for $\alpha = 1 \sim 5$.

α	$R(\rho)$	$\rho(R)$	$r'(R)$
1	$\sqrt{\rho^2+d^2}$	$\sqrt{R^2-d^2}$	R
2	$\log \sqrt{\rho^2+d^2}$	$\sqrt{e^{2R}-d^2}$	e^R
3	$-\dfrac{1}{\sqrt{\rho^2+d^2}}$	$\sqrt{\dfrac{1}{R^2}-d^2}$	$-\dfrac{1}{R}$
4	$-\dfrac{1}{2(\rho^2+d^2)}$	$\sqrt{-\dfrac{1}{2R}-d^2}$	$\sqrt{-\dfrac{1}{2R}}$
5	$-\dfrac{1}{3(\rho^2+d^2)^{3/2}}$	$\sqrt{(-3R)^{-2/3}-d^2}$	$(-3R)^{-1/3}$

an accurate result, independent of the source distance d. In other words, the integration in the radial variable was done analytically. In this sense, the method is semi-analytical.

From this point of view, for a planar element S, $(r=r')$, with $f \equiv$constant, the radial component of the integrals

$$I_{\alpha,\gamma} = \int_S \frac{f\rho^{\gamma}}{r^{\alpha}} \, dS \tag{5.53}$$

where $\gamma = 0$; $\alpha = 1,3,5$ and $\gamma = 1$; $\alpha = 3,5$ (cf. Table 3.2) which occur in three dimensional potential problems can be calculated analytically as follows.

$$I_{\alpha,\gamma} = \sum_j |\det L_j| \, I_{\alpha,\gamma,j} \tag{5.54}$$

$$I_{\alpha,\gamma,j} = \int_0^{\Delta\theta_j} d\theta \int_0^{\rho_j(\theta)} \frac{f\rho^{\gamma+1}}{r^{\alpha}} \, d\rho$$

$$= \int_0^{\Delta\theta_j} J_{\alpha,\gamma,j}(\theta)\, d\theta \qquad (5.55)$$

where

$$J_{\alpha,\gamma,j} = \int_0^{\rho_j(\theta)} \frac{f\rho^\delta}{r^\alpha}\, d\rho$$

$$= f \int_0^{\rho_j(\theta)} \frac{\rho^\delta}{\sqrt{\rho^2+d^2}^{\,\alpha}}\, d\rho$$

$$= f \cdot \left[R_{\alpha,\delta}(\rho_j(\theta)) - R_{\alpha,\delta}(0) \right] \qquad (5.56)$$

where

$$R_{\alpha,\delta}(\rho) = \int \frac{\rho^\delta}{\sqrt{\rho^2+d^2}^{\,\alpha}}\, d\rho \qquad (5.57)$$

and $\delta = \gamma + 1$, so that

$\delta = 1$; $\alpha = 1, 3, 5$ and

$\delta = 2$; $\alpha = 3, 5$

For $\delta = 1$,

$$R_{\alpha,1}(\rho) = \frac{\sqrt{\rho^2+d^2}^{\,2-\alpha}}{2-\alpha} \quad ; \quad \alpha = 1, 3, 5 \qquad (5.58)$$

from equation (5.49).

For $\delta = 2$, which occurs in flux calculations

$$R_{3,2}(\rho) = \int \frac{\rho^2}{\sqrt{\rho^2+d^2}^{\,3}}\, d\rho$$

$$= \log(\rho + \sqrt{\rho^2+d^2}) - \frac{\rho}{\sqrt{\rho^2+d^2}} \qquad (5.59)$$

and

$$R_{5,2}(\rho) = \int \frac{\rho^2}{\sqrt{\rho^2+d^2}^{\,5}}\, d\rho$$

$$= \frac{\rho^3}{3d^2\sqrt{\rho^2+d^2}^{\,3}} \qquad (5.60)$$

from equations (3.141) and (3.142) respectively.

For general curved elements, one can also use the radial variable transformations of equations (5.50), (5.58) and (5.59). In this case, the radial variable transformations no longer cancell the (near) singularity exactly, since the element is curved. Hence, more than one integration points are required for the integration in the transformed variable R.

For instance, numerical results in Chapter 10 show that, for a spherical quadrilateral element S, with f = constant, the approach works efficiently when the source projection $\hat{x}_s$ is near the centre of the element, although it requires additional radial integration points for the case $d \ll 1$. However, as $\hat{x}_s$ moves away from the centre of the element towards the edge of the element, the method seems to require more radial integration points and becomes inefficient.

Problems also arise for the case of planar quadrilateral elements which are not parallelograms. This is caused by the fact that the mapping from the square in the (η_1, η_2)-space to an element is linear only when the element is a planar parallelogram.

Similarly, for curved elements the linear mapping L_j defined for each region $\bar{\Delta}_j$ in equation (5.34) does not give the exact point on the curved element whose projection matches the integration point on the tangent plane, since this inverse projection is defined by a nonlinear mapping.

At first thought, inaccuracy of the inverse mapping appears to be the main reason for causing inefficient cancellation of the (near) singularity.

(2) Consideration of exact inverse projection and curvature of the element in the radial variable transformation

In order to overcome these difficulties, the following modifications were considered.

(i) Exact projection of the curved element S on to the plane tangent at $\hat{x}_s$.

(ii) Exact inverse projection from the integration point on the tangent plane to the curved element using the Newton-Raphson method to account for the nonlinear mapping.

(iii) A more accurate approximation of the distance r by taking the curvature of the element at $\hat{x}_s$ into account in the approximating distance r' and the radial variable transformation $R(\rho)$ based on this r'.

The combination of these modifications resulted in a significant decrease of the number of necessary radial integration points, which remain almost constant for very small values of the distance d, for the case when f =constant in the integration

$$\int_S \frac{f}{r^\alpha}\, dS \quad .$$

However, this approach has the following draw backs :

(i) It was found that when $f \neq$ constant, for instance for integrals containing the interpolation function :

$$\int_S \frac{\phi_{ij}}{r^\alpha}\, dS \quad ,$$

the simple radial variable transformation

$$R(\rho) = \int \frac{\rho}{\sqrt{\rho^2 + d^2}}\, d\rho$$

with the linear mapping of equation (5.23) based on L_j, requires more than 32 Gauss points to achieve a relative error $< 10^{-6}$, for a planar square element, as will be shown in Chapter 10.

For planar square elements, the 'approximate' projection of the element S to S, the inverse projection using the linear mapping L_j, and the 'approximating' distance $r' = \sqrt{\rho^2 + d^2}$ are all exact. Hence, the failure to integrate $\int_S \phi_{ij}/r^\alpha\, dS$ indicates that the above modifications are not sufficient to calculate the integrals $\int_S f/r^\alpha\, dS$ for general curved elements, let alone planar elements.

In fact numerical experiments on curved elements showed that the above modifications do not help to decrease the necessary integration points to calculate $\int f/r^\alpha\, dS$ over curved elements when $f \neq$ constant.

(ii) The two variable Newton-Raphson iteration has to be applied for each integration point in order to find the inverse projection, which results in excessive CPU time.

(iii) Since an exact projection of the curved element S to the tangent plane at $\hat{x}_s$ is performed, the projected quadrilateral $\bar{S}$ generally has curved edges. This causes many complexities when performing the integration in $\bar{S}$.

Another disadvantage of the singularity cancelling radial transformation proposed so far is the fact that they require a different transformation for different order of singularities $\alpha = 1 \sim 5$. This implies that different sets of integration points and calculation of the quantities like r, $|G|$, ϕ_{ij} for them are required for each α. For instance, different sets of integration points are required for the computation of near singular integrals $g_{e'e}^{kl}$ and $h_{e'e}^{kl}$ of equation (2.38) and (2.39) in order to obtain the influence matrices G and H.

Consequently a more simple but robust radial transformation is desired.

(3) Adaptive logarithmic radial variable transformation (log-L_2)

In order to overcome the above difficulties, one resorts to the approximate projection and the linear mapping from the tangent plane to the curved element mentioned in sections 5.2 and 5.3.

However, this time, instead of using the same degree α of the radial transformation as the (near) singularity $1/r^{\alpha}$, as in equations (5.43) and (5.44), radial transformations with different degrees $\beta \neq \alpha$ were attempted, i.e.

$$\rho \, \mathrm{d}\rho = r'^{\beta} \mathrm{d}R \tag{5.61}$$

and

$$J(\theta) = \int_{R(0)}^{R(\rho_j(\theta))} \frac{f|\mathrm{G}|}{r^{\alpha}} r'^{\beta} \mathrm{d}R \tag{5.62}$$

where $\alpha = 1 \sim 5$ and $\beta = 1 \sim 5$ independently.

As a result, it was found (cf. Chapter 10) that the transformation corresponding to $\beta = 2$:

$$\rho \, \mathrm{d}\rho = r'^{2} \mathrm{d}R \tag{5.63}$$

or

$$R(\rho) = \log \sqrt{\rho^2 + \mathrm{d}^2} \quad , \tag{5.64}$$

which gives

$$\rho(R) = \sqrt{\mathrm{e}^{2R} - d^2} \tag{5.65}$$

$$r'(R) = \mathrm{e}^{R} \tag{5.66}$$

works most efficiently for different types of near singularities $1/r^{\alpha}$, ($\alpha = 1,2,3,4,5$). We shall refer to this transformation as the adaptive logarithmic transformation (log-L_2), since $R(\rho)$ is the logarithm of the L_2 - norm in the (ρ, d)-space.

As will be shown in the numerical results in Chapter 10, this log-L_2 transformation works efficiently for general curved elements, with arbitrary position of the source projection $\hat{\mathbf{x}}_s$. It also enables one to calculate accurately and

efficiently nearly singular integrals whose kernels include the interpolation functions ϕ_{ij} even when $0 < d \ll 1$, which was not possible with previous methods. The log-L_2 radial variable transformation also has the virtue that only one radial transformation is necessary for kernels with near singularities of different orders, such as in $g_{e'e}^{kl}$ and $h_{e'e}^{kl}$ in equations (2.38) and (2.39) for the G and H matrices, or g_e^{sl}, h_e^{sl} in equations (2.50) and (2.51) for the potential at an internal point $\mathbf{x}_s$.

The reason why the adaptive logarithm radial transformation (log-L_2) works efficiently for nearly singular integrals of the type $\int_S 1/r^{\alpha} \mathrm{d}S$, ($\alpha = 1,2,3, \cdots$) seems to be the following:

(i) For $0 < d \ll 1$, r'^2 is sufficient to weaken the near singularity of $1/r^{\alpha}$ ($\alpha = 1 \sim 5$).

(ii) Since the lower and upper bounds of the radial integration is

$$R(0) = \log d \tag{5.67}$$

and

$$R(\rho_j(\theta)) = \log \sqrt{\rho_j(\theta)^2 + d^2} \tag{5.68}$$

respectively, the range of integration does not expand drastically as d becomes very small. This enable the Gauss-Legendre quadrature formula to work efficiently in the transformed variable R.

For higher degree transformations this is not the case, for example,

$$R(0) = -\frac{1}{d} \qquad (\beta = 3) \quad , \tag{5.69}$$

$$R(0) = -\frac{1}{2d^2} \qquad (\beta = 4) \quad , \tag{5.70}$$

$$R(0) = -\frac{1}{3d^3} \qquad (\beta = 5) \quad . \tag{5.71}$$

However, a more rigorous explanation for the optimality of the $\beta = 2$ (log-L_2) transformation will be given in Chapter 6.

(4) Adaptive logarithmic radial variable transformation (log-L_1)

As will be shown by numerical experiments in Chapter 10, and explained by the error analysis in section 6.2 , the adaptive logarithmic transformation (log-L_2)

$$R(\rho) = \log \sqrt{\rho^2 + d^2} \tag{5.64}$$

which was proposed in the previous section (3) , works efficiently for nearly singular integrals arising from the calculation of the potential $u(\mathbf{x}_s)$ at a point $\mathbf{x}_s$ very near the boundary.

However, the log-L_2 transformation of equation (5.64) does not work so efficiently for nearly singular integrals arising from the calculation of the flux (eg. electrostatic field E, magnetostatic field B) or the potential derivative $\partial u/\partial \mathbf{x}_s$ at a point $\mathbf{x}_s$ very near the boundary. This is demonstrated by numerical experiments in Chapter 10. The reason for the inefficiency of the log-L_2 transformation for the potential derivative is given in the error analysis of section 6.8.

In short, the near singular integrals for the potential derivative $\partial u/\partial \mathbf{x}_s$ include integrals of the type

$$J_{\alpha,2} = \int_0^{\rho_j} \frac{\rho^2}{r^\alpha} \, d\rho \quad ; \quad (\alpha = 3,5) \tag{5.72}$$

in the radial variable ρ , where

$$\rho_j = \rho_j(\theta) \tag{5.73}$$

The integral $J_{\alpha,2}$ of equation (5.72) is transformed by the log-L_2 transformation

$$R(\rho) = \log \sqrt{\rho^2 + d^2} \tag{5.64}$$

to give

$$J_{\alpha,2} = \int_{R(0)}^{R(\rho_j)} \rho \, r^{2-\alpha} \, dR \tag{5.74}$$

where

$$r = \sqrt{\rho^2 + d^2} \tag{5.75}$$

for planar elements ,

$$F(R) = \rho \, r^{2-\alpha} \tag{5.76}$$

and

$$\frac{dF}{dR} = \frac{dF}{d\rho} \frac{d\rho}{dR} \tag{5.77}$$

so that

$$\left. \frac{dF}{dR} \right|_{\rho=+0} = +\infty \tag{5.78}$$

and similarly

$$\left(\frac{dF}{dR} \right)^{(2\alpha)} \Big|_{\rho=+0} = -\infty \tag{5.79}$$

which means that the application of the Gauss-Legendre formula to the numerical integration of $F(R) = \rho \, r^{2-\alpha}$ with respect to the variable R in the integral of equation (5.74) is expected to be inaccurate, or inefficient in that it requires a lot of integration points.

The basic reason for this is that for the log-L_2 transformation

$$R(\rho) = \log \sqrt{\rho^2 + d^2} \tag{5.64}$$

$$\frac{dR}{d\rho} = \frac{\rho}{r^2} = \frac{\rho}{\rho^2 + d^2} \tag{5.80}$$

and

$$\left. \frac{dR}{d\rho} \right|_{\rho=+0} = +0 \tag{5.81}$$

as shown in Fig. 5.13 , so that

$$\frac{d\rho}{dR} = \frac{\rho^2 + d^2}{\rho} \tag{5.82}$$

which results in

$$\left. \frac{d\rho}{dR} \right|_{\rho=+0} = +\infty \tag{5.83}$$

in equations (5.77) and (5.78) .

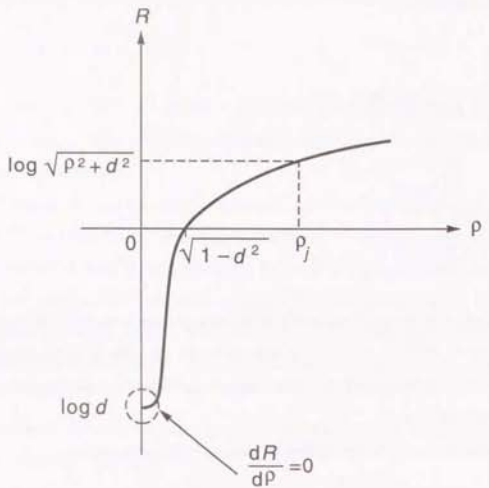

Fig. 5.13 The log-L_2 transformation :
$R(\rho) = \log \sqrt{\rho^2+d^2}$

In order to avoid this defect of the log-L_2 transformation of equation (5.64), one would like to have a radial variable transformation which retains the nice logarithmic character of the log-L_2 transformation and yet has the property

$$\left.\frac{dR}{d\rho}\right|_{\rho=+0} \neq +0 \quad , \tag{5.84}$$

so that $d\rho/dR$ has a finite value at $\rho=+0$.

This can be satisfied by the transformation

$$R(\rho) = \log(\rho+d) \quad , \tag{5.85}$$

which we shall refer to as the adaptive logarithmic radial variable transformation (log-L_1), or the log-L_1 transformation, since it is the logarithm of the L_1-norm in the (ρ, d)-space. Note that

$$R(0) = \log d \tag{5.86}$$

$$R(\rho_j) = \log(\rho_j + d) \quad . \tag{5.87}$$

From equation (5.85),

$$\frac{dR}{d\rho} = \frac{1}{\rho+d} \quad , \tag{5.88}$$

which satisfies

$$\left.\frac{dR}{d\rho}\right|_{\rho=0} = \frac{1}{d} \neq 0 \quad , \tag{5.89}$$

as shown in Fig. 5.14, so that

$$\left.\frac{d\rho}{dR}\right|_{\rho=0} = d \neq \infty \tag{5.90}$$

As will be shown in section 6.8, the essential nature of the radial component of the near singular integrals in three dimensional potential problems can be represented by

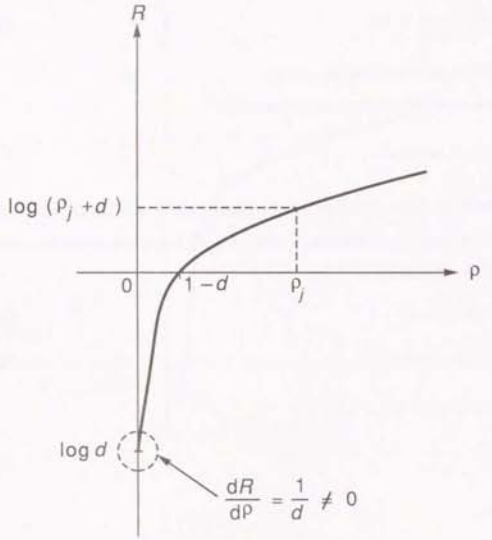

Fig. 5.14 The log-L_1 transformation :
$R(\rho) = \log(\rho + d)$

$$J_{\alpha,\delta} = \int_0^{\rho_j} \frac{\rho^\delta}{r^\alpha} \, d\rho \tag{5.91}$$

where

$$\delta = 1 ; \quad \alpha = 1, 3$$

for the calculation of the potential $u(\mathbf{x}_s)$ and

$$\delta = 1 ; \quad \alpha = 3, 5$$

$$\delta = 2 ; \quad \alpha = 3, 5$$

for the potential derivative $\partial u / \partial \mathbf{x}_s$. (cf. Table 3.3 of Chapter 3)

The integral of equation (5.91) is transformed by the log-L_1 transformation of equation (5.85) as

$$J_{\alpha,\delta} = \int_{R(0)}^{R(\rho_j)} \frac{\rho^\delta}{r^\alpha} e^R \, dR \quad , \tag{5.92}$$

since from equations (5.85) and (5.88)

$$\frac{d\rho}{dR} = \rho + d = e^R \quad . \tag{5.93}$$

Let the integrand of equation (5.92) be

$$F(R) \equiv \frac{\rho^\delta e^R}{r^\alpha} = \frac{\rho^\delta (\rho + d)}{r^\alpha} \quad , \tag{5.94}$$

where

$$\log d \leq R \leq \log(\rho_j + d) \quad , \tag{5.95}$$

and

$$\frac{dF}{dR} = \frac{e^R \rho^{\delta-1}}{r^{\alpha+2}} \left| r^2 \left\{ (\delta+1)\rho + \delta d \right\} - \alpha \rho^2 e^R \right|$$

$$= \frac{(\rho + d)\rho^{\delta-1}}{r^{\alpha+2}} \left\{ (\delta - \alpha + 1)\rho^3 + (\delta - \alpha) d\rho^2 + (\delta+1) d^2 \rho + \delta d^3 \right\} \tag{5.81}$$

so that

$$\left. \frac{dF}{dR} \right|_{\rho=0} = \delta \rho^{\delta-1} d^{2-\alpha} = \begin{cases} d^{2-\alpha} & : (\delta = 1) \\ 0 & : (\delta = 2) \end{cases} \quad . \tag{5.97}$$

and dF/dR remains finite for the interval of R in equation (5.95), in contrast with equation (5.78) for the log-L_2 transformation.

Hence, the adaptive logarithmic radial variable transformation (log-L_1) stands a good chance for the efficient calculation of near singular integrals for the potential derivative $\partial u/\partial \mathbf{x}_s$ as well as the potential $u(\mathbf{x}_s)$. This will be demonstrated by numerical experiments in Chapter 10.

In fact, it turns out that the log-L_1 transformation is more efficient than the log-L_2 transformation, not only for the flux calculation but also for the potential calculation when curved elements and/or high order interpolation functions are used. This can be explained by the presence of terms with $\delta \geqq 2$ in equation (5.91) for such cases.

The log-L_1 transformation is also more robust against the change of the source distance d and the position of the source projection $\bar{\mathbf{x}}_s$, compared to the log-L_2 transformation.

Thus, the log-L_1 radial variable transformation is preferred to the log-L_2 transformation.

(5) $L_1^{-1/5}$ transformation

A natural question to ask then, is whether the log-L_1 transformation is the optimum radial variable transformation based on the Gauss -Legende formula, whether there are still better transformations.

Looking at the convergence results for the L_2-type transformation in Fig. 10.18~10.22, we observe that, although the log-L_2 transformation $R(\rho)=\log\sqrt{\rho^2+d^2}$ corresponding to $\beta=2$ is most robust for integrals $\int_S 1/r^\alpha \, dS$, ($\alpha=1\sim5$), the transformation $R(\rho)=-(\rho^2+d^2)^{-1/2}$ corresponding to $\beta=3$ shows better convergence for the case $\alpha=4, 5$.

This leads us to try the corresponding L_1-type transformation

$$R(\rho)=-(\rho+d)^{-1} \tag{5.98}$$

Numerical experiments on the model radial variable integrals

$$I_{\alpha,\delta}=\int_0^{\beta_j}\frac{\rho^\delta}{r^\alpha}\,d\rho \tag{10.45}$$

where

$$r=\sqrt{\rho^2+d^2} \tag{10.46}$$

show that the transformation (5.98) gives better results for $\alpha=3, \delta=1$; $\alpha=5, \delta=1$ and $\alpha=5, \delta=2$ compared to the log-L_1, transformation. However, the results for $\alpha=1, \delta=1$ and $\alpha=3, \delta=2$ are very bad as shown in Table 10.25.

This then leads us to seek for L_1-type transformation which lie between $\log(\rho+d)$ and $(\rho+d)^{-1}$.

When we look at the transformation as functions of $x=\rho+d$, the functions posses singularities of order $\log x$ and $1/x$, respectively. Then, it seems reasonable to expect better transformations among functions with order of singularities in between $\log x$ and $1/x$, i.e. $x^{-1/m}$ where $m>1$. Hence, we arrive at the radial variable transformation of the form

$$R(\rho)=-(\rho+d)^{-\frac{1}{m}}, \quad m>1 \tag{5.99}$$

Numerical experiments in Chapter 10 (cf. Tables 10.26~10.38 and Fig. 10.29) show that optimum results are obtained for $m=5$,

$$R(\rho)=-(\rho+d)^{-\frac{1}{5}} \tag{5.100}$$

which we shall call the $L_1^{-1/5}$ transformation. Comparing Tables 10.24 and 10.32 or Fig. 10.28. and 10.29, we can expect that the $L_1^{-1/5}$ transformation gives better results than the log-L_1 transformation for the integration of both the potential kernels u^*, q^* and the flux kernels $\partial u^*/\partial \mathbf{x}_s$ and $\partial q^*/\partial \mathbf{x}_s$. This is confirmed for the flux kernels by numerical results over curved elements in section 10.7.

However, for the potential kernels, the log-L_1 transformation gives better results than the $L_1^{-1/5}$ transformation. Hence, the best strategy is to use the log-L_1 transformation for the calculation of potential or H, G matrices, and to use the $L_1^{-1/5}$ transformation when flux calculation is involved.

(6) Single and double exponential radial variable transformations

In order to weaken the near singularity in the radial variable near $\rho=0$, we can also use exponential type radial transformations [37]. The exponential type transformations themselves are not original [36, 13, 32, 14, 26, 16, 30, 27], but the fact that they are applied in the radial variable ρ in the tangent plane S is new.

There are basically two ways of performing the exponential type radial transformations in the radial variable ρ. The first way is to map the radial variable $\rho:[0, \rho_j(\theta)]$ on to the half-infinite interval $R:[-\infty, 0]$. The second way is to map ρ on to the whole infinite interval $R:[-\infty, \infty]$. Numerical experiments in Chapter 10 show that the second procedure gives better results for different nearly singular integrands F and different source distances d. This is because the numerical integration error near the end point $\rho=\rho_j(\theta)$ in equation (5.39) and (5.42) is effectively reduced by the second procedure.

Given the transformation to the whole infinite interval $R:[-\infty, +\infty]$, there is another choice of using the single or double exponential transformation.

(a) Single Exponential radial variable transformation (SE)

First consider the single exponential transformation

$$\rho(R)=\frac{\rho_j}{2}(1+\tanh R)$$

$$=\frac{\rho_j}{1+e^{-2R}} \quad . \tag{5.101}$$

where

$$\rho_j=\rho_j(\theta) \quad . \tag{5.102}$$

Here $\rho:[0, \rho_j]$ is mapped on to $R:[-\infty, +\infty]$ as shown in Fig. 5.15.

From equation (5.101),

$$\rho(0)=\frac{\rho_j}{2} \quad , \tag{5.103}$$

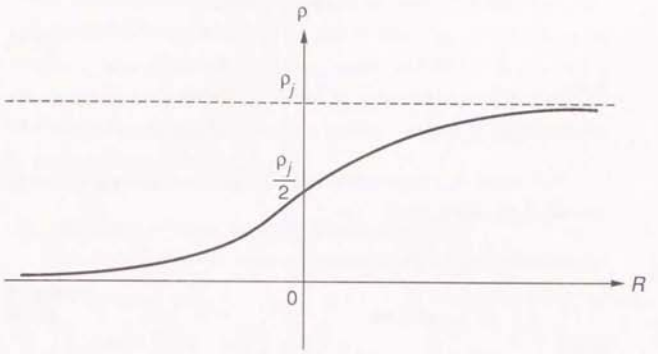

Fig. 5.15 The Single Exponential Transformation $\rho(R)=\frac{\rho_j}{2}(1+\tanh R)$

$$\rho(R) \sim \rho_j (1 - e^{-2R}) \qquad \text{for} \quad R \to +\infty \quad , \tag{5.104}$$

$$\rho(R) \sim \rho_j e^{-2|R|} \qquad \text{for} \quad R \to -\infty \quad , \tag{5.105}$$

so that $\rho(R)$ converges exponentially to ρ_j as $R \to +\infty$, and to 0 as $R \to -\infty$, respectively. From equation (5.101),

$$\frac{d\rho}{dR} = \frac{\rho_j}{2\cosh^2 R} \quad , \tag{5.106}$$

so that

$$\left.\frac{d\rho}{dR}\right|_{\rho=0} = \frac{\rho_j}{2} \quad . \tag{5.107}$$

The integration in the radial variable ρ in equation (5.42) is transformed by equation (5.101) and (5.106) as

$$J(\theta) = \int_0^{\rho_j} \frac{f|G|}{r^\alpha} \rho \, d\rho$$

$$= \int_{-\infty}^{\infty} g(R) \, dR \quad , \tag{5.108}$$

where

$$g(R) = \frac{f|G|\rho}{r^\alpha} \frac{d\rho}{dR} \quad . \tag{5.109}$$

Therefore, the integral $J(\theta)$ can be approximated by the truncated trapezium rule for the infinite interval $R : [-\infty, +\infty]$;

$$J(\theta) \sim J_{h,n} = h \sum_{k=-n}^{n} g(kh) \tag{5.110}$$

It can be seen from Fig. 5.15 that, since the integration points for the trapezium rule in the variable R in equation (5.10) is equally spaced, the corresponding integration points in the variable ρ are concentrated around the near singularity at $\rho=0$ so that, effectively, the near singularity is weakened when transformed to the variable R. Hence, the numerical integration in equation (5.10) results in high precision and efficiency.

As mentioned before, this single exponential transformation of equation (5.90) is superior to the 'half-infinite single exponential transformation'

$$\rho(R) = \rho_j (1 + \tanh R) \tag{5.111}$$

which maps $\rho : [0, \rho_j]$ on to $R : [-\infty, 0]$, since the transformation of equation (5.111) results in inaccuracy due to the truncation error at the end point $\rho = \rho_j$, where as for the transformation of equation (5.101), integration points in the variable ρ are concentrated, not only around the near singularity at $\rho=0$, but also around the end point $\rho = \rho_j$, so that the truncation error of the numerical integration near the end point $\rho = \rho_j$ is significantly reduced. This will be shown in the numerical results in Chapter 10.

(b) Double Exponential radial variable transformation (DE)

Consider next the double exponential transformation [32] applied to the radial variable ρ :

$$\rho(R) = \frac{\rho_j}{2} \left\{ (1 + \tanh\left(\frac{\pi}{2} \sinh R \right) \right\} \tag{5.112}$$

Here again, $\rho : [0, \rho_j]$ is mapped on to $R : [-\infty, +\infty]$ as shown in Fig. 5.16 . From equation (5.112) ,

$$\rho(0) = \frac{\rho_j}{2} \quad , \tag{5.113}$$

$$\rho(R) \sim \rho_j (1 - e^{-\frac{\pi}{2} e^R}) \qquad \text{for} \quad R \to +\infty \quad , \tag{5.114}$$

$$\rho(R) \sim \rho_j \, e^{-\frac{\pi}{2} e^{|R|}} \qquad \text{for} \quad R \to -\infty \quad , \tag{5.115}$$

so that $\rho(R)$ converges to ρ_j as $R \to +\infty$, and $\rho(R)$ converges to 0 as $R \to -\infty$, double exponentially, which is a faster convergence compared to the single exponential transformation of equations (5.101), (5.104) and (5.105). From equation (5.109) ,

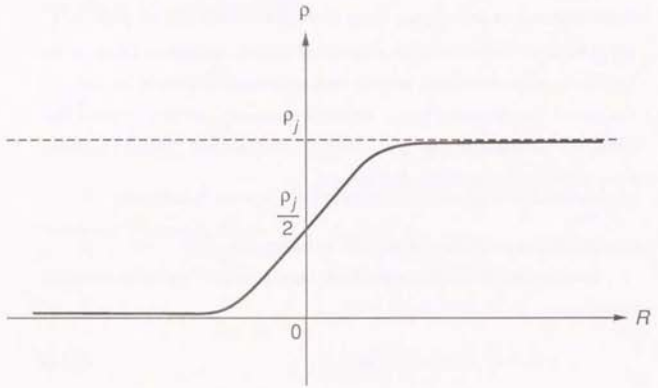

Fig. 5.16 The Double Exponential Transformation

$$\rho(R) = \frac{\rho_j}{2}\left\{1 + \tanh\left(\frac{\pi}{2}\sinh R\right)\right\}$$

$$\frac{d\rho}{dR} = \frac{\pi}{4}\rho_j \frac{\cosh R}{\cosh^2\left(\frac{\pi}{2}\sinh R\right)} \tag{5.116}$$

so that

$$\left.\frac{d\rho}{dR}\right|_{\rho=0} = \frac{\pi}{4}\rho_j \tag{5.117}$$

Equations (5.108), (5.109) and (5.110) can be similarly applied to calculate the integral $J(\theta)$ numerically.

(c) Implementation of the single and double exponential transformations

In the numerical integration using the single exponential or double exponential transformation, the interval h and the number of integration points $2n+1$ in equation (5.110) can be determined for a specific integrand function as follows:

Set $h=1$, for example, and calculate $J_{h,n}$ with increasing n until

$$\frac{|J_{h,n} - J_{h,n-1}|}{|J_{h,n}|} < \epsilon_n \tag{5.118}$$

is satisfied to obtain $J_h \equiv J_{h,n}$.

Repeat the process for $h = 1/2,\ 1/4,\ 1/8, \cdots$ until

$$\frac{|J_{h/2} - J_h|}{|J_{h/2}|} < \epsilon_h \tag{5.119}$$

is satisfied to obtain the final result.

The threshold value ϵ_h may be set equal to the required accuracy ϵ of the integration. It is advisable to set $\epsilon_n \leqq \epsilon_h$.

In order to speed up calculations, it is recommended to calculate the exponential type function such as $\cosh(x)$ by

$ex = \exp(x)$

$ei = 1/ex$

$$\cosh x = (ex + ei)/2 \quad , \tag{5.120}$$

instead of calling the internal function cosh(x), so that ex and ei can be reused to calculate other required exponential type functions such as sinh(x) or tanh(x). For instance, for the single exponential transformation,

$$\rho(R) = \frac{\rho_j e^R}{e^R + 1/e^R} \tag{5.121}$$

$$\cosh R = \frac{e^R + 1/e^R}{2} \tag{5.122}$$

should be used, where e^R and $1/e^R$ are computed only once for a given value for R.

Further CPU-time can be saved by calculating $g(R)$ of equation (5.109) for $R=k$ and $R=-k, (k=1\sim n)$ at the same time, using the fact that

$$\cosh(-R) = \cosh R \tag{5.123}$$

$$\sinh(-R) = -\sinh R \tag{5.124}$$

$$\tanh(-R) = -\tanh R \tag{5.125}$$

etc.

However, in doing so one must make sure that the addition

$$g(-kh) + g(kh) \tag{5.126}$$

does not involve substantial rounding error, since from equation (5.109),

$$|g(-kh)| \gg |g(kh)| \tag{5.127}$$

for relatively large k, since $1/r^a$ becomes dominant when $R \to -\infty$ i.e. when $\rho \to 0$. In order to minimize such sources of error, it is best to perform the addition in equation (5.110) from $k=N$ down to $k=-N$ consecutively. This will result in

adding small quantities together first, instead of adding small numbers to large numbers as in equation (5.126), thus minimizing round off errors.

The advantage of using the single or double exponential transformation in combination with the truncated trapezium rule, is that they do not require any integration tables (such as that of Gauss-Legendre formula), and also they have the advantage that the results used for interval h can be reused for the calculation with interval $h/2$ etc., where as in the Gauss-Legendre formula, the position of the integration points are independent for different numbers of integration points used.

However, the single and double exponential transformations consume significantly more CPU-time per integration point, compared to the log-L_1 and log-L_2 transformations combined with the Gauss-Legendre formula. This is shown in Table 5.2. Chapter 10. (To further speed up the single/double exponential transformations, one may prepare a table of values for ρ and $d\rho/dR$ of equations (5.101) and (5.106) before hand.)

Table 5.2 Comparison of computation per integration point

	Double Exponential	Single Exponential	log-L_2	log-L_1
exponential	1	0.5	1	1
square root			1	
division	2	1.5		
multiplication	2.5	1		
addition/subtraction	2	1	1	1
divide/multiply by 2	1.5		1	
CPU time per integration time (μ seconds on SX-2)	7.6	5.4	~0.2	~0.9

Hence, over all, the log-L_1 radial variable transformation in combination with the Gauss-Legendre formula seems to be the best, considering accuracy, robustness to different types of near singularity and CPU-time.

5.6 Angular Variable Transformation

As will be shown in the numerical results in Chapter 10, when using polar coordinates, the number of integration points required for the angular variable to produce accurate results increases rapidly as the source projection $\hat{\mathbf{x}}_s = \mathbf{x}(\bar{\eta}_1, \bar{\eta}_2)$ approaches the edge of the projected quadrilateral $\bar{S}$.

This causes a problem not only for nearly singular integrals but also for singular integrals resulting from discontinuous elements [1], for which case the source can be very near the element edges.

This phenomenon may be considered as a near singularity in the angular variable and can be explained as follows.

When $\hat{\mathbf{x}}_s$ is very close to the edge $\hat{\mathbf{x}}_{j+1} - \hat{\mathbf{x}}_j$ of the projected quadrilateral $\bar{S}$ as shown in Fig. 5.17, the value of $\rho_j(\theta)$, and hence the integrand with respect to the angular variable θ in the integral

$$I_j = | l_{11}^j l_{22}^j - l_{12}^j l_{21}^j | \int_0^{\Delta\theta_j} \int_0^{\rho_j(\theta)} \frac{f|\mathbf{G}|}{r^a} \rho \, d\rho \, d\theta \tag{5.39}$$

can vary rapidly as θ varies from 0 to $\Delta\theta_j$. Thus, a large number of integration points are necessary to perform the angular integration numerically.

In order to overcome this difficulty of near singularity in the angular variable, strategies similar to those taken in the case of near singularity in the radial variable discussed in section 5.5, are proposed. Namely, a transformation of the angular variable is introduced in order to weaken the near singularity in the angular variable.

(1) Adaptive logarithmic angular variable transformation

First we propose a logarithmic angular variable transformation which weakens the angular near singularity before applying the Gauss-Legendre quadrature formula.

In order to do so, let us assume in equation (5.39) that

$$J(\theta) = \int_0^{\rho_j(\theta)} \frac{f|\mathbf{G}|}{r^a} \rho \, d\rho \sim \rho_j(\theta) \quad , \tag{5.128}$$

since $\rho_j(\theta)$ dominates the behaviour of the integral $J(\theta)$ when $\hat{\mathbf{x}}_s$ is very near an edge of $\bar{S}$.

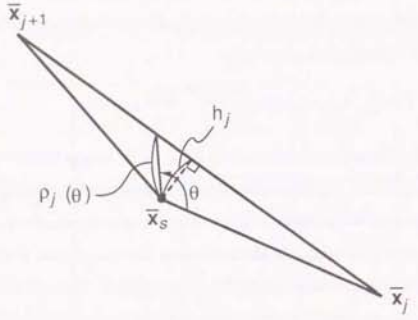

Fig. 5.17 Near singularity in the angular variable θ

Consider next an angular transformation $t = t(\theta)$ such that

$$\frac{d\theta}{dt} = \frac{1}{\rho_j(\theta)} = \frac{\cos(\theta - \alpha_j)}{h_j} \quad , \tag{5.129}$$

where $t(\theta)$ is given for each region Δ_j by

$$t(\theta) = \int \rho_j(\theta)\, d\theta$$

$$= \frac{h_j}{2} \log \left\{ \frac{1+\sin(\theta-\alpha_j)}{1-\sin(\theta-\alpha_j)} \right\} \quad . \tag{5.130}$$

Using t as the new variable for the angular integration in equation (5.39), we obtain

$$\int_o^{\Delta\theta_j} J(\theta)\, d\theta = \int_{t(0)}^{t(\Delta\theta_j)} J(\theta) \frac{d\theta}{dt}\, dt$$

$$= \int_{t(0)}^{t(\Delta\theta_j)} \frac{J(\theta)}{\rho_j(\theta)}\, dt \quad . \tag{5.131}$$

Since

$$\frac{J(\theta)}{\rho_j(\theta)} \sim 1 \quad ,$$

the integrand in (5.131) is expected to be a smooth function of t compared to the original strong variation of $J(\theta)$ with respect to θ. $t(\theta)$ acts as a transformation that weakens the near singularity in the angular variable θ.

Here it is interesting to note that both the radial and angular variable transformations

$$R(\rho) = \log \sqrt{\rho^2 + d^2} \quad , \tag{5.64}$$

$$R(\rho) = \log(\rho + d) \tag{5.64}$$

and

$$t(\theta) = \frac{h_j}{2} \log \left\{ \frac{1+\sin(\theta-\alpha_j)}{1-\sin(\theta-\alpha_j)} \right\} \quad , \tag{5.130}$$

which work efficiently for the radial and angular near singularities respectively, are logarithmic functions related to the near singularity so that

$$R(\rho) \to \infty \quad \text{as} \quad r' = \sqrt{\rho^2 + d^2} \to 0 \tag{5.132}$$

and

$$t(\theta) \to \pm\infty \quad \text{as} \quad \theta - \alpha_j \to \pm\frac{\pi}{2} \quad . \tag{5.133}$$

Hence, the logarithmic function efficiently weakens the near singularity by magnifying the scale of the integration variable in an optimal manner, when $\sqrt{\rho^2+d^2} \ll 1$ and $1 \pm \sin(\theta - a_j) \ll 1$, which are the causes for the radial and angular near singularities respectively. By doing so, enough information is sampled to accurately integrate the rapidly changing integrand in the near singular range.

When $\hat{\mathbf{x}}_s$ is right on the edge, the triangular region $\bar{\Delta}_j$ collapses to a line and it has no contribution to the integral. Hence, one can simply skip the integration loop for that particular j when $\mathrm{sgn}(j)=0$ as defined by (5.27). Using this $\mathrm{sgn}(j)$ makes the programming simple, since it defines the position of $\hat{\mathbf{x}}_s$ with respect to the edge-j.

Numerical experiments in Chapter 10 confirm the accuracy and efficiency of the use of the logarithmic angular variable transformation of equation (5.130) in combination with the Gauss-Legendre formula.

(2) Single and double exponential angular variable transformations

Just as in the case of the radial variable, one can also apply the single/double exponential transformation to the integration in the angular variable, in order to weaken the angular near singularity. The truncated trapezium rule can then be applied to integrate in the infinite interval of the transformed angular variable.

For the integration in the angular variable in equation (5.39), one can apply the single exponential (SE) transformation

$$\theta(t) = \frac{\Delta\theta_j}{2}(1+\tanh t) \tag{5.134}$$

or the double exponential (DE) transformation

$$\theta(t) = \frac{\Delta\theta_j}{2}\left\{1+\tanh\left(\frac{\pi}{2}\sinh t\right)\right\} \quad , \tag{5.135}$$

which map θ: $[0, \Delta\theta_j]$ onto t :$[-\infty, +\infty]$. Hence, the integration in the angular variable is transformed as

$$\int_0^{\Delta\theta_j} J(\theta)\,\mathrm{d}\theta = \int_{-\infty}^{\infty} J(\theta)\frac{\mathrm{d}\theta}{\mathrm{d}t}\,\mathrm{d}t \quad , \tag{5.136}$$

where

$$J(\theta) = \int_0^{\Delta\theta_j(\theta)} \frac{f|\mathrm{G}|}{r^\alpha}\,\rho\,\mathrm{d}\rho \tag{5.42}$$

and

$$\frac{\mathrm{d}\theta}{\mathrm{d}t} = \frac{\Delta\theta_j}{2}\frac{1}{\cosh^2 t} \tag{5.137}$$

for the single exponential transformation of equation (5.134), and

$$\frac{\mathrm{d}\theta}{\mathrm{d}t} = \frac{\pi}{4}\Delta\theta_j \frac{\cosh t}{\cosh^2\left(\frac{\pi}{2}\sinh t\right)} \tag{5.138}$$

for the double exponential transformation of equation (5.135).
In both cases,

$$\int_0^{\Delta\theta_j} J(\theta)\,\mathrm{d}\theta = \int_{-\infty}^{\infty} a(t)\,\mathrm{d}t \tag{5.139}$$

where

$$a(t) = J\{\theta(t)\}\frac{\mathrm{d}\theta}{\mathrm{d}t} \quad . \tag{5.140}$$

Hence, the integral of equation (5.139) can be calculated numerically using the truncated tapezium rule as

$$\int_{-\infty}^{\infty} a(t)\,\mathrm{d}t \sim h\sum_{k=-N}^{N} a(kh) \quad , \tag{5.141}$$

where h and N are determined by the required accuracy as in equations (5.118) and (5.119).

5.7 Implementation of the PART Method

To sum up, the integral of equation (5.1) which we want to calculate, is transformed as follows,

$$I = \int_S \frac{f}{r^\alpha}\,\mathrm{d}S$$

$$= \int_{-1}^{1}\int_{-1}^{1} \frac{f|G|}{r^{\alpha}} \, d\eta_1 \, d\eta_2$$

$$= \sum_{j=1}^{4} I_j \qquad (5.142)$$

where

$$I_j = |\det L_j| \int_0^{\Delta\theta^j} d\theta \int_0^{\rho_j(\theta)} \frac{f|G|}{r^{\alpha}} \, \rho \, d\rho$$

$$= |\det L_j| \int_{t(0)}^{t(\Delta\theta^j)} \frac{d\theta}{dt} \, dt \int_{R(0)}^{R\{\rho_j(\theta(t))\}} \frac{f|G|\rho}{r^{\alpha}} \frac{d\rho}{dR} \, dR \qquad (5.143)$$

and

$$\det L_j = L_{11}^j L_{22}^j - L_{12}^j L_{21}^j \qquad (5.144)$$

$R(\rho)$ is the radial variable transformation which serves to cancel or weaken the (near) singularity due to $1/r^{\alpha}$. $t(\theta)$ is the angular variable transformation which serves to weaken the angular near singularity which arises when $\bar{x}_s$ is near the edges of the approximately projected element $\overline{S}$.

Now that the radial and angular (near) singularities have been weakened by the transformation $R(\rho)$ and $t(\theta)$, the integral I_j of equation (5.143) can be calculated accurately and efficiently by applying standard numerical integration formulas to the integration in the variables R and t.

(1) The use of Gauss-Legendre formula

The best recommended way is to apply the Gauss-Legendre formula [3] to $R(\rho)$ and $t(\theta)$.

The radial variable transformation $R(\rho)$ should be chosen as follows:

(i) For weakly singular integrals ($d=0, \alpha=1$),

e.g. $\int_S \frac{f}{r} \, dS$ and $\int_S \frac{(r,n)}{r^3} f \, dS$

in potential problems,

$$R(\rho) = \rho \qquad (5.145)$$

(ii) For nearly singular integrals ($0<d\ll 1$),

e.g. $\int_S u^* f \, dS$ and $\int_S q^* f \, dS$

for potential calculations and

e.g. $\int_S \frac{\partial u^*}{\partial \mathbf{x}_s} f \, dS$ and $\int_S \frac{\partial q^*}{\partial \mathbf{x}_s} f \, dS$

for flux calculation in potential problems,

$$R(\rho) = \log(\rho + d) \qquad (\log\text{-}L_1 \text{ transformation}) \qquad (5.85)$$

(iii) For planar elements with $f \equiv$ constant in equation (5.142),

$$R(\rho) = \begin{cases} \dfrac{(\rho^2+d^2)^{\frac{2-\alpha}{2}}}{2-\alpha} & \text{for } \alpha \neq 2 \\ \dfrac{1}{2}\log(\rho^2+d^2) & \text{for } \alpha = 2 \end{cases} \qquad (5.50)$$

for integrals of the type $\int_S 1/r^{\alpha} \, dS$, where $\alpha = 1, 3$ occur in potential calculations and $\alpha = 3, 5$ occur in flux calculations in three dimensional potential problems (cf. Table 3.2 and equation (5.50)), and

$$R(\rho) = \begin{cases} \log(\rho + \sqrt{\rho^2+d^2}) - \dfrac{\rho}{\sqrt{\rho^2+d^2}} & \text{for } \alpha = 3 \\ \dfrac{\rho^3}{3d^2\sqrt{\rho^2+d^2}^{\,3}} & \text{for } \alpha = 5 \end{cases} \qquad (5.146)$$

for integrals of the type $\int_S \rho/r^{\alpha} \, dS$, $(\alpha=3,5)$, which occur in flux calculations of three dimensional potential problems. The transformation of equations (5.50) and (5.146) correspond to performing the radial integral analytically. Hence, only one integration point is required in the radial direction to obtain the exact value.

The angular variable transformation $t(\theta)$ is given by

$$t(\theta) = \frac{h_j}{2} \log\left\{\frac{1+\sin(\theta-\alpha_j)}{1-\sin(\theta-\alpha_j)}\right\} \tag{5.130}$$

(logarithmic angular variable transformation) for each region $\bar{\Delta}_j$ $(j=1\sim4)$.

Now that the radial and angular (near) singularities have been weakened (or cancelled) by the variable transformations $R(\rho)$ and $t(\theta)$, the product Gauss-Legendre quadrature formula can be safely applied to the integration in the variables R and t of equation (5.143), i.e.

$$I_j \sim \tilde{I}_j = |\det L_j| \frac{t(\Delta\theta_j)-t(0)}{2} \sum_{k=1}^{N_t} \frac{w(k,N_t)}{\rho_j(t_k)} \frac{R[\rho_j(t_k)]-R(0)}{2} \times$$

$$\sum_{l=1}^{N_R} w(l,N_R) \frac{f(\eta_{1kl},\eta_{2kl})\,|\mathbf{G}(\eta_{1kl},\eta_{2kl})|\,\rho(R_{kl})}{r^a(\eta_{1kl},\eta_{2kl})} \frac{\mathrm{d}\rho}{\mathrm{d}R}(R_{kl}) \tag{5.147}$$

for each region $\bar{\Delta}_j$. $\tilde{I}_j$ need not be computed when $\mathrm{sgn}(j)=0$, in which case the source projection $\bar{x}_s$ lies on the line defined by edge-j so that the area of region $\bar{\Delta}_j$ is zero and $I_j=0$.

In the transformed angular variable $t(\theta)$, the integration points t_k, $(k=1\sim N_t)$ are given by

$$t_k = \frac{t(\Delta\theta_j)-t(0)}{2} g(k,N_t) + \frac{t(\Delta\theta_j)+t(0)}{2} \tag{5.148}$$

where

$$t(\Delta\theta_j) = \frac{h_j}{2} \log\left\{\frac{1+\sin(\Delta\theta_j-\alpha_j)}{1-\sin(\Delta\theta_j-\alpha_j)}\right\} \tag{5.149}$$

$$t(0) = \frac{h_j}{2} \log\left\{\frac{1-\sin\alpha_j}{1+\sin\alpha_j}\right\} \tag{5.150}$$

and

$$\sin(\Delta\theta_j-\alpha_j) = \sin\Delta\theta_j\cos\alpha_j - \cos\Delta\theta_j\sin\alpha_j \tag{5.151}$$

Note also that

$$\rho_j(t_k) \equiv \rho_j\{\theta(t_k)\} = \frac{h_j}{\cos(\theta-\alpha_j)} = h_j\cosh\left(\frac{t_k}{h_j}\right) \tag{5.152}$$

where h_j, $\sin\Delta\theta_j$, $\sin\alpha_j$ etc. are given in equations (5.25) and (5.26). The inverse transform $\theta(t_k)$, which maps the integration point t_k to the angle $\theta(t_k)$ defined in Fig. 5.10 for each triangular region $\bar{\Delta}_j$ in $\bar{S}$, is given by

$$\sin\theta(t_k) = \cos\alpha_j \tanh\left(\frac{t_k}{h_j}\right) + \frac{\sin\alpha_j}{\cosh\left(\frac{t_k}{h_j}\right)} \tag{5.153}$$

$$\cos\theta(t_k) = \frac{\cos\alpha_j}{\cosh\left(\frac{t_k}{h_j}\right)} - \sin\alpha_j \tanh\left(\frac{t_k}{h_j}\right) , \tag{5.154}$$

since

$$\sin(\theta-\alpha_j) = \frac{e^{\frac{2t}{h_j}}-1}{e^{\frac{2t}{h_j}}+1} = \tanh\left(\frac{t}{h_j}\right) \tag{5.155}$$

and

$$\cos(\theta-\alpha_j) = \sqrt{1-\tanh^2\left(\frac{t}{h_j}\right)} = \frac{1}{\cosh\left(\frac{t}{h_j}\right)} \tag{5.156}$$

where

$$\cos(\theta-\alpha_j) > 0 , \quad \text{since} \quad -\frac{\pi}{2} < \theta-\alpha_j < \frac{\pi}{2} .$$

The $\tanh(t_k/h_j)$ and $\cosh(t_k/h_j)$ in equations (5.153) and (5.154) should be calculated using $\exp(t_k/h_j)$ and its reciprocal to save CPU-time, as was done in equation (5.120).

$g(k, N_t)$ and $w(k, N_t)$ in equations (5.148) and (5.147) are respectively the position and weight of the k-th integration point of the N_t point Gauss-Legendre quadrature formula for the interval $[-1, 1]$, which in this case is used for the integration in the transformed angular variable t.

In the transformed radial variable $R(\rho)$, the integration points R_{kl} $(l=1\sim N_l)$ for a given angular direction t_k are given by

$$R_{kl} = \frac{R[\rho_j(t_k)] - R(0)}{2} g(l, N_R) + \frac{R[\rho_j(t_k)] + R(0)}{2} \qquad (5.157)$$

$g(l, N_R)$ and $w(l, N_R)$ are respectively the position and weight of the l-th integration point of the N_R point Gauss-Legendre formula for the interval $[-1,1]$, which in this case is used for the integration in the transformed radial variable R.

In order to calculate f, r and $|G|$ in equation (5.147), we need to know the point (η_{1kl}, η_{2kl}) in region Δ_j of the (η_1, η_2) parameter space, which is mapped linearly from the integration point $(\theta(t_k), \rho(R_{kl}))$ in region Δ_j. To do so, we use equations (5.40), (5.153) and (5.154) to obtain

$$\eta_{1kl} = \rho(R_{kl}) \left\{ l_{11}^j \cos\theta(t_k) + l_{12}^j \sin\theta(t_k) \right\} + \bar{\eta}_1$$

$$\eta_{2kl} = \rho(R_{kl}) \left\{ l_{21}^j \cos\theta(t_k) + l_{22}^j \sin\theta(t_k) \right\} + \bar{\eta}_2 \quad , \qquad (5.158)$$

where

$$\bar{\mathbf{x}}_s = \mathbf{x}(\bar{\eta}_1, \bar{\eta}_2)$$

and

(i) For $R(\rho) = \rho$ of equation (5.145),

$$\rho(R) = R \qquad (5.159)$$

$$\frac{d\rho}{dR} = 1 \quad . \qquad (5.160)$$

(ii) For the log-L_2 transformation

$$R(\rho) = \log\sqrt{\rho^2+d^2} \qquad (5.64)$$

$$\rho(R) = \sqrt{e^{2R}-d^2} \quad = \quad \sqrt{r'^2-d^2} \qquad (5.161)$$

where

$$r' = \sqrt{\rho^2+d^2} = e^R \qquad (5.162)$$

$$\rho\frac{d\rho}{dR} = r'^2 = e^{2R} \qquad (5.163)$$

(iii) For the log-L_1 transformation $R(\rho) = \log(\rho+d)$ of equation (5.85),

$$\rho(R) = e^R - d \qquad (5.164)$$

$$\frac{d\rho}{dR} = e^R = \rho + d \qquad (5.165)$$

(iv) For the $L_1^{-1/m}$ transformation $R(\rho) = -(\rho+d)^{-1/m}$ of equation (5.99),

$$\rho(R) = (-R)^{-m} - d \qquad (5.166)$$

$$\frac{d\rho}{dR} = m(-R)^{-m-1} \qquad (5.167)$$

(2) <u>The use of truncated trapezium rule</u>

In this case, equation (5.143) gives

$$I_j = |\det L_j| \int_{-\infty}^{\infty} \frac{d\theta}{dt} dt \int_{-\infty}^{\infty} \frac{f|G|\rho}{r^\alpha} \frac{d\rho}{dR} dR \quad , \qquad (5.168)$$

so that

$$I_j \sim \tilde{I}_j = |\det L_j| h_t h_R \sum_{k=-N_t}^{N_t} \frac{d\theta}{dt}\bigg|_{t=kh_t} \sum_{l=-N_R}^{N_R} F\left\{\rho(lh_R), \theta(kh_t)\right\} \frac{d\rho}{dR}\bigg|_{R=lh_R} , \qquad (5.169)$$

where

$$F(\rho,\theta) = \frac{f|G|\rho}{r^\alpha} \qquad (5.170)$$

and h_t and h_R are the interval for the trapezium rule for the angular variable t and the radial variable R, respectively.

For the single exponential transformation,

$$\theta(t) = \frac{\Delta\theta_j}{2}(1+\tanh t) \tag{5.134}$$

$$\frac{d\theta}{dt} = \frac{\Delta\theta_j}{2}\frac{1}{\cosh^2 t} \tag{5.137}$$

for the angular variable, and

$$\rho(R) = \frac{\rho_j\{\theta(t)\}}{2}(1+\tanh R) \tag{5.171}$$

$$\frac{d\rho}{dR} = \frac{\rho_j(\theta)}{2}\frac{1}{\cosh^2 R} \tag{5.172}$$

for the radial variable.

For the double exponential transformation,

$$\theta(t) = \frac{\Delta\theta_j}{2}\left\{1+\tanh\left(\frac{\pi}{2}\sinh t\right)\right\} \tag{5.135}$$

$$\frac{d\theta}{dt} = \frac{\pi}{4}\Delta\theta_j\frac{\cosh t}{\cosh^2\left(\frac{\pi}{2}\sinh t\right)} \tag{5.138}$$

for the angular variable, and

$$\rho(R) = \frac{\rho_j\{\theta(t)\}}{2}\left\{1+\tanh\left(\frac{\pi}{2}\sinh R\right)\right\} \tag{5.173}$$

$$\frac{d\rho}{dR} = \frac{\pi}{4}\rho_j\{\theta(t)\}\frac{\cosh R}{\cosh^2\left(\frac{\pi}{2}\sinh R\right)} \tag{5.174}$$

Numerical experiments in Chapter 10 show that the single exponential transformation (SE) is more efficient compared to the double exponential

transformation, in the number of integration points and CPU time, particularly for nearly singular integrals ($0<d\ll 1$) in the radial variable.

However, it is also shown in Chapter 10 that the log-L_1 and log-L_2 radial variable transformations with the Gauss-Legendre formula is more efficient compared to the single/double exponential transformation with the truncated trapezium rule for the integration in the radial variable. Further, the log-L_1 radial variable transformation is more robust compared to the log-L_2 transformation against different types of kernel and element geometry.

The organization of a program to calculate a (nearly) singular integral $\int_S f/r^\alpha dS$ would be the following.

Given the nodes $\mathbf{x}^{i,k}$ ($i,k=-1, 0, 1$) of the curved quadrilateral element S, and the source point $\mathbf{x}_s$ and a table containing weights and positions of the Gauss-Legendre quadrature formula,

(1) Find the source projection $\hat{\mathbf{x}}_s = \mathbf{x}(\hat{\eta}_1, \hat{\eta}_2)$ by the Newton-Raphson method.

(2) Determine $\mathrm{sgn}(j)$, ($j=1\sim4$).

(3) Calculate the unit normal $\mathbf{n}_s$ to the curved element S at $\hat{\mathbf{x}}_s$.

(4) Find the projection $\hat{\mathbf{x}}_j$, ($j=1\sim4$) of the four corner nodes of S on to the plane tangent to S at $\hat{\mathbf{x}}_s$.

(5) Determine the geometry of the projected quadrilateral $\bar{S}$ and the four triangular regions $\bar{\Delta}_j$ ($j=1\sim4$) defined by $\hat{\mathbf{x}}_s$, $\hat{\mathbf{x}}_j$ ($j=1\sim4$). Then, determine the linear mapping matrices L_j ($j=1\sim4$).

(6) Perform the numerical integration for each triangular region $\bar{\Delta}_j$, $j=1\sim4$ (if $\mathrm{sgn}(j)\neq 0$) in the angular and radial transformed variables t and R respectively, according to equation (5.147).

Similar procedures can be taken for a curved triangular element (and arbitrary curved polygonal elements). For triangular elements, the method is

even more attractive since there are generally only three regions $\bar{\Delta}_j$ ($j=1\sim3$) to perform the integration instead of four for quadrilateral elements.

5.8 Moving the Source Projection to the Edge

The angular variable transformation $t(\theta)$ of equation (5.30) was introduced in order to weaken the angular near singularity and reduce the number of angular integration points when the source projection $\hat{\mathbf{x}}_s$ is near the edge of the element.

Although this has a considerable effect, the method still requires many angular integration points when $\hat{\mathbf{x}}_s$ is very near the edge of the element. In order to overcome this problem, the effect of deliberately moving the source projection $\hat{\mathbf{x}}_s$ to the closest edge of the element S was examined.

The procedure is as follows:

Taking the example when $\hat{\mathbf{x}}_s=\mathbf{x}(\tilde{\eta}_1, \tilde{\eta}_2)$ is closest to the edge corresponding to $\eta_1=1$,

1. Let $\hat{\mathbf{x}}'_s=\mathbf{x}(1, \tilde{\eta}_2)$
2. Approximately project S on the polygon $\bar{S}'$ on the plane tangent to S at $\hat{\mathbf{x}}'_s$
3. Define the new source distance as $d'=|\mathbf{x}_s-\hat{\mathbf{x}}'_s|$
4. Introduce polar coordinates (ρ, θ) in $\bar{S}'$, centred at $\hat{\mathbf{x}}'_s$, apply the radial and angular variable transformation and integrate with respect to the transformed variables. In the radial variable transformation, the updated source distance d' is used.

If the initial source projection $\hat{\mathbf{x}}_s$ is close to two edges (i.e. a corner) of the element S, $\hat{\mathbf{x}}_s$ is moved to the corner.

The above procedure is advantageous, not only because it reduces the number of angular integration points, but also because it reduces the number of triangular regions in $\bar{S}$ to integrate over.

Numerical experiment results in Chapter 10 indicate that when the source projection $\hat{\mathbf{x}}_s$ is either outside the element S, or when it is inside S but very close to the edge (namely when $h_j<d$, where h_j is the distance between $\hat{\mathbf{x}}_s$ and the nearest edge-j of the projected element $\bar{S}$), moving the source projection $\hat{\mathbf{x}}_s$ to the edge of the element S leads to a considerable reduction of the number of integration points.

5.9 Variable Transformation in the Parametric Space

So far, we have introduced polar coordinates (ρ, θ) and radial and angular variable transformations $R(\rho)$, $t(\theta)$ in the plane $\bar{S}$ tangent to the curved element S at the source projection $\hat{\mathbf{x}}_s$.

In a similar manner, we can also introduce polar coordinates (ρ, θ) and radial and angular variable transformations in the parametric space (η_1, η_2) which describes the curved element $\mathbf{x}(\eta_1, \eta_2)$.

For instance, for a curved quadrilateral element S defined by $\{\mathbf{x}(\eta_1, \eta_2) \mid -1\leq \eta_1, \eta_2 \leq 1\}$, one can proceed as follows:

(1) Find the point $\hat{\mathbf{x}}_s=\mathbf{x}(\tilde{\eta}_1, \tilde{\eta}_2)$ on S, closest to the source point $\mathbf{x}_s$.

(2) Introduce polar coordinates (ρ, θ) centered at $(\tilde{\eta}_1, \tilde{\eta}_2)$ in the square defined by $-1\leq \tilde{\eta}_1, \tilde{\eta}_2 \leq 1$.

(3) Divide the square in to four triangular regions Δ_j, ($j=1\sim4$) as shown in Fig. 5.7.

(4) In each region Δ_j, introduce radial and angular variable transformations $R(\rho)$, $t(\theta)$ similar to those defined in sections 5.5 and 5.6 for $\bar{\Delta}_j$ in the tangent plane, in order to weaken the (near) singularity.

(5) For each region Δ_j, perform numerical integration with respect to the transformed variables $R(\rho)$ and $t(\theta)$.

For radial variable transformations $R(\rho)$ which make use of the source distance $d=|\mathbf{x}_s-\hat{\mathbf{x}}_s|$, the equivalent source distance D can be defined for the parametric space (η_1, η_2) by,

$$l_1 = |\mathbf{x}(1, \bar{\eta}_2) - \mathbf{x}(-1, \bar{\eta}_2)| \quad , \tag{5.175}$$

$$l_2 = |\mathbf{x}(\bar{\eta}_1, 1) - \mathbf{x}(\bar{\eta}_1, -1)| \quad , \tag{5.176}$$

$$D = \frac{d}{\max(l_1, l_2)} \quad , \tag{5.177}$$

for example. Using such an equivalent source distance D, a log-L_1 transformation

$$R(\rho) = \log(\rho + D) \tag{5.178}$$

and a $L_1^{-1/5}$ transformation

$$R(\rho) = -(\rho + D)^{-1/5} \tag{5.174}$$

can be defined.

Similar transformations can be introduced for curved triangular elements in the parametric space (η_1, η_2) by defining an equivalent distance D similar to equation (5.177) if necessary.

This variable transformation in the parametric space (η_1, η_2) may seem simpler compared to the PART method, which employs variable transformations in the approximately projected element $\bar{S}$ in the tangent plane. However, the concept of the equivalent distance D becomes vague when the element has a large aspect ratio, whereas the source distance d is always clearly defined for all kinds of element geometry, so that the radial variable transformation in $\bar{S}$ using the source distance d itself is preferred, so long as the source distance is employed in the radial variable transformation, such as in the log-L_1 and $L_1^{-1/5}$ transformations.

CHAPTER 6

ELEMENTARY ERROR ANALYSIS

6.1 The Use of Error Estimate for Gauss-Legendre Quadrature Formula

In this section we will perform an error analysis of the proposed numerical integration (PART) method and explain why the log-L_2 radial transformation

$$R(\rho) = \log\sqrt{\rho^2 + d^2} \tag{5.64}$$

corresponding to $\beta=2$ in

$$\rho\, d\rho = r^{\beta}\, dR \tag{5.46}$$

leads to accurate numerical integration results with relatively few integration points for integrals of the type $\int_S 1/r^{\alpha}\, dS$, whilst the radial transformations corresponding to $\beta \neq 2$ (cf. Table 5.1) give poor results. (cf. Chapter 10)

Since we are interested in the integration in the radial direction, consider the integral

$$J = \int_0^{\rho_j} \frac{f|G|}{r^{\alpha}}\, \rho\, d\rho \tag{6.1}$$

where $\rho_j = \rho_j(\theta)$ is the upper limit of the radial variable in equation (5.42).

For simplicity, take the case of constant planar elements (parallelogram or triangular) so that the radial integration of equation (6.1) reduces to

$$J = \int_0^{\rho_j} \frac{\rho}{r^{\alpha}}\, d\rho \tag{6.2}$$

where

$$r = r' = \sqrt{\rho^2 + d^2} \quad . \tag{6.3}$$

Applying the radial variable transformation corresponding to

$$\rho \, d\rho = r^{\beta} \, dR \tag{5.46}$$

we obtain

$$J = \int_{R(0)}^{R(\rho_j)} r^{\beta - \alpha} \, dR \tag{6.4}$$

We are now interested in estimating the error when applying the Gauss-Legendre quadrature formula to equation (6.4).

The error estimate for the n-point Gauss-Legendre formula when applied to the integration over the interval $[-1, 1]$:

$$\int_{-1}^{1} f(x) \, dx = \sum_{i=1}^{n} w_i f(x_i) + e_n(f) \tag{6.5}$$

is given by [3, 33]

$$e_n(f) = \frac{2^{2n+1}(n!)^4}{(2n+1)\{(2n)!\}^3} f^{(2n)}(\eta)$$

for some $-1 < \eta < 1$, (6.6)

where

$$f^{(m)}(x) \equiv \frac{d^m f}{dx^m}$$

Hence, the error $E_n(F)$ of applying the Gauss-Legendre quadrature formula of equation (6.5) to the integration of a function $F(t)$ over a general interval $t \in [a,b]$ is given as follows:

$$\begin{aligned} \int_a^b F(t) dt &= \frac{b-a}{2} \int_{-1}^{1} F\left\{\frac{a+b+x(b-a)}{2}\right\} dx \\ &= \frac{b-a}{2} \int_{-1}^{1} g(x) \, dx \\ &= \frac{b-a}{2} \left\{ \sum_{i=1}^{n} w_i g(x_i) + e_n(g) \right\} \\ &= \frac{b-a}{2} \sum_{i=1}^{n} w_i g(x_i) + E_n(F) \end{aligned} \tag{6.7}$$

where

$$t(x) = \frac{a+b+x(b-a)}{2} \tag{6.8}$$

$$\frac{dt}{dx} = \frac{b-a}{2} \tag{6.9}$$

and

$$g(x) = F\left\{t(x)\right\} = F\left\{\frac{a+b+x(b-a)}{2}\right\} \tag{6.10}$$

Here, $t(x)$ maps the interval $x \in [-1, 1]$ to $t \in [a, b]$. From equation (6.9) and (6.10),

$$\frac{dg}{dx} = \frac{dF}{dt} \frac{dt}{dx} = \frac{b-a}{2} \frac{dF}{dt} \tag{6.11}$$

and

$$g^{(m)} \equiv \frac{d^m g}{dx^m} = \left(\frac{b-a}{2}\right)^m F^{(m)} \tag{6.12}$$

where

$$F^{(m)} \equiv \frac{d^m F}{dt^m} \tag{6.13}$$

so that the error $E_n(F)$ of equation (6.7) is given, from equation (6.12) by

$$\begin{aligned} E_n(F) &= \frac{b-a}{2} e_n(g) \\ &= \frac{b-a}{2} \epsilon_n g^{(2n)}(\xi) \\ &= \left(\frac{b-a}{2}\right)^{2n+1} \epsilon_n F^{(2n)}(\tau) \end{aligned}$$

for some $a < \tau < b$, $(-1 < \xi < 1)$, (6.14)

where

$$\epsilon_n \equiv \frac{2^{2n+1}(n!)^4}{(2n+1)\{(2n)!\}^3} \tag{6.15}$$

Recall Stirling's formula

$$n! \sim e^{-n} n^n \sqrt{2\pi n} \tag{6.16}$$

or

$$\lim_{n\to\infty} \frac{e^{-n} n^n \sqrt{2\pi n}}{n!} = 1 \tag{6.17}$$

which means that $n!$ is asymptotically equivalent to $e^{-n}n^n\sqrt{2\pi n}$. The approximation (6.16) is reasonably accurate for small values of n as well, as shown in Table 6.1.

Table 6.1 Accuracy of Stirling's formula for small n

n	$\frac{e^{-n} n^n \sqrt{2\pi n}}{n!}$
1	0.922
2	0.960
3	0.973
4	0.980
5	0.983
6	0.986
7	0.988
8	0.990
9	0.991
10	0.992

In fact equation (6.16) can be expressed by the following asymptotic expansion

$$n! = e^{-n} n^n \sqrt{2\pi n}\left(1 + \frac{1}{12n} + \frac{1}{288n^2} - \frac{139}{5180n^3} + \cdots\right) \tag{6.18}$$

Substituting Stirling's formula (6.16) in equation (6.15), one obtains

$$\epsilon_n = \frac{2^{2n+1}(n!)^4}{(2n+1)\{(2n)!\}^3}$$

$$\sim \frac{\sqrt{\pi}}{2}\left(\frac{e}{4}\right)^{2n} n^{-2n-\frac{1}{2}} \tag{6.19}$$

Hence, from equation (6.14),

$$E_n(F) = p_n F^{(2n)}(\tau)$$

for some $a < \tau < b$, (6.20)

where

$$p_n = \left(\frac{b-a}{2}\right)^{2n+1} \epsilon_n$$

$$\sim \frac{b-a}{4}\sqrt{\frac{\pi}{n}}\left\{\frac{(b-a)e}{8n}\right\}^{2n} \tag{6.21}$$

From equation (6.20), the lower bound $L_n(F)$ and upper bound $U_n(F)$ for $|E_n(F)|$ are given by

$$L_n(F) = \min_{a \le \tau \le b} |E_n(F)|$$

$$= p_n \min_{a \le \tau \le b} |F^{(2n)}(\tau)| \tag{6.22}$$

and

$$U_n(F) = \max_{a \le \tau \le b} |E_n(F)|$$

$$= p_n \max_{a \le \tau \le b} |F^{(2n)}(\tau)| \tag{6.23}$$

respectively, so that,

$$L_n(F) \le |E_n(F)| \le U_n(F) \tag{6.24}$$

Now we are ready to apply the error analysis to the integral

$$J = \int_{R(0)}^{R(\rho_j)} r^{\beta-\alpha}\, dR \quad , \tag{6.4}$$

where,

$$F(R) \equiv r(R)^{\beta-\alpha} \tag{6.25}$$

$$a = R(0) \tag{6.26}$$

and

$$b = R(\rho_j) \quad . \tag{6.27}$$

6.2 Case $\beta=2$ (Adaptive Logarithmic Transformation : log-L_2)

First, the error analysis will be performed for the log-L_2 radial variable transformation corresponding to $\beta=2$:

$$R(\rho) = \log \sqrt{\rho^2 + d^2} \quad . \tag{5.64}$$

Since $\beta=2$ and

$$r = r' = \sqrt{\rho^2 + d^2} = e^R \quad , \tag{6.28}$$

we have

$$F(R) = r^{2-\alpha} = e^{(2-\alpha)R} \quad , \tag{6.29}$$

which is shown in Fig. 6.1.

Also,

$$a = R(0) = \log d$$

$$b = R(\rho_j) = \log \sqrt{\rho_j^2 + d^2} = \log r_j \tag{6.30}$$

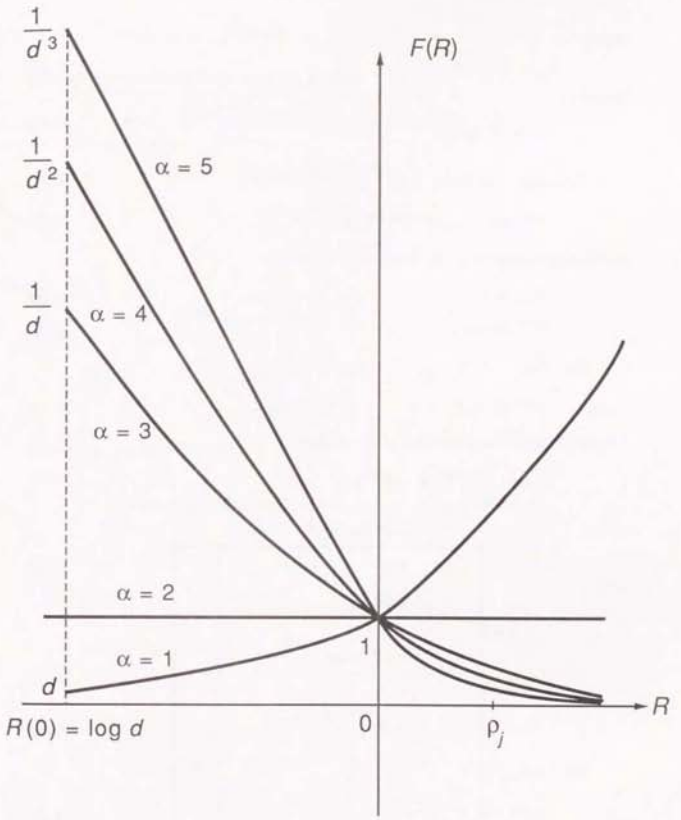

Fig. 6.1 Graph of $F(R) \equiv r^{\beta-\alpha} = e^{(2-\alpha)R}$ for $\beta = 2$, $\alpha = 1 \sim 5$

where

$$r_j = \sqrt{\rho_j^2 + d^2} \quad . \tag{6.31}$$

Hence,

$$b - a = \log \frac{r_j}{d} \quad . \tag{6.32}$$

From equation (6.29),

$$F^{(2n)}(R) = (2-\alpha)^{2n}\ e^{(2-\alpha)R} \geqq 0 \quad , \tag{6.33}$$

which also stands for $\alpha = 2$, when

$$F(R) = 1 \quad , \tag{6.34}$$

$$F^{(2n)}(R) = 0 \quad . \tag{6.35}$$

For $\alpha = 1$,

$$F^{(2n)}(R) = e^R > 0 \tag{6.36}$$

is a strictly increasing function of R, so that

$$\begin{aligned} \min_{a \leqq R \leqq b} |F^{(2n)}(R)| &= F^{(2n)}(a) \\ &= F^{(2n)}(\log d) \\ &= d \end{aligned} \tag{6.37}$$

and

$$\begin{aligned} \max_{a \leqq R \leqq b} |F^{(2n)}(R)| &= F^{(2n)}(b) \\ &= F^{(2n)}(\log r_j) \\ &= r_j \\ &= \sqrt{\rho_j^2 + d^2} \quad . \end{aligned} \tag{6.38}$$

For $\alpha = 2$,

$$E_n(F) = p_n F^{(2n)}(\tau) = 0 \tag{6.39}$$

where $a \leqq \tau \leqq b$.

For $\alpha \geqq 3$,

$$F^{(2n)}(R) = (2-\alpha)^{2n}\ e^{(2-\alpha)R} > 0 \tag{6.33}$$

is a strictly decreasing function of R, so that

$$\begin{aligned} \min_{a \leqq R \leqq b} |F^{(2n)}(R)| &= F^{(2n)}(b) \\ &= (2-\alpha)^{2n}\ e^{(2-\alpha)\log r_j} \\ &= (2-\alpha)^{2n}\ r_j^{\,2-\alpha} \\ &= (2-\alpha)^{2n} \sqrt{\rho_j^2 + d^2}^{\,2-\alpha} \end{aligned} \tag{6.40}$$

and

$$\begin{aligned} \max_{a \leqq R \leqq b} |F^{(2n)}(R)| &= F^{(2n)}(a) \\ &= (2-\alpha)^{2n}\ e^{(2-\alpha)\log d} \\ &= (2-\alpha)^{2n}\ d^{2-\alpha} \quad . \end{aligned} \tag{6.41}$$

To sum up, we have Table 6.2.

Table 6.2 Minimum and maximum value of $F^{(2n)}(\tau)$ $(a \leqq \tau \leqq b)$ for $\beta = 2$, $\alpha = 1 \sim 5$

α	$\min_{a \leqq \tau \leqq b} F^{(2n)}(\tau)$	$\max_{a \leqq \tau \leqq b} F^{(2n)}(\tau)$
1	d	r_j
2	0	0
3	r_j^{-1}	d^{-1}
4	$2^{2n} r_j^{-2}$	$2^{2n} d^{-2}$
5	$3^{2n} r_j^{-3}$	$3^{2n} d^{-3}$

where

$$r_j = \sqrt{\rho_j^2 + d^2}$$

From equations (6.21) and (6.32),

$$P_n \sim \frac{\log \frac{r_j}{d}}{4} \sqrt{\frac{\pi}{n}} \left(\frac{e \log \frac{r_j}{d}}{8n} \right)^{2n} \quad (6.42)$$

If we define

$$\frac{r_j}{d} = 10^k \quad , \quad (6.43)$$

$$\log \frac{r_j}{d} = k \log 10 \quad (6.43)$$

$$\sim 2.30\, k \quad (6.44)$$

For nearly singular integrals $d \ll \rho_j$

$$\frac{r_j}{d} = \frac{\sqrt{\rho_j^2 + d^2}}{d} \sim \frac{\rho_j}{d} \gg 1 \quad , \quad (6.45)$$

so that $k > 0$.

Hence,

$$P_n \sim \frac{\log 10}{4} k \sqrt{\frac{\pi}{n}} \left(\frac{k\, e \log 10}{8n} \right)^{2n}$$

$$\sim \frac{1.81\, k}{\sqrt{n}} \left(\frac{0.782\, k}{n} \right)^{2n} \quad (6.46)$$

From Table 6.2 and equations (6.22), (6.23) and (6.46), the lower bound L_n and the upper bound U_n for the error $E_n(F)$ of applying the n-point Gauss-Legendre quadrature formula and the radial variable transformation

$$R(\rho) = \log \sqrt{\rho^2 + d^2} \quad , \quad (\beta = 2) \quad (5.64)$$

to the integral

$$I = \int_0^{\rho_j} \frac{\rho}{r^\alpha} \, d\rho \quad (6.2)$$

is given by Table 6.3.

Table 6.3 Lower bound $L_n(F)$ and upper bound $U_n(F)$ of numerical integration error $E_n(F)$ for $\beta = 2$

α	$L_n(F)$	$U_n(F)$
1	$\frac{1.81\, k\, d}{\sqrt{n}} \left(\frac{0.782\, k}{n} \right)^{2n}$	$\frac{1.81\, k\, r_j}{\sqrt{n}} \left(\frac{0.782\, k}{n} \right)^{2n}$
2	0	0
3	$\frac{1.81\, k}{r_j \sqrt{n}} \left(\frac{0.782\, k}{n} \right)^{2n}$	$\frac{1.81\, k}{d \sqrt{n}} \left(\frac{0.782\, k}{n} \right)^{2n}$
4	$\frac{1.81\, k}{r_j^2 \sqrt{n}} \left(\frac{1.56\, k}{n} \right)^{2n}$	$\frac{1.81\, k}{d^2 \sqrt{n}} \left(\frac{1.56\, k}{n} \right)^{2n}$
5	$\frac{1.81\, k}{r_j^3 \sqrt{n}} \left(\frac{2.35\, k}{n} \right)^{2n}$	$\frac{1.81\, k}{d^3 \sqrt{n}} \left(\frac{2.35\, k}{n} \right)^{2n}$

To sum up, for $\beta = 2$, since

$$L_n(F) \leq E_n(F) \leq U_n(F) \quad , \quad (6.24)$$

equation (6.40), (6.41) and (6.42) gives

$$E_n(F) \sim \left\{ \frac{(\alpha - 2)\, e \log \frac{r_j}{d}}{8n} \right\}^{2n} \quad (6.42)$$

$$= \left\{ \frac{0.783\, (\alpha - 2)\, k}{n} \right\}^{2n} \xrightarrow[n \to \infty]{} 0 \quad . \quad (6.47)$$

where

$$k = \frac{\log \frac{r_j}{d}}{\log 10} \sim 0.434 \log \frac{r_j}{d} \quad . \tag{6.48}$$

Table 6.3 and equation (6.47) show that the adaptive logarithmic radial variable transformation (log-L_2)

$$R(\rho) = \log \sqrt{\rho^2 + d^2} \quad , \quad (\beta = 2) \tag{5.64}$$

in combination with the Gauss-Legendre quadrature formula has the very good convergence behaviour of order $O(n^{-2n})$, for the integration in the radial variable :

$$J = \int_0^{r_j} \frac{\rho}{r^\alpha} \, d\rho \qquad (\alpha = 1, 2, 3, \cdots) \quad , \tag{6.2}$$

where n is the number of integration points for the transformed radial variable R . This explains why the radial variable transformation $R(\rho)$ corresponding to $\beta = 2$ (log-L_2) works well for nearly singular integrals of the type

$$I = \int_S \frac{dS}{r^\alpha} \qquad (\alpha = 1, 2, 3, \cdots)$$

$$= \int_0^{2\pi} d\theta \int_0^{\rho_j(\theta)} \frac{\rho}{r^\alpha} \, d\rho \quad . \tag{6.49}$$

6.3 Case $\beta = 1$ Transformation

For the radial variable transformation corresponding to $\beta = 1$ (cf. Table 5.1) :

$$R(\rho) = \sqrt{\rho^2 + d^2} \quad , \tag{6.50}$$

we have

$$r = r' = R \tag{6.51}$$

$$F(R) = r^{\beta - \alpha} = R^{1-\alpha} \tag{6.52}$$

and

$$a = R(0) = d$$

$$b = R(\rho_j) = \sqrt{\rho_j^2 + d^2} = r_j \quad . \tag{6.53}$$

From equation (6.52), for $\alpha = 1$,

$$F(R) = 1 \tag{6.54}$$

$$F^{(2n)}(R) = 0 \tag{6.55}$$

and for $\alpha \geqq 2$,

$$F^{(2n)}(R) = \frac{(2n+\alpha-2)!}{(\alpha-2)!} R^{-2n-\alpha+1} > 0 \quad . \tag{6.56}$$

Since $F^{(2n)}(R)$ is a strictly decreasing function of $R \in [\, d, r_j \,]$ for $\alpha \geqq 2$,

$$\min_{a \leqq R \leqq b} F^{(2n)}(R) = F^{(2n)}(r_j)$$

$$= \frac{(2n+\alpha-2)!}{(\alpha-2)!} r_j^{-2n-\alpha+1} > 0 \tag{6.57}$$

and

$$\max_{a \leqq R \leqq b} F^{(2n)}(R) = F^{(2n)}(d)$$

$$= \frac{(2n+\alpha-2)!}{(\alpha-2)!} d^{-2n-\alpha+1} > 0 \tag{6.58}$$

for $\alpha \geqq 2$.

Since

$$b - a = r_j - d \tag{6.59}$$

equation (6.21) gives

$$p_n \sim \frac{r_j - d}{4} \sqrt{\frac{\pi}{n}} \left\{ \frac{(r_j - d)e}{8n} \right\}^{2n} \tag{6.60}$$

and

$$\frac{(2n+\alpha-2)!}{(\alpha-2)!} = (2n)!\ f_\alpha(n)$$

$$\sim e^{-2n}\,(2n)^{2n}\sqrt{4\pi n}\ f_\alpha(n) \tag{6.61}$$

where

$$f_\alpha(n) = \frac{(2n+\alpha-2)!}{(2n)!\,(\alpha-2)!} \quad , \quad (\alpha \geq 2) \tag{6.62}$$

as shown in Table 6.4 .

Table 6.4 $f_\alpha(n)$, ($\beta=1$, $\alpha \geq 2$)

α	f_α
2	1
3	$2n+1$
4	$(2n+1)(n+1)$
5	$\frac{(2n+1)(n+1)(2n+3)}{3}$

From equations (6.22), (6.23), (6.57), (6.58), (6.60) and (6.61), for $\alpha \geq 2$,

$$L_n(F) \sim \frac{\pi}{2}\,(r_j - d)\,r_j^{\,1-\alpha}\ f_\alpha(n)\left(\frac{1-\frac{d}{r_j}}{4}\right)^{2n} \tag{6.63}$$

$$U_n(F) \sim \frac{\pi}{2}\,(r_j - d)\,d^{\,1-\alpha}\ f_\alpha(n)\left(\frac{\frac{r_j}{d}-1}{4}\right)^{2n} \quad . \tag{6.64}$$

Hence, to sum up for the radial transformation $R(\rho)$ corresponding to $\beta=1$,

$$E_n(F) = 0 \qquad \text{for} \qquad \alpha=1 \tag{6.65}$$

and for $\alpha \geq 2$,

$$L_n(F) \leq E_n(F) \leq U_n(F) \quad , \tag{6.24}$$

where, for nearly singular integrals, for which

$$0 < \frac{d}{r_j} \ll 1 \quad \text{or} \quad \frac{r_j}{d} \gg 1 \quad , \tag{6.66}$$

$$L_n(F) \sim \left(\frac{1}{4}\right)^{2n} \xrightarrow[n\to\infty]{} 0 \tag{6.67}$$

$$U_n(F) \sim \left(\frac{1}{4}\cdot\frac{r_j}{d}\right)^{2n} \xrightarrow[n\to\infty]{} \infty \quad . \tag{6.68}$$

This suggests that the $\beta=1$ transformation does not work as efficiently as the $\beta=2$ (log-L_2), since

$$E_n(F) \sim \left(\frac{1}{4}\right)^{2n} \gg \left(\frac{1}{n}\right)^{2n} \quad , \tag{6.69}$$

except for the case when $\alpha=1$, for which

$$E_n(F) = 0 \quad .$$

This is shown in the numerical results (Chapter 10) where the $\beta=1$ transformation is out-performed by the $\beta=2$ (log-L_2) transformation, except for the case of weakly singular integrals ($d=0$, $\alpha=1$).

6.4 Case $\beta=3$ Transformation

For $\beta=3$ (cf. Table 5.1),

$$R(\rho) = -\frac{1}{\sqrt{\rho^2+d^2}} \tag{6.70}$$

so that

$$a = R(0) = -\frac{1}{d} \tag{6.71}$$

$$b = R(\rho_j) = -\frac{1}{\sqrt{\rho_j^2 + d^2}} = -\frac{1}{r_j} \tag{6.72}$$

and

$$b - a = \frac{1}{d} - \frac{1}{r_j} \tag{6.73}$$

Since

$$r = r' = -\frac{1}{R} \quad , \tag{6.74}$$

$$F(R) = r^{\beta-\alpha} = (-R)^{\alpha-3} \tag{6.75}$$

Hence, for

$$\alpha \geq 3 \quad \left(, n > \frac{\alpha-3}{2} \right) \quad ,$$

$$F^{(2n)}(R) \equiv 0 \tag{6.76}$$

and

$$E_n(F) \equiv 0 \tag{6.77}$$

For $\alpha = 1, 2$

$$F^{(2n)}(R) = \frac{(2n+2-\alpha)!}{(2-\alpha)!} (-R)^{\alpha-3-2n} \tag{6.78}$$

Since

$$\frac{1}{r_j} \leq -R \leq \frac{1}{d} \tag{6.79}$$

where $0 < d \ll r_j$ for nearly singular integrals, and $F^{(2n)}(R)$ is a strictly increasing function of

$$R \in \left[-\frac{1}{d}, -\frac{1}{r_j} \right] \quad ,$$

one obtains

$$\min_{a \leq R \leq b} F^{(2n)}(R) = F^{(2n)}\left(-\frac{1}{d}\right) = \frac{(2n+2-\alpha)!}{(2-\alpha)!} d^{2n+3-\alpha} > 0 \tag{6.80}$$

and

$$\max_{a \leq R \leq b} F^{(2n)}(R) = F^{(2n)}\left(-\frac{1}{r_j}\right) = \frac{(2n+2-\alpha)!}{(2-\alpha)!} r_j^{2n+3-\alpha} > 0 \quad . \tag{6.81}$$

Here

$$\frac{(2n+2-\alpha)!}{(2-\alpha)!} = (2n)!\, f_\alpha(n)$$

$$\sim e^{-2n} (2n)^{2n} \sqrt{4\pi n}\, f_\alpha(n) \tag{6.82}$$

where

$$f_\alpha(n) = \frac{(2n+2-\alpha)!}{(2-\alpha)!(2n)!} \tag{6.83}$$

or

$$f_1(n) = 2n+1 \tag{6.84}$$

$$f_2(n) = 1 \quad . \tag{6.85}$$

From equation (6.21),

$$p_n \sim \frac{\frac{1}{d} - \frac{1}{r_j}}{4} \sqrt{\frac{\pi}{n}} \left\{ \frac{\left(\frac{1}{d} - \frac{1}{r_j}\right) e}{8n} \right\}^{2n} \quad . \tag{6.86}$$

Thus, for nearly singular integrals $(0 < d \ll r_j)$ and $\alpha = 1,2$,

$$L_n(F) = p_n F^{(2n)}\left(-\frac{1}{d}\right)$$

$$\sim \frac{\pi}{2} \left(\frac{1}{d} - \frac{1}{r_j}\right) d^{3-\alpha} f_\alpha(n) \left(\frac{1 - \frac{d}{r_j}}{4}\right)^{2n}$$

$$\sim \left(\frac{1}{4}\right)^{2n} \xrightarrow[n \to \infty]{} 0 \tag{6.87}$$

and

$$U_n(F) = p_n F^{(2n)}\left(-\frac{1}{r_j}\right)$$

$$\sim \frac{\pi}{2}\left(\frac{1}{d}-\frac{1}{r_j}\right) r_j^{3-\alpha} f_\alpha(n) \left(\frac{\frac{r_j}{d}-1}{4}\right)^{2n}$$

$$\sim \left(\frac{1}{4}\cdot\frac{r_j}{d}\right)^{2n} \xrightarrow[n\to\infty]{} \infty \quad , \tag{6.88}$$

where

$$L_n(F) \leq E_n(F) \leq U_n(F) \quad . \tag{6.89}$$

To sum up for R(ρ) ; $\beta=3$, good convergence is expected for $\alpha = 3,4,5,\cdots$ (for planar elements), while for $\alpha=1, 2$, equations (6.87), (6.88) and (6.89) suggest that the $\beta=3$ transformation does not work as well as the $\beta=2$ (log-L_2) transformation, for which it was shown in section 6.2 that

$$E(f) \sim L_n(F) \sim U_n(F) \sim \left(\frac{1}{n}\right)^{2n} \tag{6.90}$$

6.5 Case $\beta=4$ Transformation

For $\beta=4$ (cf. Table 5.1),

$$R(\rho) = -\frac{1}{2(\rho^2+d^2)} \quad , \tag{6.91}$$

so that

$$a = R(0) = -\frac{1}{2d^2} \tag{6.92}$$

$$b = R(\rho_j) = -\frac{1}{2r_j^2} \quad , \tag{6.93}$$

where

$$r_j = \sqrt{\rho_j^2 + d^2} \tag{6.94}$$

and

$$b - a = \frac{1}{2}\left(\frac{1}{d^2} - \frac{1}{r_j^2}\right) \tag{6.95}$$

Since

$$r = r' = (-2R)^{-\frac{1}{2}} \quad , \tag{6.96}$$

$$F(R) = r'^{\beta-\alpha} = (-2R)^{\frac{\alpha}{2}-2}$$

$$= 2^{\frac{\alpha}{2}-2}(-R)^{\frac{\alpha}{2}-2} \quad , \tag{6.97}$$

or

$$F(R) = 2^{-\frac{3}{2}}(-R)^{-\frac{3}{2}} \quad , \quad \alpha = 1 \tag{6.98}$$

$$F(R) = 2^{-1}(-R)^{-1} \quad , \quad \alpha = 2 \tag{6.99}$$

$$F(R) = 2^{-\frac{1}{2}}(-R)^{-\frac{1}{2}} \quad , \quad \alpha = 3 \tag{6.100}$$

$$F(R) = (-R)^0 = 1 \quad , \quad \alpha = 4 \tag{6.101}$$

$$F(R) = 2^{\frac{1}{2}}(-R)^{-\frac{1}{2}} \quad , \quad \alpha = 5 \tag{6.102}$$

etc.

Hence, for $\alpha = 4$, ($n \geq 1$)

$$F^{(2n)}(R) = 0 \tag{6.103}$$

and

$$E_n(F) = 0 \quad . \tag{6.104}$$

For $\alpha \neq 4$,

$$F^{(2n)}(R) = 2^{\frac{\alpha}{2}-2} \left| \prod_{i=1}^{2n} \left(\frac{\alpha}{2}-1-i\right) \right| \frac{1}{(-R)^{2n+2-\frac{\alpha}{2}}} \quad (6.105)$$

Hence $|F^{(2n)}(R)|$ is a strictly increasing function of

$$R \in \left| -\frac{1}{2d^2} , -\frac{1}{2r_j^2} \right| ,$$

so that

$$\min_{a \le R \le b} |F^{(2n)}(R)| = |F^{(2n)}\left(-\frac{1}{2d^2}\right)|$$

$$= d^{4-\alpha} \left| \prod_{i=1}^{2n} \left(\frac{\alpha}{2}-1-i\right) \right| (2d^2)^{2n} \quad (6.106)$$

and

$$\max_{a \le R \le b} \left|F^{(2n)}(R)\right| = \left|F^{(2n)}\left(-\frac{1}{2r_j^2}\right)\right|$$

$$= r_j^{4-\alpha} \left| \prod_{i=1}^{2n} \left(\frac{\alpha}{2}-1-i\right) \right| (2r_j^2)^{2n} . \quad (6.107)$$

From equation (6.14),

$$E_n(F) = \left(\frac{b-a}{2}\right)^{2n+1} e_n \frac{F^{(2n)}(R)}{(2n)!} \quad (6.108)$$

for some $R \in [a, b]$, where

$$e_n = \frac{2^{2n+1}(n!)^4}{(2n+1)\{(2n)!\}^2} \sim \frac{\pi}{2^{2n}} \quad (6.109)$$

using Stirling's formula of equation (6.16).

Hence,

$$E_n(F) \sim \frac{\pi}{4d^2} \left\{1-\left(\frac{d}{r_j}\right)^2\right\}^{2n+1} \left(\frac{1}{8d^2}\right)^{2n} \frac{F^{(2n)}(R)}{(2n)!} \quad (6.110)$$

for some $R \in [a,b]$,

so that,

$$L_n(F) = \min_{a \le R \le b} |E_n(F)|$$

$$= \frac{\pi}{4} d^{2-\alpha} \left\{1-\left(\frac{d}{r_j}\right)^2\right\}^{2n+1} t_n \left(\frac{1}{4}\right)^{2n} \quad (6.111)$$

$$U_n(F) = \max_{a \le R \le b} |E_n(F)|$$

$$= \frac{\pi}{4} \frac{r_j^{4-\alpha}}{d^2} \left\{1-\left(\frac{d}{r_j}\right)^2\right\}^{2n+1} t_n \left(\frac{r_j}{2d}\right)^{4n} , \quad (6.112)$$

where

$$t_n = \frac{\left| \prod_{i=1}^{2n} \left(\frac{\alpha}{2}-1-i\right) \right|}{(2n)!} \quad (6.110)$$

$$= \prod_{i=1}^{2n} \left| 1+\frac{2-\alpha}{2i} \right| . \quad (6.113)$$

For nearly singular integrals

$$0 < \frac{d}{r_j} \ll 1 ,$$

so that

$$L_n(F) \sim \frac{\pi}{4} d^{2-\alpha} t_n \left(\frac{1}{4}\right)^{2n} \quad (6.114)$$

and

$$U_n(F) \sim \frac{\pi}{4} \frac{r_j^{4-\alpha}}{d^2} t_n \left(\frac{r_j}{2d}\right)^{4n} . \quad (6.115)$$

t_n can be estimated by the following theorem.

Theorem 6.1

$$t_n = \prod_{i=1}^{2n} \left| 1+\frac{a}{i} \right| \sim O(n^a) \tag{6.116}$$

as $n \to \infty$.

Proof

(1) Case $a>0$

Since

$$t_n = \prod_{i=1}^{2n} \left(1+\frac{a}{i} \right) \quad , \tag{6.117}$$

let us define

$$S_1^{2n} = \log t_n = \sum_{i=1}^{2n} \log\left(1+\frac{a}{i} \right) \tag{6.118}$$

and

$$f(x) = \log\left(1+\frac{a}{x} \right) \quad , \tag{6.119}$$

where

$$f(+0) = +\infty \tag{6.120}$$

$$f(+\infty) = +0 \tag{6.121}$$

$$f'(x) = -\frac{a}{x(x+a)} < 0 \quad , \tag{6.122}$$

so that $f(x)$ is a strictly decreasing function of $x>0$, as shown in Fig. 6.2.

Hence we have

$$\int_1^{2n+1} \log\left(1+\frac{a}{x} \right) dx < S_1^{2n} < \int_0^{2n} \log\left(1+\frac{a}{x} \right) dx \quad , \tag{6.123}$$

where

$$\int \log\left(1+\frac{a}{x} \right) dx = (x+a)\log(x+a) - x\log x \quad , \tag{6.124}$$

so that

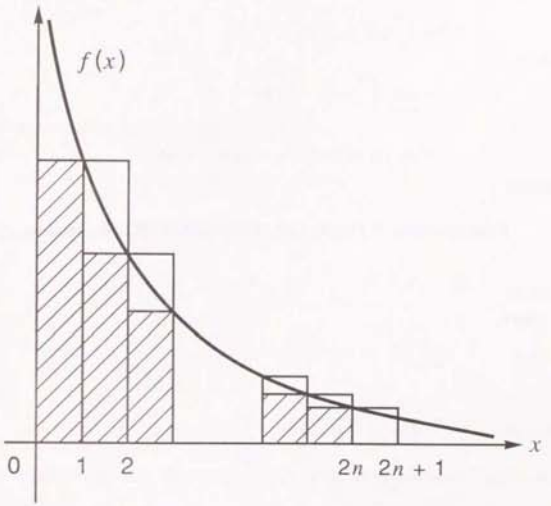

Fig. 6.2 $f(x) = \log(1 + \frac{a}{x})$, $a > 0$

$$\underline{S}_1^{2n} = \int_1^{2n+1} \log\left(1+\frac{a}{x}\right)dx$$

$$= (2n+1+a)\log(2n+1+a) - (2n+1)\log(2n+1) - (1+a)\log(1+a) \qquad (6.125)$$

and

$$\bar{S}_1^{2n} = \int_0^{2n} \log\left(1+\frac{a}{x}\right)dx$$

$$= \lim_{\varepsilon \to +0} \int_\varepsilon^{2n} \log\left(1+\frac{a}{x}\right)dx$$

$$= (2n+a)\log(2n+a) - 2n\log 2n - a\log a \qquad (6.126)$$

From equations (6.118), (6.123), (6.125) and (6.126), one obtains

$$\underline{t}_n < t_n < \bar{t}_n \qquad (6.127)$$

where

$$\underline{t}_n = e^{\underline{S}_1^{2n}}$$

$$= \frac{(2n+1+a)^{2n+1+a}}{(2n+1)^{2n+1}(1+a)^{1+a}}$$

$$\underset{n\to\infty}{\sim} \frac{\left[e(2n+1+a)\right]^a}{(1+a)^{1+a}}$$

$$\sim \frac{(2e)^a}{(1+a)^{1+a}} n^a$$

$$\sim O(n^a) \qquad (6.128)$$

and

$$\bar{t}_n = e^{\bar{S}_1^{2n}}$$

$$= \frac{(2n+a)^{2n+a}}{(2n)^{2n} a^a}$$

$$= \left(1+\frac{a}{2n}\right)^{2n} \left(\frac{2n+a}{a}\right)^a$$

$$\underset{n\to\infty}{\sim} \left(\frac{e}{a}\right)^a (2n+a)^a$$

$$\sim \left(\frac{2e}{a}\right)^a n^a$$

$$\sim O(n^a) \qquad (6.129)$$

From equations (6.127), (6.128) and (6.129),

$$t_n = \prod_{i=1}^{2n} \left|1+\frac{a}{i}\right| \sim O(n^a) \quad \text{for} \quad a > 0 \qquad (6.130)$$

(2) Case $a=0$

$$t_n = \prod_{i=1}^{2n} \left|1+\frac{a}{i}\right| = 1 = n^0 = n^a \qquad (6.131)$$

(3) Case $a < 0$

Let $b \equiv -a$. Then,

$$t_n = \prod_{i=1}^{2n} \left|1-\frac{b}{i}\right| \quad , \quad b > 0 \qquad (6.132)$$

If b is an integer less than $2n$, $t_n = 0 < O(n^a)$, so let us assume that b is not an integer and let

$$S_1^{2n} = \log t_n$$

$$= S_1^{k-1} + S_k^{2n} \qquad (6.133)$$

where

$$S_1^{k-1} = \sum_{i=1}^{k-1} \log\left|1-\frac{b}{i}\right| \qquad (6.134)$$

and

$$S_k^{2n} = \sum_{i=k}^{2n} \log\left(1-\frac{b}{i}\right) \tag{6.135}$$

where k is defined as the integer which satisfies

$$k-1 < b < k \quad . \tag{6.136}$$

Then, if we define

$$f(x) = \log\left(1-\frac{b}{x}\right) \quad , \quad b>0 \quad , \tag{6.137}$$

we have

$$f(b+0) = -\infty \quad , \tag{6.138}$$

$$f(+\infty) = -0 \quad , \tag{6.139}$$

and

$$f'(x) = \frac{b}{x(x-b)} > 0 \quad \text{for} \quad x>b \quad , \tag{6.140}$$

i.e. $f(x)$ is a strictly increasing function of x for $x>b$, as shown in Fig. 6.3 .

Hence,

$$\underline{S}_k^{2n} < S_k^{2n} < \overline{S}_k^{2n} \quad . \tag{6.141}$$

where

$$\underline{S}_k^{2n} = \log\left(1-\frac{b}{k}\right) + \int_k^{2n} \log\left(1-\frac{b}{x}\right) dx \tag{6.142}$$

and

$$\overline{S}_k^{2n} = \int_k^{2n+1} \log\left(1-\frac{b}{x}\right) dx \quad , \tag{6.143}$$

where

$$\int \log\left(1-\frac{b}{x}\right) dx = (x-b)\log(x-b) - x\log x \quad , \tag{6.144}$$

so that

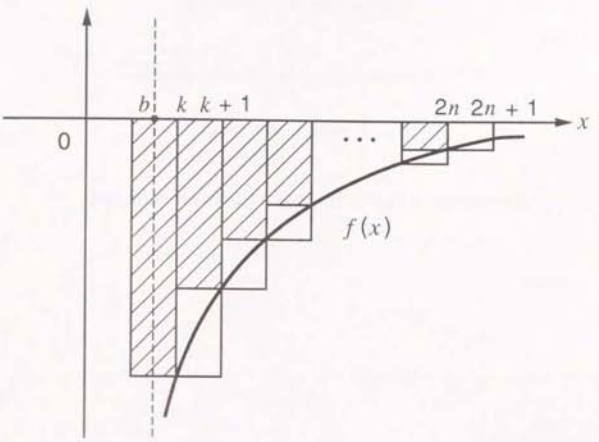

Fig. 6.3 $f(x) = \log(1-\frac{b}{x})$, $b>0$

$$\underline{S}_k^{2n} = (2n-a)\log(2n-a) - 2n\log 2n$$

$$-(k-a-1)\log(k-a) + (k-1)\log k \qquad (6.145)$$

and

$$\bar{S}_k^{2n} = (2n+1-a)\log(2n+1-a) - (2n+1)\log(2n+1)$$

$$-(k-a)\log(k-a) + k\log k \quad . \qquad (6.146)$$

From equations (6.132), (6.133), (6.141), (6.145) and (6.146),

$$\underline{t}_n < t_n < \bar{t}_n \quad , \qquad (6.147)$$

where

$$\underline{t}_n \equiv e^{S_1^{k-1} + \underline{S}_k^{2n}} \quad , \qquad (6.148)$$

$$\bar{t}_n \equiv e^{S_1^{k-1} + \bar{S}_k^{2n}} \quad , \qquad (6.149)$$

and

$$e^{S_1^{k-1}} = \prod_{i=1}^{k-1} \left|1 - \frac{b}{i}\right| \quad , \qquad (6.150)$$

$$e^{\underline{S}_k^{2n}} = \frac{(2n-b)^{2n-b}}{(2n)^{2n}} \frac{k^{k-1}}{(k-b)^{k-b-1}}$$

$$= \frac{(1-\frac{b}{2n})^{2n}}{(2n-b)^b} \frac{(k-b)^b}{(1-\frac{b}{k})^{k-1}} \qquad (6.151)$$

$$\underset{n\to\infty}{\sim} \left\{\frac{e(k-b)}{2n-b}\right\}^b \left(1-\frac{b}{k}\right)^{1-k}$$

$$\sim \left(1-\frac{b}{k}\right)^{1-k} \left\{\frac{e(k-b)}{2}\right\}^b n^{-b}$$

$$\sim O(n^{-b})$$

$$\sim O(n^a) \quad , \qquad (6.152)$$

$$e^{\bar{S}_k^{2n}} = \frac{(2n+1-b)^{2n+1-b}}{(2n+1)^{2n+1}} \frac{k^k}{(k-b)^{k-b}}$$

$$= \frac{(1-\frac{b}{2n+1})^{2n+1}}{(2n+1-b)^b} \frac{k^k}{(1-\frac{b}{k})^{k-b}}$$

$$\underset{n\to\infty}{\sim} \left(\frac{ek}{2n+1-b}\right)^b \left(1-\frac{b}{k}\right)^{b-k}$$

$$\sim \left(1-\frac{b}{k}\right)^{b-k} \left(\frac{ek}{2}\right)^b n^{-b}$$

$$\sim O(n^{-b})$$

$$\sim O(n^a) \quad . \qquad (6.153)$$

Hence,

$$\underline{t}_n \sim O(n^a) \quad , \qquad (6.154)$$

$$\bar{t}_n \sim O(n^a) \quad , \qquad (6.155)$$

which imply that

$$t_n \sim O(n^a) \quad \text{for} \quad a < 0 \quad . \qquad (6.156)$$

From equations (6.130), (6.131) and (6.156),

$$t_n \sim O(n^a) \quad \text{for } \forall a \in R \qquad (6.157)$$

Q.E.D.

Returning to equations (6.113), (6.114) and (6.115), for the radial variable transformation $R(\rho)$ corresponding to $\beta=4$, Theorem 6.1 implies that

$$t_n = \prod_{i=1}^{2n} \left| 1+\frac{2-a}{2i} \right| \sim O\left(n^{1-\frac{a}{2}}\right) \qquad (6.158)$$

Hence, for $a \neq 4$

$$L_n(F) \sim \frac{\pi}{4} d^{2-a} n^{1-\frac{a}{2}} \left(\frac{1}{4}\right)^{2n}$$

$$\sim \left(\frac{1}{4}\right)^{2n} \xrightarrow[n\to\infty]{} 0 \qquad (6.159)$$

and

$$U_n(F) \sim \frac{\pi}{4} \frac{r_j^{4-a}}{d^2} n^{1-\frac{a}{2}} \left(\frac{r_j}{2d}\right)^{4n}$$

$$\sim \left(\frac{r_j}{2d}\right)^{4n} \xrightarrow[n\to\infty]{} \infty \qquad (6.160)$$

for nearly singular integrals i.e.

$$0 < \frac{d}{r_j} \ll 1 \quad ,$$

where

$$L_n(F) \leq |E_n(F)| \leq U_n(F) \qquad (6.161)$$

To sum up, the radial variable transformation $R(\rho)$ corresponding to $\beta=4$ is not expected to give good results for the integration of

$$I = \int_0^{r_j} \frac{\rho}{r^a} d\rho \quad , \qquad (6.2)$$

compared to the $\beta=2$ (log-L_2) transformation, except for the case of $a=4$ for planar elements, when $E_n(F)=0$.

6.6 Case $\beta=5$ Transformation

For $\beta=5$,

$$R(\rho) = -\frac{1}{3\sqrt{\rho^2+d^2}^3} \qquad (6.162)$$

(cf. Table 5.1), so that

$$a = R(0) = -\frac{1}{3d^3} \quad , \qquad (6.163)$$

$$b = R(\rho_j) = -\frac{1}{3r_j^3} \quad , \qquad (6.164)$$

where

$$r_j = \sqrt{\rho_j^2 + d^2} \qquad (6.165)$$

and

$$b-a = \frac{1}{3}\left(\frac{1}{d^3} - \frac{1}{r_j^3}\right) \qquad (6.166)$$

Since

$$r = r' = (-3R)^{-\frac{1}{3}} \qquad (6.167)$$

$$F(R) = r^{\beta-a} = 3^{-\frac{5-a}{3}} (-R)^{-\frac{5-a}{3}} \quad , \qquad (6.168)$$

for $a = 5$,

$$F(R) = 1 \qquad (6.169)$$

and

$$F^{(2n)}(R) = 0 \qquad (6.170)$$

so that

$$E_n(F) = 0 \quad . \qquad (6.171)$$

For $\alpha \neq 5$,

$$F^{(2n)}(R) = 3^{\frac{\alpha-5}{3}} \left\{ \prod_{i=1}^{2n} \left(\frac{2}{3} - \alpha + i \right) \right\} (-R)^{\frac{\alpha-5}{3}-2n} \tag{6.172}$$

Hence, $|F^{(2n)}(R)|$ is a strictly increasing function of

$$R \in \left| -\frac{1}{3d^3} , -\frac{1}{3r_j^3} \right| \quad , \tag{6.172}$$

so that

$$\min_{a \leq R \leq b} |F^{(2n)}(R)| = |F^{(2n)}\left(-\frac{1}{3d^3}\right)|$$

$$= 3^{2n} \left\{ \prod_{i=1}^{2n} \left| \frac{2}{3} - \alpha + i \right| \right\} d^{6n+5-\alpha} \tag{6.173}$$

and

$$\max_{a \leq R \leq b} \left| F^{(2n)}(R) \right| = \left| F^{(2n)}\left(-\frac{1}{3r_j^3}\right) \right|$$

$$= 3^{2n} \left\{ \prod_{i=1}^{2n} \left| \frac{2}{3} - \alpha + i \right| \right\} r_j^{6n+5-\alpha} \quad . \tag{6.173}$$

From equations (6.108) and (6.109),

$$E_n(F) \sim \left(\frac{b-a}{2} \right)^{2n+1} \frac{\pi}{2^{2n}} \frac{F^{(2n)}(R)}{(2n)!} \tag{6.175}$$

for some $R \in [a,b]$,

where

$$\left(\frac{b-a}{2} \right)^{2n+1} = \left(\frac{1}{6d^3} \right)^{2n+1} \left\{ 1 - \left(\frac{d}{r_j} \right)^3 \right\}^{2n+1} \quad . \tag{6.176}$$

Hence ,

$$L_n(F) \leq |E_n(F)| \leq U_n(F) \tag{6.177}$$

where

$$L_n(F) = \min_{a \leq R \leq b} |E_n(F)|$$

$$\sim \frac{\pi}{6d^3} \left\{ 1 - \left(\frac{d}{r_j} \right)^3 \right\} \left\{ \frac{1 - \left(\frac{d}{r_j} \right)^3}{4d^3} \right\}^{2n} \quad d^{6n+5-\alpha} \left\{ \prod_{i=1}^{2n} \left| 1 + \frac{\frac{2}{3} - \alpha}{i} \right| \right\} \tag{6.178}$$

Since

$$\prod_{i=1}^{2n} \left| 1 + \frac{\frac{2}{3} - \alpha}{i} \right| \sim n^{\frac{2}{3} - \alpha} \tag{6.179}$$

from Theorem 6.1 ,

$$L_n(F) \sim n^{\frac{2}{3}-\alpha} \left\{ \frac{1 - \left(\frac{d}{r_j} \right)^3}{4} \right\}^{2n} \sim \left(\frac{1}{4} \right)^{2n} \xrightarrow[n \to \infty]{} 0$$

and

$$U_n(F) \sim n^{\frac{2}{3}-\alpha} \left\{ \frac{1 - \left(\frac{d}{r_j} \right)^3}{4} \right\}^{2n} \left(\frac{r_j}{d} \right)^{6n}$$

$$\sim \left\{ \frac{1}{4} \left(\frac{r_j}{d} \right)^3 \right\}^{2n} \xrightarrow[n \to \infty]{} \infty \tag{6.180}$$

for nearly singular integrals i. e.

$$0 < \frac{d}{r_j} \ll 1 \quad . \tag{6.181}$$

Hence, the transformation $R(\rho)$ corresponding to $\beta=5$ is expected to give poor results compared to the $\beta=2$ (log-L_2) transformation for the integration of

$$I = \int_0^{s_j} \frac{\rho}{r^\alpha} d\rho \quad , \tag{6.2}$$

except for the case of $\alpha=5$ for planar elements, when $E_n(F)=0$.

6.7 Summary of Error Estimates for $\beta=1\sim5$ transformations

To sum up, we have been considering the error estimate E_n when applying the Gauss-Legendre formula after applying the radial variable transforamtion

$$\rho d\rho = r^{\beta} dR \quad ; \quad (\beta = 1 \sim 5) \quad , \tag{5.46}$$

to the integration in the radial variable

$$J = \int_0^{\rho_j} \frac{\rho}{r^{\alpha}} d\rho \quad ; \quad (\alpha = 1 \sim 5) \tag{6.2}$$

which occurs in the nearly singular integral

$$I = \int_S \frac{dS}{r^{\alpha}}$$

$$= \int_0^{2\pi} d\theta \int_0^{\rho_j} \frac{\rho}{r^{\alpha}} d\rho \tag{6.49}$$

where S is a planar element, so that

$$r = r' = \sqrt{\rho^2 + d^2} \tag{6.3}$$

The error estimate E_n for the radial variable transformations : $\beta=1\sim5$, is given for different orders of near singularity : $\alpha=1\sim5$, in Table 6.5 .

Table 6.5 Error estimate E_n of integration using radial variable transformation $\beta=1\sim5$

β \ α	1	2	3	4	5
1	0	$4^{-2n} < E_n < (r_j/4d)^{2n}$			
2	n^{-2n}	0	n^{-2n}		
3	$4^{-2n} < E_n < \{r_j/(4d)\}^{2n}$	0			
4	$4^{-2n} < E_n < \{(r_j/(2d)\}^{4n}$		0	$4^{-2n} < E_n < \{r_j/(2d)\}^{4n}$	
5	$4^{-2n} < E_n < \{r_j/(4^4 d)\}^{6n}$			0	

Here,

$$r_j = \sqrt{\rho_j^2 + d^2} \tag{6.31}$$

and

$$\frac{r_j}{d} \gg 1 \tag{6.45}$$

for nearly singular integrals.

From Table 6.1, the $\beta=2$ transformation :

$$R(\rho) = \log \sqrt{\rho^2 + d^2} \tag{5.64}$$

gives good convergence for all near singularities $\alpha=1\sim5$ of the type in equations (6.2) or (6.49), as will be confirmed by numerical results in Chapter 10 .

The $\beta=3$ transformation also seems promising for $\alpha\geqq3$. However, it should be reminded that the above error analysis was performed for planar constant elements. The effect of curvature and high order polynomial interpolation functions in the integrand are not taken in to account. For instance, although the error is $E_n\equiv0$ for $\beta=1$, $\alpha=1$ for planar constant elements, it is found in the numerical results in Chapter 10 that, the $\beta=1$ radial variable transformation

$$R(\rho) = \sqrt{\rho^2 + d^2} \tag{6.50}$$

does not give accurate results compared to the $\beta=2$ (log-L_2) transformation

$$R(\rho) = \log \sqrt{\rho^2 + d^2} \tag{5.64}$$

for the integration

$$I = \int_S \frac{dS}{r} \tag{6.182}$$

over a curved quadrilateral patch. This seems to indicate that the n^{-2n} convergence of the $\beta=2$ (log-L_2) transformation is robust, not only with respect to the value of α but also with respect to the curvature of the boundary element.

6.8 Error Analysis for Flux Calculations

As will be shown in the numerical results in Chapter 10, the adaptive logarithmic transformation (log-L_2) of the type :

$$R(\rho) = \log \sqrt{\rho^2 + d^2} \tag{5.64}$$

works efficiently for nearly singular integrals arising in the calculation of the potential $u(\mathbf{x}_s)$ at a point $\mathbf{x}_s$ very near the boundary. However, the radial transformation of equation (5.64) does not work so efficiently for nearly singular integrals arising from the calculation of the flux or the potential derivative $\partial u/\partial \mathbf{x}_s$ at a point $\mathbf{x}_s$ very near the boundary.

This can be explained as follows if we recall the nature of nearly singular integrals discussed in Chapter 3 [37,40]. Since in the vicinity of the source point $\mathbf{x}_s$ which is very near to the curved boundary,

$$u^* \sim \frac{1}{4\pi r} \tag{3.127}$$

$$q^* \sim -\frac{d}{4\pi r^3} \tag{3.128}$$

and

$$\frac{\partial u^*}{\partial \mathbf{x}_s} \sim \frac{1}{4\pi} \begin{pmatrix} \dfrac{\rho \cos\theta}{r^3} \\ \dfrac{\rho \sin\theta}{r^3} \\ -\dfrac{d}{r^3} \end{pmatrix} \tag{3.129}$$

$$\frac{\partial q^*}{\partial \mathbf{x}_s} \sim \frac{1}{4\pi} \left[\begin{pmatrix} 0 \\ 0 \\ -\dfrac{1}{r^3} \end{pmatrix} + \begin{pmatrix} -3d & \dfrac{\rho \sin\theta}{r^5} \\ -3d & \dfrac{\rho \sin\theta}{r^5} \\ 3d^2 & \dfrac{1}{r^5} \end{pmatrix} \right] \tag{3.130}$$

where the potential $u(\mathbf{x}_s)$ and the potential derivative $\partial u/\partial \mathbf{x}_s$ at an internal point $\mathbf{x}_s$ near the boundary S are given by

$$u(\mathbf{x}_s) = \int_S (q\,u^* - u\,q^*)\, dS \tag{2.45}$$

and

$$\frac{\partial u}{\partial \mathbf{x}_s} = \int_S \left(q \frac{\partial u^*}{\partial \mathbf{x}_s} - u \frac{\partial q^*}{\partial \mathbf{x}_s} \right) dS \tag{2.46}$$

Since the near singularity is essentially related to r and the radial variable ρ, the nature of integral kernels in equations (2.45) and (2.46) can be summarized as in Table 3.2. In other words,

$$\int_S u^*\, dS \sim \int_S \frac{1}{r}\, dS \tag{6.183}$$

$$\int_S q^*\, dS \sim \int_S \frac{1}{r^3}\, dS \quad , \tag{6.184}$$

where as

$$\int_S \frac{\partial u^*}{\partial \mathbf{x}_s}\, dS \sim \int_S \frac{1}{r^3}\, dS + \int_S \frac{\rho}{r^3}\, dS \tag{6.185}$$

$$\int_S \frac{\partial q^*}{\partial \mathbf{x}_s}\, dS \sim \int_S \frac{1}{r^5}\, dS + \int_S \frac{\rho}{r^5}\, dS \quad , \tag{6.186}$$

regarding the order of near singularity.

Since

$$I = \int_S F\, dS$$

$$= \int_0^{2\pi} d\theta \int_0^{\rho_{\max}(\theta)} F\, \rho\, d\rho \tag{6.187}$$

where (ρ,θ) are the polar coordinates in the plane tangent to S at $\hat{\mathbf{x}}_s$ (cf. equation (5.39) of section 5.4) , the radial component of the integrals of equations (6.183) to (6.186) can be summarized as

$$\int_S u^* \, dS \;\rightarrow\; J_1 = \int_0^{\rho_j} \frac{\rho}{r} \, d\rho \quad , \tag{6.188}$$

$$\int_S q^* \, dS \;\rightarrow\; J_3 = \int_0^{\rho_j} \frac{\rho}{r^3} \, d\rho \quad , \tag{6.189}$$

whereas

$$\int_S \frac{\partial u^*}{\partial x_s} \, dS \;\rightarrow\; \begin{cases} J_3 \\ J_{3,2} = \int_0^{\rho_j} \frac{\rho^2}{r^3} \, d\rho \end{cases} \quad , \tag{6.190}$$

$$\int_S \frac{\partial q^*}{\partial x_s} \, dS \;\rightarrow\; \begin{cases} J_5 \\ J_{5,2} = \int_0^{\rho_j} \frac{\rho^2}{r^5} \, d\rho \end{cases} \quad , \tag{6.191}$$

where the extra ρ compared to quations (6.183) to (6.186) accounts for the Jacobian introduced by the polar coordinate system in equation (6.187), i.e.

$$dS = \rho \, d\rho \, d\theta \quad , \tag{6.192}$$

and

$$\rho_j = \rho_{max}(\beta) \quad . \tag{6.193}$$

It was shown in the error analysis in section 6.2 that for the radial integration :

$$J_\alpha = \int_0^{\rho_j} \frac{\rho}{r^\alpha} \, d\rho \quad ; \quad (\alpha = 1 \sim 5) \quad , \tag{6.2}$$

the adaptive logarithmic transformation of the type

$$R(\rho) = \log \sqrt{\rho^2 + d^2} \tag{5.49}$$

corresponding to $\beta = 2$ (log-L_2) reduces the error E_n of the radial numerical integration by the Gauss-Legendre formula to an order of

$$E_n \sim O(n^{-2n}) \tag{6.194}$$

where n is the number of integration points in the radial variable. This guarantees the efficiency of the logarithmic transformation (log-L_2) of equation (5.64) for the integration of the radial integration J_α, ($\alpha = 1 \sim 5$) of equation(6.2), and hence of the integration

$$I_\alpha = \int_S \frac{dS}{r^\alpha} \quad ; \quad (\alpha = 1 \sim 5) \tag{6.195}$$

and

$$u(\mathbf{x}_s) = \int_S (q\,u^* - u\,q^*) \, dS \tag{2.45}$$

for potentials near the boundary, which involve radial integrations J_1 and J_3, as demonstrated by the numerical results in Chapter 10 .

However, for flux (potential derivative) calculations involving the integral of equation (2.46), radial integrals of the type

$$J_{\alpha,2} = \int_0^{\rho_j} \frac{\rho^2}{r^\alpha} \, d\rho \quad ; \quad (\alpha = 3, 5) \tag{6.196}$$

as well as

$$J_\alpha = \int_0^{\rho_j} \frac{\rho}{r^\alpha} \, d\rho \quad ; \quad (\alpha = 3, 5) \tag{6.197}$$

are required, as shown in equations (6.190) and (6.191). Hence, let us perform an error analysis of the numerical integration of equation (6.196) when using radial variable transformations of the type

$$\rho \, d\rho = r' \, dR \tag{5.61}$$

where

$$r' = \sqrt{\rho^2 + d^2} = r \tag{6.197}$$

for planar elements. The integral of equation (6.196) is transformed by equation (5.61) to give

$$J_{\alpha,2} = \int_{R(0)}^{R(\rho_j)} \rho \, r^{\beta - \alpha} \, dR \quad . \tag{6.198}$$

Let the kernel of the integral of equation (6.198) be notified by

$$F(R) = \rho\, r^{\beta-\alpha} \tag{6.199}$$

as a function of the transformed variable R.

Since from equation(5.61)

$$\frac{d\rho}{dR} = \frac{r^{\beta}}{\rho} \quad , \tag{6.200}$$

and from equation (6.199)

$$\frac{dF}{d\rho} = r^{\beta-\alpha} + \rho\,(\beta-\alpha)\, r^{\beta-\alpha-1}\, \frac{dr}{d\rho} \tag{6.200}$$

$$= \left\{ (\beta-\alpha+1)\,\rho^2 + d^2 \right\} r^{\beta-\alpha-2} \quad , \tag{6.201}$$

where

$$\frac{dr}{d\rho} = \frac{d}{d\rho}\left(\sqrt{\rho^2+d^2}\right) = \frac{\rho}{\sqrt{\rho^2+d^2}} = \frac{\rho}{r} \quad . \tag{6.202}$$

Hence, from equations (6.200) and (6.201), one obtains

$$\frac{dF}{dR} = \frac{dF}{d\rho}\,\frac{d\rho}{dR}$$

$$= \frac{1}{\rho}\left\{ (\beta-\alpha+1)\,\rho^2 + d^2 \right\} r^{2\beta-\alpha-2} \tag{6.203}$$

Hence ,

$$\left.\frac{dF}{dR}\right|_{\rho=+0} = \left.\frac{d^{2\beta-\alpha}}{\rho}\right|_{\rho=+0} = +\infty \quad , \tag{6.204}$$

so long as $d>0$. This results from the fact that, from equation (6.200),

$$\left.\frac{d\rho}{dR}\right|_{\rho=+0} = \left.\frac{d^{\beta}}{\rho}\right|_{\rho=+0} = +\infty \quad , \tag{6.205}$$

while from equation (6.201)

$$\left.\frac{dF}{d\rho}\right|_{\rho=+0} = d^{\beta-\alpha} > 0 \tag{6.206}$$

for $d>0$.

Similarly, for higher derivatives

$$F^{(n)}(R) = \frac{d^n F}{dR^n} \quad , \tag{6.206}$$

we obtain the following theorem :

Theorem 6.2

For integers $n \geqq 0$,

$$F^{(n)}(R) = r^{(n+1)\beta-\alpha-2n} \sum_{k=0}^{n} a_{1-2k}^{n}\, \rho^{1-2k} \quad , \tag{6.207}$$

where $a_{1-2k}{}^{n}$ are constants which do not depend on ρ or R, and

$$a_{1-2n}^{n} = \left\{ \prod_{i=1}^{n-1} (1-2i) \right\} d^{2n} \tag{6.208}$$

where

$$\prod_{i=1}^{m} b_i = 1 \quad \text{for} \quad m<1 \quad . \tag{6.209}$$

Proof

For $n=0$, equation (6.207) gives

$$F^{(0)}(R) = r^{\beta-\alpha}\, a_1^0\, \rho \quad , \tag{6.210}$$

where, from equations (6.208) and (6.209),

$$a_1^0 = \left\{ \prod_{i=1}^{-1} (1-2i) \right\} = 1 \quad , \tag{6.211}$$

so that

$$F^{(0)}(R) = F(R) = r^{\beta-\alpha}\rho \quad , \tag{6.212}$$

which corresponds to equation (6.199).

For $n=1$, equation (6.207) gives

$$F^{(1)}(R) = (a_1^1\,\rho + a_{-1}^1\,\rho^{-1})\,r^{2\beta-\alpha-2} \quad , \tag{6.213}$$

and equation (6.208) and (6.209) give

$$a_{-1}^1 = \left\{\prod_{i=1}^{0}(1-2i)\right\} d^2 = d^2 \quad , \tag{6.214}$$

which agrees with equation (6.203).

For $n \geqq 2$, we use mathematical induction. Assume that equations (6.207) and (6.208) hold for $n=m$, i.e.

$$F^{(m)}(R) = r^{(m+1)\beta-\alpha-2m}\sum_{k=0}^{m} a_{1-2k}^m\,\rho^{1-2k} \quad , \tag{6.215}$$

and

$$a_{1-2m}^m = \left\{\prod_{i=1}^{m-1}(1-2i)\right\} d^{2m} \quad . \tag{6.216}$$

Then, for $n=m+1$ one obtains,

$$F^{(m+1)}(R) = \frac{\mathrm{d}F^{(m)}}{\mathrm{d}R} = \frac{\mathrm{d}}{\mathrm{d}R}(fg) \tag{6.215}$$

$$= \frac{df}{dR}\,g + f\,\frac{dg}{dR} \tag{6.217}$$

where

$$f = r^{(m+1)\beta-\alpha-2m} \tag{6.218}$$

and

$$g = \sum_{k=0}^{m} a_{1-2k}^m\,\rho^{1-2k} \quad . \tag{6.219}$$

Since

$$r = r' = \sqrt{\rho^2 + d^2} \quad , \tag{6.220}$$

$$\rho\,\mathrm{d}\rho = r'^{\beta}\mathrm{d}R = r^{\beta}\mathrm{d}R \quad ; \tag{6.221}$$

and from equation (6.220)

$$r^2 = \rho^2 + d^2 \quad , \tag{6.222}$$

so that

$$r\,\mathrm{d}r = \rho\,\mathrm{d}\rho \quad . \tag{6.223}$$

From equation (6.221),

$$\frac{\mathrm{d}\rho}{\mathrm{d}R} = \frac{r^{\beta}}{\rho} \quad , \tag{6.224}$$

and from equations (6.221) and (6.223)

$$\frac{\mathrm{d}r}{\mathrm{d}R} = r^{\beta-1} \quad . \tag{6.225}$$

Hence,

$$\frac{df}{dR} = \frac{df}{dr}\,\frac{dr}{dR} \tag{6.224}$$

$$= \left\{(m+1)\beta-\alpha-2m\right\} r^{(m+2)\beta-\alpha-2(m+1)} \tag{6.226}$$

and

$$\frac{dg}{dR} = \frac{dg}{d\rho}\,\frac{d\rho}{dR}$$

$$= \frac{r^{\beta}}{\rho}\sum_{k=0}^{m} a_{1-2k}^m\,(1-2k)\,\rho^{1-2k}$$

$$= r^{\beta}\sum_{k=0}^{m}(1-2k)\,a_{1-2k}^m\,\rho^{-1-2k} \quad . \tag{6.227}$$

From equations (6.217), (6.226) and (6.227),

$$F^{(m+1)}(R) = r^{(m+2)\beta - \alpha - 2(m+1)} \left[\sum_{k=0}^{m} \left\{ (m+1)\beta - \alpha - 2m + 1 - 2k \right\} a_{1-2k}^{m} \rho^{1-2k} + \sum_{k=0}^{m} (1-2k)\, d^2\, a_{1-2k}^{m} \rho^{-1-2k} \right]$$

$$= r^{(m+2)\beta - \alpha - 2(m+1)} \sum_{k=0}^{m+1} a_{1-2k}^{m+1} \rho^{1-2k} \qquad (6.228)$$

where, for $k = 0$

$$a_{1}^{m+1} = d^2\, a_{1}^{m} \qquad (6.229)$$

and for $1 \leqq k \leqq m$

$$a_{1-2k}^{m+1} = \left\{ (m+1)\beta - \alpha - 2m + 1 - 2k + (3-2k)\, d^2\, a_{3-2k}^{m} \right\} \qquad (6.230)$$

and for $k = m+1$

$$a_{1-2(m+1)}^{m+1} = (1-2m)\, d^2\, a_{1-2m}^{m} \qquad (6.230)$$

$$= \left\{ \prod_{i=1}^{m} (1-2i) \right\} d^{2(m+1)} \qquad (6.231)$$

from equation (6.216).

Hence, equaions (6.207) and (6.208) hold for $n = m+1$. Since equations (6.207) and (6.208) hold for $n = 1$, by mathematical induction they are satisfied for all integers $n \geqq 1$. Q.E.D.

From Theorem 6.2, the following corollaries are obtained.

Corollary 6.2.1

For integers $n \geqq 0$,

$$F^{(n)}(R) \Big|_{\rho=+0} \sim \left\{ \prod_{i=1}^{n-1} (1-2i) \right\} d^{(n+1)\beta - \alpha} \rho^{1-2n} \,, \qquad (6.232)$$

Proof Since $r = \sqrt{\rho^2 + d^2} = d$ for $\rho = 0$ and since the term including ρ^{1-2n} is the dominant term in equation (6.207) for $\rho = +0$, equation (6.232) is asymptotically true for $\rho = +0$.

Corollary 6.2.2

For $n \geqq 1$,

$$F^{(2n)}(R) \Big|_{\rho=+0} \sim \left\{ \prod_{i=1}^{2n-1} (1-2i) \right\} d^{(2n+1)\beta - \alpha} \rho^{1-4n}$$

$$\rho \to +0 \quad -\infty \,. \qquad (6.233)$$

Applying Stirling's formula :

$$n! \sim e^{-n} n^{n} \sqrt{2\pi n} \qquad (6.234)$$

to

$$\prod_{i=1}^{2n-1} (1-2i) = -\frac{(4n-3)!}{(2n-1)!\, 2^{2n-1}} \,, \qquad (6.235)$$

one obtains

$$\prod_{i=1}^{2n-1} (1-2i) \sim -2(2e)^{-2n} n^{2n-2} \,, \qquad (6.236)$$

which gives

Corollary 6.2.3

For relatively large integers $n \geqq 1$,

$$F^{(2n)}(R) \Big|_{\rho=+0} \sim -2\, d^{\beta - \alpha} n^{-2} \left(\frac{nd}{2e} \right)^{2n} \frac{1}{\rho^{4n-1}} \,. \qquad (6.237)$$

From equation (6.20), the error $E_R(F)$ of applying the Gauss-Legendre formula to the integral $J_{\alpha,2}$ in the radial variable R in equation (6.198) is

$$E_n(F) = p_n F^{(2n)}(R) \tag{6.238}$$

for some $R \in [a,b]$ and for some $\rho \in [0, \rho_j]$, where

$$\begin{aligned} a &= R(0) \\ b &= R(\rho_j) \end{aligned} \tag{6.239}$$

and from equation (5.50),

$$R(\rho) = \begin{cases} \dfrac{(\rho^2+d^2)^{1-\frac{\beta}{2}}}{2-\beta} & \text{for} \quad \beta \neq 2 \qquad (6.240) \\ \log(\rho^2+d^2)^{\frac{1}{2}} & \text{for} \quad \beta = 2 \qquad (6.241) \end{cases}$$

and

$$p_n \sim \frac{b-a}{4}\sqrt{\frac{\pi}{n}}\left|\frac{(b-a)\,e}{8n}\right|^{2n} . \tag{6.242}$$

Equations (6.238), (6.242) and Corollary 6.2.3 suggest that if the value $\rho \in [0, \rho_j]$ of equation (6.238) is near 0, i.e. $0 \leqq \rho \ll \rho_j$,

$$E_n(F) \sim n^{-\frac{5}{2}}\left|\frac{\{R(\rho_m)-R(0)\}\,d}{16\rho^2}\right|^{2n}_{\rho} . \tag{6.243}$$

Nothing that for $0 < d \ll \rho_j < r_j = \sqrt{\rho_j^2+d^2}$,

$$R(\rho_j)-R(0) = \begin{cases} r_j - d \sim r_j & (\beta=1) \\ \log r_j - \log d \sim -\log d & (\beta=2) \\ -\dfrac{1}{r_j} + \dfrac{1}{d} \sim \dfrac{1}{d} & (\beta=3) \\ -\dfrac{1}{2r_j^2} + \dfrac{1}{2d^2} \sim \dfrac{1}{2d^2} & (\beta=4) \\ -\dfrac{1}{3r_j^3} + \dfrac{1}{3d^3} \sim \dfrac{1}{3d^3} & (\beta=5) \end{cases} , \tag{6.244}$$

equation (6.243) suggests that many integration points n are required for the accurate integration of $J_{\alpha,2}$ of equation (6.198), compared to the integration of J_α of equation (6.4) by the log-L$_2$ ($\beta=2$) transformation, whre $E_n(F) \sim n^{-2n}$ as in equation (6.47) and Table 6.5.

To sum up, although $|E_n(F)| \neq \infty$, the fact that

$$\left(\frac{dF}{dR}\right)^{(m)}\Big|_{\rho=+0} = (-1)^{m-1}\infty \quad , \qquad (m \geqq 1) \tag{6.245}$$

has a bad effect on the efficiency of the use of the Gauss-Legendre formula for the integration of equation (6.198). Therefor it is clear that the radial variable transformation $R(\rho)$ of the type

$$\rho\, d\rho = r^{\beta}\, dR \tag{5.46}$$

does not stand a good chance of accurately calculating the integral $J_{\alpha,2}$, ($\alpha=3,5$) of equation (6.196) and hence the potential gradient at an internal point near the boundary.

This is true even for the adaptive logarithmic radial variable transformation (log-L$_2$) corresponding to $\beta=2$:

$$R(\rho) = \log\sqrt{\rho^2+d^2} \quad , \tag{5.64}$$

which was so successful in calculating integrals J_α for the potential. This fact is depicted in Figure 6.4 which shows the kernel function

$$F(R) = \rho\, r^{\beta-\alpha} \tag{6.199}$$

of equation (6.198) for $\beta=2$; $\alpha=3,5$, i.e.

$$F(R) = \rho\, r^{-1} = \sqrt{1-d^2}\, e^{-2R} \quad ; \qquad (\alpha=3) \tag{6.246}$$

$$F(R) = \rho\, r^{-4} = \sqrt{1 - d^2 e^{-2R}}\;\; e^{-2R} \qquad ; \qquad (\alpha = 5)\ , \tag{6.247}$$

where, from equation (5.64),

$$\rho(R) = \sqrt{e^{2R} - d^2} \tag{5.65}$$

$$r(R) = e^{R} \tag{6.248}$$

Comparing Fig. 6.4 with Fig. 6.1, it is seen that for the flux related kernel of equation (6.196), the log-L_2 transformation of the equation (5.64) ($\beta = 2$) has a problem, since the transformed kernel $F(R) = \rho\, r^{\beta-\alpha}$ of equation (6.199) has an infinite derivative at $\rho = 0$ or $R = R(0) = \log d$, so that the Gauss-Legendre formula applied to the variable R is not expected to work as efficiently as it did for the potential related kernel of equation (6.197) which renders a transformed kernel $F(R) = r^{\beta-\alpha}$ as seen in equation (6.25). This problem can be overcome by using the log-L_1 radial variable transformation which was proposed in Chapter 5.

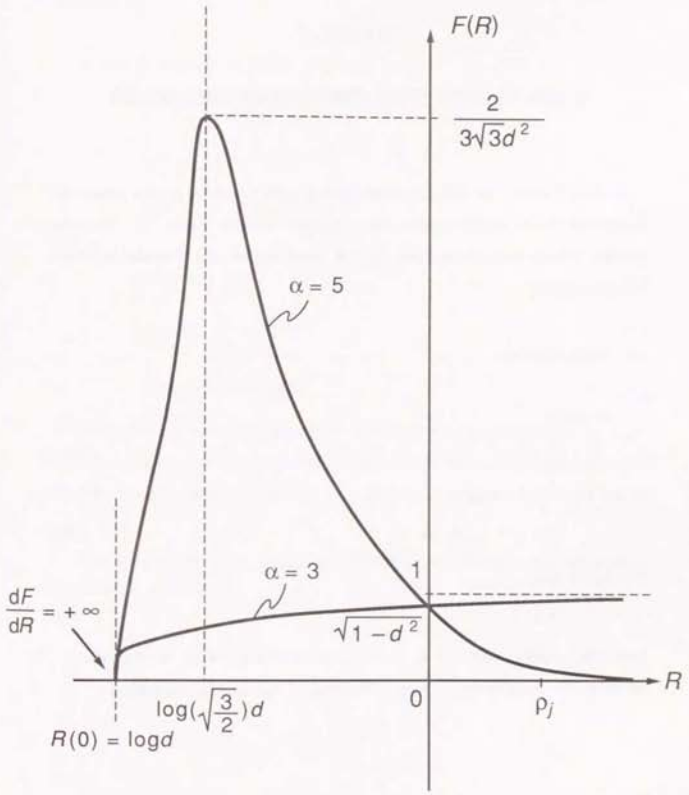

Fig. 6.4 Graph of $F(R) = \rho r^{\beta-\alpha}$ for $\beta = 2$, $\alpha = 3, 5$

CHAPTER 7

ERROR ANALYSIS USING COMPLEX FUNCTION THEORY

In this chapter, we will give more precise error estimates for the numerical integration in the radial variable, using complex function theory [42,52]. This also renders a firm theoretical basis for the optimization of the radial variable transformation.

7.1 Basic Theorem

The error

$$E_n(f) = I - I_n \tag{7.1}$$

of the numerical integration formula

$$I \sim I_n = \sum_{j=1}^{n} A_j f(a_j) \tag{7.2}$$

for the integral

$$I = \int_{-1}^{1} f(x)\,dx \tag{7.3}$$

over the interval $J=(-1,1)$ on the real axis is given by the following theorem [43-48], considering $f(z)$ as a function of the complex variable z.

Theorem 7.1

If $f(z)$ is regular on $K=[\,-1,\ 1\,]$,

$$I = \frac{1}{2\pi i} \oint_C \Psi(z)\, f(z)\,dz \tag{7.4}$$

$$I_n = \frac{1}{2\pi i} \oint_C \Psi_n(z)\, f(z)\,dz \tag{7.5}$$

$$E_n(f) = \frac{1}{2\pi i} \oint_C \Phi_n(z)\, f(z)\,dz \tag{7.6}$$

where

$$\Psi(z) = \int_{-1}^{1} \frac{dz}{z-x} \tag{7.7}$$

$$\Psi_n(z) = \sum_{j=1}^{n} \frac{A_j}{z-a_j} \tag{7.8}$$

$$\Phi_n(z) = \Psi(z) - \Psi_n(z) \tag{7.9}$$

and the path C of the complex integrals encircles the integration points $a_1, a_2, \cdots, a_n$ in the positive direction, as shown in Fig.7.1, and there are no singularities of the function $f(z)$ inside the path C.

$\Phi_n(z)$ is called the error characteristic function of the numerical integration formula of equation (7.2).

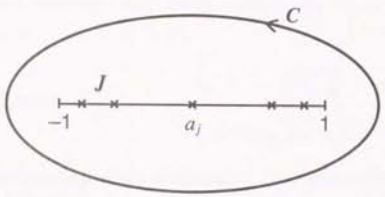

Fig. 7. 1 The integration path C

For the Gauss-Legendre formula, which we are using,

$$\Phi_n(z) = \frac{1}{p_n(z)} \int_{-1}^{1} \frac{p_n(x)}{z-x}\, dx$$

$$= \frac{1}{p_n(z)} \sum_{k=n}^{\infty} \frac{1}{z^{k+1}} \int_{-1}^{1} x^k p_n(x)\, dx \qquad (7.10)$$

Here, $p_n(x)$ is the n-th order Legendre polynomial defined on the interval $J=(-1, 1)$, and we adopt the zero points of this polynomial as the integration points $a_1, a_2, \cdots, a_n$.

7.2 Asymptotic Expressions for the Error Characteristics Function $\Phi_n(z)$

In order to derive theoretical error estimates of the numerical integration using Theorem 7.1, asymtotic expressions for the error characteristics function $\Phi_n(z)$ as $n \gg 1$ and/or $|z| \gg 1$ becomes necessary. In the following, we give known asymptotic expressions for $\Phi_n(z)$ for the Gauss-Legendre formula [46, 45, 47].

(1) Case $|z| \gg 1$

$$\Phi_n(z) = c_n z^{-2n-1} \left\{ 1 + b_n^{-2} z^{-2} + O(z^{-4}) \right\} \qquad (7.11)$$

where

$$b_n^{-2} = \frac{2n^3 + 3n^2 - n - 1}{(2n+3)(2n-1)} \qquad (7.12)$$

and

$$c_n = \frac{2^{2n+1} (n!)^4}{(2n)!\,(2n+1)!} \qquad (7.13)$$

Using Stirling's formula :

$$n! \sim \sqrt{2\pi n}\, n^n e^{-2n} \qquad (7.14)$$

for $n \gg 1$, we obtain

$$c_n \sim \frac{\pi}{2^{2n}} \quad , \quad (n \gg 1) \qquad (7.15)$$

(2) Case $n \gg 1$

(i) For all $z \in \mathbf{C}$ except for an arbitrary neighbourhood of the real segment $K=[-1, 1]$,

$$\Phi_n(z) \sim 2\pi \left(z + \sqrt{z^2-1}\right)^{-2n-1} \qquad (7.16)$$

(ii) For all z except for an arbitrary neighbourhood of $z=1$,

$$\Phi_n(z) \sim 2e^{-i\pi} \frac{K_0(2k\zeta)}{I_0(2k\zeta)} \qquad (7.17)$$

where

$$z = e^{i\pi} \cosh 2\zeta \qquad (7.18)$$

$$k = n + \frac{1}{2} \qquad (7.19)$$

and $I_0(z)$ and $K_0(z)$ are the modified Bessel function of the first and second kind, resectively.

7.3 Use of the Elliptic Contour as the Integral Path

In the estimation of the numerical integration error $E_n(f)$ by Theorem 7.1, it is often useful to take the ellipse $\mathcal{E}_\sigma$:

$$\left| z + \sqrt{z^2-1} \right| = \sigma, \quad (\sigma > 1) \qquad (7.20)$$

as the path C of the complex contour integral in equation (7.6).

The ellipse $\mathcal{E}_\sigma$ has the foci at $z = \pm 1$ and encircles the interval $K=[-1, 1]$. In fact, it collapses to the interval $K=[-1, 1]$ when $\sigma=1$ in equation (7.20). The major axis of $\mathcal{E}_\sigma$ is

$$x_0 = \frac{1}{2}\left(\sigma + \frac{1}{\sigma}\right) \qquad (7.21)$$

and the minor axis is

$$y_0 = \frac{1}{2}\left(\sigma - \frac{1}{\sigma}\right) \qquad (7.22)$$

If the function $f(z)$ is regular inside $\mathcal{E}_\sigma$, equation (7.6) of Theorem 7.1 and the asymptotic ($n \gg 1$) expression of $\Phi_n(z)$ in equation (7.16) gives [4]

$$E_n(f) \sim \frac{1}{i} \oint_{\mathcal{E}_\sigma} \frac{f(z)}{\left(z + \sqrt{z^2-1}\right)^{2n+1}} \, dz \quad , \quad (n \gg 1) \quad , \qquad (7.23)$$

which gives

$$|E_n(f)| \leq \frac{\ell(\mathcal{E}_\sigma)}{\sigma^{2n+1}} \max_{z \in \mathcal{E}_\sigma} |f(z)| \qquad (7.24)$$

where $\ell(\mathcal{E}_\sigma)$ is the length of $\mathcal{E}_\sigma$.

Since

$$\ell(\mathcal{E}_\sigma) \leq 2\pi \cdot \frac{1}{2}\left(\sigma + \frac{1}{\sigma}\right) = \pi\left(\sigma + \frac{1}{\sigma}\right) < 2\pi\sigma \quad , \qquad (7.25)$$

we have

$$|E_n(f)| < 2\pi\sigma^{-2n} \max_{z \in \mathcal{E}_\sigma} |f(z)| \qquad (7.26)$$

Hence, it becomes important to estimate the maximum value of σ (size of the ellipse $\mathcal{E}_\sigma$), such that there are no singularities of $f(z)$ inside the ellipse $\mathcal{E}_\sigma$. In order to do so, we derive the expression of $\sigma = \sigma(x, y)$ for the ellipse $\mathcal{E}_\sigma$ which passes through the point $z = x + iy$, in the following.

Equation (7.20) is equivalent to

$$\frac{x^2}{\left\{\frac{1}{2}\left(\sigma + \frac{1}{\sigma}\right)\right\}^2} + \frac{y^2}{\left\{\frac{1}{2}\left(\sigma - \frac{1}{\sigma}\right)\right\}^2} = 1 \quad , \qquad (7.27)$$

which gives

$$\frac{x^2}{s} + \frac{y^2}{s-1} = 1 \qquad (7.28)$$

where

$$s = \left[\frac{1}{2}\left(\sigma + \frac{1}{\sigma}\right)\right]^2 > 1 \quad \text{for} \quad \sigma > 1 \qquad (7.29)$$

Solving equation (7.28) for s under the constraint $s>1$ gives

$$s = \frac{x^2 + y^2 + 1 + \sqrt{\{(x+1)^2 + y^2\}\{(x-1)^2 + y^2\}}}{2}$$

$$= \left[\frac{\sqrt{(x+1)^2 + y^2} + \sqrt{(x-1)^2 + y^2}}{2}\right]^2 \qquad (7.30)$$

Next, solving equation (7.29) under the condition $\sigma>1$, $s>1$ gives

$$\sigma = \gamma + \sqrt{\gamma^2 - 1} \qquad (7.31)$$

where

$$\gamma = \sqrt{s} = \frac{\sqrt{(x+1)^2 + y^2} + \sqrt{(x-1)^2 + y^2}}{2} > 1 \qquad (7.32)$$

Note that $\sigma(\gamma)$ is a strictly increasing function of $\gamma>1$ and $\sigma(1)=1$.

7.4 The Saddle Point Method

Another technique which proves useful in the theoretical estimation of the numerical integration error using Theorem 7.1, is the saddle point method [43, 44].

The saddle point s of a complex function $f(z)$ is the point $z=s$ at which $f(z)$ is regular and

$$f'(s) = 0, \qquad f''(s) \neq 0 \qquad (7.33)$$

As long as $f(z) \neq 0$, we can express $f(z)$ as

$$f(z) = \exp g(z) \qquad (7.34)$$

which gives

$$f'(z) = g'(z) \exp g(z) \qquad (7.35)$$

Since

$$g'(s) = 0 \Leftrightarrow f'(s) = 0 \qquad (7.36)$$

the saddle points of $g(z)$ and $f(z)$ coincide.

In the neighbourhood $|z-s| \ll 1$ of $z=s$,

$$f(z) = \exp g(z)$$

$$\sim \exp g(s) \exp\left\{\frac{1}{2} g''(s)(z-s)^2\right\} \qquad (7.37)$$

Let

$$g''(s) = |g''(s)| e^{i\alpha}, \quad \alpha = \arg g''(s), \quad -\pi < \alpha \leq \pi \qquad (7.38)$$

$$z - s = re^{i\theta}, \quad r = |z-s|, \quad \theta = \arg(z-s) \qquad (7.39)$$

Then,

$$g(z) \sim g(s) + \frac{|g''(s)|}{2} r^2 e^{i(\alpha + 2\theta)} \qquad (7.40)$$

$$f(z) = \exp g(z)$$

$$\sim \exp g(s) \exp\left\{\frac{g''(s)}{2} r^2 \cos(\alpha + 2\theta)\right\} \exp\left\{i \frac{g''(s)}{2} r^2 \sin(\alpha + 2\theta)\right\} \qquad (7.41)$$

Now, let us consider the complex contour integral

$$I = \int_C f(z)\, dz \qquad (7.42)$$

along a path C. Let $z=s$ be the saddle point of $f(z)$, where $f(z)$ is expressed as

$$f(z) = \exp g(z) \qquad (7.34)$$

in the neighbourhood of $z=s$. Move the integration path C, without crossing any singular points of $f(z)$, so that it passes through the saddle point $z=s$ in the direction

$$\theta = -\frac{\alpha}{2} \pm \frac{\pi}{2} \qquad (7.43)$$

($\pm$ depends on the direction of the path), so that

$$f(z) \sim \exp\left\{g(s)\right\} \exp\left\{-\frac{|g''(s)|}{2} |z-s|^2\right\} \qquad (7.44)$$

and

$$dz = e^{i\left(-\frac{\alpha}{2}\pm\frac{\pi}{2}\right)} dr \tag{7.45}$$

in the neighbourhood $|z-s|<\delta$ of $z=s$.

Then,

$$\begin{aligned} I &= \int_C f(z)\,dz \\ &\sim e^{\frac{i(-\alpha\pm\pi)}{2}} \exp\left[g(s)\right] \int_{-\delta}^{\delta} \exp\left[-\frac{|g''(s)|}{2} r^2\right] dr \\ &\sim e^{\frac{i(-\alpha\pm\pi)}{2}} \exp\left[g(s)\right] \int_{-\infty}^{\infty} \exp\left[-\frac{|g''(s)|}{2} r^2\right] dr \\ &= e^{\frac{i(-\alpha\pm\pi)}{2}} \sqrt{\frac{2\pi}{|g''(s)|}}\, f(s) \end{aligned} \tag{7.46}$$

where

$$g''(s) = \left[\frac{d^2}{dz^2}\left\{\log f(z)\right\}\right]_{z=s} . \tag{7.47}$$

The contribution to the integral I from $|z-s|<\delta$ is dominant, provided $|g''(s)|$ is sufficiently large. Note that equation (7.46) gives an evaluation of the complex integral I by the information of $f(z)$ at its saddle point $z=s$. If there are several saddle points of $f(z)$, the sum of the last expression in equation (7.46) is taken for these saddle points.

7.5 Integration in the Transformed Radial Variable : R

Using Theorem 7.1 and the techniques mentioned above, we will derive theoretical error estimates for numerical integration using different radial variable transformations.

The essence of the radial component of the boundary element integrals for three dimensional potential problems can be expressed as

$$I = \int_0^{\rho_j} \frac{\rho^\beta}{r^\alpha} d\rho \tag{7.48}$$

where $r=\sqrt{\rho^2+d^2}$ for planar elements. α and β are given in Table 7.1, according to Table 3.3. $\rho_j=\rho_j(\theta)$ is the upper limit of the radial integral in equation (5.42).

Table 7.1 Nature of nearly singular kernels of the radial component integrals in 3-D potential problems

	α	β
u^*	1	1
q^*	3	1
$\frac{\partial u^*}{\partial x_s}$	3	1 2
$\frac{\partial q^*}{\partial x_s}$	3	1
	5	1 2

The application of the radial variable transformation to equation (7.48) gives

$$I = \int_{R(0)}^{R(\rho_j)} \frac{\rho^\beta}{r^\alpha} \frac{d\rho}{dR} dR \tag{7.49}$$

Further, transforming R to x so that the interval $R:[R(0), R(\rho_j)]$ is mapped onto $x:[-1,1]$, we obtain

$$I = \int_{-1}^{1} \frac{\rho^\beta}{r^\alpha} \frac{d\rho}{dR} \frac{dR}{dx} dx = \int_{-1}^{1} f(x)\,dx , \tag{7.50}$$

where

$$f(x) = \frac{\rho^\beta}{r^\alpha} \frac{d\rho}{dR} \frac{dR}{dx} \tag{7.51}$$

and

$$x = \frac{2R - \{R(\rho_j)+R(0)\}}{R(\rho_j)-R(0)} \tag{7.52}$$

or

$$R = \frac{\{R(\rho_j) - R(0)\}\, x + R(\rho_j) + R(0)}{2} \quad , \tag{7.53}$$

so that

$$\frac{dR}{dx} = \frac{R(\rho_j) - R(0)}{2} \quad . \tag{7.54}$$

Now, Theorem 7.1 and the related techniques can be applied to the numerical integration of $f(x)$ in equation (7.50) using the Gauss-Legendre rule.

7.6 Error Analysis for the Identity Transformation : $R(\rho)=\rho$

First, theoretical error estimates will be derived for the basic case of the identity transformation : $R(\rho)=\rho$, which is equivalent to using just polar coordinates in the projected plane $\overline{S}$ (cf. Chapter 5) without any radial variable transformation. This will clarify the nature of the (radial) near singularity and the difficulty which results from applying the Gauss-Legendre formula directly to the radial variable ρ.

Since

$$R(0) = 0 \quad , \quad R(\rho_j) = \rho_j \quad , \tag{7.55}$$

we have

$$R(\rho) = \rho = \frac{\rho_j\,(x+1)}{2} \tag{7.56}$$

and

$$\frac{d\rho}{dx} = \frac{\rho_j}{2} \quad , \tag{7.57}$$

so that

$$r = \frac{\rho_j}{2}\,(x+1+2\,D\,i)^{\frac{1}{2}}\,(x+1-2\,D\,i)^{\frac{1}{2}} \quad , \tag{7.58}$$

where

$$D = \frac{d}{\rho_j} \tag{7.59}$$

is equivalent to the source distance relative to the element size. This relative source distance : D is the parameter which essentially determines the degree of near singularity.

Hence, we obtain

$$I = \int_0^{\rho_j} \frac{\rho^\beta}{r^\alpha}\, d\rho = \int_{-1}^{1} f(x)\, dx \tag{7.57}$$

where

$$\boxed{f(z) = \left(\frac{\rho_j}{2}\right)^{\beta+1-\alpha} \frac{(z+1)^\beta}{\{z-(-1+2Di)\}^{\alpha/2}\,\{z-(-1-2Di)\}^{\alpha/2}}} \tag{7.58}$$

or

$$f(z) = A\,(z+1)^\beta\,(z-z_1)^{-\frac{\alpha}{2}}\,(z-\bar{z}_1)^{-\frac{\alpha}{2}} \tag{7.59}$$

where

$$A = \left(\frac{\rho_j}{2}\right)^{\beta+1-\alpha} \quad . \tag{7.60}$$

The singularities of $f(z)$ are

$$z_1 = -1+i\frac{2d}{\rho_j} = -1+2Di$$

$$\bar{z}_1 = -1-i\frac{2d}{\rho_j} = -1-2Di \quad . \tag{7.61}$$

z_1 and $\bar{z}_1$ are also branching points when α is odd.

The estimate for numerical integration error is obtained by

$$E_n(f) = \frac{1}{2\pi i}\oint_C \Phi_n(z)\, f(z)\, dz \tag{7.7}$$

where the path C for the complex contour integral is taken as an ellipse $\mathcal{E}_\sigma$:

$$|\, z+\sqrt{z^2-1}\,| = \sigma \quad , \quad (\sigma > 1) \tag{7.20}$$

which does not contain the singular points z_1 , $\bar{z}_1$ inside or on the ellipse, as shown in Fig.7.2.

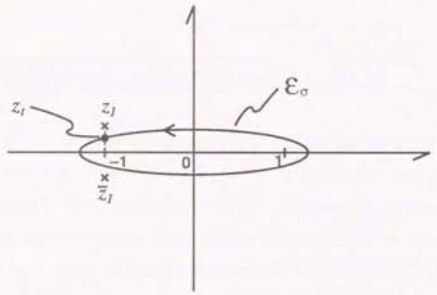

Fig. 7. 2 Singularities of $f(z)$ and integration path $\mathcal{E}_\sigma$ for the identity radial variable transformation : $R(\rho)=\rho$

Using the asymptotic expression

$$\Phi_n(z) \sim 2\pi\,(z+\sqrt{z^2-1})^{-2n-1} \quad , \tag{7.16}$$

we obtain

$$|E_n(f)| \leq 2\pi\,\sigma^{-2n} \max_{z\in\mathcal{E}_\sigma} |f(z)| \quad . \tag{7.24}$$

(1) Estimation of the size σ of the ellipse $\mathcal{E}_\sigma$

First, we will determine the size σ of the ellipse $\mathcal{E}_\sigma$ which passes through the point

$$z_t = -1+2Dti \quad , \quad 0<t<1$$
$$= x+yi \quad . \tag{7.62}$$

It is clear that this ellipse $\mathcal{E}_\sigma$ does not contain z_1 or $\bar{z}_1$ inside or on itself.

From equations (7.31) and (7.32), we obtain

$$\gamma(D,t) = \sqrt{1+(D\theta)^2}+Dt \tag{7.63}$$

and,

$$\sigma(D,t) = \gamma+\sqrt{\gamma^2-1}$$
$$= \sqrt{1+(D\theta)^2}+\sqrt{2\{Dt\sqrt{1+(D\theta)^2}+(D\theta)^2\}}+Dt \quad \geq 1 \quad , \quad (0<t<1) \tag{7.64}$$

so that

$$\frac{\partial\sigma}{\partial D} = \frac{t\{1+2Dt\sqrt{1+(D\theta)^2}+2(Dt)^2\}}{\sqrt{1+(D\theta)^2}\,\sqrt{2\{Dt\sqrt{1+(D\theta)^2}+(D\theta)^2\}}}+t+\frac{Dt^2}{\sqrt{1+(D\theta)^2}}$$
$$> \quad 0 \quad , \quad (0<t<1) \quad . \tag{7.65}$$

Hence , $\sigma(D, t)$ is a strictly increasing function of both D and t for $0<t<1$, with the following properties :

$$\sigma(D=0) = 1 \tag{7.66}$$

$$\sigma(0<D\ll 1) \sim 1+\sqrt{2Dt} \tag{7.67}$$

$$\frac{\partial\sigma}{\partial D}(0<D\ll 1) \sim \sqrt{\frac{t}{2D}} \xrightarrow[D\to 0_+]{} +\infty \tag{7.68}$$

$$\sigma\ (D \gg 1) \sim 4Dt \qquad (7.69)$$

The graph of $\sigma(D, t)$ vs D for the case $t=0.6$ is shown in Fig.7.3.

(2) Estimation of $\max_{z \in \mathcal{E}_\sigma} |f(z)|$

From equation (7.58),

$$f(\bar{z}) = A^{\delta+1-\alpha}\ (\bar{z}+1)^{\beta}\ (\bar{z}-z_1)^{-\frac{\alpha}{2}}\ (\bar{z}-\bar{z}_1)^{-\frac{\alpha}{2}} = \overline{f(z)} \qquad (7.70)$$

so that

$$|f(\bar{z})| = |f(z)| \qquad (7.71)$$

Hence, we need only consider $\mathrm{Im}(z) \geqq 0$ on the ellipse $\mathcal{E}_\sigma$. Since $f(z)$ has a singularity of order $(z-z_1)^{-\alpha/2}$ at z_1, it is obvious that $|f(z)|$ takes the maximum value on $\mathcal{E}_\sigma$ when z is nearest to z_1.

Let $z=z_1+\Delta z$. Then, for $|\Delta z| \ll 1$,

$$|f(z)| \sim A^{\delta+1-\alpha}\ 2^{\beta-\alpha}\ D^{\delta-\frac{\alpha}{2}}\ |\Delta z|^{-\frac{\alpha}{2}}$$

$$= 2^{-1} \rho_j^{\delta+1-\alpha}\ D^{\delta-\frac{\alpha}{2}}\ |\Delta z|^{-\frac{\alpha}{2}} \qquad (7.72)$$

Then, for $z_t = -1+2Dt\,\mathrm{i}$, $0<t<1$, we have

$$\Delta z = z_t - z_1 = -2D(1-t)\mathrm{i} \qquad (7.73)$$

and

$$|\Delta z| = 2D(1-t) \qquad (7.74)$$

Hence, for $|\Delta z| = 2D|1-t| \ll 1$, which is the case for nearly singular integrals, where $0 < D \equiv d/\rho_j \ll 1$, $|f(z)|$ is nearly maximum at $z=z_t$ for all $z \in \mathcal{E}_\sigma$, and

$$\max_{z \in \mathcal{E}_\sigma} |f(z)| \sim |f(z_t)|$$

$$\sim 2^{-\alpha-1} \rho_j^{\delta+1-\alpha}\ D^{\delta-\frac{3\alpha}{2}}\ |1-t|^{-\frac{\alpha}{2}} \qquad (7.75)$$

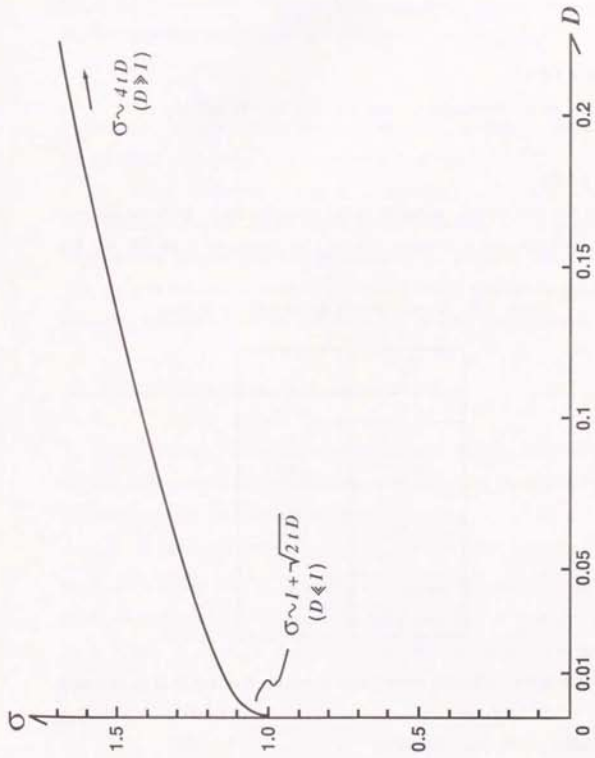

Fig. 7.3 Graph of $\sigma(D, t=0.6)$ vs D for the identity radial transformation : $R(\rho)=\rho$

(3) Error estimate $E_n(f)$

From equations (7.24) and (7.75), we obtain the error estimate

$$|E_n(f)| \lesssim \frac{\pi\, 2^{-\alpha}\, \rho_j^{\delta+1-\alpha}\, D^{\delta-\frac{3\alpha}{2}}\, (1-t)^{-\frac{\alpha}{2}}}{\sigma^{2\alpha}} \tag{7.76}$$

where $0 < t < 1$.

Since we are interested in cases $\alpha = 1,3,5$ (cf. Table 7.1),

$$(1-t)^{-\frac{\alpha}{2}} < 10 \tag{7.77}$$

implies $t < 0.6$.

For the case $t = 0.6$, equation (7.64) gives values of $\sigma(D)$ for different values of relative source distance $D \equiv d/\rho_j$, as shown in Table 7.2 (cf. Fig. 7.3).

Table 7.2 Values of $\sigma(D)$ for $t = 0.6$, for $R(\rho) = \rho$

D	σ
10^{-4}	1.01
10^{-3}	1.04
3×10^{-3}	1.06
10^{-2}	1.12
3×10^{-2}	1.21
10^{-1}	1.42
3×10^{-1}	1.85
1	3.22

For nearly singular integrals whose relative source distance D is in the range

$$D: 10^{-3} \sim 10^{-1}, \tag{7.78}$$

σ in equation (7.76) takes the value

$$\rho: 1.04 \sim 1.42 \tag{7.79}$$

In summary, we have obtained an error estimate :

$$\boxed{|E_n(f)| \lesssim D^{\delta-\frac{3\alpha}{2}}\, \sigma^{-2\alpha} \sim \sigma^{-2\alpha} \quad \text{where} \quad \sigma = 1.04 \sim 1.42 \quad \text{for} \quad D: 10^{-3} \sim 10^{-1}} \tag{7.80}$$

for the numerical integration

$$I = \int_0^{\rho_j} \frac{\rho^\delta}{r^\alpha}\, d\rho \tag{7.45}$$

in the radial variable, (which characterizes the 3-D potential problem,) using the identity radial variable transformation $R(\rho) = \rho$.

The above theoretical estimate corresponds well with numerical experiment results, as will be demonstrated in Chapter 10. Equation (7.80) explains why the use of polar coordinates in the projected plane $\bar{S}$, alone, does not give efficient or accurate results for nearly singular integrals, thus indicating the necessity of an efficient radial variable transformation $R(\rho)$.

7.7 Error Analysis for the log-L_2 Transformation

In this section, theoretical error estimates will be derived for the numerical integration in the radial variable using the Gauss-Legendre rule after applying the log-L_2 transformation

$$R(\rho) = \log \sqrt{\rho^2 + d^2} \tag{5.64}$$

The analysis will clarify quantitatively, the reason why the log-L_2 transformation works so efficiently for the integration of potential kernels, while it fails to do so for flux kernels and kernels including interpolation functions.

Equation (5.64) gives

$$R(0) = \ln d \tag{7.81}$$

$$R(\rho_j) = \ln r_j \tag{7.82}$$

where

$$r_j = \sqrt{\rho_j^2 + d^2} \tag{7.83}$$

and

$$\rho \mathrm{d}\rho = r^2 \mathrm{d}r \tag{7.84}$$

for planar elements, where

$$r = r' = \sqrt{\rho^2 + d^2} = \mathrm{e}^R \tag{7.85}$$

and

$$\rho(R) = (\mathrm{e}^{2R} - d^2)^{\frac{1}{2}} \tag{7.86}$$

Hence,

$$I = \int_0^{\rho_j} \frac{\rho^\delta}{r^\alpha} \mathrm{d}\rho = \int_{R(0)}^{R(\rho_j)} \frac{\rho^{\delta-1}}{r^{\alpha-2}} \mathrm{d}R \tag{7.87}$$

Equations (7.52) and (7.53) for the linear trasformation which maps $R:[R(0), R(\rho_j)]$ onto $x:[-1, 1]$ gives

$$x = \frac{2R - \ln(r_j d)}{\ln(r_j/d)} \tag{7.88}$$

and

$$R = \frac{\left[\ln(r_j/d)\right] x + \ln(r_j d)}{2} \tag{7.89}$$

and

$$\frac{\mathrm{d}R}{\mathrm{d}x} = \frac{\ln(r_j/d)}{2} \tag{7.90}$$

Thus, the integral of equation (7.87) can be expressed as

$$I = \int_{-1}^{1} f(x) \mathrm{d}x \tag{7.91}$$

where

$$f(z) = b\,(\mathrm{e}^{z \ln a} - a^{-1})^{\frac{\delta-1}{2}}\, \mathrm{e}^{\left(\frac{2-\alpha}{2} \ln a\right) z} \tag{7.92}$$

$$b = \frac{\ln a}{2} (r_j d)^{\frac{\delta+1-\alpha}{2}} > 0 \tag{7.93}$$

$$a = \frac{r_j}{d} = \frac{\sqrt{\rho_j^2 + d^2}}{d} > 1 \tag{7.94}$$

(1) Case : δ = odd

When δ is a (positive) odd number, as in the integration of u^* and q^* for the potential, where $\delta = 1$ (cf. Table 7.1), the function $f(z)$ of equation (7.92) is regular in the whole complex plane except for $z = \infty$, since $(\delta - 1)/2$ is a non-negative integer.

Hence, we can take the integration path as $C: \{z \mid |z| = R \gg 1\}$ in

$$E_n(f) = \frac{1}{2\pi i} \oint_C \Phi_n(z)\, f(z)\, \mathrm{d}z \tag{7.6}$$

of Theorem 7.1, and apply the asymptotic expression of $\Phi_n(z)$ for $|z| \gg 1$ in equation (7.11), and expand $f(z)$ in Taylor series as

$$f(z) = \sum_{k=1}^{\infty} a_\ell\, z^\ell \tag{7.95}$$

for $z \neq \infty$, so that we obtain the error estimate

$$E_n(f) \sim c_n (a_{2n} + b_n^{-2} a_{2n+2}) \tag{7.96}$$

Here, we have used the fact that

$$\frac{1}{2\pi i} \oint_c z^m \mathrm{d}z = \begin{cases} 1 & ; \ m = -1 \\ 0 & ; \ m \neq -1 \end{cases} \tag{7.97}$$

for any integration path C that encircles $z = 0$ in the positive direction once.

The a_ℓ in equation (7.95) can be obtained as follows. In equation (7.92),

$$(\mathrm{e}^{z \ln a} - a^{-1})^{\frac{\delta-1}{2}} = \sum_{k=0}^{\frac{\delta-1}{2}} {}_{\frac{\delta-1}{2}}C_k\, \mathrm{e}^{\left(\frac{\delta-1}{2} - k\right)(\ln a) z} (-a^{-1})^k \tag{7.98}$$

where

$${}_mC_k = \frac{m!}{(m-k)!\, k!} \tag{7.99}$$

is the coefficient of binomial expansion. Hence,

$$f(z) = b \sum_{k=0}^{\frac{\delta-1}{n}} \frac{\delta-1}{2} C_k \, e^{\left(\frac{\delta-\alpha+1}{2}-k\right)(\ln a)z} (-a^{-1})^k$$

$$= b \sum_{k=0}^{\frac{\delta-1}{n}} \frac{\delta-1}{2} C_k (-a^{-1})^k \sum_{\ell=0}^{\infty} \frac{\left\{\left(\frac{\delta-\alpha+1}{2}-k\right)(\ln a)z\right\}^\ell}{\ell!} \quad , \tag{7.100}$$

since

$$e^z = \sum_{\ell=0}^{\infty} \frac{z^\ell}{\ell!} \quad . \tag{7.101}$$

Thus, we have

$$a_\ell = b \sum_{k=0}^{\frac{\delta-1}{n}} \frac{\delta-1}{2} C_k (-a^{-1})^k \frac{\left\{\left(\frac{\delta+1-\alpha}{2}-k\right)\ln a\right\}^\ell}{\ell!} \quad , \tag{7.102}$$

so that in equation (7.96),

$$a_{2n} = b \sum_{k=0}^{\frac{\delta-1}{2}} C_{\delta,k} \frac{(d_{\delta,k})^{2n}}{(2n)!} \quad , \tag{7.103}$$

$$b_n^{-2} a_{2n+2} = b \frac{2n^3+3n^2-n-1}{(2n+3)(2n-1)} \sum_{k=0}^{\frac{\delta-1}{n}} C_{\delta,k} \frac{(d_{\delta,k})^{2n+2}}{(2n+2)!}$$

$$\underset{n\gg 1}{\sim} b \sum_{k=0}^{\frac{\delta-1}{n}} \frac{(d_{\delta,k})^2}{8n} C_{\delta,k} \frac{(d_{\delta,k})^{2n}}{(2n)!} \quad , \tag{7.104}$$

where

$$C_{\delta,k} = \frac{\delta-1}{2} C_k (-a^{-1})^k \quad ,$$

$$d_{\delta,k} = \left(\frac{\delta+1-\alpha}{2}-k\right)\ln a \quad . \tag{7.105}$$

Since

$$\frac{2-\alpha}{2} \le \frac{\delta+1-\alpha}{2} - k \le \frac{\delta+1-\alpha}{2}$$

for

$$\frac{\delta-1}{2} \ge k \ge 0 \quad , \tag{7.106}$$

and

$$-\frac{3}{2} \le \frac{2-\alpha}{2} \le \frac{1}{2} \quad , \quad \frac{\delta-4}{2} \le \frac{\delta+1-\alpha}{2} \le \frac{\delta}{2} \tag{7.107}$$

for $\alpha = 1,3,5$ (for 3-D potential problems), we have

$$\left|\frac{\delta+1-\alpha}{2}-k\right| \le \frac{\max(3,\delta)}{2} \quad , \tag{7.108}$$

which gives

$$\frac{(d_{\delta,k})^2}{8n} \le \frac{\{\max(3,\delta)\ln(r_j/d)\}^2}{32n} \quad . \tag{7.109}$$

Hence, for $n \gg 1$,

$$b_n^{-2} a_{2n+2} \ll a_{2n} \tag{7.110}$$

in equation (7.96), so that

$$E_n(f) \sim c_n a_{2n}\{1+O(1/n)\}$$

$$\underset{n\gg 1}{\sim} c_n a_{2n}$$

$$= (r_j d)^{\frac{\delta+1-\alpha}{2}} \ln(r_j/d) \left\{2\ln(r_j/d)\right\}^{2n} \frac{(n!)^4}{(2n)!\,(2n+1)!}$$

$$\sum_{k=0}^{\frac{\delta-1}{n}} \frac{\delta-1}{2} C_k (-d/r_j)^k \left(\frac{\delta-\alpha+1}{2}-k\right)^{2n}$$

$$\underset{n\gg 1}{\sim} \frac{1}{4}\sqrt{\frac{\pi}{n}} (r_j d)^{\frac{\delta+1-\alpha}{2}} \ln(r_j/d) \left\{\frac{e\ln(r_j/d)}{4n}\right\}^{2n}$$

$$\sum_{k=0}^{\frac{\delta-1}{n}} \frac{\delta-1}{2} C_k (-d/r_j)^k \left(\frac{\delta-\alpha+1}{2}-k\right)^{2n} \quad , \tag{7.111}$$

using Stirling's formula.

For $\delta = 1$, equation (7.111) gives

$$E_n(f) \sim \left\{\frac{(\alpha-2)\,e\ln(r_j/d)}{8n}\right\}^{2n} \quad , \tag{7.112}$$

which matches with equation (6.42), obtained by elementary error analysis in Chapter 6.

For the nearly singular case, where the source distance d is very small compared to the element size, i.e. $0 < D \equiv d/\rho_j \ll 1$,

$$\frac{r_j}{d} = \frac{\sqrt{\rho_j^2 + d^2}}{d} \sim D^{-1} \quad , \tag{7.113}$$

$$r_j d \sim {\rho_j}^2 D \quad , \tag{7.114}$$

so that equation (7.111) for δ : odd gives

$$E_n(f) \underset{D \ll 1}{\sim} \rho_j^{\delta+1-\alpha} D^{\frac{\delta+1-\alpha}{2}} (-\ln D)(2\ln D)^{2n} \frac{(n!)^4}{(2n)!(2n+1)!} \sum_{k=0}^{\frac{\delta-1}{n}} {}_{\frac{\delta-1}{2}}C_k (-D)^k \left(\frac{\delta-\alpha+1}{2} - k\right)^{2n}$$

$$\underset{n \gg 1}{\sim} \frac{1}{4}\sqrt{\frac{\pi}{n}} \rho_j^{\delta+1-\alpha} D^{\frac{\delta+1-\alpha}{2}} (-\ln D) \left(\frac{\mathrm{e} \ln D}{4n}\right)^{2n} \sum_{k=0}^{\frac{\delta-1}{n}} {}_{\frac{\delta-1}{2}}C_k (-D)^k \left(\frac{\delta-\alpha+1}{2} - k\right)^{2n} \tag{7.115}$$

Further, using equation (7.108) for $1 \leqq \alpha \leqq 5$,

and since

$$\sum_{k=0}^{\frac{\delta-1}{n}} {}_{\frac{\delta-1}{2}}C_k (-D)^k = (1-D)^{\frac{\delta-1}{2}} \quad , \tag{7.116}$$

we obtain

$$| E_n(f) | \underset{\sim}{<} \frac{1}{4}\sqrt{\frac{\pi}{n}} \rho_j^{\delta+1-\alpha} D^{\frac{\delta+1-\alpha}{2}} (1-D)^{\frac{\delta-1}{2}} (-\ln D) \left[\frac{\max(3,\delta)\, \mathrm{e} \ln D}{8n}\right]^{2n} \tag{7.117}$$

In summary, for δ : odd we obtain the following theoretical error estimates when using the log-L_2 radial variable transformation :

For δ : odd

$$| E_n(f) | \underset{\sim}{<} (-\ln D) D^{\frac{\delta+1-\alpha}{2}} \left[\frac{\max(3,\delta)\, \mathrm{e} \ln D}{8n}\right]^{2n} , \quad (n \gg 1,\ D \gg 1) . \tag{7.118}$$

For $\delta = 1$

$$| E_n(f) | \underset{\sim}{<} (-\ln D) D^{\frac{2-\alpha}{2}} \left[\frac{3\, \mathrm{e} \ln D}{8n}\right]^{2n} . \tag{7.119}$$

Roughly speaking,

$$\boxed{| E_n(f) | \underset{\sim}{<} D^{\frac{\delta+1-\alpha}{2}} \left(\frac{\ln D}{n}\right)^{2n} \sim n^{-2n}} \tag{7.120}$$

for δ : odd .

These estimates correspond well with numerical results in Chapter 10, and explain why the log-L_2 radial variable transformation gives efficient results for the integration of potential kernels u^* and q^* (which do not include any interpolation functions).

(2) Case : δ = even

When δ is a (positive) even number, as in the integration of $\partial u^*/\partial x_s$ and $\partial q^*/\partial x_s$ for the flux, where $\delta = 2$ (cf. Table 7.1), the function $f(z)$ of equation (7.84) has a branch point (singularity)

$$z_m = -1 + \mathrm{i} \frac{2\pi m}{\ln(r_j/d)} \quad , \ (m : \text{integer}) \tag{7.121}$$

as shown in Fig.7.4.

In this case, we can modify the condition of Theorem 7.1 to allow a singularity of $f(z)$ at the end point $z = -1$ of the interval $K = [-1, 1]$ of integration [45,47] . The path C of the contour integral is taken as

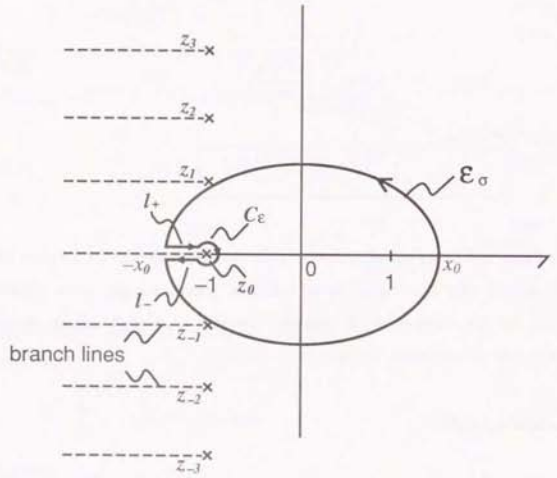

Fig. 7. 4 Branching singularities z_m of $f(z)$ and integration path for log-L_2 transformation, δ = even

$$C = \sigma + \ell_+ + C_\varepsilon + \ell_- \quad , \tag{7.122}$$

as shown in Fig.7.4. $\mathcal{E}\sigma$ is an ellipse

$$|\, z+\sqrt{z^2-1}\,| = \sigma \quad , \quad \sigma>1 \tag{7.20}$$

which has $z=\pm 1$ as its foci, and the branch points z_1, z_{-1} are outside the ellipse. ℓ_+ and ℓ_- are the real segment $(-x_0, -1-\varepsilon)$ in the positive and negative directions, respectively.

$$x_0 = \frac{1}{2}(\sigma + \frac{1}{\sigma}) \tag{7.123}$$

is the major axis of $\mathcal{E}\sigma$. $C\varepsilon$ is a circle of radius $0<\varepsilon\ll 1$, with its centre at $z=-1$.

In the following, we will estimate the error $E_n(f)$ according to Theorem 7.1, considering the contribution of each component of the path C.

(i) Contribution from the branch line ℓ_+, ℓ_-

In the equation

$$E_n(f) = \frac{1}{2\pi i} \oint_C \Phi_n(z)\, f(z)\, dz \tag{7.6}$$

of Theorem 7.1, the contribution from the branch lines ℓ_+ and ℓ_- is

$$E_{\ell_+\ell_-} = \frac{1}{2\pi i}\left\{ \int_{-x_0}^{-1-\varepsilon} f(z_+)\Phi_n(z_+)\, dz + \int_{-1-\varepsilon}^{-x_0} f(z_-)\Phi_n(z_-)\, dz \right\}$$

$$= \frac{1}{2\pi i} \int_{-x_0}^{-1-\varepsilon} \{\, f(z_+)\Phi_n(z_+) - f(z_-)\Phi_n(z_-)\,\}\, dz \tag{7.124}$$

where $z_+ \in \ell_+$ and $z_- \in \ell_-$.

Applying the asymptotic expression

$$\Phi_n(z_+) \sim 2e^{\pm i\pi} \frac{K_0(2k\zeta)}{I_0(2k\zeta)} \quad , \quad (n\gg 1) \tag{7.17}$$

where

$$z_\pm = e^{\pm i\pi}\cosh 2\zeta \quad \text{on} \quad \ell_\pm \quad . \tag{7.125}$$

and

$$k = n + \frac{1}{2} \gg 1 \quad , \tag{7.19}$$

we obtain

$$\Phi_n(z_+) = \Phi_n(z_-) = -2\,\frac{K_0(2k\zeta)}{I_0(2k\zeta)} \tag{7.126}$$

and equation (7.124) can be written as

$$E_{\ell+,\ell-} = \frac{1}{2\pi i}\int_{-x_0}^{-1-\varepsilon} \{ f(z_+) - f(z_-) \}\, \Phi_n(z_\pm)\, dz \quad . \tag{7.127}$$

Next, equations (7.92~94) can be rewritten as

$$f(z) = \tilde{b}\left[e^{(x+1)\ln a} - 1 \right]^{\frac{\delta-1}{2}} e^{\left(\frac{2-\alpha}{2}\ln a\right)x} \tag{7.128}$$

$$\tilde{b} = \frac{\ln a}{2}\, r_j^{\frac{2-\alpha}{2}}\, d^{\frac{2\delta-\alpha}{2}} > 0 \tag{7.129}$$

$$a = \frac{r_j}{d} > 1 \quad . \tag{7.130}$$

If we choose $x_0 > 1$ such that

$$x_0 - 1 \ll 1 \tag{7.131}$$

so that

$$0 < \zeta \ll 1 \quad \text{for} \quad -x_0 \leq x = e^{\pm i\pi}\cosh 2\zeta \leq -1-\varepsilon \quad . \tag{7.132}$$

we obtain

$$x = e^{\pm i\pi}\cosh 2\zeta \sim e^{\pm i\pi}(1+2\zeta^2) \tag{7.133}$$

$$dx \sim 4e^{\pm i\pi}\zeta\, d\zeta = -4\zeta\, d\zeta \quad . \tag{7.134}$$

Hence, in equation (7.128),

$$e^{(x+1)\ln a} - 1 = e^{e^{\pm i\pi} 2\zeta^2 \ln a} - 1$$

$$\sim e^{\pm i\pi}\, 2\zeta^2 \ln a \quad , \quad (0 < \zeta \ll 1) \, , \tag{7.135}$$

so that

$$\left[e^{(x+1)\ln a} - 1 \right]^{\frac{\delta-1}{2}} \sim e^{\pm i\frac{(\delta-1)\pi}{2}} (2\ln a)^{\frac{\delta-1}{2}}\, \zeta^{\delta-1} \tag{7.136}$$

and

$$e^{\left(\frac{2-\alpha}{2}\ln a\right)x} \sim e^{\frac{\alpha-2}{2}\ln a\,(1+2\zeta^2)}$$

$$\sim a^{\frac{\alpha-2}{2}}\, \{1 + O(\zeta^2)\} \quad . \tag{7.137}$$

Thus, equation (7.128) can be expressed as

$$f(z_\pm) \sim \tilde{A}\, e^{\pm i\frac{(\delta-1)\pi}{2}}\, \zeta^{\delta-1} \quad , \quad (0 < \zeta \ll 1) \quad , \tag{7.138}$$

$$\tilde{A} = 2^{\frac{\delta-3}{2}} (\ln a)^{\frac{\delta+1}{2}}\, d^{\frac{\delta+1-\alpha}{2}} \quad . \tag{7.139}$$

Hence, in equation (7.127),

$$f(z_+) - f(z_-) \sim \tilde{A}\left[e^{i\frac{(\delta-1)\pi}{2}} - e^{-i\frac{(\delta-1)\pi}{2}} \right] \zeta^{\delta-1} \quad , \quad (0 < \zeta \ll 1) \quad , \tag{7.140}$$

which gives

$$f(z_+) - f(z_-) \sim \tilde{B}\, \zeta^{\delta-1} \quad , \tag{7.141}$$

$$\tilde{B} = i\,(-1)^{\frac{\delta+2}{2}}\, 2^{\frac{\delta-1}{2}}\, (\ln a)^{\frac{\delta+1}{2}}\, d^{\frac{\delta+1-\alpha}{2}} \quad . \tag{7.142}$$

Now, equation (7.127) can be expressed as

$$E_{\ell+,\ell-} \sim \frac{1}{2\pi i}\int_{\zeta_0}^{\sqrt{\frac{\varepsilon}{2}}} \tilde{B}\, \zeta^{\delta-1}\left[-2\,\frac{K_0(2k\zeta)}{I_0(2k\zeta)} \right](-4\zeta)\, d\zeta$$

$$\sim \tilde{C}\int_{\sqrt{\frac{\varepsilon}{2}}}^{\zeta_0} \zeta^{\delta}\,\frac{K_0(2k\zeta)}{I_0(2k\zeta)}\, d\zeta \quad . \tag{7.143}$$

where

$$\tilde{C} = \frac{(-1)^{\frac{\delta}{2}}\, 2^{\frac{\delta+3}{2}}}{\pi}\, (\ln a)^{\frac{\delta+1}{2}}\, d^{\frac{\delta+1-\alpha}{2}} \quad , \tag{7.144}$$

$$\zeta_0 = \frac{1}{2}\cosh^{-1} x_0 \sim \sqrt{\frac{x_0 - 1}{2}}$$

and we have assumed

$$n \gg 1 \quad \text{i.e.} \quad k = n + \frac{1}{2} \gg 1 \quad , \tag{7.145}$$

$$0 < x_0 - 1 \ll 1 \quad \text{i.e.} \quad 0 < \zeta_0 \ll 1 \quad , \tag{7.146}$$

$$0 < \varepsilon \ll 1 \quad . \tag{7.147}$$

For $0 \leq \zeta \leq \sqrt{\frac{\varepsilon}{2}}$, if we take $\varepsilon > 0$ such that

$$2k\zeta \leq (2n+1)\sqrt{\frac{\varepsilon}{2}} \ll 1 \quad , \tag{7.148}$$

i.e.

$$\varepsilon \ll \frac{2}{(2n+1)^2} \quad , \tag{7.149}$$

equation (7.189) gives

$$\frac{K_0(2k\zeta)}{I_0(2k\zeta)} \sim -\log(k\zeta) - \gamma + O(k\zeta)^2 \quad . \tag{7.150}$$

Hence, if we take the limit as $\varepsilon \to 0$,

$$\int_0^{\sqrt{\frac{\varepsilon}{2}}} \zeta^\delta \frac{K_0(2k\zeta)}{I_0(2k\zeta)}\, d\zeta \sim O\left(\varepsilon^{\frac{\delta+1}{2}} \log \varepsilon\right) \to 0 \quad , \tag{7.151}$$

so that equation (7.143) gives

$$E_{\ell+,\ell-} \sim \tilde{C} \int_0^{\zeta_0} \zeta^\delta \frac{K_0(2k\zeta)}{I_0(2k\zeta)}\, d\zeta \quad . \tag{7.152}$$

If we further choose x_0 so that it satisfies

$$2k\zeta_0 = (2n+1)\zeta_0 \sim (2n+1)\sqrt{\frac{x_0-1}{2}} \gg 1 \quad , \tag{7.153}$$

we obtain

$$\frac{K_0(2k\zeta)}{I_0(2k\zeta)} \sim \pi e^{-4k\zeta} \quad \text{for} \quad \zeta \geq \zeta_0 \tag{7.154}$$

(cf. ref [49]) so that

$$0 < \int_{\zeta_0}^{\infty} \zeta^\delta \frac{K_0(2k\zeta)}{I_0(2k\zeta)}\, d\zeta \sim \int_{\zeta_0}^{\infty} \zeta^\delta \pi e^{-4k\zeta} d\zeta \quad . \tag{7.155}$$

Since

$$0 < \int_{\zeta_0}^{\infty} \zeta^\delta \pi e^{-4k\zeta}\, d\zeta < \int_0^{\infty} \zeta^\delta \pi e^{-4k\zeta} d\zeta = \frac{\pi\,\delta!}{(4k)^{\delta+1}} \quad , \tag{7.156}$$

we have

$$0 < \int_{\zeta_0}^{\infty} \zeta^\delta \frac{K_0(2k\zeta)}{I_0(2k\zeta)}\, d\zeta < O(k^{-\delta-1}) \quad . \tag{7.157}$$

Note also that if we let $t = 2k\zeta$,

$$\int_0^{\infty} \zeta^\delta \frac{K_0(2k\zeta)}{I_0(2k\zeta)}\, d\zeta = \frac{1}{(2k)^{\delta+1}} \int_0^{\infty} t^\delta \frac{K_0(t)}{I_0(t)}\, dt \sim O(k^{-\delta-1}) \quad , \tag{7.158}$$

since

$$\int_0^{\infty} t^\delta \frac{K_0(t)}{I_0(t)}\, dt$$

is a constant which is independent of k.

From equations (7.157) and (7.158), we have

$$\int_0^{\zeta_0} \zeta^\delta \frac{K_0(2k\zeta)}{I_0(2k\zeta)}\, d\zeta = \int_0^{\infty} \zeta^\delta \frac{K_0(2k\zeta)}{I_0(2k\zeta)}\, d\zeta - \int_{\zeta_0}^{\infty} \zeta^\delta \frac{K_0(2k\zeta)}{I_0(2k\zeta)}\, d\zeta$$

$$\sim O(k^{-\delta-1})$$

$$\sim O(n^{-\delta-1}) \quad . \tag{7.159}$$

Hence, equation (7.152) gives

$$E_{\ell+,\ell-} \sim O\left\{(\ln a)^{\frac{\delta+1}{2}}\, d^{\delta+1-\alpha}\, n^{-\delta-1}\right\}$$

$$\tilde{}_{D<1}\, O\left\{(-\ln D)^{\frac{\delta+1}{2}}\, D^{\delta+1-\alpha}\, n^{-\delta-1}\right\} \tag{7.160}$$

(ii) Contribution from the ellipse $\mathcal{E}_\sigma$

For the contribution $E_{\mathcal{E}_\sigma}$ to the error $E_n(f)$, from the ellipse $\mathcal{E}_\sigma$ of equation (7.20), we have

$$|E_{\mathcal{E}_\sigma}| < 2\pi\sigma^{-2n} \max_{z\in\mathcal{E}_\sigma} |f(z)| \quad , \tag{7.161}$$

from equation (7.24).

① Estimation of the size σ of the ellipse

According to equation (7.92), $|f(z)|$ is boumded as long as z is finite and $\delta \geqq 1$. Hence, the ellipse $\mathcal{E}_\sigma$ can be taken as close as possible to the branch points :

$$z_{\pm 1} = -1 \pm i\frac{2\pi}{\ln a} \quad , \tag{7.162}$$

so long as the points $z_{\pm 1}$ are just outside the ellipse $\mathcal{E}_\sigma$. Thus, we will estimate the size σ of the ellipse which has its foci at $z=\pm 1$ and passes through

$$z_t = -1 + i\frac{2\pi t}{\ln a} \quad , \qquad (0<t<1) \tag{7.163}$$

From equations (7.29, 30), we obtain

$$\sigma = q + \sqrt{1+q^2} + \sqrt{2q(q+\sqrt{1+q^2})} \tag{7.164}$$

where

$$q = \frac{\pi t}{\ln a} = \frac{\pi t}{\ln(\frac{r_j}{d})} = \frac{2\pi t}{\ln(1+D^{-2})} \tag{7.165}$$

and $D \equiv d/\rho_j$ is the relative souce distance.

Equations (7.164, 165) give

$$\frac{d\sigma}{dq} = 1 + \frac{q}{\sqrt{1+q^2}} + \frac{1+q+q^2+(1+q)\sqrt{1+q^2}}{\sqrt{1+q^2}\sqrt{2q(q+\sqrt{1+q^2})}} > 0 \tag{7.166}$$

and

$$\frac{dq}{dD} = \frac{4\pi t}{D(D^2+1)\{\ln(1+D^{-2})\}^2} \quad . \tag{7.167}$$

Hence, $\sigma(D)$ is a strictly increasing function of $D>0$, where

$$\sigma(D \ll 1) \sim 1 + \sqrt{\frac{2\pi t}{-\ln D}} \quad , \tag{7.168}$$

$$\sigma(D \gg 1) \sim 8\pi t D^2 \quad , \tag{7.169}$$

and

$$\frac{d\sigma}{dD}(D \ll 1) \sim \frac{\sqrt{2\pi t}}{D(-\ln D)^{3/2}} \xrightarrow[D\to+0]{} +\infty \quad . \tag{7.170}$$

Note also that $\sigma(D,t)$ is also a strictly increasing function of $0<t<1$, so that

$$\sigma(D,t) < \sigma(D,1) \quad . \tag{7.171}$$

The table and graph of $\sigma(D,t)$ for $t=1.0$ are given in Table 7.3 and Fig. 7.5, respectively.

Table 7.3 Values of $\sigma(D)$ for $t=1.0$, for the log-L_2 transformation (δ : even)

D	σ
10^{-4}	2.37
10^{-3}	2.74
3×10^{-3}	3.02
10^{-2}	3.50
3×10^{-2}	4.24
10^{-1}	5.93
3×10^{-1}	10.4
1	36.3

Since $\forall\varepsilon>0$, $^3\delta>0$;

$$|\sigma(D,t=1)-\sigma(D,t=1-\delta)| < \varepsilon \quad , \tag{7.172}$$

we may conclude that, for the nearly singular case, σ in equation (7.161) takes the value

$$\sigma : 2.74 \sim 5.93 \quad \text{for} \quad D : 10^{-3} \sim 10^{-1} \quad . \tag{7.173}$$

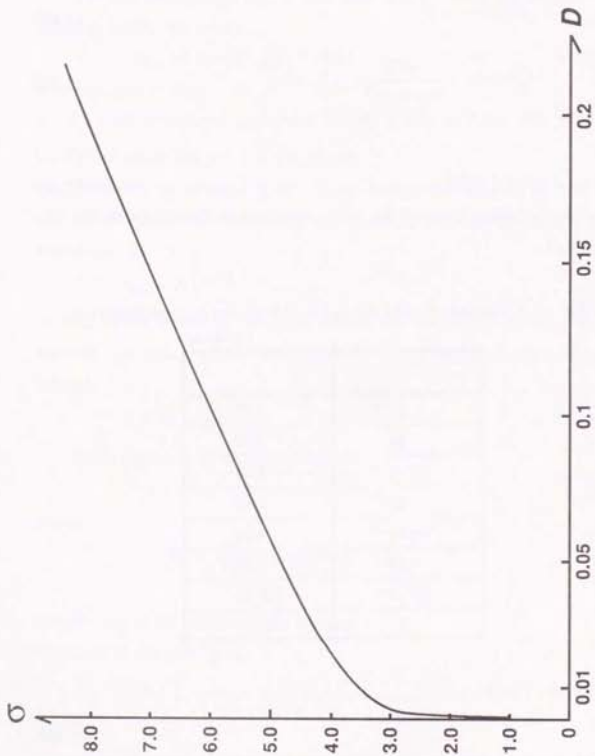

Fig. 7.5 Graph of $\sigma(D, t = 1.0)$ vs D for the log-L_2 transformation (δ : even)

② Estimation of $\max_{z \in \mathcal{E}_\sigma} |f(z)|$

We will estimate $\max_{z \in \mathcal{E}_\sigma} |f(z)|$ using

$$f(z) = \tilde{b}\left\{e^{(z+1)\ln a} - 1\right\}^{\frac{\delta-1}{2}} e^{\left(\frac{2-\sigma}{2}\ln a\right) z} \quad , \tag{7.128}$$

$$\tilde{b} = \frac{\ln a}{2} r_j^{\frac{2-\sigma}{2}} d^{\frac{2\delta-\sigma}{2}} \underset{D<1}{\sim} \frac{1}{2}\rho_j^{\delta+1-\sigma}(-\ln D) D^{\delta-\frac{\sigma}{2}} > 0 \tag{7.174}$$

and

$$|x| \leq x_0 = \frac{1}{2}\left(\sigma + \frac{1}{\sigma}\right) \tag{7.175}$$

$$|y| \leq y_0 = \frac{1}{2}\left(\sigma - \frac{1}{\sigma}\right) \tag{7.176}$$

where $z = x + iy$, and x_0 and y_0 are the major and minor axes of the ellipse $\mathcal{E}_\sigma$, respectively.

Since, if c is real,

$$|e^{cz}| = e^{|c|x} \leq e^{|c| x_0} \quad , \tag{7.177}$$

we have

$$|e^{\left(\frac{2-\sigma}{2}\ln a\right) z}| \leq e^{\left(\frac{|2-\sigma|}{2}\ln a\right) x_0} = a^{\frac{|2-\sigma|}{2} x_0} \quad . \tag{7.178}$$

Similarly, we obtain

$$\begin{aligned} |e^{(z+1)\ln a} - 1| &\leq 2 e^{(x_0+1)\ln a} + 1 \\ &= 2 a^{x_0+1} + 1 \\ &\leq 3 a^{x_0+1} \end{aligned} \quad , \tag{7.179}$$

since $a > 1$.

Hence, for $\delta \geqq 1$, we have

$$\begin{aligned} \max_{z \in \mathcal{E}_\sigma} |f(z)| &\leq \tilde{b}\, 3^{\frac{\delta-1}{2}} a^{(x_0+1)\frac{\delta-1}{2} + \frac{|2-\sigma|}{2} x_0} \\ &\underset{D<1}{\sim} \frac{3^{\frac{\delta-1}{2}}}{2}\rho_j^{\delta+1-\sigma}(-\ln D) D^{ind(\sigma,\delta)} \end{aligned} \quad , \tag{7.180}$$

where

$$ind(\alpha,\delta) = \frac{\delta+1-\sigma-(\delta-1+|2-\alpha|)x_0}{2} \quad . \tag{7.181}$$

Summing up for the contribution from the ellipse $\mathcal{E}_\sigma$, equations (7.161) and (7.180) give

$$|E_{\mathcal{E}_\sigma}| < \pi 3^{\frac{\delta-1}{2}} \rho_j^{\delta+1-\sigma}(-\ln D)\, D^{ind(\alpha,\delta)}\, \sigma^{-2n} \quad , \tag{7.182}$$

where

$$\sigma : 2.74 \sim 5.93 \quad for \quad D : 10^{-3} \sim 10^{-1} \quad . \tag{7.173}$$

Comparing equation (7.182) with (7.160), we have

$$|E_{\mathcal{E}_\sigma}| \ll |E_{\ell_+,\ell_-}| \tag{7.183}$$

for $n \gg 1$.

(iii) Contribution from the small circle C_ε

Finally, we will estimate the contribution E_{C_ε} from the small circle C_ε.

From equations (7.92~94), it can be proved that for $z=-1+\Delta z$ such that $|\Delta z| \ll 1$,

$$f(z) \sim \tilde{A}\, \Delta z^{\frac{\delta-1}{2}} + O(\Delta z^{\frac{\delta+1}{2}}) \quad , \tag{7.184}$$

where

$$\tilde{A} = \frac{1}{2}(\ln\alpha)^{\frac{\delta+1}{2}} d^{\frac{\delta-\alpha+1}{2}} \quad . \tag{7.185}$$

As the asymptotic expression for $\Phi_n(z)$, we adopt

$$\Phi_n(z) \sim 2e^{-ix} \frac{K_0(2k\zeta)}{I_0(2k\zeta)} \quad , \qquad (n \gg 1) \tag{7.17}$$

where

$$z = -1+\Delta z = e^{i\pi}\cosh 2\zeta \quad , \qquad k = n+\frac{1}{2} \quad . \tag{7.186}$$

Noting that[49]

$$K_0(Z) \sim -I_0(Z)\left(\gamma + \log\frac{Z}{2}\right) + \frac{Z^2}{4} + O(Z^4) \quad , \quad (|Z| \ll 1) \quad , \tag{7.187}$$

$$I_0(Z) \sim 1 + \frac{Z^2}{4} + O(Z^4) \quad , \quad (|Z| \ll 1) \quad , \tag{7.188}$$

where $\gamma = 0.577$ is the Euler's constant, we obtain

$$\frac{K_0(Z)}{I_0(Z)} \sim -\log\frac{Z}{2} - \gamma + O(Z^2) \quad , \qquad (|Z| \ll 1) \quad . \tag{7.189}$$

Thus, if we take $0<\varepsilon \ll 1$ such that $|2k\zeta| \ll 1$ for $z \in C_\varepsilon$, we obtain

$$\Phi_n(z) \sim 2\log k\zeta + 2\gamma + O(k\zeta)^2 \quad . \tag{7.190}$$

Since $|\zeta| \ll 1$, we have

$$\Delta z = z+1 = 1-\cosh 2\zeta \sim -2\zeta^2 \quad , \tag{7.191}$$

$$|\Delta z| \ll 1 \quad , \tag{7.192}$$

and

$$dz = -4\zeta d\zeta \quad . \tag{7.193}$$

Hence, for $n \gg 1$ and $|2k\zeta| \ll 1$, we obtain

$$E_{C_\varepsilon} = \frac{1}{2\pi i}\int_{C_\varepsilon} \Phi_n(z) f(z)\, dz$$

$$\sim O\left\{\varepsilon^{\frac{\delta+1}{2}} \log(k\varepsilon)\right\} \xrightarrow[\varepsilon\to 0]{} 0 \quad . \tag{7.194}$$

Hence, the contribution from C_ε, $(\varepsilon \to 0)$ is zero.

(iv) Summary

In summary, the contribution E_{ℓ_+,ℓ_-} from the branch line ℓ_+,ℓ_- is dominant in $E_n(f)$. Hence, from equation (7.160), the theoretical error estimate for the radial numerical integration using the log-L_2 transformation with the Gauss-Legendre rule for the case : δ=even, is given by

$$E_n(f) \sim E_{\ell_+,\ell_-}$$

$$\underset{n\ll 1}{\sim} O\left[\{\ln(r_j/d)\}^{\frac{\delta+1}{2}} d^{\delta+1-\sigma} n^{-\delta-1}\right]$$

$$\underset{D\ll 1}{\sim} O\left[(-\ln D)^{\frac{\delta+1}{2}} D^{\delta+1-\sigma} n^{-\delta-1}\right]$$

$$\sim O(n^{-\delta-1}) \quad , \tag{7.195}$$

where n is the number of integration points in the radial variable.

This theoretical estimate corresponds well with numerical results in Chapter 10, and explains why the log-L_2 radial variable transformation is inefficient and gives inaccurate results for the integration of flux kernels $\partial u^*/\partial x_s$ and $\partial q^*/\partial x_s$, which include terms corresponding to $\delta=2$.

Equation (7.195) also explains why the log-L_2 transformation tends to be inefficient for the integration of kernels including interpolation functions such as ϕ_{ij} of equation (9.17). Since $\phi_{ij}(\eta_1, \eta_2)$ are polynomials of η_1 and η_2, which in turn include first order terms of ρ as in equation (5.40), ϕ_{ij} include terms of order $\rho, \rho^2, \rho^3, \rho^4$, which correspond to $\delta=2, 3, 4, 5$ in the radial integral of equation (7.48). According to equation (7.190), this means that the numerical integration error drops only at the rate of $O(n^{-3})$ and $O(n^{-5})$ for the components corresponding to $\delta=2$ and 4, respectively. This matches with numerical experiment results for $\int_s \phi_{ij} u^* dS$ and $\int_s \phi_{ij} q^* dS$ in Chapter 10.

7.8 Error Analysis for the log-L_1 Transformation

In this section, theoretical error estimates will be derived for the numerical integration in the radial variable using the Gauss-Legendre rule after applying the log-L_1 transformation :

$$R(\rho)=\log(\rho+d) \tag{5.85}$$

The analysis will clarify quantitatively, the reason why the log-L_1 transformation is a robust transformation which works efficiently for the integration of flux kernels as well as potential kernels and kernels including interpolation functions.

Equation (5.85) gives

$$R(0)=\ln d \ , \tag{7.196}$$

$$R(\rho_j)=\ln(\rho_j+d) \tag{7.197}$$

and

$$\rho(R)=e^R-d \ , \tag{7.198}$$

$$\frac{d\rho}{dR}=e^R \ . \tag{7.199}$$

Hence, the radial component integral of equation (7.48) can be expressed as

$$I=\int_0^{\rho_j}\frac{\rho^\delta}{r^\alpha}\,d\rho$$

$$=\int_{R(0)}^{R(\rho_j)}\frac{(e^R-d)^\delta e^R}{\sqrt{(e^R-d)^2+d^2}^{\,\alpha}}\,dR \ . \tag{7.200}$$

Then, equations (7.52, 53, 54) give

$$x=\frac{2R-\ln(1+\frac{\rho_j}{d})-2\ln d}{\ln(1+\frac{\rho_j}{d})} \ , \tag{7.201}$$

$$R=\frac{x\ln(1+\frac{\rho_j}{d})+\ln(1+\frac{\rho_j}{d})+2\ln d}{2} \ . \tag{7.202}$$

and

$$\frac{dR}{dx} = \frac{\ln\left(1+\frac{\rho_j}{d}\right)}{2} \tag{7.203}$$

Hence, the integral of equation (7.200) can be expressed as

$$I = \int_{-1}^{1} f(x)\,dx \tag{7.204}$$

where

$$f(z) = \frac{b'(w-1)^{\beta} w}{\{w-(1-i)\}^{\alpha/2}\{w-(1+i)\}^{\alpha/2}} \quad , \tag{7.205}$$

$$w = e^{\frac{z+1}{2}\ln a'} \quad , \tag{7.206}$$

$$b' = \frac{\ln a'}{2} d^{\beta-\alpha+1} > 0 \quad , \tag{7.207}$$

$$a' = 1 + \frac{\rho_j}{d} > 1 \quad . \tag{7.208}$$

$f(z)$ has singularities at

$$w = e^{\frac{z+1}{2}\ln a'} = 1 \pm i \quad , \tag{7.209}$$

which are equivalent to

$$z = z_m^{\pm} = -1 + \frac{\ln 2}{\ln a'} + i\frac{(4m \pm 1/2)\pi}{\ln a'} \quad , \quad (m: \text{integer}) \ . \tag{7.210}$$

The singularities $z = z_m^{\pm}$, $(m = 0, \pm 1, \pm 2, \cdots)$ are also branch points when α is odd, as shown in Fig.7.6

Using the relative source distance :

$$D = \frac{d}{\rho_j} \quad , \tag{7.211}$$

we have

$$a' = 1 + D^{-1} \underset{D \ll 1}{\sim} D^{-1}$$

so that

$$\ln a' = \ln(1+D^{-1}) \underset{D \ll 1}{\sim} -\ln D \quad , \tag{7.212}$$

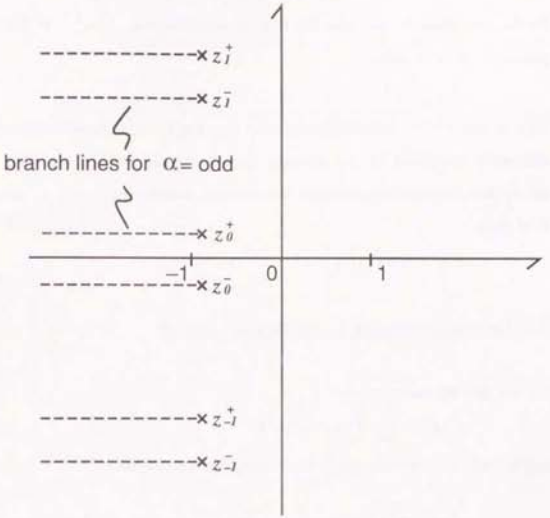

Fig. 7.6 Singularities $z_m^{\pm}$ and branch lines (for α = odd) of $f(z)$ for the log-L_1 transformation

which gives

$$z_0^{\pm}+1 \sim \frac{\ln 2 \pm i\frac{\pi}{2}}{-\ln D} \quad . \tag{7.213}$$

Hence, the distance between the nearest singularities $z=z_0^{\pm}$ to the end point $z=-1$ is of order

$$O\left(\frac{1}{-\ln D}\right) \quad .$$

This is the key to understanding why the log-L_1 transformation works far efficiently compared to the identity transformation, where equation (7.61) shows that the distance between the nearest singularities $z=z_1, \bar{z}_1$ to $z=-1$ is of order

$$O(D) \ll O\left(\frac{1}{-\ln D}\right) \quad .$$

(1) Error analysis using the saddle point method

In the equation

$$E_n(f) = \frac{1}{2\pi i}\oint_C \Phi_n(z)\, f(z)\, dz \tag{7.6}$$

of Theorem 7.1, we can apply the asymptotic expression

$$\Phi_n(z) \sim \frac{c_n}{z^{2n+1}} \tag{7.214}$$

of equation (7.11) for $z \in \mathbb{C}$; $|z| \gg 1$.

If we define

$$F(z) \equiv \Phi_n(z)\, f(z)$$

$$\sim \frac{A'}{z^{2n+1}} \frac{(w-1)^{\delta} w}{\{w-(1-i)\}^{\alpha/2}\{w-(1+i)\}^{\alpha/2}} \quad , \quad (|z| \gg 1) \tag{7.215}$$

from equations (7.205) and (7.214), where

$$w \equiv e^{\frac{z+1}{2}\ln a'} \quad , \tag{7.206}$$

$$A' \equiv c_n b' = \frac{\ln a'}{2} d^{\delta+1-\alpha} c_n \quad , \tag{7.216}$$

we obtain

$$g(z) \equiv \log F(z)$$

$$\sim \ln A' - (2n+1)\log z + \delta \log(w-1) + \log w$$

$$-\frac{\alpha}{2}\log(w-1+i) - \frac{\alpha}{2}\log(w-1-i) \quad , \quad (|z| \gg 1) \tag{7.217}$$

and

$$\frac{dg}{dz} \sim -\frac{2n+1}{z} + \frac{\ln a'}{2}\left[\delta+1-\alpha+\frac{\delta}{w-1}-\frac{\alpha}{2}\left(\frac{1-i}{w-1+i}+\frac{1+i}{w-1-i}\right)\right] \tag{7.218}$$

$$, \quad (|z| \gg 1) \quad .$$

(i) Case $\mathrm{Re}(z) \gg 1$

In this case,

$$|w| = e^{\frac{\ln a'}{2}(\mathrm{Re}(z)+1)} \gg 1 \tag{7.219}$$

where

$$a' \equiv 1 + \frac{\rho_j}{d} > 1 \quad . \tag{7.208}$$

If $|\mathrm{Im}(z)| \sim 1$, we have

$$|z| \sim \mathrm{Re}(z) \gg 1 \quad , \tag{7.220}$$

which gives

$$|w| \gg |z| \gg 1 \quad , \tag{7.221}$$

or

$$\frac{1}{|w|} \ll \frac{1}{|z|} \ll 1 \quad . \tag{7.222}$$

Hence, equation (7.218) gives

$$g'(z) \equiv \frac{dg}{dz} \sim -\frac{2n+1}{z} + \frac{\ln a'}{2}(\delta+1-\alpha) \quad , \quad (\mathrm{Re}(z) \gg 1) \quad . \tag{7.223}$$

Thus, the saddle point of $F(z)$ of equation (7.215), which is given by

$$\left.\frac{dg}{dz}\right|_{z=s} = 0 \tag{7.224}$$

is

$$s \sim \frac{2(2n+1)}{(\delta+1-\alpha)\ln a'} \quad . \tag{7.225}$$

The condition $\mathrm{Re}(s) \gg 1$ implies

$$\delta+1-\alpha>0, \quad n \gg 1 \quad , \tag{7.226}$$

since $\ln a' > 0$. From Table 7.1, for the basic integral kernels in three dimensional potential problems, α, δ and $\delta+1-\alpha$ take the values shown in Table 7.4.

Table 7.4 Values for 3-D potential problem

kernels	α	δ	$\delta+1-\alpha$
u^*	1	1	1
q^*	3	1	-1
$\dfrac{\partial u^*}{\partial x_s}$	3	1	
		2	0
$\dfrac{\partial q^*}{\partial x_s}$	3	1	-1
	5	1	-3
		2	-2

Hence, only the case $\alpha=\delta=1$ for the u^* kernel gives a saddle point of equation (7.225) satisfying $\mathrm{Re}(s) \gg 1$ for $n \gg 1$.

Equation (7.223) gives

$$g''(z) \sim \frac{2n+1}{z^2} \quad , \quad (\mathrm{Re}(z) \gg 1) \quad , \tag{7.227}$$

so that at the saddle point $z=s$,

$$g''(s) \sim \frac{2n+1}{s^2} = \frac{\{(\delta+1-\alpha)\ln a'\}^2}{4(2n+1)} \quad . \tag{7.228}$$

Equations (7.38) and (7.45) give

$$\alpha = \arg g''(s) = 0 \quad , \tag{7.229}$$

$$dz = e^{i(+\frac{\pi}{2})} dr = i\,dr \quad . \tag{7.230}$$

Applying the saddle point method along the contour C shown in Fig.7.7,

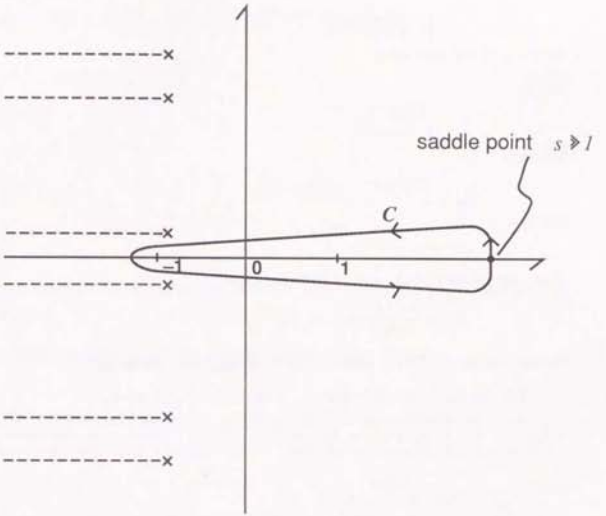

Fig. 7.7 Integration path C for the saddle point method for the log-L_1 transformation

$$E_n(f) = \frac{1}{2\pi i} \oint_C F(z)\,dz$$

$$\sim \frac{1}{2\pi i}\, e^{\frac{\pi}{2}i} \sqrt{\frac{2\pi}{|\, g''(s)\,|}}\, F(s)$$

$$\sim \sqrt{\frac{s^2}{2\pi(2n+1)}}\; A'\; s^{-2n-1} w^{\delta+1-\alpha}$$

$$= \frac{A'}{\sqrt{2\pi(2n+1)}}\, s^{-2n} w^{\delta+1-\alpha} \qquad (7.231)$$

for $\delta-\alpha+1>0$ and $n \gg 1$.

Since,

$$s \sim \frac{2(2n+1)}{(\delta+1-\alpha)\ln a'} \quad , \qquad (7.225)$$

we have

$$w(s) = e^{\frac{s+1}{2}\ln a'} = e^{\frac{2n+1}{\delta+1-\alpha} + \frac{\ln a'}{2}} \quad , \qquad (7.232)$$

$$w^{\delta+1-\alpha} = e^{2n+1}\, a'^{\frac{\delta+1-\alpha}{2}} \quad . \qquad (7.233)$$

From equations (7.216) and (7.15), we have

$$A' = \frac{\pi(\ln a')\, d^{\delta+1-\alpha}}{2^{2n+1}} \quad . \qquad (7.234)$$

Hence, equation (7.231) renders the following error estimate :

For the log-L_1 transformation, with $\delta-\alpha+1>0$, $n \gg 1$,

$$E_n(f) \sim \frac{e}{4}\sqrt{\frac{\pi}{n+1/2}}\, \{\ln(1+\rho_j/d)\}\, (d\sqrt{1+\rho_j/d})^{\delta+1-\alpha} \left[\frac{(\delta+1-\alpha)e\,\ln(1+\rho_j/d)}{4(2n+1)}\right]^{2n}$$

$$\underset{D\gg 1}{\sim} (-\ln D)\, D^{\frac{\delta+1-\alpha}{2}} \left(\frac{\ln D}{n}\right)^{2n}$$

$$\sim O(n^{-2n}) \quad , \qquad (7.235)$$

where $D \equiv d/\rho_j$ is the relative source distance.

This estimate corresponds well with numerical results for the integration of u^*, $(\alpha=\delta=1)$ in Chapter 10.

(ii) Case $\mathrm{Re}(z) \ll -1$

In this case,

$$|\, w\,| = e^{\frac{\ln a'}{2}(\mathrm{Re}(z)+1)} \ll 1 \quad , \qquad (7.236)$$

which implies

$$\frac{dg}{dz} \sim \frac{2n+1}{z} + \frac{\ln a'}{2}\left[\delta-\alpha+1-\delta-\frac{\alpha}{2}\left(\frac{1-i}{-1+i}+\frac{1+i}{-1-i}\right)\right]$$

$$= -\frac{2n+1}{z} + \frac{\ln a'}{2} \quad . \qquad (7.237)$$

Hence,

$$\left.\frac{dg}{dz}\right|_{z=s} = 0 \qquad (7.224)$$

implies

$$s \sim \frac{2(2n+1)}{\ln a'} > 0 \quad , \qquad (7.238)$$

which contradicts with $\mathrm{Re}(s) \ll -1$.

Hence, there are no saddle points of $F(z) \equiv \Phi_n(z)\, f(z)$ in the region $\mathrm{Re}(z) \ll -1$.

(2) Error analysis using the elliptic contour : $\mathcal{E}_\sigma$

In order to obtain error estimates for general natural numbers α, δ, using equation (7.6) of Theorem 7.1, we turn to the asymptotic expression

$$\Phi_n(z) \sim 2\pi\,(z+\sqrt{z^2-1}\,)^{-2n-1} \quad , \qquad (7.16)$$

which is valid for $n \gg 1$ and $z \in \mathbf{C}$ except for an arbitrary neighbourhood of $K=[-1,1]$. The integration path C is taken as the ellipse $\mathcal{E}_\sigma$:

$$|\, z+\sqrt{z^2-1}\,| = \sigma \quad , \quad (\sigma>1) \quad , \qquad (7.20)$$

which does not contain any singularities of $f(z)$ of equation (7.205), inside. More specifically, we will choose the ellipse $\mathcal{E}_\sigma$ which passes through the point

$$z_t \equiv -1 + \frac{\ln 2}{\ln a'} + i\frac{\pi t}{2\ln a'} \quad , \quad (0<t<1) \quad , \qquad (7.239)$$

which is located just below the singular point :

$$z_0^+ = -1 + \frac{\ln 2}{\ln a'} + i\frac{\pi}{2\ln a'} \quad , \tag{7.240}$$

as shown in Fig.7.8. Then, we can use the equation

$$|E_n(f)| \leq 2\pi\sigma^{-2n} \max_{z\in\mathcal{E}_\sigma} |f(z)| \tag{7.24}$$

to estimate the error of numerical integration.

(i) Estimation of $\max_{z\in\mathcal{E}_\sigma} |f(z)|$

Since

$$\overline{w} = e^{\frac{\bar{z}+1}{2}\ln a'} \quad , \tag{7.241}$$

equation (7.205) gives

$$f(\bar{z}) = \overline{f(z)} \quad , \tag{7.242}$$

which implies

$$|f(\bar{z})| = |f(z)| \quad . \tag{7.243}$$

Hence, we need only consider the region $\mathrm{Im}(z)\geqq 0$.

It is also clear from equation (7.205) that $|f(z_0^+)| = +\infty$, where z_0^+ is the singular point given by equation (7.210). Thus, we obtain

$$\max_{z\in\mathcal{E}_\sigma} |f(z)| \sim |f(z_t)| \quad \text{for} \quad |1-t| \ll 1 \quad . \tag{7.244}$$

If we define

$$\Delta z = z_t - z_0^+ = -\frac{(1-t)\pi}{2\ln a'}\,i \quad , \tag{7.245}$$

we have

$$z_t + 1 = z_0^+ + 1 + \Delta z = \frac{\ln 2 + \frac{\pi}{2}i}{2\ln a'} + \Delta z \tag{7.246}$$

so that

$$w(z_t) = e^{\frac{z_t+1}{2}\ln a'} = (1+i)\,e^{\frac{\ln a'}{2}\Delta z} \quad . \tag{7.247}$$

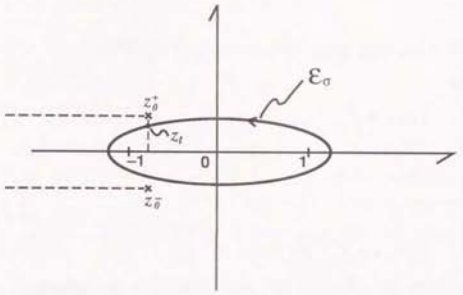

Fig. 7.8 Singularities of $f(z)$ and integration path $\mathcal{E}_\sigma$ for the $\log$-L_1 transformation

Hence, for

$$|\Delta z| \ll \frac{2}{\ln a'} \quad , \tag{7.248}$$

we have

$$w(z_t) = (1+i)\left\{1+\frac{\ln a'}{2}\Delta z + O\left(\frac{\ln a'}{2}\Delta z\right)^2\right\} \quad , \tag{7.249}$$

so that equation (7.205) gives

$$f(z_t) = B'\left[\Delta z^{-\frac{\alpha}{2}} + \frac{\ln a'}{2}\{1+(1-i)\delta\}\,\Delta z^{1-\frac{\alpha}{2}}\right] \tag{7.250}$$

where

$$B' = (i+1)\,i^{\delta}\,2^{-1-\frac{\alpha}{4}}\,d^{\delta+1-\alpha}\,(\ln a')^{1-\frac{\alpha}{2}}\,e^{-\frac{3}{8}\alpha\pi i} \quad . \tag{7.251}$$

Thus, for

$$|\Delta z| \ll \frac{2}{\ln a'} \quad ,$$

$$|f(z_t)| \sim |B'|\,|\Delta z|^{-\frac{\alpha}{2}} \tag{7.252}$$

where

$$|B'| = 2^{-\frac{1}{2}-\frac{\alpha}{4}}\,d^{\delta+1-\alpha}\,(\ln a')^{1-\frac{\alpha}{2}} \quad . \tag{7.253}$$

Finally, equation (7.244), (7.248) and (7.252) give the following :

For $1-t \ll 1$, $\quad 0<t<1$,

$$\max_{z\in\mathcal{E}_\sigma}|f(z)| \sim |f(z_t)| \sim 2^{\frac{\alpha-2}{4}}\,\pi^{-\frac{\alpha}{2}}\left[\ln\left(1+\frac{\rho_j}{d}\right)\right] d^{\delta+1-\alpha}\,(1-t)^{-\frac{\alpha}{2}} \quad . \tag{7.254}$$

For $0<D \ll 1$, equation (7.254) gives

$$\max_{z\in\mathcal{E}_\sigma}|f(z)| \sim |f(z_t)| \sim 2^{\frac{\alpha-2}{4}}\,\pi^{-\frac{\alpha}{2}}\,\rho_j^{\delta+1-\alpha}\,(-\ln D)\,D^{\delta+1-\alpha}\,(1-t)^{-\frac{\alpha}{2}} \quad . \tag{7.255}$$

(ii) Estimation of σ

Next, we estimate the size σ of the ellipse $\mathcal{E}_\sigma$ of equation (7.20) which passes through the point $z=z_t$ of equation (7.239). Since,

$$z_t = x + iy \tag{7.256}$$

where

$$x = \frac{\ln 2}{\ln a'} - 1 \quad , \qquad y = \frac{\pi t}{2\ln a'} \quad , \tag{7.257}$$

equations (7.31) and (7.32) give

$$\sigma = \frac{c}{2}p + \sqrt{\frac{c^2}{4}p^2 - p\ln 2 + 1} + \sqrt{\frac{c^2}{2}p^2 - p\ln 2 + cp\sqrt{\frac{c^2}{4}p^2 - p\ln 2 + 1}} \quad , \tag{7.258}$$

where

$$p \equiv \frac{1}{\ln(1+D^{-1})} \quad , \qquad D \equiv \frac{d}{\rho_j} > 0 \tag{7.259}$$

and

$$c \equiv \sqrt{(\ln 2)^2 + \left(\frac{\pi t}{2}\right)^2} \quad , \qquad 0<t<1 \quad . \tag{7.260}$$

It can be shown that $\sigma(D)$ is a strictly increasing function of $D>0$, i.e.

$$\frac{d\sigma}{dD} > 0 \quad \text{for} \quad D>0 \quad . \tag{7.261}$$

For $D \ll 1$,

$$\sigma(D) \sim 1 + \sqrt{c-\ln 2}\,\sqrt{\frac{1}{-\ln D}} \xrightarrow[D\to+0]{} 1 \tag{7.262}$$

and

$$\frac{d\sigma}{dD} \sim O\left\{\frac{1}{D(-\ln D)^{23}}\right\} \xrightarrow[D\to+0]{} +\infty \quad . \tag{7.263}$$

For $D \gg 1$,

$$\sigma(D) \sim 2cD \quad . \tag{7.264}$$

The graph of $\sigma(D, t)$ vs D for the case $t=0.6$ is shown in Fig.7.9.

(iii) Error estimate $E_n(f)$

From equations (7.24) and (7.254), we obtain

$$|E_n(f)| \lesssim 2^{\frac{\alpha+2}{4}}\,\pi^{1-\frac{\alpha}{2}}\left[\ln\left(1+\frac{\rho_j}{d}\right)\right] d^{\delta+1-\alpha}\,(1-t)^{-\frac{\alpha}{2}}\,\sigma^{-2n}$$

$$\underset{D\ll 1}{\sim} 2^{\frac{\alpha+2}{4}}\,\pi^{1-\frac{\alpha}{2}}\,\rho_j^{\delta+1-\alpha}\,(-\ln D)\,D^{\delta+1-\alpha}\,(1-t)^{-\frac{\alpha}{2}}\,\sigma^{-2n} \quad . \tag{7.265}$$

From equations (3.138~142), the analytical expression for

$$I_{n,\delta} = \int_0^{\rho_j}\frac{\rho^{\delta}}{r^{\alpha}}\,d\rho \tag{7.266}$$

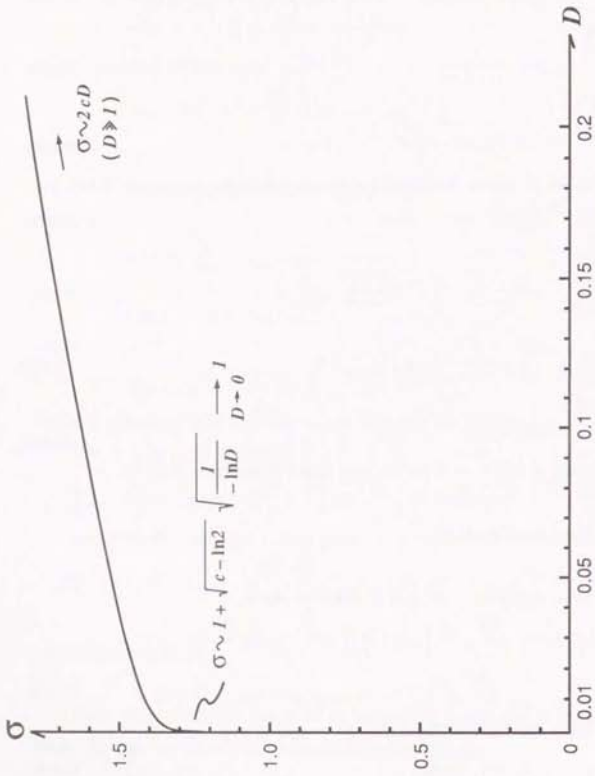

Fig. 7.9 Graph of $\sigma(D, t=0.6)$ vs D for the log-L_1 transformation : $R(\rho)=\log(\rho+d)$

is given by Table 7.5.

Table 7.5. Closed form for $I_{\alpha,\delta}=\int_0^{\rho_j}\frac{\rho^\delta}{r^\alpha}\,d\rho$

α	δ	$I_{\alpha,\delta}$ (exact)	$I_{\alpha,\delta}$ $(D\ll 1)$
1	1	$\rho_j(\sqrt{1+D^2}-D)$	ρ_j
3	1	$(1/D-1/\sqrt{1+D^2})/\rho_j$	$1/(\rho_j D)$
	2	$\ln\{(1+\sqrt{1+D^2})/D\}-1/\sqrt{1+D^2}$	$-\ln D$
5	1	$\{1/D^3-1/(1+D^2)^{3/2}\}/(3\rho_j{}^3)$	$1/\{3(\rho_j D)^3\}$
	2	$1/\{3(\rho_j D)^2(1+D^2)^{3/2}\}$	$1/\{3(\rho_j D)^2\}$

Then, equation (7.265) and Table 7.5 give the estimate for the relative error as in Table 7.6.

Table 7.6. Estimates for relative error $E_n(f)/I_{\alpha,\delta}$

α	δ	$E_n(f)/I_{\alpha,\delta}$
1	1	$3.0(-\ln D)\,D\,(1-t)^{-1/2}\,\sigma^{-2n}$
3	1	$1.3(-\ln D)\quad(1-t)^{-3/2}\,\sigma^{-2n}$
	2	$1.3\qquad(1-t)^{-3/2}\,\sigma^{-2n}$
5	1	$1.8(-\ln D)\quad(1-t)^{-5/2}\,\sigma^{-2n}$
	2	$1.8(-\ln D)\quad(1-t)^{-5/2}\,\sigma^{-2n}$

To maintain the constant coefficient of the error estimates at a reasonable size,

$$(1-t)^{-\frac{\alpha}{2}} < 10 \quad , \tag{7.267}$$

gives

$$0 < t < 1-10^{-\alpha/2} = \begin{cases} 0.99 & (\alpha=1) \\ 0.78 & (\alpha=3) \\ 0.60 & (\alpha=5) \end{cases} \quad . \tag{7.268}$$

The values of $\sigma(D)$ for $t=0.6$ are given in Table 7.7 (cf. graph of Fig.7.9).

Table 7.7 Values of $\sigma(D)$ for $t=0.6$, for the log-L_1 transformation

D	σ
10^{-10}	1.16
10^{-8}	1.18
10^{-6}	1.21
10^{-4}	1.26
3×10^{-4}	1.28
10^{-3}	1.31
3×10^{-3}	1.35

D	σ
10^{-2}	1.40
3×10^{-2}	1.48
10^{-1}	1.63
3×10^{-1}	1.94
1	3.05
3	7.23
10	23.4

For nearly singular integrals, one typically has relative source distances of the range

$$D : 10^{-3} \sim 10^{-1} \quad , \tag{7.269}$$

for which the size σ of the ellipse E_σ is

$$\sigma : 1.31 \sim 1.63 \quad . \tag{7.270}$$

In summary, we obtain the following error estimate for the numerical integration of

$$I_{\alpha,\delta} = \int_0^{\rho_j} \frac{\rho^\delta}{r^\alpha} d\rho \tag{7.266}$$

using the log-L_1 radial variable transformation

$$R(\rho) = \log(\rho+d) \tag{5.85}$$

and the Gauss-Legendre formula, for general natural numbers α, δ :

$$\begin{aligned} |E_n(f)| &\lesssim 2^{\frac{\alpha+2}{4}} \pi^{1-\frac{\alpha}{2}} \rho_j^{\delta+1-\alpha} \ln(1+D^{-1}) D^{\delta+1-\alpha} (1-t)^{-\frac{\alpha}{2}} \sigma^{-2n} \\ &\sim \ln(1+D^{-1}) D^{\delta+1-\alpha} \sigma^{-2n} \\ &\underset{D\ll1}{\sim} (-\ln D) D^{\delta+1-\alpha} \sigma^{-2n} \end{aligned}$$

where

$$\sigma : 1.31 \sim 1.63$$

for

$$D : 10^{-3} \sim 10^{-1} \quad , \tag{7.271}$$

where we have taken $t=0.6$.

From Table 7.6, the estimate for the relative error ε is given by

$$\boxed{\varepsilon \sim \sigma^{-2n}} \tag{7.272}$$

for the same values for σ.

The theoretical estimate of equation (7.272) corresponds fairly well with numerical experiment results in Chapter 10. The estimate also clarifies quantatively, why the log-L_1 radial variable transformation is, by far, more efficient and robust compared to the log-L_2 and identity transformations.

7.9 Error Analysis for the $L_1^{-1/m}$ Transformation

In this section, theoretical error estimates will be derived for the numerical integration in the radial variable using the Gauss-Legendre rule after applying the $L_1^{-1/m}$ transformation :

$$R(\rho) = -(\rho+d)^{-\frac{1}{m}}, \quad m>1 \tag{5.99}$$

To make the analysis easier, we will treat

$$R(\rho) = (\rho + d)^{-\frac{1}{m}}, \qquad m > 1 \tag{7.273}$$

which is an equivalent transformation with a difference of signs. Then,

$$R(0) = d^{-\frac{1}{m}} \tag{7.274}$$

$$R(\rho_j) = (\rho_j + d)^{-\frac{1}{m}} \tag{7.275}$$

and

$$\rho(R) = R^{-m} - d \tag{7.276}$$

$$\frac{\mathrm{d}\rho}{\mathrm{d}R} = -mR^{-m-1} \tag{7.277}$$

Hence, the radial component integral of equation (7.48) can be expressed as

$$\begin{aligned} I &= \int_0^{\rho_j} \frac{\rho^\delta}{r^\alpha}\,\mathrm{d}\rho \\ &= \int_{R(0)}^{R(\rho_j)} \frac{(R^{-m}-d)^\delta\,(-mR^{-m-1})}{\{(R^{-m}-d)^2+d^2\}^{\alpha/2}}\,\mathrm{d}R \\ &= \int_{-1}^{1} f(z)\,\mathrm{d}z \end{aligned} \tag{7.278}$$

where

$$R = 2^{-1}\rho_j^{-\frac{1}{m}}(-az+b) \tag{7.279}$$

$$a = D^{-\frac{1}{m}} - (1+D)^{-\frac{1}{m}} > 0$$

$$b = D^{-\frac{1}{m}} + (1+D)^{-\frac{1}{m}} > 0 \tag{7.280}$$

$$D = \frac{d}{\rho_j} \tag{7.281}$$

$$f(z) = C' \frac{\left(R^m - \dfrac{1}{\rho_j D}\right)^\delta R^{(\alpha-\delta-1)m-1}}{\left\{R^m - \dfrac{1}{(1-\mathrm{i})\rho_j D}\right\}^{\alpha/2}\left\{R^m - \dfrac{1}{(1+\mathrm{i})\rho_j D}\right\}^{\alpha/2}}$$

$$C' = m(-1)^\delta\, 2^{-1-\frac{\alpha}{2}}\,\rho_j^{\delta-\alpha-\frac{1}{m}}\,D^{\delta-\alpha}\left\{D^{-\frac{1}{m}} - (1+D)^{-\frac{1}{m}}\right\} \tag{7.282}$$

which gives

$$\begin{aligned} f(z) = C &\left\{(z-z_1)^m - a_1^m\right\}^\delta \quad (z-z_1)^{(\alpha-\delta-1)m-1} \\ &\left\{(z-z_1)^m - 2^{-\frac{1}{2}}\mathrm{e}^{\frac{\pi}{4}\mathrm{i}}a_1^m\right\}^{-\frac{\alpha}{2}} \left\{(z-z_1)^m - 2^{-\frac{1}{2}}\mathrm{e}^{-\frac{\pi}{4}\mathrm{i}}a_1^m\right\}^{-\frac{\alpha}{2}} \end{aligned} \tag{7.283}$$

where

$$z_1 = \frac{b}{1-a} = \frac{1+\Delta^{1/m}}{1-\Delta^{1/m}}$$

$$a_1 = -\frac{2}{1-\Delta^{1/m}} \tag{7.285}$$

$$C = m(-1)^{\delta-m-1}\,2^{m-\frac{\alpha}{2}}(\rho_j D)^{\delta-\alpha+1}(1-\Delta^{1/m})^{-m} \tag{7.286}$$

$$\Delta = \frac{D}{1+D} \tag{7.287}$$

where $0 \leqq \Delta < 1$

The singularities of $f(z)$ in the complex plane are analyzed in the following.

Let $m \in \mathbf{N}$, then the term $\{(z-z_1)^m - a_1^m\}^\delta$ in equation (7.283) does not give rise to singularities except for $z = \infty$.

The second term $(z-z_1)^{(\alpha-\delta-1)m-1}$ will be treated next. For the potential kernels u^*, q^* and the flux kernels $\partial u^*/\partial \mathbf{x}_s$, $\partial q^*/\partial \mathbf{x}_s$, the exponent $(\alpha-\delta-1)m-1$ take the values shown in Table 7.8.

Table 7.8 Singularity at $z = z_1$

	α	δ	$(\alpha-\delta-1)m-1$	
u^*	1	1	$-m-1<0$	singularity
q^*	3	1	$m-1$	
$\dfrac{\partial u^*}{\partial \mathbf{x}_s}$	3	1	$m-1$	
		2	$-1<0$	singularity
$\dfrac{\partial q^*}{\partial \mathbf{x}_s}$	3	1	$m-1$	
	5	1	$3m-1$	
		2	$2m-1$	

Hence, $z=z_1=(1+\Delta^{1/m})/(1-\Delta^{1/m})$ becomes a singularity for $\alpha=\delta=1$ (u^* kernel) and $\alpha=3, \delta=2$ ($\partial u^*/\partial x_k$ kernel).

Next, the third and the fourth terms in equation (7.283) has singularities at

$$z=z_k^{\pm}{}_m = z_1 + \frac{2^{1-\frac{1}{2m}}}{1-\Delta^{1/m}} e^{\left(1\pm\frac{1}{4m}+\frac{2k}{m}\right)\pi i} \tag{7.288}$$

where $k\in\mathbf{Z}$, $m\in\mathbf{N}$.

For the case $m=5$ ($L_1^{-1/5}$ transformation), the approximate values of the singularities z_1 and z_0^- are given in Table 7.9 for different values of the relative source distance D.

Table 7.9 Singularities z_1, z_0^- for $m=5$

D	z_1	z_0^-
1	14.5	0.217+2.26 i
0.1	4.25	−0.589+0.766 i
0.01	2.32	−0.740+0.484 i
0.001	1.67	−0.791+0.390 i
0.0001	1.38	−0.813+0.347 i

The position of the singularities $z=z_1, z_k^{\pm}$ ($k\in\mathbf{Z}$) of $f(z)$ for the case $m=5$ ($L_1^{-1/5}$ transformation), $D=0.01$ is shown in Fig. 7.10.

The efficiency of the $L_1^{-1/5}$ transformation in combination with the Gauss-Legendre rule is determined by the maximum size σ of the ellipse $\mathcal{E}_\sigma$

$$|z+\sqrt{z^2-1}|=\sigma \tag{7.20}$$

with foci at $z=\pm1$, which does not have any singularities z_1, z_k inside itself.

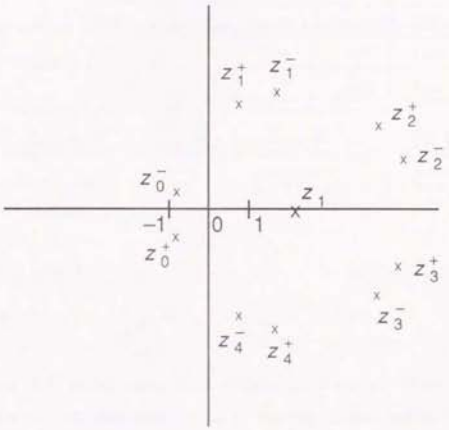

Fig. 7.10 Singularities of $f(z)$ for $L_1^{-1/5}$ tranasformation ($D=0.01$)

From equations (7.31) and (7.32), the size of the ellipse $\mathcal{E}\sigma$ which passes through $z=z_1$ is given by

$$\sigma_1 = \gamma_1 + \sqrt{\gamma_1^2 - 1} = \frac{\left(1+\Delta^{\frac{1}{2m}}\right)^2}{1-\Delta^{1/m}} \tag{7.289}$$

where

$$\gamma_1 = z_1 = \frac{1+\Delta^{1/m}}{1-\Delta^{1/m}} \tag{7.290}$$

Similarly, the size of the ellipse $\mathcal{E}\sigma$ which passes through $z=z_0^{\pm}$ is given by

$$\sigma_0 = \gamma_0 + \sqrt{\gamma_0^2 - 1} \tag{7.291}$$

where

$$\gamma_0 = \frac{1}{1-\Delta^{1/m}}\left\{ \sqrt{1+2^{-\frac{1}{m}} - 2^{1-\frac{1}{2m}}\cos\frac{\pi}{4m}} + \sqrt{\Delta^{\frac{2}{m}} + 2^{-\frac{1}{m}} - 2^{1-\frac{1}{2m}}\Delta^{\frac{1}{m}}\cos\frac{\pi}{4m}} \right\}$$

$$= \frac{\sqrt{(x_0+1)^2+y_0^2} + \sqrt{(x_0-1)^2+y_0^2}}{2} \tag{7.292}$$

where

$$z_0^{-} = x_0 + \mathrm{i}y_0 \tag{7.293}$$

$$= \frac{1+\Delta^{-1/m} - 2^{1-\frac{1}{2m}}\cos\frac{\pi}{4m}}{1-\Delta^{1/m}} + \mathrm{i}\,\frac{2^{1-\frac{1}{2m}}\sin\frac{\pi}{4m}}{1-\Delta^{1/m}}$$

Table 7.10 gives the values of γ_0, γ_1, σ_0, σ_1 for different values of D, which indicate that the ellipse passing through $z=z_0^{-}$ is smaller than the one which passes through $z=z_1$. This indicates that the singularity at $z=z_0^{-}$ dominates the convergence behaviour of the L_1^{-15} transformation.

Table 7.10 Size of ellipse σ_0, σ_1 passing through $z=z_0^{-}$, z_1

D	$\gamma_1=z_1$	γ_0	σ_1	σ_0
1	14.5	2.47	28.9	4.74
0.1	4.25	1.32	8.38	2.17
0.01	2.32	1.18	4.41	1.80
0.001	1.67	1.14	3.01	1.68
0.0001	1.38	1.12	2.32	1.62

To treat the problem more rigorously, note that σ is a strictly increasing function of γ, since

$$\frac{\mathrm{d}\sigma}{\mathrm{d}\gamma} = 1 + \frac{\gamma}{\sqrt{\gamma^2-1}} > 0 \quad \text{for} \quad \gamma > 1 \tag{7.294}$$

Noting that $1-\Delta^{1/m} > 0$, let

$$F(x) = (1-\Delta^{1/m})(\gamma_1 - \gamma_0)$$

$$= 1+\Delta^{1/m} - \sqrt{1+2^{-\frac{1}{m}} - 2^{1-\frac{1}{2m}}\cos\frac{\pi}{4m}} - \sqrt{\Delta^{\frac{2}{m}} + 2^{-\frac{1}{m}} - 2^{1-\frac{1}{2m}}\Delta^{\frac{1}{m}}\cos\frac{\pi}{4m}}$$

$$= 1+x - \sqrt{1+2^{-\frac{1}{m}} - 2^{1-\frac{1}{2m}}\cos\frac{\pi}{4m}} - \sqrt{x^2 + 2^{-\frac{1}{m}} - 2^{1-\frac{1}{2m}}x\cos\frac{\pi}{4m}} \tag{7.295}$$

where

$$x = \Delta^{1/m} = \left(\frac{D}{1+D}\right)^{1/m} \tag{7.296}$$

and $0 \leqq x < 1$.

Since

$$F(0) = 1 - \sqrt{1+2^{-\frac{1}{m}} - 2^{1-\frac{1}{2m}}\cos\frac{\pi}{4m}} - 2^{-\frac{1}{2m}} < 0 \tag{7.297}$$

for $m \neq \infty$,

and

$$F(1) = 2\left(1 - \sqrt{1 + 2^{-\frac{1}{m}} - 2^{1-\frac{1}{2m}} \cos\frac{\pi}{4m}}\right) > 0 \tag{7.298}$$

for $m=5$,

and

$$\frac{dF}{dx} = -\left(1 - \sqrt{\frac{x^2 - 2^{1-\frac{1}{2m}}\, x\cos\frac{\pi}{4m} + 2^{-\frac{1}{m}}\cos^2\frac{\pi}{4m}}{x^2 - 2^{1-\frac{1}{2m}}\, x\cos\frac{\pi}{4m} + 2^{-\frac{1}{m}}}}\right) > 0 \tag{7.299}$$

we have

$$\begin{aligned} F(x) &< 0 \quad 0 < x < x^* \\ &= 0 \quad x = x^* \\ &> 0 \quad x^* < x < 1 \end{aligned} \tag{7.300}$$

where x^* is given from equation (7.295) by

$$x^* = \frac{2^{-\frac{1}{2m}}\cos\frac{\pi}{4m} + \sqrt{1 + 2^{-\frac{1}{m}} - 2^{1-\frac{1}{2m}}\cos\frac{\pi}{4m}} - 1}{2^{-\frac{1}{2m}}\cos\frac{\pi}{4m} - \sqrt{1 + 2^{-\frac{1}{m}} - 2^{1-\frac{1}{2m}}\cos\frac{\pi}{4m}} + 1} \doteqdot 0.0497 \tag{7.301}$$

and

$$D^* = \frac{x^{*m}}{1 - x^{*m}} \doteqdot 3\times 10^{-7} \tag{7.302}$$

so that

$$\begin{aligned} \gamma_1 &< \gamma_0 \quad for \quad 0 \leqq D < D^* \\ \gamma_1 &= \gamma_0 \quad for \quad D = D^* \\ \gamma_1 &> \gamma_0 \quad for \quad D^* < D \end{aligned} \tag{7.303}$$

i.e.

$$\sigma_0 < \sigma_1 \quad for \quad D > D^* = 3\times 10^{-7}, \quad m=5 \tag{7.304}$$

This means that for $m=5$, $D>D^*=3\times 10^{-7}$, the ellipse passing though $z=z_0^-$ is smaller than the one passing through $z=z_1$, and hence the former is the critical one.

Hence, for the case $D>D^*$, we will consider the ellipse of equation (7.20) which passes through the point

$$z_t = x_0 + t y_0$$

$$= \frac{1 + \Delta^m - 2^{1-\frac{1}{2m}}\cos\frac{\pi}{4m}}{1 - \Delta^{1/m}} + i\,\frac{2^{1-\frac{1}{2m}}\sin\frac{\pi}{4m}}{1 - \Delta^{1/m}}\, t \quad , \quad (0 < t < 1) \tag{7.305}$$

which is located just below the singular point z_0^-, as shown in Fig. 7.11.

(i) Estimation of $\max_{z \in \mathcal{E}_\sigma} |f(z)|$

From equation (7.283), we have

$$|f(\bar{z})| = \overline{f(z)} \tag{7.306}$$

which implies

$$|f(\bar{z})| = |f(z)| \tag{7.307}$$

Hence, we need only consider the region $\mathrm{Im}(z) \geqq 0$.

If we take $0 < |1-t| 1$, z_0^- is the closest singularity to the ellipse $\mathcal{E}_\sigma$ and

$$\max_{z \in \mathcal{E}_\sigma} |f(z)|$$

$$\sim |f(z_t)|$$

$$\sim m^{1-\frac{\sigma}{2}} 2^{-\frac{3}{4}\sigma + \frac{1}{2m} - \frac{1}{2}} (\rho_j D)^{\sigma - s + 1} (1 - \Delta^{1/m}) \left(\sin\frac{\pi}{4m}\right)^{-\frac{\sigma}{2}} (1-t)^{-\frac{\sigma}{2}} \tag{7.308}$$

from equation (7.283)

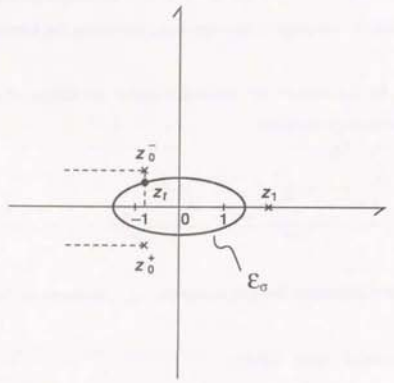

Fig. 7. 11 Integration path $\mathcal{E}_\sigma$ for the $L_1^{-1/5}$ transformation

(ii) Estimation of σ

Next, the size σ of the ellipse $\mathcal{E}_\sigma$ of equation (7.20) passing through the point $z=z_t$ of equation (7.305) is estimated.

This can be done by using

$$z_t = x + iy$$

$$x = \frac{1+\Delta^{1/m} - 2^{1-\frac{1}{2m}} \cos\frac{\pi}{4m}}{1-\Delta^{1/m}} \quad ,$$

$$y = \frac{2^{1-\frac{1}{2m}} \sin\frac{\pi}{4m}}{1-\Delta^{1/m}}\, t \quad , \qquad (7.309),$$

$$\gamma = \frac{\sqrt{(x+1)^2+y^2} + \sqrt{(x-1)^2+y^2}}{2} \qquad (7.32)$$

and

$$a = \gamma + \sqrt{\gamma^2 - 1} \qquad (7.31)$$

(iii) Error estimate $E_n(f)$

The error $E_n(f)$ for $D>D^*$ can now be obtained from

$$|E_n(f)| < 2\pi a^{-2n} \max_{z \in \mathcal{E}_\sigma} |f(z)| \qquad (7.26)$$

In order to maintain

$$(1-t)^{-\frac{\alpha}{2}} < 10 \qquad (7.267)$$

for $\alpha=1, 3, 5$ in equation (7.307), we set $t=0.6$ as in equation (7.268). The values and the graph of $\sigma(D)$ for $t=0.6$ are given in Table 7.11 and Fig. 7.12, respectively.

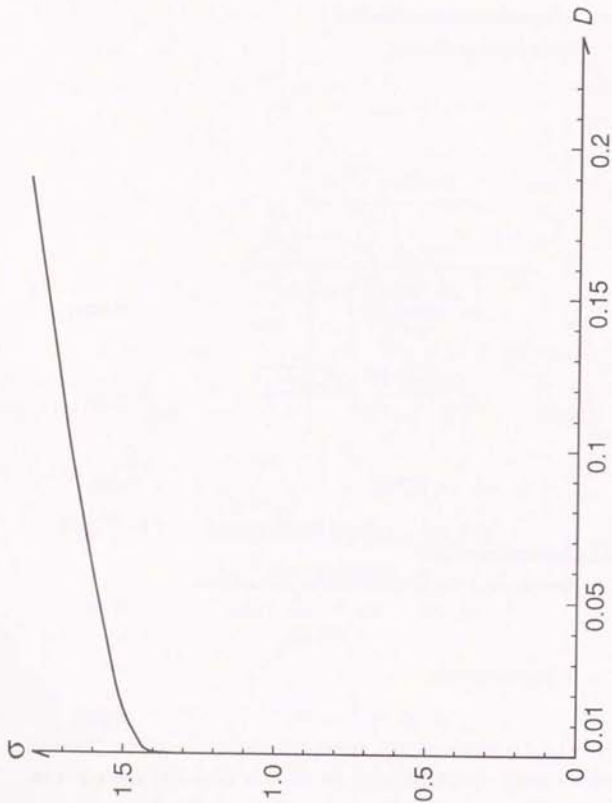

Fig. 7. 12 Graph of σ(D, t = 0.6) vs D for the $L_1^{-1/5}$ transformation : $R(\rho) = -(\rho+d)^{-1/5}$

Table 7.11 Value of $\sigma(D)$ for $t=0.6$, for the $L_1^{-1/5}$ transformation

D	σ	D	σ
10^{-6}	1.36	10^{-2}	1.48
10^{-5}	1.36	3×10^{-2}	1.54
3×10^{-5}	1.37	10^{-1}	1.67
10^{-4}	1.38	3×10^{-1}	1.96
3×10^{-4}	1.39	1	3.06
10^{-3}	1.41	3	7.30
3×10^{-3}	1.44	10	23.6

For nearly singular integrals with typical relative source distances of the range

$$D : 10^{-3} \sim 10^{-1}$$

the size σ of the ellipse $\mathcal{E}_\sigma$ is in the range

$$\sigma : 1.41 \sim 1.67 \tag{7.310}$$

which is slightly larger than the corresponding ellipse for the log-L_1 transformation.

Hence, from equations (7.26) and (7.308), we obtain the following error estimate for the numerical integration of

$$I_{\alpha,\delta} = \int_0^{\rho_j} \frac{\rho^\delta}{r^\alpha}\, d\rho \tag{7.266}$$

using the $L_1^{-1/m}$ ($m=5$) radial variable transformation

$$R(\rho) = (\rho+d)^{-\frac{1}{5}} \tag{5.100}$$

and the Gauss-Legendre formula, for general natural numbers α, δ :

$$|E_n(f)| \lesssim m^{1-\frac{\alpha}{2}}\, 2^{\frac{1}{2}+\frac{1}{2m}-\frac{3}{4}\alpha}\, \pi\, (\rho_j D)^{\delta-\alpha+1}\, (1-\Delta^{1/m}) \left(\sin\frac{\pi}{4m}\right)^{-\frac{\alpha}{2}} (1-t)^{-\frac{\alpha}{2}}\, e^{-2n}$$

$$= 5^{1-\frac{\sigma}{2}} 2^{\frac{3}{5}-\frac{3}{4}\sigma} \pi (\rho_j D)^{\delta-\sigma+1} (1-\Delta^{1/5}) \left(\sin\frac{\pi}{20}\right)^{-\frac{\sigma}{2}} (1-t)^{-\frac{\sigma}{2}} \sigma^{-2n}$$

$$\sim D^{\delta+1-\sigma} (1-\Delta^{1/5}) \sigma^{-2n}$$

$$\sim (1-D^{1/5})\, D^{\delta+1-\sigma} \sigma^{-2n}$$

$D \ll 1$

where

$$\sigma : 1.41 \sim 1.67$$

for

$$D : 10^{-3} \sim 10^{-1} \qquad (7.311)$$

where we have taken $t=0.6$.

From Table 7.6, the estimate of the relative error ε is given by

$$\varepsilon \sim \sigma^{-2n} \qquad (7.312)$$

for the same values for σ.

The theoretical estimate of equation (7.312) corresponds fairly well with numerical experiment results in Chapter 10. The estimate explains why the $L_1{}^{-1/5}$ transformation is slightly better compared to the log-L_1 transformation for the model radial integral of equation (7.266) (cf. Tables 10.24, 10.32 and Fig. 10) and for the flux integral $\int_S \phi_{ij} \frac{\partial q^*}{\partial x_s} dS$ (cf. Table 10.50 and Fig. 10.39).

7.10 Summary of Theoretical Error Estimates

In this chapter, we derived theoretical error estimates for numerical integration by means of the theory of complex functions.

The basic radial component integrals

$$I_{\alpha,\delta} = \int_0^{\rho_j} \frac{\rho^\delta}{r^\alpha} d\rho$$

where

$$r = \sqrt{\rho^2+d^2} \quad , \quad \alpha, \delta \in N \quad , \qquad (7.313)$$

characterize the nearly singular integrals occurring in the boundary element analysis of three dimensional potential problems.

We obtained the following error estimates E_n for the numerical integration of $I_{\alpha,\delta}$ using the Gauss-Legendre rule after applying each radial variable transformation $R(\rho)$.

Let n be the number of integration points in the radial variable, and

$$D = \frac{d}{\rho_j} > 0$$

be the relative source distance.

Then, for $n \gg 1$ and $D \ll 1$ (nearly singular),

(1) Identity tranformation : $R(\rho)=\rho$

$$E_n \lesssim D^{\delta-\frac{3}{2}\sigma} \sigma^{-2n}$$

$$\sim \sigma^{-2n}$$

where

$$\sigma : 1.04 \sim 1.42$$

for

$$D: 10^{-3} \sim 10^{-1} \qquad (7.80)$$

(2) log-L_2 transformation : $R(\rho)= \log\sqrt{\rho^2+d^2}$

For δ=odd (potential),

$$E_n \lesssim (-\ln D)\, D^{\frac{\delta+1-\alpha}{2}} \left[\frac{\max(3,\delta)\, e \ln D}{8n}\right]^{2n}$$

$$\sim D^{\frac{\delta+1-\alpha}{2}} \left(\frac{\ln D}{n}\right)^{2n}$$

$$\sim n^{-2n} \quad . \qquad (7.118,120)$$

For δ=even (flux, interpolation functions),

$$E_n \sim (-\ln D)^{\frac{\delta+1}{2}} D^{\delta+1-\alpha} n^{-\delta-1}$$

$$\sim n^{-\delta-1} \quad . \tag{7.195}$$

(3) log-L_1 transformation : $R(\rho)=\log(\rho+d)$

For $\delta+1-\alpha>0$ (e.g. $\alpha=\delta=1$ for potential),

$$E_n \sim (-\ln D) D^{\frac{\delta+1-\alpha}{2}} \left\{ \frac{(\delta+1-\alpha)\, e \ln D}{8n} \right\}^{2n}$$

$$\sim D^{\frac{\delta+1-\alpha}{2}} \left(\frac{\ln D}{n} \right)^{2n}$$

$$\sim n^{-2n} \tag{7.235}$$

For general $\alpha, \delta \in \mathbf{N}$,

$$E_n \lesssim (-\ln D)\, D^{\delta+1-\alpha}\, \sigma^{-2n}$$

$$\sim \sigma^{-2n}$$

where

$$\sigma : 1.31 \sim 1.63$$

for

$$D : 10^{-3} \sim 10^{-1} \quad . \tag{7.271}$$

(4) $L_1^{-1/5}$ transformation : $R(\rho) = -(\rho+d)^{-1/5}$

$$E_n \sim (1-D^{\frac{1}{5}})\, D^{\delta+1-\alpha}\, \sigma^{-2n}$$

$$\sim \sigma^{-2n}$$

where

$$\sigma : 1.41 \sim 1.67$$

for

$$D : 10^{-3} \sim 10^{-1} \quad . \tag{7.311}$$

These theoretical error estimates are compared with numerical experiment results on one dimensional radial variable integration and boundary element surface integrals with potential and flux kernels, in Chapter 10. The theoretical estimates bear remarkable resemblance with the numerical experiment results, demonstrating the validity of the estimates derived in this chapter.

The theoretical estimates in this chapter also give a clear insight regarding the optimization of the radial variable transformation $R(\rho)$ for nearly singular integrals arising in boundary element analysis in general.

To be more precise, the singularities $\rho_\pm = \pm d\,i \in \mathbf{C}$, inherent in the near singularity of

$$\frac{1}{r^\alpha} = \frac{1}{\sqrt{\rho^2+d^2}^{\,\alpha}} \quad , \tag{7.314}$$

are mapped to $R_\pm = R(\rho_\pm)$ by the radial variable transformation $R(\rho)$. $R_\pm$ in turn, are mapped to $z_\pm = x(R_\pm)$ by the transformation

$$x = \frac{2R - \{R(\rho_j) + R(0)\}}{R(\rho_j) - R(0)} \quad , \tag{7.49}$$

in the process of mapping the interval $R:[R(0), R(\rho_j)]$ to the interval $x:[-1,1]$ in order to apply the standard Gauss-Legendre rule.

As shown, for example, by equation (7.80) for $R(\rho)=\rho$ and equation (7.271) for $R(\rho)=\log(\rho+d)$, the numerical integration error is governed by the maximum size σ of the ellipse $\mathcal{E}_\sigma$

$$|\, z + \sqrt{z^2-1}\,| = \sigma, \quad (\sigma>1) \tag{7.20}$$

in the complex plane, which does not include the singularities $z_\pm$ inside.

Therefore, roughly speaking, the optimum radial variable transformation $R(\rho)$ is the transformation which maps the singularities $\rho_\pm = \pm d\,i$, inherent in the near singularity, to $z_\pm = x\{R(\rho_\pm)\}$ which are as far away as possible from the real interval $z:[-1,1]$, allowing an ellipse $\mathcal{E}_\sigma$ of maximum size σ.

PART II

APPLICATIONS AND NUMERICAL RESULTS

CHAPTER 8

NUMERICAL EXPERIMENT PROCEDURES AND ELEMENT GEOMETRY

In the following chapters, results of numerical experiments performed on the numerical integration methods proposed in Chapter 5 are given with comparison with previous methods. Weakly singular integrals, nearly singular integrals and hyper singular integrals (Cauchy principal value) arising in three dimensional potential problems are treated. In this chapter the numerical experiment procedures and types of elements used in the experiments are given.

8.1 Notes on Procedures for Numerical Experiments

All the numerical experiments were done on the NEC supercomputer SX-2 (peak performance 1.3GFLOPS) in double precision (except when stated otherwise). The results for CPU-time presented in milliseconds (msec) were consistent within a relative difference of about 1% for most cases and within 5% for some exceptional cases.

When the Gauss-Legendre formula was used as the basic quadrature rule, the number of integration points N was increased in the following series:

$$N = 1, 2, 3, 4, 5, 6, 7, 8, 9, 10, 11, 12, 14, 16, 20, 25, 28, 32, 35, 40, 45, 50, 55, 60, 64, 72, 80, 90, 100, 1110, 120, 128, 140, 150, 160, 170, 180, 190, 200, 210, 220, 230, 240, 250, 256, 300, 250, 400, 450, 500, \quad (8.1)$$

until the numerical integration results converged. The integration table in Stroud and Secrest[3] and the IMSL mathematical library[39] based on the subroutine GAUSSQUADRULE by Golub and Welsch[38] were used to generate the integration points and weights for the formula.

The relative error e_n of the numerical integration result I_n was measured by comparing it with the true value of the integral I^*, which was obtained either by analytical integration, when it was possible, or by using the converged result using the best method with sufficient number of integration points. For instance, for nearly singular integrals, the result obtained by the PART method with the angular variable transformation $t(\theta)$ of equation (5.130) and the log-L_1 radial variable transformation $R(\rho)$ of equation (5.85), was used to obtain the converged numerical integration result. Then the relative error e_n was measured by

$$e_n = \left| \frac{I_n - I^*}{I^*} \right| \tag{8.2}$$

When the value of the true (converged) integral I^* itself is zero (or when $|I^*|$ is less than a certain threshold value e.g. 10^{-10}), the absolute error

$$E_n = |I_n - I^*| \tag{8.3}$$

was used as the measure of convergence, instead of the relative error.

In most tables, the minimum number of integration points required to obtain a relative error less than $\varepsilon = 10^{-6}$ is given with the CPU-time consumed, as a measure of the efficiency of the method.

In order to obtain the minimum number of integration points in each variable required to achieve a relative error less than ε, the following procedure was taken. Taking the example of the PART method with integration in the angular variable $t(\theta)$ and the radial variable $R(\rho)$, where N_t and N_R are the number of integration points in the angular and radial variables, respectively,

(1) increase N_t and N_R as $N_t = N_R = 1, 2, 3, \cdots$, according to the sequence of equation (8.1), until the relative error becomes less than ε at $N_t = N_R = N_{\max}(1)$,

(2) set $N_R = N_{\max}(1)$ and increase $N_t = 1, 2, 3, \cdots$, according to the sequence of equation (8.1), until the relative error becomes less than ε at $N_t = N_{\max}(2)$,

(3) set $N_t = N_{\max}(2)$ and increase $N_R = 1, 2, 3, \cdots$, according to the sequence of equation (8.1), until the relative error becomes less than ε at $N_R = N_{\max}(3)$, so that the minimum number of integration points required are $N_t = N_{\max}(2)$ and $N_R = N_{\max}(3)$ for the angular and radial variables, respectively.

When there are more than one component in the integral concerned, such as in integrals related to the flux e.g. $\int_s \partial u^*/\partial \mathbf{x}_s \, dS$, $\int_s \partial q^*/\partial \mathbf{x}_s \, dS$ or in integrals containing interpolation functions e.g. $\int_s \phi_{ij} u^* \, dS$, $(i, j = -1, 0, 1)$, the maximum relative error among all the components concerned is taken as the (maximum) relative error.

8.2 Geometry of Boundary Elements used for Numerical Experiments

In all cases, the 9-point Lagrangian element defined by equations (5.2), (5.3) and (5.4), and shown in Fig. 5.1 is used to model the following (curved) quadrilateral patches.

(1) Planar rectangle (PLR)

A planar rectangle in the xy-plane defined by $[-a, a] \times [-b, b]$, or

$$\begin{aligned} -a &\le x \le a \\ -b &\le y \le b \\ z &= 0 \end{aligned} \tag{8.4}$$

as shown in Fig. 8.1. The source point $\mathbf{x}_s$ is given by

$$\mathbf{x}_s = (x, y, d) \tag{8.5}$$

where d is the source distance. The above planar rectangle will be called PLR(a, b).

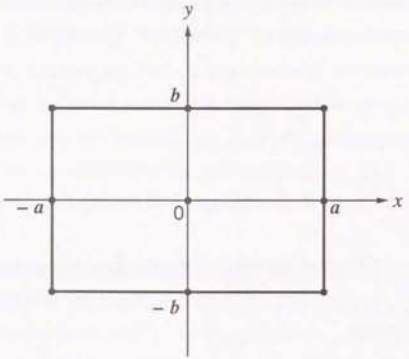

Fig. 8.1 Planar rectangle PLR (a, b)

As a special case, the planar square of size 1 can be defined by PLR (0.5, 0.5). The planar rectangle PLR (a, b) is modelled by the 9-point Lagrangian element of equation (5.4) by setting

$$\mathbf{x}^{j,k} = \mathbf{x}(j,k) = (ja, kb, 0) \; ; \; j,k = -1, 0, 1 \quad . \tag{8.6}$$

(2) 'Spherical' quadrilateral (SPQ)

A spherical quadrilateral on the spherical surface of radius a defined by

$$\begin{aligned} x &= a \sin\Psi \cos\Phi \\ y &= a \sin\Psi \sin\Phi \\ z &= a \cos\Psi \end{aligned} \tag{8.7}$$

where Ψ determines the latitude and Φ is the longitude, as shown in Fig. 8.2, where Ψ and Φ are bounded by

$$\begin{aligned} \Psi(1) \leq \Psi \leq \Psi(-1) \\ \Phi(-1) \leq \Phi \leq \Phi(1) \end{aligned} \quad . \tag{8.8}$$

The spherical quadrilateral is approximated by the 9-point Lagrangian element of equation (5.4) such that parameters η_1 and η_2 correspond with angles Φ and Ψ, respectively, as

$$\begin{aligned} \eta_1 = -1 \quad &\leftrightarrow \quad \Phi = \Phi(-1) \\ \eta_1 = 0 \quad &\leftrightarrow \quad \Phi = \Phi(0) \\ \eta_1 = 1 \quad &\leftrightarrow \quad \Phi = \Phi(1) \end{aligned}$$

and

$$\begin{aligned} \eta_2 = -1 \quad &\leftrightarrow \quad \Psi = \Psi(-1) \\ \eta_2 = 0 \quad &\leftrightarrow \quad \Psi = \Psi(0) \\ \eta_2 = 1 \quad &\leftrightarrow \quad \Psi = \Psi(1) \end{aligned} \quad , \tag{8.9}$$

as shown in Fig. 8.3.

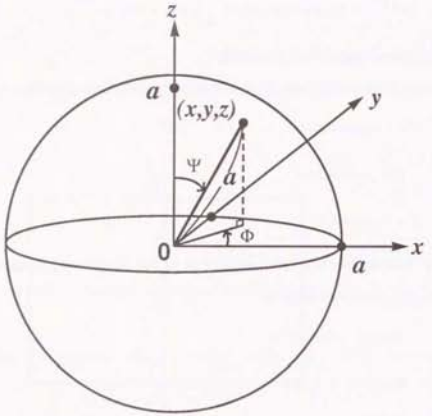

Fig. 8.2 Sphere with radius a

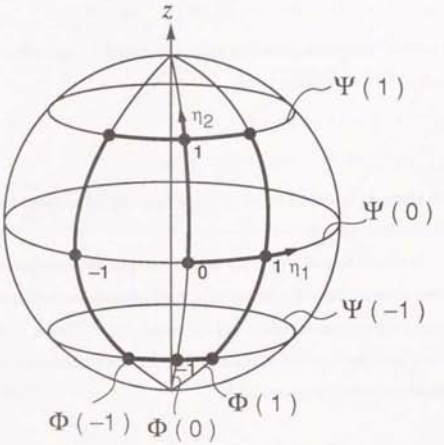

Fig. 8.3 Spherical quadrilateral (SPQ)

For instance, if we take

$$a = 1 \quad ,$$

$$\Phi(-1) = -30^\circ \quad , \quad \Phi(-1) = -30^\circ \quad , \quad \Phi(1) = 30^\circ \quad ,$$

$$\Psi(-1) = 120^\circ \quad , \quad \Psi(0) = 90^\circ \quad , \quad \Psi(1) = 60^\circ \quad , \tag{8.10}$$

we obtain a spherical quadrilateral subtending 60° in each direction Φ and Ψ, and the size of the element is 1, i.e.

$$| \mathbf{x}(1,0) - \mathbf{x}(-1,0) | = 1 \quad ,$$

$$| \mathbf{x}(0,1) - \mathbf{x}(0,-1) | = 1 \quad . \tag{8.11}$$

This element, modelled by the 9-point Lagrangian element as in equation (8.8), will be called SPQ60.

It should be noted that the maximum relative discrepancy between the real spherical quadrilateral and the 'spherical' quadrilateral SPQ60 (modelled by the 9 point Lagrangian element), is of the order of 10^{-3}. Hence, in actual applications a more accurate geometrical modelling becomes necessary, depending on the required accuracy of the analysis.

(3) Hyperbolic quadrilateral (HYQ)

A hyperbolic quadrilateral is defined as the 9-point Lagrangian element (cf. equation (5.4)) whose nine nodes $\mathbf{x}^{j,k}$; $j, k = -1, 0, 1$ are given in x, y, z coordinates as

$$x^{j,k} = ja \quad , \quad (j,k = -1,0,1) \quad ,$$

$$y^{j,k} = kb \quad , \quad (j,k = -1,0,1) \quad ,$$

and

$$z^{-1,1} = -h \quad , \quad z^{0,1} = 0 \quad , \quad z^{1,1} = h \quad ,$$

$$z^{-1,0} = 0 \quad , \quad z^{0,0} = 0 \quad , \quad z^{0,1} = 0 \quad ,$$

$$z^{-1,-1} = h \quad , \quad z^{0,-1} = 0 \quad , \quad z^{1,-1} = -h \quad , \tag{8.12}$$

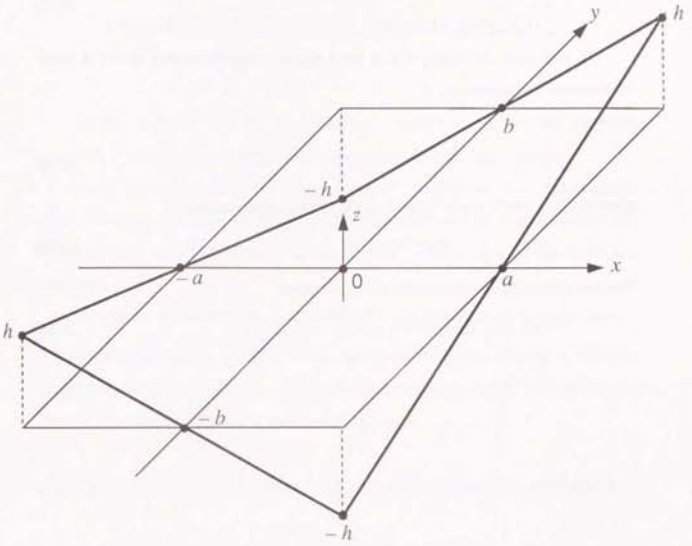

Fig. 8.4 Hyperbolic quadrilateral (HYQ)

as shown in Fig. 8.4.

This element HYQ is described by

$$z = \frac{h}{ab} xy \qquad (8.13)$$

In this case, the modelling of the hyperbolic quadrilateral by the 9 point Lagrangian element is exact.

Setting

$$a = b = 0.5 \quad , \quad h = 0.25 \qquad (8.14)$$

gives the hyperbolic quadrilateral HYQ 1, which is described by

$$z = xy \quad , \quad -0.5 \leq x, y \leq 0.5 \qquad (8.15)$$

The size of the element is considered to be 1, since

$$|\mathbf{x}(1,0) - \mathbf{x}(-1,0)| = |\mathbf{x}(0,1) - \mathbf{x}(0,-1)| = 1 \qquad (8.16)$$

CHAPTER 9

APPLICATIONS TO WEAKLY SINGULAR INTEGRALS

In this chapter, results of numerical experiments on weakly singular integrals arising in three dimensional potential problems are presented.

Although weakly singular integrals are not as difficult to calculate as the nearly singular integrals, difficulty may arise using polar coordinates, when the source point is very near the edge of the element, as is the case for discontinuous elements.

It will be demonstrated in this chapter that the method of using polar coordinates in the plane $\bar{S}$ tangent to the element S at the source point $\mathbf{x}_s$, with the angular variable transformation $t(\theta)$ introduced in Chapter 5 (PART method with $R(\rho) = \rho$), overcomes the above mentioned difficulty.

9.1 Check with Analytical Integration Formula for Constant Planar Element

First, the analytical integration formula for the integral

$$I_{u^*} = 4\pi \int_S u^* \, dS = \int_S \frac{dS}{r} \qquad (9.1)$$

for a constant planar quadrilateral element is presented, so that the method and code for numerical integration can be checked.

Using polar coordinates (ρ, θ) centered at the source point $\mathbf{x}_s$, in each triangle ($j=1\sim4$), as shown in Fig. 9.1,

$$I_{u^*} = \int_S \frac{dS}{r}$$

$$= \sum_{j=1}^{4} \int_0^{\Delta\theta_j} d\theta \int_0^{\rho_j(\theta)} \frac{\rho}{r}\, d\rho \qquad (9.2)$$

where

$$r = \sqrt{\rho^2 + d^2} = \rho \quad , \qquad (9.3)$$

for singular integrals ($d=0$) over planar elements. Hence,

$$I_{u^*} = \sum_{j=1}^{4} \int_0^{\Delta\theta_j} d\theta \int_0^{\rho_j(\theta)} d\rho$$

$$= \sum_{j=1}^{4} \int_0^{\Delta\theta_j} \rho_j(\theta)\, d\rho$$

$$= \sum_{j=1}^{4} \int_0^{\Delta\theta_j} \frac{h_j}{\cos(\theta - \alpha_j)}\, d\theta$$

$$= \sum_{j=1}^{4} \frac{h_j}{2} \log \left| \frac{\{1+\sin(\Delta\theta_j - \alpha_j)\}(1+\sin\alpha_j)}{\{1-\sin(\Delta\theta_j - \alpha_j)\}(1-\sin\alpha_j)} \right| \qquad (9.4)$$

For a rectangular planar element PLR (a, b) with the source point at $\mathbf{x}_s=(x_s, y_s, 0)$, as shown in Fig. 9.2, equation (9.4) can be expressed as

$$I_{u^*} = \sum_{j=1}^{4} \frac{h_j}{2} \log \left(\frac{a_{j+1}+h_{j+1}}{a_{j+1}-h_{j+1}} \cdot \frac{a_j+h_{j-1}}{a_j-h_{j-1}} \right) \quad , \qquad (9.5)$$

since

$$\sin(\Delta\theta_j - \alpha_j) = \frac{h_{j+1}}{a_{j+1}} \quad , \qquad (9.6)$$

$$\sin\alpha_j = \frac{h_{j-1}}{a_j} \quad , \quad (j=1\sim4) \quad , \qquad (9.7)$$

where

$$h_0 = h_4 \quad , \quad h_5 = h_1 \quad , \quad a_5 = a_1 \quad . \qquad (9.8)$$

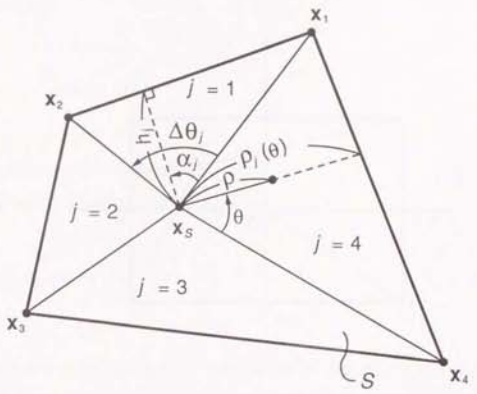

Fig. 9.1 Planar quadrilateral element

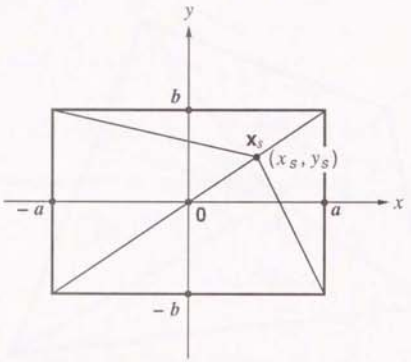

Fig. 9.2 Planar rectangle PLR (a, b) with source point at (x_s, y_s)

When the source point $\mathbf{x}_s$ is on the j-th edge of the element, i.e. $\mathrm{sgn}(j)=0$, the j-th component of the summation in equations (9.4) and (9.5) is set to zero.

As an example, we take the planar square element S : PLR(0.5, 0.5), which is described by

$$\begin{aligned} -0.5 \leq x \leq 0.5 \quad , \\ -0.5 \leq y \leq 0.5 \quad , \\ z = 0 \quad . \end{aligned} \tag{9.9}$$

The typical size of the element is 1.

In Table 9.1, the result of calculating

$$\int_S u^* \, dS \tag{9.10}$$

is given, where

$$u^* = \frac{1}{4\pi r} \tag{9.11}$$

and the source point $\mathbf{x}_s = \mathbf{x}(\eta_1, \eta_2)$ is set to $\mathbf{x}(0, 0)$, $\mathbf{x}(1, 0)$, $\mathbf{x}(1, 1)$ and $\mathbf{x}(0, 1)$, as shown in Fig. 9.3. The numerical result obtained by using polar coordinates (ρ, θ) around the source point, and further using the angular transformation

$$t(\theta) = \frac{h_j}{2} \log \left\{ \frac{1 + \sin(\theta - \alpha_j)}{1 - \sin(\theta - \alpha_j)} \right\} \tag{5.127}$$

introduced in Chapter 5, are compared with the analytical integration of equation (9.4). The basic quadrature rule used for the integration in ρ, θ and $t(\theta)$ is the Gauss-Legendre rule. The minimum number of integration points, N_ρ, N_θ and $N_{t(\theta)}$, required in each variable to achieve a relative error (compared to the analytical results) less than 10^{-6} are given with the CPU-time.

Only one integration point is required in the radial variable. This is because for planar elements $r = \rho$, so that

$$\begin{aligned} \int u^* \, dS &= \int d\theta \int \frac{1}{4\pi r} \, \rho \, d\rho \\ &= \frac{1}{4\pi} \int d\theta \int d\rho \quad . \end{aligned} \tag{9.12}$$

Table 9.1 Weakly singular integral $\int_S u^* \, dS$ over the unit planar square : PLR (0.5, 0.5)

Source point (η_1, η_2)	Polar Coordinates				Angular Transformation				Integral (analytical)
	$N_\theta \times N_\rho$	total	CPU (msec)	relative error	$N_{t(\theta)} \times N_\rho$	total	CPU (msec)	relative error	$4\pi \int_S u^* \, dS$
(0, 0)	6×1	24	0.69	3×10^{-7}	1×1	4	0.20	3×10^{-16}	3.5254943
(1, 0)	6×1	18	0.54	3×10^{-7}	1×1	3	0.17	7×10^{-16}	2.4060591
(1, 1)	4×1	8	0.28	9×10^{-7}	1×1	2	0.13	6×10^{-16}	1.7627472
(0, 1)	6×1	18	0.54	3×10^{-7}	1×1	3	0.17	7×10^{-16}	2.4060591

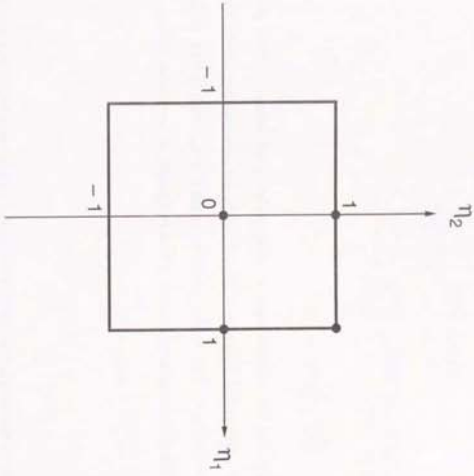

Fig. 9.3 Position of source point

With the angular transformation $t(\theta)$, only one integration point is required in the angular variable. This is because

$$\int_S u^* \, d\theta = \frac{1}{4\pi} \sum_{j=1}^{4} \int_0^{\Delta\theta_j} d\theta \int_0^{\rho_j(\theta)} d\rho$$

$$= \frac{1}{4\pi} \sum_{j=1}^{4} \int_{t(0)}^{t(\Delta\theta_j)} \rho_j(\theta) \frac{d\theta}{dt} \, dt$$

$$= \frac{1}{4\pi} \sum_{j=1}^{4} \int_{t(0)}^{t(\Delta\theta_j)} dt \qquad (9.13)$$

since

$$\frac{d\theta}{dt} = \frac{1}{\rho_j(\theta)} \qquad (5.126)$$

In Fig. 9.4 the relative error ϵ using polar coordinates (ρ, θ) is plotted (in log-scale) against the number of Gauss-Legendre integration points N_θ in the angular variable θ. The source point is located at $\mathbf{x}_s = \mathbf{x}(0, 0) = (0, 0, 0)$ at the centre of the planar square element. From the graph, it is estimated that

$$\log_{10} \epsilon \simeq 0.15 - 1.1 N_\theta \qquad (9.14)$$

so that

$$\epsilon \simeq 1.4 \times \left(\frac{1}{13}\right)^{N_\theta} \qquad (9.15)$$

(From now on the relative error will be plotted in log-scale in all the convergence graphs showing the relative error vs. number of integration points.)

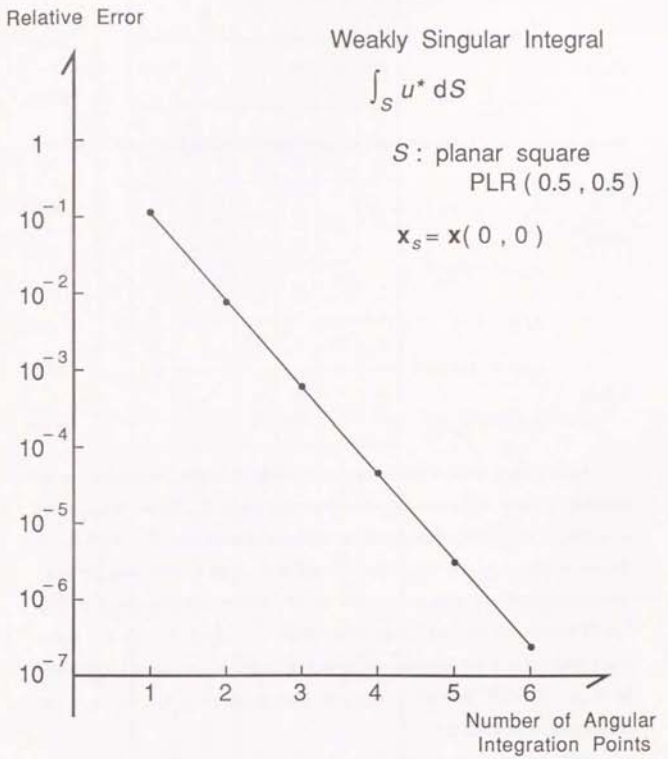

Fig. 9.4 Relative error vs. Number of angular integration points using polar coordinates (ρ, θ)

9.2 Planar Rectangular Element with Interpolation Function ϕ_{ij}

Next, numerical integration is performed for the weakly singular integrals

$$\int_S \phi_{ij} u^* \, dS \quad , \quad (i,j=-1,0,1) \tag{9.16}$$

where

$$u^* = \frac{1}{4\pi r} \tag{9.11}$$

and ϕ_{ij}, $(i,j=-1,0,1)$ are the 9-point Lagrangian interpolation functions defined by

$$\phi_{ij}(\eta_1, \eta_2) = \phi_i(\eta_1)\, \phi_j(\eta_2) \tag{9.17}$$

where

$$\phi_{-1}(\eta) = \eta(\eta-1)/2$$

$$\phi_0(\eta) = 1-\eta^2$$

$$\phi_1(\eta) = \eta(\eta+1)/2 \tag{5.3}$$

so that

$$\phi_{ij}(k,l) = \delta_{ik}\, \delta_{jl} \quad . \tag{9.18}$$

Again taking the unit planar square S: PLR(-0.5, 0.5), Table 9.2 gives the minimum number of Gauss-Legendre integration points N_ρ, N_θ and $N_{t\,(\theta)}$ in the variables, ρ, θ and $t\,(\theta)$, respectively, to achieve a relative error $\epsilon < 10^{-6}$ for all the components $i, j=-1$, 0, 1 of the integral of equation (9.16), using the polar coordinates (ρ, θ) and with the angular transformation $t\,(\theta)$ of equation (5.130). The CPU-time and the maximum relative error for $i, j=-1$, 0, 1 are also given. The actual value of the integral corresponding to the ϕ_{11} component, calculated by $N_{t\,(\theta)} = N_\rho = 128$ points is also given. The source point $\mathbf{x}_s = \mathbf{x}(\eta_1, \eta_2)$ was chosen similar to Table 9.1.

This time, more than one integration point is required in each variable, because of the interpolation function ϕ_{ij}. However, only 3 integration points are required in the radial variable, and the transformation $t\,(\theta)$ decreases the

Table 9.2 Weakly singular integral $\int_S \phi_{ij} u^* \, dS$ over the unit planar square: PLR(0.5, 0.5)

Source point (η_1, η_2)	Polar Coordinates (ρ, θ)					Angular Transformation $(\rho, t\,(\theta))$				$\frac{N_\theta}{N_{t\,(\theta)}}$	Integral $4\pi \int_S \phi_{11} u^* \, dS$ $(128\times128\text{pts.}, t\,(\theta)\times\rho)$
	$N_\theta \times N_\rho$	total	CPU (msec)	CPU/point (μsec)	relative error	$N_{t\,(\theta)} \times N_\rho$	total	CPU (msec)	CPU/point (μsec)	relative error	
(0, 0)	8×3	96	2.8	29	4×10^{-7}	5×3	60	1.8	30	2×10^{-7}	1.6	5.3283998×10^{-2}
(1, 0)	9×3	81	2.4	30	3×10^{-7}	5×3	45	1.4	30	6×10^{-8}	1.8	8.1962173×10^{-2}
(1, 1)	7×3	42	1.3	30	5×10^{-8}	4×3	24	0.75	31	9×10^{-7}	1.8	2.7602986×10^{-1}
(0, 1)	9×3	81	2.4	30	3×10^{-7}	5×3	45	1.4	30	6×10^{-8}	1.8	8.1962173×10^{-2}

angular integration points by a factor of 1.6~1.8. The extra CPU-time for the angular variable transformation is shown to be negligible.

Fig. 9.5 shows the relative error against the number of radial integration points, and Fig. 9.6 shows the relative error against the number of integration points in the angular variables θ and $t(\theta)$, for the case of $\mathbf{x}_s = \mathbf{x}(0, 0)$.

Next, the effect of the position of the source point $\mathbf{x}_s$, on the efficiency of the numerical integration is investigated. Moving the source point $\mathbf{x}_s = \mathbf{x}(\bar{\eta}, \bar{\eta})$ from $\bar{\eta} = 0$ to $\bar{\eta} = 1.0$ along the diagonal of the planar square element, Table 9.3 shows the minimum number of integration points N_ρ, N_θ and $N_{t(\theta)}$ in each variable to achieve a relative error less than 10^{-6}, for the integrals $\int_S \phi_{ij} u^* \, dS$, $(i, j = -1, 0, 1)$. Fig. 9.7 shows the number of angular integration points N_θ using the ordinary angular variable θ, and $N_{t(\theta)}$ using the transformed angular variable $t(\theta)$ against $\bar{\eta}$, which indicates the position of the source point $\mathbf{x}_s = \mathbf{x}(\bar{\eta}, \bar{\eta})$ along the diagonal of the element.

It is evident that as the source point approaches the corner (or edge) of the element the number of angular integration points N_θ increases rapidly. This is due to the angular near singularity mentioned in section 5.6. This problem is overcome by introducing the angular variable transformation $t(\theta)$ of equation (5.130), which weakens the near singularity in the angular variable θ. Table 9.3 and Fig. 9.7 show that the transformation $t(\theta)$ is robust against the change of position of the source point in the element, and that the number of integration points (, and hence the CPU-time,) can be reduced by a factor of more than 6 by integrating in the transformed variable $t(\theta)$ instead of θ, as the source point approaches the corner of the element ($\bar{\eta} > 0.9$). Hence, this angular transformation $t(\theta)$ becomes particularly useful when using discontinuous elements, which employ source points near the edge or corner of the element.

For the case $\mathbf{x}_s = \mathbf{x}(0.9, 0.9)$ (or $\bar{\eta} = 0.9$ in Table 9.3), the maximum relative error (for $i, j = -1, 0, 1$) is plotted against the number of radial integration points

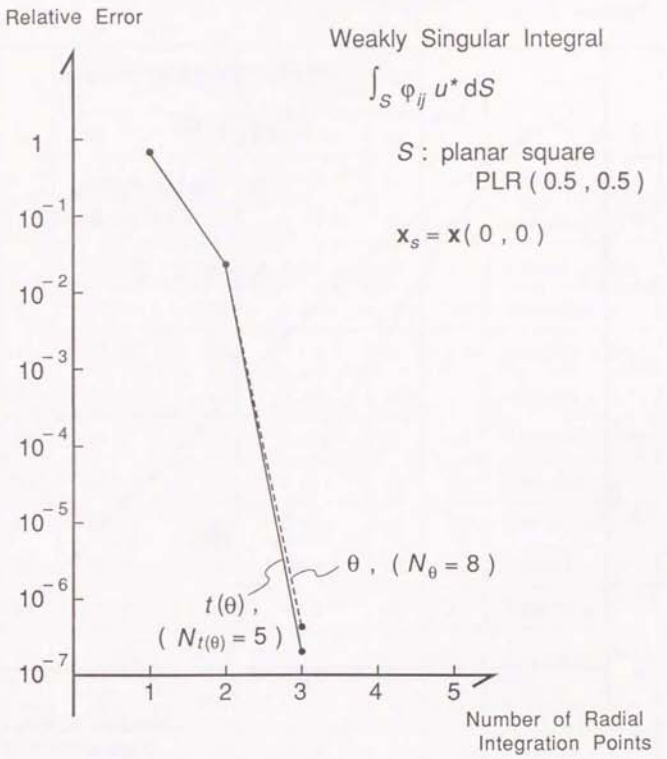

Fig. 9.5 Relative error vs. Number of radial integration points

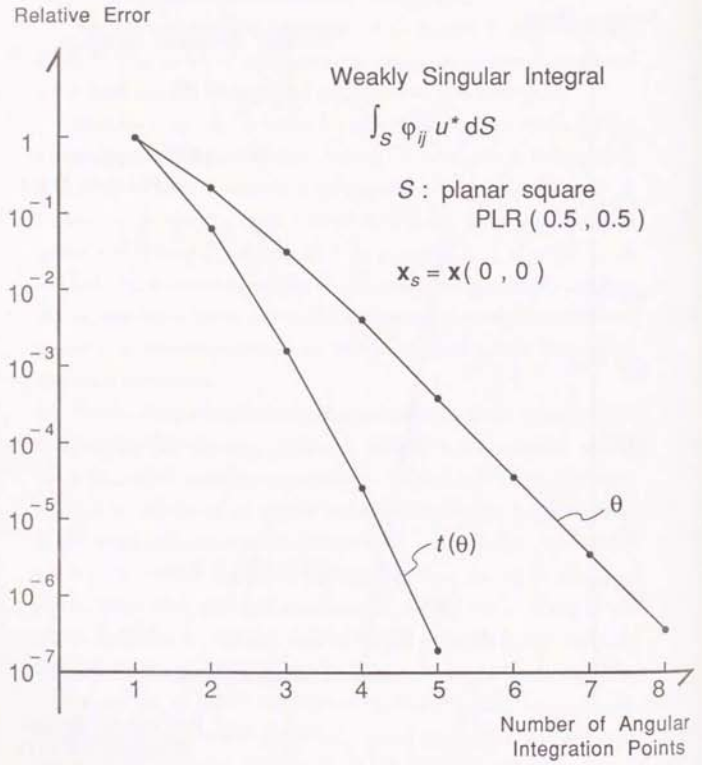

Fig. 9.6 Relative error vs. Number of angular integration points

Table 9.3 Weakly singular integral $\int_S \phi_{ij} u^* dS$ over the unit planar square: PLR(0.5, 0.5) (effect of position of source point)

$\tilde{\eta}$	Polar Coordinates (ρ, θ)		Angular Transformation ($\rho, t(\theta)$)		$\frac{N_\theta}{N_{t(\theta)}}$	Integral $4\pi\int_S \phi_{11}\, u^*\, dS$ (128×128pts., $t(\theta)\times\rho$)
	$N_\theta \times N_\rho$	total	$N_{t(\theta)} \times N_\rho$	total		
0	8×3	96	5×3	60	1.6	5.3283998×10^{-2}
0.2	9×3	108	5×3	60	1.8	9.5485251×10^{-2}
0.4	12×3	144	6×3	72	2.0	1.8719597×10^{-1}
0.6	16×3	192	6×3	72	2.7	3.2822709×10^{-1}
0.8	25×3	300	7×3	84	3.6	4.6027876×10^{-1}
0.9	40×3	480	7×3	84	5.7	4.6096971×10^{-1}
0.92	45×3	540	8×3	96	5.6	4.4780849×10^{-1}
0.94	50×3	600	8×3	96	6.3	4.2744234×10^{-1}
0.96	55×3	660	8×3	96	6.9	3.9746827×10^{-1}
0.98	80×3	960	8×3	96	10	3.5329583×10^{-1}
0.99	100×3	1,200	8×3	96	13	3.2243822×10^{-1}
0.995	$(128) \times 3$ $\varepsilon = 2\times10^{-6}$	(1,536)	8×3	96	(16)	3.0295234×10^{-1}
0.999	$(128) \times 3$ $\varepsilon = 5\times10^{-4}$	(1,536)	8×3	96	(16)	2.8307336×10^{-1}
1.0	7×3	42	4×3	24	1.8	2.7602986×10^{-1}

Position of source point: $\mathbf{x}_s = \mathbf{x}(\tilde{\eta}, \tilde{\eta})$. Relative error $\varepsilon < 10^{-6}$.

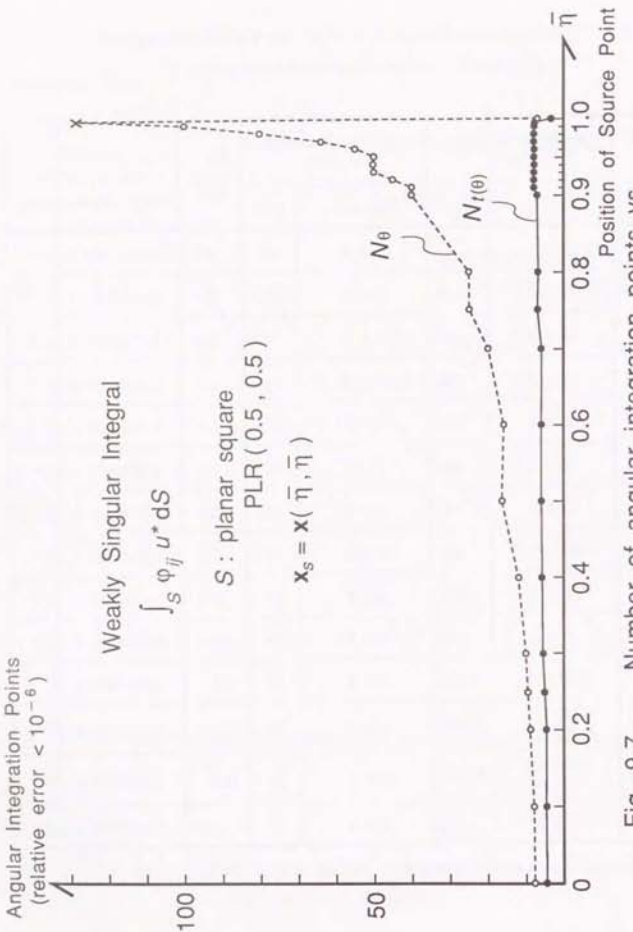

Fig. 9.7 Number of angular integration points vs. Position of source point

in Fig. 9.8, and against the number of angular integration points in Fig. 9.9, respectively.

Comparing Fig.9.6 ($\bar{\eta}=0$) with Fig. 9.9 ($\bar{\eta}=0.9$), the angular near singularity and the effect of the angular variable transformation $t(\theta)$ is more pronounced in the latter ($\bar{\eta}=0.9$).

Next, the effect of the aspect ratio b/a of the planar rectangular element PLR (a, b), on the efficiency of the numerical integration is investigated. Setting $a=0.5$ constant, b is varied from 0.5 to 5, so that the aspect ratio ranges from 1 to 10 . In each case, the minimum number of integration points required to achieve relative errors less than 10^{-6} for $i,j=-1,0,1$ for the integral $\int_S \phi_{ij} u^* dS$ by the method of polar coordinates (ρ, θ) and the method using the angular variable transformation (ρ, $t(\theta)$), in Table 9.4. Fig. 9.10 gives the convergence graph of the maximum relative error for $i,j=-1,0,1$ vs. the number of integration points in the angular variable, for the case when the aspect ratio is 5 ($a=0.5$, $b=2.5$).

It is evident that as the aspect ratio increases, the number of integration points in the angular variable θ in the method using polar coordinates (ρ, θ) increases rapidly, whereas with the method using the transformed angular variable $t(\theta)$ of equation (5.130) the number of integration points increases very slowly.

From the above numerical experiments on weakly singular integrals $\int_S u^* dS$ and $\int_S \phi_{ij} u^* dS$ over the unit planar square and planar rectangles, the robustness of the angular transformation $t(\theta)$ against the position of the source point and the aspect ratio of the element is verified.

As for the weakly singular integrals $\int_S q^* dS$ and $\int_S \phi_{ij} q^* dS$, results are not given for planar elements, since $(\mathbf{r}, \mathbf{n})=0$ and $q^*=-(\mathbf{r}, \mathbf{n})/(4\pi r^3)=0$ for $r\neq 0$ so that the integrals take the value of zero, excluding the Cauchy principal value, which is defined as the limit as the source distance $d\to 0$ of the corresponding nearly singular integral. This will be mentioned in Chapter 10.

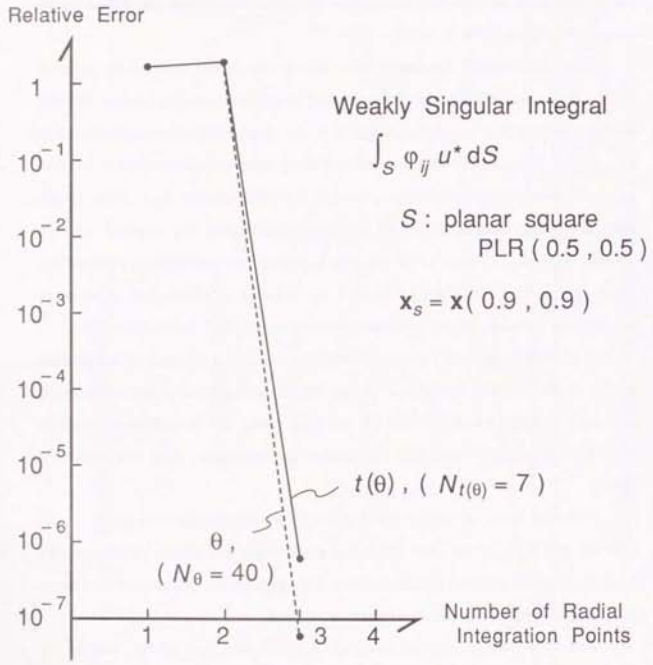

Fig. 9.8 Relative error vs. Number of radial integration points

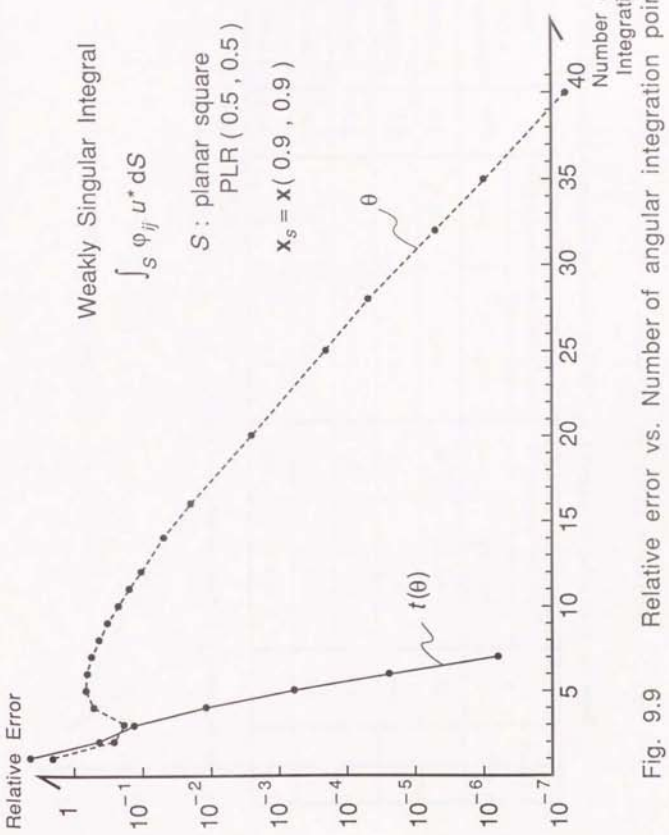

Fig. 9.9 Relative error vs. Number of angular integration points

Table 9.4 Weakly singular integral $\int_S \phi_{ij} u^* \, dS$ over the planar rectangular element : PLR (0.5, b)

Aspect ratio	b	Polar Coordinates (ρ, θ)		Angular Transformation (ρ, $t(\theta)$)		$\frac{N_\theta}{N_{t(\theta)}}$	Integral $4\pi \int_S \phi_{11} u^* \, dS$ (128×128pts., $t(\theta)\times\rho$)
		$N_\theta \times N_\rho$	total	$N_{t(\theta)} \times N_\rho$	total		
1	0.5	8 × 3	96	5 × 3	60	1.6	5.3283998×10^{-2}
2	1.0	11 × 3	132	6 × 3	72	1.8	6.8978324×10^{-2}
3	1.5	14 × 3	168	6 × 3	72	2.3	7.4886094×10^{-2}
5	2.5	20 × 3	240	7 × 3	84	2.9	7.9307007×10^{-2}
10	5	28 × 3	336	8 × 3	96	3.5	8.1984132×10^{-2}

Source point $x_s = (0, 0, 0)$, relative error $< 10^{-6}$.

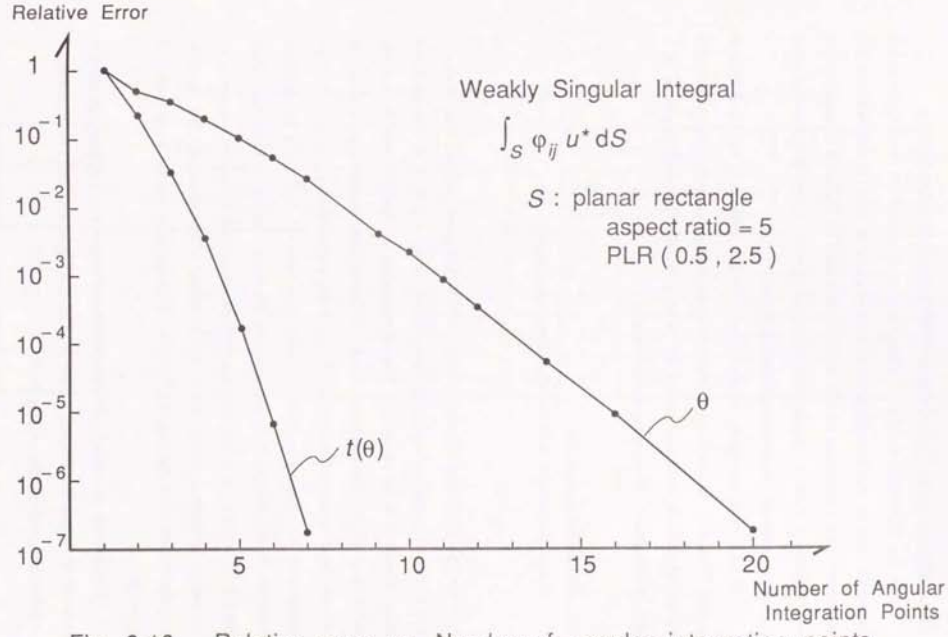

Fig. 9.10 Relative error vs. Number of angular integration points

9.3 'Spherical' Quadrilateral Element with Interpolation Function ϕ_{ij}

In the following, results of numerical experiments on weakly singular integrals over curved boundary elements are given in order to demonstrate the efficiency and robustness of the method proposed in Chapter 5 using polar coordinates (ρ, θ) in the plane S tangent to the curved element at the source point $\mathbf{x}_s$ and the angular variable transformation $t(\theta)$.

First, numerical results on the element SPQ60 defined in section 8.2 (2) is given. This element is a 9 point Lagrangian element obtained by interpolating a spherical quadrilateral subtending 60° in both the latitude and longitude on a sphere of radius 1. The typical element size is 1.

(1) Results for $\int_S \phi_{ij} u^* \, dS$

Numerical results on the weakly singular integral

$$\int_S \phi_{ij} u^* \, dS \quad , \quad (i,j=-1,0,1) \tag{9.16}$$

over the 'spherical' quadrilateral element SPQ60 are given in Table 9.5, where u^* and the 9 point Lagrangian interpolation functions ϕ_{ij}, $(i,j=-1, 0, 1)$ are defined as in equations (9.11) and (9.17). The source point $\mathbf{x}_s$ is set to $\mathbf{x}(0, 0)$, $\mathbf{x}(1, 0)$, $\mathbf{x}(1,1)$ and $\mathbf{x}(0,1)$. The minimum number of Gauss-Legendre integration points to achieve relative errors less than 10^{-6} for all the components ϕ_{ij}, $(i,j=-1, 0, 1)$, using polar coordinates (ρ, θ) in the tangential plane S, and using the angular variable transformation $t(\theta)$ are given in the table, similar to Table 9.2. This time, 5~7 integration points are required (compared to 3 for planar elements) in the radial variable ρ, due to the curved geometry of the element. The angular transformation $t(\theta)$ reduces the number of integration points by a factor of 1.3~1.7.

For the case $\mathbf{x}_s = \mathbf{x}(0, 0)$, the (maximum) relative error is plotted against the number of radial integration points in Fig. 9.11 and against the number of angular integration points in Fig. 9.12.

Table 9.5 Weakly singular integral $\int_S \phi_{ij} u^* \, dS$ over a 'spherical' quadrilateral: SPQ60

Source point (η_1, η_2)	Polar Coordinates (ρ, θ)					Angular Transformation $(\rho, t(\theta))$					$\frac{N_\theta}{N_{t(\theta)}}$	Integral $4\pi \int_S \phi_{11} u^* \, dS$ $(128\times128\text{pts.}, t(\theta)\times\rho)$
	$N_\theta \times N_\rho$	total	CPU (msec)	CPU/point (μsec)	relative error	$N_{t(\theta)} \times N_\rho$	total	CPU (msec)	CPU/point (μsec)	relative error		
(0,0)	8×5	160	4.4	28	1×10^{-7}	6×5	120	3.4	28	7×10^{-7}	1.3	5.6759090×10^{-2}
(1,0)	8×6	144	4.0	28	3×10^{-7}	6×6	108	3.0	28	2×10^{-7}	1.3	8.5749232×10^{-2}
(1,1)	7×7	98	2.8	29	4×10^{-7}	6×7	84	2.4	29	2×10^{-7}	1.2	2.8827304×10^{-1}
(0,1)	10×6	180	5.0	28	3×10^{-7}	6×6	108	3.0	28	3×10^{-7}	1.7	9.3577679×10^{-2}

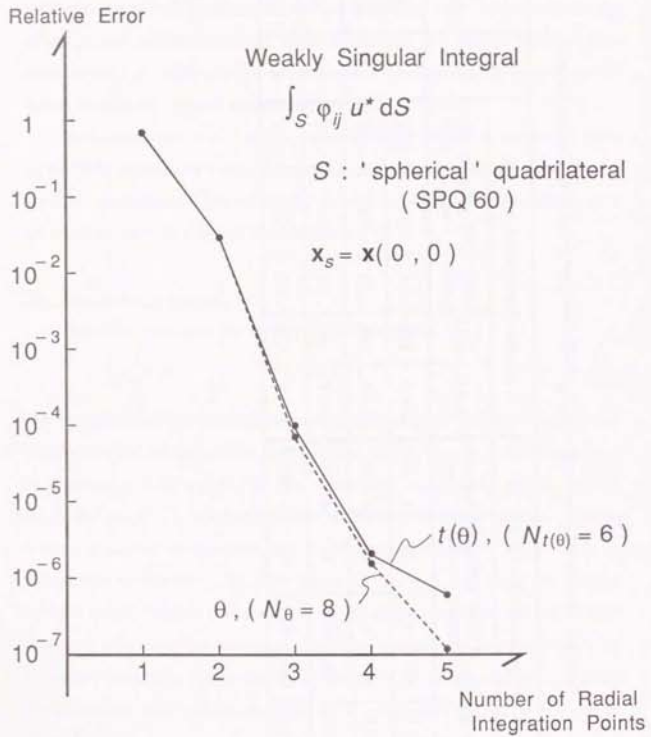

Fig. 9.11 Relative error vs. Number of radial integration points

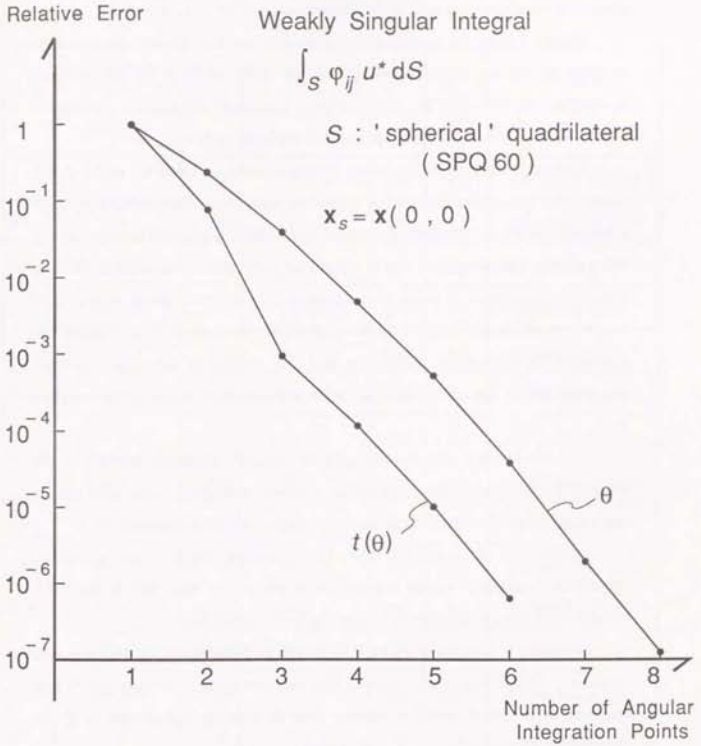

Fig. 9.12 Relative error vs. Number of angular integration points

Next, the effect of the position of the source point $\mathbf{x}_s$ is investigated by moving it along the 'diagonal' of the element i.e. $\mathbf{x}_s=\mathbf{x}(\bar{\eta}, \bar{\eta})$, $0 \leqq \bar{\eta} \leqq 1$.

Table 9.6 gives the number of integration points N_ρ, N_θ and $N_{t(\theta)}$ in each variable to obtain a maximum relative error less than 10^{-6}, for the integrals $\int_S \phi_i \phi_j u^* \, dS$, $(i, j=-1, 0, 1)$. Fig. 9.13 plots the number of angular integration points N_θ and $N_{t(\theta)}$ against the position of the source point $\bar{\eta}$.

Similar to the case of the planar square element in Table 9.3 and Fig. 9.7, the number of angular integration points N_θ using just polar coordinates (ρ, θ) increases rapidly as the source point approaches the corner of the element $(\bar{\eta} \to 1)$. The angular transformation $t(\theta)$ of equation (5.130) has a remarkable effect in reducing the number of angular integration points. The graph of Fig. 9.13 roughly traces that of Fig. 9.7 for the planar square element except that at the maximum 14 integration points are required for $t(\theta)$ in the spherical case, compared to 8 in the planar case, to obtain a maximum relative error less than 10^{-6}.

Also the number of radial integration points N_ρ increases slightly as the source point approaches the corner of the element, which was not seen for planar elements. This is considered to be due to the curvature of the element.

For the case of $\mathbf{x}_s=\mathbf{x}(0.9, 0.9)$, the maximum relative error is plotted against the number of radial integration points in Fig. 9.14, and against the number of angular integration points in Fig. 9.15, respectively.

Compared to the case of $\mathbf{x}_s=\mathbf{x}(0, 0)$ in Fig. 9.11 and Fig. 9.12, the necessary number of radial integration points (for relative error less than 10^{-6}) has increased from 5 to 7, and the angular near singularity and the effect of the angular variable transformation $t(\theta)$ is more pronounced.

Table 9.6 Weakly singular integral $\int_S \phi_i \phi_j u^* \, dS$ over a 'spherical' quadrilateral : SPQ60 (effect of position of source point)

$\bar{\eta}$	Polar Coordinates (ρ, θ)		Angular Transformation $(\rho, t(\theta))$		$\frac{N_\theta}{N_{t(\theta)}}$	Integral $4\pi \int_S \phi_{11} u^* \, dS$ $(128\times128\text{pts.}, t(\theta)\times\rho)$
	$N_\theta \times N_\rho$	total	$N_{t(\theta)} \times N_\rho$	total		
0	8 × 5	160	6 × 5	120	1.3	5.6759090×10^{-2}
0.2	9 × 5	180	7 × 5	140	1.1	7.2742430×10^{-2}
0.4	11 × 5	220	8 × 5	160	1.4	1.9162439×10^{-1}
0.6	16 × 6	384	10 × 6	240	1.6	3.3693243×10^{-1}
0.8	20 × 7	560	11 × 6	264	2.1	4.7758224×10^{-1}
0.9	40 × 7	1,120	14 × 7	392	2.9	4.8092765×10^{-1}
0.92	50 × 9	1,800	14 × 7	392	3.5	4.6761673×10^{-1}
0.94	50 × 7	1,400	14 × 7	392	3.6	4.4668974×10^{-1}
0.96	45 × 7	1,260	14 × 7	392	3.2	4.1559238×10^{-1}
0.98	64 × 7	1,792	12 × 7	336	5.3	3.6945555×10^{-1}
0.99	90 × 7	2,520	14 × 7	392	6.4	3.3709633×10^{-1}
0.995	120 × 7	3,360	14 × 7	392	8.6	3.1662071×10^{-1}
0.999	(128) × 7	(3,584)	12 × 7	336	(11)	2.9569854×10^{-1}
1.0	7 × 7	98	6 × 7	84	1.2	2.8827304×10^{-1}

Position of source point: $\mathbf{x}_s=\mathbf{x}(\bar{\eta}, \bar{\eta})$. Relative error $\varepsilon < 10^{-6}$.

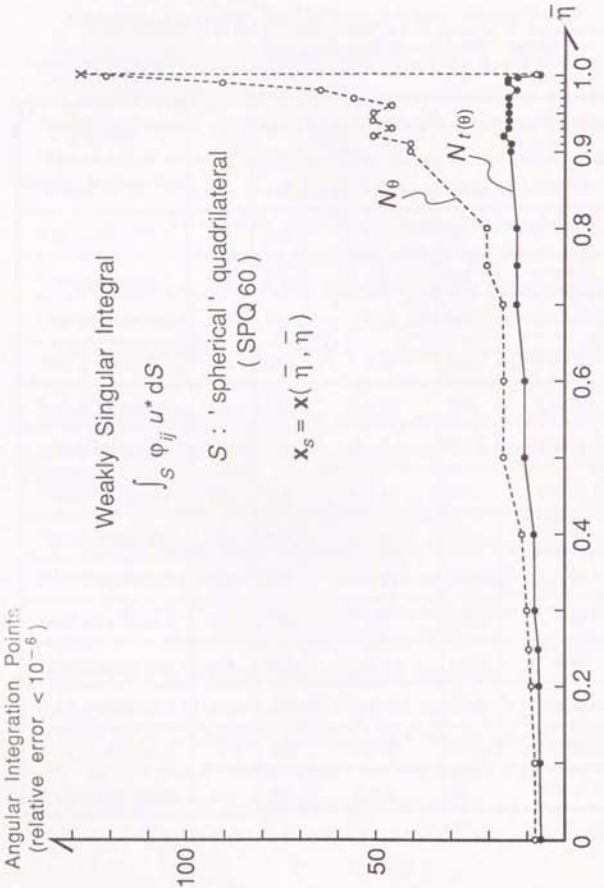

Fig. 9.13 Number of angular integration points vs. Position of source point

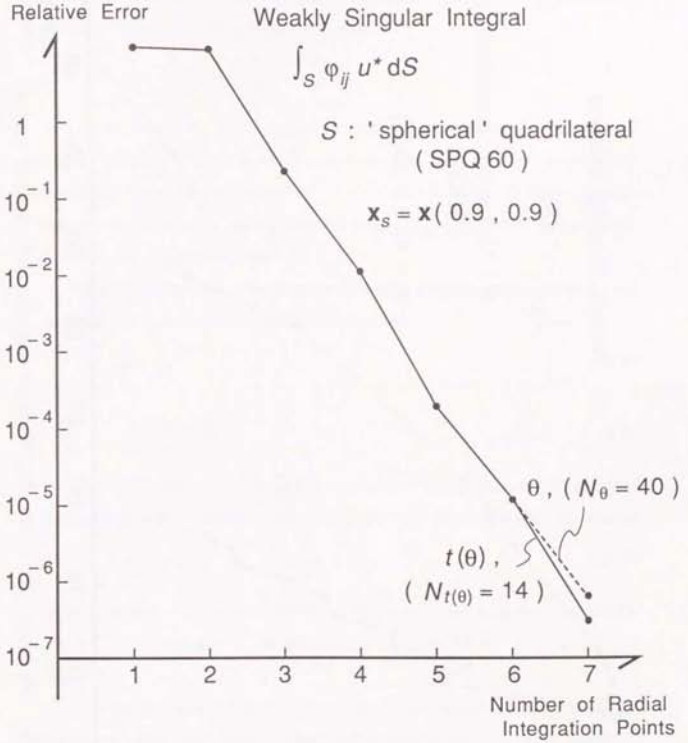

Fig. 9.14 Relative error vs. Number of radial integration points

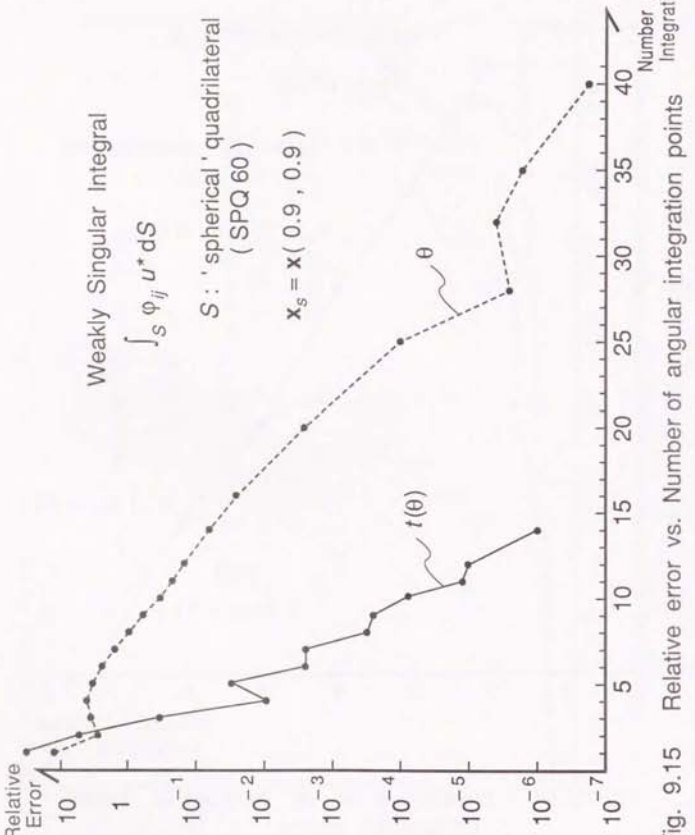

Fig. 9.15 Relative error vs. Number of angular integration points

(2) Results for $\int_S \phi_{ij} q^* \, dS$

For planar elements we had $(\mathbf{r}, \mathbf{n}) \equiv 0$, $r \neq 0$ and hence $q^* \equiv 0$, $r \neq 0$. However, for curved elements, $(\mathbf{r}, \mathbf{n}) \equiv 0$ as shown in Fig. 9.16, so that $q^* \equiv 0$. In fact it was proved in Theorem 3.1 (equation (3.10)) that

$$q^* \equiv -\frac{(\mathbf{r}, \mathbf{n})}{4\pi r^3} \sim -\frac{K_n}{8\pi r} = -\frac{K_n}{2}\, u^* \tag{9.19}$$

for $0 < r \ll 1$, where K_n is the normal curvature at $\mathbf{x} = \mathbf{x}_s$. Hence, it is expected that the integration of the weakly singular integral $\int_S \phi_{ij} q^* \, dS$ gives numerical results similar to that of $\int_S \phi_{ij} u^* \, dS$, for curved elements. In the following, numerical results for the weakly singular integral $\int_S \phi_{ij} q^* \, dS$ over the 'spherical' quadrilateral SPQ60 are given.

In all the numerical experiments with weakly singular integrals over curved elements, the unit outward normal $\mathbf{n}$ is defined by

$$\mathbf{n} = \frac{\mathbf{G}}{|\mathbf{G}|} \tag{9.20}$$

where

$$\mathbf{G} = \frac{\partial \mathbf{x}}{\partial \eta_1} \times \frac{\partial \mathbf{x}}{\partial \eta_2} \tag{9.21}$$

Table 9.7 gives the number of integration points N_θ, $N_{t(\theta)}$ and N_ρ required to obtain a maximum relative error less than 10^{-6}, for the weakly singular integral

$$\int_S \phi_{ij} q^* \, dS \quad , \quad (i, j = -1, 0, 1) \tag{9.22}$$

over the 'spherical' quadrilateral SPQ 60. The source point $\mathbf{x}_s$ is chosen as $\mathbf{x}(0, 0)$, $\mathbf{x}(1, 0)$, $\mathbf{x}(1, 1)$ and $\mathbf{x}(0, 1)$. Results similar to Table 9.5 for $\int_S \phi_{ij} u^* \, dS$ are obtained.

For the case $\mathbf{x}_s = \mathbf{x}(0, 0)$, the maximum relative error is plotted against the number of radial and angular integration points in Fig. 9.17 and Fig. 9.18, respectively.

The effect of the position of the source point $\mathbf{x}_s$ is shown in Table 9.8 and Fig. 9.19, similar to Table 9.6 and Fig. 9.13.

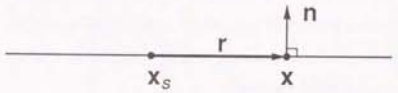

planar element $(\mathbf{r},\mathbf{n}) \equiv 0$

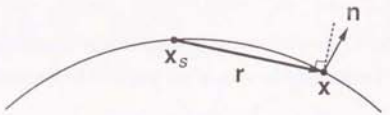

curved element $(\mathbf{r},\mathbf{n}) \not\equiv 0$

Fig. 9.16 $(\mathbf{r},\mathbf{n})$ on planar and curved elements

Table 9.7 Weakly singular integral $\int_S \phi_\theta q^*\,dS$ over the 'spherical' quadrilateral: SPQ60

Source point	Polar Coordinates (ρ,θ)					Angular Transformation $(\rho, t(\theta))$					$\frac{N_\theta}{N_{t(\theta)}}$	Integral $4\pi \int_S \phi_{11}\, u^*\,dS$ $(128\times128\text{pts.}, t(\theta)\times\rho)$
(γ_1,γ_2)	$N_\theta \times N_\rho$	total	CPU (msec)	CPU/point (μsec)	relative error	$N_{t(\theta)}\times N_\rho$	total	CPU (msec)	CPU/point (μsec)	relative error		
(0,0)	8 × 5	160	4.5	28	6×10^{-7}	6 × 4	96	2.8	29	5×10^{-7}	1.3	-2.6807077×10^{-2}
(1,0)	7 × 6	126	3.5	28	7×10^{-7}	6 × 6	108	3.1	29	9×10^{-7}	1.2	-4.0201067×10^{-2}
(1,1)	7 × 6	84	2.4	29	6×10^{-7}	6 × 6	72	2.1	29	4×10^{-7}	1.2	-1.1608845×10^{-1}
(0,1)	10 × 6	180	5.0	28	1×10^{-7}	7 × 5	105	3.0	29	9×10^{-7}	1.4	-4.4071135×10^{-2}

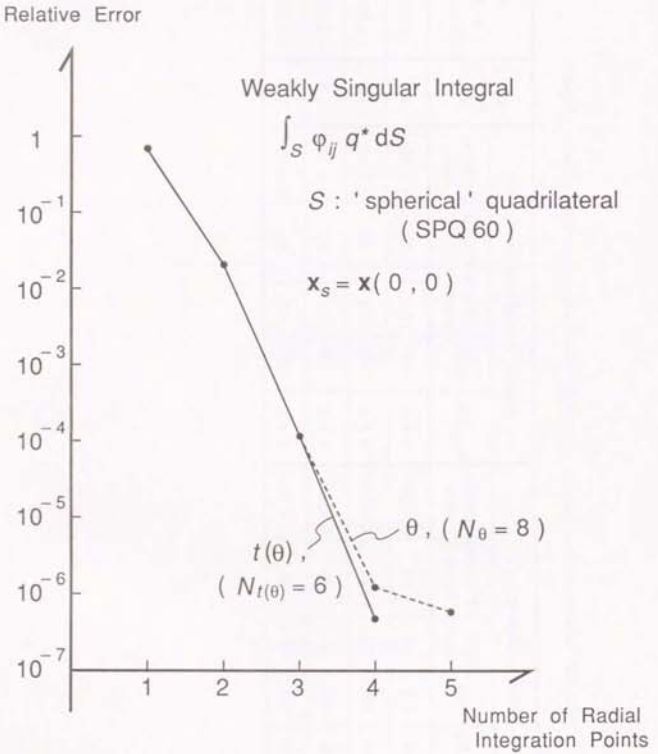

Fig. 9.17 Relative error vs. Number of radial integration points

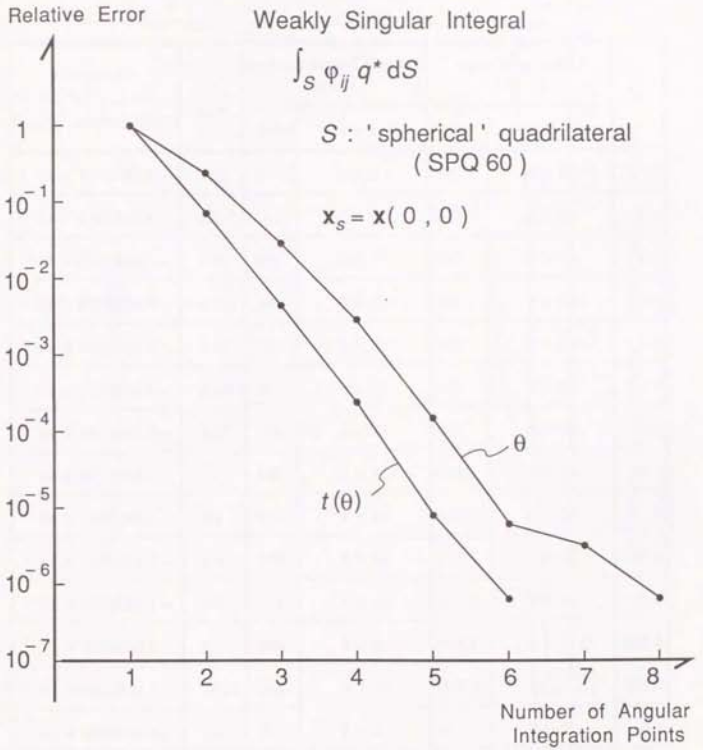

Fig. 9.18 Relative error vs. Number of angular integration points

Table 9.8 Weakly singular integral $\int_S \phi_{ij} q^* \, dS$ over the 'spherical' quadrilateral : SPQ60 (effect of position of source point)

$\bar{\eta}$	Polar Coordinates (ρ, θ)		Angular Transformation $(\rho, t(\theta))$		$\frac{N_\theta}{N_{t(\theta)}}$	Integral $4\pi \int_S \phi_{11} q^* \, dS$ $(128\times128\text{pts.}, t(\theta)\times\rho)$
	$N_\theta \times N_\rho$	total	$N_{t(\theta)} \times N_\rho$	total		
0	8×5	160	6×4	96	1.3	$-2.6807077 \times 10^{-2}$
0.2	10×5	200	7×5	140	1.4	$-4.5622416 \times 10^{-2}$
0.4	12×6	288	9×5	180	1.3	$-8.6645831 \times 10^{-2}$
0.6	20×6	480	11×6	264	1.8	$-1.4822399 \times 10^{-1}$
0.8	25×6	600	12×6	288	2.1	$-2.0071886 \times 10^{-1}$
0.9	40×6	960	14×6	336	2.9	$-1.9613109 \times 10^{-1}$
0.92	40×6	960	14×6	336	2.9	$-1.8953344 \times 10^{-1}$
0.94	45×6	1,080	11×6	264	4.1	$-1.8000174 \times 10^{-1}$
0.96	55×6	1,320	14×6	336	3.9	$-1.6664471 \times 10^{-1}$
0.98	72×6	1,728	14×6	336	5.1	$-1.4774935 \times 10^{-1}$
0.99	90×7	2,520	14×6	336	6.4	$-1.3492079 \times 10^{-1}$
0.995	110×6	2,640	14×6	336	7.9	$-1.2694574 \times 10^{-1}$
0.999	$(128) \times 6$ $\varepsilon = 3 \times 10^{-4}$	(3,072)	10×6	240	(13)	$-1.1890655 \times 10^{-1}$
1.0	7×6	84	6×6	72	1.2	$-1.1608845 \times 10^{-1}$

Position of source point: $\mathbf{x}_s = \mathbf{x}(\bar{\eta}, \bar{\eta})$. Relative error $\varepsilon < 10^{-6}$.

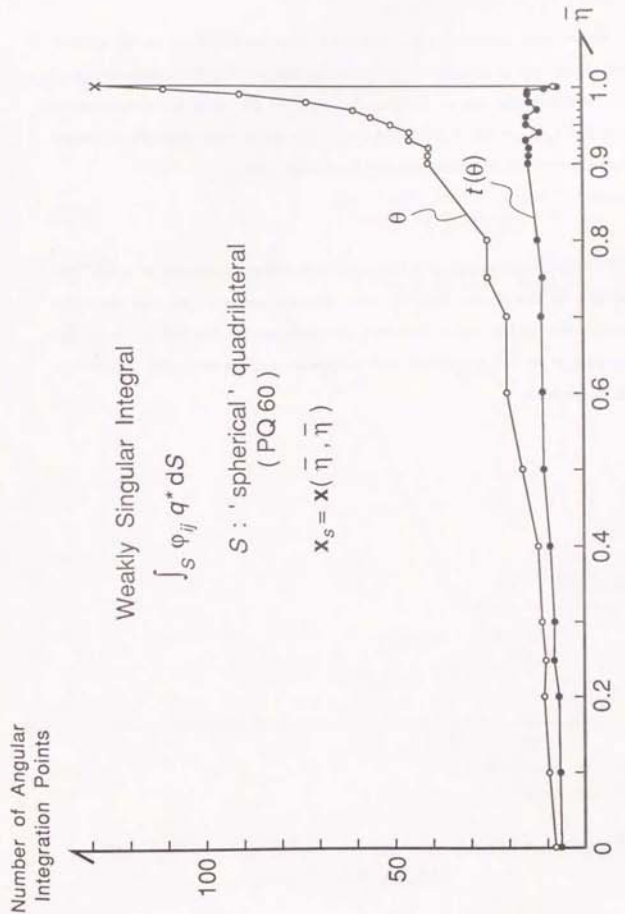

Fig. 9.19 Number of angular integration points vs. Position of source point

For the case $x_s = x(0.9, 0.9)$, the relative error is plotted against the number of radial and angular integration points in Fig. 9.20 and Fig. 9.21, respectively.

Comparing the results obtained for $\int_S \phi_{ij}\, q^*\, dS$ with the corresponding results for $\int_S \phi_{ij}\, u^*\, dS$, it is observed that they show very close resemblances. This can be explained by the resemblance of the kernels

$$q^* \sim -\frac{K_n}{2}\, u^* \qquad for \quad 0 < r \ll 1 \tag{9.23}$$

(cf. Theorem 3.1 and equation (9.19)), and the fact that the kernels u^* and q^* are dominant in the region $0<r\ll 1$ near the source point x_s, so that the characteristics in the region $0<r\ll 1$ are reflected in the behaviour of the integrals $\int_S \phi_{ij}\, u^*\, dS$, $\int_S \phi_{ij}\, q^*\, dS$, and the precision of the numerical integration methods for them.

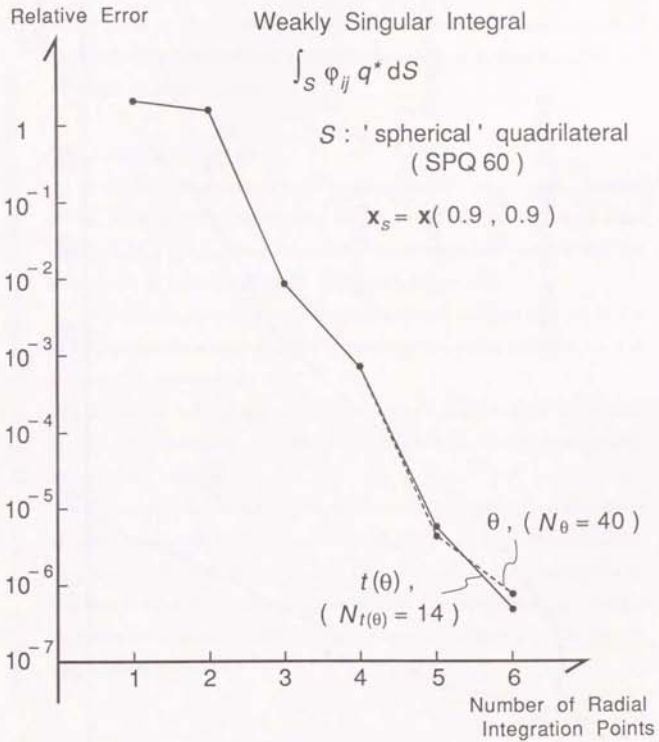

Fig. 9.20 Relative error vs. Number of radial integration points

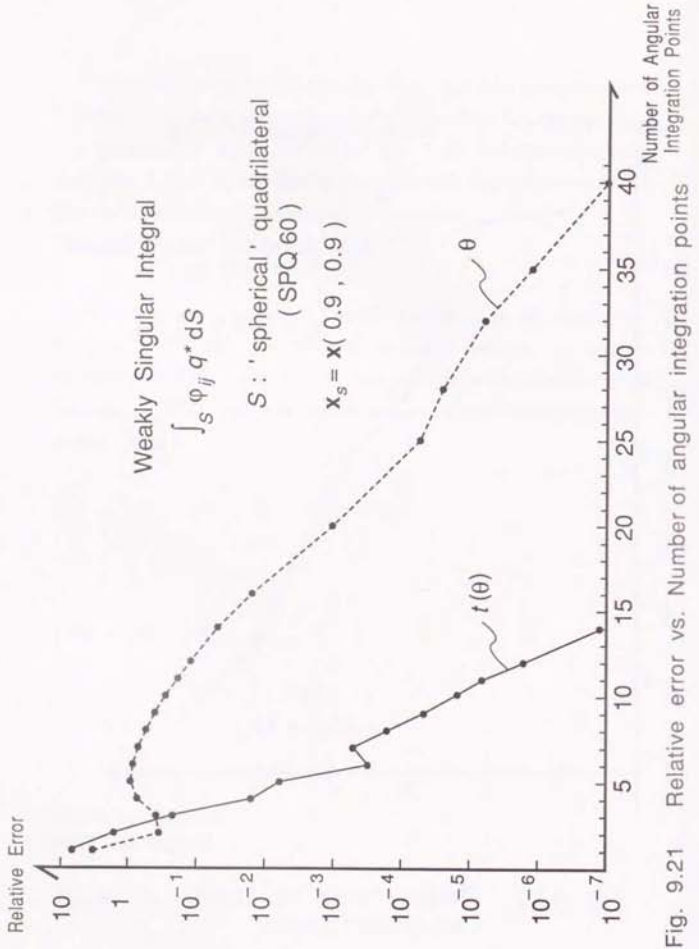

Fig. 9.21 Relative error vs. Number of angular integration points

9.4 Hyperbolic Quadrilateral Element with Interpolation Function ϕ_{ij}

As another type of curved element, numerical experiment results on the hyperbolic quadrilateral element HYQ1 defined in equation (8.15) of section 8.2 (3) are given in order to show the efficiency and robustness against element geometry, of the method of polar coordinates with the angular transformation $t(\theta)$ for weakly singular integrals.

(1) Results for $\int_S \phi_{ij}\, u^*\, dS$

Table 9.9 gives the number of integration points N_θ, $N_{t(\theta)}$ and N_ρ, required to obtain a maximum relative error less than 10^{-6} for the weakly singular integral $\int_S \phi_{ij}\, u^*\, dS$, $(i, j = -1, 0, 1)$ over the hyperbolic quadrilateral HYQ1. The source point $\mathbf{x}_s$ is located at $\mathbf{x}(0, 0)$, $\mathbf{x}(1, 0)$, $\mathbf{x}(1, 1)$ and $\mathbf{x}(0, 1)$.

For the case $\mathbf{x}_s = \mathbf{x}(0, 0)$, the maximum relative error for $i, j = -1, 0, 1$ is plotted against the number of radial and angular integration points in Fig. 9.22 and Fig. 9.23, respectively.

Table 9.10 and Fig. 9.24 show the effect of the position of the source point $\mathbf{x}_s = \mathbf{x}(\bar{\eta}, \bar{\eta})$, $\bar{\eta} = 0 \to 1$, on the numerical integration and compare the use of θ and $t(\theta)$ as the angular variable.

For the case $\mathbf{x}_s = \mathbf{x}(0.9, 0.9)$, the relative error is plotted against the number of radial and angular integration points in Fig. 9.25 and Fig. 9.26, respectively. Compared to the case $\mathbf{x}_s = \mathbf{x}(0, 0)$, the number of radial integration points N_ρ (required to achieve a relative error less than 10^{-6}) increases from 4 to 7, and the angular near singularity and the effect of the angular variable transformation $t(\theta)$ becomes more pronounced.

Table 9.9 Weakly singular integral $\int_S \phi_{ij} u^* dS$ over the hyperbolic quadrilateral: HYQ1

Source point (η_1, η_2)	Polar Coordinates (ρ, θ)					Angular Transformation ($\rho, t(\theta)$)					$\frac{N_\theta}{N_{t(\theta)}}$	Integral $4\pi \int_S \phi_{11} u^* dS$ (128×128pts., $t(\theta)\times\rho$)
	$N_\theta \times N_\rho$	total	CPU (msec)	CPU/point (μsec)	relative error	$N_{t(\theta)} \times N_\rho$	total	CPU (msec)	CPU/point (μsec)	relative error		
(0, 0)	8×5	160	4.4	28	6×10^{-7}	6×4	96	2.8	29	4×10^{-7}	1.7	5.8486239×10^{-2}
(1, 0)	9×6	162	4.5	28	4×10^{-7}	6×6	108	3.1	28	1×10^{-7}	1.5	8.6850181×10^{-2}
(1, 1)	6×7	84	2.4	28	1×10^{-7}	5×7	70	2.0	29	7×10^{-7}	1.2	2.7591133×10^{-1}
(0, 1)	9×6	162	4.5	28	4×10^{-7}	6×6	108	3.1	28	1×10^{-7}	1.5	8.6850181×10^{-2}

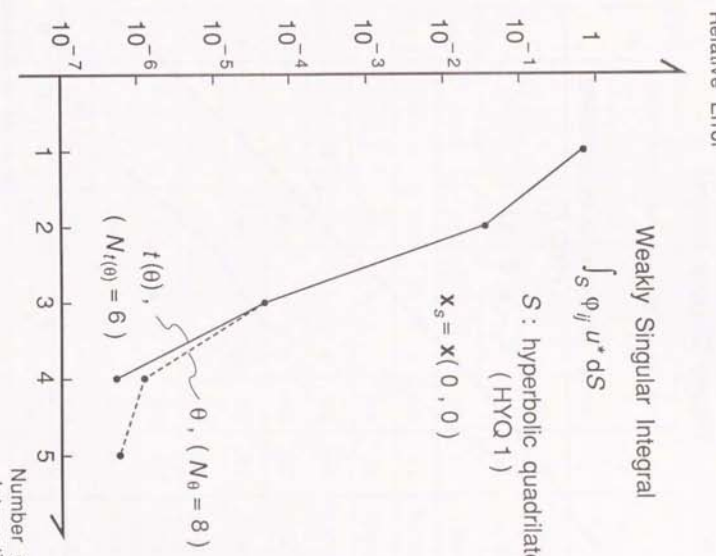

Fig. 9.22 Relative error vs. Number of radial integration points

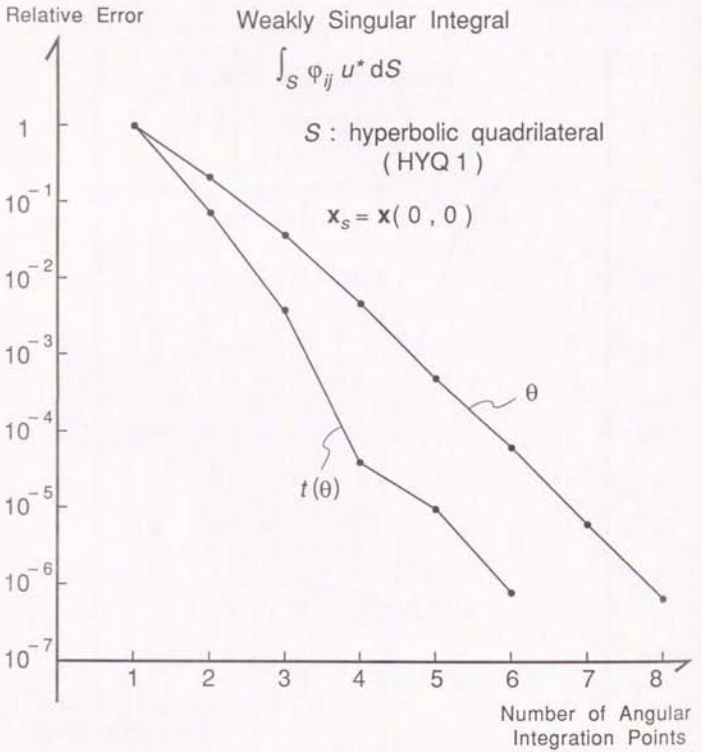

Fig. 9.23 Relative error vs. Number of angular integration points

Table 9.10 Weakly singular integral $\int_S \phi_{ij}\, u^*\, dS$ over the hyperbolic quadrilateral: HYQ1 (effect of position of source point)

$\bar{\eta}$	Polar Coordinates (ρ , θ)		Angular Transformation (ρ , $t(\theta)$)		$\frac{N_\theta}{N_{t(\theta)}}$	Integral $4\pi \int_S \phi_{11}\, u^*\, dS$ (128×128pts., $t(\theta)\times\rho$)
	$N_\theta \times N_\rho$	total	$N_{t(\theta)} \times N_\rho$	total		
0	8 × 5	160	6 × 4	96	1.3	5.8486239×10^{-2}
0.2	10 × 5	200	7 × 5	140	1.4	1.0198064×10^{-1}
0.4	14 × 5	280	7 × 5	140	2.0	1.9736308×10^{-1}
0.6	20 × 6	480	8 × 6	192	2.5	3.4712015×10^{-1}
0.8	25 × 6	600	9 × 6	216	2.8	4.9061557×10^{-1}
0.9	40 × 7	1,120	9 × 7	252	4.4	4.8962891×10^{-1}
0.92	50 × 8	1,600	8 × 7	224	6.3	4.7417784×10^{-1}
0.94	50 × 8	1,600	8 × 8	256	6.3	4.5040850×10^{-1}
0.96	60 × 7	1,680	9 × 7	252	6.7	4.1555278×10^{-1}
0.98	80 × 7	2,240	9 × 7	252	8.9	3.6439300×10^{-1}
0.99	110 × 7	3,080	9 × 7	252	12	3.2883544×10^{-1}
0.995	(128) × 7 $\epsilon = 4\times10^{-6}$	(3,584)	9 × 7	252	(14)	3.0649529×10^{-1}
0.999	(128) × 7 $\epsilon = 6\times10^{-4}$	(3,584)	10 × 7	280	(13)	2.8385477×10^{-1}
1.0	6 × 7	84	5 × 7	70	1.2	2.7591133×10^{-1}

Position of source point: $x_s = x(\bar{\eta}, \bar{\eta})$. Relative error $\epsilon < 10^{-6}$.

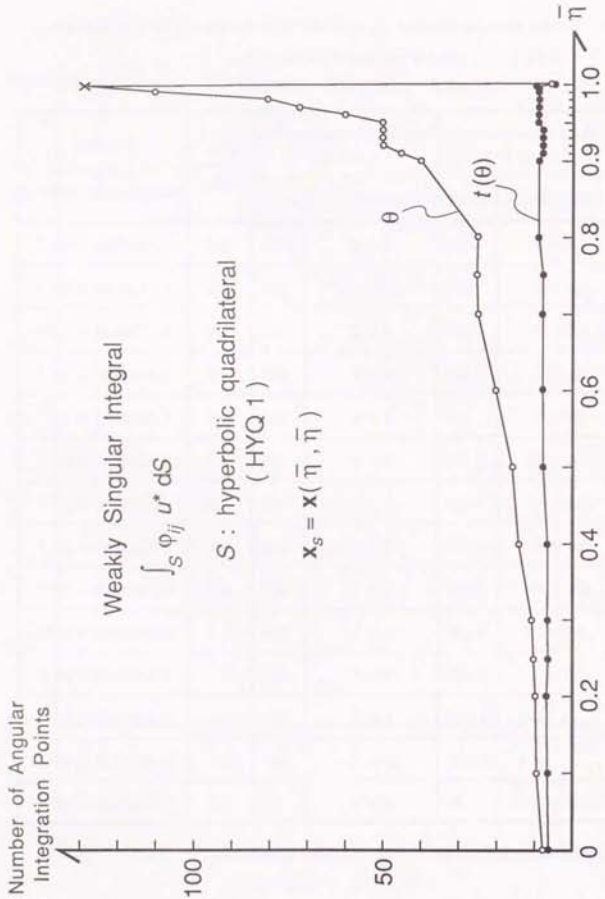

Fig. 9.24 Number of angular integration points vs. Position of source point

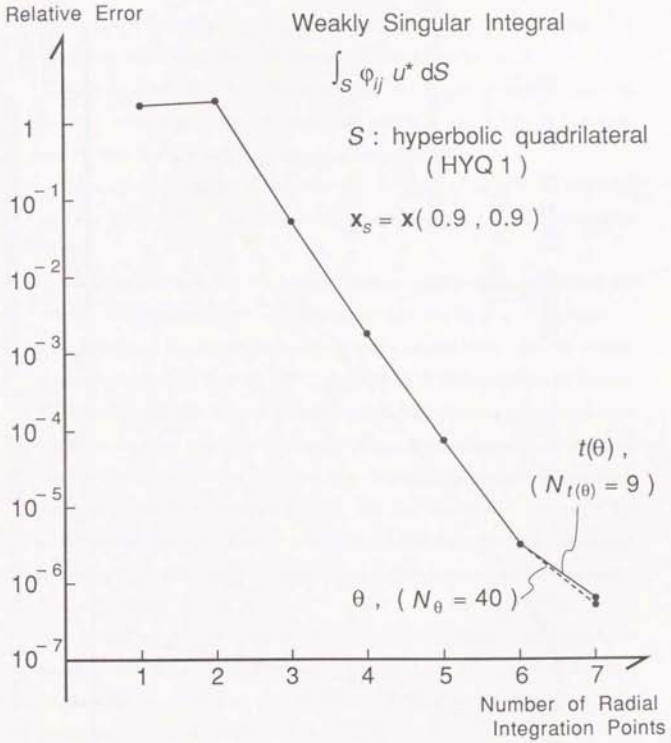

Fig. 9.25 Relative error vs. Number of radial integration points

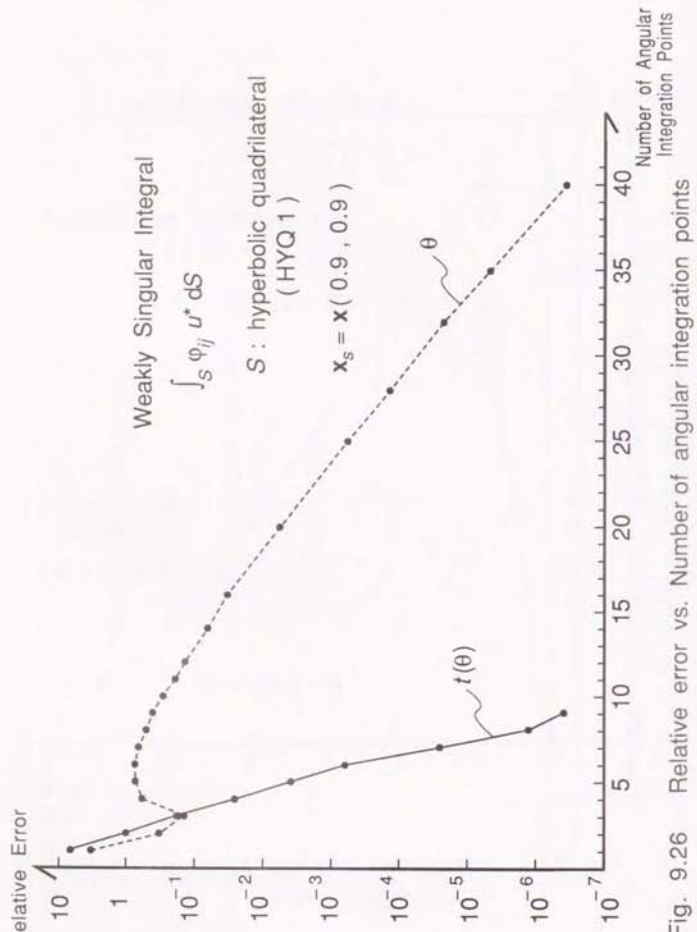

Fig. 9.26 Relative error vs. Number of angular integration points

(2) Results for $\int_S \phi_{ij} q^* \, dS$

Table 9.11 gives the number of integration points required to achieve a relative error less than 10^{-6} for the integral $\int_S \phi_{ij} q^* \, dS$ over the hyperbolic quadrilateral HYQ1 for the same set of source points as in Table 9.9.

For the case $\mathbf{x}_s = \mathbf{x}(0, 0)$, the maximum relative error is plotted aginst the number of radial and angular integration points in Fig. 9.27 and Fig. 9.28, respectively. For this case, N_θ happens to be less than $N_{t(\theta)}$.

Table 9.12 and Fig. 9.29 show the effect of the position of the source point $\mathbf{x}_s = \mathbf{x}(\bar{\eta}, \bar{\eta})$, $\bar{\eta} = 0 \rightarrow 1$, on the numerical integration by the angular variables θ and $t(\theta)$.

For the case $\mathbf{x}_s = \mathbf{x}(0.9, 0.9)$, the relative error is plotted against the number of radial and angular integration points in Fig. 9.30 and Fig. 9.31, respectively.

Results on the hyperbolic quadrilateral element HYQ1 for the weakly singular integrals $\int_S \phi_{ij} u^* \, dS$ and $\int_S \phi_{ij} q^* \, dS$, give similar results as those on the spherical element SPQ60. Namely, the method of using polar coordinates (ρ, θ) on the plane tangent to the element at $\mathbf{x}_s$, works efficiently. However, as the source point approaches the corner of the element, the number of integration points required in θ increases rapidly. On the other hand, the use of the transformed angular variable $t(\theta)$ of equation (5.130) overcomes this problem, i.e. relatively few angular integration points are required even when the source point is near the corner.

Compared to the 'spherical' quadrilateral (SPQ60), the hyperbolic quadrilateral (HYQ1) requires less (9 compared to 14) angular integration points in the variable $t(\theta)$ as $\bar{\eta} \rightarrow 1$ for the integral $\int_S \phi_{ij} u^* \, dS$, and slightly more (16 compared to 14) for the integral $\int_S \phi_{ij} q^* \, dS$.

Table 9.11 Weakly singular integral $\int_S \phi_{ij} q^* \, dS$ over the hyperbolic quadrilateral: HYQ1

Source point (η_1, η_2)	Polar Coordinates (ρ, θ)					Angular Transformation ($\rho, t(\theta)$)					$\frac{N_\theta}{N_{t(\theta)}}$	Integral $4\pi \int_S \phi_{11} u^* \, dS$ (128×128pts., $t(\theta) \times \rho$)
	$N_\theta \times N_\rho$	total	CPU (msec)	CPU/point (μsec)	relative error	$N_{t(\theta)} \times N_\rho$	total	CPU (msec)	CPU/point (μsec)	relative error		
(0, 0)	6×4	96	2.8	29	7×10^{-7}	8×4	128	3.7	29	4×10^{-7}	0.75	5.4181104×10^{-2}
(1, 0)	8×5	120	3.4	28	5×10^{-7}	7×5	105	3.0	29	2×10^{-7}	1.1	$-3.8030661 \times 10^{-2}$
(1, 1)	6×6	72	2.1	29	3×10^{-7}	6×6	72	2.1	29	4×10^{-7}	1.0	5.5451645×10^{-2}
(0, 1)	8×5	120	3.4	28	5×10^{-7}	7×5	105	3.0	29	2×10^{-7}	1.1	$-3.8030661 \times 10^{-2}$

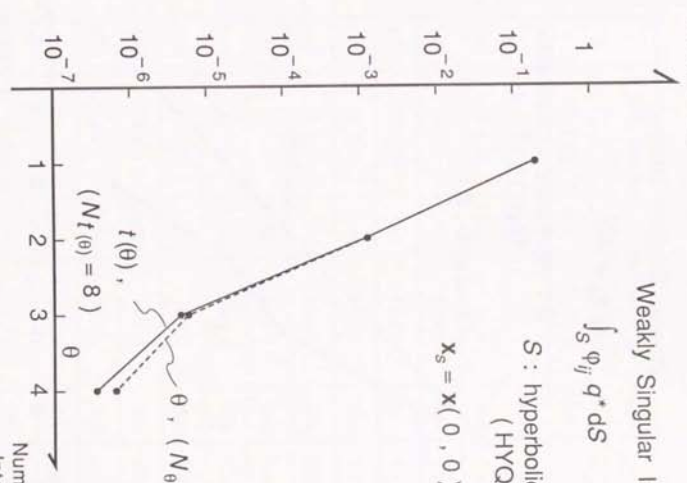

Fig. 9.27 Relative error vs. Number of radial integration points

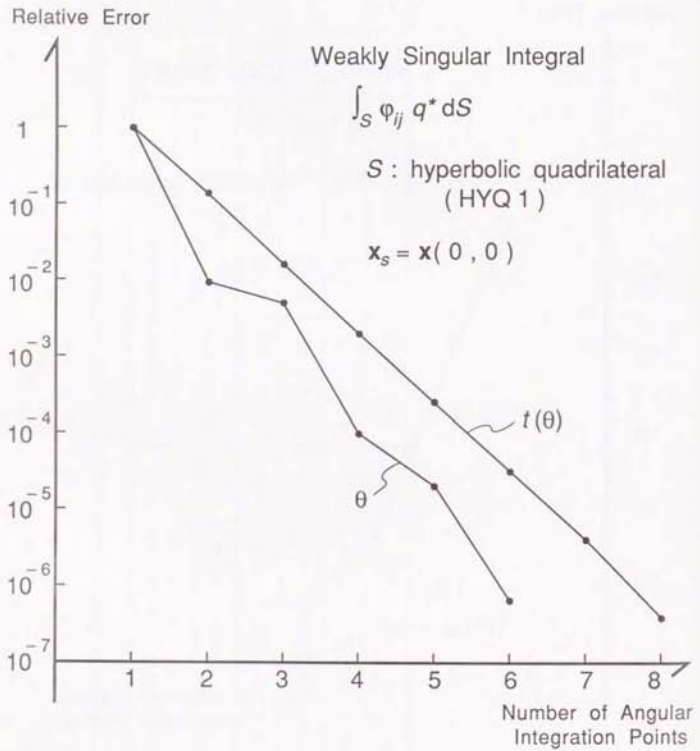

Fig. 9.28 Relative error vs. Number of angular integration points

Table 9.12 Weakly singular integral $\int_S \phi_{ij}\, q^*\, dS$ over the hyperbolic quadrilateral: HYQ1 (effect of position of source point)

$\tilde{\eta}$	Polar Coordinates (ρ, θ)		Angular Transformation ($\rho, t(\theta)$)		$\frac{N_\theta}{N_{t(\theta)}}$	Integral $4\pi \int_S \phi_{11}\, u^*\, dS$ (128×128pts., $t(\theta)\times\rho$)
	$N_\theta \times N_\rho$	total	$N_{t(\theta)} \times N_\rho$	total		
0	6×4	96	8×4	128	0.75	5.4181104×10^{-2}
0.2	9×5	180	9×5	180	1.0	5.6473892×10^{-2}
0.4	10×5	200	10×5	200	1.0	3.9303177×10^{-2}
0.6	16×6	384	12×6	288	1.3	5.2697491×10^{-3}
0.8	25×7	700	12×7	336	2.1	-1.6637769×10^{-2}
0.9	32×7	896	16×6	384	2.0	-1.1809626×10^{-3}
0.92	32×6	896	16×6	384	2.0	5.9762477×10^{-3}
0.94	35×7	980	14×6	336	2.5	1.4922905×10^{-2}
0.96	40×7	1,120	16×6	384	2.5	2.5909095×10^{-2}
0.98	55×6	1,320	14×6	336	3.9	3.9253216×10^{-2}
0.99	64×7	1,792	16×6	384	4.0	4.6947305×10^{-2}
0.995	80×7	2,240	16×6	384	5.0	5.1087330×10^{-2}
0.999	100×7	2,800	16×6	384	6.3	5.4558558×10^{-2}
1.0	6×6	72	6×6	72	1.0	5.5451645×10^{-2}

Position of source point : $x_s = x(\tilde{\gamma}, \tilde{\gamma})$. Relative error $\varepsilon < 10^{-6}$.

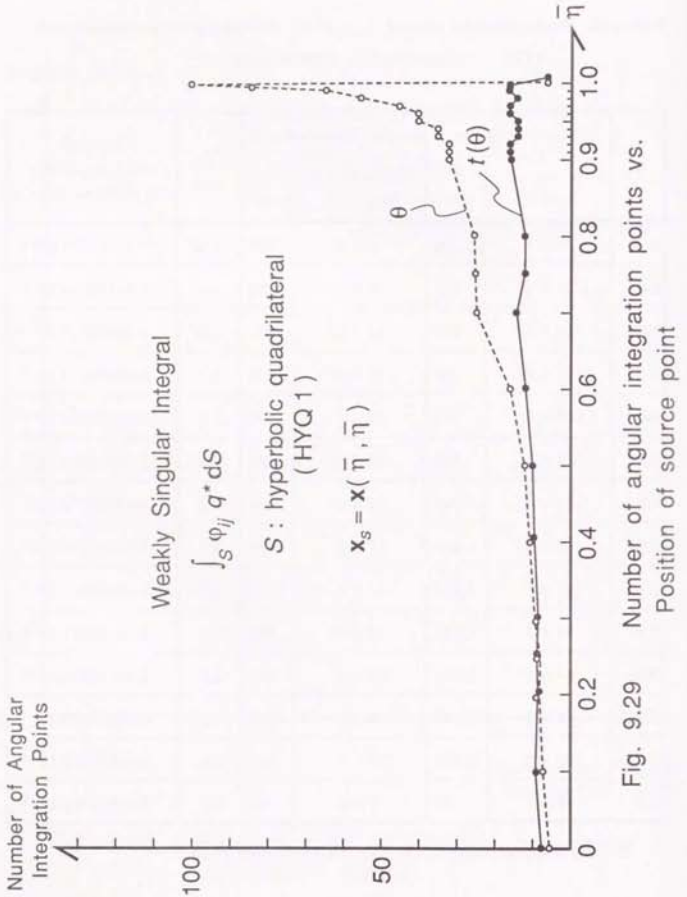

Fig. 9.29 Number of angular integration points vs. Position of source point

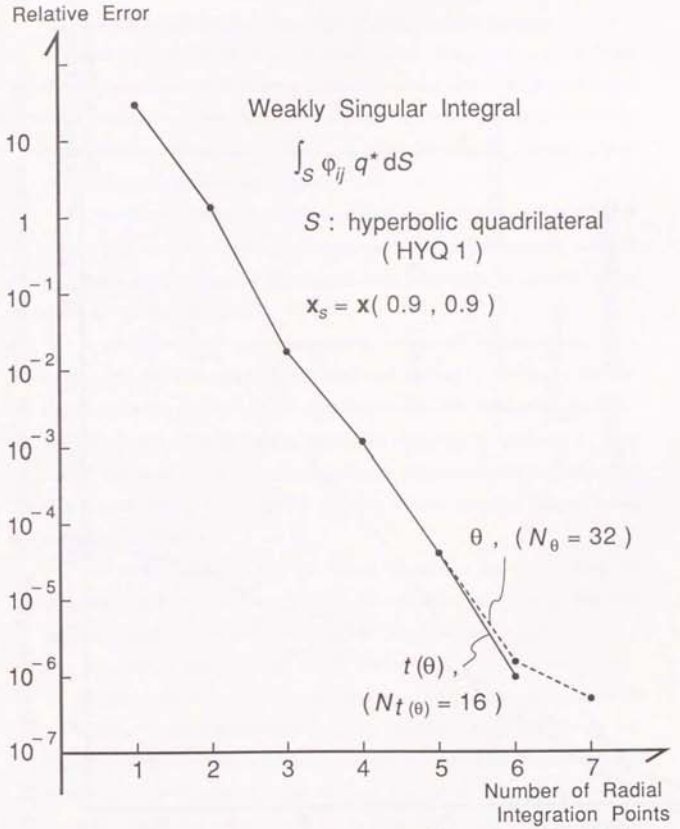

Fig. 9.30 Relative error vs. Number of radial integration points

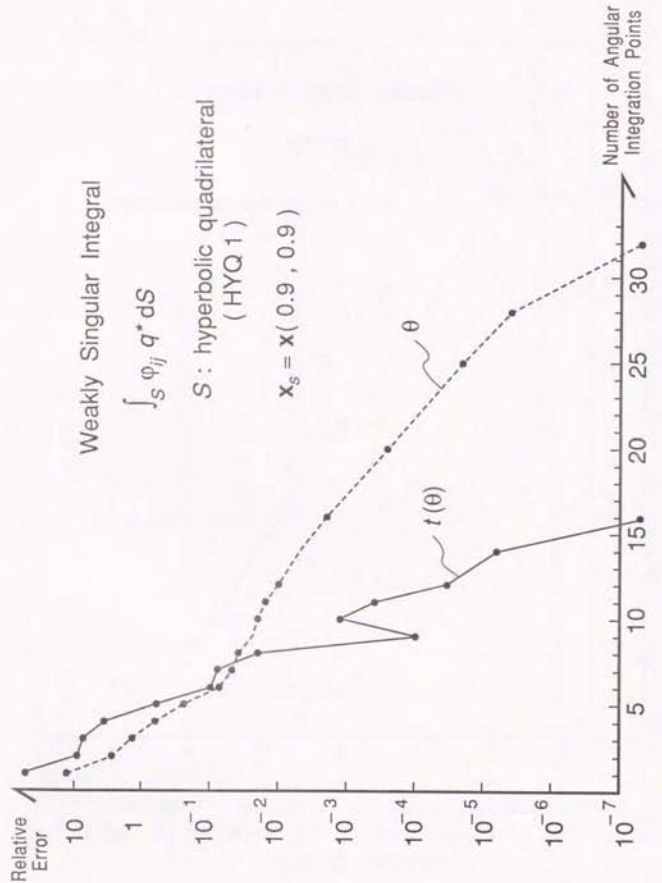

Fig. 9.31 Relative error vs. Number of angular integration points

9.5 Summary of Numerical Results for Weakly Singular Integrals

In this chapter, numerical experiment results were presented to verify the effectiveness of the method of using polar coordinates (ρ, θ) in the plane tangent to the boundary element at the source point $\mathbf{x}_s$, with the angular variable transformation $t(\theta)$ proposed in Chapter 5, for weakly singular integrals arising in three dimensional potential problems.

It was shown that the use of polar coordinates alone[9,15,16] requires excessive number of integration points in the angular variable θ, when the source point $\mathbf{x}_s$ is near the corner or edge of the element as in discontinuous elements, or for elements with high aspect ratio.

It was also shown that the proposed angular variable transformation $t(\theta)$ of equation (5.130) overcomes the above mentioned problem by weakening the near singularity in the angular variable by the transformation. Numerical results for kernels u^* and q^* with 9 point Lagrangian interpolation functions ϕ_{ij} over planar, 'spherical' and hyperbolic quadrilateral elements showed the robustness of the transformation $t(\theta)$ against the position of the source point, integral kernel and element geometry.

The effectiveness of using the radial variable ρ for weakly singular integrals with kernels u^* and q^* with interpolation functions ϕ_{ij} was also verified, in accordance with Theorem 3.1, which implies that

$q^* \sim -K_n/2\ u^* \sim O(1/r) \sim O(1/\rho)$ for $0 < \rho \ll 1$.

Summing up, the use of polar coordinates (ρ, θ) in the tangent plane with the angular variable transformation $t(\theta)$, in combination with the Gauss-Legendre quadrature rule, is a robust and efficient method for the calculation of weakly singular integrals $\int_S \phi_{ij}\, u^*\, dS$ and $\int_S \phi_{ij}\, q^*\, dS$ over general curved elements. Hence, the method can be safely applied to weakly singular integrals which arise in the calculation of H, G matrices for three dimensional boundary element analysis (e.g. potential problem).

Other methods for weakly singular integrals [6, 8, 19, 20] have not been compared with the present method, which gives good enough results, mainly because the stress of this thesis is on nearly singular integrals, which are more difficult to calculate, and also because the present method of polar coordinates with angular variable transformation can be considered as a special case of the proposed PART (Projection and Angular & Radial Transformation) method for nearly singular integrals, indicating a unified approach to weakly singular and nearly singular as well as hyper singular integrals, as will be shown in the following chapters.

CHAPTER 10

APPLICATIONS TO NEARLY SINGULAR INTEGRALS

In this chapter, results of numerical experiments on nearly singular integrals arising in three dimensional potential problems, which is the main interest of this thesis, are presented. The PART (Projection and Angular & Radial Transformation) method proposed in Chapter 5, with its different types of radial variable transformations $R(\rho)$ and the angular transformation $t(\theta)$, will be evaluated.

10.1 Analytical Integration Formula for Constant Planar Elements

First, the analytical integration formula for the integral

$$I_{u^*} = 4\pi \int_S u^* \, dS = \int_S \frac{dS}{r} \tag{10.1}$$

for a constant planar quadrilateral element is presented, so that the numerical integration methods / codes can be checked.

Using polar coordinates (ρ, θ) centered at the source projection $\bar{\mathbf{x}}_s$, in each triangle $\bar{\Delta}_j$, $(j=1\sim4)$, as shown in Figures 5.4, 5.5, 5.8 and 5.10,

$$I_{u^*} = \sum_{j=1}^{4} I_{u^*,j} \tag{10.2}$$

where

$$I_{u^*,j} = \int_0^{\Delta\theta_j} d\theta \int_0^{\rho_j(\theta)} \frac{\rho}{r} \, d\rho \tag{10.3}$$

where

$$r = \sqrt{\rho^2 + d^2} \tag{10.4}$$

for planar elements, where d is the source distance, or the distance of the source point $\mathbf{x}_s$ from the element S.

Since,

$$J_{u^*,j}(\theta) = \int_0^{\rho_j(\theta)} \frac{\rho}{r}\, d\rho$$

$$= \int_0^{\rho_j(\theta)} \frac{\rho}{\sqrt{\rho^2+d^2}}\, d\rho$$

$$= \left[\sqrt{\rho^2+d^2}\right]_0^{\rho_j(\theta)}$$

$$= \sqrt{\rho_j^2(\theta)+d^2} - d$$

$$= \sqrt{\frac{h_j^2}{\cos^2(\theta-\alpha_j)}+d^2} - d \quad , \tag{10.5}$$

where

$$\rho_j(\theta) = \frac{h_j}{\cos(\theta-\alpha_j)} \quad , \tag{10.6}$$

$$I_{u^*,j} = \int_0^{\Delta\theta_j} J_{u^*,j}(\theta)\, d\theta$$

$$= \int_0^{\Delta\theta_j} \frac{\sqrt{h_j^2+d^2\cos^2(\theta-\alpha_j)}}{\cos(\theta-\alpha_j)}\, d\theta - \Delta\theta_j\, d$$

$$= h_j \log\left| \frac{\cos(\Delta\theta_j-\alpha_j)\cdot(h_j\sin\alpha_j+\sqrt{h_j^2+d^2\cos^2\alpha_j})}{\cos\alpha_j\cdot\{-h_j\sin(\Delta\theta_j-\alpha_j)+\sqrt{h_j^2+d^2\cos^2(\Delta\theta_j-\alpha_j)}\}}\right|$$

$$+ d\left[\cos^{-1}\left\{\frac{-d\sin(\Delta\theta_j-\alpha_j)}{\sqrt{h_j^2+d^2}}\right\} - \cos^{-1}\left(\frac{d\sin\alpha_j}{\sqrt{h_j^2+d^2}}\right) - \Delta\theta_j\right] \tag{10.7}$$

for $\mathrm{sgn}(j)\neq 0$. Note that

$$\cos(\Delta\theta_j-\alpha_j) > 0 \quad , \tag{10.8}$$

since

$$-\frac{\pi}{2} < \Delta\theta_j-\alpha_j < \frac{\pi}{2} \quad , \tag{10.9}$$

for $\mathrm{sgn(j)}\neq 0$. $\Delta\theta_j$ can be calculated from

$$\Delta\theta_j = \mathrm{sgn}(j)\cos^{-1}(\cos\Delta\theta_j) \quad , \tag{10.10}$$

where $\cos\Delta\theta_j$ is given by equation (5.26). For $\mathrm{sgn}(j)=0$, $\mathbf{x}_s$ lies on edge-j of $S=\bar{S}$, so that the area of $\bar{\Delta}_j$ becomes zero, i.e. $I_{u^*,j}=0$.

Similarly, for the kernel q^*,

$$I_{q^*} = 4\pi\int_S q^*\, dS$$

$$= -\int_S \frac{(\mathbf{r},\mathbf{n})}{r^3}\, dS$$

$$= \sum_{j=1}^{4} I_{q^*,j} \quad , \tag{10.11}$$

where

$$I_{q^*,j} = \int_0^{\Delta\theta_j} d\theta \int_0^{\rho_j(\theta)} \frac{-d\cdot\rho}{r^3}\, d\rho \tag{10.12}$$

since $(\mathbf{r},\mathbf{n})=d$, where the outward unit normal $\mathbf{n}$ to the planar element S is taken so that $\mathbf{n}$ points to the other side of S regarding the source point $\mathbf{x}_s$.

Since, $r=\sqrt{\rho^2+d^2}$ for planar elements,

$$J_{q^*,j}(\theta) = -d\int_0^{\rho_j(\theta)} \frac{\rho}{r^3}\, d\rho$$

$$= -d\left[-\frac{1}{\sqrt{\rho^2+d^2}}\right]_0^{\rho_j(\theta)}$$

$$= \frac{d}{\sqrt{\rho_j(\theta)^2+d^2}} - 1$$

$$= \frac{d\cos(\theta-\alpha_j)}{\sqrt{h_j^2+d^2\cos^2(\theta-\alpha_j)}} - 1 \quad , \tag{10.13}$$

$$I_{q^*,j}(\theta) = \int_0^{\Delta\theta_j} J_{q^*,j}(\theta)\, d\theta$$

$$= \sin^{-1}\left\{\frac{d\sin(\Delta\theta_j-\alpha_j)}{\sqrt{h_j^2+d^2}}\right\} + \sin^{-1}\left(\frac{d\sin\alpha_j}{\sqrt{h_j^2+d^2}}\right) - \Delta\theta_j \tag{10.14}$$

for $\mathrm{sgn}(j)\neq 0$, where $\Delta\theta_j$ is calculated by equation (10.10).

For $\mathrm{sgn}(j)=0$, $I_{q^*,j}=0$.

It is interesting to note that, from equations (10.11) and (10.14), the limit

$$\lim_{d\to 0_+}\int_S q^*\,\mathrm{d}S = -\frac{1}{4\pi}\sum_{j=1}^{4}\Delta\theta_j = -\frac{1}{2} \tag{10.15}$$

gives the Cauchy principal value of the weakly singular integral $\int_S q^*\,\mathrm{d}S\,;\,d=0$, with the source point $\mathbf{x}_s$ just inside the region V regarding S. This corresponds to equation (2.18) with $\omega=2\pi$, where the limit was taken with the source point $\mathbf{x}_s$ inside a small hemisphere of radius $\varepsilon(\to 0)$. (Refer also to the end of section 9.2.)

10.2 Singularity Cancelling Radial Variable Transformation for Constant Planar Elements

In this section, numerical experimental results are given to show the effectiveness of the singularity cancelling radial variable transformation proposed in Chapter 5:

$$\rho\,\mathrm{d}\rho = r'^{a}\,\mathrm{d}R \tag{5.43}$$

or

$$R(\rho) = \int \frac{\rho}{\sqrt{\rho^2+d^2}^{\,a}}\,\mathrm{d}\rho \quad , \tag{5.45}$$

for calculating the integrals

$$\int_S u^*\,\mathrm{d}S = \frac{1}{4\pi}\int_S \frac{\mathrm{d}S}{r^a} \quad , \quad (a=1) \tag{10.16}$$

and

$$\int_S q^*\,\mathrm{d}S = -\frac{1}{4\pi}\int_S \frac{(\mathbf{r},\mathbf{n})}{r^3} = -\frac{d}{4\pi}\int_S \frac{\mathrm{d}S}{r^a} \quad , \quad (a=3) \tag{10.17}$$

over constant planar elements S, for which

$$r' = \sqrt{\rho^2+d^2} = r \quad . \tag{10.18}$$

From Table 5.1, for $a=1$ we have

$$R(\rho) = \sqrt{\rho^2+d^2} \tag{10.19}$$

and for $a=3$

$$R(\rho) = -\frac{1}{\sqrt{\rho^2+d^2}} \quad . \tag{10.20}$$

As an example, we take the planar square element S : PLR $(-0.5, 0.5)$, which is defined by

$$-0.5 \leq x \leq 0.5\,,\quad -0.5 \leq y \leq 0.5\,,\quad z=0 \quad . \tag{8.24}$$

The element size is 1, so that the source distance d is equivalent to the relative source distance.

The source point $\mathbf{x}_s=(0.25, 0.25, d)$ will be set so that the source projection is always

$$\bar{\mathbf{x}}_s = -(0.25, 0.25, 0) = \mathbf{x}(0.5, 0.5) \qquad (10.21)$$

as shown in Fig. 10.1 , and the source distance d is varied from 10 to 10^{-3} in order to see the effect of the source distance on the difficulty of numerical integration. $\bar{\mathbf{x}}_s$ is set off the centre in order to represent the general unsymmetric case where $\bar{\mathbf{x}}_s \neq \mathbf{x}(0, 0)$.

Numerical integration results for the integral $\int_S u^* \, dS$ using the singularity cancelling radial variable transformation $R(\rho) = \sqrt{\rho^\alpha + d^\alpha}$, $(\alpha = 1)$, with and without the angular variable transformation $t(\theta)$ of equation (5.130) ; the product type Gauss-Legendre formula [3, 38, 39] of equation (4.24) and Telles' cubic transformation method [16] of equation (4.51) are compared in Table 10.1. The minimum number of integration points in each variable required to obtain a relative error less than 10^{-6} is shown. Fig. 10.2 gives the convergence graph of relative error (in log scale) vs. the number of integration points, for the case when the source distance $d = 0.1$.

As shown in Table 9.1, only one radial integration point is required for the integration

$$\int_S u^* \, dS = \frac{1}{4\pi} \int_S \frac{dS}{r^\alpha} \qquad (10.22)$$

when the radial variable transformation

$$R(\rho) = \sqrt{\rho^2 + d^2} \quad , \qquad (10.19)$$

corresponding to

$$\rho \, d\rho = r'^{\alpha} \, dR \quad , \quad (\alpha = 1) \qquad (10.23)$$

is used, irrespective of the source distance d , whereas with the Gauss and Telles' methods increasing number of integration points are required as the source distance decreases. This is because for planar elements, $r = r'$ in equations (5.43) and (5.44), so that the near singularity due to $1/r$ in equation (5.44) and (10.22) is exactly cancelled by the r' in the Jacobian due to the transformation of equation (10.19) and (10.23). In other words, the radial integration is done analytically.

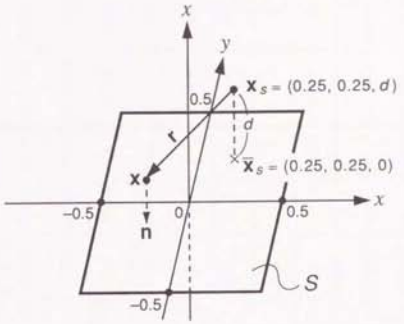

Fig. 10.1 Unit planar square element S and source point $\mathbf{x}_S$

Table 10.1 Nearly singular integral $\int_S u^* \, dS$ over the unit planar square: PLR(0.5, 0.5)

Source distance d	$R(\rho)=\sqrt{\rho^2+d^2}$, $(\alpha=1)$							Gauss			Telles			Integral $4\pi \int_S u^* \, dS$ (analytical)
	Angular variable θ			$t(\theta)$			$\frac{N_\theta}{N_{t(\theta)}}$							
	$N_\theta \times N_R$	total	CPU (msec)	$N_{t(\theta)} \times N_R$	total	CPU (msec)		$N_{\gamma_1} \times N_{\gamma_2}$	total	CPU (msec)	$N_{\gamma_1} \times N_{\gamma_2}$	total	CPU (msec)	
10	10×1	40	1.3	4×1	16	0.68	2.5	2×2	4	0.091	2×2	4	0.29	9.9854681×10^{-2}
3	10×1	40	1.3	5×1	20	0.81	2.0	3×3	9	0.20	3×3	9	0.40	3.2813410×10^{-1}
1	10×1	40	1.3	4×1	16	0.68	2.5	4×5	20	0.44	2×3	6	0.35	8.8974473×10^{-1}
0.3	9×1	36	1.2	5×1	20	0.81	1.8	9×9	81	1.8	6×6	36	0.99	1.8868165
0.1	9×1	36	1.2	5×1	20	0.81	1.8	25×25	625	13	9×10	90	2.2	2.6127678
0.03	9×1	36	1.2	6×1	24	0.92	1.5	64×64	4,096	88	11×11	121	2.8	2.9818223
0.01	9×1	36	1.2	3×1	12	0.57	3.0	160×160	25,600	554	20×20	400	8.8	3.1011123
0.003	9×1	36	1.2	3×1	12	0.57	3.0	250×250	62,500	1,350	35×35	1,225	27	3.1443680
0.001	9×1	36	1.2	3×1	12	0.57	3.0	256×256 $(\varepsilon=2\times10^{-4})$	65,536	1,410	45×50	2,250	49	3.1568704
0	9×1	36	1.2	1×1	4	0.35	9.0	——	—	—	——	—	—	3.1631456

Source point $\mathbf{x}_S=(0.25, 0.25, d)$, relative error $\varepsilon<10^{-6}$

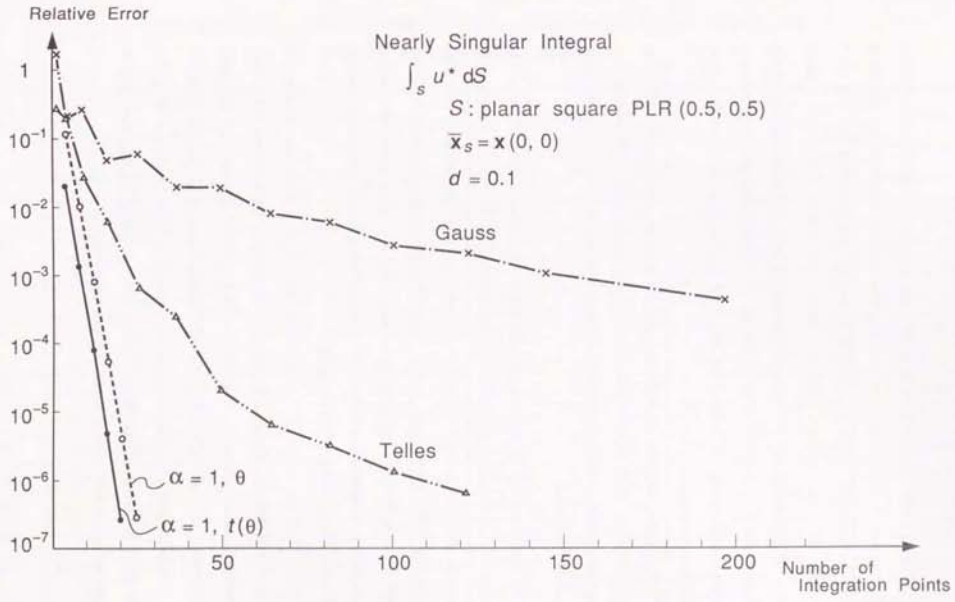

Fig. 10.2 Relative error vs. Number of integration points

Table 10.1 and Fig. 10.2 also show that the angular variable transformation $t(\theta)$ of equation (5.130) is useful in reducing the number of integration points in the angular variable. This is shown more clearly in Table 10.2 and Fig. 10.3 where the effect of moving the position of the source projection $\hat{\mathbf{x}}_s = \mathbf{x}(\bar{\eta}, \bar{\eta})$ from centre $\bar{\eta}=0$ to the corner $\bar{\eta}=1$ along the diagonal is shown, keeping the source distance constant at $d=10^{-1}$. Fig. 10.4 shows the convergence graph for the case when the source projection is near the corner of the element i.e. $\hat{\mathbf{x}}_s = \mathbf{x}(0.9, 0.9)$, with the source distance $d=10^{-1}$.

The angular variable transformation $t(\theta)$ becomes particularly effective when the source projection $\hat{\mathbf{x}}_s$ is situated near the corner or edge of the element $\bar{S}$. Hence, the transformation $t(\theta)$ gives a robust numerical integration method for the angular variable.

For the Gauss and Telles methods, the required number of integration points decreases as $\hat{\mathbf{x}}_s$ approaches the corner or edge of the element. This is because the integration points of the Gauss and Telles methods are concentrated near the corner or edge of the element, so that the near singular integral is integrated more accurately when the source projection (around which the integral kernel changes most rapidly) is situated near the corner or edge of the element, compared to when it is situated in the centre of the element.

Table 10.3 shows the effect of the aspect ratio of the element on the numerical integration. The source projection is set to $\hat{\mathbf{x}}_s = \mathbf{x}(0, 0)$ and the source distance is fixed at $d=10^{-1}$. Again, the robustness of the angular variable transformation $t(\theta)$ against the aspect ratio of the element is shown, compared to using θ as the angular variable or using the Gauss and Telles' methods. With the product type formulas of Gauss and Telles, the number of integration points increases approximately proportionally to the aspect ratio.

Table 10.2 Nearly singular integral $\int_S u^* \, dS$ over the unit planar square: PLR(0.5, 0.5)
(Effect of position of source projection $\hat{\mathbf{x}}_s$)

$\bar{\eta}$	$R(\rho)=\sqrt{\rho^2+d^2}$, $(a=1)$			$t(\theta)$			$\frac{N_\theta}{N_{t(\theta)}}$	Gauss			Telles			Integral $4\pi \int_S u^* \, dS$ (analytical)
	Angular variable θ													
	$N_\theta \times N_R$	total	CPU (msec)	$N_{t(\theta)} \times N_R$	total	CPU (msec)		$N_{\bar{\eta}1} \times N_{\bar{\eta}2}$	total	CPU (msec)	$N_{\bar{\eta}1} \times N_{\bar{\eta}2}$	total	CPU (msec)	
0	6×1	24	0.88	5×1	20	0.78	1.2	28×28	784	17	10×8	80	1.9	2.9532809
0.2	7×1	28	1.0	5×1	20	0.82	1.4	28×28	784	17	9×9	81	2.0	2.8993301
0.4	8×1	32	1.1	5×1	20	0.81	1.6	25×25	625	13	9×10	90	2.2	2.7362864
0.6	10×1	40	1.3	6×1	24	0.91	1.7	25×25	625	13	8×9	72	1.8	2.4603894
0.8	16×1	64	2.0	6×1	24	0.91	2.7	20×20	400	8.6	9×10	90	2.2	2.0690631
0.9	25×1	100	3.0	8×1	32	1.2	3.1	16×16	256	5.5	9×9	81	2.0	1.8390272
0.92	25×1	100	3.0	8×1	32	1.2	3.1	14×14	196	4.2	7×8	56	1.4	1.7923194
0.94	28×1	112	3.3	8×1	32	1.2	3.5	14×14	196	4.2	9×9	81	2.0	1.7460078
0.96	32×1	128	3.7	8×1	32	1.2	4.0	12×12	144	3.1	8×8	64	1.6	1.7004233
0.98	45×1	180	5.2	9×1	36	1.2	5.0	9×12	108	2.4	6×8	48	1.3	1.6558955
0.99	60×1	240	6.9	8×1	32	1.2	7.5	12×12	144	3.1	8×8	64	1.6	1.6341235
0.995	80×1	320	9.0	8×1	32	1.2	10	12×12	144	3.1	8×8	64	1.6	1.6233753
0.999	150×1	600	17	6×1	24	0.91	25	12×12	144	3.1	8×8	64	1.6	1.6148463
1.0	4×1	8	0.43	3×1	6	0.38	1.3	12×12	144	3.1	8×8	64	1.6	1.6127239
1.05	20×1	80	2.4	6×1	24	0.91	3.3	10×10	100	2.2	7×7	49	1.3	1.5121155
1.1	14×1	56	1.8	5×1	20	0.80	2.8	9×10	90	2.0	6×6	36	0.99	1.4229312

Position of source projection: $\hat{\mathbf{x}}_s = \mathbf{x}(0, 0)$. Source distance $d=10^{-1}$. Relative error $<10^{-6}$.

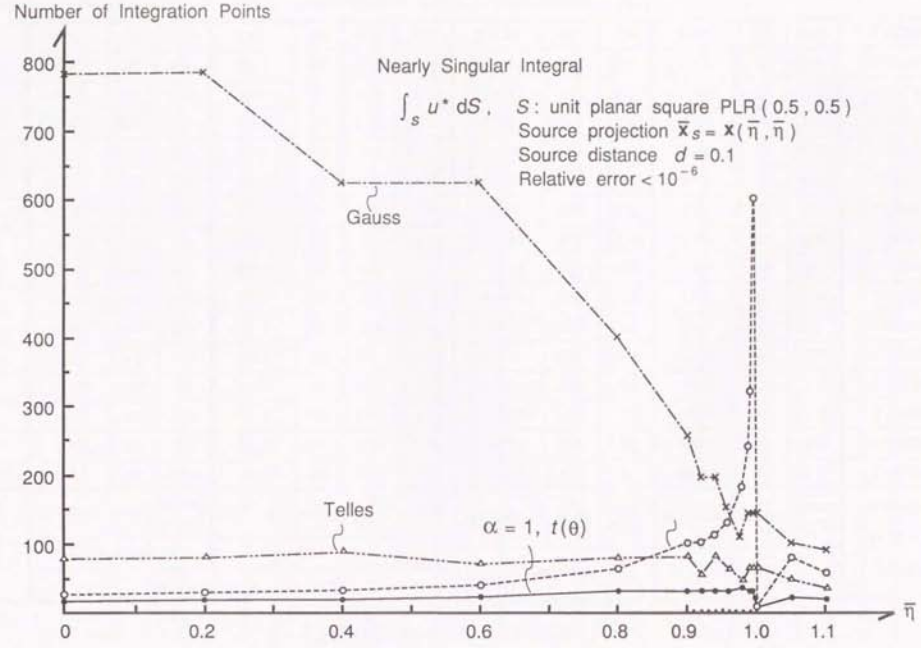

Fig.10.3 Number of integration points vs. Position of source projection $\bar{x}_S$

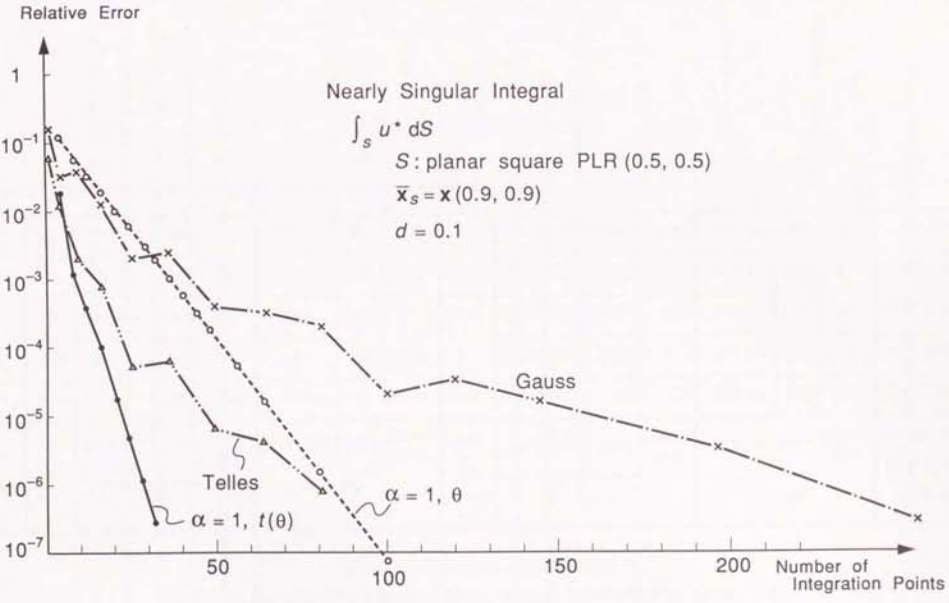

Fig. 10.4 Relative error vs. Number of integration points

Table 10.3 Nearly singular integral $\int_S u^* \, dS$ over the planar rectangle: PLR(0.5, b)
(Effect of the aspect ratio of the element)

Aspect ratio	b	$R(\rho)=\sqrt{\rho^2+d^2}$, $(\alpha=1)$						Gauss			Telles			Integral
		Angular variable θ			$t(\theta)$									$4\pi \int_S u^* \, dS$ (analytical)
		$N_\theta \times N_R$	total	CPU (msec)	$N_{t(\theta)} \times N_R$	total	CPU (msec)	$\frac{N_\theta}{N_{t(\theta)}}$	$N_{\eta_1} \times N_{\eta_2}$	total	CPU (msec)	$N_{\gamma_1} \times N_{\gamma_2}$	total	CPU (msec)	
1	0.5	6×1	24	0.89	5×1	20	0.80	1.2	28×28	784	17	10×8	80	1.9	2.9532809
2	1.0	8×1	32	1.1	7×1	28	0.99	1.1	28×55	1,540	34	8×9	72	1.7	4.2282421
3	1.5	10×1	40	1.3	8×1	32	1.1	1.3	25×72	1,800	39	8×16	128	2.9	5.0151730
5	2.5	14×1	56	1.8	9×1	36	1.2	1.6	25×120	3,000	65	8×25	200	4.4	6.0239885
10	5.0	20×1	80	2.4	12×1	48	1.6	1.7	25×240	6,000	130	8×28	224	4.9	7.4047459

Source projection: $\bar{x}_s = x(0, 0)$. Source distance $d = 10^{-1}$. Relative error $<10^{-6}$.

Next, the effectiveness of the radial variable transformation

$$R(\rho) = -\frac{1}{\sqrt{\rho^2+d^2}} \quad . \tag{10.20}$$

corresponding to

$$\rho \, d\rho = r^{1-\alpha} \, dR \quad , \quad (\alpha=3) \tag{10.24}$$

for the integration

$$\int_S q^* \, dS = -\frac{1}{4\pi} \int_S \frac{(r, n)}{r^\alpha} dS$$

$$= -\frac{d}{4\pi} \int_S \frac{dS}{r^\alpha} \quad , \quad (\alpha=3) \tag{10.17}$$

over a constant planar element S, is demonstrated in Table 10.4 .

Again, the unit planar square element PLR(0.5, 0.5) with the source point at $\mathbf{x}_s=(0.25, 0.25, d)$ is taken as an example. In this case, the unit outward normal $\mathbf{n}$ is defined as

$$\mathbf{n} = -\frac{\mathbf{G}}{|\mathbf{G}|} \tag{10.25}$$

where

$$\mathbf{G} = \frac{\partial \mathbf{x}}{\partial \eta_1} \times \frac{\partial \mathbf{x}}{\partial \eta_2} \quad , \tag{10.26}$$

as shown in Fig. 10.1, so that

$$(\mathbf{r}, \mathbf{n}) = d \quad . \tag{10.27}$$

Similar to the case of $\int_S u^* \, dS$, $\alpha=1$ in Table 10.1, only one integration point is required for the radial variable, independent of the source distance d. For the Gauss and Telles' methods, even more integration points are required when $0<d \ll 1$, since the order of near singularity is $\alpha=3$ for q^*, compared to $\alpha=1$ for u^*. Fig. 10.5 shows the convergence graph for the case when the source distance is $d=10^{-1}$ and the source projection $\bar{\mathbf{x}}_s=\mathbf{x}(0, 0)$.

Table 10.4 Nearly singular integral $\int_S q^* \, dS$ over the unit planar square: PLR(0.5, 0.5)

Source distance d	$R(\rho)=-1/\sqrt{\rho^2+d^2}$, $(\alpha=3)$						$\frac{N_\theta}{N_{t(\theta)}}$	Gauss			Telles			Integral $4\pi\int_S q^* \, dS$ (analytical)
	Angular variable θ			$t(\theta)$				$N_{\eta_1}\times N_{\eta_2}$	total	CPU (msec)	$N_{\gamma_1}\times N_{\gamma_2}$	total	CPU (msec)	
	$N_\theta\times N_R$	total	CPU (msec)	$N_{t(\theta)}\times N_R$	total	CPU (msec)								
10	10×1	40	1.4	4×1	16	0.70	2.5	3×3	9	0.20	3×3	9	0.40	-9.9565067×10^{-2}
3	10×1	40	1.4	5×1	20	0.88	2.0	3×4	12	0.27	3×4	12	0.47	-1.0603981×10^{-1}
1	7×1	28	1.0	5×1	20	0.81	1.4	5×6	30	0.68	4×4	16	0.58	-7.1920527×10^{-1}
0.3	6×1	24	0.91	7×1	28	1.0	0.86	12×12	144	3.1	8×8	64	1.6	−2.7346419
0.1	5×1	20	0.80	7×1	28	1.2	0.71	32×32	1024	22	14×14	196	4.5	−4.7608104
0.03	3×1	12	0.57	7×1	28	1.0	0.43	100×110	11,000	240	25×25	625	14	−5.8061327
0.01	3×1	12	0.57	7×1	28	1.0	0.43	256×256 ($\varepsilon=2\times10^{-6}$)	65,536	1,430	45×45	2,025	45	−6.1235154
0.003	3×1	12	0.57	3×1	12	0.58	1.0	256×256 ($\varepsilon=2\times10^{-3}$)	65,536	1,420	72×72	5,184	113	−6.2352619
0.001	3×1	12	0.57	7×1	28	1.0	0.43	256×256 ($\varepsilon=2\times10^{-1}$)	65,536	1,430	100×100	10,000	217	−6.2672102

Source point $\mathbf{x}_s=(0.25, 0.25, d)$. Relative error $\varepsilon<10^{-6}$.

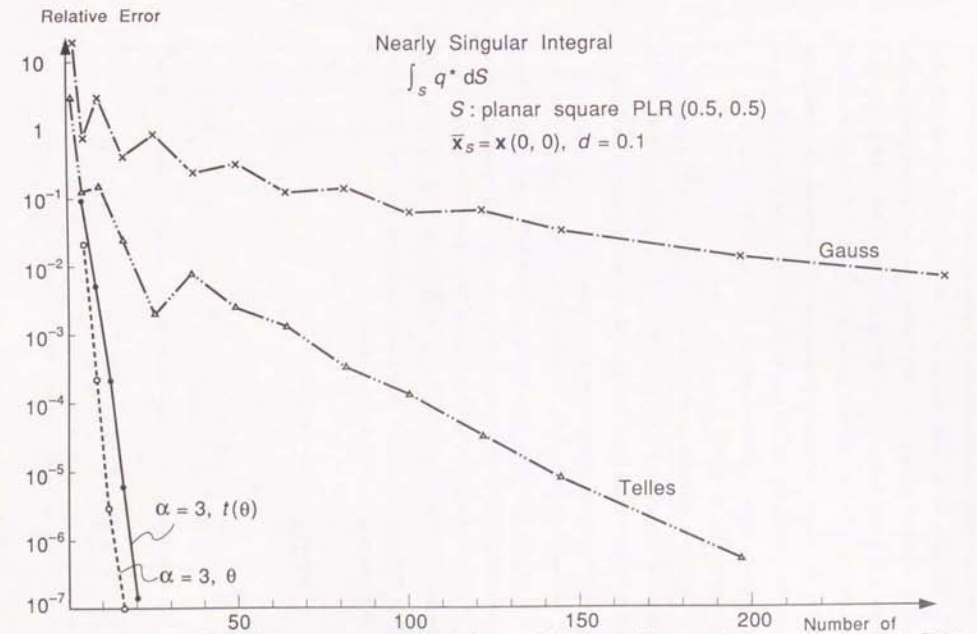

Fig. 10.5 Relative error vs. Number of integration points

This time, the angular variable transformation $t(\theta)$ does not pay off when $d \leqq 0.3$. However, Table 10.5 and Fig. 10.6 show that when the source projection $\hat{\mathbf{x}}_s = \mathbf{x}(\hat{\gamma}, \hat{\eta})$ is near the corner of the element ($0.96 \leqq \hat{\gamma} \leqq 1.0$), the transformation $t(\theta)$ helps to reduce the number of integration points in the angular variable. Hence, the angular variable transformation $t(\theta)$ ensures the robustness of the numerical integration method against the position of the source projection $\hat{\mathbf{x}}_s$. This is demonstrated in the convergence graph in Fig. 10.7 for the case $\hat{\mathbf{x}}_s = \mathbf{x}(0.99, 0.99)$, $d = 10^{-1}$.

Table 10.6 demonstrates the effect of the aspect ratio of the element on the numerical integration of $\int_S q^* \, dS$. It is shown that the radial variable transformation method is robust against the aspect ratio, where as the Gauss and Telles' methods are strongly affected by the aspect ratio.

Summing up, it has been demonstrated that the singularity cancelling radial variable transformations of equations (10.19) and (10.20) require only one radial integration point for the exact evaluation of the nearly singular integrals $\int_S u^* \, dS$, ($\alpha = 1$) and $\int_S q^* \, dS$ ($\alpha = 3$), respectively, when S is a constant planar element. The effectiveness of the angular variable transformation $t(\theta)$, for cases where the source projection $\hat{\mathbf{x}}_s$ is very near the element edge, and for elements with high aspect ratio, was also demonstrated.

Table 10.5 Nearly singular integral $\int_S q^* \, dS$ over the unit planar square: PLR(0.5, 0.5)
(Effect of position of source projection $\hat{\mathbf{x}}_s$)

$\hat{\gamma}$	$R(\rho) = -1/\sqrt{\rho^2 + d^2}$, ($\alpha = 3$)					Gauss		Telles		Integral $4\pi \int_S q^* \, dS$ (analytical)
	Angular variable θ		$t(\theta)$		$\frac{N_\theta}{N_{t(\theta)}}$					
	$N_\theta \times N_R$	total	$N_{t(\theta)} \times N_R$	total		$N_{\gamma_1} \times N_{\gamma_2}$	total	$N_{\gamma_1} \times N_{\gamma_2}$	total	
0	4×1	16	5×1	20	0.80	40×40	1,600	14×14	196	−5.1701980
0.2	4×1	16	5×1	20	0.80	35×35	1,225	12×14	168	−5.1164294
0.4	4×1	16	7×1	28	0.57	35×40	1,400	14×14	196	−4.9305174
0.6	5×1	20	8×1	32	0.63	32×32	1,024	11×12	132	−4.5063249
0.8	7×1	28	9×1	36	0.78	25×28	700	14×14	196	−3.4966631
0.9	9×1	36	10×1	40	0.90	25×25	625	14×14	196	−2.5457765
0.92	10×1	40	8×1	32	1.3	20×20	400	12×11	132	−2.3192253
0.94	11×1	44	11×1	44	1.0	20×20	400	12×12	144	−2.0880565
0.96	14×1	56	11×1	44	2.3	20×20	400	12×12	144	−1.8583067
0.98	20×1	80	12×1	48	1.7	20×20	400	11×11	121	−1.6367757
0.99	28×1	112	11×1	44	2.5	10×20	200	9×11	99	−1.5311679
0.995	35×1	140	14×1	56	2.5	20×20	400	9×11	99	−1.4799752
0.999	60×1	240	14×1	56	4.3	20×20	400	11×11	121	−1.4398658
1.0	3×1	6	3×1	6	1.0	20×20	400	11×11	121	−1.4299605
1.05	7×1	28	8×1	32	0.88	14×16	224	10×10	100	−1.0046306
1.1	5×1	20	7×1	28	0.71	12×12	144	8×8	64	$-7.1518008 \times 10^{-1}$
Average CPU-time per point	38 μsec		38 μsec			22 μsec		23 μsec		

Source projection: $\hat{\mathbf{x}}_s = \mathbf{x}(\hat{\gamma}, \hat{\eta})$. Source distance $d = 10^{-1}$. Relative error $< 10^{-6}$.

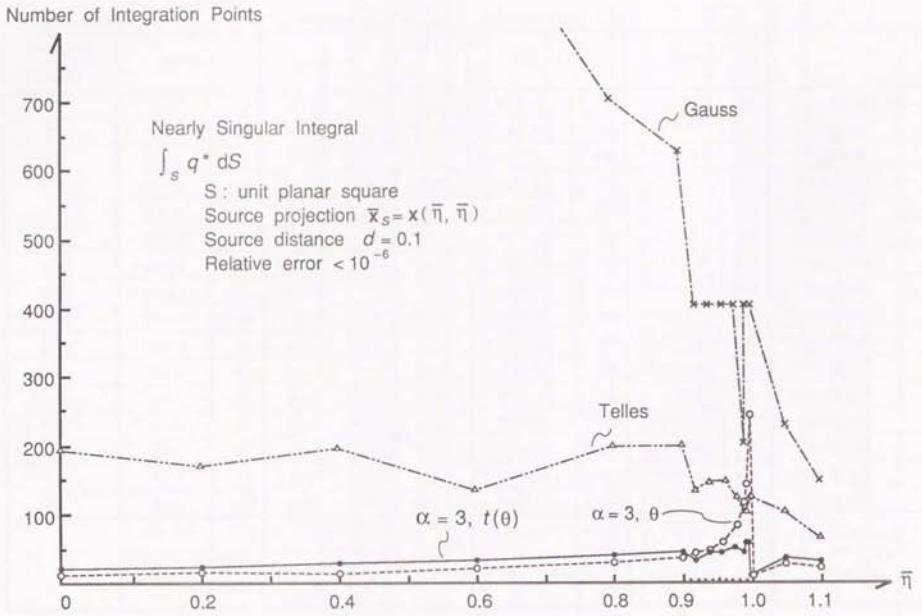

Fig.10.6 Number of integration points vs. Position of source projection $\bar{x}_S$

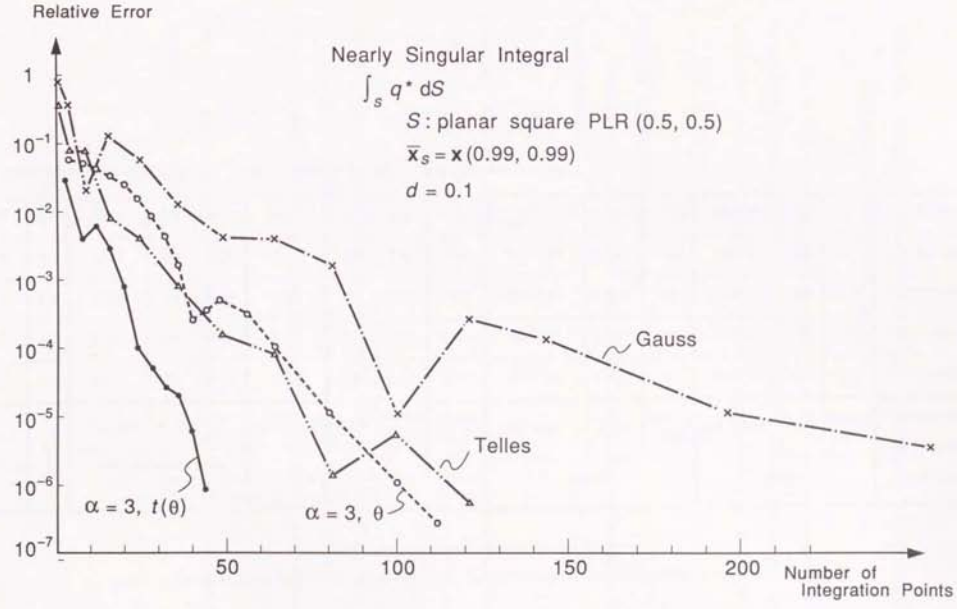

Fig. 10.7 Relative error vs. Number of integration points

Table 10.6 Nearly singular integral $\int_S q^* \, dS$ over the planar rectangle: PLR(0.5, b)
(Effect of the aspect ratio of the element)

Aspect ratio	b	$R(\rho)=-1/\sqrt{\rho^2+d^2}$, $(\alpha=3)$							Gauss			Telles			Integral
		Angular variable θ			$t(\theta)$			$\frac{N_\theta}{N_{t(\theta)}}$							$4\pi \int_S q^* \, dS$ (analytical)
		$N_\theta \times N_R$	total	CPU (msec)	$N_{t(\theta)} \times N_R$	total	CPU (msec)		$N_{\eta_1} \times N_{\eta_2}$	total	CPU (msec)	$N_{\gamma_1} \times N_{\gamma_2}$	total	CPU (msec)	
1	0.5	4×1	16	0.67	5×1	20	0.79	0.80	40×40	1,600	35	14×14	196	4.5	−5.1701980
2	1.0	4×1	16	0.67	6×1	24	0.92	0.67	40×80	3,200	70	14×20	280	6.3	−5.3998335
3	1.5	5×1	20	0.78	9×1	36	1.3	0.56	35×110	3,850	84	14×25	350	7.8	−5.4504683
5	2.5	5×1	20	0.78	11×1	44	1.5	0.45	40×190	7,600	167	16×32	512	11	−5.4777787
10	5.0	5×1	20	0.79	14×1	56	1.9	0.36	256×256 ($\varepsilon=8\times10^{-5}$)	65,536	1,420	14×40	560	12	−5.4896142

Source projection: $\hat{\mathbf{x}}_s=(0, 0)$. Source distance $d=10^{-1}$. Relative error $<10^{-6}$.

10.3 Application of the Singularity Cancelling Transformation to Elements with Curvature and Interpolation Functions

The success of the singularity cancelling radial variable transformation $R(\rho)$ of equations (10.19) and (10.20) for constant planar elements, encourages us to apply the method to curved elements and integrals including interpolation functions $\phi_{ij}(\eta_1, \eta_2)$.

(1) Application to curved elements

Results of applying the singularity cancelling radial variable transformation

$$R(\rho)=\sqrt{\rho^2+d^2} \quad , \qquad (\alpha=1) \tag{10.19}$$

in combination with the angular variable transformation $t(\theta)$ of equation (5.130), to the nearly singular integral

$$\int_S u^* \, dS = \frac{1}{4\pi}\int_S \frac{dS}{r} \tag{10.22}$$

over the 'spherical' quadrilateral element SPQ60 defined in section 8.2, are given in Tables 10.7, 10.8 and 10.9. In each case, the source projection was set to $\hat{\mathbf{x}}=\mathbf{x}(\tilde{\eta}, \tilde{\eta})$ with $\tilde{\eta}=0, 0.5$ and 0.9, respectively. The source point $\mathbf{x}_s$ was located at

$$\mathbf{x}_s = \bar{\mathbf{x}}_s + d\,\mathbf{n} \quad , \tag{10.28}$$

where the source distance d was varied from 10 to 10^{-3}. The unit outward normal $\mathbf{n}$ is defined by

$$\mathbf{n} = \mathbf{G}/|\mathbf{G}| \tag{10.29}$$

$$\mathbf{G} = \frac{\partial \mathbf{x}}{\partial \eta_1} \times \frac{\partial \mathbf{x}}{\partial \eta_2} \quad . \tag{10.30}$$

Table 10.7 Nearly singular integral $\int_S u^* \, dS$ over the 'spherical' quadrilateral: SPQ60

(Source projection $\bar{\mathbf{x}}_s = \mathbf{x}(0, 0)$)

Source distance d	$R(\rho)=\sqrt{\rho^2+d^2}$, $(\alpha=1)$ Angular variable: $t(\theta)$			Telles			Integral $4\pi \int_S u^* \, dS$ (log-L_1, 128×128)
	$N_{t(\theta)} \times N_{R(\rho)}$	total	CPU (msec)	$N_{\gamma_1} \times N_{\gamma_2}$	total	CPU (msec)	
10	5×3	60	1.7	4×5	20	0.62	1.0519218×10^{-1}
3	5×3	60	1.7	4×5	20	0.62	3.5505101×10^{-1}
1	5×3	60	1.7	5×5	25	0.72	1.0458484
0.3	5×4	80	2.2	7×7	49	1.2	2.3999977
0.1	5×6	120	3.1	10×11	110	2.5	3.1707996
0.03	5×12	240	5.9	16×20	320	6.9	3.4722881
0.01	4×20	320	7.7	28×28	784	17	3.5598394
0.003	4×35	560	13	25×25	625	13	3.5905652
0.001	5×45	900	21	50×50	2,500	53	3.5993500
Average CPU -time per point :			26μsec	〃		25μsec	

Relative error $\varepsilon < 10^{-6}$. Source distance $d = 0.01$, towards centre of sphere.

Table 10.8 Nearly singular integral $\int_S u^* \, dS$ over the 'spherical' quadrilateral: SPQ60

(Source projection $\bar{\mathbf{x}}_s = \mathbf{x}(0.5, 0.5)$)

Source distance d	$R(\rho)=\sqrt{\rho^2+d^2}$, $(\alpha=1)$; Angular variable: $t(\theta)$			Telles			Integral $4\pi \int_S u^* \, dS$ (log-L_1, 128×128)
	$N_{t(\theta)} \times N_{R(\rho)}$	total	CPU (msec)	$N_{\gamma_1} \times N_{\gamma_2}$	total	CPU (msec)	
10	6×20	480	12	4×5	20	0.68	1.0576605×10^{-1}
3	6×20	480	12	4×5	20	0.68	3.6025808×10^{-1}
1	6×20	480	11	5×4	20	0.62	1.0467642
0.3	5×20	400	9.6	6×6	36	1.0	2.1748271
0.1	5×14	280	6.8	9×9	81	2.0	2.8377859
0.03	6×20	480	12	11×16	176	4.0	3.1353675
0.01	6×28	672	16	20×20	400	8.7	3.2263821
0.003	6×40	960	23	35×35	1,225	26	3.2587902
0.001	6×60	1,440	34	45×50	2,250	47	3.2680995
Average CPU -time per point :			24μsec	〃		27μsec	

Relative error $< 10^{-6}$. Source point $\mathbf{x}_s$, towards centre of sphere.

Table 10.9 Nearly singular integral $\int_S u^* dS$ over the 'spherical' quadrilateral: SPQ60

(Source projection $\bar{x}_s = x(0.9, 0.9)$)

Source distance d	$R(\rho)=\sqrt{\rho^2+d^2}$, $(a=1)$; Angular variable: $t(\theta)$			Telles			Integral $4\pi \int_S u^* dS$ (log-L_1, 128×128)
	$N_{t(\theta)} \times N_{R(\rho)}$	total	CPU (msec)	$N_{\gamma_1} \times N_{\gamma_2}$	total	CPU (msec)	
10	6×20	480	12	4×5	20	0.68	1.0687784×10^{-1}
3	5×25	500	12	4×5	20	0.68	3.7004261×10^{-1}
1	5×20	400	10	4×4	16	1.1	1.0298690
0.3	6×25	600	14	6×6	36	1.0	1.7293821
0.1	6×20	480	12	7×7	49	1.3	2.0268382
0.03	7×25	700	17	9×12	108	2.6	2.2105752
0.01	9×32	1,152	27	20×20	400	8.7	2.2935015
0.003	10×55	2,200	51	28×28	784	17	2.3276379
0.001	10×90	3,600	85	40×25	1,000	21	2.3379046
Average CPU -time per point :			24μsec	"		31μsec	

Relative error $<10^{-6}$. Source point x_s, towards centre of sphere.

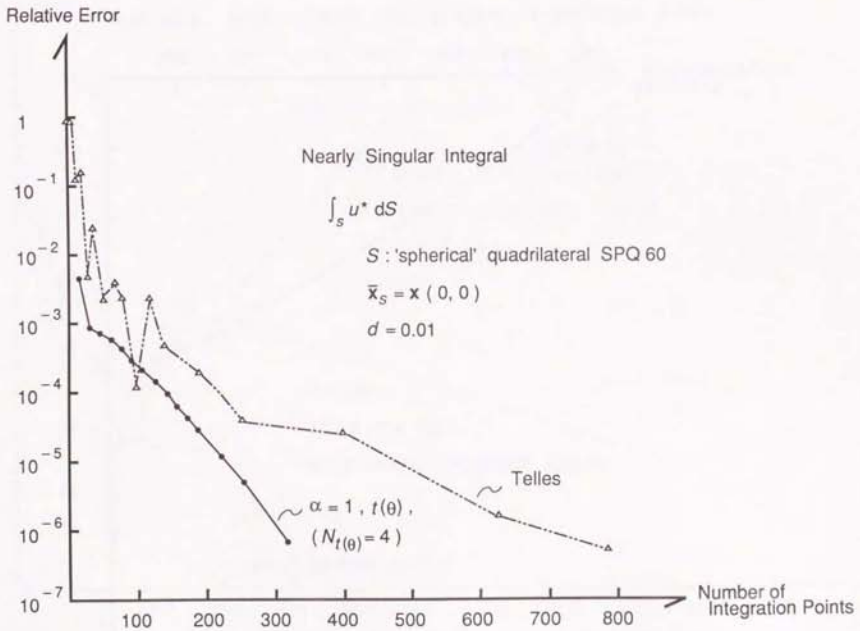

Fig.10.8 Relative error vs. Number of integration points

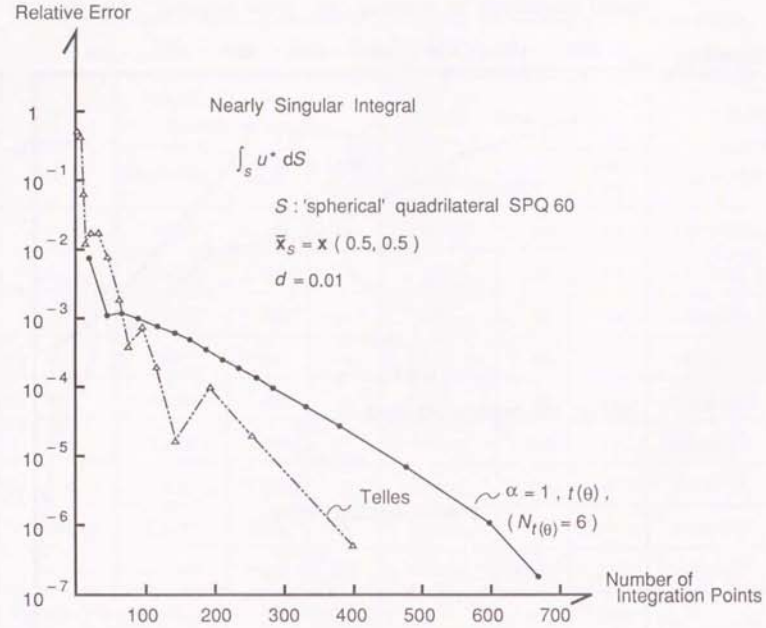

Fig. 10.9 Relative error vs. Number of integration points

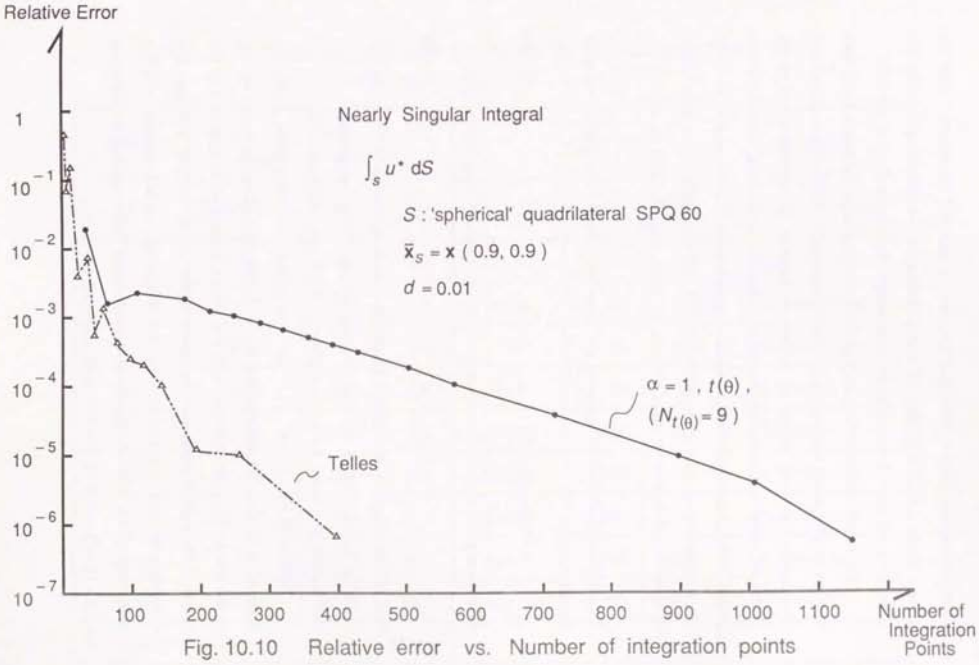

Fig. 10.10 Relative error vs. Number of integration points

Hence the source point x_s is located towards the centre of the sphere (inside the sphere when $d \leqq 1$). Fig. 10.8, 10.9 and 10.10 give convergence graphs for the cases $\tilde{\eta}=0$, 0.5 and 0.9, respectively, with the source distance fixed at $d=0.01$.

The results indicate that, unlike for constant planar elements, more than one integration points are required in the transformed radial variable R and that the number increases rapidly as the source distance d decreases, and as the source projection $\hat{x}_s$ approaches the corner of the curved elements. Compared with Telles' cubic transformation method of equation (4.51), the radial variable transformation method of equation (10.19) ($a=1$) requires less number of integration points only for cases $d \leqq 0.03$ for $\tilde{\eta}=0$, and $d \leqq 0.003$ for $\tilde{\eta}=0.5$.

Similarly, results of applying the singularity cancelling radial variable transformation

$$R(\rho) = -\frac{1}{\sqrt{\rho^2 + d^2}} \quad , \quad (a=3) \tag{10.20}$$

with the angular variable transformation $t(\theta)$, to the nearly singular integral

$$\int_S q^* \, dS = -\frac{1}{4\pi} \int_S \frac{(r, n)}{r^3} \, dS \tag{10.31}$$

over the 'spherical' quadrilateral SPQ60, are given in Tables 10.10, 10.11 and 10.12 for the cases $\tilde{\eta}=0$, 0.5 and 0.9, respectively. The corresponding convergence graphs for $d=0.01$ are given in Fig. 10.11, 10.12 and 10.13.

Similar to the case of $\int_S u^* \, dS$, more than one integration points are required in the transformed radial variable R, and the number increases rapidly as the source distance decreases and the source projection $\hat{x}_s$ approaches the corner of the curved element. Compared to the Telles' method, this time the singularity cancelling radial variable transformation method becomes slightly more competitive. Namely, the method outperforms Telles' method for the cases $d \leqq 0.1$ ($\tilde{\eta}=0$), $d \leqq 0.01$ ($\tilde{\eta}=0.5$) and $d \leqq 0.001$ ($\tilde{\eta}=0.9$).

Table 10.10 Nearly singular integral $\int_S q^* \, dS$ over the 'spherical' quadrilateral: SPQ60

(Source projection $\hat{x}_s = x(0, 0)$)

Source distance d	$R(\rho) = -1/\sqrt{\rho^2+d^2}$, $(a=3)$; Angular variable: $t(\theta)$			Telles			Integral $4\pi \int_S q^* \, dS$ ($\log\text{-}L_1$, 128×128)
	$N_{t(\theta)} \times N_{R(\rho)}$	total	CPU (msec)	$N_{\gamma_1} \times N_{\gamma_2}$	total	CPU (msec)	
10	5×2	40	1.3	3×4	12	0.45	-9.8697960×10^{-3}
3	5×3	60	1.8	4×4	16	0.54	-1.1618876×10^{-1}
1	6×3	72	2.1	5×5	25	0.74	−1.0481517
0.3	5×5	100	2.7	8×8	64	1.6	−4.7854723
0.1	5×8	160	4.1	14×16	224	5.1	−7.0239076
0.03	6×16	384	9.5	25×28	700	15	−7.7894255
0.01	6×28	672	17	40×45	1,800	40	−7.9974845
0.003	6×50	1,200	29	64×72	4,608	100	−8.0689484
0.001	6×90	2,160	52	110×110	12,100	262	−8.0892319
Average CPU -time per point :			27 μsec	"		26 μsec	

Relative error $<10^{-6}$. Source point x_s, towards centre of sphere.

Table 10.11 Nearly singular integral $\int_S q^* \, dS$ over the 'spherical' quadrilateral: SPQ60

(Source projection $\hat{\mathbf{x}}_s = \mathbf{x}(0.5, 0.5)$)

Source distance d	$R(\rho) = -1/\sqrt{\rho^2 + d^2}$, $(\alpha = 3)$; Angular variable: $t(\theta)$			Telles			Integral $4\pi \int_S q^* \, dS$ (log-L_1, 128×128)
	$N_{t(\theta)} \times N_{R(\rho)}$	total	CPU (msec)	$N_{\gamma_1} \times N_{\gamma_2}$	total	CPU (msec)	
10	5×20	400	9.8	3 × 4	12	0.52	$-9.4067128 \times 10^{-3}$
3	5×20	400	9.9	4 × 4	16	0.60	$-1.1562058 \times 10^{-1}$
1	6×20	480	12	5 × 5	25	0.74	−1.0499297
0.3	6×14	336	8.4	7 × 7	49	1.3	−4.0862770
0.1	6×7	168	4.4	14 × 14	196	4.5	−6.4265768
0.03	8×20	640	16	25 × 25	625	14	−7.4555989
0.01	8×32	1,024	25	40 × 45	1,800	40	−7.7480149
0.003	8×45	1,440	35	64 × 72	4,608	100	−7.8489797
0.001	9×110	3,960	95	100 × 100	10,000	217	−7.8776623
Average CPU -time per point :			25 μsec	"		28 μsec	

Relative error $< 10^{-6}$. Source point $\mathbf{x}_s$, towards centre of sphere.

Table 10.12 Nearly singular integral $\int_S q^* \, dS$ over the 'spherical' quadrilateral: SPQ60

(Source projection $\hat{\mathbf{x}}_s = \mathbf{x}(0.9, 0.9)$)

Source distance d	$R(\rho) = -1/\sqrt{\rho^2 + d^2}$ Angular variable: $t(\theta)$			Telles			Integral $4\pi \int_S q^* \, dS$ (log-L_1, 128×128)
	$N_{t(\theta)} \times N_{R(\rho)}$	total	CPU (msec)	$N_{\gamma_1} \times N_{\gamma_2}$	total	CPU (msec)	
10	6×32	768	19	3×4	12	0.52	$-8.5565994 \times 10^{-3}$
3	6×28	672	17	4×4	16	0.60	$-1.1487449 \times 10^{-1}$
1	6×16	384	10	5×5	25	1.3	−1.0162495
0.3	7×14	392	9.7	7×8	56	1.5	−2.5547829
0.1	8×7	224	5.8	11×14	154	3.6	−3.7059921
0.03	10×25	1,000	24	14×16	224	5.2	−5.5991854
0.01	10×40	1,600	39	28×32	896	20	−6.7346103
0.003	14×72	4,032	96	50×55	2,750	60	−7.1833142
0.001	10×128	5,120	122	80×72	5,760	125	−7.3129500
Average CPU -time per point :			25 μsec	"		30 μsec	

Relative error $< 10^{-6}$. Source point $\mathbf{x}_s$, towards centre of sphere.

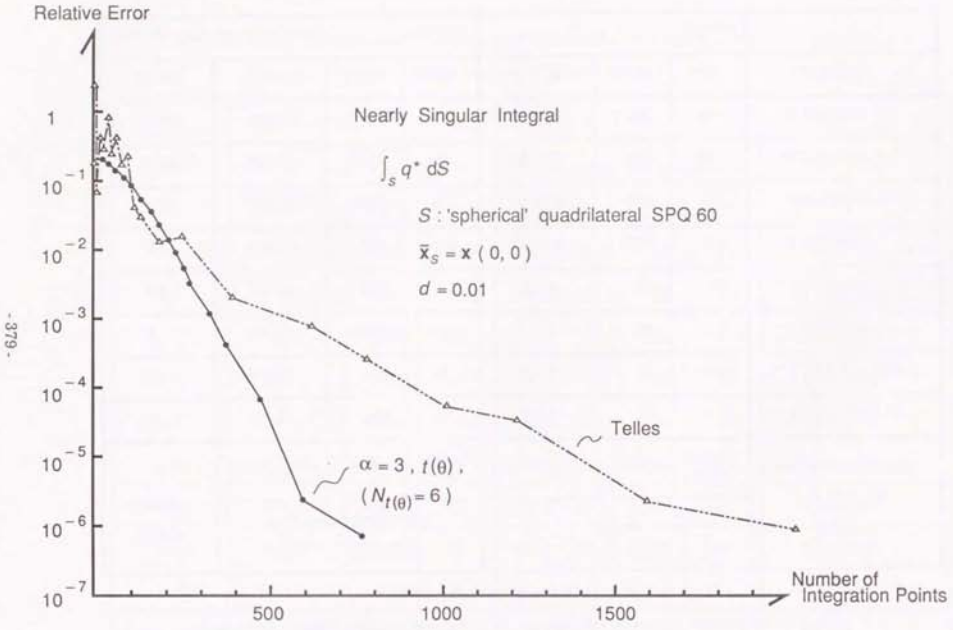

Fig. 10.11 Relative error vs. Number of integration points

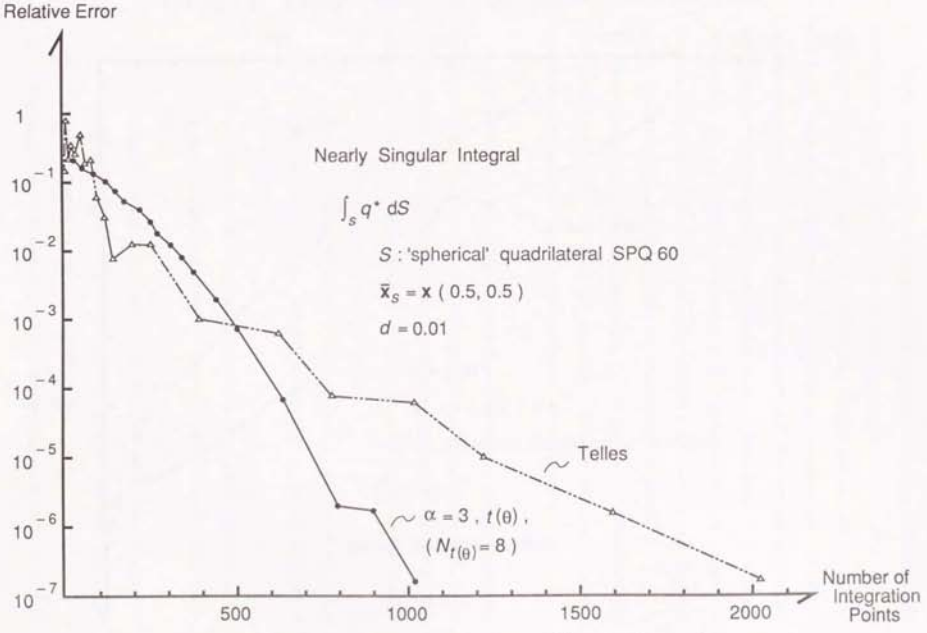

Fig. 10.12 Relative error vs. Number of integration points

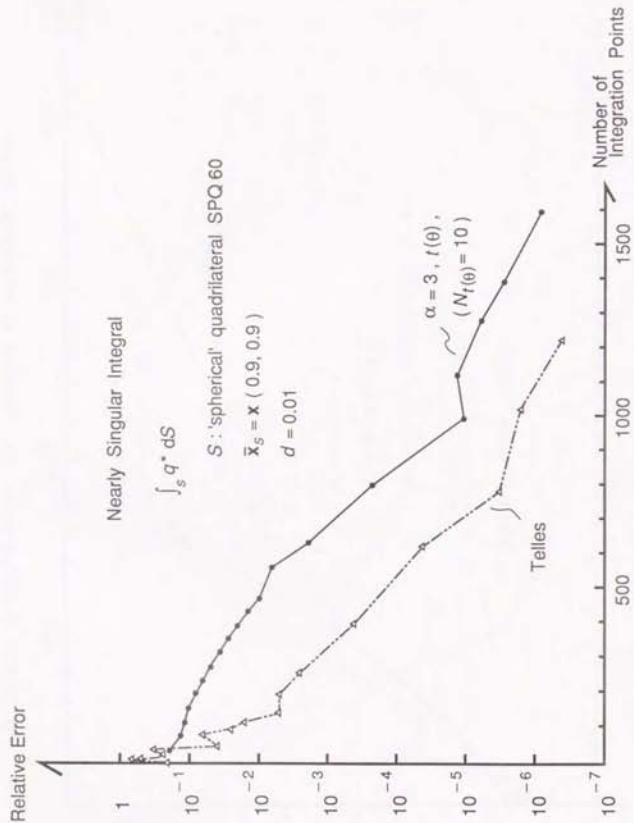

Fig. 10.13 Relative error vs. Number of integration points

Summing up, for curved elements, the singularity cancelling radial variable transformations $R(\rho)=\sqrt{\rho^2+d^2}$, $(\alpha=1)$ for u^* and $R(\rho)=-1/\sqrt{\rho^2+d^2}$, $(\alpha=3)$ for q^* do not perform as dramatically or efficiently as they did on constant planar elements. Particularly, these radial variable transformations are not robust against the position of the source projection $\bar{\mathbf{x}}_s$, although the $\alpha=3$ transformation is slightly more robust than the $\alpha=1$ transformation. The other shortcoming of the singularity cancelling transformation is that different sets of integration points are required for the kerneles u^* and q^*, unlike the Telles' method. Hence, a more robust and efficient radial variable transformation is required.

The angular variable transformation $t(\theta)$ of equation (5.130) is robust against the position of $\bar{\mathbf{x}}_s$, since the number of angular integration points increases only slightly as $\bar{\mathbf{x}}_s$ approaches the corner of the element.

At this point, a more accurate cancellation of the near singularity by taking into consideration the curvature of the element at the source projection $\bar{\mathbf{x}}_s$, in the radial variable transformation was attempted, as mentioned in Chapter 5. This approach showed some effect in decreasing the number of radial integration points. However, it has the following shortcomings.

(a) Exact cancellation of u^* or q^* does not work efficiently when the integral kernel includes interpolation functions ϕ_ψ, as will be shown in the next section.

(b) Much CPU-time is required in determining the exact projection of the integration point $\mathbf{x}$ on the curved element, to the plane $\bar{S}$ tangent to S at $\bar{\mathbf{x}}_s$.

(c) The exact (instead of approximate) projection of the curved element S on to the tangent plane $\bar{S}$ becomes complicated, since the edge of the projected element is, in general, a curve in $\bar{S}$.

(d) Different sets of integration points are required for the kernels u^* and q^*.

(2) Application to integrals including interpolation functions

Next, the effect of applying the singularity cancelling radial transformations of equation (10.19) and (10.20), to nearly singular integrals including the interpolation functions ϕ_{ij} is tested.

For simplicity, the unit planar square PLR(0.5, 0.5) is taken as the element, and the source point is set at $\mathbf{x}_s=(0.25, 0.25, d)$ with various source distances $10^{-3} \leqq d \leqq 10$. The source projection is fixed at $\bar{\mathbf{x}}_s=\mathbf{x}(0.5, 0.5)$.

The 9-point Lagrangian interpolation function

$$\phi_{ij}(\eta_1, \eta_2) = \phi_i(\eta_1)\ \phi_j(\eta_2) \quad , \quad i, j = -1, 0, 1 \tag{10.32}$$

where

$$\begin{aligned} \phi_{-1}(\eta) &= \eta(\eta-1)/2 \\ \phi_0(\eta) &= 1-\eta^2 \\ \phi_1(\eta) &= \eta(\eta+1)/2 \quad , \end{aligned} \tag{5.3}$$

is used as the interpolation function.

First, the effect of the singularity cancelling radial variable transformation

$$R(\rho) = \sqrt{\rho^2 + d^2} \quad , \quad (a=1) \tag{10.19}$$

in combination with the angular variable transformation $t(\theta)$ of equation (5.127) on the nearly singular integral

$$\int_S \phi_{ij}\, u^*\, dS \quad , \quad i, j = -1, 0, 1 \tag{10.33}$$

is shown in Table 10.13. The number of integration points required to achieve a relative error less than 10^{-6} for all the components ϕ_{ij}, ($i, j=-1, 0, 1$) is compared with the product type Telles' cubic transformation method of equation (4.51). (The relative error was estimated by comparing with results obtained by $N_t=128$, $N_R=128$ points with the log-L_1 radial variable transformation method, mentioned later.)

Table 10.13 Nearly singular integral $\int_S \phi_{ij}\, u^*\, dS$ over the unit planar square: PLR(0.5, 0.5)

Source distance d	$R(\rho)=\sqrt{\rho^2+d^2}$, $(a=1)$; Angular variable: $t(\theta)$			Telles			Integral $4\pi \int_S \phi_{11}\, u^*\, dS$ (log-L_1, 128×128pts.)
	$N_{t(\theta)} \times N_{R(\rho)}$	total	CPU (msec)	$N_{\gamma_1} \times N_{\gamma_2}$	total	CPU (msec)	
10	8×128	4,096	112	3×3	9	0.45	2.7788157×10^{-3}
3	7×128	3,584	98	4×4	16	0.63	9.2963434×10^{-3}
1	6×90	2,160	60	5×5	25	0.85	2.8520099×10^{-2}
0.3	8×90	2,880	80	7×8	56	1.7	9.2787798×10^{-2}
0.1	7×80	2,240	61	10×10	100	2.8	1.7670453×10^{-1}
0.03	9×110	3,960	109	25×25	625	16	2.2756348×10^{-1}
0.01	9×150	5,400	147	35×40	1,400	36	2.4436723×10^{-1}
0.003	7×80	2,240	61	55×55	3,025	79	2.5045883×10^{-1}
0.001	6×64	1,536	43	72×72	5,184	134	2.5221794×10^{-1}

Source point $\mathbf{x}_s=(0.25, 0.25, d)$, relative error $<10^{-6}$.

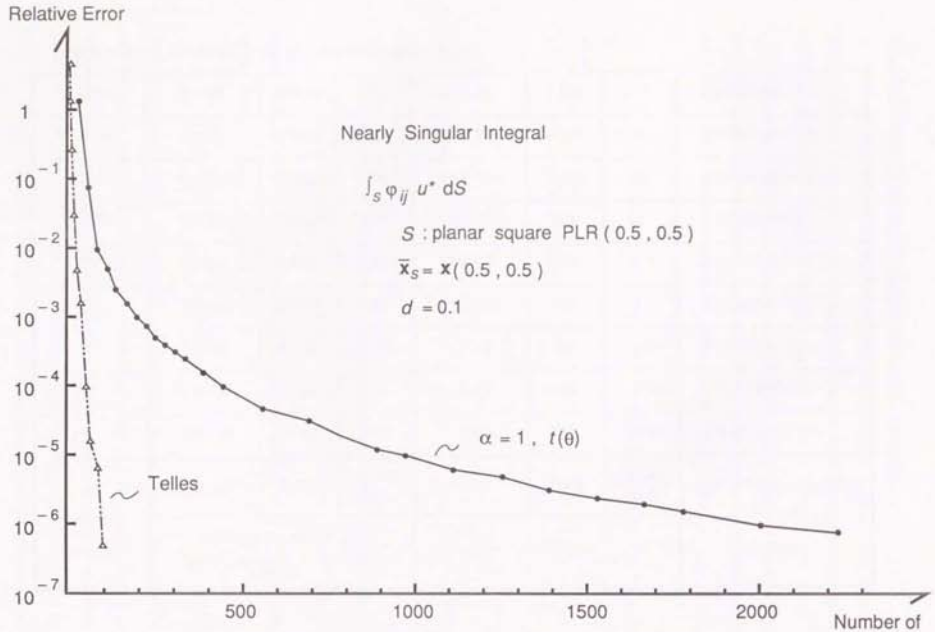

Fig. 10.14 Relative error vs. Number of integration points

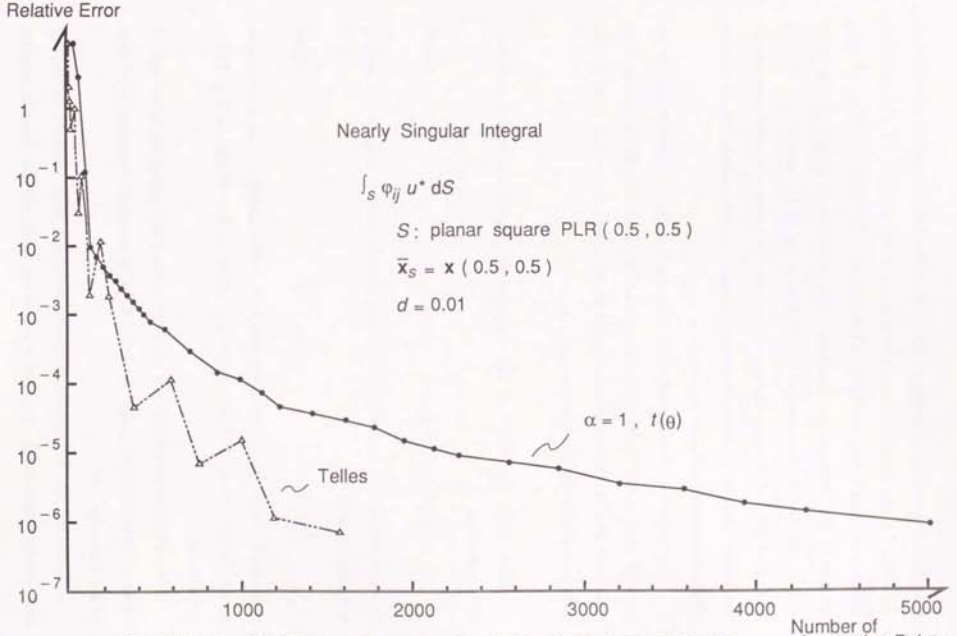

Fig. 10.15 Relative error vs. Number of integration points

The singularity cancelling radial variable transformation of equation (10.19), $\alpha=1$, which was so successful with the integral $\int_S u^* \, dS$ over constant planar elements turns out to be inefficient for the integral $\int_S \phi_{ij} \, u^* \, dS$, containing the interpolation function. The convergence graphs for the case $d=0.1$ and $d=0.01$ are shown in Fig. 10.14 and Fig. 10.15, respectively. Only in cases $d=0.003, 0.001$ where the source distance d is extremely small compared to the element, the radial variable transformation $R(\rho)$ of equation (10.19) is more efficient compared to Telles' method.

The reason for this is that when applying the Gauss-Legendre rule to the variable R, obtained by the transformation of equation (10.19), the integration points are ideally positioned to integrate $1/r$ but they are far from ideal for the polynomial interpolation function $\phi_{ij}(\eta_1, \eta_2)$.

Similarly, the effect of the singularity cancelling radial variable transformation

$$R(\rho) = -\frac{1}{\sqrt{\rho^2 + d^2}} \quad , \quad (\alpha = 3) \tag{10.20}$$

in combination with the angular variable transformation $t(\theta)$, on the nearly singular integral

$$\int_S \phi_{ij} \, q^* \, dS \quad , \quad (i, j = -1, 0, 1) \tag{10.34}$$

is shown in Table 10.14, in comparison with Telles' method. The convergence graphs for the cases $d=0.1$ and 0.01 are shown in Fig. 10.16 and Fig. 10.17, respectively.

Many integration points are required in the transformed radial variable R because the integration points are not optimally placed to integrate ϕ_{ij}/r^3 as a whole, instead of $1/r^3$.

Summing up, for nearly singular integrals with kernels including interpolation functions ϕ_{ij}, the exactly cancelling radial variable transformations

$$R(\rho) = \sqrt{\rho^2 + d^2} \quad , \quad (\alpha = 1 \text{ for } u^*) \tag{10.19}$$

$$R(\rho) = -\frac{1}{\sqrt{\rho^2 + d^2}} \quad , \quad (\alpha = 3 \text{ for } q^*) \tag{10.20}$$

do not give efficient numerical integration results. Hence, a more effective and robust radial variable transformation (against interpolation function ϕ_{ij}, curvature of element and position of source point) is required.

Table 10.14 Nearly singular integral $\int_S \phi_{ij}\, q^*\, dS$ over the unit planar square: PLR(0.5, 0.5)

Source distance d	$R(\rho)=-1/\sqrt{\rho^2+d^2}$, $(\alpha=3)$; Angular variable: $t(\theta)$			Telles			Integral $4\pi \int_S \phi_{11}\, q^*\, dS$ (log-L_1, 128×128pts.)
	$N_{t(\theta)}\times N_{R(\rho)}$	total	CPU (msec)	$N_{\gamma_1}\times N_{\gamma_2}$	total	CPU (msec)	
10	8×128	4,096	114	3×4	12	0.53	-2.7808842×10^{-4}
3	7×120	3,360	93	4×5	20	0.75	-3.1225319×10^{-3}
1	8×100	3,200	89	6×6	36	1.2	-2.9528453×10^{-2}
0.3	8×72	2,304	64	9×10	90	2.6	-2.5686670×10^{-1}
0.1	8×25	800	23	14×14	196	5.3	-6.3441539×10^{-1}
0.03	7×28	784	22	25×28	700	19	-8.1669590×10^{-1}
0.01	8×45	1,440	40	45×45	2,025	53	-8.6279332×10^{-1}
0.003	8×72	2,304	64	72×72	5,184	136	-8.7752422×10^{-1}
0.001	8×120	3,840	106	100×100	10,000	262	-8.8157517×10^{-1}

Source point $\mathbf{x}_s=(0.25, 0.25, d)$, relative error $<10^{-6}$.

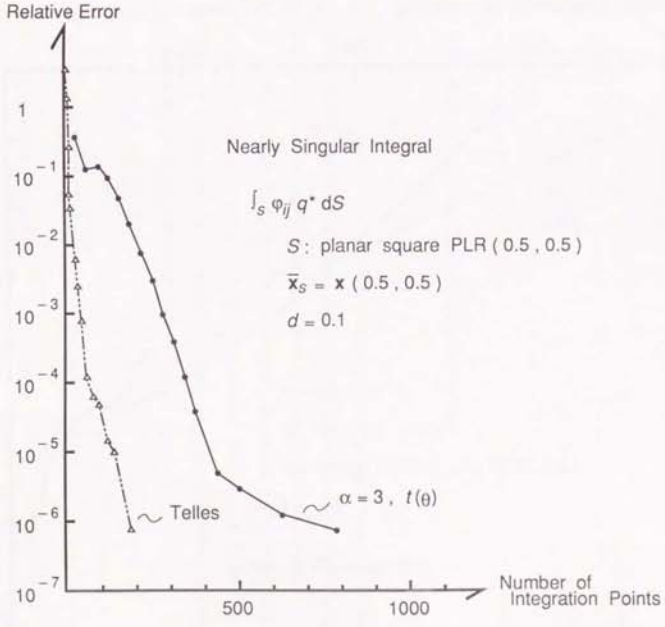

Fig. 10.16 Relative error vs. Number of integration points

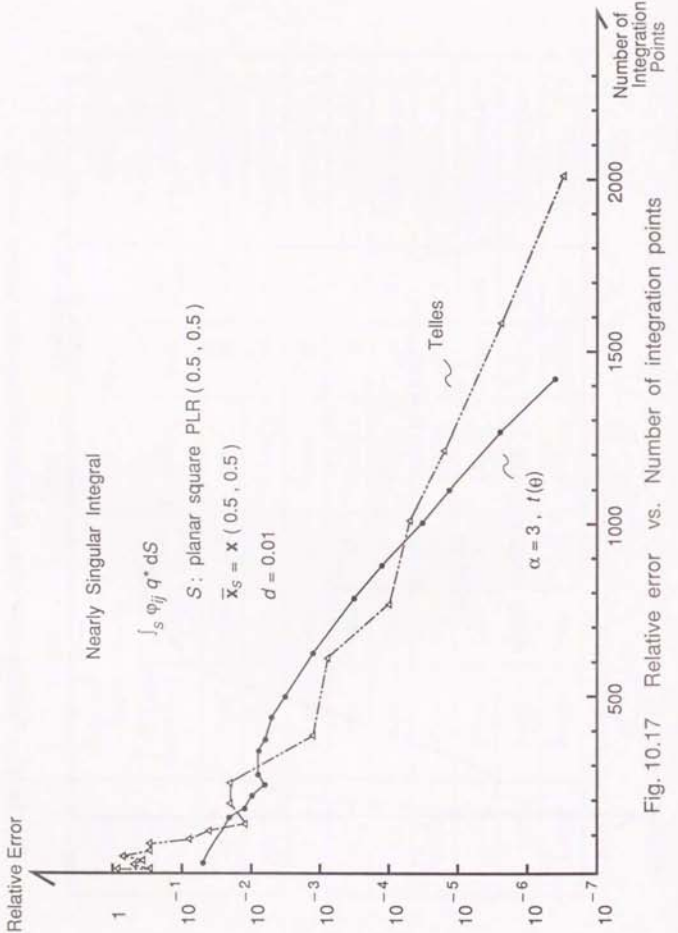

Fig. 10.17 Relative error vs. Number of integration points

10.4 The Derivation of the log-L_2 Radial Variable Transformation

(1) Application of radial variable transformations $\rho\, d\rho = r'^{\beta}\, dR$ $(\beta \neq \alpha)$ to integrals $\int_S 1/r^{\alpha}\, dS$ over curved elements

In search for a more effective and robust radial variable transformation, transformations of the type

$$\rho\, d\rho = r'^{\beta}\, dR \tag{5.61}$$

or

$$R(\rho) = \int \frac{\rho}{r'^{\beta}}\, d\rho \tag{5.71}$$

where

$$r' = \sqrt{\rho^2 + d^2} \tag{5.46}$$

were attempted on nearly singular integrals of the type

$$\int_S \frac{dS}{r^{\alpha}} \tag{10.35}$$

over curved elements. This time, β is not necessarily equal to α, unlike the exactly cancelling transformation. All the combinations of the transformation: β and order of nearly singular integral: α were attempted for $\beta = 1 \sim 5$, $\alpha = 1 \sim 5$.

Tables 10.15~10.19 give the number of integration points required to achieve relative error $\varepsilon < 10^{-6}$ for the calculation of the integrals $\int_S 1/r^{\alpha}\, dS$, $(\alpha = 1 \sim 5)$; by the radial variable transformations of equation (5.61) with $\beta = 1 \sim 5$, respectively. The transformations are given by

$$R(\rho) = \sqrt{\rho^2 + d^2} \quad , \quad (\beta = 1)$$

$$R(\rho) = \log \sqrt{\rho^2 + d^2} \quad , \quad (\beta = 2)$$

$$R(\rho) = -\frac{1}{\sqrt{\rho^2 + d^2}} \quad , \quad (\beta = 3)$$

$$R(\rho) = -\frac{1}{2(\rho^2 + d^2)} \quad , \quad (\beta = 4)$$

$$R(\rho) = -\frac{1}{3\sqrt{\rho^2+d^2}^3} \quad , \quad (\beta=5) \quad . \tag{10.36}$$

The curved element S was chosen as the 'spherical' quadrilateral SPQ60. The source point $\mathbf{x}_s$ was given such that the source projection is $\hat{\mathbf{x}}_s=\mathbf{x}(0.5, 0.5)$, and the source distance $d=10,\ 1,\ 0.1,\ 0.01,\ 0.001$ towards the centre of the sphere.

Table 10.20 gives the actual values of the integrals $\int_S 1/r^\alpha\, dS$, $(\alpha=1\sim5)$ calculated by the PART method with the log-L_1 radial variable transformation of equation (5.85) (, which is the most robust and reliable transformation, as will be shown later on) and the angular variable transformation $t(\theta)$ of equation (5.130), with $N_R=N_t=128$ integration points.

For the case: source distance $d=0.01$, Table 10.21 gives the number of integration points N_R in the transformed radial variable R required to achieve relative error $\varepsilon<10^{-6}$ for the calculation of the integrals $\int_S 1/r^\alpha\, dS$, $(\alpha=1\sim5)$ with the transformations: $\beta=1\sim5$. Fig. 10.18~10.22 give the convergence graphs of relative error ε vs. the number of integration points to calculate the integrals

$\int_S 1/r^\alpha\, dS$, $(\alpha=1\sim5)$ by the radial variable transformations: $\beta=1\sim5$, respectively.

The results show that the radial variable transformation corresponding to $\beta=2$:

$$R(\rho) = \log\sqrt{\rho^2+d^2} \tag{5.64}$$

gives good results for all types of near singularity $\alpha=1\sim5$, (particularly for $d\leqq0.1$). This log-L_2 radial variable transformation requires relatively few integration points, regardless of the order of near singularity α, curvature of the element and source distance d.

As an exception, for the case $\alpha=4$, and 5, the radial variable transformation corresponding to $\beta=3$:

$$R(\rho) = -\frac{1}{\sqrt{\rho^2+d^2}} \tag{10.37}$$

gives better results than the $\beta=2$ (log-L_2) transformation. (The required number of radial integration points is less than a half.)

These results can be explained by the error analysis in Chapter 6 (Table 6.5), where it was shown for planar elements that the numerical integration error $E_n(F)$ in the radial variable is given by

$$E_n(F) \sim \begin{cases} n^{-2\alpha} & , \quad (\alpha=1,3,4,5) \\ 0 & , \quad \alpha=2 \end{cases} \tag{10.38}$$

for the $\beta=2$ (log-L_2) transformation, and

$$E_n(F) \begin{cases} > 4^{-2n} & , \quad (\alpha=1,2) \\ = 0 & , \quad (\alpha=3,4,5) \end{cases} \tag{10.39}$$

for the $\beta=3$ transformation, and

$$E_n(F) \begin{cases} > 4^{-2n} & , \quad (\alpha\neq\beta) \\ = 0 & , \quad (\alpha=\beta) \end{cases} \tag{10.40}$$

for the $\beta=1, 4, 5$ transformation.

For curved elements, $E_n(F)=0$ does not hold strictly, even for $\alpha=\beta$. However, the convergence graphs of Fig. 10.18~10.22 indicate that for $\alpha=\beta$, either the initial relative error is smaller or the initial rate of convergence is faster compared to $\alpha\neq\beta$.

To sum up, the radial variable transformation: $\beta=2$ (log-L_2) is the most robust transformation concerning the order of near singularity $\alpha=1\sim5$. The $\beta=2$ transformation gives best results for $\alpha=1\sim3$, and the $\beta=3$ transformation gives best results for $\alpha=4, 5$.

Considering the robustness for $\alpha=1\sim5$ and the optimality for $\alpha=1\sim3$, the $\beta=2$ (log-L_2) radial variable transformation appears to be the most attractive transformation.

Table 10.15 Nearly singular integral $\int_S 1/r^\alpha \, dS$ over the 'spherical' quadrilateral: SPQ60

(Radial variable transformation $\beta=1$: $R(\rho)=\sqrt{\rho^2+d^2}$)

Source distance d	$\alpha=1$		$\alpha=2$		$\alpha=3$		$\alpha=4$		$\alpha=5$	
	$N_{I(\theta)}\times N_{R(\rho)}$	total	$N_{I(\theta)}\times N_{R(\rho)}$	total	$N_{I(\theta)}\times N_{R(\rho)}$	total	$N_{I(\theta)}\times N_{R(\rho)}$	total	$N_{I(\theta)}\times N_{R(\rho)}$	total
10	6 × 20	480	6 × 20	480	6 × 20	480	5 × 16	320	4 × 20	320
1	6 × 20	480	6 × 20	480	6 × 20	480	6 × 20	480	6 × 20	480
0.1	5 × 14	280	6 × 25	600	7 × 32	896	7 × 35	980	7 × 35	980
0.01	6 × 28	672	7 × 40	1,120	9 × 50	1,800	9 × 60	2,160	9 × 64	2,304
0.001	6 × 60	1,440	9 × 120	4,320	9 × 150	5,400	9 × 170	6,120	9 × 190	6,840
Average CPU-time per point	24 μsec		23 μsec		24 μsec		23 μsec		24 μsec	

Number of integration points necessary for relative error $<10^{-6}$.
Source projection : $\hat{\mathbf{x}}_s=\mathbf{x}(0.5, 0.5)$, source point towards centre of sphere.

Table 10.16 Nearly singular integral $\int_S 1/r^\alpha \, dS$ over the 'spherical' quadrilateral: SPQ60

(Radial variable transformation $\beta=2$: $R(\rho)=\log\sqrt{\rho^2+d^2}$)

Source distance d	$\alpha=1$		$\alpha=2$		$\alpha=3$		$\alpha=4$		$\alpha=5$	
	$N_{I(\theta)}\times N_{R(\rho)}$	total	$N_{I(\theta)}\times N_{R(\rho)}$	total	$N_{I(\theta)}\times N_{R(\rho)}$	total	$N_{I(\theta)}\times N_{R(\rho)}$	total	$N_{I(\theta)}\times N_{R(\rho)}$	total
10	6 × 20	480	5 × 16	320	6 × 20	480	5 × 16	320	4 × 20	320
1	6 × 20	480	6 × 20	480	6 × 20	480	6 × 20	480	6 × 20	480
0.1	5 × 5	100	8 × 12	384	8 × 16	512	7 × 20	560	7 × 20	560
0.01	6 × 8	192	7 × 8	224	9 × 11	396	9 × 14	504	9 × 14	504
0.001	6 × 10	240	9 × 10	360	9 × 14	504	9 × 16	576	9 × 16	576
Average CPU-time per point	26 μsec		25 μsec		25 μsec		24 μsec		26 μsec	

Number of integration points necessary for relative error $<10^{-6}$.
Source projection : $\hat{\mathbf{x}}_s=\mathbf{x}(0.5, 0.5)$, source point towards centre of sphere.

Table 10.17 Nearly singular integral $\int_S 1/r^\alpha \, dS$ over the 'spherical' quadrilateral: SPQ60

(Radial variable transformation $\beta=3$: $R(\rho)=-1/\sqrt{\rho^2+d^2}$)

Source distance d	$\alpha=1$		$\alpha=2$		$\alpha=3$		$\alpha=4$		$\alpha=5$	
	$N_{I(\theta)}\times N_{R(\rho)}$	total	$N_{I(\theta)}\times N_{R(\rho)}$	total	$N_{I(\theta)}\times N_{R(\rho)}$	total	$N_{I(\theta)}\times N_{R(\rho)}$	total	$N_{I(\theta)}\times N_{R(\rho)}$	total
10	6×20	480	6×20	480	6×20	480	5×16	320	4×20	320
1	6×20	480	6×20	480	6×20	480	6×16	384	6×16	384
0.1	6×10	240	6×9	216	7×8	224	7×11	308	7×11	308
0.01	6×35	840	8×25	800	8×14	448	9×6	216	9×6	216
0.001	6×110	2,640	8×80	2,560	9×35	1,260	9×5	180	9×6	216
Average CPU-time per point	24 μsec		24 μsec		24 μsec		25 μsec		25 μsec	

Number of integration points necessary for relative error $<10^{-6}$.
Source projection : $\bar{\mathbf{x}}_s=\mathbf{x}(0.5, 0.5)$, source point towards centre of sphere.

Table 10.18 Nearly singular integral $\int_S 1/r^\alpha \, dS$ over the 'spherical' quadrilateral: SPQ60

(Radial variable transformation $\beta=4$: $R(\rho)=-1/\{2(\rho^2+d^2)\}$)

Source distance d	$\alpha=1$		$\alpha=2$		$\alpha=3$		$\alpha=4$		$\alpha=5$	
	$N_{I(\theta)}\times N_{R(\rho)}$	total	$N_{I(\theta)}\times N_{R(\rho)}$	total	$N_{I(\theta)}\times N_{R(\rho)}$	total	$N_{I(\theta)}\times N_{R(\rho)}$	total	$N_{I(\theta)}\times N_{R(\rho)}$	total
10	6×20	480	6×20	480	6×20	480	5×16	320	4×20	320
1	6×16	384	6×16	384	6×16	384	6×16	384	6×16	384
0.1	6×32	768	6×25	600	7×20	560	7×14	392	8×12	384
0.01	$(6\times 256$ $\varepsilon=5\times 10^{-6}$	6,144)	7×220	6,160	9×150	5,400	9×50	1,800	8×25	800
0.001	$(6\times 256$ $\varepsilon=4\times 10^{-1}$	6,144)	$(9\times 256$ $\varepsilon=5\times 10^{-2}$	9,216)	$(9\times 256$ $\varepsilon=3\times 10^{-4}$	9,216)	8×5	160	10×50	2,000
Average CPU-time per point	24 μsec		23 μsec		24 μsec		24 μsec		24 μsec	

Number of integration points necessary for relative error $<10^{-6}$.
Source projection : $\bar{\mathbf{x}}_s=\mathbf{x}(0.5, 0.5)$, source point towards centre of sphere.

Table 10.19 Nearly singular integral $\int_S 1/r^\alpha \, dS$ over the 'spherical' quadrilateral: SPQ60

(Radial variable transformation $\underline{\beta=5}$: $R(\rho)=-1/\{3(\rho^2+d^2)^{3/2}\}$)

Source distance d	$\alpha=1$		$\alpha=2$		$\alpha=3$		$\alpha=4$		$\alpha=5$	
	$N_{t(\theta)}\times N_{R(\rho)}$	total	$N_{t(\theta)}\times N_{R(\rho)}$	total	$N_{t(\theta)}\times N_{R(\rho)}$	total	$N_{t(\theta)}\times N_{R(\rho)}$	total	$N_{t(\theta)}\times N_{R(\rho)}$	total
10	6×20	480	6×20	480	6×20	480	5×16	320	4×20	320
1	6×16	384	6×16	384	6×16	384	6×16	384	6×16	384
0.1	6×80	1,920	6×72	1,728	7×60	1,680	7×40	1,120	7×16	448
0.01	$(6\times 256$ $\varepsilon=2\times 10^{-1}$	6,144)	$(8\times 256$ $\varepsilon=3\times 10^{-2}$	8,192)	$(9\times 256$ $\varepsilon=1\times 10^{-3}$	9,216)	9×256 $\varepsilon=2\times 10^{-5}$	9,216	10×28	1,120
0.001	$(6\times 256$ $\varepsilon=9\times 10^{-1}$	6,144)	$(9\times 256$ $\varepsilon=3\times 10^{-1}$	9,216)	$(9\times 256$ $\varepsilon=1\times 10^{-2}$	9,216)	9×256 $\varepsilon=1\times 10^{-4}$	9,216	10×20	800
Average CPU-time per point	27 μsec		26 μsec		27 μsec		26 μsec		28 μsec	

Number of integration points necessary for relative error $<10^{-6}$.
Source projection : $\hat{\mathbf{x}}_s=\mathbf{x}(0.5, 0.5)$, source point towards centre of sphere.

Table 10.20 Value of nearly singular integral $\int_S 1/r^\alpha \, dS$ over the 'spherical' quadrilateral: SPQ60

(Source projection: $\hat{\mathbf{x}}_s=\mathbf{x}(0.5, 0.5)$)

Source distance d	$\alpha=1$	$\alpha=2$	$\alpha=3$	$\alpha=4$	$\alpha=5$
10	1.0576605×10^{-1}	1.0722041×10^{-2}	1.0870732×10^{-3}	1.1022767×10^{-4}	1.1178239×10^{-5}
1	1.0467642	1.0501187	1.0534972	1.0569000	1.0603272
0.1	2.8377859	1.0589840×10	5.2819788×10	3.2411271×10^2	2.2689253×10^3
0.01	3.2263821	2.4321063×10	6.1913243×10^2	3.1700026×10^4	2.1147560×10^6
0.001	3.2680995	3.8615209×10	6.2741356×10^3	3.1446057×10^6	2.0964182×10^9

Calculated by the log-L_1 radial variable transformation : $R(\rho)=\log(\rho+d)$, and the angular variable transformation : $t(\theta)$ with $N_{R(\rho)}=N_{t(\theta)}=128$ points.

Table 10.21 Nearly singular integral $\int_S 1/r^{\alpha}\,dS$ over the 'spherical' quadrilateral : SPQ60

(Number of radial integration points N_R by the transforamtion : β)

	$\alpha=1$	$\alpha=2$	$\alpha=3$	$\alpha=4$	$\alpha=5$
$\beta=1$	28	40	50	60	64
$\beta=2$	8	8	11	14	14
$\beta=3$	35	25	14	6	6
$\beta=4$	(256) $\varepsilon=5\times10^{-6}$	220	150	50	25
$\beta=5$	(256) $\varepsilon=9\times10^{-1}$	(256) $\varepsilon=3\times10^{-2}$	(256) $\varepsilon=1\times10^{-3}$	(256) $\varepsilon=2\times10^{-5}$	28

Relative error $\varepsilon<10^{-6}$. Source projection $\bar{x}_s=x(0.5, 0.5)$.
Source distance $d=0.01$, towards centre of sphere.

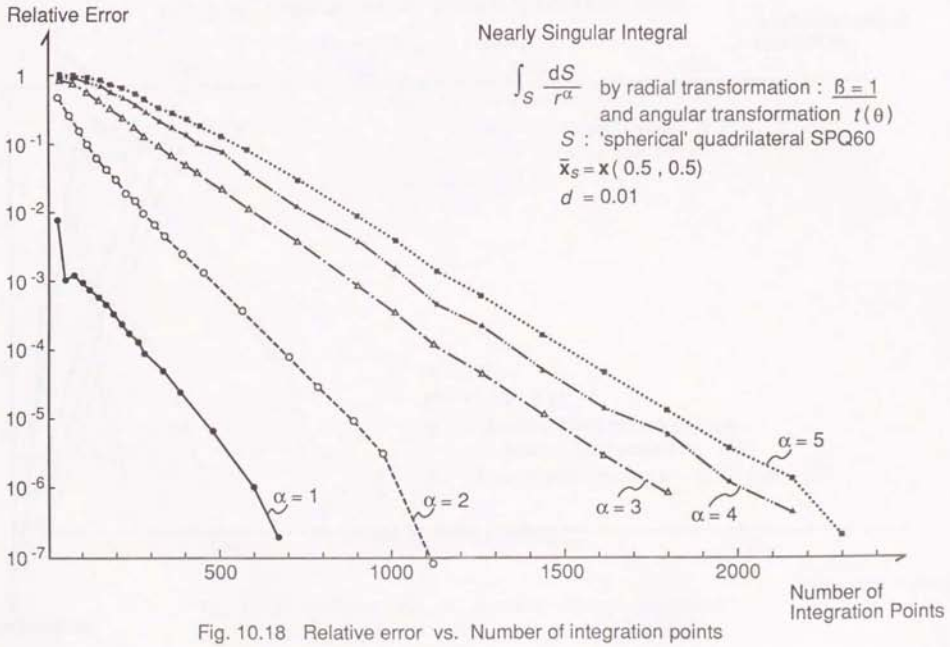

Fig. 10.18 Relative error vs. Number of integration points

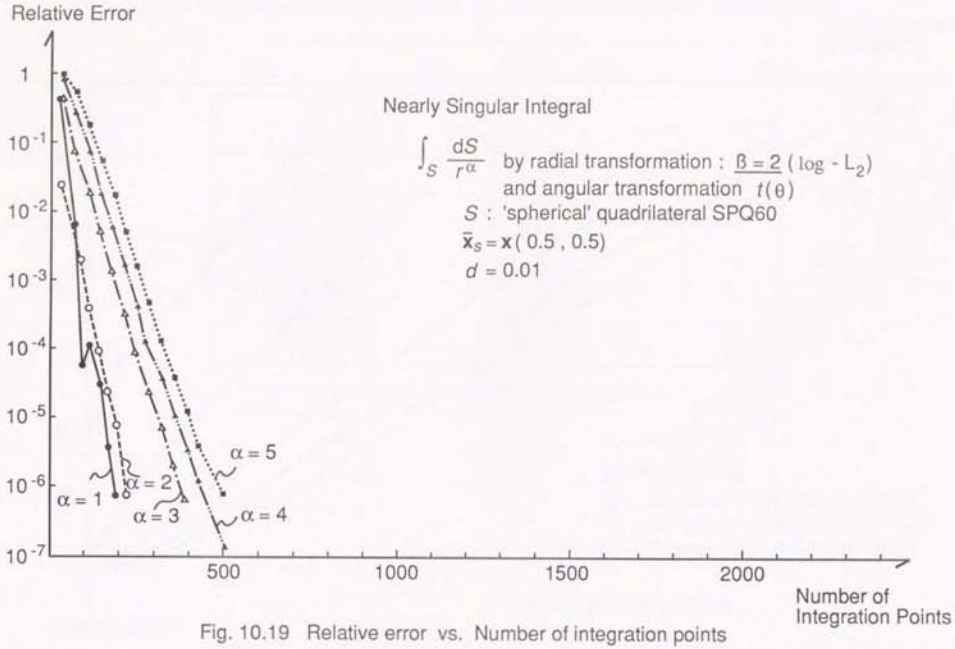

Fig. 10.19 Relative error vs. Number of integration points

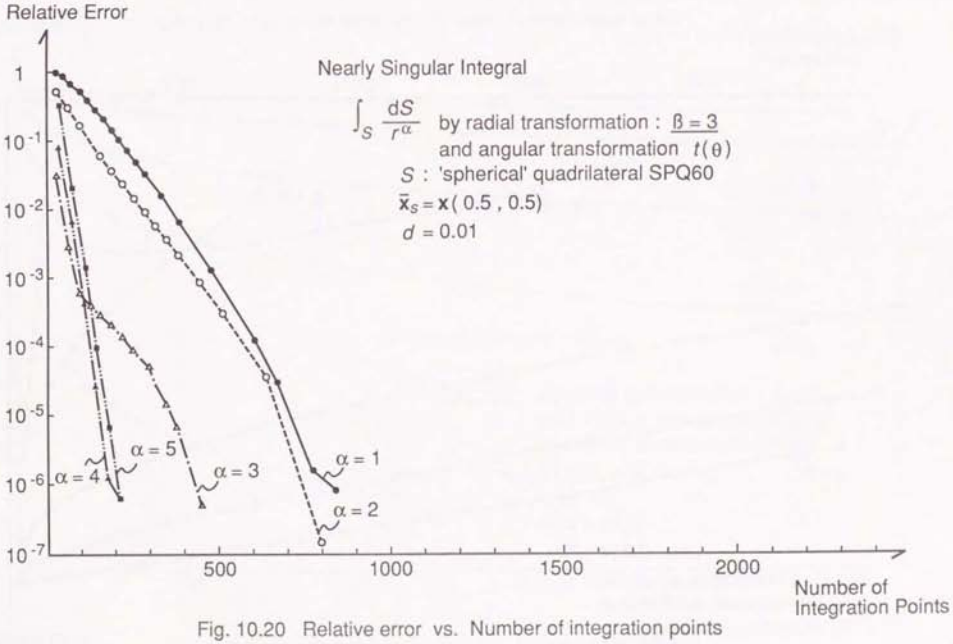

Fig. 10.20 Relative error vs. Number of integration points

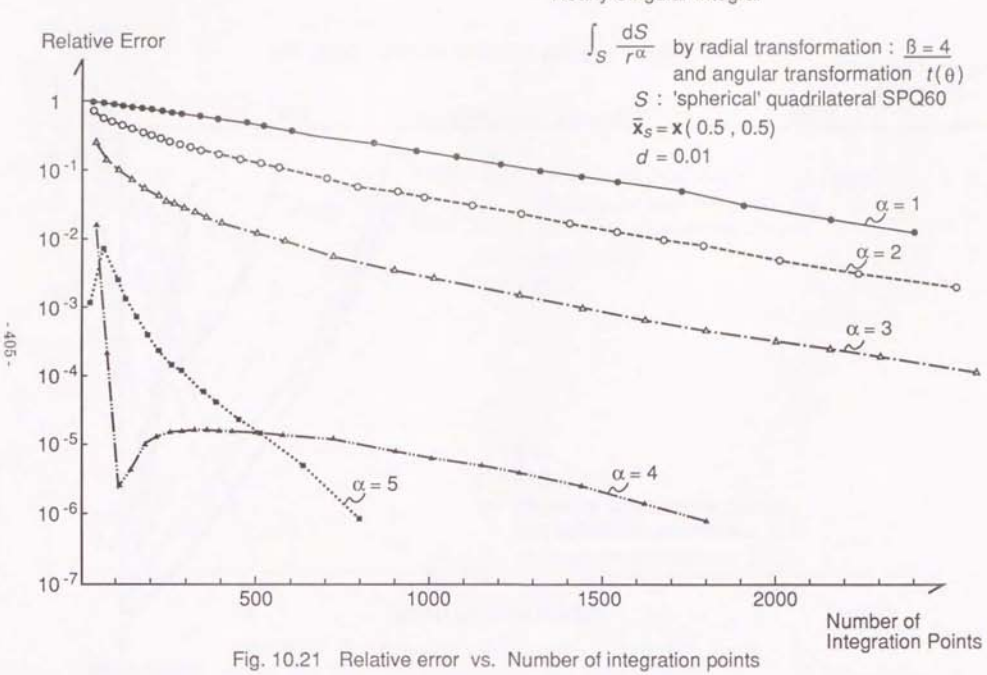

Fig. 10.21 Relative error vs. Number of integration points

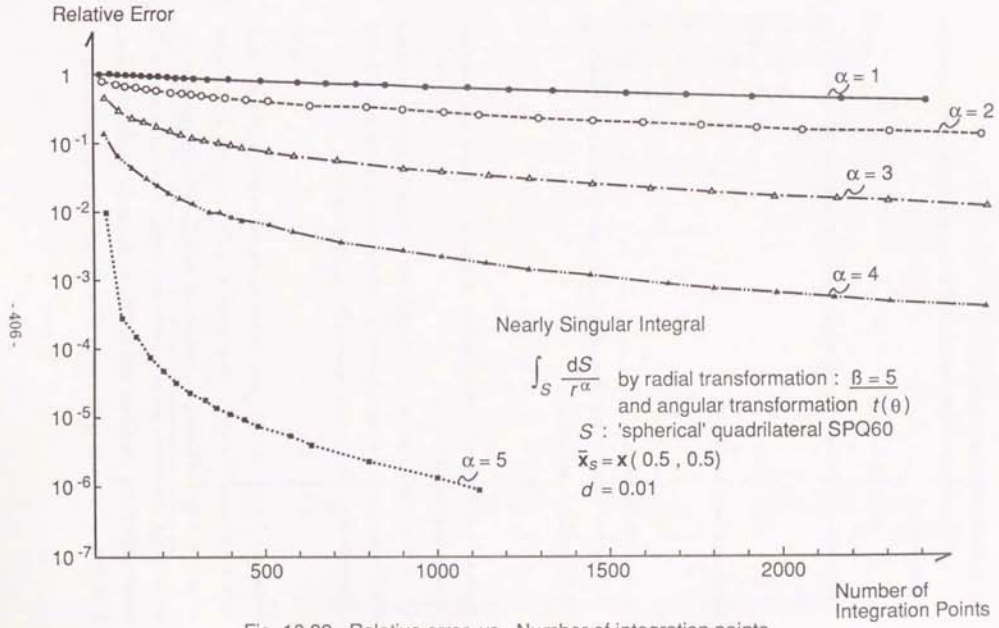

Fig. 10.22 Relative error vs. Number of integration points

(2) Difficulty with flux calculation

In the previous section, it was shown that the log-L_2 radial variable transformation:

$$R(\rho) = \log \sqrt{\rho^2 + d^2} \tag{5.64}$$

corresponding to $\beta=2$ is the most robust radial variable transformation of the type

$$\rho \, d\rho = r^{*\beta} \, dR \tag{5.61}$$

for the calculation of integrals

$$\int_S \frac{dS}{r^\alpha} \quad , \quad (\alpha = 1 \sim 5)$$

over a curved element S.

However, the log-L_2 transformation of equation (5.64) works very poorly for nearly singular integrals like

$$\int_S \frac{\partial u^*}{\partial \mathbf{x}_s} dS \quad , \quad \int_S \frac{\partial q^*}{\partial \mathbf{x}_s} dS \quad ,$$

which arise in the calculation of the flux $\partial u/\partial \mathbf{x}_s$ at a point $\mathbf{x}_s$ very near the boundary using equation (2.46).

In Fig. 10.23, the result of applying the log-L_2 radial variable transformation with the angular variable transformation $t(\theta)$ of equation (5.127) is shown for the constant planar square element PLR(0.5, 0.5) :

$$-0.5 \leq x, y \leq 0.5 \, , \quad z=0 \tag{10.43}$$

of size one (cf. section 8.2 (1)), with the source point at $\mathbf{x}_s=(0.25, 0.25, d)$, where the source distance is $d=0.01$. The integrals $\int_S u^* dS$, $\int_S q^* dS$ related to the calculation of the potential at $\mathbf{x}_s$, and the integrals $\int_S \partial u^*/\partial \mathbf{x}_s \, dS$, $\int_S \partial q^*/\partial \mathbf{x}_s \, dS$ related to the flux calculation at $\mathbf{x}_s$, were calculated. The relative error ε is plotted against the (necessary and sufficient) number of integration points $N=N_t \times N_R \times 4$, where N_t is the number of Gauss-Legendre integration points

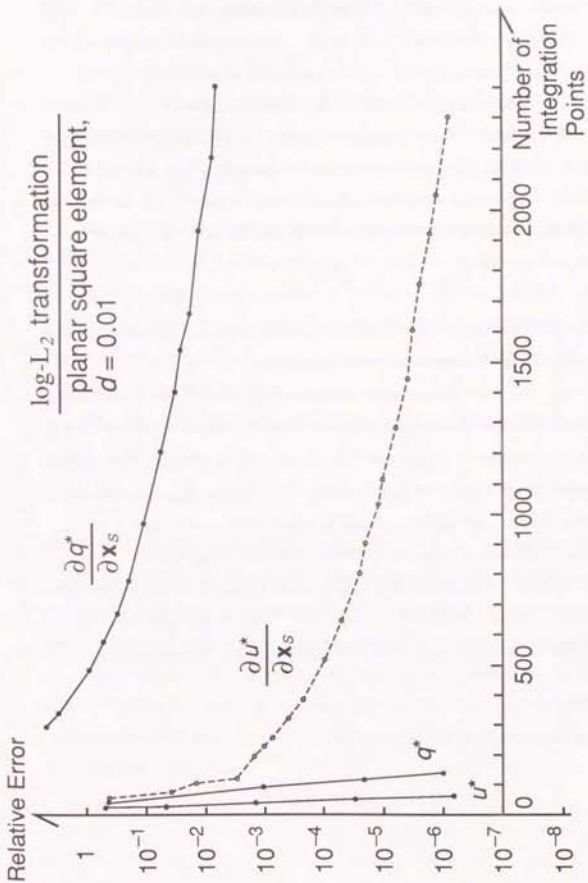

Fig. 10.23 Integration of potential and flux kernels using the log-L_2 transformation

for the angular variable t, and N_R for the radial variable R. N_t was 3, 7, 8 and 12 for the kernels u^*, q^*, $\partial u^*/\partial \mathbf{x}_s$, and $\partial q^*/\partial \mathbf{x}_s$, respectively, for relative error : $\varepsilon < 10^{-6}$.

From Fig. 10.23, it is evident that the log-L_2 radial variable transformation, which is so successful with the integration of nearly singular potential kernels u^* and q^*, turns out to be inefficient for the flux kernels $\partial u^*/\partial \mathbf{x}_s$ and $\partial q^*/\partial \mathbf{x}_s$. The reason for this was analysed in sections 5.5 (4), 6.8 and 7.7 (2). In short, the potential kernels essentially give rise to radial integrals with $\delta = 1$ only, in

$$I_{\alpha,\delta} = \int_0^{\rho_j} \frac{\rho^\delta}{r^\alpha} \, d\rho \ , \qquad r = \sqrt{\rho^2 + d^2} \ ,$$

where as the flux kernels involve radial integrals with $\delta = 2$ as well as $\delta = 1$, which causes the difficulty with the log-L_2 transformation.

In fact, for $\delta = 2$, the theoretical estimate of equation (7.190) in section 7.7 (iv) for the log-L_2 transformation predicts an error estimate of order $n^{-\delta-1} = n^{-3}$, where n is the number of integration points in the radial variable. This matches remarkably well with the convergence graphs of numerical experiment results in Fig. 10.23, where $\int_S \partial u^*/\partial \mathbf{x}_s \, dS$ gives a convergence of order $n^{-3.1}$ and $\int_S \partial q^*/\partial \mathbf{x}_s \, dS$ gives a convergence of order $n^{-3.0}$ for the relative error.

The excellent convergence of the log-L_2 transformation for the integration of the potential kernels u^* and q^*, where $\delta = 1$: odd, is also predicted by the theoretical error estimate $E_n(f) \sim n^{-2n}$ of equation (7.120) in section 7.7 (1).

10.5 The log-L_1 Radial Variable Transformation

In order to overcome the difficulty with flux calculation using the log-L_2 radial variable transformation, in section 5.5 (4) we introduced the log-L_1 radial variable transformation :

$$R(\rho) = \log(\rho + d) \qquad (5.85)$$

In Fig. 10.24, the result of calculating the same integrals as in Fig. 10.23 but with the log-L_1 instead of the log-L_2 radial variable transformation is given. Notice the remarkable improvement of the log-L_1 over the log-L_2 for the error convergence for the flux integrals $\int_S \partial u^*/\partial \mathbf{x}_s \, dS$ and $\int_S \partial q^*/\partial \mathbf{x}_s \, dS$. Note also that the log-L_1 transformation works reasonably well for the potential integrals $\int_S u^* \, dS$ and $\int_S q^* \, dS$, as well.

The theoretical error estimate of section 7.8 (2) (iii) predicts the relative error ε to be of order

$$\varepsilon \sim \sigma^{-2n} \qquad (7.266)$$

where $\sigma = 1.40$ for $d = 0.01$ from Table 7.7, and n is the number of radial integration points. This matches fairly well with the convergence graphs in Fig. 10.24, which give relative error of orders 1.6^{-n} and 1.7^{-n} approximately, for the integration of $\partial u^*/\partial \mathbf{x}_s$ and $\partial q^*/\partial \mathbf{x}_s$, respectively, for flux calculations.

The theoretical error estimate of equation (7.229) in section 7.8 (1), using the saddle point method, predicts an error of order n^{-2n} for the case $\alpha = \delta = 1$, which corresponds to the integration of u^*. This explains the excellent convergence for the u^* kernel in Fig. 10.24.

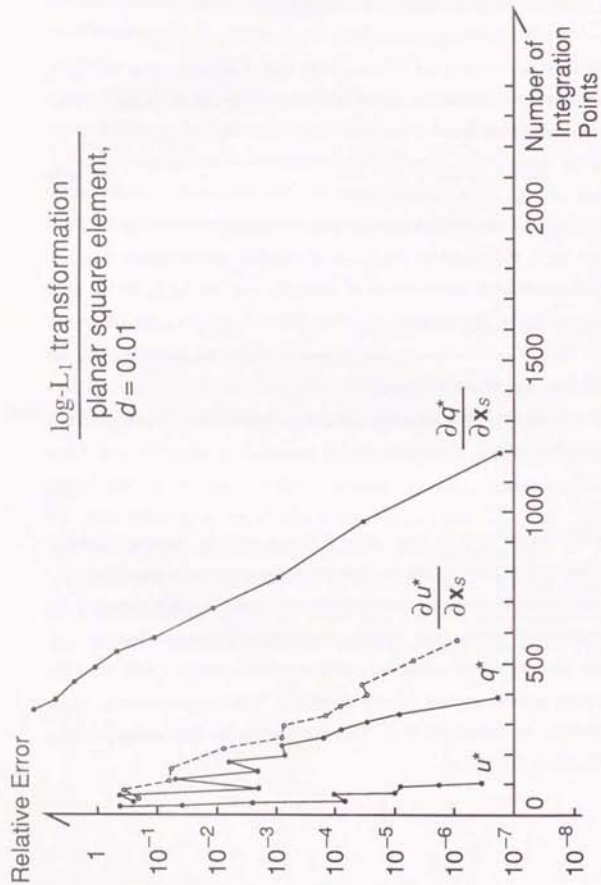

Fig. 10.24 Integration of potential and flux kernels using the log-L_1 transformation

10.6 Comparison of Radial Variable Transformations for the Model Radial Integral $I_{\alpha,\delta}$

In section 3.3 (Table 3.2, 3.3) and section 7.5 (Table 7.1), it was shown that the essential nature of nearly singular integrals occurring in the boundary element analysis of three dimensional potential problems can be characterized by the following model integral in the radial variable :

$$I_{\alpha,\delta} = \int_0^{\rho_j} \frac{\rho^\delta}{r^\alpha} \, d\rho \tag{10.45}$$

where

$$r = \sqrt{\rho^2 + d^2} \tag{10.46}$$

for planar elements, and $\rho_j \equiv \rho_j(\theta)$ is the upper limit of the radial variable of the integral in equation (5.42). The basic integral kernels in three dimensional boundary element analysis give rise to α, δ given in Table 7.1, which is reproduced below.

Table 7.1 Nature of nearly singular kernels of the radial component integrals in 3-D potential problems

	α	δ
u^*	1	1
q^*	3	1
$\frac{\partial u^*}{\partial x_s}$	3	1 2
$\frac{\partial q^*}{\partial x_s}$	3	1
	5	1 2

In the present section, we will compare the effect of different radial variable transformations on the numerical integration of $I_{\alpha,\delta}$ of equation (10.45). The transformations to be compared are

(1) Transformations based on the Gauss-Legendre rule :

(i) Identity transformation :

$$R(\rho) = \rho \tag{10.47}$$

(ii) log-L_2 transformation :

$$R(\rho) = \log \sqrt{\rho^2 + d^2} \tag{5.64}$$

(iii) log-L_1 transformation :

$$R(\rho) = \log (\rho + d) \tag{5.85}$$

(iv) $L_1^{-1/m}$ transformation :

$$R(\rho) = -(\rho + d)^{-\frac{1}{m}} \tag{5.99}$$

and

(2) Transformations based on the truncated trapezium rule :

(i) Single Exponential (SE) transformation

$$\rho(R) = \frac{\rho_j}{2}(1 + \tanh R) \tag{5.101}$$

(ii) Double Exponential (DE) Transformation

$$\rho(R) = \frac{\rho_j}{2}\left\{1 + \tanh\left(\frac{\pi}{2}\sinh R\right)\right\} \tag{5.112}$$

Numerical results will be compared with the following closed form integrals obtained in section 3.3 (equations (3.138~142)) and section 7.8 (2) (iii) (Table 7.5).

$$I_{1,1} = \sqrt{\rho_j^2 + d^2} - d = \rho_j(\sqrt{1+D^2} - D) \tag{10.48}$$

$$I_{3,1} = \frac{1}{d} - \frac{1}{\sqrt{\rho_j^2 + d^2}} = \frac{1}{\rho_j}\left(\frac{1}{D} - \frac{1}{\sqrt{1+D^2}}\right) \tag{10.49}$$

$$I_{3,2} = \log(\rho_j + \sqrt{\rho_j^2 + d^2}) - \log d - \frac{\rho_j}{\sqrt{\rho_j^2 + d^2}} \tag{10.50}$$

$$= \log\left(\frac{1+\sqrt{1+D^2}}{D}\right) - \frac{1}{\sqrt{1+D^2}} \tag{10.50}$$

$$I_{5,1} = \frac{1}{3}\left(\frac{1}{d^3} - \frac{1}{\sqrt{\rho_j^2 + d^2}^3}\right) = \frac{1}{3\rho_j^3}\left(\frac{1}{D^3} - \frac{1}{\sqrt{1+D^2}^3}\right) \tag{10.51}$$

$$I_{5,2} = \frac{\rho_j^3}{3d^2\sqrt{\rho_j^2 + d^2}^3} = \frac{1}{3\rho_j^2 D^2\sqrt{1+D^2}^3} \tag{10.52}$$

Also, theoretical error estimates for the identity, log-L_2 and log-L_1 transformations will be compared with numerical results.

Tables 10.22~41 give the number of (radial) integration points required to obtain a relative error $\varepsilon < 10^{-6}$, for the integration of the model integrals $I_{\alpha,\delta}$ of equation (10.45), using each radial variable transformation in conjunction with the Gauss-Legendre rule or the truncated trapezium rule. ρ_j was set to $\rho_j = 1$ and the source distance d was varied from 10 to 10^{-3}. The integration error was obtained by comparing with the analytical integration results of equation (10.48~52).

Table 10.42 sums up the results of Tables 10.22~41. The number of integration points required for the potential integrals ($\alpha = 1, \delta = 1$ and $\alpha = 3, \delta = 1$) and the flux integrals ($\alpha = 3; \delta = 1, 2$ and $\alpha = 5; \delta = 1, 2$) are given.

Figures 10.25~31 give the convergence graphs of the relative error of numerical integration ε (in log scale) vs the number of radial integration points n for each radial variable transformation, for the case $d=0.01$.

Table 10.22 Identity transformation :

$R(\rho)=\rho$

α	δ	Source distance : d				
		10	1	10^{-1}	10^{-2}	10^{-3}
1	1	3	5	12	35	80
3	1	3	6	16	60	190
	2	3	5	20	55	170
5	1	3	6	20	64	210
	2	3	7	25	60	190

(Number of radial integration points n for relative error $\varepsilon < 10^{-6}$.)

Table 10.23 log-L_2 transformation :

$R(\rho)=\log\sqrt{\rho^2+d^2}$

α	δ	Source distance : d				
		10	1	10^{-1}	10^{-2}	10^{-3}
1	1	2	3	4	5	6
3	1	2	3	4	5	6
	2	55	55	64	72	80
5	1	2	3	6	8	10
	2	55	64	120	170	200

(n for $\varepsilon < 10^{-6}$)

Table 10.24 log-L_1 transformation :

$R(\rho)=\log(\rho+d)$

α	δ	Source distance : d				
		10	1	10^{-1}	10^{-2}	10^{-3}
1	1	3	5	8	9	8
3	1	3	5	12	16	20
	2	3	6	11	11	16
5	1	3	6	14	20	25
	2	3	6	14	20	20

(n for $\varepsilon < 10^{-6}$)

Table 10.25 $L_1^{-1/m}$ transformation :

$(m=1)$

$R(\rho)=-\dfrac{1}{\rho+d}$

α	δ	Source distance : d				
		10	1	10^{-1}	10^{-2}	10^{-3}
1	1	3	5	14	45	150
3	1	3	6	8	9	9
	2	3	6	12	35	110
5	1	3	6	10	11	11
	2	4	6	10	11	11

(n for $\varepsilon < 10^{-6}$)

Table 10.26 $L_1^{-1/m}$ transformation : ($m=2$)

$$R(\rho) = -\frac{1}{\sqrt{\rho+d}}$$

α	δ	Source distance : d				
		10	1	10^{-1}	10^{-2}	10^{-3}
1	1	3	5	8	16	28
3	1	3	6	9	10	12
	2	3	5	7	11	20
5	1	3	6	11	12	14
	2	4	6	10	14	14

(n for $\varepsilon < 10^{-6}$)

Table 10.27 $L_1^{-1/m}$ transformation : ($m=2.5$)

$$R(\rho) = -(\rho+d)^{-\frac{1}{2.5}}$$

α	δ	Source distance : d				
		10	1	10^{-1}	10^{-2}	10^{-3}
1	1	3	5	8	14	25
3	1	3	6	8	12	14
	2	3	5	9	10	14
5	1	3	6	11	14	16
	2	4	6	12	14	16

(n for $\varepsilon < 10^{-6}$)

Table 10.28 $L_1^{-1/m}$ transformation : ($m=3$)

$$R(\rho) = -(\rho+d)^{-\frac{1}{3}}$$

α	δ	Source distance : d				
		10	1	10^{-1}	10^{-2}	10^{-3}
1	1	3	5	8	11	20
3	1	3	6	10	14	14
	2	3	6	9	11	10
5	1	3	6	12	16	16
	2	3	6	11	16	16

(n for $\varepsilon < 10^{-6}$)

Table 10.29 $L_1^{-1/m}$ transformation : ($m=3.5$)

$$R(\rho) = -(\rho+d)^{-\frac{1}{3.5}}$$

α	δ	Source distance : d				
		10	1	10^{-1}	10^{-2}	10^{-3}
1	1	3	5	7	10	16
3	1	3	6	10	12	16
	2	3	6	10	11	12
5	1	3	5	12	16	20
	2	3	6	11	16	20

(n for $\varepsilon < 10^{-6}$)

Table 10.30 $L_1^{-1/m}$ transformation : ($m=4$)

$$R(\rho) = -(\rho+d)^{-\frac{1}{4}}$$

α	δ	Source distance : d				
		10	1	10^{-1}	10^{-2}	10^{-3}
1	1	3	5	7	9	14
3	1	3	6	10	14	16
	2	3	6	10	10	11
5	1	3	5	12	16	20
	2	3	6	10	14	20

(n for $\varepsilon < 10^{-6}$)

Table 10.31 $L_1^{-1/m}$ transformation : ($m=4.5$)

$$R(\rho) = -(\rho+d)^{-\frac{1}{4.5}}$$

α	δ	Source distance : d				
		10	1	10^{-1}	10^{-2}	10^{-3}
1	1	3	5	7	9	12
3	1	3	6	10	14	16
	2	3	6	10	12	14
5	1	3	6	12	16	20
	2	3	6	12	16	16

(n for $\varepsilon < 10^{-6}$)

Table 10.32 $L_1^{-1/m}$ transformation : ($m=5$)

$$R(\rho) = -(\rho+d)^{-\frac{1}{5}}$$

α	δ	Source distance : d				
		10	1	10^{-1}	10^{-2}	10^{-3}
1	1	3	5	7	8	11
3	1	3	5	9	14	16
	2	3	6	10	12	14
5	1	3	6	11	16	20
	2	3	6	12	16	20

(n for $\varepsilon < 10^{-6}$)

Table 10.33 $L_1^{-1/m}$ transformation : ($m=5.5$)

$$R(\rho) = -(\rho+d)^{-\frac{1}{5.5}}$$

α	δ	Source distance : d				
		10	1	10^{-1}	10^{-2}	10^{-3}
1	1	3	5	7	8	11
3	1	3	5	11	14	11
	2	3	6	7	14	12
5	1	3	6	11	16	20
	2	3	6	12	20	20

(n for $\varepsilon < 10^{-6}$)

Table 10.34 $L_1^{-1/m}$ transformation : ($m=6$)

$R(\rho) = -(\rho+d)^{-\frac{1}{6}}$

α	δ	Source distance : d				
		10	1	10^{-1}	10^{-2}	10^{-3}
1	1	3	5	7	8	10
3	1	3	5	11	14	20
	2	3	6	10	14	14
5	1	3	6	14	16	20
	2	3	6	12	20	20

(n for $\varepsilon < 10^{-6}$)

Table 10.35 $L_1^{-1/m}$ transformation : ($m=7$)

$R(\rho) = -(\rho+d)^{-\frac{1}{7}}$

α	δ	Source distance : d				
		10	1	10^{-1}	10^{-2}	10^{-3}
1	1	3	5	8	8	10
3	1	3	5	11	14	16
	2	3	6	10	14	16
5	1	3	6	14	20	20
	2	3	6	12	20	20

(n for $\varepsilon < 10^{-6}$)

Table 10.36 $L_1^{-1/m}$ transformation : ($m=10$)

$R(\rho) = -(\rho+d)^{-\frac{1}{10}}$

α	δ	Source distance : d				
		10	1	10^{-1}	10^{-2}	10^{-3}
1	1	3	5	8	5	9
3	1	3	5	11	16	20
	2	3	6	10	14	16
5	1	3	6	14	20	20
	2	3	6	11	20	25

(n for $\varepsilon < 10^{-6}$)

Table 10.37 $L_1^{-1/m}$ transformation : ($m=100$)

$R(\rho) = -(\rho+d)^{-\frac{1}{100}}$

α	δ	Source distance : d				
		10	1	10^{-1}	10^{-2}	10^{-3}
1	1	3	5	8	9	8
3	1	3	5	12	14	20
	2	3	6	11	16	16
5	1	3	6	14	20	25
	2	3	6	10	16	25

(n for $\varepsilon < 10^{-6}$)

Table 10.38 Single Exponential (SE) transformation with $R(\rho) : [-\infty, +\infty]$

α	δ	Source distance : d				
		10	1	10^{-1}	10^{-2}	10^{-3}
1	1	32	66	66	30	30
3	1	32	66	56	46	54
	2	70	68	62	58	58
5	1	32	64	40	48	58
	2	70	58	50	38	48

(Number of radial integration points n for relative error $\varepsilon < 10^{-6}$)

Table 10.39 Double Exponential (DE) transformation with $R(\rho) : [-\infty, +\infty]$

α	δ	Source distance : d				
		10	1	10^{-1}	10^{-2}	10^{-3}
1	1	22	22	38	38	38
3	1	22	22	36	66	70
	2	22	22	38	36	68
5	1	22	22	32	66	72
	2	22	22	34	60	66

(n for $\varepsilon < 10^{-6}$)

Table 10.40 Single Exponential (SE) transformation with $R(\rho) : [-\infty, 0]$

α	δ	Source distance : d				
		10	1	10^{-1}	10^{-2}	10^{-3}
1	1	1916	1015	64	21	13
3	1	1916	1185	1260	410	128
	2	3016	743	1032	1196	752
5	1	1917	2318	202	26	31
	2	1370	858	521	84	26

(n for $\varepsilon < 10^{-6}$)

Table 10.41 Double Exponential (DE) transformation with $R(\rho) : [-\infty, 0]$

α	δ	Source distance : d				
		10	1	10^{-1}	10^{-2}	10^{-3}
1	1	1688	872	55	17	17
3	1	1688	883	498	266	72
	2	1360	717	825	479	528
5	1	1689	1741	126	35	38
	2	1360	728	439	32	68

(n for $\varepsilon < 10^{-6}$)

Table 10.42 Number of radial integration points for potential and flux integrals ($\varepsilon < 10^{-6}$.)

radial transformation	Potential integral $\alpha=1,\ \delta=1$; $\alpha=3,\ \delta=1$ Source distance : d					flux integral $\alpha=3,\ \delta=1,2$ $\alpha=5,\ \delta=1,2$ Source distance : d				
	10	1	10^{-1}	10^{-2}	10^{-3}	10	1	10^{-1}	10^{-2}	10^{-3}
identity	3	6	16	60	190	3	7	25	64	210
log-L_2	2	3	4	5	6	55	64	120	170	200
log-L_1	3	5	12	16	20	3	6	14	20	25
$L_1{}^{-1}$	3	6	14	45	150	4	6	12	35	110
$L_1{}^{-1/2}$	3	6	9	16	28	4	6	11	14	20
$L_1{}^{-1/2.5}$	3	6	8	14	25	4	6	12	14	16
$L_1{}^{-1/3}$	3	6	10	14	20	3	6	12	16	16
$L_1{}^{-1/3.5}$	3	6	10	12	16	3	6	12	16	20
$L_1{}^{-1/4}$	3	6	10	14	16	3	6	12	16	20
$L_1{}^{-1/4.5}$	3	6	10	14	16	3	6	12	16	20
$L_1{}^{-1/5}$	3	5	9	14	16	3	6	12	16	20
$L_1{}^{-1/5.5}$	3	5	11	14	11	3	6	12	20	20
$L_1{}^{-1/6}$	3	5	11	14	20	3	6	14	20	20
$L_1{}^{-1/7}$	3	5	11	14	16	3	6	14	20	20
$L_1{}^{-1/10}$	3	5	11	16	20	3	6	14	20	25
$L_1{}^{-1/100}$	3	5	12	14	20	3	6	14	20	25
single exponential (SE)	32	66	66	46	54	70	68	62	58	58
double exponential (DE)	22	22	38	66	70	22	22	38	66	72

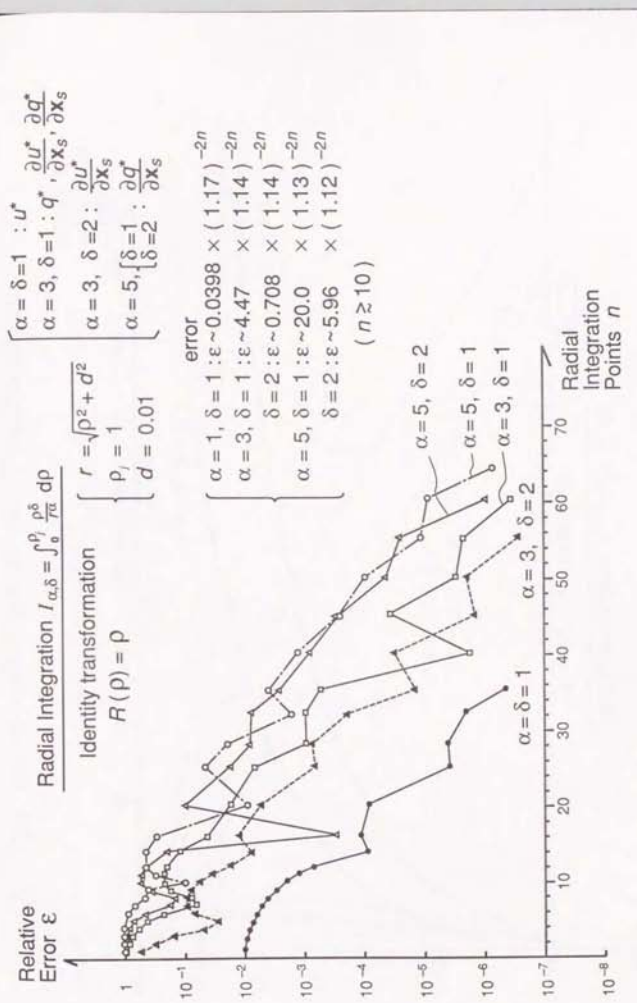

Fig. 10.25 Radial integral $I_{\alpha,\delta}$ by identity transformation

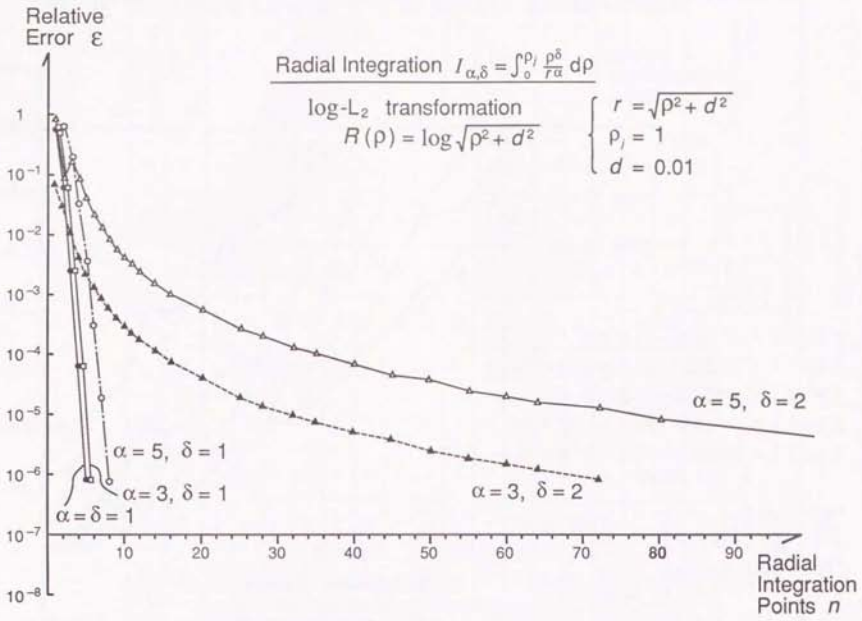

Fig. 10.26 Radial integral $I_{\alpha,\delta}$ by log-L_2 transformation

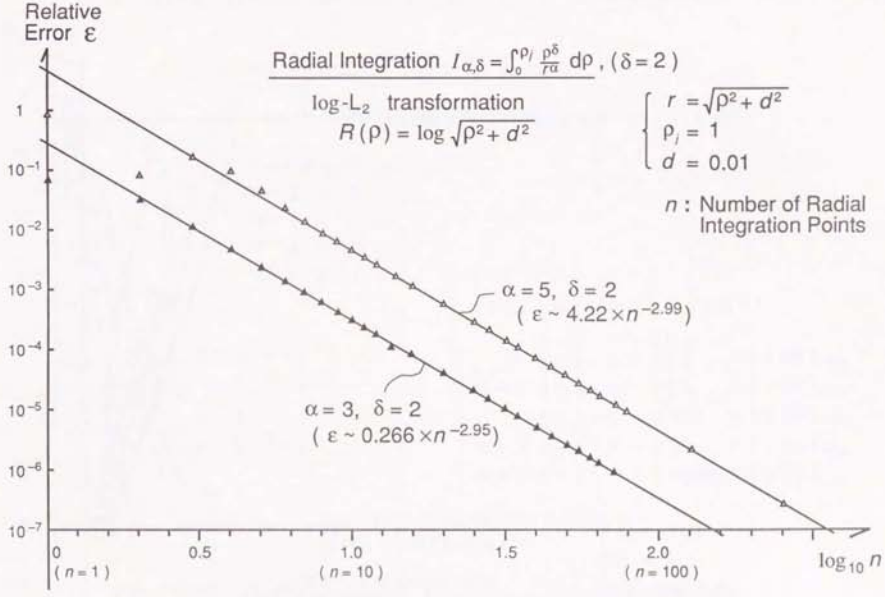

Fig. 10.27 Convergence rate for log-L_2 transformation

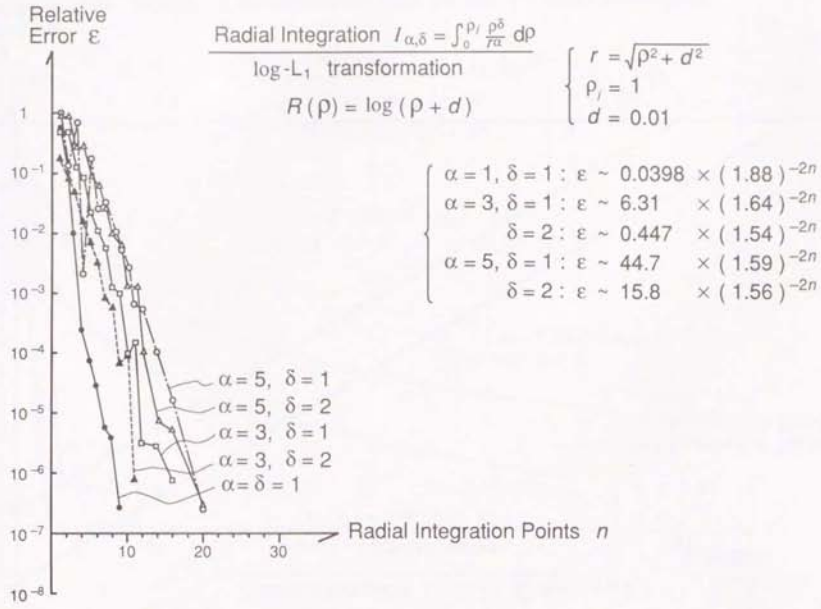

Fig. 10.28 Radial integral $I_{\alpha,\delta}$ by log-L$_1$ transformation

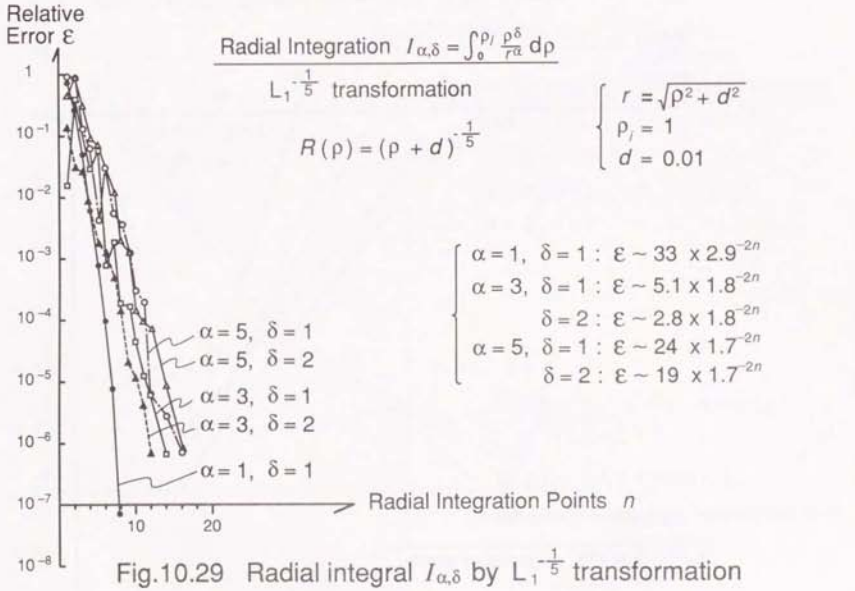

Fig.10.29 Radial integral $I_{\alpha,\delta}$ by L$_1^{-\frac{1}{5}}$ transformation

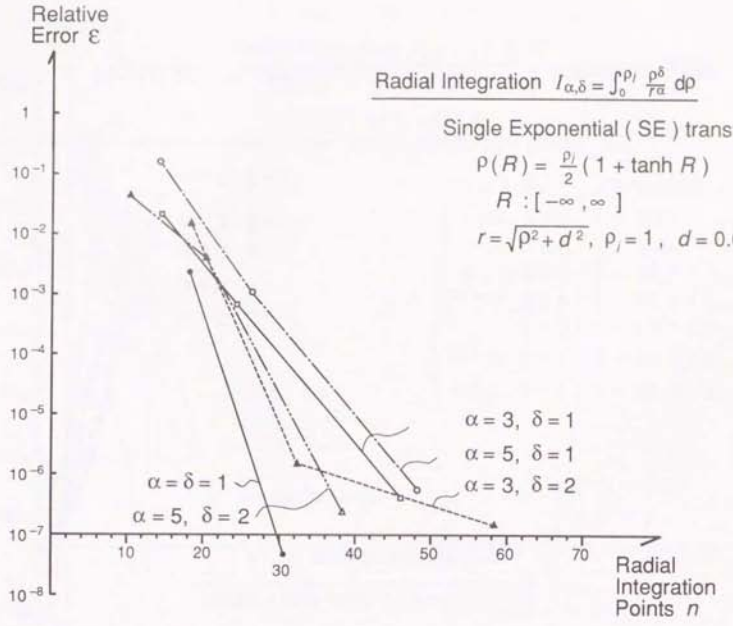

Fig. 10.30 Radial integral $I_{\alpha,\delta}$ by Single Exponential (SE) transformation

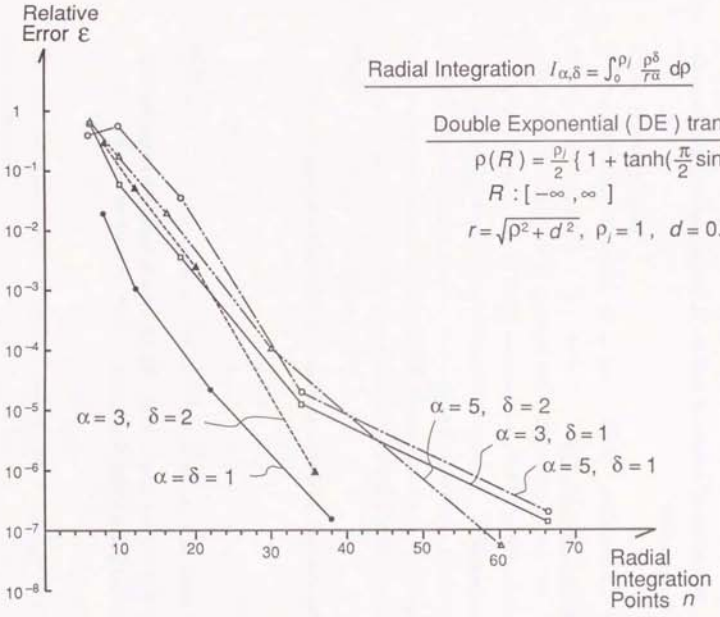

Fig. 10.31 Radial integral $I_{\alpha,\delta}$ by Double Exponential (DE) transformation

(1) Transformations based on the Gauss-Legendre rule

(i) Identity transformation

From Table 10.22 and Fig. 10.25, it is clear that the identity transformation (just polar coordinates) requires a huge number of radial integration points for nearly singular integrals ($D = d/\rho_j \ll 1$).

The theoretical estimate of the error E_n given in section 7.6 (3), equation (7.76) implies that

$$E_n \sim (1-t)^{-\frac{\alpha}{2}} \sigma^{-2n} \quad , \tag{10.53}$$

where, in order to maintain

$$(1-t)^{-\frac{\alpha}{2}} < 10 \quad , \tag{7.77}$$

t must satisfy

$$0 < t < 1-10^{-2/\alpha} = \begin{cases} 0.99 & (\alpha=1) \\ 0.78 & (\alpha=3) \\ 0.60 & (\alpha=5) \end{cases} \quad . \tag{7.268}$$

Hence, if we take the maximum values for t, equation (7.64) gives

$$\sigma = \begin{cases} 1.15 & (\alpha=1) \\ 1.13 & (\alpha=3) \\ 1.12 & (\alpha=5) \end{cases} \tag{10.54}$$

for $D=d=0.01$ in equation (10.53). This theoretical estimate matches well with numerical results in Fig. 10.25, where

$$\sigma = \begin{cases} 1.17 & (\alpha=\delta=1) \\ 1.14 & (\alpha=3, \delta=1) \\ 1.14 & (\alpha=3, \delta=2) \\ 1.13 & (\alpha=5, \delta=1) \\ 1.12 & (\alpha=5, \delta=2) \end{cases} \quad . \tag{10.55}$$

(ii) log-L_2 transformation

Table 10.23 and Fig. 10.26 show that the log-L_2 transformation is very efficient for the integration of $I_{\alpha,\delta}$ when $\delta=1$, but on the other hand very inefficient for the integration of $I_{\alpha,\delta}$ when $\delta=2$. This is in accordance with Fig. 10.23. There, the log-L_2 radial variable transformation gave remarkably good convergence for the calculation of the potential integrals $\int_S u^* \, dS$ and $\int_S q^* \, dS$, which correspond to $\alpha=\delta=1$ and $\alpha=3, \delta=1$, respectively. On the other hand, the log-L_2 transformation gave very slow convergence for the flux integrals $\int_S \partial u^*/\partial \mathbf{x}_s \, dS$ and $\int_S \partial q^*/\partial \mathbf{x}_s \, dS$, which contain components corresponding to $\alpha=3, \delta=2$ and $\alpha=5, \delta=2$, respectively (cf. Table 7.1).

The theoretical estimates of the error E_n in section 7.7 (1), equation (7.120) gives

$$E_n \sim n^{-2n} \tag{10.56}$$

for $\delta=1$. This is in good agreement with the numerical results, which show fast convergence for $\alpha=1, 3, 5$; $\delta=1$ in Fig. 10.26.

For $\delta=2$, the theoretical estimate in section 7.7 (2), equation (7.190) gives

$$E_n \sim n^{-3} \quad . \tag{10.57}$$

Fig. 10.27 shows the convergence graphs of relative error ε vs $\log_{10} n$, for $\delta=2$. The graphs give

$$\varepsilon \sim 0.266 \times n^{-2.95} \qquad (\alpha=3, \delta=2) \tag{10.58}$$

$$\varepsilon \sim 4.22 \times n^{-2.99} \quad (\alpha=5, \delta=2) \quad . \tag{10.59}$$

which matches very well with the theoretical error estimate of equation (10.57).

(iii) log-L_1 transformation

Table 10.24 and Fig. 10.28 show that the log-L_1 transformation works efficiently and robustly for all types of model kernels which appear in the three dimensional potential problem.

The theoretical estimate for the relative numerical integration error ε in section 7.8, Table 7.6 gives

$$\varepsilon \sim (1-t)^{-\frac{\alpha}{2}} \sigma^{-2n} \tag{10.60}$$

In order to maintain

$$(1-t)^{-\frac{\alpha}{2}} < 10 \tag{7.77}$$

in equation (10.60), t must satisfy

$$0 < t < 1-10^{-2/\alpha} = \begin{cases} 0.99 & (\alpha=1) \\ 0.78 & (\alpha=3) \\ 0.60 & (\alpha=5) \end{cases} \quad . \tag{7.268}$$

Hence, if we take the maximum values for t, equations (7.258~260) give

$$\sigma = \begin{cases} 1.64 & (\alpha=1) \\ 1.51 & (\alpha=3) \\ 1.40 & (\alpha=5) \end{cases} \tag{10.61}$$

for $D=d=0.01$, in equation (10.60). This theoretical estimate for the relative error corresponds well with the numerical results in Fig. 10.28, where

$$\sigma = \begin{cases} 1.88 & (\alpha=\delta=1) \\ 1.64 & (\alpha=3, \delta=1) \\ 1.54 & (\alpha=3, \delta=2) \\ 1.59 & (\alpha=5, \delta=1) \\ 1.56 & (\alpha=5, \delta=2) \end{cases} \quad . \tag{10.62}$$

(iv) $L_1^{-1/m}$ transformation

Tables 10.25~37 and Table 10.42 indicate that for the potential integral, the $L_1^{-1/m}$ transformation with $m=3.5$, 5 and 5.5 give best results and for the flux integral, $m=2$, 2.5 and 5 give best results for source distances ranging from 10 to 10^{-3}. On the whole, $m=5$ gives best results. The $L_1^{-1/5}$ transformation gives better results compared to the log-L_1 transformation except for the case $\alpha=\delta=1$, $d=10^{-3}$ and $\alpha=3, \delta=2, d=10^{-2}$. Fig. 10.29 shows that the $L_1^{-1/5}$ transformation gives better convergence compared to the log-L_1 transformation (cf Fig. 10.28) for the case $d=0.01$.

It is also interesting to note that the pattern of the number of integration points of the $L_1^{-1/m}$ transformation approaches that of the log-L_1 transformation as m increases.

The theoretical estimate of the relative error ε of numerical integration using the $L_1^{-1/5}$ transformation given by equation (7.311) and Table 7.5 is

$$\varepsilon \sim (1-t)^{-\frac{\alpha}{2}} \sigma^{-2n}$$

where t must satisfy

$$0 < t < 1-10^{-2/\alpha} = \begin{cases} 0.99 & (\alpha=1) \\ 0.78 & (\alpha=3) \\ 0.60 & (\alpha=5) \end{cases} \quad . \tag{7.268}$$

Hence, if we take the maximum values for t for each α, equations (7.31~32) and (7.309) give

$$\sigma = \begin{cases} 1.79 & (\alpha=1) \\ 1.62 & (\alpha=3) \\ 1.48 & (\alpha=5) \end{cases} \tag{10.64}$$

for $D=d=0.01$, in equation (10.63).

This theoretical estimate for the relative error corresponds with the numerical results in Fig. 10.29, where

$$\sigma = \begin{cases} 2.9 & (\alpha=1) \\ 1.8 & (\alpha=3) \\ 1.7 & (\alpha=5) \end{cases} \tag{10.65}$$

(2) Transformations based on the truncated trapezium rule

(i) Single Exponential (SE) transformation

Table 10.38 and Fig. 10.30 give numerical results for the numerical integration using the single exponential transformation

$$\rho(R) = \frac{\rho_j}{2}(1+\tanh R) \quad , \tag{5.101}$$

which maps $R:[-\infty, \infty]$ to $\rho:[0, \rho_j]$. The truncated trapezium rule is used for the integration in the transformed variable $R:[-\infty, \infty]$.

The detail of the numerical procedure is given in section 5.5 (5), together with the double exponential (DE) transformation. Although better than the identity transformation (1)(i) with the Gauss-Legendre rule for $D=d \leqq 10^{-2}$, the single exponential transformation requires more than twice as much integration points, compared to the log-L_1 transformation of (1) (iii) to obtain the same accuracy.

Table 10.40 gives numerical results for the single exponential transformation

$$\rho(R) = \rho_j(1+\tanh R) \quad , \tag{5.11}$$

which maps $R:[-\infty, 0]$ to $\rho:[0, \rho_j]$. This transformation gives poor results compared to that of equation (5.101), which reduced the integration error by concentrating the integration points near the end point $\rho=\rho_j$ as well as $\rho=0$.

(ii) Double Exponential (DE) transformation

Table 10.39 and Fig. 10.31 give numerical results for the double exponential transformation

$$\rho(R) = \frac{\rho_j}{2}\left\{1+\tanh\left(\frac{\pi}{2}\sinh R\right)\right\} \quad , \tag{5.112}$$

which maps $R:[-\infty, \infty]$ to $\rho:[0, \rho_j]$. This transformation requires even more integration points for $D=d \leqq 10^{-2}$, compared with the single exponential transformation of equation (5.98). Compared with the identity transformation, the DE transformation is more efficient for $D=10^{-3}$ and comparable for $D=10^{-2}$.

As with the SE transformation, the DE transformation

$$\rho(R) = \rho_j\left\{1+\tanh\left(\frac{\pi}{2}\sinh R\right)\right\} \quad , \tag{10.66}$$

which maps $R:[-\infty, 0]$ to $\rho:[0, \rho_j]$, gives poor results compared to the transformation of equation (5.12), as shown in Table 10.41.

(3) Summary

To sum up, numerical experiments on model radial variable integrals in this section indicate that the most efficient and robust method for the numerical integration in the radial variable, so far, is the $L_1^{-1/m}$ transformation with $m=3$~5.5 in combination with the Gauss-Legendre rule.

Also important is the fact that the numerical results match very well with the theoretical error estimates based on complex function theory, which was given in Chapter 7.

10.7 Comparison of Different Numerical Integration Methods on the 'Spherical' Element

In this section, different numerical integration methods will be compared for the integration of nearly singular integrals arising in potential calculations

$$\int_S \phi_{ij}\, u^*\, dS \quad , \quad \int_S \phi_{ij}\, q^*\, dS \tag{10.67}$$

and flux calculations

$$\int_S \phi_{ij}\, \frac{\partial u^*}{\partial x_s}\, dS \quad , \quad \int_S \phi_{ij}\, \frac{\partial q^*}{\partial x_s}\, dS \quad , \tag{10.68}$$

in three dimensional potential problems. The boundary element S is taken as the 'spherical' quadrilateral element SPQ60, which was defined in section 8.2, equation (8.9) . SPQ60 is a spherical quadrilateral subtending 60° in each direction on a sphere of radius 1, modelled by the 9- point Lagrangian element of equations (5.2) and (5.3). Its typical element size is 1 as shown by equation (8.10).

The following methods will be compared :

1. Gauss : The product Gauss-Legendre formula [3], given in section 4.2 .
2. Telles : Telles' self-adaptive cubic transformation method [15], given in section 4.4 (2) (ii) .
3. The PART method with (and without) the angular variable transformation $t(\theta)$ of equation (5.130), and with the radial variable transformations $R(\rho)$:
   (i) Identity : $R(\rho)=\rho$
   (ii) log-L_2 : $R(\rho)=\log\sqrt{\rho^2+d^2}$
   (iii) log-L_1 : $R(\rho)=\log(\rho+d)$
   (iv) $L_1^{-1/m}$: $R(\rho)=-(\rho+d)^{-1/m}$

(1) Effect of the source distance : d

First, the source point $\mathbf{x}_s$ was positioned so that its projection $\hat{\mathbf{x}}_s$ on the element S is $\hat{\mathbf{x}}_s=\mathbf{x}(0.5, 0.5)$, i.e. $\bar{\eta}_1=\bar{\eta}_2=0.5$, and $\mathbf{x}_s$ is situated towards the centre of the sphere at a distance d from the element surface S .

Figures 10.32~10.35 are the convergence graphs for the integrals $\int_S \phi_{ij}\, u^*\, dS$, $\int_S \phi_{ij}\, q^*\, dS$, $\int_S \phi_{ij}\, \partial u/\partial x_s\, dS$ and $\int_S \phi_{ij}\, \partial q/\partial x_s\, dS$, respectively, for the source distance $d=0.01$. Here, ϕ_{ij} is the 9- point Lagrangian interpolation function corresponding to the node $(\eta_1, \eta_2)=(i, j)$, i.e.

$$\phi_{ij}(\eta_1, \eta_2)=\phi_i(\eta_1)\,\phi_j(\eta_2) \quad , \tag{10.69}$$

where $\phi_i(\eta)$, $(i=-1, 0, 1)$ is defined in equation (5.3). In the graphs, the relative error is plotted against the number of integration points. The relative error is taken as the maximum relative error for all the interpolation functions $i, j=-1$, 0, 1 . The error was calculated by comparing with the result given by the PART method with the log-L_1 radial variable transformation and the logarithmic type angular variable transformation $t(\theta)$ of equation (5.130), with $N_t=N_R=128$, i.e. 128 Gauss-Legendre integration points for the variables t and R, respectively.

The PART method with the log-L_1 radial variable transformation is shown to be the most efficient and robust method for different integral kernels. Note also that for the integrals $\int_S \phi_{ij}\, u^*\, dS$ and $\int_S \phi_{ij}\, q^*\, dS$, related to potential calculations, the log-L_2 radial variable transformation does not show good convergence as it did for the potential related integrals $\int_S u^*\, dS$ and $\int_S q^*\, dS$ on the constant planar element in Fig. 10.23. The reason for this was explained using the results of theoretical error estimates in section 7.7 (2), i.e. ϕ_{ij} contain terms equivalent to ρ and ρ^3, which give rise to terms corresponding to $\delta=$even in the model radial integral kernels in equation (7.45).

For the flux kernels, Fig 10.34 and 10.35, the standard product Gauss-Legendre formula did not converge within the scope of the graphs.

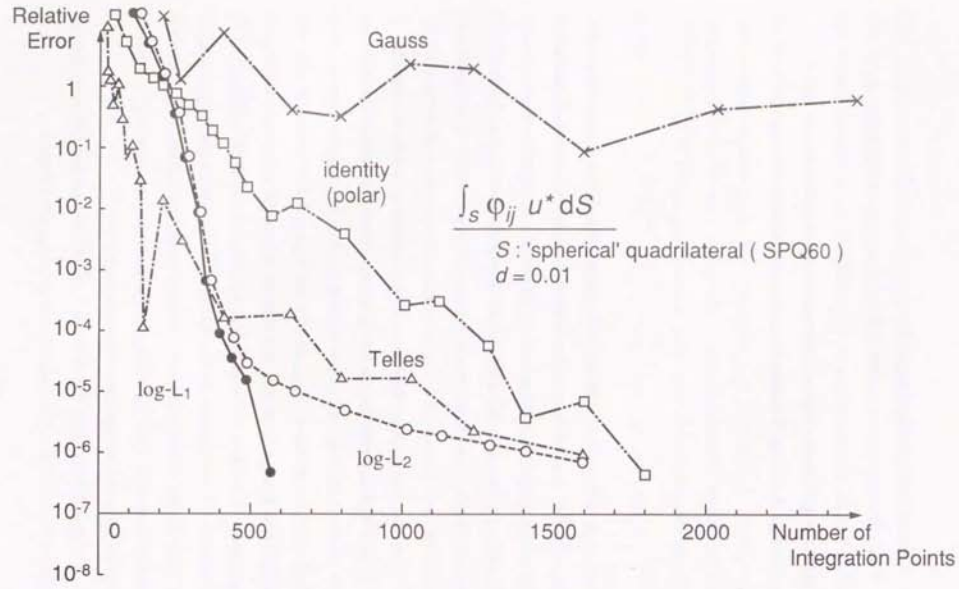

Fig. 10.32 Convergence graph for $\int_s \varphi_{ij}\, u^* \, dS$

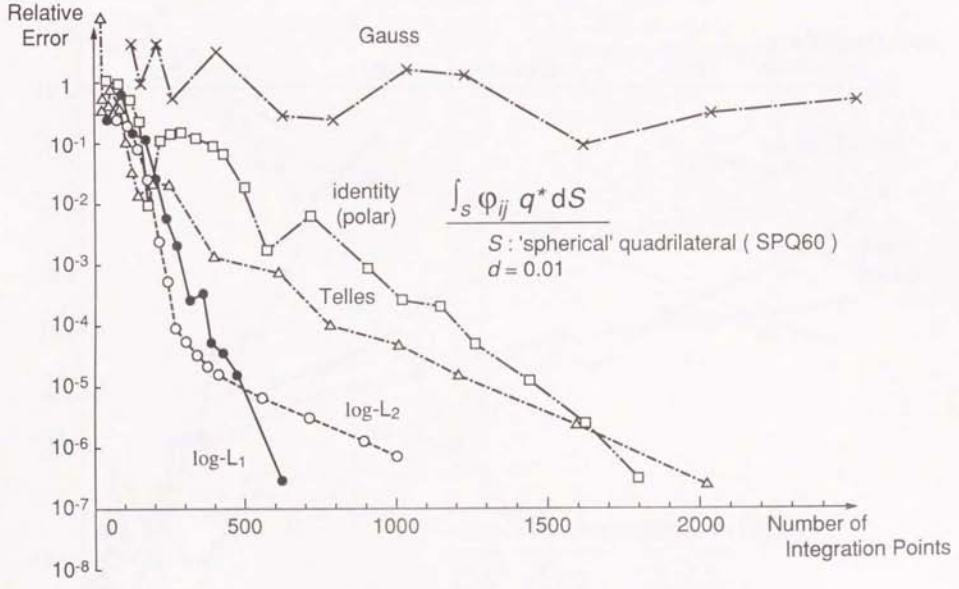

Fig. 10.33 Convergence graph for $\int_s \varphi_{ij}\, q^* \, dS$

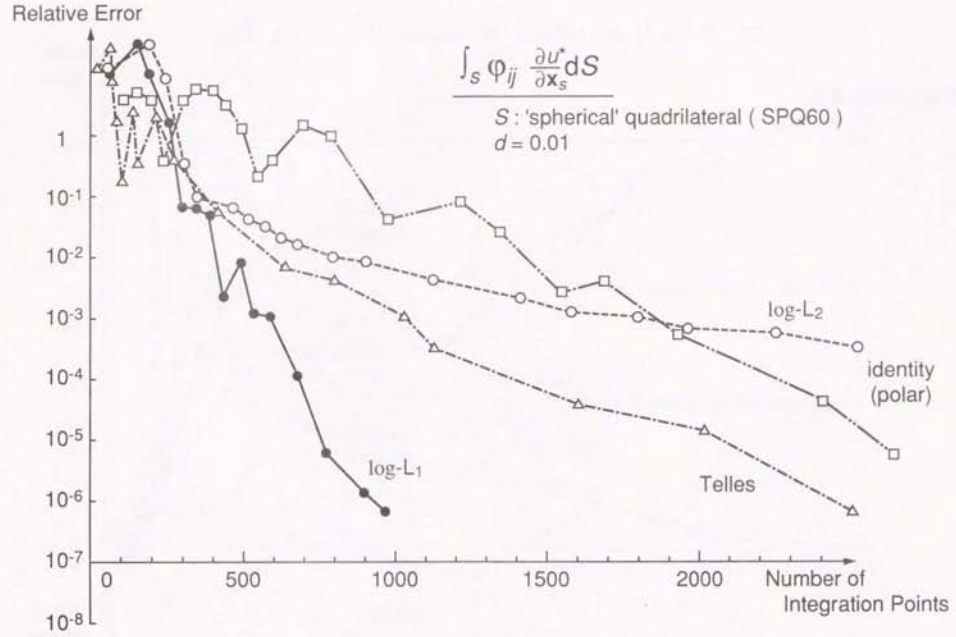

Fig. 10.34 Convergence graph for $\int_S \varphi_{ij} \frac{\partial u^*}{\partial \mathbf{x}_s} dS$

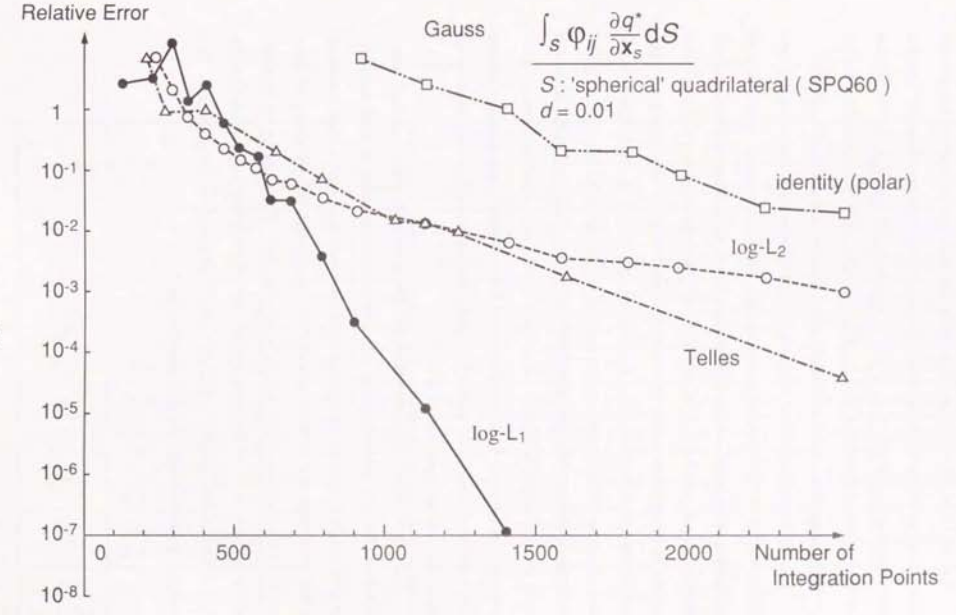

Fig. 10.35 Convergence graph for $\int_S \varphi_{ij} \frac{\partial q^*}{\partial \mathbf{x}_s} dS$

Tables 10.43, 10.44, 10.45 and 10.46 compare the number of integration points required for each method to achieve a relative error less than 10^{-6} for the same integrals $\int_S \phi_{ij} u^* \, dS$, $\int_S \phi_{ij} q^* \, dS$, $\int_S \phi_{ij} \partial u^*/\partial x_s \, dS$ and $\int_S \phi_{ij} \partial q^*/\partial x_s \, dS$, for different values of the source distance from $d=10$ to 10^{-3}. The source projection $\hat{x}_s$ was set again to $\hat{x}_s = x(0.5, 0.5)$ on the curved quadrilateral element : SPQ60.

For the Gauss and Telles methods N_1 and N_2 represent the necessary and sufficient number of integration points in the η_1 and η_2 directions, respectively, so that the total number of integration points is $N=N_1 \times N_2$. For the PART method (identity , log-L_2 and log-L_1), N_t and N_R (or N_ρ) are the necessary and sufficient number of integration points in the transformed angular variable t and the transformed radial variable R (or ρ), respectively, so that $N=N_t \times N_R \times 4$, since there are generally four triangular regions $\bar{\Delta}_j$, $(j=1 \sim 4)$ to integrate. (For triangular elements, this becomes $N=N_t \times N_R \times 3$, so that the PART methods would require only 3/4 of the integration points compared to quadrilateral elements. On the other hand, the Gauss and Telles methods basically require the same number of integration points for triangular and quadrilateral elements, so long as the product type formula is used.)

The actual value of the maximum relative error is shown in brackets when the method failed to converge even with 256 integration points in each variable. The average CPU-time per integration point is shown to be more or less the same for different methods, so that basically one may judge the efficiency of each method by the number of integration points required. The value of the integral corresponding to ϕ_{11} (of the x-component for flux integrals), calculated by the PART method (log-L_1, $t(\theta)$) with $N_t=N_R=128$, is also given for each case. The best method for each distance d is indicated by * .

Table 10.43 Comparison for different methods for $\int_S \phi_{ij} u^* \, dS$

source distance d	Gauss		Telles		Identity (Polar)		log-L_2		log-L_1		Integral $\int_S \phi_{11} u^* \, dS$
	$N_1 \times N_2$	total	$N_1 \times N_2$	total	$N_t \times N_\rho$	total	$N_t \times N_R$	total	$N_t \times N_R$	total	
10	5×6	*30	5×6	30	8×5	160	8×128	4096	8×6	192	2.3690670×10^{-4}
3	5×6	*30	5×6	30	8×6	192	8×120	3840	8×6	192	7.8512215×10^{-4}
1	5×5	*25	6×6	36	8×6	192	8×110	3520	8×7	224	2.3665596×10^{-3}
0.3	9×10	90	7×8	*56	7×8	224	8×72	2304	7×8	224	7.9340063×10^{-3}
0.1	25×28	700	9×10	*90	8×14	448	8×45	1440	8×9	288	1.4990202×10^{-2}
0.03	90×100	9000	20×25	500	7×20	560	7×32	896	7×12	*336	1.8818785×10^{-2}
0.01	220×250	55000	35×40	1400	10×45	1800	10×40	1600	10×14	*560	2.0009242×10^{-2}
0.003	256×256 (5×10^{-4})	65536	55×55	3025	11×64	2816	10×20	800	10×16	*640	2.0432292×10^{-2}
0.001	256×256 (2×10^{-3})	65536	72×72	5184	10×10	4400	10×20	*800	10×20	*800	2.0553637×10^{-2}
Average CPU-time per point	27 μsec		30 μsec		28 μsec		29 μsec		29 μsec		

Table 10.44 Comparison for different methods for $\int_S \phi_{ij}\, q^*\, dS$

source distance	Gauss		Telles		Identity (Polar)		log-L_2		log-L_1		Integral
d	$N_1 \times N_2$	total	$N_1 \times N_2$	total	$N_t \times N_\rho$	total	$N_t \times N_R$	total	$N_t \times N_R$	total	$\int_S \phi_{11}\, q^*\, dS$
10	4×5	*20	4×5	20	8×5	160	8×128	4096	8×5	160	$-2.4452062 \times 10^{-5}$
3	5×5	*25	5×5	25	8×6	192	8×128	4096	8×6	192	$-2.6509634 \times 10^{-4}$
1	6×6	*36	6×6	36	8×6	192	8×110	3520	8×7	224	$-2.3551983 \times 10^{-3}$
0.3	12×14	168	8×8	*64	8×10	320	9×110	3960	8×8	256	$-2.3437238 \times 10^{-2}$
0.1	32×35	1120	14×14	*196	7×16	448	9×55	1980	7×11	308	$-5.8702728 \times 10^{-2}$
0.03	110×110	12100	25×25	625	9×28	1008	9×40	1440	9×14	*504	$-7.4058844 \times 10^{-2}$
0.01	256×256 (3×10^{-6})	65536	45×45	2025	9×50	1800	9×28	1008	10×16	*640	$-7.7822266 \times 10^{-2}$
0.003	256×256 (4×10^{-3})	65536	72×72	5184	9×90	3240	9×28	900	9×20	*720	$-7.9027356 \times 10^{-2}$
0.001	256×256 (3×10^{-1})	65536	100×100	10000	9×150	5400	9×20	*720	10×20	800	$-7.9359758 \times 10^{-2}$
Average CPU-time per point	27 μsec		31 μsec		28 μsec		30 μsec		29 μsec		

Table 10.45 Comparison for different methods for $\int_S \phi_{ij}\, \partial u^*/\partial x_s\, dS$

source distance	Gauss		Telles		Identity (Polar)		log-L_2		log-L_1		Integral
d	$N_1 \times N_2$	total	$N_1 \times N_2$	total	$N_t \times N_\rho$	total	$N_t \times N_R$	total	$N_t \times N_R$	total	$\int_S \phi_{11}\, \partial u^*/\partial x_s\, dS$ (x-component)
10	5×6	*30	5×6	30	8×5	160	8×128	4096	8×6	192	2.1740212×10^{-5}
3	6×6	*36	6×6	36	9×7	252	9×170	6120	9×7	252	2.3158820×10^{-4}
1	6×7	*42	7×8	56	10×7	280	10×256	10240	10×9	360	1.9793103×10^{-3}
0.3	14×14	196	10×10	*100	9×11	396	9×180	6480	9×10	360	1.6292413×10^{-2}
0.1	40×40	1600	14×16	*224	9×20	720	10×210	8400	10×11	440	3.0043614×10^{-2}
0.03	150×150	22500	32×32	*1024	14×40	2240	14×256 (8×10^{-6})	14336	14×20	1120	2.9820882×10^{-2}
0.01	256×256 (2×10^{-3})	65536	50×50	2500	12×64	3072	14×256 (2×10^{-6})	14336	12×20	*960	2.8428787×10^{-2}
0.003	256×256 (13)	65536	90×100	9000	14×120	6720	14×256 (5×10^{-6})	14336	14×25	*1400	2.7777735×10^{-2}
0.001	256×256 (62)	65536	120×120	14400	16×170	10880	14×256 (4×10^{-6})	14336	14×25	*1400	2.7575715×10^{-2}
Average CPU-time per point	31 μsec		33 μsec		32 μsec		33 μsec		34 μsec		

Table 10.46 Comparison for different methods for $\int_S \phi_{ij} \partial q^*/\partial x_s \, dS$

source distance d	Gauss		Telles		Identity (Polar)		$\log\text{-}L_2$		$\log\text{-}L_1$		Integral $\int_S \phi_{11} \partial q^*/\partial x_s \, dS$ (x-component)
	$N_1 \times N_2$	total	$N_1 \times N_2$	total	$N_t \times N_\rho$	total	$N_t \times N_R$	total	$N_t \times N_R$	total	
10	5×5	*25	5×5	25	8×6	192	8×140	4480	8×6	192	$-4.7314067 \times 10^{-6}$
3	5×6	*30	5×6	30	8×6	192	8×128	4096	8×7	224	$-1.6191572 \times 10^{-4}$
1	7×7	*49	8×8	64	10×7	286	10×220	8800	10×9	360	$-3.9035821 \times 10^{-3}$
0.3	14×16	224	9×10	*90	9×12	432	9×150	5400	9×10	360	$-7.5012685 \times 10^{-2}$
0.1	40×45	1800	20×20	*400	10×20	800	11×210	9240	11×14	616	$-8.9873760 \times 10^{-2}$
0.03	160×180	28800	40×40	1600	12×45	2160	12×350 (8×10^{-6})	16800	14×20	*1120	$-7.7111343 \times 10^{-3}$
0.01	256×256 (3×10^{-5})	65536	64×64	4096	14×80	4480	14×256 (7×10^{-6})	14336	14×25	*1400	2.7794385×10^{-2}
0.003	256×256 (90)	65536	110×110	12100	14×150	8400	14×256 (3×10^{-5})	14336	14×28	*1568	4.1226837×10^{-2}
0.001	256×256 (590)	65536	170×170	28900	16×256	16384 (2×10^{-6})	16×256 (1×10^{-4})	16384	16×35	*2240	4.5148359×10^{-2}
Average CPU-time per point	30 μsec		37 μsec		32 μsec		38 μsec		38 μsec		

Similar numerical experiments were done to compare the $L_1^{-1/m}$ radial variable transformation of equation (5.99) with the log-L_1 transformation. The parameter m was varied from 2 to 7. The same 9 point Lagrangian element SPQ60 was used with the source projection at $\hat{\mathbf{x}}_s = \mathbf{x}(0.5, 0.5)$ and the source point situated at a distance d towards the centre of the sphere.

Tables 10.47~50 give the number of integration points (radial : N_R and total : N where $N = N_R \times N_t \times 4$) required to achieve a relative error $\varepsilon < 10^{-6}$ for the integrals $\int_S \phi_{ij} u^* \, dS$, $\int_S \phi_{ij} q^* \, dS$, $\int_S \phi_{ij} \partial u^*/\partial \mathbf{x}_s \, dS$ and $\int_S \phi_{ij} \partial q^*/\partial \mathbf{x}_s \, dS$, respectively. The asterisk denotes the method with the least number of integration points.

For the integral $\int_S \phi_{ij} u^* \, dS$, the log-$L_1$ transformation is the best, contrary to the results with the model radial integral with $\alpha = \delta = 1$ in Tables 10.24~37. This is probably due to terms corresponding to $\alpha = 1$, $\delta \geqq 2$, due to the interpolation function ϕ_{ij}.

For the other integrals involving q^*, $\partial u^*/\partial \mathbf{x}_s$ and $\partial q^*/\partial \mathbf{x}_s$, the $L_1^{-1/5}$ transformation gives the best results on the whole.

Fig. 10.36~39 give the convergence graphs comparing the log-L_1 and $L_1^{-1/5}$ transformations for each integral for the case $d = 0.01$.

Next, Table 10.51 gives the total number of integration points required for the integrals $\int_S \phi_{ij} u^* dS$ and $\int_S \phi_{ij} q^* \, dS$ which appear in potential calculations. Similarly, Table 10.52 gives the number of integration points for the integrals. $\int_S \phi_{ij} \partial u^*/\partial \mathbf{x}_s \, dS$ and $\int_S \phi_{ij} \partial q^*/\partial \mathbf{x}_s \, dS$ which are required in flux calculations.

Table 10.51 shows that the log-L_1 transformation is preferred to the $L_1^{-1/m}$ transformation for potential calculations. This is due to the fact that the $L_1^{-1/m}$ requires more integration points than the log-L_1 for the integral $\int_S \phi_{ij} u^* dS$ and more than $L_1^{-1/m}$ itself for the integral $\int_S \phi_{ij} q^* dS$.

Table 10.52 shows that the $L_1^{-1/5}$ transformation requires the least number of integration points for flux calculations.

To sum up, the above experiments indicate that for the calculation of nearly singular integrals, one should use the log-L_1 transformation if one only wants to calculate the potential or the H, G matrices and one should use the $L_1^{-1/6}$ transformation if one wants to calculate the flux (with or without the potential).

Table 10.47 Number of integration points for $\int_S \phi_\psi u^* dS$

(SPQ 60, $\tilde{\gamma}_1 = \tilde{\gamma}_2 = 0.5$, $\varepsilon < 10^{-6}$)

d	log-L_1		$L_1^{-1/2}$		$L_1^{-1/2.5}$		$L_1^{-1/3}$		$L_1^{-1/3.5}$		$L_1^{-1/4}$		$L_1^{-1/5}$		$L_1^{-1/5.5}$		$L_1^{-1/6}$		$L_1^{-1/7}$	
	N_R	N	N_R	N	N_R	N	N_R	N	N_R	N	N_R	N	N_R	N	N_R	N	N_R	N	N_R	N
10	6	192	6	192	6	192	6	192	6	192	6	192	6	192	6	192	6	192	6	192
3	6	192	6	192	6	192	6	192	6	192	6	192	6	192	6	192	6	192	6	192
1	7	224	8	256	7	224	7	224	7	224	7	224	7	224	7	224	7	224	7	224
0.3	8	*224	9	252	9	252	9	252	9	252	9	252	8	256	8	*224	8	*224	8	*224
0.1	9	288	12	384	12	384	11	352	11	352	11	352	10	320	10	320	10	320	10	320
0.03	12	*336	20	560	16	448	16	448	14	392	14	392	14	392	14	392	14	392	14	392
0.01	14	*560	28	1120	25	1000	25	1000	20	880	20	800	20	800	20	800	20	800	20	800
0.003	16	*640	40	1600	32	1280	28	1120	25	1100	25	1000	25	1000	25	1000	20	880	20	800
0.001	20	*800	45	1800	40	1760	35	1400	32	1280	28	1232	25	1100	25	1000	25	1000	25	1000

N_R: Number of radial integration points

N: Total number of integration points

Table 10.48 Number of integration points for $\int_S \phi_{ij}\, q^*\, dS$

(SPQ 60, $\bar{\eta}_1=\bar{\eta}_2=0.5$, $\varepsilon<10^{-6}$)

d	log-L_1		$L_1^{-1/2}$		$L_1^{-1/2.5}$		$L_1^{-1/3}$		$L_1^{-1/3.5}$		$L_1^{-1/4}$		$L_1^{-1/5}$		$L_1^{-1/5.5}$		$L_1^{-1/6}$		$L_1^{-1/7}$	
	N_R	N	N_R	N	N_R	N	N_R	N	N_R	N	N_R	N	N_R	N	N_R	N	N_R	N	N_R	N
10	5	160	5	160	5	160	5	160	5	160	5	160	5	160	5	160	5	160	5	160
3	6	192	6	192	6	192	6	192	6	192	6	192	6	192	6	192	6	192	6	192
1	7	224	8	256	8	256	8	256	7	224	7	224	7	224	7	224	7	224	7	224
0.3	8	256	9	288	9	288	8	256	8	256	8	256	8	256	8	256	8	256	8	256
0.1	11	308	11	352	11	352	10	320	10	320	10	*280	10	*280	10	*280	10	*280	10	*280
0.03	14	504	16	576	14	504	14	504	12	480	12	432	12	432	11	*396	12	480	12	480
0.01	16	640	20	800	20	720	16	640	16	576	16	576	14	*504	14	*504	14	*504	14	560
0.003	20	720	28	1120	25	900	25	900	20	720	20	720	20	720	16	640	16	*576	16	*576
0.001	20	800	40	1440	28	1120	28	1008	25	900	25	900	20	*720	20	*720	20	*720	20	*720

N_R: Number of radial integration points

N: Total number of integration points

Table 10.49 Number of integration points for $\int_S \phi_{ij}\, \partial u^*/\partial x_s\, dS$

(SPQ 60, $\bar{\eta}_1=\bar{\eta}_2=0.5$, $\varepsilon<10^{-6}$)

d	log-L_1		$L_1^{-1/2}$		$L_1^{-1/2.5}$		$L_1^{-1/3}$		$L_1^{-1/3.5}$		$L_1^{-1/4}$		$L_1^{-1/5}$		$L_1^{-1/5.5}$		$L_1^{-1/6}$		$L_1^{-1/7}$	
	N_R	N	N_R	N	N_R	N	N_R	N	N_R	N	N_R	N	N_R	N	N_R	N	N_R	N	N_R	N
10	6	192	6	192	6	192	6	192	6	192	6	192	6	192	6	192	6	192	6	192
3	7	*252	8	288	8	288	8	288	8	288	8	288	8	288	8	288	8	288	8	288
1	9	360	9	360	9	360	9	360	9	360	9	360	9	360	9	360	9	360	9	360
0.3	10	360	10	360	10	360	9	*324	9	*324	9	*324	9	*324	9	*324	9	*324	9	*324
0.1	11	440	14	504	14	504	12	432	12	432	12	432	11	*396	12	432	12	432	12	432
0.03	20	1120	25	1400	20	1120	20	1120	20	1120	16	*896	16	*896	20	1120	16	*896	16	*896
0.01	20	*960	28	1568	25	1200	25	1200	20	1120	20	*960	20	*960	20	*960	20	*960	20	*960
0.003	25	1400	40	2240	32	1792	28	1568	25	1400	25	1400	25	1400	25	1400	20	*1120	20	*1120
0.001	25	*1400	55	3080	40	2240	35	1960	32	1792	28	1568	25	*1400	25	*1400	25	*1400	25	*1400

N_R: Number of radial integration points

N: Total number of integration points

Table 10.50 Number of integration points for $\int_S \varphi_{ij}\ \partial q^*/\partial x_s^*\ dS$

(SPQ 60, $\bar{\eta}_1=\bar{\eta}_2=0.5$, $\varepsilon<10^{-6}$)

d	log-L_1		$L_1^{-1/2}$		$L_1^{-1/2.5}$		$L_1^{-1/3}$		$L_1^{-1/3.5}$		$L_1^{-1/4}$		$L_1^{-1/5}$		$L_1^{-1/5.5}$		$L_1^{-1/6}$		$L_1^{-1/7}$	
	N_R	N	N_R	N	N_R	N	N_R	N	N_R	N	N_R	N	N_R	N	N_R	N	N_R	N	N_R	N
10	6	192	6	192	6	192	6	192	6	192	6	192	6	192	6	192	6	192	6	192
3	7	224	7	224	7	224	7	224	7	224	7	224	7	224	7	224	7	224	7	224
1	9	360	9	360	9	360	9	360	9	360	9	360	9	360	9	360	9	360	9	360
0.3	10	360	9	*324	10	360	10	360	9	*324	10	360	9	*324	9	*324	10	360	10	360
0.1	14	616	12	*480	12	*480	12	528	14	560	14	560	14	560	12	528	12	528	12	*480
0.03	20	1120	16	*896	16	*896	20	1120	20	1120	20	1120	20	1120	20	1120	20	1120	20	1120
0.01	25	1400	25	1400	20	*1120	20	*1120	20	*1120	20	*1120	20	*1120	25	1400	25	1400	25	1400
0.003	28	1568	32	1792	25	1400	20	*1120	25	1400	25	1400	25	1400	25	1400	25	1400	25	1400
0.001	35	2240	40	2560	32	2048	25	*1600	25	*1600	25	*1600	25	*1600	28	1792	28	1792	28	1792

N_R: Number of radial integration points

N: Total number of integration points

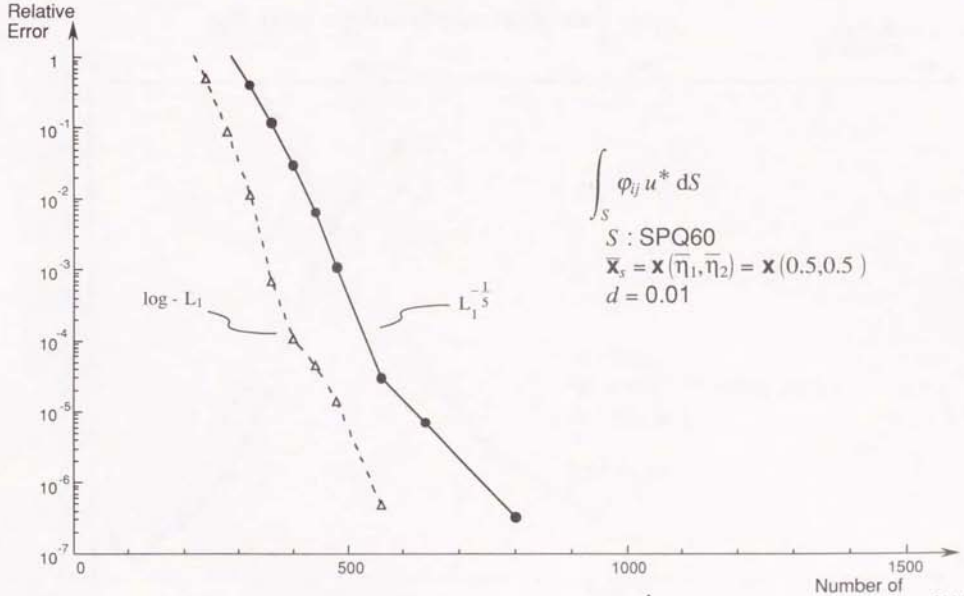

Fig.10.36 Convergence graph for $\int_S \varphi_{ij}\, u^*\, dS$

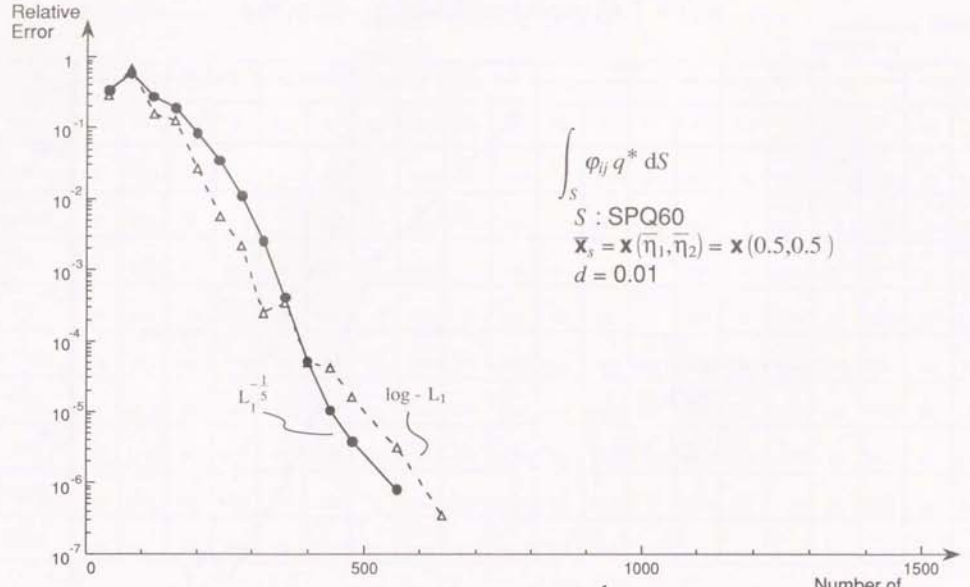

Fig.10.37 Convergence graph for $\int_S \varphi_{ij}\, q^*\, dS$

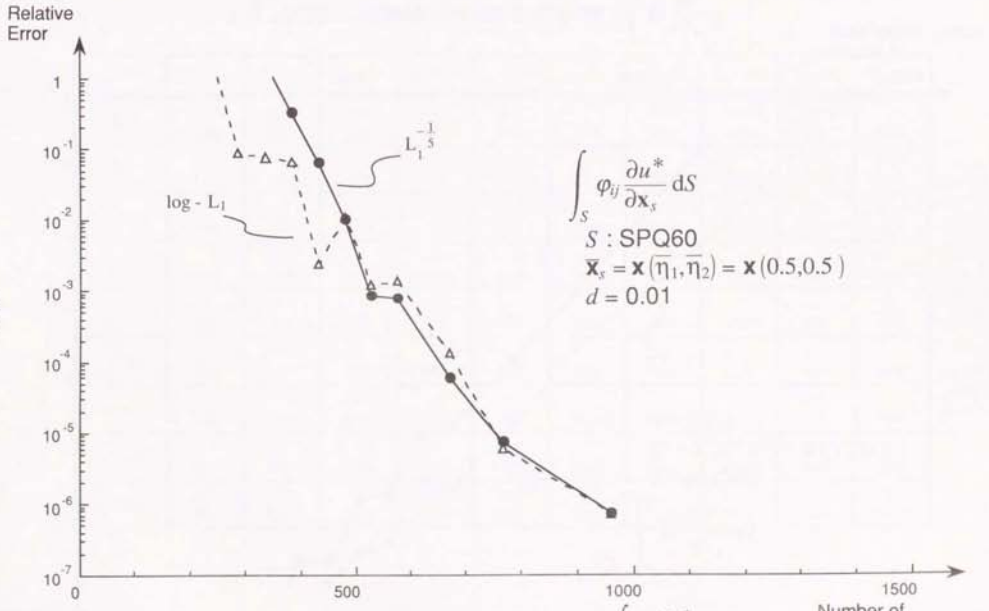

Fig.10.38 Convergence graph for $\int_S \varphi_{ij} \frac{\partial u^*}{\partial \mathbf{x}_s}\, dS$

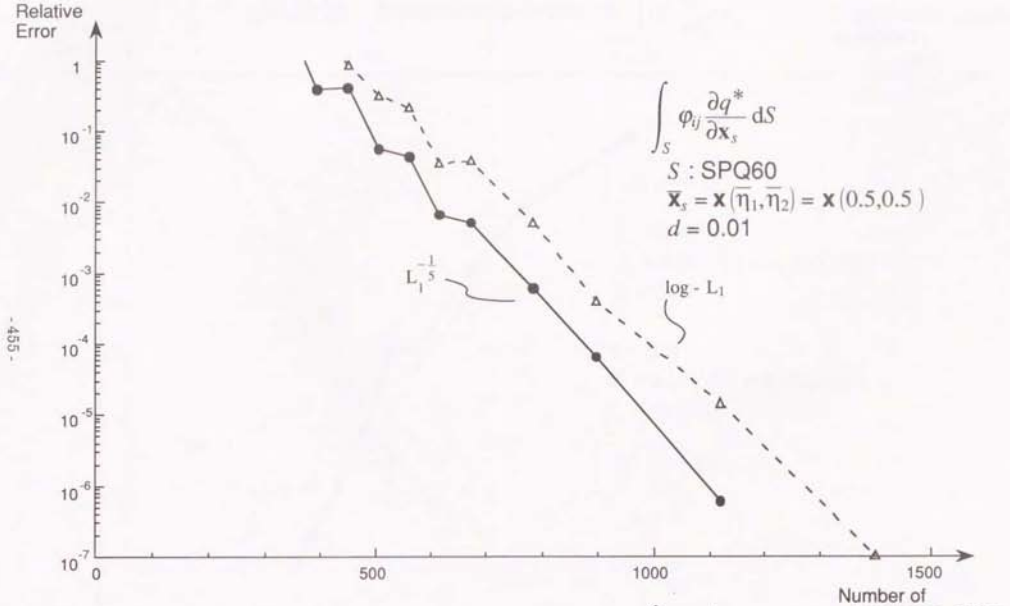

Fig.10.39 Convergence graph for $\int_S \varphi_{ij} \frac{\partial q^*}{\partial \mathbf{x}_s} dS$

Table 10.51 Number of integration points for potential integrals

(SPQ 60, $\bar{\eta}_1 = \bar{\eta}_2 = 0.5$, $\varepsilon < 10^{-6}$)

d	log-L_1	$L_1^{-1/2}$	$L_1^{-1/2.5}$	$L_1^{-1/3}$	$L_1^{-1/3.5}$	$L_1^{-1/4}$	$L_1^{-1/5}$	$L_1^{-1/5.5}$	$L_1^{-1/6}$	$L_1^{-1/7}$
10	192	192	192	192	192	192	192	192	192	192
3	192	192	192	192	192	192	192	192	192	192
1	*224	256	256	256	*224	256	*224	*224	*224	*224
0.3	256	288	288	256	256	256	256	256	256	256
0.1	*308	384	384	352	352	352	320	320	320	320
0.03	504	576	504	504	480	504	432	*396	480	480
0.01	*640	1120	1000	1000	880	800	800	800	800	800
0.003	*720	1600	1280	1120	1100	1000	1000	1000	880	800
0.001	*800	1800	1760	1400	1280	1232	1100	1000	1000	1000

Table 10.52 Number of integration points for flux integrals

(SPQ 60, $\hat{r}_1 = \hat{r}_2 = 0.5$, $\epsilon < 10^{-6}$)

d	$\log \mathrm{L}_1$	$\mathrm{L}_1^{-1/2}$	$\mathrm{L}_1^{-1/2.5}$	$\mathrm{L}_1^{-1/3}$	$\mathrm{L}_1^{-1/3.5}$	$\mathrm{L}_1^{-1/4}$	$\mathrm{L}_1^{-1/5}$	$\mathrm{L}_1^{-1/5.5}$	$\mathrm{L}_1^{-1/6}$	$\mathrm{L}_1^{-1/7}$
10	192	192	192	192	192	192	192	192	192	192
3	* 252	288	288	288	288	288	288	288	288	288
1	360	360	360	360	360	360	360	360	360	360
0.3	360	360	360	360	* 324	360	* 324	* 324	360	360
0.1	616	* 504	* 504	528	560	560	560	528	528	480
0.03	1120	1400	1120	1120	1120	1120	1120	1120	1120	1120
0.01	1400	1568	1200	1200	* 1120	* 1120	* 1120	1400	1400	1400
0.003	1568	2240	1792	1568	* 1400	* 1400	* 1400	* 1400	* 1400	* 1400
0.001	2240	3080	2240	1960	1792	* 1600	* 1600	1792	1792	1792

Fig.10.40~43 compare in more detail, the effect of the source distance d on the different methods for the calculation of $\int_S \phi_{ij}\, u^*$, $\int_S \phi_{ij}\, q^*\, dS$, $\int_S \phi_{ij}\, \partial u^*/\partial \mathbf{x}_s\, dS$ and $\int_S \phi_{ij}\, \partial q^*/\partial \mathbf{x}_s\, dS$. Similar to Tables 10.43~50, the number of integration points required for each method to obtain relative error $\varepsilon < 10^{-6}$ for all $i, j = -1, 0, 1$ (and x, y, z component), was plotted against the source distance $d = 10^{-4} \sim 10$. The element is the same 'spherical' quadrilateral SPQ60 with the source projection at $\hat{\mathbf{x}}_s = \mathbf{x}\,(0.5, 0.5)$ and the source distance is measured from the element towards the centre of the sphere. Table 10.53 summarizes the results.

Table 10.53 Range of source distance d best suited to each method

integral kernel	log - L_2	log - L_1	$\mathrm{L}_1^{-1/5}$	Telles	Gauss
$\phi_{ij}\, u^*$	$d \leqq 0.001$	$d \leqq 0.04$	–	$0.04 \leqq d \leqq 0.5$	$0.5 \leqq d$
$\phi_{ij}\, q^*$	$d \leqq 0.002$	$0.002 \leqq d \leqq 0.007$	$0.001 \leqq d < 0.06$	$0.06 \leqq d \leqq 0.7$	$0.6 \leqq d$
$\phi_{ij}\, \partial u^*/\partial \mathbf{x}_s$	–	$d \leqq 0.03$	$0.0003 \leqq d < 0.04$	$0.04 \leqq d < 0.7$	$0.7 \leqq d$
$\phi_{ij}\, \partial q^*/\partial \mathbf{x}_s$	–	–	$d \leqq 0.07$	$0.07 \leqq d < 0.8$	$0.8 \leqq d$

(S : SPQ60, $\hat{\mathbf{x}}_s = \mathbf{x}(0.5, 0.5)$, relative error $< 10^{-6}$)

In order to save CPU-time, it is advisable to use the same set of integration points for the calculation of $\int_S \phi_{ij}\, u^*\, dS$ and $\int_S \phi_{ij}\, q^*\, dS$ in order to calculate the potential $u(\mathbf{x}_s)$ at $\mathbf{x} = \mathbf{x}_s$. Similarly, the same set of integration points should be used for the calculation of $\int_S \phi_{ij}\, \partial u^*/\partial \mathbf{x}_s\, dS$ and $\int_S \phi_{ij}\, \partial q^*/\partial \mathbf{x}_s\, dS$ in order to calculate the flux (potential derivative) $\partial u/\partial \mathbf{x}_s$ at $\mathbf{x} = \mathbf{x}_s$. Further, if one wants to calculate both potential and flux at the same point $\mathbf{x} = \mathbf{x}_s$, the same set of integration points should be used for all the kernels: $\int_S \phi_{ij}\, u^*\, dS$, $\int_S \phi_{ij}\, q^*\, dS$, $\int_S \phi_{ij}\, \partial u^*/\partial \mathbf{x}_s\, dS$ and $\int_S \phi_{ij}\, \partial q^*/\partial \mathbf{x}_s\, dS$.

The strategy for the choice of numerical integration method with regard to the source distance d for each situation is given in Table 10.54.

Table 10.54 Strategy for the choice of numerical integration method

calculation item	log - L_1	$L_1^{-1/5}$	Telles	Gauss
potential only	$d < 0.06$	–	$0.06 \leqq d < 0.6$	$0.6 \leqq d$
flux only	–	$d \leqq 0.07$	$0.07 \leqq d < 0.8$	$0.8 \leqq d$
potential and flux	–	$d \leqq 0.07$	$0.07 \leqq d < 0.8$	$0.8 \leqq d$

(S: SPQ60, $\hat{x}_s = x(0.5, 0.5)$, relative error $< 10^{-6}$)

The above results may vary depending on the position of the source projection $\hat{x}_s$, the geometry of the element S. However, they may be considered as a rough guide for choosing the numerical integration method according to the (relative) source distance d.

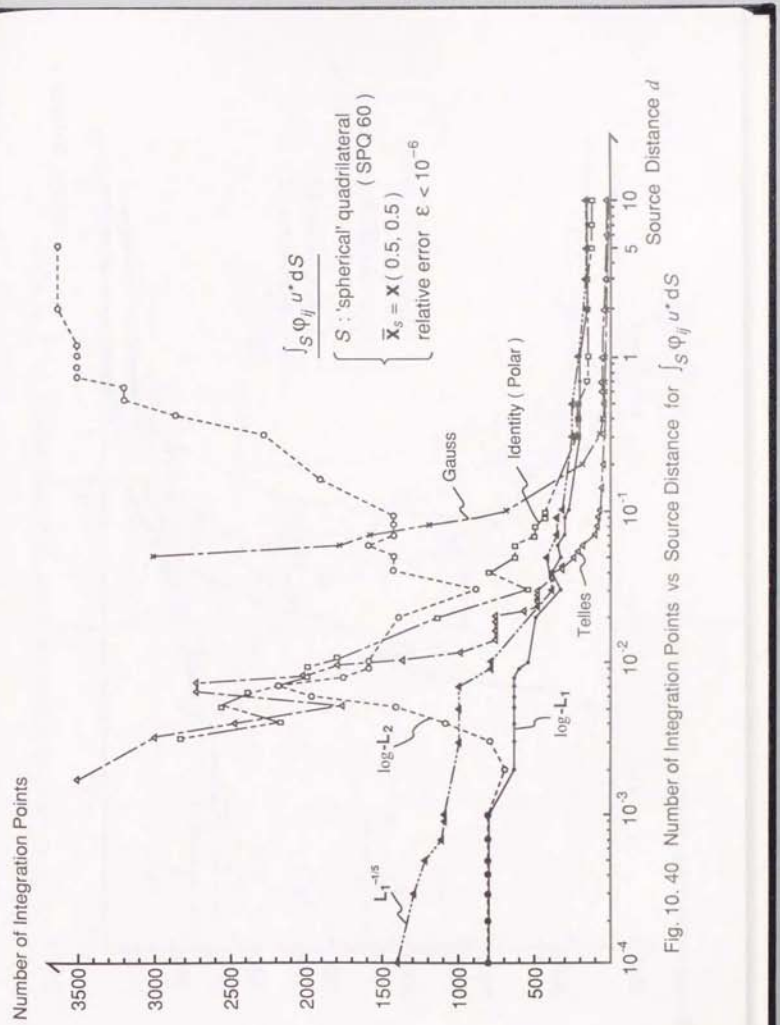

Fig. 10.40 Number of Integration Points vs Source Distance for $\int_S \varphi_{ij}\, u^* dS$

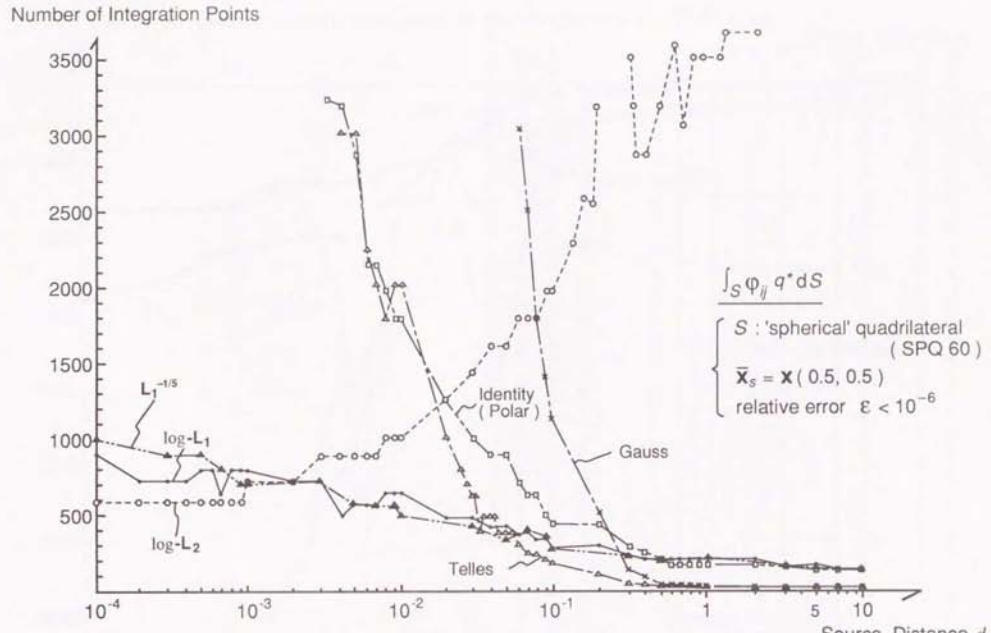

Fig. 10. 41 Number of Integration Points vs Source Distance for $\int_S \varphi_{ij}\, q^* dS$

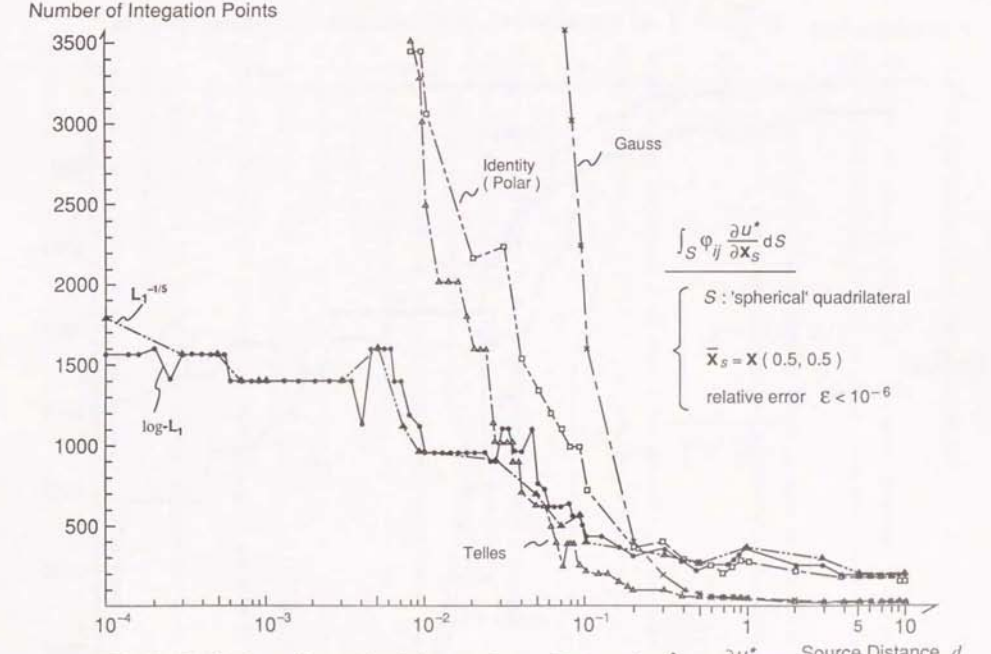

Fig. 10. 42 Number of Integration Points vs Source Distance for $\int_S \varphi_{ij} \frac{\partial u^*}{\partial \mathbf{x}_S} dS$

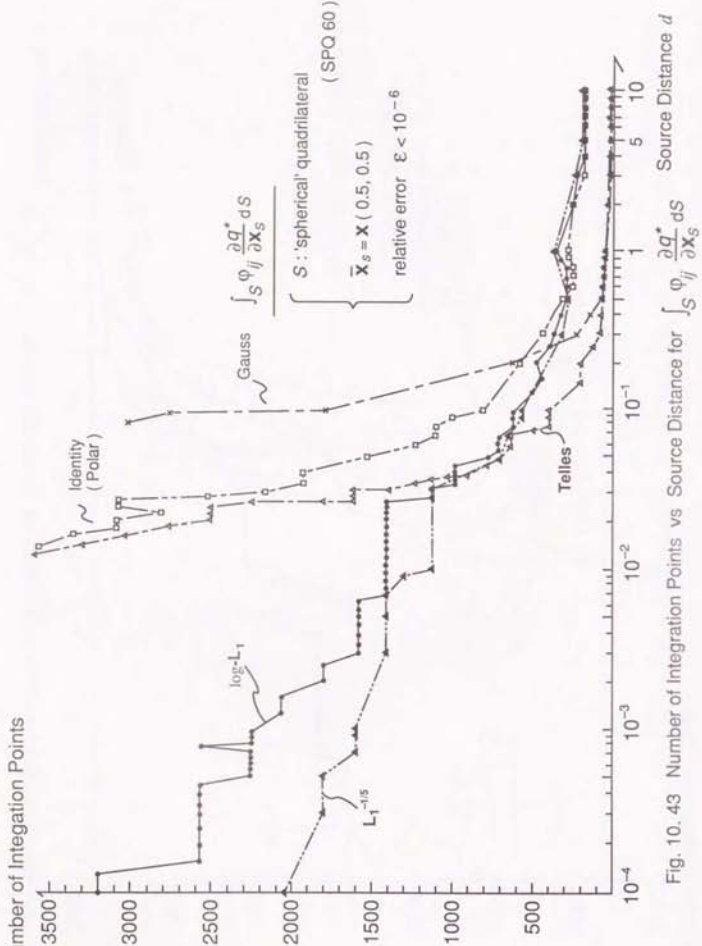

Fig. 10. 43 Number of Integration Points vs Source Distance for $\int_S \varphi_{ij} \frac{\partial q^*}{\partial x_S} dS$

(2) Effect of the position of the source projection : $\bar{x}_s$

Next , the effect of the position of the source projection $\bar{x}_s$ on the accuracy and efficiency of each numerical integration method , is investigated .

The same 'spherical' quadrilateral S : SPQ60 is taken as the curved boundary element over which the integration is performed . The source projection

$$\bar{x}_s = x(\bar{\eta}, \bar{\eta}) \tag{10.70}$$

is moved along the diagonal of the element from the centre ($\bar{\eta}=0$) to the corner ($\bar{\eta}=1$) and outside ($\bar{\eta}=1.1$) . The source point is positioned at

$$x_s = \bar{x}_s + d\,n \tag{10.71}$$

where n is the unit normal at $\bar{x}_s$ pointing towards the centre of the sphere. The source distance was fixed at $d=0.01$.

The following three methods were compared :

1. The PART method with the log-L_1 radial variable transformation and the angular variable transformation $t(\theta)$:
   (i) Identity : $t(\theta)=\theta$,
   (ii) log-type :
   $$t(\theta) = \frac{h_j}{2} \log\left\{\frac{1+\sin(\theta-\alpha_j)}{1-\sin(\theta-\alpha_j)}\right\} \quad , \tag{5.130}$$
2. Telles' self-adaptive cubic transformation method [15] , given in section 4.4 (2) (ii) .

Fig 10.44~47 are the graphs of the number of integration points required to achieve relative error $\varepsilon < 10^{-6}$ for all $i, j = -1, 0, 1$ (and x, y, z) components , vs $\bar{\eta}$ (position of the source projection $\bar{x}_s$) , for the calculation of $\int_S \phi_{ij}\, u^*\, dS$, $\int_S \phi_{ij}\, q^*\, dS$, $\int_S \phi_{ij}\, \partial u^*/\partial x_s\, dS$ and $\int_S \phi_{ij}\, \partial q^*/\partial x_s\, dS$, respectively.

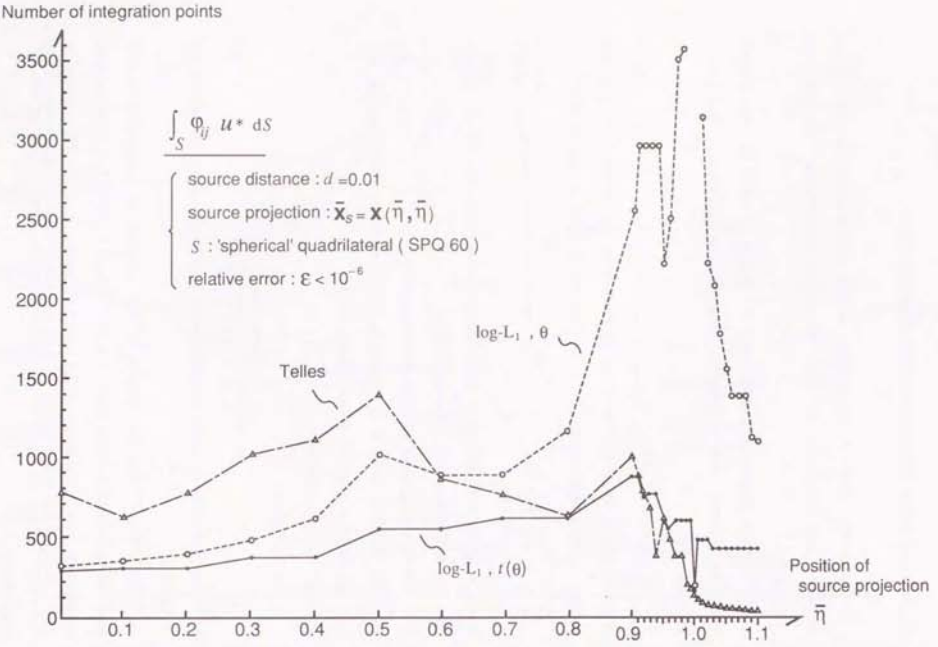

Fig. 10. 44 Number of integration points vs Position of source projection for $\int_S \varphi_{ij}\ u^*\ dS$

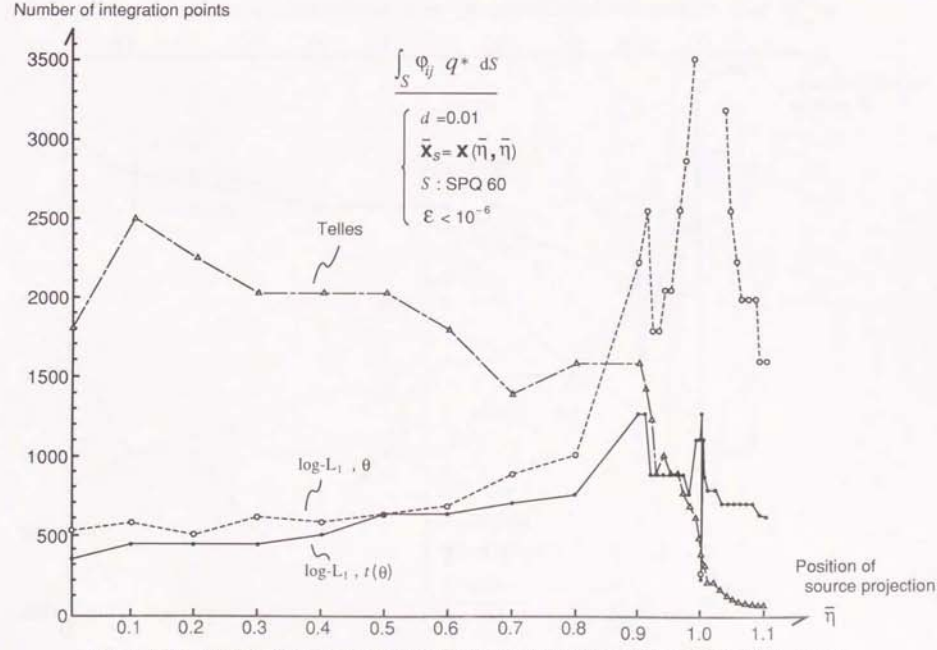

Fig. 10. 45 Number of integration points vs Position of source projection for $\int_S \varphi_{ij}\ q^*\ dS$

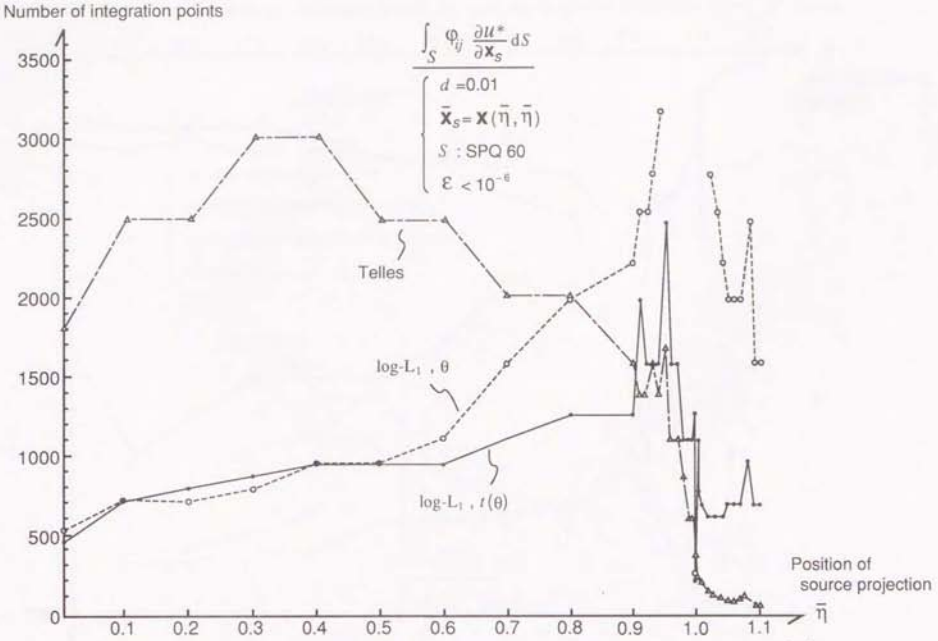

Fig. 10. 46 Number of integration points vs Position of source projection for $\int_S \varphi_{ij} \frac{\partial u^*}{\partial \mathbf{x}_s} dS$

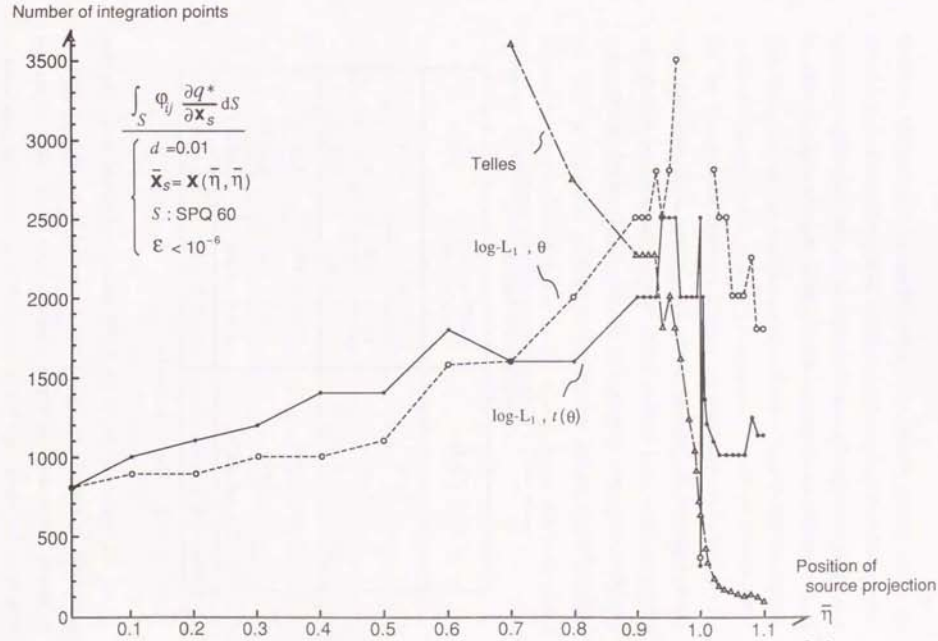

Fig. 10. 47 Number of integration points vs Position of source projection for $\int_S \varphi_{ij} \frac{\partial q^*}{\partial \mathbf{x}_s} dS$

The figures clearly show the effect of the angular variable transformation $t(\theta)$ of equation (5.130), particularly when $\bar{\eta} \gtrsim 0.7$, in reducing the number of integration points in the angular variable compared to the identity transformation $t(\theta)=\theta$, which requires a huge number of angular integration points as the source projection $\hat{\mathbf{x}}_s$ approaches the edge of the element ($\bar{\eta} \to 1$).

Telles' cubic transformation method becomes advantageous as the source projection $\hat{\mathbf{x}}_s$ approaches the edge (corner) of the element. The results are summarized in Table 10.55. However, the results are only for the case when the source distance $d=0.01$. The PART method becomes more advantageous as the source distance d decreases.

Table 10.55 Position of source projection $\hat{\mathbf{x}}_s=\mathbf{x}(\bar{\eta}, \bar{\eta})$ suited to each method

Type of kernel	PART method log-L_1, $t(\theta)$	Telles
$\phi_{ij}\, u^*$	$0 \leqq \bar{\eta} \leqq 0.92$	$0.92 < \bar{\eta}$
$\phi_{ij}\, q^*$	$0 \leqq \bar{\eta} \leqq 0.96$	$0.96 < \bar{\eta}$
potential calculation	$0 \leqq \bar{\eta} \leqq 0.96$	$0.96 < \bar{\eta}$
$\phi_{ij}\, \partial u^*/\partial \mathbf{x}_s$	$0 \leqq \bar{\eta} \leqq 0.90$	$0.90 < \bar{\eta}$
$\phi_{ij}\, \partial q^*/\partial \mathbf{x}_s$	$0 \leqq \bar{\eta} \leqq 0.93$	$0.93 < \bar{\eta}$
flux calculation	$0 \leqq \bar{\eta} \leqq 0.93$	$0.93 < \bar{\eta}$
potential & flux calculation	$0 \leqq \bar{\eta} \leqq 0.93$	$0.93 < \bar{\eta}$

(S : SPQ60, $d=0.01$)

In the implementation of the PART method and Telles' method in this experiment, the source distance d was determined as the distance between $\mathbf{x}_s$ and $\hat{\mathbf{x}}_s$, even when the source projection $\hat{\mathbf{x}}_s=\mathbf{x}(\bar{\eta}_1, \bar{\eta}_2)$ falls outside the element S, i.e. when $|\bar{\eta}_1| > 1$ or $|\bar{\eta}_2| > 1$ ($|\bar{\eta}| > 1$ in the case above).

However, since the integration is performed only inside the element S, the effective source distance between the source point $\mathbf{x}_s$ and the element S is, generally speaking, larger than the distance $|\mathbf{x}_s - \hat{\mathbf{x}}_s|$. Actually, the nearest point to $\mathbf{x}_s$ lies on the edge of the element S, in this case. Using this definition of the effective source distance, the PART method (in particular) and Telles' method can be improved.

Also, even when the source projection $\hat{\mathbf{x}}_s$ lies on the element S, but very close to the element edge, results by the PART method may be improved by artificially moving the source projection to the nearest point on the edge, provided that the distance between the original source projection $\hat{\mathbf{x}}_s$ and the closest element edge is smaller than or comparable to the source distance d. This will be shown in the next section.

(3) Moving the source projection $\bar{\mathbf{x}}_s$ to the closest element edge

As shown in the previous section, the angular variable transformation $t(\theta)$ of equation (5.130) has considerable effect in reducing the number of angular integration points when the source projection $\bar{\mathbf{x}}_s$ is near the edge of the element.

However, the method still requires many angular integration points when $\bar{\mathbf{x}}_s$ is very near the edge of the element. In order to overcome this problem, the effect of deliberately moving the source projection $\bar{\mathbf{x}}_s$ to the closest edge of the element S was examined.

The procedure is as follows:

Taking the example when $\bar{\mathbf{x}}_s = \mathbf{x}(\bar{\eta}_1, \bar{\eta}_2)$ is closest to the edge corresponding to $\bar{\eta}_1 = 1$ on a curved quadrilateral element,

1. Let $\bar{\mathbf{x}}_s' = \mathbf{x}(1, \bar{\eta}_2)$
2. Approximately project S on to the polygon $\bar{S}'$ on the plane tangent to S at $\bar{\mathbf{x}}_s'$.
3. Define the new source distance as $d' = |\bar{\mathbf{x}}_s - \bar{\mathbf{x}}_s'|$
4. Introduce polar coordinate (ρ, θ) in S' , centred at $\bar{\mathbf{x}}_s'$, apply the radial and angular variable transformation and integrate with respect to the transformed variables. In the radial transformation, the updated source distance d' is used.

If the initial source projection $\bar{\mathbf{x}}_s$ is close to two edges (i.e. a corner) of the element S, $\bar{\mathbf{x}}_s$ is moved to the corner.

The above procedure is advantageous, not only because it reduces the number of angular integration points, but also because it reduces the number of triangular regions $\bar{\Delta}_j$ in $\bar{S}$ to integrate over.

Numerical experiments were done on the previous curved element SPQ60 for the integrals $\int_S \phi_{ij}\, q^*\, dS$ and $\int_S \phi_{ij}\, \partial q^*/\partial \mathbf{x}_s\, dS$ for source distance $d = 0.1$, 0.01 and 0.001 towards the centre of the sphere. In the experiments, the

effect of moving the source projection $(\bar{\eta}_1, \bar{\eta}_2)$ to the nearest element edge for the Telles' method was also examined.

First, the source projection is situated along the diagonal of the element, i.e. $\bar{\mathbf{x}}_s = \mathbf{x}(\bar{\eta}_1, \bar{\eta}_1)$ where $\bar{\eta}_1 = \bar{\eta}_2 = 0 \sim 1.2$. Tables 10.56~61 compare the number of integration points required to achieve a relative error less than 10^{-6} for the PART and Telles' methods with and without moving the source projection $\bar{\mathbf{x}}_s$ to the element edge. N_t, N_R, N_1, N_2 indicate respectively, the number of integration points required in the angular variable t, the radial variable R, for the PART method, and variables $\gamma_1(\bar{\eta}_1)$ and $\gamma_2(\bar{\eta}_2)$ for Telles' method. N indicates the total number of integration points.

For the radial variable transformation in the PART method, the log-L_1 was used for the integral $\int_S \phi_{ij} q^* dS$, and the $L_1^{-1/5}$ for $\int_S \phi_{ij} \partial q^*/\partial \mathbf{x}_s dS$, as recommended in section 10.7 (1). For the angular variable transformation, $t(\theta)$ of equation (5.130) was used. h_1 indicates the distance between the original source projection $\bar{\mathbf{x}}_s$ and the edge-1 of the projected element $\bar{S}$, and h_4 the distance between $\bar{\mathbf{x}}_s$ and edge-4. In this case, h_4 is the distance between $\bar{\mathbf{x}}_s$ and the nearest edge of $\bar{S}$. The asterisk in the column for N indicates the method which required the least number of integration points. The asterisk in the column for h_4 indicates the value for h_4 where it becomes advantageous to move $\bar{\mathbf{x}}_s$ to the element edge with the PART method. Fig. 10.48~49 show the results in graphs for $d = 0.01$. In the present case, $\bar{\mathbf{x}}_s$ is moved to the corner, so that the number of triangular regions to integrate over is reduced from four to two.

Similar results are given in Tables 10.62~67 and Fig. 10.50~51, for the case where the source projection $\bar{\mathbf{x}}_s = \mathbf{x}(\bar{\eta}_1, \bar{\eta}_2)$ is situated along $\bar{\eta}_2 = 0$, $\bar{\eta}_1 = 0 \sim 1.2$. In this case, $\bar{\mathbf{x}}_s$ is moved to $\bar{\mathbf{x}}_s' = \mathbf{x}(1, 0)$, so that the number of triangular regions is reduced from four to three.

Results show that, for the PART method, moving the source projection $\bar{\mathbf{x}}_s$ to the element edge leads to a substantial reduction of integration points when the original source projection $\bar{\mathbf{x}}_s$ lies inside the element S and $h_j < d$ (i.e. when the

distance h_j between the original source projection $\bar{\mathbf{x}}_s$ and an edge of the projected element $\bar{S}$ is less than the original source distance d) or when $\bar{\mathbf{x}}_s$ lies outside the element S. The reduction of the necessary number of integration points can be as much as a factor of ten. The reduction is caused by the reduction of the number of triangular regions $\bar{\Delta}_j$ in the projected element to integrate over, and the reduction of the number of integration points in the transformed angular variable $t(\theta)$. On the other hand, for Telles' method, there is no substantial improvement by moving the source projection $(\bar{\eta}_1, \bar{\eta}_2)$ to the element edge. This is mainly because there is no reduction of the number of regions to integrate over for Telles' method.

Concerning the comparison between the PART method and Telles' method, the following is observed. For $d=0.1$, Telles' method is superior expect for the integration of $\int_S \phi_{ij} \partial q^*/\partial \mathbf{x}_s \, dS$ for the case $\bar{\eta}_1 = \bar{\eta}_2$, $(\bar{\eta}_1 < 1.1)$ in Table 10.59. For $d=0.01$ and $d=0.001$, the PART method is superior when the original source projection $\bar{\mathbf{x}}_s = \mathbf{x}(\bar{\eta}_1, \bar{\eta}_2)$ is inside the element S and also for $\bar{\eta}_1 \leqq 1.01$ when $\bar{\mathbf{x}}_s$ lies outside the element.

Finally a minor note for the case $\bar{\eta}_2=0$, $\bar{\eta}_1=0\sim1.2$. It is noticed, for instance in Tables 10.64 and 10.67 that as $\bar{\eta}_1$ increases from 0, h_4 decreases monotonically until it reaches a minimum of 0.00015 at $\bar{\eta}_1=0.992$, after which it starts to increase monotonically with $\bar{\eta}_1$. Note that for $\bar{\eta}_1=1$, $h_4=0.0042$ and not $h_4=0$. This phenomenon was explained in section 5.3 as being caused by the curved element, where in this case $\bar{\mathbf{x}}_s \notin \bar{S}$ even when $\bar{\mathbf{x}}_s \in S$. Hence, for the case $d=0.001$, the criterion $h_4<d$ for moving $\bar{\mathbf{x}}_s$ to the element edge becomes misleading, as shown in Tables 10.64 and 10.67. Instead, one could decide to move $\bar{\mathbf{x}}_s$ to the edge in this case if $(1-\bar{\eta}_1)/2<D$, where $D \equiv d/l$ is the relative source distance. (l is the size of the element S.) In the present case, the element size is $l=1$, which gives $(1-\bar{\eta}_1)/2<d$ as the criterion to move $\bar{\mathbf{x}}_s$. In fact, this rule matches well with all the numerical results in Tables 10.56~67. The

asterisk in the left most column for $\bar{\eta}_1=\bar{\eta}_2$ or $\bar{\eta}_1$ indicates the threshold value for $\bar{\eta}_1$ according to this criterion.

Table 10.56 Effect of moving the source projection $\hat{x}_s$ to the element edge

$\int_S \phi_\psi q^* dS$, S: SPQ60, $\tilde{\eta}_1=\tilde{\eta}_2=0\sim1.2$, $d=0.1$

$\tilde{\eta}_1=\tilde{\eta}_2$	Number of integration points for relative error $<10^{-6}$								h_1	h_4
	log-L_1				Telles					
	original $\hat{x}_s$		move $\hat{x}_s$		original $\hat{x}_s$		move $\hat{x}_s$			
	$N_t\times N_R$	N	$N_t\times N_R$	N	$N_1\times N_2$	N	$N_1\times N_2$	N		
0	6×9	* 216	11×50	1100	14×16	224	35×40	1400	0.50	0.43
0.2	8×11	* 352	11×55	1210	20×20	400	40×40	1600	0.42	0.36
0.4	8×10	320	9×45	810	14×14	* 196	32×35	1120	0.34	0.28
0.6	9×11	396	7×40	560	12×14	* 168	28×28	784	0.24	0.19
0.8 *	9×11	396	6×28	336	14×16	* 224	20×20	400	0.13	* 0.096
0.82	9×12	432	6×25	300	14×16	* 224	20×25	500	0.12	0.086
0.84	9×12	432	6×25	300	14×16	* 224	20×20	400	0.10	0.077
0.86	9×12	432	7×25	350	16×16	* 256	20×20	400	0.090	0.067
0.88	10×14	560	7×25	350	16×20	320	20×20	400	0.078	0.058
0.9	9×14	504	7×25	350	14×16	* 224	20×20	400	0.065	0.048
0.92	10×14	560	7×20	280	16×16	* 256	16×20	320	0.052	0.039
0.94	11×12	528	7×16	224	14×14	* 196	14×14	* 196	0.040	0.029
0.96	11×12	528	6×16	192	12×14	* 168	14×14	196	0.027	0.019
0.99	14×14	784	6×14	* 168	12×14	* 168	12×14	* 168	0.0067	0.0048
1.0	6×14	168	6×14	168	12×12	* 144	12×12	* 144	0	0
1.001	11×14	616	6×14	168	12×12	* 144	12×12	* 144	0.00067	0.00048
1.005	11×14	616	7×12	168	12×12	144	11×12	* 132	0.0034	0.0024
1.01	10×12	480	6×12	144	11×12	* 132	11×12	* 132	0.0067	0.0048
1.05	9×14	504	6×10	* 120	11×11	121	11×11	* 121	0.034	0.024
1.1	8×14	448	6×10	120	10×10	* 100	10×11	110	0.068	0.048
1.15	8×16	512	7×10	140	10×10	* 100	10×11	110	0.10	0.072
1.2	7×16	448	6×9	108	8×8	* 64	9×9	81	0.14	0.096

Table 10.57 Effect of moving the source projection $\hat{x}_s$ to the element edge

$\int_S \phi_\psi q^* dS$, S: SPQ60, $\tilde{\eta}_1=\tilde{\eta}_2=0\sim1.2$, $d=0.01$

$\tilde{\eta}_1=\tilde{\eta}_2$	Number of integration points for relative error $<10^{-6}$								h_1	h_4
	log-L_1				Telles					
	original $\hat{x}_s$		move $\hat{x}_s$		original $\hat{x}_s$		move $\hat{x}_s$			
	$N_t\times N_R$	N	$N_t\times N_R$	N	$N_1\times N_2$	N	$N_1\times N_2$	N		
0	6×14	* 336			40×45	1800			0.5	0.43
0.2	8×14	* 448			45×50	2250			0.42	0.36
0.4	8×16	* 512			45×45	2025			0.34	0.28
0.6	10×16	* 640			40×45	1800	200×250	55000	0.24	0.19
0.8	12×16	* 768			40×40	1600	180×170	30600	0.13	0.096
0.9	16×20	* 1280			40×40	1600	128×140	17920	0.065	0.048
0.92	14×16	* 896	10×120	2400	35×35	1225	100×110	11000	0.052	0.039
0.94	14×16	* 896	9×100	1800	32×32	1024	72×72	5184	0.040	0.029
0.96	14×16	* 896	7×72	1008	28×32	* 896	50×55	2750	0.027	0.019
0.98 *	12×16	768	6×40	* 480	25×28	700	32×35	1120	0.013	* 0.0097
0.99	14×20	1120	6×28	* 336	25×25	625	25×25	625	0.0067	0.0048
0.995	14×20	1120	6×25	* 300	20×25	500	20×25	500	0.033	0.0024
0.999	16×20	1280	6×20	* 240	20×20	400	20×20	400	0.00067	0.00048
1.0	6×20	240	6×20	* 240	20×20	400	20×20	400	0	0
1.001	14×20	1120	6×20	* 240	16×20	320	20×20	400	0.00067	0.00048
1.002	12×20	960	6×16	* 192	16×20	320	16×20	320	0.0013	0.00097
1.005	11×20	880	6×14	* 168	16×20	320	16×16	256	0.0034	0.0024
1.01	10×20	800	7×14	* 196	14×16	224	16×16	256	0.0067	0.0048
1.02	10×20	800	7×14	* 196	14×16	224	14×14	* 196	0.013	0.0097
1.04	9×20	720	6×12	144	11×12	132	11×11	* 121	0.027	0.019
1.1	8×20	640	6×10	120	8×8	* 64	10×10	100	0.068	0.048
1.2	8×20	640	6×10	120	7×8	* 56	8×9	72	0.14	0.096

Table 10.58 Effect of moving the source projection $\hat{x}_s$ to the element edge

$\int_S \phi_\psi q^* dS$, S: SPQ60, $\bar{\gamma}_1=\bar{\gamma}_2=0\sim1.2$, $d=0.001$

$\bar{\gamma}_1=\bar{\gamma}_2$	Number of integration points for relative error $<10^{-6}$								h_1	h_4
	log-L_1				Telles					
	original $\hat{x}_s$		move $\hat{x}_s$		original $\hat{x}_s$		move $\hat{x}_s$			
	$N_t\times N_R$	N	$N_t\times N_R$	N	$N_1\times N_2$	N	$N_1\times N_2$	N		
0	6×20	* 480			110×120	13200			0.5	0.433
0.2	7×20	* 560			100×120	13200			0.42	0.36
0.4	8×20	* 640			110×110	12100			0.34	0.28
0.6	10×20	* 800			100×100	10000			0.24	0.19
0.8	12×20	* 960			90×90	8100			0.13	0.096
0.9	16×20	*1280			90×90	8100			0.065	0.048
0.95	16×20	*1280			64×64	4096			0.033	0.024
0.99	20×20	*1600			55×55	3025	150×170	25500	0.0067	0.0048
0.992	20×20	*1600			60×60	3600	128×150	19200	0.0053	0.0039
0.994	20×20	*1600			60×60	3600	100×128	12800	0.0040	0.0029
0.996	20×20	1600	7×100	*1400	55×60	3300	90×100	9000	0.0027	*0.0019
0.998*	20×25	2000	7×64	* 896	60×64	3840	72×72	5184	0.0013	0.00097
0.999	16×20	1280	7×35	* 490	45×50	2250	50×50	2500	0.00067	0.00048
0.9992	16×20	1280	7×32	* 448	45×50	2250	45×50	2250	0.00054	0.00039
0.9999	20×25	2000	7×25	* 350	40×40	1600	35×40	1400	0.000067	0.000048
1.0	7×25	* 350	7×25	* 350	32×35	1120	32×35	1120	0	0
1.0001	16×25	1600	7×20	* 280	32×35	1120	32×35	1120	0.000067	0.000048
1.0005	12×25	1200	7×20	* 280	28×28	784	32×32	1024	0.00033	0.00024
1.001	11×25	1100	6×16	* 192	25×25	625	25×28	700	0.00067	0.00048
1.005	11×25	1100	6×14	* 168	20×16	320	20×20	400	0.0034	0.0024
1.01	11×25	1100	6×14	* 168	14×14	196	14×16	224	0.0067	0.0048
1.05	10×28	1120	6×11	132	10×9	* 90	10×10	100	0.034	0.024
1.1	9×28	1008	6×10	120	8×8	* 64	9×9	81	0.068	0.048
1.2	8×28	896	6×10	120	7×7	* 49	8×8	64	0.14	0.096

Table 10.59 Effect of moving the source projection $\hat{x}_s$ to the element edge

$\int_S \phi_\psi \partial q^*/\partial x_s dS$, S: SPQ60, $\bar{\gamma}_1=\bar{\gamma}_2=0\sim1.2$, $d=0.1$

$\bar{\gamma}_1=\bar{\gamma}_2$	Number of integration points for relative error $<10^{-6}$								h_1	h_4
	$L_1{}^{-1/5}$				Telles					
	original $\hat{x}_s$		move $\hat{x}_s$		original $\hat{x}_s$		move $\hat{x}_s$			
	$N_t\times N_R$	N	$N_t\times N_R$	N	$N_1\times N_2$	N	$N_1\times N_2$	N		
0	8×10	* 320	16×72	2304	25×25	625	50×55	2750	0.5	0.43
0.2	9×14	504	14×72	2016	20×25	* 500	50×50	2500	0.42	0.36
0.4	10×14	560	12×60	1440	20×20	* 400	45×45	2025	0.34	0.28
0.6	11×12	528	9×50	900	20×20	* 400	40×40	1600	0.24	0.19
0.8 *	11×14	616	7×32	448	20×20	* 400	28×28	784	0.13	*0.096
0.82	11×14	616	6×32	* 384	20×20	400	25×28	700	0.12	0.086
0.84	11×14	616	7×28	* 392	20×20	400	25×25	625	0.10	0.077
0.86	11×14	616	7×28	* 392	20×20	400	25×25	625	0.090	0.067
0.88	12×16	768	7×28	* 392	20×20	400	25×25	625	0.078	0.058
0.9	14×14	784	7×25	* 350	20×20	400	20×25	500	0.065	0.048
0.92	14×14	784	7×25	* 350	20×20	400	20×20	400	0.052	0.039
0.94	16×16	1024	7×25	* 350	20×20	400	20×20	400	0.040	0.029
0.96	14×14	784	7×20	* 280	16×20	320	20×20	400	0.027	0.019
0.99	16×14	896	7×16	* 224	16×16	256	16×16	256	0.0067	0.0048
1.0	7×14	196	7×14	* 196	16×16	256	16×16	256	0	0
1.001	14×14	784	7×14	* 196	16×16	256	16×16	256	0.00067	0.00048
1.005	14×14	784	7×14	* 196	16×16	256	16×16	256	0.0034	0.0024
1.01	12×14	672	7×14	* 196	14×16	224	14×16	224	0.0067	0.0048
1.05	10×16	640	8×12	* 192	14×14	196	14×14	196	0.034	0.024
1.1	8×16	512	7×12	168	11×12	* 132	12×12	144	0.068	0.048
1.15	8×20	640	8×12	192	10×10	* 100	10×11	110	0.10	0.072
1.2	9×20	720	7×11	154	9×9	* 81	10×10	100	0.14	0.096

Table 10.60 Effect of moving the source projection $\hat{x}_s$ to the element edge

$\int_S \phi_{ij} \partial q^*/\partial \hat{x}_s \, dS$, S: SPQ60, $\bar{\eta}_1=\bar{\eta}_2=0\sim1.2$, $d=0.01$

$\bar{\eta}_1=\bar{\eta}_2$	Number of integration points for relative error $<10^{-6}$								h_1	h_4
	$L_1^{-1/5}$				Telles					
	original $\hat{x}_s$		move $\hat{x}_s$		original $\hat{x}_s$		move $\hat{x}_s$			
	$N_t\times N_R$	N	$N_t\times N_R$	N	$N_1\times N_2$	N	$N_1\times N_2$	N		
0	8×20	* 640			60×72	4320			0.5	0.43
0.2	11×25	*1100			72×72	5184			0.42	0.36
0.4	14×20	*1120			72×72	5184			0.34	0.28
0.6	16×25	*1600			64×64	4096			0.24	0.19
0.8	16×20	*1280			60×60	3600			0.13	0.096
0.9	20×20	*1600			55×55	3025	180×190	34200	0.065	0.048
0.92	20×20	*1600			50×55	2750	150×160	24000	0.052	0.039
0.94	25×20	*2000			50×50	2500	120×128	15360	0.040	0.029
0.96	25×20	2000	10×90	*1800	45×50	2250	90×90	8100	0.027	*0.019
0.98*	20×20	1600	7×50	* 700	40×45	1800	50×55	2750	0.013	0.0097
0.99	20×20	1600	6×32	* 384	35×40	1400	35×40	1400	0.0067	0.0048
0.995	20×20	1600	6×28	* 336	32×32	1024	32×35	1120	0.0033	0.0024
0.999	25×25	2500	7×25	* 350	28×28	784	28×28	784	0.00067	0.00048
1.0	6×20	* 240	6×20	* 240	28×28	784	28×28	784	0	0
1.001	20×20	1600	6×20	* 240	25×28	700	25×28	700	0.00067	0.00048
1.002	16×20	1280	6×20	* 240	25×25	625	25×25	625	0.0013	0.00097
1.005	14×20	1120	6×16	* 192	25×25	625	25×25	625	0.0034	0.0024
1.01	12×20	960	6×16	* 192	20×20	400	20×20	400	0.0067	0.0048
1.02	11×20	880	6×16	* 192	16×20	320	14×16	224	0.013	0.0097
1.04	10×20	800	7×14	* 196	14×14	* 196	14×14	* 196	0.027	0.019
1.1	10×25	1000	7×12	168	10×9	* 90	11×11	121	0.068	0.048
1.2	11×25	1100	8×12	192	8×8	* 64	9×9	81	0.14	0.096

Table 10.61 Effect of moving the source projection $\hat{x}_s$ to the element edge

$\int_S \phi_{ij} \partial q^*/\partial \hat{x}_s \, dS$, S: SPQ60, $\bar{\eta}_1=\bar{\eta}_2=0\sim1.2$, $d=0.001$

$\bar{\eta}_1=\bar{\eta}_2$	Number of integration points for relative error $<10^{-6}$								h_1	h_4
	$L_1^{-1/5}$				Telles					
	original $\hat{x}_s$		move $\hat{x}_s$		original $\hat{x}_s$		move $\hat{x}_s$			
	$N_t\times N_R$	N	$N_t\times N_R$	N	$N_1\times N_2$	N	$N_1\times N_2$	N		
0	8×25	* 800			190×190	36100			0.5	0.043
0.2	14×28	*1568			190×190	36100			0.42	0.036
0.4	16×25	*1600			190×190	36100			0.34	0.028
0.6	20×28	*2240			170×180	30600			0.24	0.19
0.8	20×25	*2000			160×170	27200			0.13	0.096
0.9	25×25	*2500			150×150	22500			0.065	0.048
0.95	25×25	*2500			140×140	19600			0.033	0.024
0.99	28×25	*2800			110×110	12100			0.0067	0.0048
0.992	28×25	*2800			100×110	11000			0.0053	0.0039
0.994	32×25	*3200			100×110	11000	200×220	44000	0.0040	0.0029
0.996	25×25	2500	10×100	*2000	90×100	9000	150×170	25500	0.0027	*0.0019
0.998*	25×25	2500	8×64	*1024	90×90	8100	100×120	12000	0.0013	0.00097
0.999	20×25	2000	7×35	* 490	80×80	6400	80×90	7200	0.00067	0.00048
0.9992	20×25	2000	6×32	* 384	80×80	6400	80×80	6400	0.00054	0.00039
0.9999	25×25	2500	6×25	* 300	60×64	3840	60×64	3840	0.000067	0.000048
1.0	6×25	300	6×25	* 300	60×60	3600	60×60	3600	0	0
1.0001	20×25	2000	6×25	* 300	55×55	3025	55×60	3300	0.000067	0.000048
1.0005	16×25	1600	6×25	* 300	45×45	2025	50×50	2500	0.00033	0.00024
1.001	14×25	1400	6×25	* 300	40×40	1600	45×45	2025	0.00067	0.00048
1.005	12×25	1200	6×20	* 240	25×25	625	25×28	700	0.0034	0.0024
1.01	12×25	1200	6×20	* 240	20×20	400	20×20	400	0.0067	0.0048
1.05	11×25	1100	7×14	196	12×11	* 132	12×12	144	0.034	0.024
1.1	11×28	1232	7×12	168	9×9	* 81	10×11	110	0.068	0.048
1.2	11×32	1408	7×12	168	8×7	* 56	9×9	81	0.14	0.096

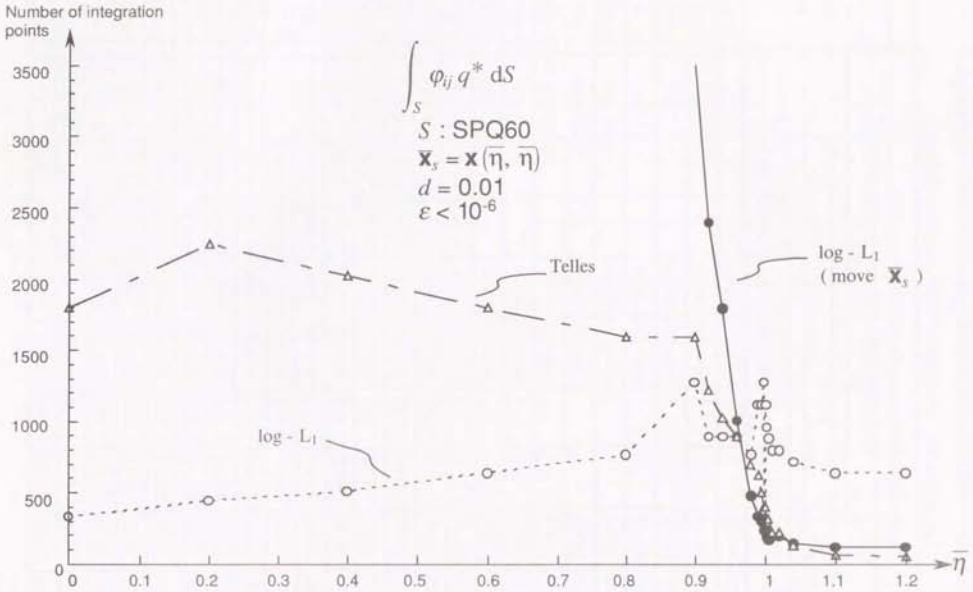

Fig.10.48 Number of integration points vs Position of source projection for $\int_S \varphi_{ij}\, q^*\, dS$

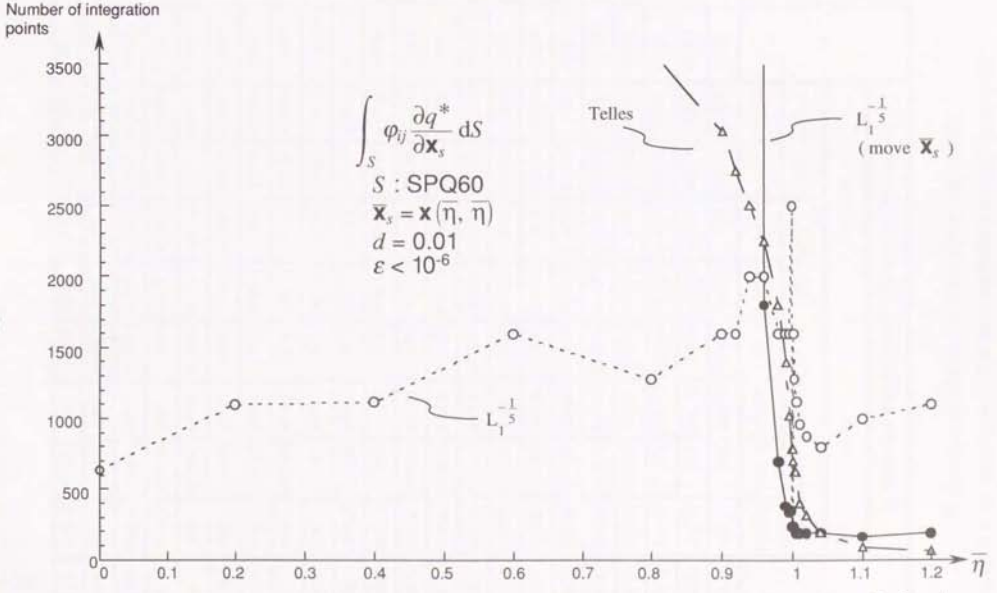

Fig.10.49 Number of integration points vs Position of source projection for $\int_S \varphi_{ij} \frac{\partial q^*}{\partial \mathbf{x}_s}\, dS$

Table 10.62 Effect of moving the source projection $\hat{x}_s$ to the element edge

$\int_S \phi_{ij} q^* dS$, S: SPQ60, $\bar{\eta}_2=0$, $\bar{\eta}_1=0\sim1.2$, $d=0.1$

$\bar{\eta}_1$	Number of integration points for relative error $<10^{-6}$								h_4
	log-L_1				Telles				
	original $\hat{x}_s$		move $\hat{x}_s$		original $\hat{x}_s$		move $\hat{x}_s$		
	$N_t\times N_R$	N	$N_t\times N_R$	N	$N_1\times N_2$	N	$N_1\times N_2$	N	
0	6×9	* 216	20×40	2400	14×16	224	35×32	1120	0.43
0.2	7×11	308	16×40	1920	14×14	* 196	40×32	1280	0.36
0.4	7×10	280	12×35	1260	14×16	* 224	32×28	896	0.28
0.6	9×10	360	8×28	672	12×16	* 192	25×25	625	0.19
0.8 *	10×11	440	7×25	525	14×16	* 224	20×20	400	0.095
0.82	9×11	396	7×20	420	14×16	* 224	20×16	320	0.085
0.84	11×11	484	7×20	420	14×16	* 224	20×16	320	* 0.076
0.86	11×11	484	6×20	360	16×16	* 256	20×14	280	0.066
0.88	11×11	484	7×16	336	14×16	* 224	16×14	* 224	0.056
0.9	11×11	484	7×16	336	14×16	* 224	16×14	* 224	0.046
0.92	13×11	572	7×16	336	14×16	* 224	16×14	* 224	0.036
0.94	12×11	528	7×14	294	14×16	224	14×14	* 196	0.026
0.96	13×12	624	7×14	294	12×14	* 168	12×14	* 168	0.016
0.99	17×11	748	7×12	252	14×14	* 196	14×14	* 196	0.00087
1.0	7×11	231	7×11	231	14×14	* 196	14×14	* 196	0.0042
1.001	9×12	432	7×11	231	14×14	* 196	14×14	* 196	0.0048
1.005	15×12	720	7×11	231	14×14	* 196	14×14	* 196	0.0068
1.01	12×11	528	7×11	231	14×14	* 196	14×14	* 196	0.0094
1.05	12×12	576	8×10	240	10×14	* 140	11×14	154	0.030
1.1	12×13	624	7×10	210	11×14	* 154	11×14	* 154	0.056
1.15	10×11	440	7×8	* 168	12×14	* 168	12×14	* 168	0.083
1.2	11×13	572	7×8	168	10×14	* 140	11×12	* 132	0.11

Table 10.63 Effect of moving the source projection $\hat{x}_s$ to the element edge

$\int_S \phi_{ij} q^* dS$, S: SPQ60, $\bar{\eta}_2=0$, $\bar{\eta}_1=0\sim1.2$, $d=0.01$

$\bar{\eta}_1$	Number of integration points for relative error $<10^{-6}$								h_4
	log-L_1				Telles				
	original $\hat{x}_s$		move $\hat{x}_s$		original $\hat{x}_s$		move $\hat{x}_s$		
	$N_t\times N_R$	N	$N_t\times N_R$	N	$N_1\times N_2$	N	$N_1\times N_2$	N	
0	6×14	* 336			40×45	1800			0.43
0.2	7×14	* 392			45×40	1800			0.36
0.4	7×14	* 392			40×45	1800			0.28
0.6	9×16	* 576			40×45	1800	220×250	55000	0.19
0.8	11×16	* 704			40×45	1800	160×180	28800	0.095
0.9	14×16	* 896	20×110	6600	35×45	1575	110×120	13200	0.046
0.92	16×16	* 1024	16×90	4320	32×45	1440	100×100	10000	0.036
0.94	16×16	* 1024	11×72	2376	35×45	1575	64×80	5120	0.026
0.96	16×16	* 1024	8×55	1320	32×45	1440	55×35	1925	0.016
0.98 *	25×16	1600	7×35	* 735	28×45	1260	35×40	1400	* 0.0060
0.99	28×16	1792	7×25	* 525	25×45	1125	28×45	1260	0.00087
0.995	25×16	1600	7×20	* 420	25×45	1125	25×40	1000	0.0017
0.999	20×20	1600	7×20	* 420	20×45	900	20×45	900	0.0037
1.0	7×20	* 420	7×20	* 420	20×45	900	20×45	900	0.0042
1.001	14×20	1120	7×16	* 336	20×45	900	20×45	900	0.0048
1.002	20×20	1600	7×16	* 336	20×45	900	20×45	900	0.0053
1.005	20×20	1600	8×16	* 384	20×45	900	20×45	900	0.0068
1.01	20×20	1600	8×14	* 336	14×45	630	16×40	640	0.0094
1.02	20×20	1600	7×12	* 252	12×40	480	12×35	420	0.015
1.04	16×20	1280	7×10	* 210	10×32	320	11×25	275	0.025
1.1	16×20	1280	7×9	189	7×25	* 175	12×20	240	0.056
1.2	14×20	1120	6×8	144	7×16	112	10×10	* 100	0.11

Table 10.64 Effect of moving the source projection $\hat{x}_s$ to the element edge

$\int_S \phi_{ij} q^* \, dS$, S: SPQ60, $\bar{\gamma}_2=0$, $\bar{\gamma}_1=0\sim1.2$, $d=0.001$

$\bar{\gamma}_1$	Number of integration points for relative error $<10^{-6}$								h_4
	log-L_1				Telles				
	original $\hat{x}_s$		move $\hat{x}_s$		original $\hat{x}_s$		move $\hat{x}_s$		
	$N_t\times N_R$	N	$N_t\times N_R$	N	$N_1\times N_2$	N	$N_1\times N_2$	N	
0	6×20	* 480			110×120	13200			0.43
0.2	6×20	* 480			100×110	11000			0.36
0.4	7×20	* 560			110×120	13200			0.28
0.6	9×20	* 720			100×110	11000			0.19
0.8	11×20	* 880			90×110	9900			0.095
0.9	12×20	* 960			72×110	7920			0.046
0.95	20×20	* 1600			90×110	9900			0.021
0.99	35×25	* 3500	20×(128)	(7680)	72×120	8640	220×100	22000	0.00087
0.992	40×20	* 3200	16×(128)	(6144)	60×120	7200	170×90	15300	0.00015
0.994	32×20	* 2560	11×100	3300	60×110	6600	140×90	12600	0.0012
0.996	25×20	2000	9×64	*1728	60×110	6600	100×90	9000	*0.0022
0.998*	80×20	6400	7×40	* 840	50×110	5500	60×110	6600	0.0032
0.999	110×20	8800	7×28	* 588	45×110	4950	50×110	5500	0.0037
0.9992	120×20	9600	7×25	* 525	45×110	4950	45×90	4050	0.0038
0.9999	120×20	9600	7×20	* 420	45×110	4950	35×110	3850	0.0042
1.0	7×20	* 420	7×20	* 420	35×110	3850	35×110	3850	0.0042
1.0001	120×20	9600	7×20	* 420	32×110	3520	35×110	3850	0.0043
1.0005	(128)×20	(10240)	7×14	* 294	25×100	2500			0.0045
1.001	(128)×20	(10240)	7×14	* 294			25×100	2500	0.0048
1.005	80×20	6400	6×14	* 252	14×72	1008	20×64	1280	0.0068
1.01	55×25	5500	7×12	* 252	12×60	720	14×50	700	0.0094
1.05	25×25	2500	7×10	* 210	10×25	250	11×25	275	0.030
1.1	20×25	2000	7×9	189	8×20	160	11×12	* 132	0.056
1.2	14×25	1400	6×8	144	7×16	112	10×10	* 100	0.11

Table 10.65 Effect of moving the source projection $\hat{x}_s$ to the element edge

$\int_S \phi_{ij} \, \partial q^*/\partial \hat{x}_s \, dS$, S: SPQ60, $\bar{\gamma}_2=0$, $\bar{\gamma}_1=0\sim1.2$, $d=0.1$

$\bar{\gamma}_1$	Number of integration points for relative error $<10^{-6}$								h_4
	$L_1^{-1/5}$				Telles				
	original $\hat{x}_s$		move $\hat{x}_s$		original $\hat{x}_s$		move $\hat{x}_s$		
	$N_t\times N_R$	N	$N_t\times N_R$	N	$N_1\times N_2$	N	$N_1\times N_2$	N	
0	8×10	* 320	25×55	4125	25×25	625	50×45	2250	0.43
0.2	8×14	448	20×50	3000	20×20	* 400	50×45	2250	0.36
0.4	9×12	432	14×45	1890	20×25	* 500	45×40	1800	0.28
0.6	12×12	576	11×40	1320	20×20	* 400	40×32	1280	0.19
*0.8	14×14	784	9×25	675	20×25	* 500	28×25	700	*0.095
0.82	14×14	784	9×25	675	20×25	* 500	28×25	700	0.085
0.84	14×14	784	8×25	600	20×25	* 500	25×25	625	0.076
0.86	14×16	896	9×25	675	20×20	* 400	25×20	500	0.066
0.88	16×14	896	9×20	540	20×20	* 400	25×20	500	0.056
0.9	20×14	1120	9×25	675	20×25	* 500	25×20	* 500	0.046
0.92	20×14	1120	9×20	540	20×25	500	20×20	* 400	0.036
0.94	16×14	896	9×20	540	20×20	* 400	20×20	* 400	0.026
0.96	20×14	1120	9×16	432	20×20	* 400	20×20	* 400	0.016
0.99	25×14	1400	9×14	* 378	20×20	400	20×20	400	0.00087
1.0	9×14	378	9×14	378	16×20	* 320	16×20	* 320	0.0042
1.001	14×14	784	9×14	378	16×20	* 320	16×20	* 320	0.0048
1.005	20×14	1120	9×14	378	16×20	* 320	16×20	* 320	0.0068
1.01	16×14	896	9×14	378	16×20	* 320	16×20	* 320	0.0094
1.05	16×14	896	9×12	324	14×20	* 280	14×20	* 280	0.030
1.1	16×16	1024	8×11	* 264	14×20	280	14×20	280	0.056
1.15	14×16	896	9×11	297	12×20	240	14×16	* 224	0.083
1.2	14×16	896	9×10	270	11×16	* 176	12×16	192	0.11

Table 10.66 Effect of moving the source projection $\hat{x}_s$ to the element edge

$\int_S \phi_{ij} \partial q^*/\partial \hat{x}_s \, dS$, S: SPQ60, $\bar{\eta}_2=0$, $\bar{\eta}_1=0\sim1.2$, $d=0.01$

$\bar{\eta}_1$	Number of integration points for relative error $<10^{-6}$								h_4
	$L_1^{-1/5}$				Telles				
	original $\hat{x}_s$		move $\hat{x}_s$		original $\hat{x}_s$		move $\hat{x}_s$		
	$N_t \times N_R$	N	$N_t \times N_R$	N	$N_1 \times N_2$	N	$N_1 \times N_2$	N	
0	8×20	* 640			60×72	4320			0.43
0.2	10×20	* 800			72×72	5184			0.36
0.4	10×20	* 800			72×60	4320			0.28
0.6	12×20	* 960			64×72	4608			0.19
0.8	14×20	*1120			60×60	3600			0.095
0.9	20×20	*1600			55×60	3300	180×200	36000	0.046
0.92	20×20	*1600	20×110	6600	55×60	3300	150×160	24000	0.036
0.94	20×20	*1600	16×100	4800	55×60	3300	120×128	15360	0.026
0.96	25×20	*2000	12×72	2592	50×60	3000	90×60	5400	0.016
*0.98	32×25	3200	9×50	*1350	45×60	2700	60×64	3840	*0.0060
0.99	32×20	2560	8×28	* 672	40×60	2400	40×64	2560	0.00087
0.995	32×20	2560	7×25	* 525	35×72	2520	35×72	2520	0.0017
0.999	20×20	1600	8×20	* 480	32×72	2304	32×72	2304	0.0037
1.0	8×20	* 480	8×20	* 480	28×72	2016	28×72	2016	0.0042
1.001	25×20	2000	8×16	* 384	28×72	2016	28×72	2016	0.0048
1.002	25×20	2000	8×16	* 384	28×72	2016	28×72	2016	0.0053
1.005	28×20	2240	8×16	* 384	25×72	1800	25×72	1800	0.0068
1.01	28×20	2240	8×16	* 384	25×64	1600	20×64	1280	0.0094
1.02	28×20	2240	8×14	* 336	16×55	880	20×55	1100	0.015
1.04	25×20	2000	8×14	* 336	16×45	720	16×40	640	0.025
1.1	20×20	1600	8×11	* 264	9×32	288	14×25	350	0.056
1.2	16×25	1600	8×10	240	8×25	200	12×16	* 192	0.11

Table 10.67 Effect of moving the source projection $\hat{x}_s$ to the element edge

$\int_S \phi_{ij} \partial q^*/\partial \hat{x}_s \, dS$, S: SPQ60, $\bar{\eta}_2=0$, $\bar{\eta}_1=0\sim1.2$, $d=0.001$

$\bar{\eta}_1$	Number of integration points for relative error $<10^{-6}$								h_4
	$L_1^{-1/5}$				Telles				
	original $\hat{x}_s$		move $\hat{x}_s$		original $\hat{x}_s$		move $\hat{x}_s$		
	$N_t \times N_R$	N	$N_t \times N_R$	N	$N_1 \times N_2$	N	$N_1 \times N_2$	N	
0	8×25	* 800			190×190	36100			0.43
0.2	11×25	*1100			190×190	36100			0.36
0.4	11×25	*1100			190×190	36100			0.28
0.6	14×25	*1400			180×190	34200			0.19
0.8	14×25	*1400			170×190	32300			0.095
0.9	25×25	*2500			150×190	28500			0.046
0.95	25×25	*2500			140×190	26600			0.021
0.99	45×25	*4500			110×190	20900			0.00087
0.992	45×25	*4500			110×190	20900			0.00015
0.994	40×25	*4000			110×190	20900	240×150	36000	0.0012
0.996	40×25	4000	11×90	*2970	100×190	19000	180×170	30600	*0.0022
*0.998	110×25	11000	8×50	*1200					0.0032
0.999	150×25	7500	8×32	* 768					0.0037
0.9992			8×28	* 672					0.0038
0.9999			8×25	* 600					0.0042
1.0	8×25	* 600	8×25	* 600	64×190	12160	64×190	12160	0.0042
1.0001			8×25	* 600					0.0043
1.0005			8×25	* 600					0.0045
1.001			8×25	* 600					0.0048
1.005	100×25	10000	8×20	* 480	25×120	3000	28×110	3080	0.0068
1.01	72×25	7200	8×20	* 480	20×90	1800	20×80	1600	0.0094
1.05	32×25	3200	8×14	* 336	11×45	495	16×32	512	0.03
1.1	25×25	2500	8×11	* 264	9×32	288	16×20	320	0.056
1.2	20×28	2240	8×11	264	8×25	200	12×16	* 192	0.11

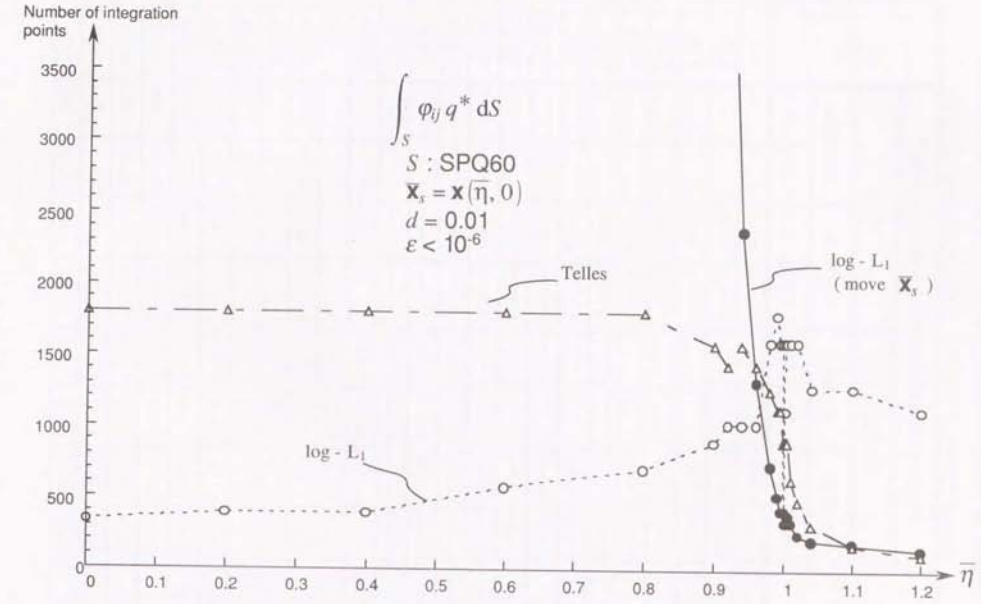

Fig.10.50 Number of integration points vs Position of source projection for $\int_S \varphi_{ij}\, q^*\, dS$

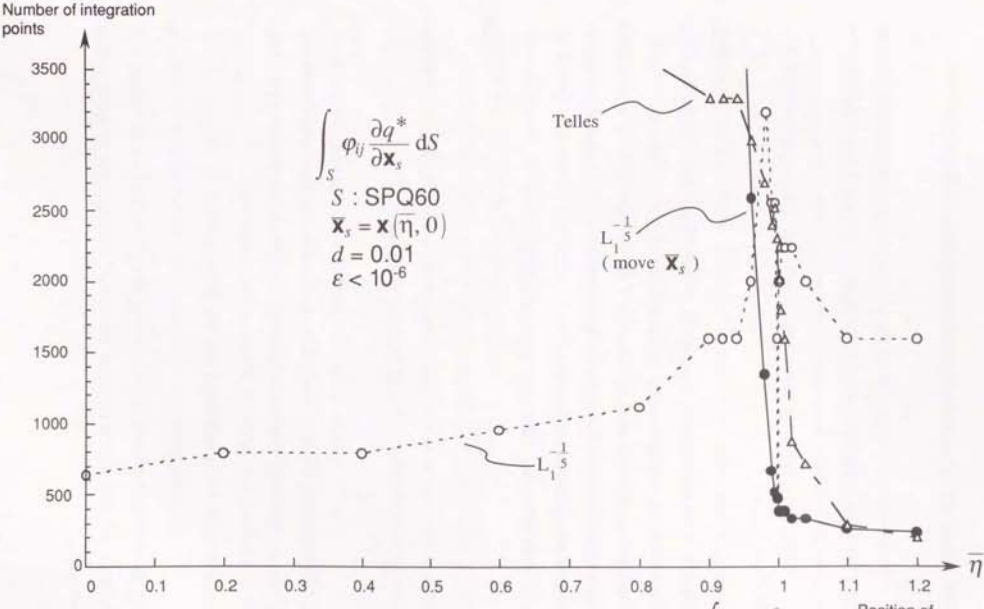

Fig.10.51 Number of integration points vs Position of source projection for $\int_S \varphi_{ij} \frac{\partial q^*}{\partial \mathbf{x}_s}\, dS$

10.8 Summary of Numerical Results for Nearly Singular Integrals

In this chapter, numerical experiment results were presented to evaluate the numerical integration methods (PART) proposed for nearly singular integrals in Chapter 5, in comparison with previous methods.

First, the singularity cancelling radial variable transformation $R(\rho)$ corresponding to

$$\rho\, d\rho = r^{1+\alpha}\, dR \quad , \tag{5.43}$$

where α is the order of near singularity of the integral kernel, was shown to require only one radial integration point for the accurate integration of u^* and q^* over constant planar elements. However, for curved elements and kernels including interpolation functions ϕ_{ij}, the method does not work as efficiently as Telles' cubic transformation method.

Then the log-L_2 radial variable transformation

$$R(\rho) = \log \sqrt{\rho^2 + d^2} \quad , \tag{5.64}$$

which corresponds to the singularity cancelling transformation for $\alpha = 2$, was shown to work efficiently for nearly singular integrals

$$\int_S \frac{dS}{r^\alpha} \quad , \quad (\alpha = 1 \sim 5) \tag{10.35}$$

of different orders of near singularity over the 'spherical' quadrilateral element SPQ60. However, the method is shown to be inefficient for the integration of the kernels $\partial u^*/\partial \mathbf{x}_s$ and $\partial q^*/\partial \mathbf{x}_s$ arising from flux calculation.

Next, the log-L_1 radial variable transformation

$$R(\rho) = \log(\rho + d) \tag{5.85}$$

was shown to work efficiently for the integration of the flux kernels $\partial u^*/\partial \mathbf{x}_s$ and $\partial q^*/\partial \mathbf{x}_s$, as well as the potential kernels u^* and q^*, over constant planar elements.

Further, the $L_1^{-1/m}$ radial variable transformations

$$R(\rho) = -(\rho + d)^{-\frac{1}{m}} \quad , \quad (m > 1) \tag{5.99}$$

were introduced to improve on the log-L_1 transformation.

Different radial variable transformations were tested for the model radial variable integrals

$$I_{\alpha,\delta} = \int_0^{\rho_j} \frac{\rho^\delta}{r^\alpha}\, d\rho \quad . \tag{10.45}$$

Results showed that the log-L_1 and $L_1^{-1/5}$ radial variable transformations with the Gauss-Legendre rule perform far better compared to the identity and log-L_2 transformations with the Gauss-Legendre rule, and the single and double exponential transformations with the truncated trapezium rule. The $L_1^{-1/5}$ transformation gave better results compared to the log-L_1 transformation except for the case $\alpha = \delta = 1$, $d = 10^{-3}$ and $\alpha = 3, \delta = 2$, $d = 10^{-2}$. It was also shown that the theoretical error estimates of Chapter 7 based on complex function theory, matches well with numerical experiment results.

Finally, different numerical integration methods were tested for the integration of

$$\int_S \phi_{ij}\, u^*\, dS \, , \quad \int_S \phi_{ij}\, q^*\, dS \, , \quad \int_S \phi_{ij} \frac{\partial u^*}{\partial \mathbf{x}_s}\, dS \quad \textit{and} \quad \int_S \phi_{ij} \frac{\partial q^*}{\partial \mathbf{x}_s}\, dS$$

over the 'spherical' quadrilateral element SPQ60 of unit size.

First, the effect of the source distance d, with the source projection fixed at $\hat{\mathbf{x}}_s = \mathbf{x}$ (0.5, 0.5), was tested. As a result, it was shown that for potential and flux calculations,

(1) For $d \leq 0.06$, the PART method with the log-L_1 and $L_1^{-1/5}$ radial variable transformations and the log-type angular variable transformation

$$t(\theta) = \frac{h_j}{2} \log \left\{ \frac{1 + \sin(\theta - \alpha_j)}{1 - \sin(\theta - \alpha_j)} \right\} \tag{5.130}$$

works most efficiently.

The log-L_1 transformation is suited to potential calculations involving the integrals $\int_S \phi_{ij} u^* \, dS$ and $\int_S \phi_{ij} q^* \, dS$, while the $L_1^{-1/5}$ transformation is suited to flux calculations involving the integrals $\int_S \phi_{ij} \partial u^*/\partial \mathbf{x}_s \, dS$ and $\int_S \phi_{ij} \partial q^*/\partial \mathbf{x}_s \, dS$.

(2) For $0.06 \leq d \leq 0.8$, Telles' cubic transformation method works most efficiently.

(3) For $d \geq 0.8$, the product Gauss-Legendre method works most efficiently.

Next, the effect of the position of the source projection $\bar{\mathbf{x}}_s = \mathbf{x}(\bar{\eta}_1, \bar{\eta}_2)$ was examined for $\bar{\eta}_1 = \bar{\eta}_2 = 0 \sim 1.2$ and $\bar{\eta}_2 = 0$, $\bar{\eta}_1 = 0 \sim 1.2$, with source distance, $d = 0.1$, 0.01 and 0.001.

It was shown that the number of integration points for the PART method with the log-L_1 and $L_1^{-1/5}$ radial variable transformations can be reduced considerably by deliberately moving the source projection $\bar{\mathbf{x}}_s$ to the nearest edge of the element S, when $\bar{\mathbf{x}}_s \notin S$ or when $\bar{\mathbf{x}}_s \in S$ and $h_j < d$ where h_j is the distance between the original source projection $\bar{\mathbf{x}}_s$ and the nearest edge-j of the projected element $\bar{S}$.

Further, it was shown that the PART method thus improved, is superior to Telles' method for $\bar{\mathbf{x}}_s \in S$ and $\bar{\mathbf{x}}_s \notin S$, $\bar{\eta}_1 < 1.01$, for source distances $d = 0.01$ and 0.001.

It was also shown that the log-type angular variable transformation $t(\theta)$ of equation (5.130) works very effectively and is indispensable when the source projection $\bar{\mathbf{x}}_s$ lies near the element edge i.e. when $0.7 \lesssim \bar{\eta} \lesssim 1.1$.

CHAPTER 11

APPLICATION TO CAUCHY PRINCIPAL VALUE INTEGRALS

Because of the robustness and efficiency of the PART method with the log-L_1 and $L_1^{-1/5}$ radial variable transformations, one is tempted to see how close one can let the source point $\mathbf{x}_s$ approach the element surface ($d \to 0$) and still obtain the accurate value of the nearly singular integral.

This is of particular interest for the flux integrals $\int_S \partial u^*/\partial \mathbf{x}_s \, dS$ and $\int_S \partial q^*/\partial \mathbf{x}_s \, dS$, since in the limit of $d \to 0$, or when the source point $\mathbf{x}_s$ is on the element, they become strongly singular, and they exist only in the Cauchy principal value sense, whereas the potential integrals $\int_S u^* \, dS$ and $\int_S q^* dS$ are only weakly singular, i.e. $u^* \sim O(1/r)$ for $d = 0$ (cf. section 3.1) and can be easily calculated just using polar coordinates centered at $\mathbf{x}_s$ in the plane tangent to the element at $\mathbf{x}_s$ (PART method with $R(\rho) = \rho$).

In fact, it turns out that one can calculate these Cauchy principal value integrals by setting the source distance d sufficiently small and calculating the corresponding nearly singular integral by the PART (log-L_1) method. To be more specific, let

$$\mathbf{x}_s' = \mathbf{x}_s + d\mathbf{n}_s \tag{11.1}$$

where $0 < d \ll 1$ and $\mathbf{n}_s$ is the unit normal to the boundary surface S at $\mathbf{x}_s \in S$, and calculate the corresponding integral with the source point at $\mathbf{x}_s'$.

First, we will calculate the nearly singular integral for the planar square element PLR (0.5, 0.5), mentioned before, letting the source point $\mathbf{x}_s' = (0.25, 0.25, d)$ approach the element surface ($d \to 0$). In order to see how the nearly singular integral converges to the Cauchy principal value of the

hypersingular integral as $d \to 0$, we will compare the former with the latter, which can be calculated analytically as follows :

For a planar rectangular element

$S : \{ \mathbf{x} = (x, y, z) \mid -a \leqq x \leqq a\ ,\ -b \leqq y \leqq b, z = 0 \}$, with the source point $\mathbf{x}_s = (x_s\ ,\ y_s\ ,\ 0)$ on the element S, the Cauchy principal value integral can be calculated as the limit of $d \to 0$, where $\mathbf{x}_s = (x_s, y_s, d)$, to give

$$\int_S \partial u^*/\partial \mathbf{x}_s \, \mathrm{d}S = (I_{\partial u^*, x}\ ,\ I_{\partial u^*, y}\ ,\ I_{\partial u^*, z})^T$$

where

$$I_{\partial u^*, x} = \frac{1}{4\pi} \sum_{j=1}^{4} \left[(\sin\theta_{j+1}) \log\left\{ \frac{h_j}{\cos(\theta_{j+1} - \alpha_j)} \right\} - (\sin\theta_j) \log\left\{ \frac{h_j}{\cos(\theta_j - \alpha_j)} \right\} \right.$$

$$\left. - (\cos\alpha_j) \log \left| \frac{\tan\left(\frac{\theta_{j+1} - \alpha_j}{2} + \frac{\pi}{4} \right)}{\tan\left(\frac{\theta_j - \alpha_j}{2} + \frac{\pi}{4} \right)} \right| \right| \tag{11.3}$$

$$I_{\partial u^*, y} = \frac{1}{4\pi} \sum_{j=1}^{4} \left[-(\cos\theta_{j+1}) \log\left\{ \frac{h_j}{\cos(\theta_{j+1} - \alpha_j)} \right\} + (\cos\theta_j) \log\left\{ \frac{h_j}{\cos(\theta_j - \alpha_j)} \right\} \right.$$

$$\left. - (\sin\alpha_j) \log \left| \frac{\tan\left(\frac{\theta_{j+1} - \alpha_j}{2} + \frac{\pi}{4} \right)}{\tan\left(\frac{\theta_j - \alpha_j}{2} + \frac{\pi}{4} \right)} \right| \right| \tag{11.4}$$

$$I_{\partial u^*, z} = -\frac{1}{2} \tag{11.5}$$

and

$$\int_S \partial q^*/\partial \mathbf{x}_s \, \mathrm{d}S = \frac{1}{4\pi} \begin{bmatrix} 0 \\ 0 \\ \sum_{j=1}^{4} \left\{ \sin(\theta_{j+1} - \alpha_j) - \sin(\theta_j - \alpha_j) \right\} / h_j \end{bmatrix} \tag{11.6}$$

where

$$\theta_1 = \tan^{-1}\left(\frac{b - y_s}{a - x_s} \right), \qquad \theta_2 = \pi - \tan^{-1}\left(\frac{b - y_s}{x_s + a} \right),$$

$$\theta_3 = \pi + \tan^{-1}\left(\frac{y_s + b}{x_s + a} \right), \qquad \theta_4 = \frac{3}{2}\pi + \tan^{-1}\left(\frac{a - x_s}{y_s + b} \right),$$

$$\theta_5 = \theta_1 + 2\pi\ , \tag{11.7}$$

$$\alpha_1 = \frac{\pi}{2}, \quad \alpha_2 = \pi, \quad \alpha_3 = \frac{3}{2}\pi, \quad \alpha_4 = 2\pi \tag{11.8}$$

and

$$h_1 = b - y_s\ , \quad h_2 = x_s + a\ , \quad h_3 = y_s + b\ , \quad h_4 = a - x_s\ . \tag{11.9}$$

For the planar square element PLR (0.5, 0.5), $a = b = 1/2$ and $x_s = y_s = 1/4$.

The result of numerical experiments on the planar square element PLR (0.5, 0.5) is given in Table 11.1, where the source distance d and the number of integration points for the angular (t) and radial (R) variables using the PART (log-L_1 transformation) method, required to achieve an accuracy of (relative error $< 10^{-6}$ compared to the analytical value of the hypersingular integral ($d = 0$), are shown. For the x, y, component integrals (*) of $\int_S \partial q^*/\partial \mathbf{x}_s \, \mathrm{d}S$, partial quadruple precision was necessary, and the absolute error was taken, since the true values are both zero.

Table 11.1 Convergence of nearly singular integrals to Cauchy principal value integrals (planar square element : PLR(0.5, 0.5))

Integral	Component	Source distance	Number of integration points		Value of integral
		d	$N_t \times N_R$	total	(analytical, $d=0$)
$\int_S \partial u^*/\partial \mathbf{x}_s \, \mathrm{d}S$	$x\ ,y$	10^{-4}	8×25	800	$-1.1122013 \times 10^{-1}$
	z	10^{-7}	10×32	1280	$-5.0000000 \times 10^{-1}$
$\int_S \partial q^*/\partial \mathbf{x}_s \, \mathrm{d}S$	$^*x\ ,y$	10^{-8}	20×80	6400	0
	z	10^{-4}	20×50	4000	1.2712670

Similarly, one can calculate the Cauchy principal value integrals $\int_S \partial u^*/\partial \mathbf{x}_s \, \mathrm{d}S$ and $\int_S \partial q^*/\partial \mathbf{x}_s \, \mathrm{d}S$ over curved elements, as the limit as $d \to 0$ of nearly singular integrals . As an example, we take the 'spherical' quadrilateral element

SPQ60 mentioned before with the source point on the element at $\mathbf{x}_s = \mathbf{x}(\bar{\eta}_1, \bar{\eta}_2)$, where $\bar{\eta}_1 = \bar{\eta}_2 = 0.5$. Numerical results are shown in Table 11.2. The value of the source distance d and the required number of integration points to achieve a relative error $< 10^{-6}$ compared to the converged result ($d \to 0$) is given. The actual value of the converged result for the Cauchy principal value integrals are also given. In this case, partial quadruple precision was necessary for calculating the integral $\int_S \partial q^*/\partial \mathbf{x}_s \, dS$. This is because $\partial q^*/\partial \mathbf{x}_s$ contains terms like $\rho \cos\theta / r^5$ (cf. equation 3.130), which take very large absolute values near the source point $\mathbf{x}_s$ and cancel each other when integrated in the angular direction, so that rounding error becomes significant.

Table 11.2 Convergence of nearly singular integrals to Cauchy principal value integrals ('spherical' quadrilateral element : SPQ60)

Integral	Component	Source distance	Number of integration points		Value of integral
		d	$N_\ell \times N_R$	total	(converged)
$\int_S \partial u^*/\partial \mathbf{x}_s \, dS$	x	10^{-6}	16×40	2560	4.0224494×10^{-1}
	y	10^{-8}	16×45	2880	$-9.9926710 \times 10^{-2}$
	z	10^{-8}	16×45	2880	$-6.1706620 \times 10^{-1}$
$\int_S \partial q^*/\partial \mathbf{x}_s \, dS$	x	10^{-7}	25×80	8000	-1.0959943
	y	10^{-8}	25×90	9000	2.221675×10^{-1}
	z	10^{-7}	25×80	8000	$-2.3174413 \times 10^{-1}$

The above numerical experiments demonstrate the robustness of the PART (log-L_1 transformation) method with regard to the source distance d, by applying it successfully to the calculation of Cauchy principal value integrals as the limit ($d \to 0$) of nearly singular integrals. This may prove useful especially when calculating Cauchy principal value integrals with the source point at the corner or on the edge of the element, in which case previous techniques [28] would not work.

CHAPTER 12

CONCLUSIONS

This thesis was primarily concerned with the numerical integration method for the accurate and efficient calculation of nearly singular integrals over general curved surfaces, which plays an important role in three dimensional boundary element analysis.

Nearly singular integrals frequently arise in engineering problems, when analysing thin structures or thin gaps, when using boundary elements with high aspect ratio and when calculating the potential or flux very near the boundary.

The thesis is divided into two parts. In the first part, the theory and formulation of three dimensional boundary element method (BEM) for potential problems is presented, and the nature of nearly singular, weakly singular and hypersingular integral kernels is analysed by focusing on the radial component of the kernels. Previous work on numerical integration methods for three dimensional BEM is briefly reviewed before proceeding to describe the new technique developed to deal with nearly singular integrals. This technique has been described in detail in Chapter 5 and is referred to as the "Projection and Angular & Radial Transformation (PART) method". The method consists of the following stages:

(1) Find the closest point $\hat{\mathbf{x}}_s$ on the curved element S from the source point $\mathbf{x}_s$.

(2) Approximately project the element S on to a polygon $\overline{S}$ in the plane tangent to S at $\hat{\mathbf{x}}_s$.

(3) Introduce polar coordinates (ρ, θ) centred at $\hat{\mathbf{x}}_s$ in $\overline{S}$.

(4) Apply a radial variable transformation $R(\rho)$ in order to weaken the near singularity inherent in the integral kernel.

(5) Apply the log-type angular variable transformation

$$t(\theta) = \frac{h_j}{2} \log \left\{ \frac{1+\sin(\theta-a_j)}{1-\sin(\theta-a_j)} \right\}$$

in order to weaken the angular near singularity, which arises when $\hat{\mathbf{x}}_s$ is very near the edge of $\bar{S}$ or when $\bar{S}$ has a high aspect ratio.

(6) Use the Gauss-Legendre formula in the transformed radial and angular variables R and t.

For weakly singular integrals, which appear in the calculation of the diagonals of H and G matrices for three dimensional potential problems, the identity radial variable transformation $R(\rho)=\rho$ gives efficient results.

For nearly singular integrals, the singularity cancelling radial variable transformation gives the exact result with only one integration point in the radial variable for constant planar elements. For curved elements, the log-L_2 radial variable transformation $R(\rho)=\log\sqrt{\rho^2+d^2}$, where d is the source distance, gives more efficient results for near singularities of different orders. For general kernels, including kernels arising in flux calculation or kernels with interpolation functions, the log-L_1 transformation $R(\rho)=\log(\rho+d)$ and the $L_1^{-1/5}$ transformation $R(\rho) = -(\rho+d)^{-1/5}$ are more robust and efficient, where the former is more suited to potential calculations and the latter to flux calculations.

The possibility of using the single or double exponential transformation with the truncated trapezium rule for the radial and angular variable integration is also discussed. Finally, the detailed implementation of the PART method is discussed. The advantage of the method lies in the fact that the radial and angular (near) singularities are separated so that they can be analysed and treated independently from each other.

An elementary error analysis was presented in Chapter 6, explaining why the log-L_2 radial variable transformation (corresponding to order $\beta=2$) gives best results among other singularity cancelling transformations corresponding to $\beta\neq 2$. In Chapter 7, complex function theory was used to derive more rigorous

theoretical error estimates for different radial variable transformations. The analysis showed that the PART method using the log-L_2 radial variable transformation converges with error of the order n^{-2n}, where n is the number of radial integration points, for integrations arising from potential calculations, whereas the method converges only at a rate of n^{-3} for integrations arising from flux calculations. For the log-L_1 transformation, the theoretical error estimate is of the order σ^{-2n} for both types of integrals, where σ : 1.31~1.63 for D : 10^{-3}~10^{-1}, where D is the source distance relative to the element size. Similarly, for the $L_1^{-1/5}$ transformation, the error is predicted to be of the order σ^{-2n}, where σ: 1.41~1.67 for D: 10^{-3}~10^{-1}. These error estimates match well with numerical experiment results. This method of using complex function theory for the theoretical error estimate also gives a clear perspective for the construction of the optimum radial variable transformation.

The second part of the thesis presented numerical experiment results for the new numerical integration technique. In Chapter 9, the PART method with the identity radial variable transformation and the log-type angular variable transformation was applied to weakly singular integrals and gave accurate and efficient results for planar and curved elements with interpolation functions. In particular, the effect of the angular variable transformation $t(\theta)$ in decreasing the number of angular integration points when the source point $\mathbf{x}_s$ is near the element edge, as in discontinuous elements and elements with high aspect ratio, was demonstrated.

Chapter 10 presented numerical results for nearly singular integrals, which was the primary concern of this thesis. First, results for constant planar elements were presented, together with the closed form integral. The singularity cancelling radial variable transformation corresponding to $\rho\,\mathrm{d}\rho = r^{\alpha}\mathrm{d}R$, where $r=\sqrt{\rho^2+d^2}$ is the source distance and α is the order of near singularity, proved to be more efficient compared to the Telles and Gauss methods when the relative

source distance $D \leqq 0.1$. The log-type angular variable transformation $t(\theta)$ was shown to be effective when the source projection $\hat{\mathbf{x}}_s$ is near the element edge.

The same singularity cancelling radial variable transformation corresponding to $\rho\, d\rho = r^n dR$, where $r' = \sqrt{\rho^2 + d^2}$ is the approximate source distance, was applied to curved elements and kernels with interpolation functions, and was shown to be inefficient compared to Telles' cubic transformation method. To overcome this difficulty, the log-L_2 radial variable transformation $R(\rho) = \log\sqrt{\rho^2 + d^2}$, which corresponds to the singularity cancelling transformation for $\alpha = 2$, was introduced and shown to be most efficient and robust among other transformations corresponding to $\alpha \neq 2$, for integrals of the type $\int_S 1/r^{\alpha}\, dS$ with different orders of near singularity $\alpha = 1 \sim 5$ over a curved element S.

However, numerical experiments on a planar element showed that the log-L_2 radial variable transformation is inefficient for integrals arising from flux calculations. In fact, the convergence was of order n^{-3}, where n is the number of radial integration points, as predicted in Chapter 7. To solve this difficulty, the log-L_1 radial variable transformation $R(\rho) = \log(\rho + d)$ was introduced and was shown to work efficiently for flux integrals as well as potential integrals over a constant planar element.

Next, different radial variable transformations were compared for the model radial component integrals $I_{\alpha,\beta} = \int_0^{\hat{\rho}} \rho^{\beta} / r^{\alpha}\, d\rho$ for potential and flux kernels. For transformations based on the Gauss-Legendre rule, the identity transformation $R(\rho) = \rho$, the log-L_2 transformation, the log-L_1 transformation and the $L_1^{-1/m}$ ($m \geqq 1$) transformations were compared. Numerical results showed that the log-L_1 transformation is a robust and efficient transformation with error convergence of order σ^{-2n} where σ : 1.56~1.88 for $\alpha = 5$ ~1 and $D = 0.01$. This corresponds well with the theoretical estimate of Chapter 7 which predicts σ : 1.40~1.64 . The $L_1^{-1/5}$ transformation showed error convergence of the order σ^{-2n} where σ: 1.7~2.9 for $\alpha = 5 \sim 1$ and $D = 0.01$. This corresponds with the

theoretical error estimates of Chapter 7 which predicts σ: 1.48~1.79. The identity and log-L_2 transformations also gave convergence results which were consistent with the theoretical estimates. The single and double exponential transformations based on the truncated trapezium rule were also compared. As a result, they required 2~3 times as many integration points compared to the log-L_1 transformation to obtain the same level of accuracy. On the whole, the $L_1^{-1/m}$ transformation with $m = 5$ gave best results for the model radial integrals.

Finally, the product type Gauss, Telles' methods and the PART method with the identity, log-L_2, log-L_1 and $L_1^{-1/m}$ ($m \geqq 2$) radial variable transformations and identity, log-type angular variable transformations were compared for the nearly singular integrals $\int_S \phi_{\hat{y}}\, u^*\, dS$, $\int_S \phi_{\hat{y}}\, q^*\, dS$ arising from potential calculations and $\int_S \phi_{\hat{y}}\, \partial u^*/\partial \mathbf{x}_s\, dS$, $\int_S \phi_{\hat{y}}\, \partial q^*/\partial \mathbf{x}_s\, dS$ from flux calculations over a curved surface element S. Results showed that the PART method with the log-L_1 or $L_1^{-1/5}$ radial variable transformation and the log-type angular variable transformation is the most robust method with regard to the type of integral kernels, source distance d and the position of the source projection $\hat{\mathbf{x}}_s$ in S .

To be more precise, the effect of the relative source distance D with the source projection fixed at $\hat{\mathbf{x}}_s = \mathbf{x}(0.5, 0.5)$ was investigated for a 'spherical' quadrilateral element S . As a result, we obtained the following guide for the choice of numerical integration methods :

For $D < 0.06$, use the proposed PART method with the log-L_1 or $L_1^{-1/5}$ radial variable transformation and the log-type angular variable transformation. (The log-L_1 gives better results for potential integrals and the $L_1^{-1/5}$ gives better results for flux integrals.)

For $0.06 \leqq D \leqq 0.8$, use Telles' cubic transformation method.

For $D > 0.8$, use the product Gauss-Legendre method.

The effect of the position of the source projection $\hat{\mathbf{x}}_s = \mathbf{x}(\hat{\eta}_1, \hat{\eta}_2)$ was also examined for $\hat{\eta}_1 = \hat{\eta}_2 = 0 \sim 1.2$ and $\hat{\eta}_2 = 0$, $\hat{\eta}_1 = 0 \sim 1.2$, with source distances $d = 0.1$, 0.01 and 0.001. Results showed that the PART method can be substantially

improved by deliberately moving the source projection $\hat{\mathbf{x}}_s$ to the element edge when $\hat{\mathbf{x}}_s \notin S$, or $\hat{\mathbf{x}}_s \in S$ and $h_j < d$, i.e. when the original $\hat{\mathbf{x}}_s$ is outside the element, or inside the element but closer to an edge of the projected element than the source point $\mathbf{x}_s$. Using this strategy, the PART method becomes superior to Telles' method when $\hat{\mathbf{x}}_s \in S$ and $\hat{\mathbf{x}}_s \notin S$, $\bar{\gamma}_1 < 1.01$ for source distances $d = 0.01$ and 0.001.

The effect of the log-type angular variable transformation in the PART method was also verified by comparing with results obtained by the identity angular variable transformation ($t(\theta) = \theta$). The effect becomes pronounced when the source projection approaches the element edge ($\bar{\gamma} \gtrsim 0.7$).

Chapter 11 showed that the PART method with the log-L_1 radial variable transformation can be applied to the calculation of Cauchy principal value integrals arising from flux calculations on the boundary. This was done by taking the source distance d sufficiently small to give an approximation of the limit as $d \to 0$. Numerical results matched with analytical integration results for a planar element. Results on a curved element with interpolation functions were also presented.

In summary, the thesis proposed a robust and efficient numerical integration method for nearly singular integrals with arbitrary small source distance d, which had been an open problem in three dimensional boundary element analysis. The thesis treated the three dimensional potential problem as an example, but the method can also be applied to other problems such as elastostatics. The method may also be applied to two dimensional problems by using the log-L_1 or $L_1^{-1/5}$ transformation. These topics are left for future research.

REFERENCES

1. BREBBIA, C.A., TELLES, J.C.F. and WROBEL, L.C. (1984) Boundary Element Techniques: Theory and Applications in Engineering, Springer-Verlag, Berlin.
2. KUWAHARA, T. and TAKEDA, T. (1985) Calculation of Potential and Potential Gradient for 3-Dimensional Field by B.E.M. using Analytical Integration, Proc. on Rotary Machines and Stational Apparatus, JECM., SA-85-47, 211-216. (In Japanese)
3. STROUD, A.H. and SECREST, D. (1966) Gaussian Quadrature Formulas, Prentice-Hall, New York.
4. CRISTESCU, M. and LOUBIGNAC, G. (1978) Gaussian Quadrature Formulas for Functions with Singularities in 1/r over Triangles and Quadrangles, in Recent Advances in Boundary Element Methods, Ed. C. Brebbia, Pentech Press, London.
5. PINA, H.L.G., FERNANDES, J.L.M. and BREBBIA, C.A. (1981) Some Numerical Integration Formulae over Triangles and Squares with a 1/R Singularity, Appl. Math. Modelling, 5, 209-211.
6. ALIABADI, M.H., HALL, W.S. and PHEMISTER, T.G. (1985) Taylor Expansion for Singular Kernels in the Boundary Element Method, Int. J. Num. Meth. Engng., 21, 2221-2236.
7. LACHAT, J.C. and WATSON, J.O. (1976) Effective Numerical Treatment of Boundary Integral Equations: A Formulation for Three Dimensional Elastostatics, Int. J. Num. Meth. Engng., 10, 273-289.
8. LEAN, M.H. and WEXLER, A. (1985) Accurate Numerical Integration of Singular Boundary Element Kernels over Boundaries with Curvature, Int. J. Num. Meth. Engng., 21, 211-228.

9. RIZZO, F.J. and SHIPPY, D.J. (1977) An Advanced Boundary Integral Equation Method for Three Dimensional Thermoelasticity, Int. J. Num. Meth. Engng., 11, 1753-1768.

10. KUTT, H.R. (1975) Quadrature Formulae for Finite Part Integrals, Report WISK 178, The National Institute for Mathematical Sciences, Pretoria.

11. SCHWAB, C.H. and WENDLAND, W.L. (1985) 3-D BEM Numerical Integration, in C. Brebbia and G. Maier (eds), Boundary Elements VII, Proc. 7th Int. Conf., Como, Italy, Springer Verlag, Berlin & CML Publications, Southampton, 2, 13-85-101.

12. JUN, L., BEER, G. and MEEK, J.L. (1985) Efficient Evaluation of Integrals of Order 1/r, $1/r^2$, $1/r^3$ using Gauss Quadrature, Engineering Analysis, 2, 118-123.

13. TAKAHASHI, M. and MORI, M. (1973) Quadrature Formulas obtained by Variable Transformation, Numer. Math., 21, 206-219.

14. HIGASHIMACHI, T., OKAMOTO, N., EZAWA, Y., AIZAWA, T. and ITO, A. (1983) Interactive Structural Analysis System using the Advanced Boundary Element Method, in Boundary Elements, Proc. 5th Int. Conf., Hiroshima, Japan, eds. C. Brebbia, T. Futagami and M. Tanaka, Springer-Verlag, Berlin & CML Publications, Southampton.

15. TELLES, J.C.F. (1987) A Self-Adaptive Co-ordinate Transformation for Efficient Numerical Evaluations of General Boundary Element Integrals, Int. J. Num. Meth. Engng., 24, 959-973.

16. KOIZUMI, M. and UTAMURA, M. (1987) A Polar Coordinate Integration Scheme with a Hierarchical Correction Procedure to Improve Accuracy, Proc. IUTAM Symp. on Advanced Boundary Element Methods, San Antonio, Texas, ed. T.A. Cruse, 215-222.

17. HAYAMI, K. and BREBBIA, C.A. (1987) A New Coordinate Transformation Method for Singular and Nearly Singular Integrals over General Curved Boundary Elements, in C.A. Brebbia, W.L. Wendland, G. Kuhn (eds.), Boundary Elements IX, Proc. 9th Int. Conf., Stuttgart, Germany, 1, 379-399.

18. HAYAMI, K. and BREBBIA, C.A. (1988) Quadrature Methods for Singular and Nearly Singular Integrals in 3-D Boundary Element Method, (Invited Paper) in C.A. Brebbia (ed.), Boundary Elements X, Proc. 10th Int. Conf., Southampton, U.K., 1, 237-264.

19. PEREIRA, M.F.S., SOARES, C.A.M. and FARIA, L.M.O. (1981) A Comparative Study of Several Boundary Element Methods, Proc. 3rd Int. Seminar on Boundary Element Methods, Irvine, California, Springer-Verlag.

20. ALIABADI, M.A. and HALL, W.S. (1987) Weighted Gaussian Methods for Three Dimensional Boundary Element Kernel Integration, Comm. Appl. Num. Meth., 3, 89-96.

21. JENG, G. and WEXLER, A. (1977) Isoparametric, Finite Element, Variational Solution of Integral Equations for Three-Dimensional Fields, Int. J. Num. Meth. Engng., 11, 1455-1471.

22. AMINI, S. and WILTON, D.T. (1986) An Investigation of Boundary Element Methods for the Exterior Acoustic Problem, Computer Methods in Applied Mechanics and Engineering, 54, 49-65.

23. HALL, W.S. (1988) Integration Methods for Singular Boundary Element Integrals, (Invited Paper), in C.A. Brebbia (ed.), Boundary Elements X, Proc. 10th Int. Conf., Southampton, U.K., 1, 219-236.

24. KRAUS, H. (1967) Thin Elastic Shells, John Wiley & Sons.

25. UTAMURA, M. and KOIZUMI, M. (1985) Development of Computer Program for Analyzing Three-Dimensional Pressure Field in Pressure Suppression System, J. Nucl. Sci., Technol., 22, 733-741.

26. JUN, L., BEER, G. and MEEK, J.L. (1985) The Application of Double Exponential Formulas in the Boundary Element Method, in C. Brebbia and

G. Maier (eds), Boundary Elements VII, Proc. 7th Int. Conf., Como, Italy, Springer-Verlag/CMP, Berlin, 2, 13-3-17.

27. KUNO, Y., YAGI, A., MORISHIMA, T. and UCHIKAWA, Y., (1988) Fundamental Study for High Accuracy Calculation of 3-D Electromagnetic Field, IEEE Trans. Mag., MAG-24, 1, 295-298.
28. GRAY, L.J. and GILES, G.E., (1988) Application of the Thin Cavity Method in Electroplating, in C.A. Brebbia (ed.), Boundary Element X, Proc. 10th Int. Conf., Southampton, U.K., 441-452 .
29. KUWAHARA, T. and TAKEDA, T. (1987) An Effective Analysis for Three-Dimensional Boundary Element Method Using Analytically Integrated Higher-Order Elements, The Transactions of the Institute of Electrical Engineers of Japan, 107-A, 6, 275-282 (in Japanese).
30. AMINI, S. (1986) Efficient Quadrature Rules with A Priori Error Estimates for Integrals with End Point Singularities, BIT 26, 200-208.
31. DAVIS, P.J. and RABINOWITZ, P. (1984) Methods of Numerical Integration, Academic Press, New York.
32. TAKAHASHI, H. and MORI, M. (1974) Double Exponential Formulas for Numerical Integration, Publ. RIMS, Kyoto Univ., 9, 721-741.
33. ATKINSON, K.E. (1978) An Introduction to Numerical Analysis, John Wiley & Sons .
34 HAYAMI, K., and BREBBIA, C.A. Projection and Angular & Radial Transformation Method for Singular and Nearly Singular Integrals in 3D-Boundary Element Method (to be published).
35. HADAMARD, J. (1923) Lectures on Cauchy's Problem in Linear Partial Differential Equations, Yale University Press .
36. IRI, M., MORIGUTI, S., and TAKASAWA, Y. (1970) On a Certain Quadrature Formula, Kokyuroku of Res. Inst. for Math. Sci., Kyoto Univ.
37. HAYAMI, K. (1990) High Precision Numerical Integration Methods for 3-D Boundary Element Analysis, IE^3 Trans. Mag., MAG-26, 2, 603-606.

38. GOLUB, G.H., and WELSCH, J. H. (1969) Calculation of Gauss Quadrature Rules, Mathematics of Computation, 23, 221-230 .
39. IMSL, (1987) User's Manual Math/Library, Fortran Subroutines for Mathematical Applications.
40. HAYAMI, K. (1989) Improvement and Error Analysis of the High Precision Numerical Integration Method: PART, Proc. 6th Japan National Symposium on Boundary Element Methods, 37-42 (in Japanese).
41. HAYAMI, K. (1990) A Robust Numerical Integration Method for Three Dimensional Boundary Element Analysis, in M. Tanaka, C.A.Brebbia and T. Honma (eds.), Boundary Elements XII, Proc. 12th Int. Conf., Sapporo, Japan, 1, 33-51.
42. HAYAMI, K. (1991) High Precision Numerical Integration Method for the Boundary Element Method and its Error Analysis, Kokyuroku of Res. Inst. for Math. Sci., Kyoto Univ., 744, 188-206 (in Japanese).
43. MORI, M. (1975) Numerical Analysis and Complex Function Theory, Chikuma-shobo, (in Japanese).
44. TAKAHASHI, H. and MORI, M. (1970) Error Estimation in the Numerical Integration of Analytic Functions, Report of the Computer Centre, Univ. of Tokyo, 3, 41-108.
45. BARRET, W., (1960) Convergence Properties of Gaussian Quadrature Formulae, Comput. J., 3, 272-277.
46. MCNAMEE, J. (1964) Error-Bounds for the Evaluation of Integrals by the Euler-Maclaurin Formula and by Gauss-Type Formulae, Math, Comp., 18, 368-381.
47. DONALDSON, J.D. and ELLIOT, D., (1972) A Unified Approach to Quadrature Rules with Asymptotic Estimates of their Remainders, SIAM J. Num. Anal., 9 No.4, 573-602.
48. DAVIS, P.J. and RABINOWITZ P. (1984) Methods of Numerical Integration, Second Edition, Academic Press.

49. MORIGUTI, S., UDAGAWA, K. and HITOTSUMATSU, S. (1960) Mathematical Formulae, Iwanami-shoten, (in Japanese).

50. HADAMARD, J. (1923) Lectures on Cauchy's Problem in Linear Partial Differential Equations, Yale University Press.

51. RUDOLPHI, T. J., KRISHNASAMY, G., SCHMERR, L. W. and RIZZO, F. J. (1988) On the Use of Strongly Singular Integral Equations for Crack Problems, (Invited Paper), in C. A. Brebbia (ed.), Boundary Elements X, Proc. 10th Int. Conf., Southampton, U. K., 3, 249-263.

52. HAYAMI, K. (1992) A Robust Numerical Integration Method for 3-D Boundary Element Analysis and its Error Analysis using Complex Function Theory, in T. O. Espelid and A. Genz (eds.), NATO ASI Series, Numerical Integration : Recent Developments, Software and Applications, Kluwer Academic Publishers, 235-248.

53. HAYAMI, K. (1992) A Projection Transformation Method for Nearly Singular Surface Boundary Element Integrals, C. A. Brebbia and S. A. Orszag (eds.), Lecture Notes in Engineering, Vol.73, Springer-Verlag.

54. HAYAMI, K., MATSUMOTO, H. and MOROGA, K. (1992) Improvement and Implementation of PART: Numerical Quadrature for Nearly Singular Boundary Element Integrals, in C. A. Brebbia, J. Dominguez and F. Paris (eds.), Boundary Elements XIV, Proc. 14th Int. Conf., Seville, Spain, 1, 605-617.